Numerical simulation of strain localization in irradiated polycristals

Aldo Marano

PSL★
UNIVERSITÉ PARIS

THÈSE DE DOCTORAT
DE L'UNIVERSITÉ PSL
Préparée à MINES ParisTech

Numerical simulation of strain localization in irradiated polycrystals
-
Simulation numérique de la localisation intra granulaire de la déformation au sein de polycristaux Irradiés

Soutenance par
Aldo MARANO
Soutenue le 20 novembre 2019

Ecole doctorale n° 621
Ingénierie des Systèmes, Matériaux, Mécanique Énergétique

Spécialité
Mécanique

Composition du jury :

Maurine MONTAGNAT
Directrice de recherche CNRS   *Présidente*

Renald BRENNER
Directeur de Recherche CNRS   *Rapporteur*

Ricardo A. LEBENSOHN
Directeur de Recherche   *Rapporteur*

Stéphane BERBENNI
Directeur de Recherche CNRS   *Examinateur*

Christophe DENOUAL
Ingénieur - Chercheur   *Examinateur*

Samuel FOREST
Directeur de Recherche CNRS   *Directeur de thèse*

Lionel GÉLÉBART
Ingénieur - Chercheur HDR   Co-d*irecteur de thèse*

Ghiath MONNET
Chercheur-Ingénieur   *Invité*

MINES ParisTech ★ | PSL★

ii

Al mio caro nonno, Sergio

REMERCIEMENTS

Il est certes banal de le rappeler, mais la valeur symbolique et affective d'un manuscrit de thèse, pour celui qui l'a écrit, ne se réduit pas à l'affinité intellectuelle avec le sujet d'étude. A ce titre, le mien ne fait pas exception. Plus que l'aboutissement d'un long travail, il restera pour moi un souvenir de ces trois années de vie, qui furent traversées par de nombreuses rencontres, et tressées de précieuses relations. Avant que la science reprenne ses droits, je vais tâcher de leur rendre ici hommage.

Mes premiers remerciements vont aux membres de mon jury de thèse. Je remercie en premier lieu, Maurine Montagnat d'avoir accepté de présider ce jury. Son savoir expérimental et son expertise de la glace, matériau crucial pour l'étude des fameuses bandes en genou, ont apporté une analyse de mon travail complémentaire et indispensable, compte tenu de la dominante numérique et métallique qui caractérise ce jury et cette thèse. Je remercie ensuite, Ricardo A. Lebensohn, d'avoir accepté de rapporter mon travail, ainsi que pour leurs remarques lors de la soutenance. J'ai beaucoup apprécié, lors les échanges que j'ai pu avoir avec lui sur les méthodes FFT lors de nos deux rencontres, sa grande disponibilité. Je remercie également Renald Brenner pour avoir accepté d'être le second rapporteur, pour ses remarques lors de la soutenance, et pour les échanges que nous avons pu avoir en Suède, sur la vie de chercheur, qui m'ont beaucoup enrichi. Je remercie enfin, Stéphane Berbenni, Christophe Denoual, et Ghiath Monnet pour leur participation à ce jury, leur enthousiasme à examiner mon travail, et leurs remarques et questions très enrichissantes.

Cette thèse est issue d'une collaboration entre le Service de Recherches Métallurgiques Appliquées (SRMA) du CEA Saclay, et le Centre des Matériaux de l'Ecole des Mines ParisTech. Je remercie chaleureusement Laurence Portier, chef du SRMA, de m'avoir accueilli au sein du service pour réaliser cette thèse, ainsi que Ludovic Vincent, chef du Laboratoire d'étude du Comportement Mécanique des Matériaux (LC2M) , avec qui il a toujours été plaisant d'échanger au sujet de mes recherches, et dont j'ai apprécié l'ouverture et l'honnêteté durant ces 3 ans. Je remercie également Cristophe Galle, pour son soutien précieux pour le financement

ACRONYMS

CCP Classical Crystal Plasticity

CCRT Centre de Calcul Recherche et Technologie

CISH Cascade Induced Source Hardening

DBH Dispersed Barrier Hardening

DFT Discrete Fourier Transform

DIC Digital Image Correlation

DPA Displacement Per Atom

DVC Digital Volume Correlation

EBSD Electron backscatter diffraction

FDM Field Dislocation Mechanics

FEM Finite Element Method

FFT Fast Fourier Transform

GND Geometrically Necessary Dislocations

IASCC Irradiation Assisted Stress Corrosion Cracking

PDE Partial Differential Equations

PWR Pressurized Water Reactors

SGP Strain Gradient Plasticity

SRMA Service de Recherche Métallurgiques Appliquées

TEM Transmission Electron Microscopy

Notation

j	Complex unit
a	Scalar
$\boldsymbol{a}$	Vector a_i
$\underline{\boldsymbol{A}}$	Second order tensor A_{ij}
$\underline{\boldsymbol{A}}^{\diamond}$	Symmetric part of second order tensor $\underline{\boldsymbol{A}}$
$\underline{\boldsymbol{A}}^{\times}$	Skew-symmetric part of order tensor $\underline{\boldsymbol{A}}$
$\underline{\boldsymbol{A}}$	Third order tensor A_{ijk}
$\underline{\underline{\boldsymbol{A}}}$	Fourth order tensor A_{ijkl}
A_{uv}	Component $(1,2)$ of tensor A in the frame defined by unit vectors $(\boldsymbol{u}, \boldsymbol{v})$

$\underline{\boldsymbol{1}}$	Second order identity tensor
$\underline{\underline{\boldsymbol{1}}}$	Fourth order Identity tensor (*on* symmetric tensors)
$\underline{\underline{\mathcal{K}}}$	Spherical projection tensor
$\underline{\underline{\mathcal{J}}}$	Deviatoric projection tensor
$\underline{\boldsymbol{\epsilon}}$	Levi-Civita permutation tensor

$\dot{a}$	Time derivative of tensor a
$a_{,i}$	Derivative of a with respect to i^{th} coordinate
$a_{,ij}$	Second derivative of a with respect to i^{th} and j^{th} coordinate
$a_{,u}$	Derivative of a in the direction of unit vector $\boldsymbol{u}$
$a_{,uv}$	Second derivative of a in the direction of unit vectors $\boldsymbol{u}$ and $\boldsymbol{v}$
$\overline{a}$	Spatial mean value of tensor a

$\hat{a}$ Fourier transform of tensor a

$\text{tr}(\underline{\boldsymbol{A}})$ Trace of second order tensor $\underline{\boldsymbol{A}}$
$\det(\underline{\boldsymbol{A}})$ Determinant of second order tensor $\underline{\boldsymbol{A}}$

Symbols

$\underline{\boldsymbol{F}}$ Deformation gradient tensor
$\underline{\boldsymbol{H}}$ Displacement gradient tensor
$\underline{\boldsymbol{L}}$ Velocity gradient tensor
$\underline{\boldsymbol{\varepsilon}}$ Small strain tensor
$\underline{\boldsymbol{\mathcal{E}}}$ Green Lagrange strain tensor

$\underline{\boldsymbol{\sigma}}$ Cauchy stress tensor
$\underline{\boldsymbol{S}}$ Boussinesq stress tensor (or first Piola-Kirchhoff stress)
$\underline{\boldsymbol{\Pi}}$ Piola-Kirchoff stress
$\underline{\boldsymbol{\Pi}}^M$ Mandel stress tensor

$\boldsymbol{m}^s$ Slip direction for slip system s
$\boldsymbol{n}^s$ Normal to the slip plane direction for slip system s
$\underline{\boldsymbol{\mu}}^s$ Schmid tensor for slip system s ($\underline{\boldsymbol{\mu}}^s = \boldsymbol{m}^s \otimes \boldsymbol{n}^s$)
γ^s Slip on slip system s
γ^s_{cum} Cumulated slip on slip system s
τ^s Resolved shear stress on slip system s
τ^s_c Critical resolved shear stress on slip system s

$\underline{\boldsymbol{\alpha}}$ Nye tensor (geometrically necessary dislocation density tensor)
$\underline{\boldsymbol{s}}$ Microstress tensor
$\underline{\boldsymbol{M}}$ Double stress tensor

E Young's Modulus
ν Poisson's ratio
μ Shear modulus
$\underline{\underline{\boldsymbol{\Lambda}}}$ Tensor of elastic moduli

TABLE OF CONTENTS

CHAPTER 1

INTRODUCTION

1.1 Industrial context

Nuclear energy is by far the most important primary source in France's electric power generation mix. In 2018, nuclear power plants generated 72% of France's electric energy[1], for a total amount of 380 TWh. This energy is currently provided by 58 operating Pressurized Water Reactors (PWR), with an average age of 30 years. Initially designed to ensure a 40-years lifetime, the present objective of public authorities to achieve a 50% share of nuclear energy in the electric power production by 2050 raises the question of the extension of currently operating reactors life. In recent years, it has led to significant research efforts aimed at extending the operating lifetime of these reactors to 60 years. This implies that the structural integrity of the reactor vessel and internal structures must be guaranteed in all operating and accidental conditions for this extra-lifetime period. Besides, preventing failure of the cladding tubes containing the nuclear fuel, which are regularly changed parts, is essential for the reduction of maintenance costs.

The parts in question are the components of the reactor most exposed to irradiation. The fuel cladding tubes, made of Zirconium alloys, containing fuel rods, are the first containment barrier of the radioactive elements. They are grouped by hundreds in fuel assemblies through which the pressurized water flows and extract the heat of the nuclear reaction. For this reason, their geometry must be maintained to avoid any perturbation of the water flow which would locally degrade cooling of fuel rods and subsequent dramatic increase in temperature. They are submitted

---

[1] https://bilan-electrique-2018.rte-france.com/total-generation/?lang=en#
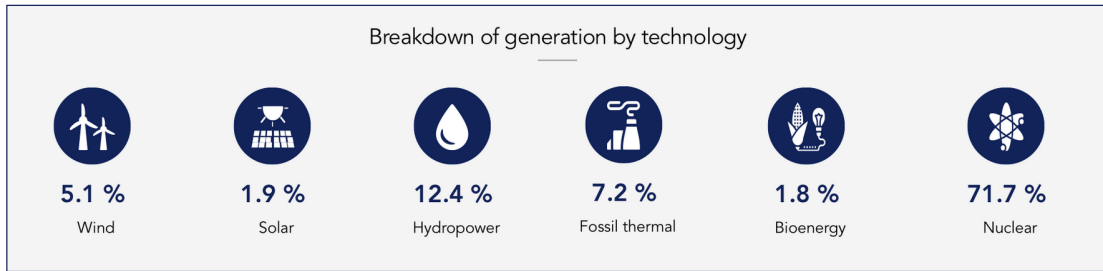
Figure 1.1 – France electricity production per source
(source : *RTE Eletric Report 2018*)

to complex solicitations such as fuel expansion (pellet-cladding interactions), high temperature gradients and irradiation induced swelling. During their 3 to 4 years operating life, they receive a high neutron flux, absorbing irradiation doses of the order of 4 dpa per year. Fuel assemblies are supported and protected by the core internals, mainly baffle plates, former plates and bolts made of austenitic stainless steels. Despite being in the vicinity to the core, they are not designed to be replaced during the life of a reactor, which results in irradiation doses up to 80 dpa after a 40-year service duration (Féron, Herms, and B. Tanguy (2012); Benoit Tanguy, Sefta, and Joly (2015)). The extension of PWR life to 60 years will result in increased doses experienced by these parts. Finally, the F/M steel pressure vessel, contains the reactor core. Its integrity is mandatory during the complete life of the reactor and must be guaranteed even after it has absorbed a high irradiation dose. All of these parts are submitted to the reactor severe conditions (water flow under 155 bar and 320 °C that can induce oxidation, hydriding ...) and complex loads during power transients or accidental conditions.

Furthermore, nuclear energy is part of the European Union long-term strategy to achieve decarbonisation of the electricity production system while meeting high energy needs. Indeed, it offers the lowest greenhouse gas emissions of all energy sources and a high power output with low intermittency. In this view, next generation nuclear fission reactors and fusion technology play a crucial role: generation IV reactors are considered to demonstrate fission as a sustainable option while fusion is a potential candidate for a clean and large-scale power generation towards the end of the century. These new technologies will rely on higher neutron fluxes and thus expose internal structures to increased irradiation doses during their life, raising new concerns to maintain the structural integrity of the new generation reactors.

Materials science research is a key factor to meet the numerous issues linked to these innovative technologies. One of the main challenges involved is the understanding, modeling and prediction of the evolution of material proper-
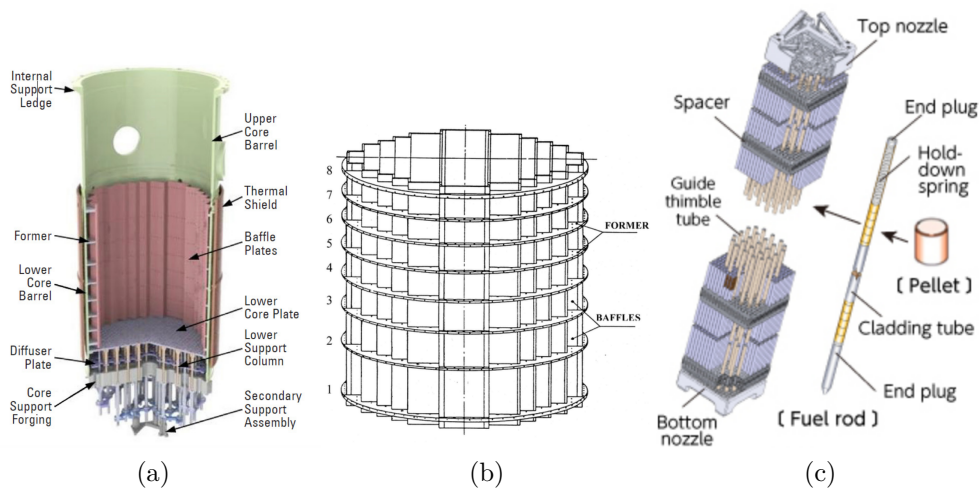
Figure 1.2 – PWR core internals (a-b) and Fuel assemblies (c)

ties induced by irradiation. It is long known that irradiation induces significant modifications on metallic crystals microstructure, through the production of large amounts of point defects. Their rearrangements result in the formation of numerous larger defects in the microstructure inducing a significant evolution of mechanical properties, as for instance a progressive hardening with increasing dose (Blewitt et al. (1960); T. Onchi, Kanayo, and Y. Higashiguchi (1977)). In particular, it is now well established that with irradiation, deformation becomes increasingly localized at the grain scale in irradiated metals (M. Wechsler (1973)). This is suspected to be a first order cause for the strong irradiation induced loss of ductility as well as factor influencing the Irradiation Assisted Stress Corrosion Cracking (IASCC), two critical issues regarding design of core parts.

In this context, materials science aims at predicting neutron irradiation hardening of steels and its impact on loss of uniform elongation by means of a physical-based multiscale modeling approach. The present PhD thesis forms one of CEA's contributions towards this goal, and takes part in the effort to build numerical models at the polycrystalline scale, able to predict the radiation induced plastic flow localization, relying on full-field homogenization techniques and physically based constitutive equations.

1.2   High performance simulation of materials behavior

Numerical simulation has been a central part of material modeling for decades. The progress of computer technologies and numerical methods has progressively made possible the simulation of increasingly rich equations on unit-cells of growing size and complexity. They have supported the fast development of full-field homogenization techniques, which have become a very powerful tool for materials science research. Indeed, they allow to explore model predictions beyond cases where analytical solutions can be found, and on the contrary to classical homogenization techniques, they can explicitly account for complex heterogenous microstructures and local stress-strain fields. For this reason, they are perfectly suited for parametric studies that explore the influence of various material or microstructural parameters on material properties, a key factor to gain new insights into material behavior. They have thus become essential in material design processes, especially in cases where experimental results are rare or come with a very high cost, such as experiments on irradiated materials.

Besides, the exponential development of modern imaging techniques such as X-ray tomography, high resolution Electron backscatter diffraction (EBSD) together with the advance of image processing (Digital Image Correlation (DIC), Digital Volume Correlation (DVC) ...) has made it possible to obtain high resolution field measurements, even from in-situ experiments. Being able to observe simultaneously the macroscopic behavior of a sample and its local state evolution at microscopical scales represents a new and formidable source of information on material behavior. In order to gain the most from these new possibilities, material modeling techniques must evolve to provide comparable outputs. In particular, it implies a change of paradigm in the construction of material models, as now they must provide field predictions that are locally representative of what is observed at the microscopic scale in addition to the prediction of the macroscopic behavior of the studied materials.

In practice, this requires numerical simulations to rely on a precise description of both scales. Intense efforts have been carried out in recent years in this direction. For instance, image processing combined to advance meshing techniques can be used to build a Finite Element model from EBSD maps or tomographic images (Proudhon, Li, et al. (2016)). In parallel, the development of numerical random microstructure generation algorithms, such as Voronoi-Laguerre tessellation techniques for polycrystalline materials, can build a large number of realizations of realistic microstructures to run simulations. However, to accurately represent microscopical phenomenon in simulations requires very refined meshes, that come with a high computational cost.
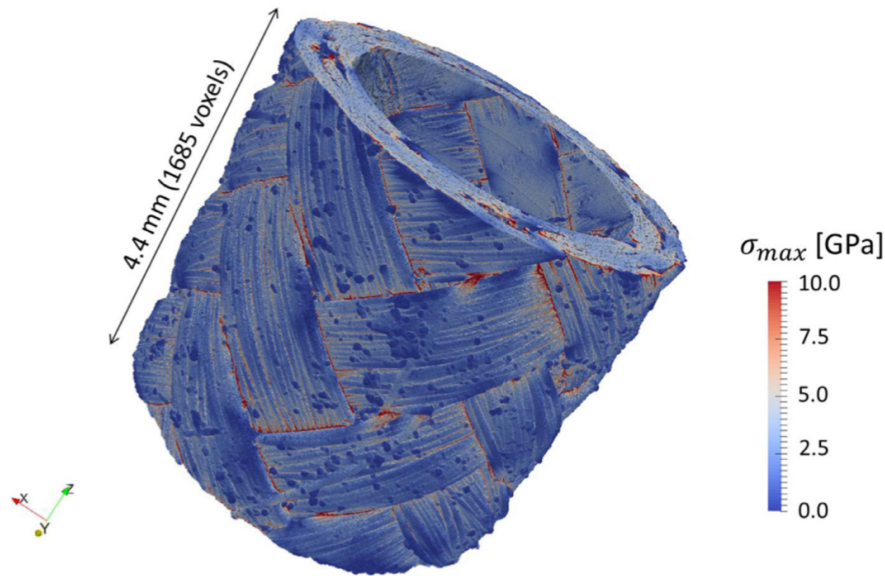
Figure 1.3 – Elastic calculation of a porous SiC/SiC composite tube carried out with AMITEX_FFTP, the unit cell is composed of 6.7 billions voxels (Yang Chen et al. (2019)).

The recent progression of parallel computing implementations and the resulting multiplication of supercomputing facilities is a decisive technological improvement that greatly helps to reduce computational costs inherent to this kind of modeling approaches. In this context, FFT-based homogenization solvers have gained increasing interest. They generally offer better performances than FEM for homogenization of periodic materials and their parallelization is extremely efficient, making them the ideal candidate to benefit from supercomputer performances for the simulation of material behavior. The CEA-Service de Recherche Métallurgiques Appliquées (SRMA) actively participates to the rise of these methods through the development of the AMITEX_FFTP code, the central tool used in the present work, which is designed for high performance simulations. Figure 1.3 presents a shining example: a calculation carried out on a huge unit cell of 6.7 billions voxels with this solver on the CEA supercomputer Cobalt (1680 processors used), for a computational time of 21 minutes (Yang Chen et al. (2019)).

1.3 Objectives and Manuscript Outline

This thesis follows the high performance modeling strategy described in the previous section, in order to improve the simulation of localized deformation in

irradiated polycrystals. Hence, it intensively relies on the SRMA local computing facility (21 nodes of 28 processors) and CEA's Centre de Calcul Recherche et Technologie (CCRT) Cobalt[2] supercomputer in conjunction with the use of the massively parallel AMITEX_FFTP solver. These tools are used too compute simulations of high resolution polycrystalline aggregates in order to get a fine description of phenomena occurring at the grain scale. These multiscale simulations allow to study the overall mechanical behavior of the polycrystal, the macroscopic scale, as well as the model prediction of intragranular plastic flow localization, the microscopic scale.

The first objective of this work is to use this high performance framework to study the accuracy of the state-of-art models of irradiated metals, regarding their ability to predict intragranular strain localization. AMITEX_FFTP allows to run simulations over realistic three dimensional polycrystalline unit cells with high resolution. Under these conditions, intragranular localization predictions can be thoroughly compared to the experimental observations in order to characterize to what extent existing models are able to capture correctly the features of plastic flow localization, as such study is lacking in the literature.

The second objective is the natural follow-up: set up clear guidelines for the development of future irradiated metals models, in order to overcome the limitations evidenced by this work. As will be discussed in the first chapter, slip localization occurs in a large variety of irradiated metals where it shows very similar characteristics. Observations point out plastic flow in irradiated metals as an extreme case of the intrinsic heterogeneity of plastic flow in crystals exhibiting microscopic softening mechanisms. Likewise, the limits of irradiated metals models are linked to the current shortcomings of crystal plasticity models regarding slip localization simulation. For this reason, this work will focus on investigating new generic developments aiming at improving the modeling of intragranular slip band formation in polycrystalline materials. Improvement of irradiated metal models will result from the application of these generic developments to the specific case of these materials. As a result, all developments have been made considering generic and simple crystal plasticity laws. No specific material has been studied in this context even so some studies are directly inspired from nuclear applications.

Finally, this thesis is also dedicated to the development of the AMITEX_FFTP solver. This code is becoming increasingly important in SRMA material modeling strategy, as it provides a massively parallel FFT-based solver which shows promising performances for full-field homogenization of heterogeneous non-linear materials. It will play a central role in the future development of predictive models for irradiated metals behavior at CEA, and as an Open-source solver,

---

[2] http://www-ccrt.cea.fr/fr/moyen_de_calcul/index.htm

is intended to be increasingly used by the material science community. In this view, a third objective of this thesis is to design and implement all the developments realized to improve slip band modeling as generic features of this solver, compatible with its parallel implementation. Thus, all potential future users of the code will benefit from the tools implemented during this thesis in AMITEX_FFTP.

This thesis is organized as follows. Chap. 2 is dedicated to a detailed review of observation and simulation of slip localization in unirradiated and irradiated metals. It aims first at considering localized deformation in irradiated metals in the general context of intragranular slip localization, with a specific emphasis put on intragranular localization modes: the so-called slip and kink bands. It is followed by a review of the irradiation induced evolution of the mechanical behavior of metals, with a specific emphasis on the associated intense localization of plastic slip, and its manifestation: the clear bands. Then, we recall the state-of-the-art regarding irradiated metal modeling, and particularly irradiation induced localization simulation. Finally, we introduce the reader to FFT-based homogenization methods and the specific algorithms used in the AMITEX_FFTPsolver, to set the ground of all numerical works presented in this work.

Chap. 3 focuses on softening Classical Crystal Plasticity (CCP) models, as they are the underlying framework of most irradiated metal models. In particular, it aims at gaining deeper insight into their ability to simulate accurately the apparition of slip and kink bands, introduced in Chap. 2. For that purpose, specific plastic localization modes analysis methodologies are proposed as potential processing techniques for direct comparison with field measurements techniques. They are then applied to simulations performed with a generic softening CCP model. This analysis leads to the identification of slip and kink modes formation underlying mechanism inherent to CCP. On this basis, by comparing the results to experimental observations of intragranular slip localization, we evidence fundamental limits of CCP models preventing them from predicting accurately intragranular localization modes for locally softening polycrystals, and thus for irradiated metals.

Chap. 4 explores the use of gradient crystal plasticity models to solve some shortcomings of CCP evidenced in Chap. 3. It focuses on a model accounting for Nye's tensor in the free energy of the crystal. After describing the model, this chapter presents the details of the generic development introduced in the AMITEX_FFTP solver to extend its features to non-local modeling, the numerical validation of the model and discusses the numerical issues involved with its integration with FFT-based solvers. We present then a detailed study of its predictions of intragranular localization, and discuss its promising capacity to simulate intragranular localization in locally softening polycrystals.

In Chap. 5, we propose, as an alternative, a geometrically explicit method

for slip band modeling in polycrystals. The composite voxel technique is used in order to reduce the computational cost of the simulations. First, we present the development of generic, multiphase and non-linear composite voxels models, and their implementation in the AMITEX_FFTPsolver. Then, we present the methodology to generate polycrystalline unit cells containing explicit potential slip bands discretized with or without composite voxels, before evidencing the improved performances obtained when using laminate composite voxels. Finally we apply this methodology to a simplified modeling of irradiated ZR alloys (used for fuel cladding tubes in the nuclear industry) in order to study the influence of slip localization on the mechanical behavior.

Finally, in the Conclusion (Chap. 6) section, we bring together the main results of the present work and propose several perspectives for the modeling of slip localization in crystals in general, in irradiated metals, and for FFT-based modeling. An extended Appendix section provides many additional details on analytical calculations and numerical details involved in this work, as well as a specific section to recall useful formulas of tensor calculus, analysis and discrete Fourier transform operations. All mathematical notations used in this document are summarized in a specific section at the beginning of the document.

1.4 Introduction : résumé en français

1.4.1 Contexte industriel

La nécessité de l'extension de la durée de vie opérationnelle à 60 ans des réacteurs nucléaires du parc français est un enjeu majeur en France, où plus de 70% de l'énergie électrique est issue de la filière nucléaire. Elle donne lieu à de nombreux travaux de recherches dont l'objectif est de garantir l'intégrité des pièces cruciales au fonctionnement du coeur du réacteur pendant cette durée supplémentaire. Ceci implique notamment d'accroître la durée de vie des structures internes du réacteur, en acier austénitiques, et d'autre part, de réduire la fréquence de maintenance des tubes de gainage du combustible en alliage de Zirconium pour la maitrise des coûts.

Une durée d'exploitation accrue dans le coeur du réacteur résultera en une irradiation plus importante des pièces en question. D'autre part, les autres technologies envisagées pour la production d'électricité nucléaire, les réacteurs de génération IV à neutrons rapides, ou, à très long terme, les réacteurs à fusion, induisent des flux d'irradiation beaucoup plus importants et soumettrons elles aussi les structures à des niveaux d'irradiation accrus. Ses effets sur les métaux sont maintenant bien connus : elle est responsable de la production d'un grand

nombre de défauts dans leur structure cristalline, qui ont un impact de premier ordre sur leurs propriétés mécaniques, réduisant par exemple leur ductilité ou leur ténacité. Ainsi, la compréhension de l'évolution sous irradiation du comportement des matériaux concernés est d'une importance cruciale pour faire face aux enjeux industriels de la filière nucléaire.

Cette thèse constitue l'une des contributions du CEA à la science des matériaux irradiés, plus particulièrement à la construction de modèle numériques permettant de prédire à l'échelle polycristalline, la localisation intra-granulaire de la déformation plastique induite par l'irradiation et ses conséquences sur le comportement des polycristaux irradiés.

1.4.2 Simulation haute performance du comportement mécanique des matériaux

Les progrès de l'informatique et des méthodes numériques ont permis l'essor de la simulation numérique des matériaux au cours des dernières décennies, qui est devenu une composante centrale de la science des matériaux. Le développement des méthodes d'homogénéisation numérique à champ complet qui en a résulté permet aujourd'hui de simuler le comportement de matériaux fortement non-linéaires en tenant compte de la forte hétérogénéité microscopique qui les caractérise. Par ailleurs, les progrès concomitants des techniques d'imagerie expérimentale et de traitement d'image permettent aujourd'hui d'obtenir des informations nouvelles et précieuses sur le comportement des matériaux à l'échelle microscopique, en fournissant par exemple des images 3D à haute résolution d'échantillons expérimentaux in-situ lors d'essais mécaniques. En conséquence, les modèles utilisés aujourd'hui pour décrire le comportement des matériaux doivent s'adapter afin de pouvoir rendre compte des phénomènes observés à cette échelle microscopique.

Dans ce contexte, les méthodes FFT ont émergé comme une technique très prometteuse. En effet, très adaptées au calcul parallèle, elles permettent d'obtenir des performances supérieures aux méthodes éléments finis pour l'homogénéisation périodique des matériaux, et de tirer le meilleur parti des supercalculateurs modernes. Elles rendent accessibles les simulations à très haute résolution, et ainsi, l'étude des prédictions locales des modèles numériques. Le CEA-SRMA participe activement à leur essor, à travers le développement du code AMITEX_FFTP, un solveur FFT massivement parallèle, au coeur des travaux réalisés au cours de la présente thèse.

1.4.3   Objectifs de la thèse

Le premier objectif de ce travail est d'étudier la précision des modèles de
l'état de l'art pour les métaux irradiés, en ce qui concerne leur capacité à prédire la
localisation intra-granulaire de la déformation plastique. Pour y arriver, les résultats
de simulations réalisées avec AMITEX_FFTP sur des cellules polycristallines
tridimensionnelles réalistes à haute résolution seront comparés aux observations
expérimentales afin de caractériser dans quelle mesure les modèles existants sont
capables de saisir les caractéristiques de la localisation de la plasticité.

Le deuxième objectif est la conséquence naturelle du premier : établir
des lignes directrices claires pour le développement de futurs modèles de métaux
irradiés, afin de surmonter les limites mises en évidence par ces travaux. Dans
une perspective de recherche fondamentale sur la localisation de la déformation
plastique, ce travail se concentre sur l'étude de nouveaux développements génériques
visant à améliorer la modélisation de la formation de bandes de glissement intra-
granulaires. L'application ultérieure de ces développements génériques au cas
spécifique des matériaux irradiés permettra d'améliorer la modélisation de ces
matériaux. Ainsi, tous les développements ont été réalisés en tenant compte des
lois génériques et simples de plasticité cristalline. Aucun matériau spécifique n'a
été étudié dans ce contexte, même si certaines études s'inspirent directement des
applications nucléaires.

Enfin, cette thèse est également consacrée au développement du solveur
AMITEX_FFTP. Ce code prend de plus en plus d'importance dans la stratégie
de modélisation des matériaux au SRMA, étant un solveur FFT massivement
parallèle ayant des performances prometteuses pour l'homogénéisation en champ
complet des matériaux non linéaires hétérogènes. Il jouera un rôle central dans le
développement futur de modèles prédictifs du comportement des métaux irradiés
au CEA, et en tant que solveur Open-source, il est destiné à être de plus en
plus utilisé par la communauté de la science des matériaux. Dans cette optique,
le troisième objectif de cette thèse est de concevoir et de mettre en œuvre tous
les développements réalisés pour améliorer la modélisation de façon générique
dans le solveur, en préservant son implémentation parallèle. Ainsi, tous les futurs
utilisateurs potentiels du code bénéficieront des outils mis en œuvre lors de cette
thèse.

CHAPTER 2

LITERATURE REVIEW

Chapter Outline

11

Résumé en français

Cette revue bibliographique présente les éléments permettant d'analyser
le comportement des métaux irradiés en termes de modes de localisation intra-
granulaire du glissement plastique, que sont les bandes de glissement, et les bandes
en genou. Cette analyse permet de lier la simulation du comportement mécanique
des métaux irradiés au problème fondamental de la simulation des mécanismes
élémentaires du glissement plastique dans les polycristaux. Les résultats de cette
étude bibliographique sont synthétisés ci-après, ainsi que les lignes directrices qu'ils
suggèrent pour ce travail de thèse.

L'observation détaillée des manifestations intra-granulaires du glissement
plastique révèle qu'il est par nature intrinsèquement hétérogène, localisé. À l'échelle
continue du cristal, son mécanisme élémentaire est la formation de bandes de
glissement dans lesquelles la déformation est beaucoup plus élevée que la déformation
macroscopique accommodée par les grains, et séparée par des régions ne montrant
aucun signe de glissement plastique. La nature lamellaire de ce processus est très
probablement liée à des mécanismes adoucissants microscopiques influençant le
mouvement des dislocations à l'échelle du plan de glissement.

Dans cette optique, la localisation accrue de la déformation plastique
observée dans les métaux irradiés apparaît comme une intensification des carac-
téristiques intrinsèques du glissement plastique. Ceci est corrélé à des mécanismes
microscopiques très fortement adoucissants, liés phénomène de canalisation des
dislocations. Ce phénomène, consistant en un balayage des défauts d'irradiation
par les dislocations sur les plans de glissement actifs, favorisant ainsi le passage
d'autre dislocations sur ce même plan, se caractérise par la formation de bandes
de localisation de la déformation, appelées bandes claires, du fait de l'absence de
défaut en leur sein. L'examen de leurs caractéristiques rapportées dans la littérature
expérimentale, révèle clairement leur nature. Elles peuvent être caractérisées sans

ambiguïté comme des bandes de glissement très intenses, au sens du mode de localisation plastique intra-granulaire présenté au section 2.1. Cela implique que les bandes claires ne sont pas des bandes en genou.

Le processus de déformation des métaux irradiés semble ainsi être un cas exacerbé de la nature intrinsèquement localisée des processus plastiques classiques des métaux, sans pour autant en être différent en nature. Par conséquent, la simulation de la localisation de la déformation dans les métaux irradiés, plus précisément la formation de bandes claires, dépend fondamentalement de la capacité à simuler fidèlement la localisation intra-granulaire du glissement plastique dans les polycristaux en général.

Par ailleurs, les bandes de glissement intenses peuvent induire des niveaux de déformation élevés capables localement d'initier une coalescence de cavités ou de fortes concentrations de contraintes aux joints des grains, même pour des niveaux de déformation globaux faibles. Ce problème devient critique pour les métaux irradiés où la localisation extrême est associée à une forte perte de ductilité, et reliée à l'Irradiation Assisted Stress Corrosion Cracking. (IASCC). Par conséquent, la simulation fidèle de la formation des bandes de glissement intense semble cruciale pour la prédiction de la rupture ductile ou inter-granulaire de ces matériaux.

Cependant, l'analyse de bifurcation indique que les modèles de plasticité cristalline classique, largement utilisés pour la simulation numérique de tels phénomènes, ne sont pas en mesure de distinguer correctement les bandes de glissement des bandes en genou, au moins au point de bifurcation. Cette analyse est généralement négligée dans la littérature sur les simulations de plasticité cristalline. En particulier, elle n'est jamais mentionnée dans les études de simulation de la canalisation des dislocations, et ce, malgré le fait que la plupart des travaux semblent prédire la formation bandes claires correspondant à des bandes en genou. Plus généralement, les bandes de glissement et les bandes en genou étant des phénomènes physiques très différents, il pourrait s'agir d'une lacune cruciale de la plasticité cristalline classique, impliquant la nécessité d'utiliser des modèles fondés sur des milieux continus d'ordre supérieur.

Ainsi, nous sommes convaincus que le traitement de ces questions fondamentales et générales est une étape nécessaire vers une meilleure compréhension du comportement des métaux irradiés, et détermine les lignes directrices de ce travail, détaillées ci-après :

Tout d'abord, il est nécessaire d'étudier en toute généralité les liens entre les modèles de plasticité cristalline classique, et leurs prédictions quant à la formation les modes de localisation intra-granulaires de la déformation plastique qu'ils induisent dans les simulations.

Deuxièmement, sur la base de ces résultats, évoluer vers des formulations plasticité cristalline à gradient afin de développer des modèles plus réalistes visant à simuler les processus de glissement élémentaires à l'échelle du continuum dans les polycristaux.

Troisièmement, explorer une piste alternative consistant en la modélisation explicite des bandes de glissement pour étudier directement les conséquences de la localisation intra-granulaire de la déformation plastique.

Les développements récents des mesures de champ fournissent une description multi-échelle très riche des processus élémentaires de la plasticité des polycristaux, et ont pu être appliqués avec succès aux métaux irradiés. La richesse des informations qu'ils délivrent implique que les modèles numériques doivent être validés non seulement sur la base du comportement macroscopique, comme c'est le cas pour la plupart des études sur les métaux irradiés, mais également en confrontant les prédictions locales des champs simulés à ces observations, à des échelles pertinentes. **Ceci met en évidence la nécessité de simulations à très haute résolution permettant une comparaison directe entre les mesures expérimentales et les champs simulés.**

L'utilisation des solveur FFT semble donc un choix naturel pour cette étude. En particulier, le solveur AMITEX_FFTP, couplé à un supercalculateur, ouvre la voie à de telles comparaisons. Les deux principaux atouts de ce solveur sont son implémentation massivement parallèle et sa structure générique, conçue pour la simulation d'un large éventail de problèmes physiques et mécaniques. Son développement revêt une grande importance pour les travaux basés sur la simulation numérique au SRMA, et pourrait être utile à toute la communauté de la science des matériaux. Ainsi, un objectif supplémentaire de ce travail est **l'introduction au sein de ce solveur de tous les développements nécessaires à l'amélioration de la modélisation des métaux irradiés, sous forme générique et compatible avec sa structure massivement parallèle.**

2.1 Intragranular slip localization modes in polycrystals

This thesis is devoted to the modeling and simulation of intragranular slip localization in irradiated metals. Therefore, before examining the detailed modification of the mechanical behavior of polycrystals induced by irradiation, an introduction to slip localization in crystals is necessary. The aim is to present the fundamental mechanisms necessary to properly analyze slip localization in

polycrystals and in particular introduce the notion of intragranular localization modes that will be the guideline of this thesis.

A general overview of plastic localization is first presented, before moving into the definition of intragranular localization modes, through the review of their various observations. Finally, the state-of-the art for their numerical simulation is briefly reviewed.

2.1.1 Plastic slip localization

The heterogeneous nature of plastic slip has been well known for decades. Passed their elastic domain, metals deformation occurs by the relative slide of two domains along specific atomic planes. This sliding is related to the glide of linear crystal defects, the dislocations, that propagate a certain amount of glide in a specific direction, defined by their Burger's vectors. Hence, plastic slip is intrinsically a discrete phenomenon. Thus, two directions suffice to describe this elementary deformation process: the glide direction indicating the direction of the displacement propagated by dislocations, and the normal to the slip plane in which dislocation glide.

Neuhäuser (1983) has provided a precise description of these phenomena: deformation occurs by formation of discrete surface steps caused by the emergence of dislocations, and can be observed on a wide range of lengths. Elementary steps are typically of nanometric width and are called slip lines. These lines can cluster in larger steps, typically of micrometric size, called slip bands. These slip bands may also cluster and form slip band bundles.

From the macroscopic point of view, polycrystals can deform in a homogenous way which requires the formation of evenly distributed slip bands over the whole sample. However, heterogeneous plastic deformation at the macroscopic scale has been observed countless times. Typical slip localization structures observed at the macroscopic scale are necking, formation of Lüders bands or shear bands, as illustrated on fig. 2.1.

However, these macroscopic features are known to be structural effects induced by the microscopic nature of plastic slip. Indeed, as they can form on polycrystalline macroscopic specimens, they are not elementary plastic slip processes. These are intrinsically linked to crystal structure of metals and should thus be examined at the grain scale in polycrystalline materials. We call intragranular plastic slip modes these elementary microscopic slip processes. Hence aforementioned macroscopic slip localization modes, like shear bands, are out of the scope of this work and will not be discussed in the following.
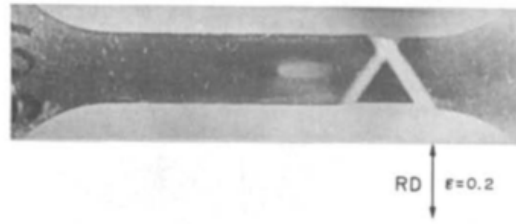
Figure 2.1 – Formation of a macroscopic shear band in a prestrained low carbon steel tensile test (Korbel and P. Martin (1988))

2.1.2   Intragranular localization modes

Two specific plastic localization modes have been observed in polycrystalline metals. They both involve slip localization in a band. In this paragraph, we present their characteristics through examples taken from the experimental literature.

Slip bands

When intense dislocation glide occurs on a few crystallographic planes, a sharp localization band parallel to dislocation glide planes, called *slip band*, forms. They are by far the most observed sign of plastic activity in crystals. As mentioned earlier, they are a direct manifestation of elementary slip processes, and thus are observed in all crystals plastically deformed.

They are thin structures, typically of micron or submicron scale, and are found parallel to active slip planes of the deformed crystal. Their formation and characteristics have been extensively studied by B. Jaoul (1964). An example of a slip band in a Aluminium alloy can be seen in fig. 2.2. It has been observed by Korbel and P. Martin (1986), who have highlighted their role in the formation of macroscopic shear bands. Their work has evidenced that macroscopic shear bands are formed through the multiplication and propagation of microscopic shear bands at the grain scale.

Recent tomographic advances have allowed a direct and non destructive observation of slip bands at incipient plasticity in the bulk of a few grains in a binary Al-Li polycrystal (Proudhon, Guéninchault, et al. (2018)). As shown on fig. 2.3, they have a very thin width compared to the grain size (100 µm), and are parallel to the slip systems of the crystal structure.
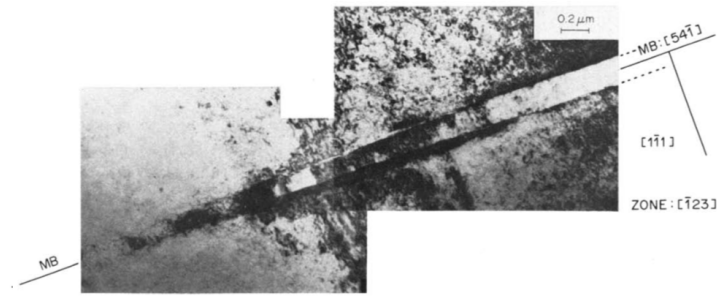
Figure 2.2 – TEM image of a microscopic slip band in a Al-4.8Mg alloy (Korbel and P. Martin (1986))
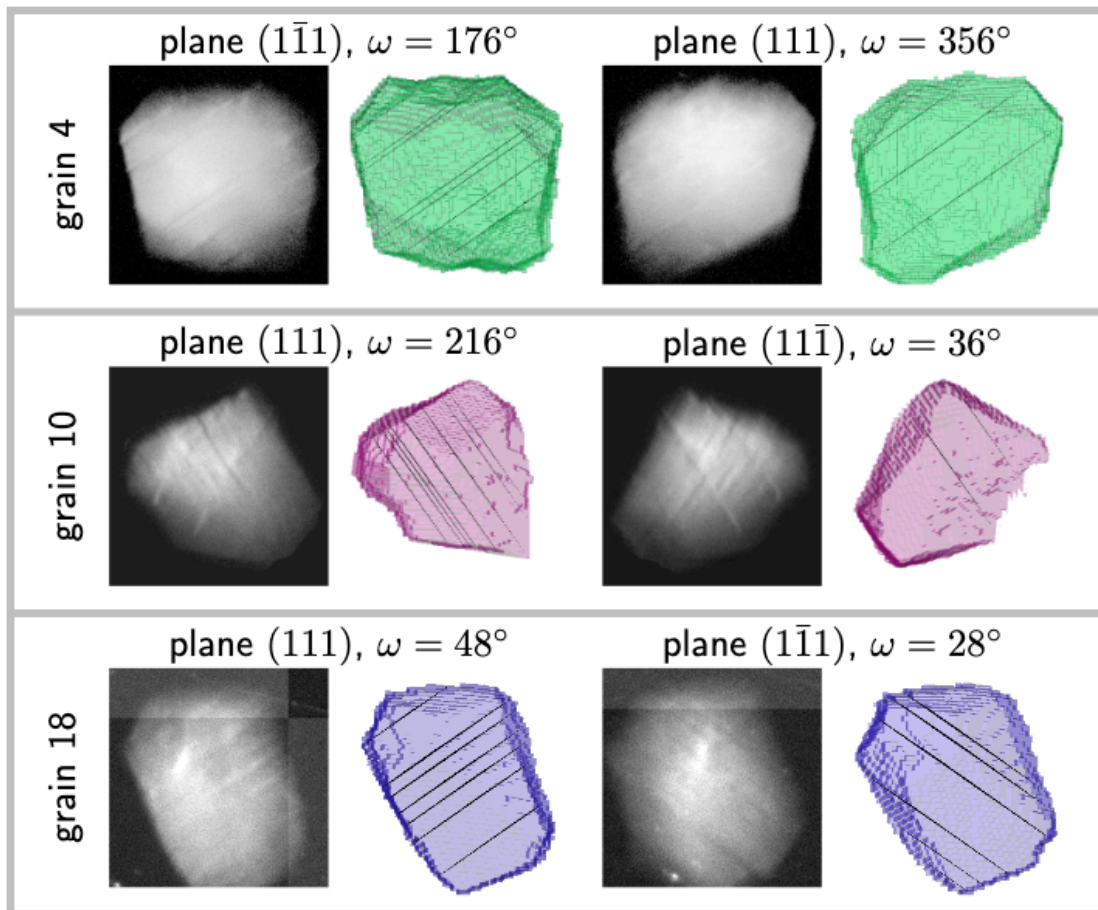
Figure 2.3 – In situ tomographic observation of bulk incipient plasticity in a binary Al-Li alloy showing distinct slip bands (Proudhon, Guéninchault, et al. (2018))

Kink bands

Another type of slip localization band observed in deformed crystals, are the so-called *kink bands*, known to form in metals since the work of OROWAN (1942) on Cadmium single crystals. They are characterized by the localization of plastic slip in a band orthogonal to the glide direction of the activated slip system. They are also associated with high crystal lattice rotation within them. All observations report a homogeneous rotation angle inside the kink bounded by two layers of high lattice curvature. These structures involve therefore the formation of walls of geometrically necessary dislocations within their boundaries.

Kink bands are reported in strongly anisotropic hexagonal crystals deforming mainly through basal slip, such as ice (Mansuy, Philip, and Meyssonier (2001); Montagnat et al. (2011); Wilson, Burg, and Mitchell (1986)), Zinc (Gilman (1954); Hagihara, Mayama, et al. (2016); Hess and Barrett (1949)), Magnesium (Hagihara, Okamoto, et al. (2016)) or Titanium (Churchman (1955)). The latter has evidence their role in the geometrical softening of Titanium single crystal deformed at high strain rate. They have also been noticed by Jaoul (P. B. Jaoul (1961); P. B. Jaoul and Gonzalez (1961)) in iron bicrystals and Aluminium single crystals strained in a direction close to the <111> direction B. Jaoul (1964). He has defined them as lattice rotation bands without activation of a secondary slip system. Other observations of kink bands are reported as crack-tip deformation modes in notched single crystals (Crone and Shield (2001); Flouriot et al. (2003); Kysar and Briant (2002); Patil, Narasimhana, and R. K. Mishra (2009)).

These observations show that kinks arise in regions where strong strain incompatibilities arise and cannot be accommodated by classical slip bands. These incompatibilities are due for instance to the polycrystalline microstructure and a strong anisotropy in ice, the loading (compression parallel to the glide plane) for zinc or magnesium single crystals, and the strong strain fields induced at crack tips.

Several examples are shown on fig. 2.4. All show that kink bands have a characteristic width that is much larger than slip bands. They also illustrate the presence of a dense distribution of very close slip bands superimposed in the direction normal to the slip plane. Hence, a kink band can be viewed as a very dense succession of parallel short slip bands, inducing locally a strong rotation of the crystal lattice. This definition of kinks highlight an important feature: slips bands appear as the elementary process leading to the formation of kinks.

(a)

(b)

(c)
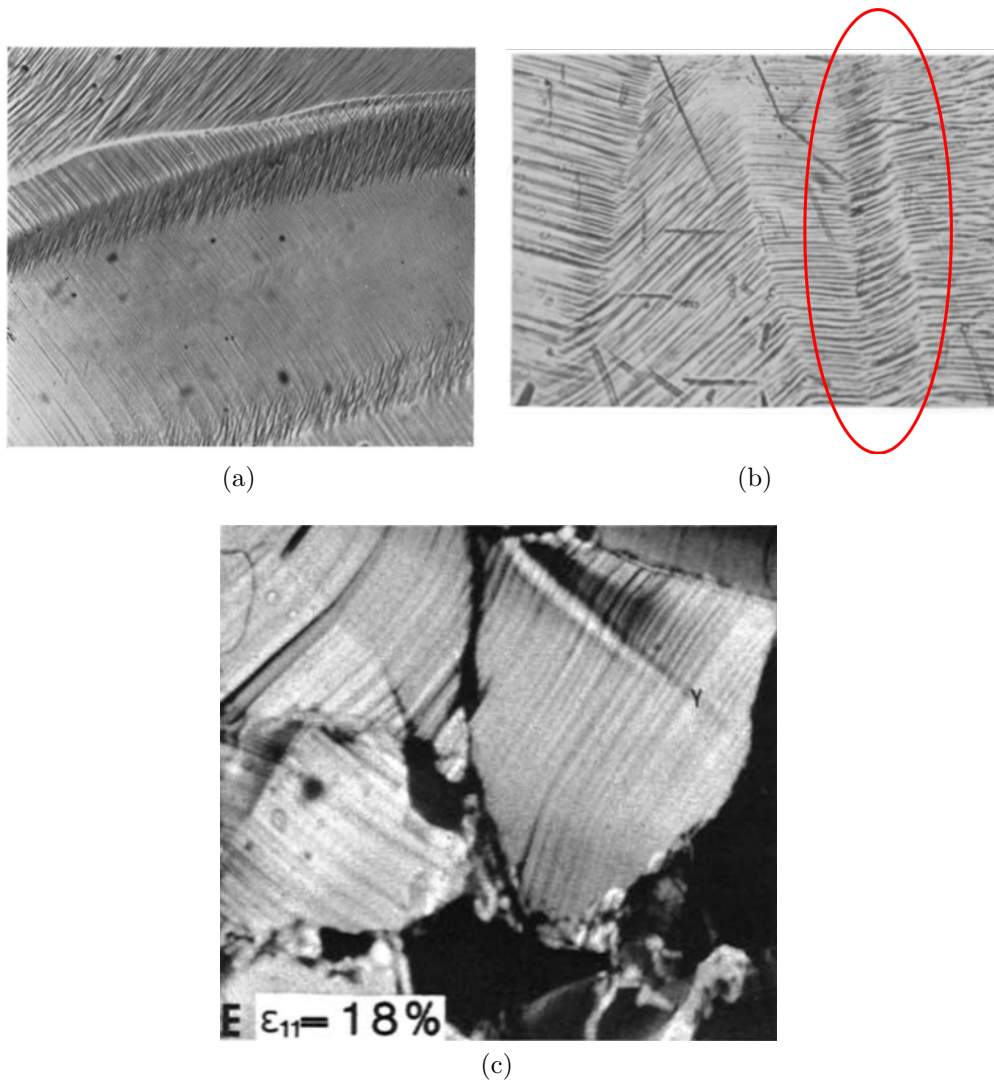
Figure 2.4 – (a): kink band in a pure iron bicrystal extended in a direction parallel to grain boundary (P. B. Jaoul (1961)) (b): Kink band observed in a Ti alloy (Churchman (1955)) (c): Observation of kink bands in polycrystalline ice (Wilson, Burg, and Mitchell (1986))

Recent advances in observation of intragranular localization modes in polycrystals: observation of kink band like areas

The modern developments of field measurement techniques have yielded a rich characterization of intragranular localization modes in polycrystals. Combining high resolution Digital Image Correlation (DIC) with automated SEM image correlation and Electron backscatter diffraction, Gioacchino and Fonseca (2015) have produced very detailed maps of the strain localization and lattice rotation in austenitic stainless steels, shown on fig. 2.5. Results evidence that the fundamentally heterogeneous nature of plastic slip is maintained from incipient plasticity to higher levels of overall strain.

All grains deform through a lamellar process: the formation of intense and evenly spaced slip bands (typical spacing is around a few µm, and width around 1 µm), separated by regions showing no plastic activity, with a multiplication of slip bands with increasing overall strain. The strain measured in the slip bands is one order of magnitude higher than the overall applied strain, demonstrating the intrinsic localized nature of plastic slip.

A key observation found in this work is that the higher the local density of slip bands, the higher the local rotation of the crystal lattice. In particular, the grains marked 21,22 and 23 in fig. 2.5 (in the lower left part of the figure) illustrate the formation of a transgranular rotation band. The authors report it as a "kink band like area". In particular, the region denoted P2 in the grain 23 (fig (b)), referred to by the authors as a "kind of kink band", is associated with the highest density of slip bands, which are for some of them distorted, by contrast to all other that are clearly straight. This area is associated to a strong local lattice rotation, up to 10-15°. The authors demonstrated that material rotation coincide with lattice rotation between slip bands. A striking fact when comparing the rotation and shear band map is the homogeneous aspect of the lattice rotation compared to the strong heterogeneity of the shear strain, due to slip bands. The authors concluded that lattice curvature bounding this area is produced by varying the intensity and spatial distribution of slip on only one slip plane. This supports the idea that kinks are formed through a dense superposition of slips.

The "kink of kink band" region (marked P2 in grain 23) is formed close to a triple point, associated thus to strong strain incompatibilities. Additionally, deformation process is dominated by single slip in this region. In other regions of the 'kink band like area' (grains marked 21,22 and 23), the activation of a secondary slip system can be observed, also inducing lattice curvature. All of these features are in very good agreement with those of the aforementioned kinks. It also shows that rotation bands can spread over a few grains. Similar measurements, shown on
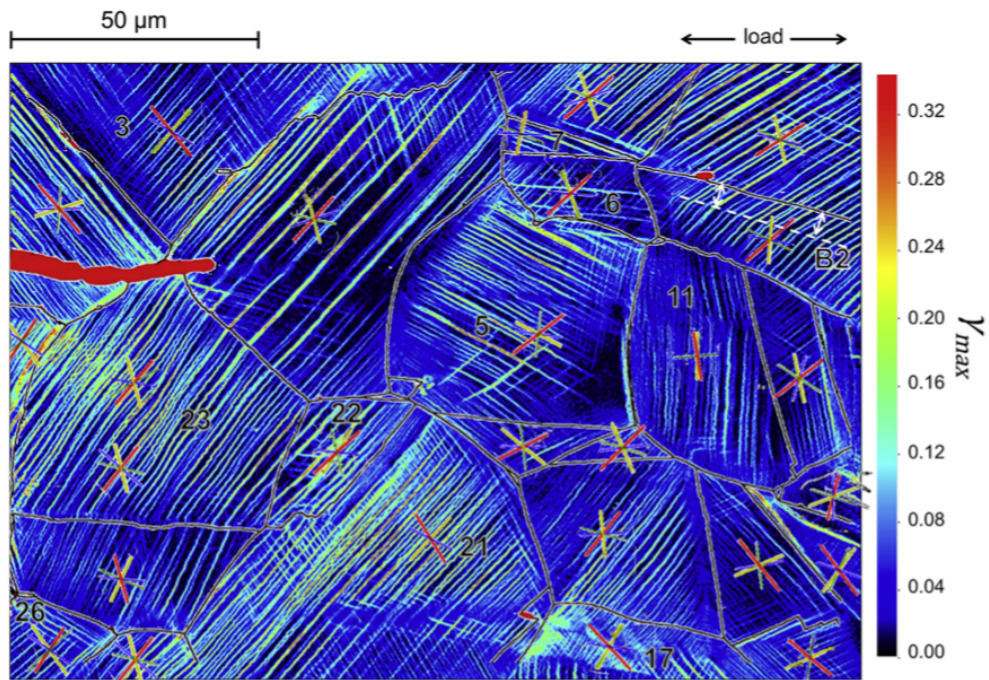
(a)
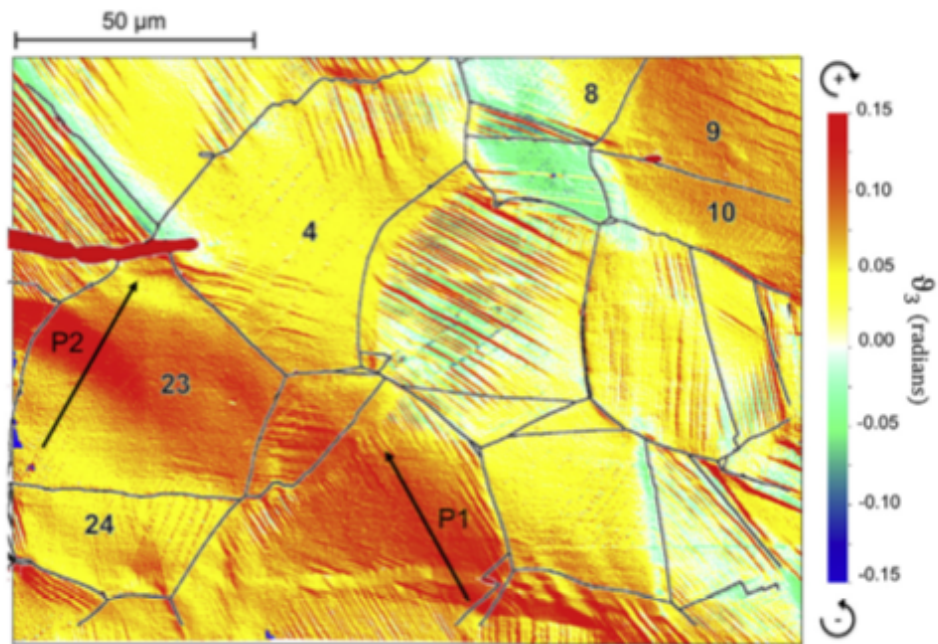
(b)

Figure 2.5 – Shear strain (a) and lattice rotation (b) surface maps of a 304L austenitic stainless steel after 6% tensile strain (Gioacchino and Fonseca (2015)).

fig. 2.6 (Orozco-Caballero et al. (2017)), evidence the slip localization modes in a
magnesium polycrystal, deforming mainly through basal slip. Even if the authors
do not mention it as such, it is clear from the previous observations and remarks
that the area shown on fig. 2.6 is a kink band like area, that is most likely similar
to the one forming in ice or Zn / Mg crystals.

Such observations provide invaluable informations on the elementary
processes of intragranular localization of plastic slip, and should be regarded as a
central test for slip localization model validations.
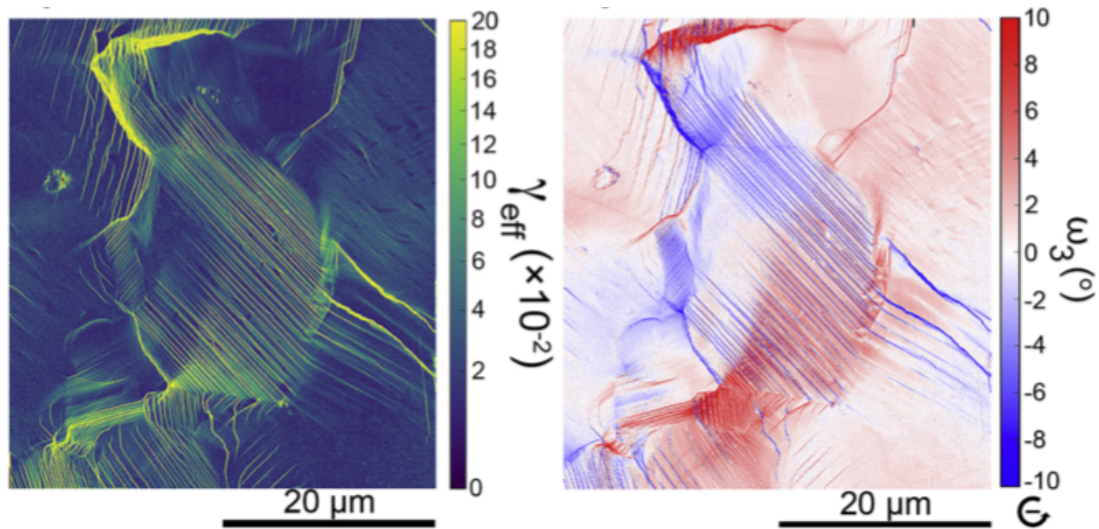
Figure 2.6 – Shear strain and material rotation surface maps of a magnesium single
crystal after 2% tensile strain (Orozco-Caballero et al. (2017)) revealing a kink
band like area on the right part of the central grain.

2.1.3   Slip localization modes modeling

Local softening mechanisms

The evidence of lamellar patterns forming during plastic deformation of
metals supports the idea that elementary mechanisms of plasticity at low scales
are associated to local softening, as well as several modeling approches. Estrin
and Kubin (1986) have investigated averaged properties of dislocations over a local
volume, and computed associated strain hardening. They found the local strain
hardening rate to be significantly lower than the bulk (macroscopic) hardening
rate. Moreover, they conducted a bifurcation analysis and concluded that this local
hardening rate is negative at incipient plasticity, which implies that plastic flow

necessarily begins in a non-uniform manner. Y.J.M Brechet, Canova, and Kubin (1993) investigated the condition for the apparition of localized plastic flow in a three dimensional dislocation dynamics study, and also evidenced the necessity of local softening mechanisms to obtain a localized plastic flow and predominance of single slip. Recently, continuum descriptions based on a non-convex energy have allowed to reproduce the formation of such lamellar deformation structures in numerical simulations (Klusemann and D. M. Kochmann (2014); Klusemann and Yalçinkaya (2013)).

Asaro and Rice's bifurcation analysis

This link between plasticity and softening mechanisms, associated to the overwhelming evidence of plastic instabilities at all scales in polycrystalline materials have drawn an important attention on them. Rice (1976) has proposed to consider plastic instabilities as bifurcations of the constitutive relations from an homogeneous deformation state into a highly concentrated band. Such bifurcation should verify Hadamard jump conditions as well as equilibrium, which leads, for a bifurcation between two planes surfaces of normal direction $\boldsymbol{n}$, to the following jump conditions:

$$[\![\mathrm{grad}(\dot{\boldsymbol{u}})]\!] = \boldsymbol{g} \otimes \boldsymbol{n} \tag{2.1}$$

$$[\![\underline{\dot{\sigma}}]\!] \cdot \boldsymbol{n} = 0 \tag{2.2}$$

where $[\![a]\!]$ denotes the jump of a across the bifurcation surface. eq. (2.1) states that the jump across the surface should be of rank one, and defined by the bifurcation mode vector $\boldsymbol{g}$. A shear band correspond to the case where $\boldsymbol{g}$ and $\boldsymbol{n}$ are orthogonal. Let us introduce now the local tangent modulus of the constitutive equations $\underline{\underline{L}}$, so that $\underline{\dot{\sigma}} = \underline{\underline{L}} : \underline{\dot{\varepsilon}}$. Then combining eqs. (2.1) and (2.2) yields the following condition to have a compatible bifurcation:

$$(\boldsymbol{n} \cdot \underline{\underline{L}} \cdot \boldsymbol{n}) \cdot \boldsymbol{g} = 0 \text{ with } \boldsymbol{g} \neq 0 \tag{2.3}$$

$(\boldsymbol{n} \cdot \underline{\underline{L}} \cdot \boldsymbol{n})$ is the acoustic tensor associated to constitutive relations. The solutions are found when the acoustic tensor becomes singular. Thus according to this approach, plastic instabilities are equivalent to stationary plastic wave. Solutions are found by solving $\det(\boldsymbol{n} \cdot \underline{\underline{L}} \cdot \boldsymbol{n}) = 0$ for $\boldsymbol{n}$, and then solve the system eq. (2.3) for $\boldsymbol{g}$.

Asaro and Rice (1977) have used this approach for finite strain crystal plasticity with a linear hardening modulus, and considering single slip. They have shown that when neglecting non Schmid effects, the problem reduces to the

following acoustic tensor:

$$(\boldsymbol{n} \cdot \underline{\underline{\boldsymbol{L}}} \cdot \boldsymbol{n}) = \left[\boldsymbol{n} \cdot \underline{\underline{\boldsymbol{\Lambda}}} \cdot \boldsymbol{n} - \frac{(\boldsymbol{n} \cdot \underline{\underline{\boldsymbol{\Lambda}}} : \underline{\boldsymbol{\mu}}) \otimes (\underline{\underline{\boldsymbol{\Lambda}}} : \underline{\boldsymbol{\mu}} \cdot \boldsymbol{n})}{H + \underline{\boldsymbol{\mu}} : \underline{\underline{\boldsymbol{\Lambda}}} : \underline{\boldsymbol{\mu}}} \right] \tag{2.4}$$

where $\underline{\underline{\boldsymbol{\Lambda}}}$ is the elastic moduli tensor of the crystal, $\underline{\boldsymbol{\mu}}$ the Schmid orientation tensor of the slip system, and H the linear hardening modulus. They found, that this expression becomes singular for the critical hardening modulus $H_{cr} = 0$, associated to two specific possible bifurcations. One is a bifurcation in a band perpendicular to the normal direction to the slip plane, the other one is perpendicular to the glide direction of the slip system. In other terms, their bifurcation analysis shows that when work-hardening vanishes or when the behavior is softening, plastic slip in homogeneous crystals undergoing single slip will localize in a slip band or a kink band.

2.1.4 Kink band formation simulation

Contrary to slip bands, that are universally known and studied, kink bands are a more confidential deformation mode. Their formation has thus not been much investigated by means of numerical simulations. Among them can be noted the work of R. Lebensohn et al. (2009); Montagnat et al. (2011). Using a crystal plasticity model incorporating the strong anisotropy of ice (soft basal and hard prismatic and pyramidal slip systems), they have been able to reproduce the formation of kink bands in polycrystalline ice. Recently, Kimura, Ueta, and Shizawa (2018) have simulated the formation of kink bands in single crystal Magnesium tensile samples with a dislocation based crystal plasticity model.

However, the results of the bifurcation analysis conducted by Asaro and Rice (1977) suggest that these localization modes are equivalent from the point of view of classical crystal plasticity constitutive equations, at least at the bifurcation point. Yet, as described above, slip and kink bands are very different deformation modes. This fundamental issue has only been pointed out by the work of Forest (1998), that has shown that both modes are equivalent for numerical simulations of single crystal tubes. Additionally, building on the fact that kink bands are associated to large lattice curvature, he has demonstrated that a generalized continuum model explicitly accounting for lattice curvature yields a distinct behavior for slip and kink bands in numerical simulations. In particular, he proposed a Cosserat crystal plasticity model that delays the instability of kink bands, thus regularizing them and leaving slip bands as the first localization mode. He presented finite element simulations that have shown that kink band formation can even be precluded in these conditions.

2.2   Irradiation effects in metallic crystals

In this section, we present a detailed review of the main effects induced by irradiation in metals. A particular focus is put on the localization of plastic slip severely increased by irradiation, which is the main interest of this work.

2.2.1   Irradiation in Pressurized Water Reactors

In PWR, energy is produced by the nuclear fission of radioactive fuel. Nuclear fission consists in the splitting of heavy fuel atoms (uranium or plutonium) into two lighter nuclei, after the capture of a thermal neutron ($E \approx 0.025\,\mathrm{eV}$). This reaction produces energy by releasing heat, but also involves the emission of fast neutrons ($E > 1\,\mathrm{MeV}$). These neutrons cross their emission fuel cladding tubes, are slowed down by the surrounding water, and cross another cladding tube before being captured by another heavy atom, triggering a new fission reaction.

The neutrons in the reactor are characterized by two important parameters: their flux and their energy. The flux of neutrons $\phi(\boldsymbol{x}, t, E)$ expressed in $\mathrm{n\,m^{-2}/s}$ measures the number of neutrons of the specific energy E crossing the material at a specific location $\boldsymbol{x}$, time t, per surface unit. Additionally, integrating the flux over a time period gives another important measure, the fluence ϕ_t, expressed in $\mathrm{n\,m^{-2}}$. Regarding PWR applications, only fast neutrons ($E > 1\,\mathrm{MeV}$) are considered to study material irradiation, as they are the only ones that are sufficiently energetic to induce microstructural damages.

When fast neutrons cross fuel cladding tubes of internal structures parts, most of them interact with the atoms of their constitutive material through elastic collisions. During a collision, the neutron transfers a part of its kinematic energy to the knocked-on atom. If this energy is above the displacement threshold, the atom is knocked-out of its equilibrium position in the crystal lattice. Most of these primary knocked-out atoms (PKA) possess enough energy to initiate other atoms displacements, causing a displacement cascade, as illustrated on the schematics on fig. 2.7. Each of these displacements creates a pair of point defects in the lattice: a vacancy and an interstitial atom. Most of the displaced atoms ultimately recombine with vacancies, however the complete rearrangement of the lattice is not possible and a few defect pairs remain.

As the fluence is a parameter strongly dependent on each reactor operating conditions and geometry, the unit of displacement per atom (dpa) is preferred to characterize irradiation damage. By definition, it is the number of times an atom is moved in average from its initial site in the lattice by elastic collisions. Neutron
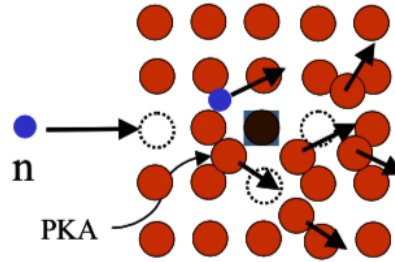
Figure 2.7 – Displacement cascade in the crystal lattice induces by an elastic collision with a fast neutron (in blue)

fluence can be converted to dpa: 1 dpa $= 7 \times 10^{24} \, \text{n m}^{-2}$ (Bruemmer et al. (1999) for austenitic stainless steels). Classically, for a PWR cycle (1 year), core internal structures receive an irradiation dose of 2.5 dpa, and fuel cladding tubes around 4dpa per cycle. Thus, after 40 years of service, internal structures will have received a dose of the order of 100 dpa. Fuel cladding tubes stay usually 3 to 4 years in the core, and hence receive doses of the order of 12-16 dpa.

2.2.2 Irradiation induced microstructural evolution of metallic alloys

Irradiation has a significant impact on the microstructures of metallic alloys. First, chemical modifications of the alloys can be induced. Indeed, inelastic neutron-atoms collision, or capture of thermal neutrons can lead to transmutation reactions, creating new elements in the lattice. Moreover, displacement cascades may lead to the amorphization or dissolution of precipitates. Conversely, irradiation induced precipitation can also be observed. However, in this work we focus on the defects that affect the most dislocation glide and thus plasticity, described in the following.

The multiplication of displacement cascades during irradiation lead to the production of a large amount of point defects. These defects, under the influence of thermal agitation, migrate, recombine or agglomerate in the crystal lattice, forming a wide range of point defects clusters. Typical radiation-induced defects in metals are:

1. Dislocation loops and black dots
2. Cavities
3. Stacking Fault Tetrahedra

The formation of dislocation loops is the most commonly observed type of irradiation induced defect. They consist in the agglomeration of point defects within a crystallographic plane, as illustrated on fig. 2.8-(a), resulting in interstitials or vacancy dislocation loops. They have been reported at least for irradiated Copper (D.J. Edwards, B.N. Singh, and Bilde-Sørensen (2005); B.N Singh, D.J Edwards, and Toft (2001)), Molybdenum (B.N. Singh, Evans, et al. (1998); Victoria et al. (2000)), pure Iron (B.N Singh, Horsewell, and Toft (1999); Victoria et al. (2000)), Vanadium (K.-i. Fukumoto, Masanari Sugiyama, and Hideki Matsui (2007)), stainless steels (Bruemmer et al. (1999); Pokor, Brechet, Dubuisson, Massoud, and Barbu (2004); Zinkle, Maziasz, and Stoller (1993)) and Zirconium alloys (Griffiths (1988); Northwood et al. (1979)).

Experimental investigations have established that in Zirconium alloys, they are mostly circular dislocation loops, located close to the prismatic planes of the Hexagonal Close Packed structure with $< 1120 >$ type Burgers vectors. Dislocation loops in stainless steels are faulted dislocation loops lying on the (111) planes of the face centered cubic structure. In those two materials, both interstitial and vacancy type loops are found.

(a)   (b)
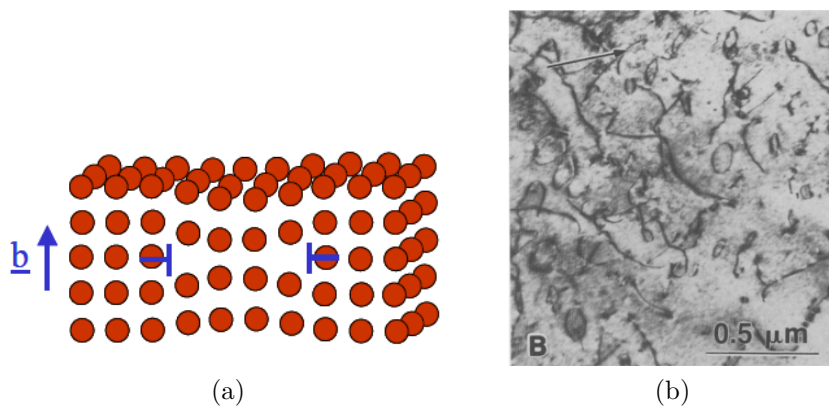
Figure 2.8 – (a): schematic representation of a dislocation vacancy loop. (b): TEM image of interstitial loops in a prismatic plane in Zirconium irradiated to a fluence of 1.51×10^{26} n m^{-2} (Griffiths (1988))

Stacking fault tetrahedra (SFT) on the other hand have been principally reported as the main irradiation induced defects in Copper (D.J. Edwards, B.N. Singh, and Bilde-Sørensen (2005); B.N Singh, D.J Edwards, and Toft (2001); Victoria et al. (2000)). These results tend to prove that the nature of the majority of irradiation induced defect is highly linked to the staking fault energy (SFE) of the metal: low SFE metals exhibiting high densities of SFT while high SFE metals will form high density of dislocation loops and black dots. Austenitic stainless
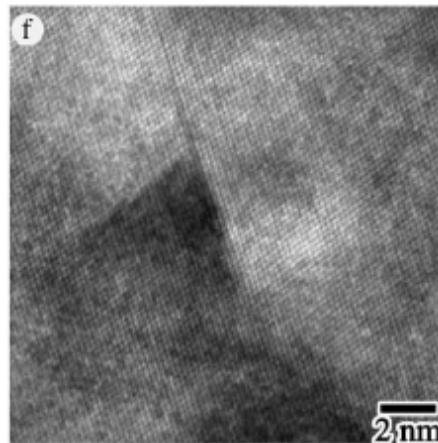
Figure 2.9 – TEM image of SFT formed in a 304 stainless steel, at 1.2 dpa (D.J Edwards, Simonen, and Bruemmer (2003))

steels are a notable exception to this rule, as their irradiation microstructure is dominated by dislocation loops. As reported by D.J Edwards, Simonen, and Bruemmer (2003), SFT constitute only about 5% of the observed defects in high purity austenitic stainless steels (an example is shown on fig. 2.9), and are not observed in commercial alloys.

Black dots are small ($\sim 3\,\mathrm{nm}$) defects that appear in early stages of irradiation where they coexist with dislocation loops, mostly reported in austenitic stainless steels. At higher irradiation doses, only irradiation loops are found. Pokor, Brechet, Dubuisson, Massoud, and Barbu (2004) have shown that size and density distribution of those defects are identical in their coexistence domain and proposed that black dots are small dislocation loops seen under different contrast conditions. The fact that black dots are found mostly for low doses is then easily explained by the small size of loops in those conditions, rendering their shape harder to observe.

Cavities are three dimensional vacancy clusters growing through the absorption of vacancies. Two categories are found, voids and bubbles:

1. Voids are agglomerations of irradiation induced vacancies (fig. 2.10).
2. Bubbles are cavities with a stabilizing gas content. They are principally observed in austenitic stainless steel under the form of Helium bubbles. In fact, irradiation induces a chain of transmutation reactions, generating Helium atoms. As they are not soluble in the lattice, they migrate in the cavities, forming bubbles. They are particularly numerous after Helium ion irradiation.

These two distinct defects can be distinguished based on their shape. Due to their internal gas pressure, bubbles are perfectly spherical whereas voids are
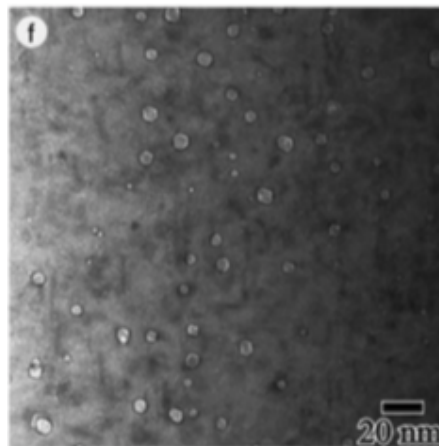
Figure 2.10 – TEM image of cavities formed in a 316 stainless steel, at 7.5 dpa (D.J Edwards, Simonen, Garner, et al. (2003))

crystallographically faceted. Their formation is highly dependent on the irradiation temperature: below 300° they are not observed but for higher temperatures their observation is frequent in austenitic stainless steels (Zinkle, Maziasz, and Stoller (1993)). At the macroscopic scale, presence of cavities may lead to swelling, which is a potential crucial issue for the design of core internals.

These defects population are specific to each irradiated metal regarding their density, size apparition dose etc... However, a general trend is observed in all metals: defects grow in density and size with increasing irradiation dose until they reach a saturation value for which an increasing dose does not affect the defect population anymore. In general the saturation is reached for a lower dose for the density than for the defect size. This is illustrated on fig. 2.11 which shows the evolution of these quantities for austenitic stainless steels and Zirconium alloys. Loop density increases up $2 \times 10^{23} \, \mathrm{m}^{-3}$ in steels for a saturation dose of approximately 1 dpa, and at $2 \times 10^{22} \, \mathrm{m}^{-3}$ for Zirconium alloys at a saturation fluence of $5 \times 10^{24} \, \mathrm{n} \, /\mathrm{m}^2$. Dislocation loop size on the contrary, saturates around 8 dpa in steels at a value of 9 nm, and saturates for fluences higher than $1 \times 10^{26} \, \mathrm{n} \, /\mathrm{m}^2$ around 8 nm.

2.2.3 Mechanical behavior of irradiated alloys

The evolution of microstructure induced by irradiation in metallic alloys go hand in hand with a significant modification of their mechanical properties. The most important evolutions observed when increasing the irradiation dose are:
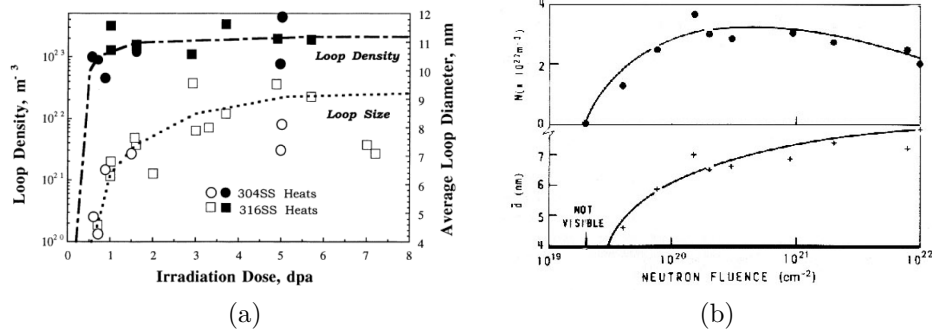
Figure 2.11 – Evolution of dislocation loop density and diameter with irradiation dose for austenitic stainless steels (a) (Bruemmer et al. (1999)) and Zirconium alloys (b) (Northwood (1977))

1. a loss a ductility

2. hardening of the material (increase of yield stress)

3. a loss of toughness

4. a reduced work hardening capacity

5. the localization of plastic flow

These general evolutions are observed for all irradiated metals. fig. 2.12 shows the evolution of the stress-strain curves experimentally obtained for an irradiated austenitic steel, a Zirconium alloy, and a Copper alloy tested until failure. The increase in yield stress with the dose is clearly evidenced by these curves, as well as the reduction of maximum elongation. These curves also highlight the lower work hardening rate induced by increase in irradiation dose. For high doses, above 0.1 dpa for Copper and above 2 dpa for austenitic steels, a pronounced stress drop following yield is observed, indicating a strongly softening behavior.

The strong decrease of maximum elongation has a direct impact on the fracture toughness. This phenomenon has not been much studied, especially under PWR conditions. A few measures of the variation of the fracture energy of austenitic stainless steels with the neutron fluence have however been provided by Torimaru et al. (2010), and are replicated here on fig. 2.13. This results highlight the severe irradiation induced loss of toughness, which is directly related to fracture energy.

One remarkable feature of this evolution of mechanical properties is that it is strongly correlated to evolution of the irradiation induced defect microstructure. Figure 2.14 presents the evolution of the observed yield stress of various alloys
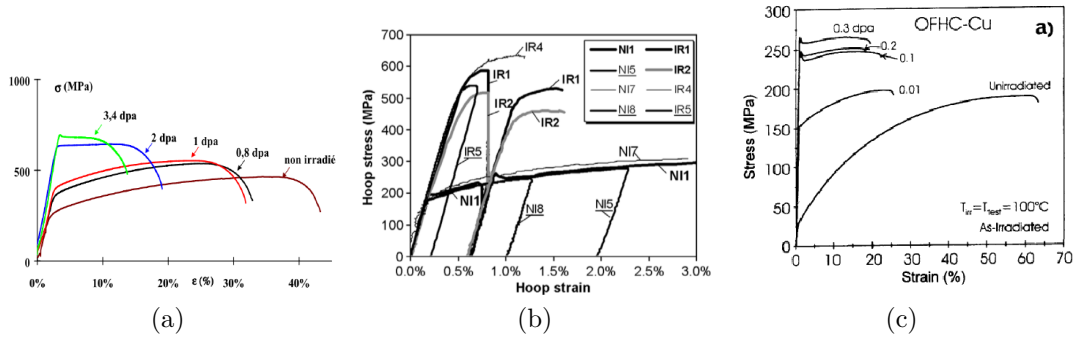
Figure 2.12 – (a): Stress–strain curves at 330 °C for a SA304 alloy after different irradiation doses (Pokor, Averty, et al. (2004)). (b): Stress-strain curves for internal pressure tests on non-irradiated (NI) and irradiated (IR) Zirconium tubes (Onimus, J. Béchade, et al. (2006)). (c): stress-strain curves for a Copper alloy after different irradiation doses (B.N. Singh, N. Ghoniem, and Trinkaus (2002))
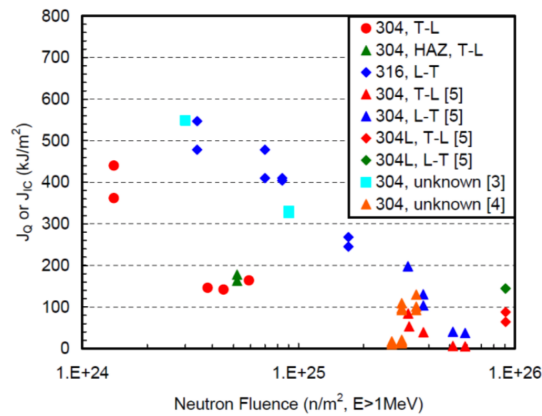
Figure 2.13 – Evolution of stainless steels fracture energy for impact tests with increasing fluence (Torimaru et al. (2010))

for different irradiation doses. The results obtained for austenitic steels (Pokor, Brechet, Dubuisson, Massoud, and Averty (2004)) (a) show a saturation of the irradiation induced increase in yield strength, obtained around 10 dpa, which is close to the saturation dose for the dislocation loops diameter, presented on fig. 2.11-(a). Similarly, Yasuda, Nakatsuka, and Yamashita (1987) have measured this evolution for Zr alloys and their results reveal a saturation fluence for irradiation induced hardening around $2 \times 10^{24} \, \mathrm{n/m^2}$, again very close to the saturation fluence of dislocation loops parameters in Zr alloys shown on fig. 2.11-(b).

Similar observations are reported regarding the evolution of the maximum elongation of deformed irradiated metals, as shown on fig. 2.15. The review of Chopra and Rao (2011) on its evolution with the radiation damage from many available experiments on austenitic stainless steels clearly demonstrates the saturation of their maximum elongation around 10 dpa, similarly to the evolution of yield stress and dislocation loops parameters. A similar study on Zirconium alloys (Rieger and D. Lee (1974)) lead to the same conclusions.

Yet, this strong loss of ductility is not associated to a change in the fracture mechanism. fig. 2.16 shows various fracture surfaces obtained after impact tests of irradiated stainless steels, revealing a ductile failure mechanism. Thus, despite loss of ductility, irradiation does not seem a brittle fracture of metallic alloys. On the contrary, this feature is the macroscopic sign a strong intragranular localization of plastic strain observed in irradiated metals. It is associated to the formation of the so-called clear channels. This particular phenomenon, which is the main focus of the present work, will be detailed in the next paragraph.

This localization is thought to be the main cause of important features of the macroscopic behavior of irradiated metals. First, while the overall strain remains low, it can locally reach very high values in the localization bands, and trigger the nucleation and coalescence of cavities. This mechanism is probably the cause of the early ductile fracture of these material. Moreover, it has been suggested by several authors that it is one of the causes of the irradiation assisted corrosion cracking (IASCC) phenomenon, observed on austenitic steels (Gupta, Hure, B. Tanguy, Laffont, M.-C. Lafont, et al. (2016); Gupta, Hure, B. Tanguy, Laffont, M.-C Lafont, et al. (2018); Hashimoto et al. (2000); Jiao and Was (2011); Karlsen, Diego, and Devrient (2010)) or Zirconium alloys (Fournier et al. (2009)). Indeed, inter-granular cracks are often associated to intense slip lines, as shown on fig. 2.17-(a). Figure 2.17-(b) shows the correlation between high slip channel heights, indicating a high degree of slip localization and intergranular cracking. It has been found to be the most correlated factor to IASCC by Jiao and Was (2011). The influence of localized deformation on grain boundary stresses is also the subject of several numerical studies Evrard and Sauzay (2010); Hure et al. (2016);

(a)

(b)
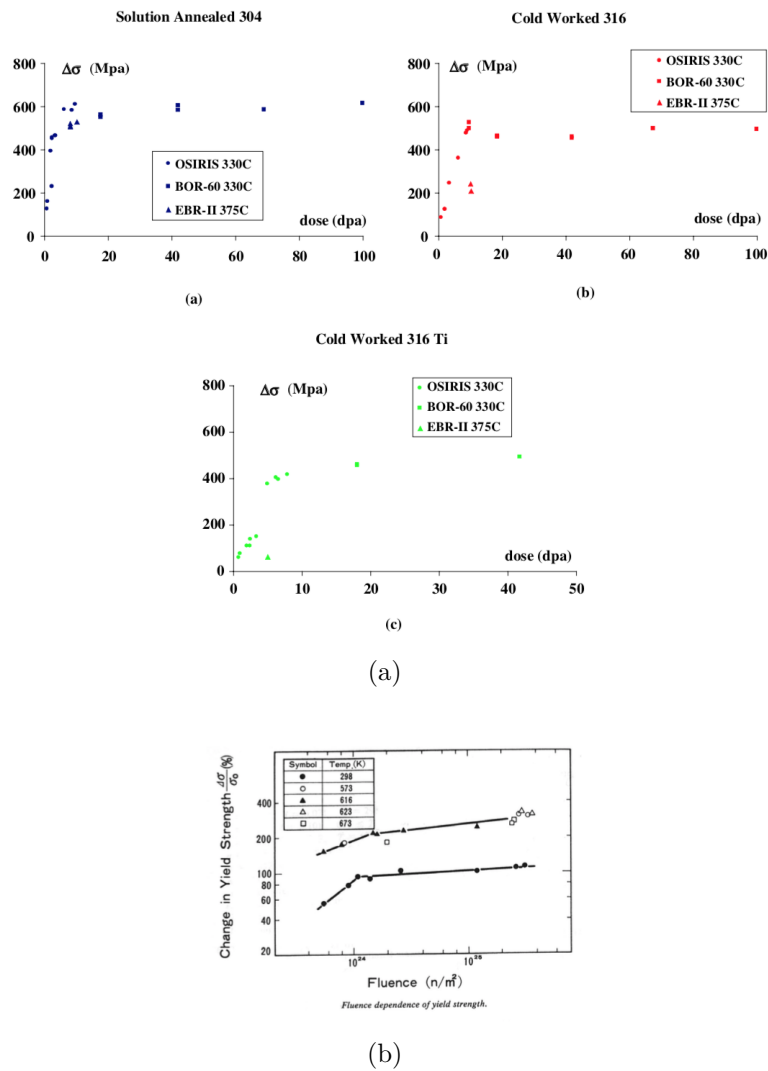
Figure 2.14 – (a): Evolution of yield stress with irradiation dose for various metallic alloys (Pokor, Brechet, Dubuisson, Massoud, and Averty (2004)). (b): Evolution of Yield strength with fluence for various test temperatures, for irradiated Zirconium alloys (Yasuda, Nakatsuka, and Yamashita (1987))
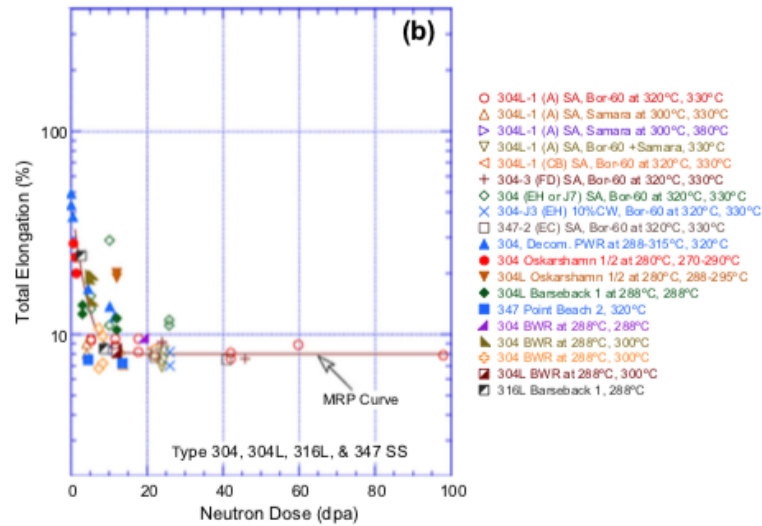
(a)
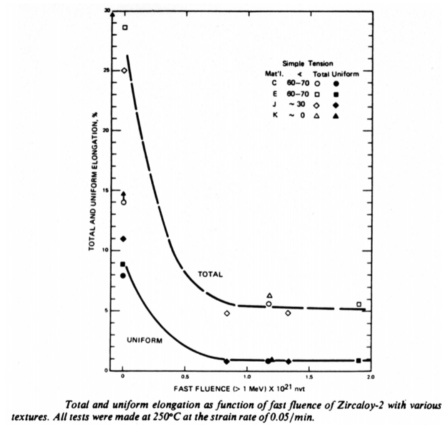
(b)

Figure 2.15 – (a): Review of the evolution of total elongation with dose for stainless steels (Chopra and Rao (2011)). (b): Evolution of maximum uniform and total elongation with fluence for Zirconium alloys (Rieger and D. Lee (1974))
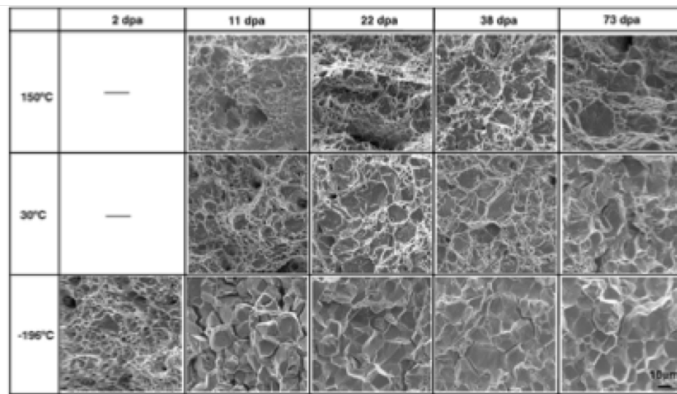
Figure 2.16 – SEM micrographs showing the fracture surface of 316 steels irradiated to different doses after impact tests at various temperatures (Fukuya et al. (2008))

Sauzay, Bavard, and Karlsen (2010). Finally, Onimus and Bechade (2009) have proposed that strain incompatibilities induced by strong plastic slip localization are responsible for the strong increase in kinematic hardening induced by irradiation on Zirconium alloys.

(a)   (b)
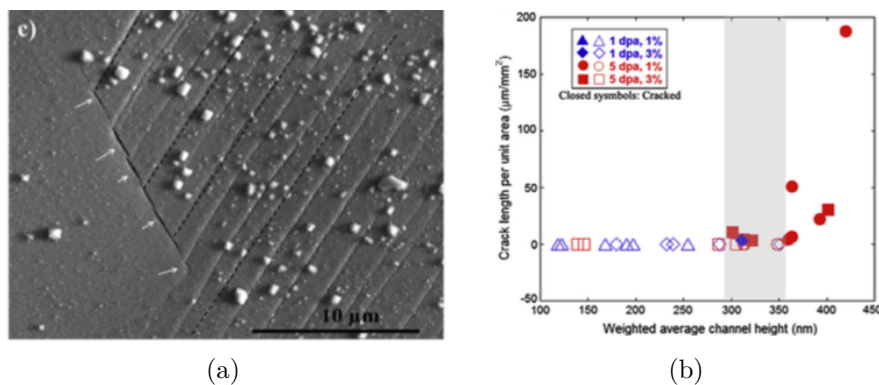
Figure 2.17 – (a): SEM image of crack in a Fe-irradiated stainless-steel in PWR environment after 4% plastic strain (Gupta, Hure, B. Tanguy, Laffont, M.-C. Lafont, et al. (2016)). (b): Correlation between average slip channel height and IASCC (Jiao and Was (2011))

Understanding strain localization appears then as a key to understand many irradiation induced mechanical phenomena. Therefore, precise prediction of its formation and characteristics is a crucial issue for the design of core reactor materials. The next paragraph focus on its precise characterization from existing observations, in various metals.

2.2.4   Irradiation induced strain localization

The nature of strain localization in irradiated metals has been progressively understood thanks to the observation of their post-deformation microstructures. They reveal the recurrent presence of bands depleted from irradiation defects, the so-called clear bands. These bands have been correlated to plastic slip activity, strongly suggesting that they are slip localization bands. This paragraph is a review of the current knowledge on this particular feature of irradiated metals. After a presentation of their characterizations, the proofs indicating their link with plastic slip are detailed. We present then the evidence of increased slip localization in irradiated alloys, and the condition in which clear bands are observed. Finally, the underlying microscopic mechanisms responsible for this phenomenon are briefly described.

Clear bands

Clear bands have been reported in TEM observations of deformed irradiated metals since the 1960s. They appear as thin channels in which the density of irradiation induced defects appears very low or null. As a result, in contrast to the surrounding matrix containing a high density of defects, they appear clearer. They get their names from this fact: clear bands or clear channels are their most used denominations. Figure 2.18 shows three examples of high magnification TEM images of clear bands in austenitic stainless steel (a), Zirconium alloy (b), and copper alloy (c). In all three, none or very few irradiation defects (loops for steel and Zr, SFTs for Copper) can be observed within the clear bands.

For the last 60 years, they have been observed in a large variety of neutron irradiated metals, such as Copper (D.J. Edwards, B.N. Singh, and Bilde-Sørensen (2005); Sharp (1972); Sharp (1972); Sharp (1974); B.N Singh, D.J Edwards, and Toft (2001); Victoria et al. (2000)), Vanadium (T. Byun, N. Hashimoto, Farrell, et al. (2006); K.-i. Fukumoto, Masanari Sugiyama, and Hideki Matsui (2007); N. Hashimoto et al. (2005); M. Sugiyama, K. Fukumoto, and H. Matsui (2004)), Molybdenum (Hasson et al. (1974); Mahajan and B. Eyre (2017); B.N. Singh, Evans, et al. (1998); Victoria et al. (2000)), Niobium (Tucker, M. S. Wechsler, and Ohr (1969)), pure iron and iron based alloys (Luppo et al. (2000); B.N Singh, Horsewell, and Toft (1999); Victoria et al. (2000)), Austenitic Steels (T. Byun, N. Hashimoto, and Farell (2006); T. Byun, N. Hashimoto, Farrell, et al. (2006); K. Field, M. N. Gussev, and J. Busby (2014); Hashimoto et al. (2000); E. Lee et al. (2001); Nishioka et al. (2008); Sauzay, Bavard, and Karlsen (2010); Victoria et al. (2000)) and Zirconium alloys (T. Onchi, Kanayo, and Y. Higashiguchi (1977); ONCHI et al. (1980); Onimus, Bechade, and Gilbon (2012); Onimus, Dupuy, and

(a)

(b)

(c)
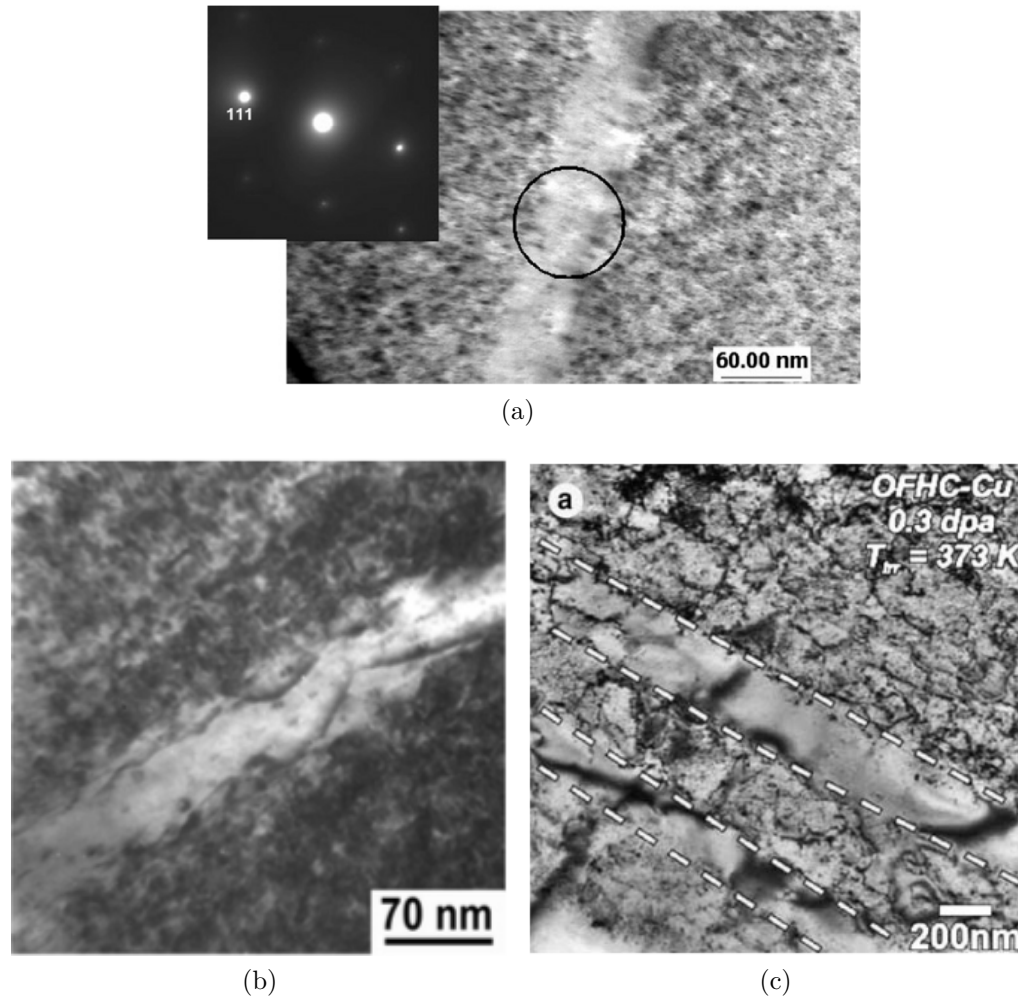
Figure 2.18 – (a): High magnification TEM image of a clear channel observed in a neutron irradiated (0.16 dpa) 304L SS sample after mild tensile strain (Sauzay, Bavard, and Karlsen (2010)). (b): Basal channel observed in a neutron irradiated Zr alloy (fluence $0.6 \times 10^{25}\,\mathrm{n\,m^{-2}}$) after tensile strain (Onimus, J. L. Béchade, and Gilbon (2012)). (c): TEM image of an neutron irradiated OFHC Copper alloy (0.3 dpa) after tensile strain showing a clear band (D.J. Edwards, B.N. Singh, and Bilde-Sørensen (2005))

Mompiou (2012); Onimus, Monnet, et al. (2004); Peterson (1982)). Clear bands
are also observed with ion irradiation (Jiao, J. Busby, and Was (2007); Miura et al.
(2009)).

(a)   (b)   (c)
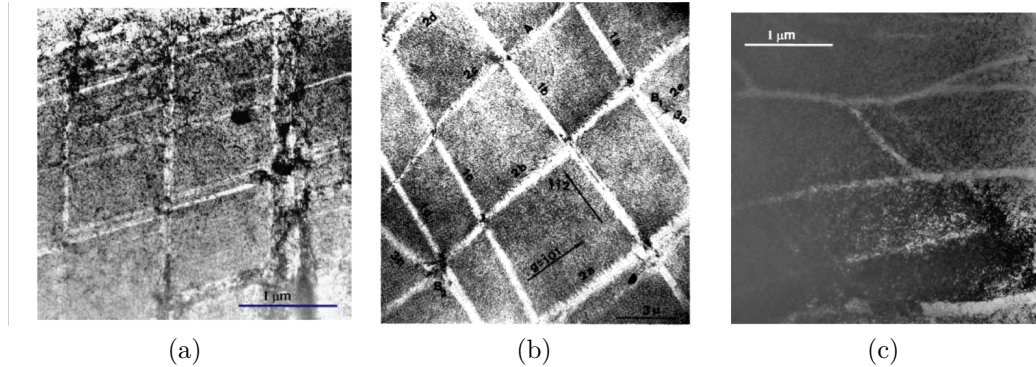
Figure 2.19 – (a): Network of clear channels in neutron irradiated 316 SS (0.78
dpa) after 32% tensile strain (T. Byun, N. Hashimoto, Farrell, et al. (2006)). (b):
Clear band patterns in neutron irradiated (0.69 dpa) Vanadium after 10% disk
bend deformation (T. Byun, N. Hashimoto, Farrell, et al. (2006)). (c): Clear band
patterns in neutron irradiated Niobium (fluence 4×10^{22} n m^{-2}) after 6.6 % tensile
strain (Tucker, M. S. Wechsler, and Ohr (1969))

All observed clear channels in the literature are found parallel to crystallo-
graphic planes. An example of clear bands parallel to the basal plane in a Zirconium
alloy grain is shown in fig. 2.20-(a). Grains exhibiting channels possess usually
several channels, that form parallel (fig. 2.20-(a)) and sometimes crossing channel
networks that strongly depend on the material, as illustrated on fig. 2.19-(a-b).
Except for the particular case of Vanadium (image (c)) deformed under multi-axial
strain, where they has been shown to exhibit curved shapes, clear bands are found
straight, with a constant width. Channels propagation at grain boundaries similar
to the one displayed in fig. 2.20-(b) have also been observed (D.J. Edwards, B.N.
Singh, and Bilde-Sørensen (2005); Jiao, J. Busby, and Was (2007); McMurtrey et al.
(2014); Onimus, Dupuy, and Mompiou (2012); Onimus, Monnet, et al. (2004)).

Typically, clear channels span the whole grain length, and have a width
of 40 nm to 250 nm and their typical spacing is of the order of the micron. In
neutron irradiated (fluence 3.2×10^{23} n m^{-2}) Zr alloys, Takeo Onchi, Kayano, and
Yasuhiro Higashiguchi (1980) observed a clear channel width of 40 nm and 100 nm.
This is consistent with the observations of Onimus, Monnet, et al. (2004), where
numerous basal channels are reported whose width span also from 40 nm to 100 nm.
They have measured an average of 3 channels per grain more or less evenly spaced,
for an average grain size of 8 µm, which yield a channel spacing of approximately
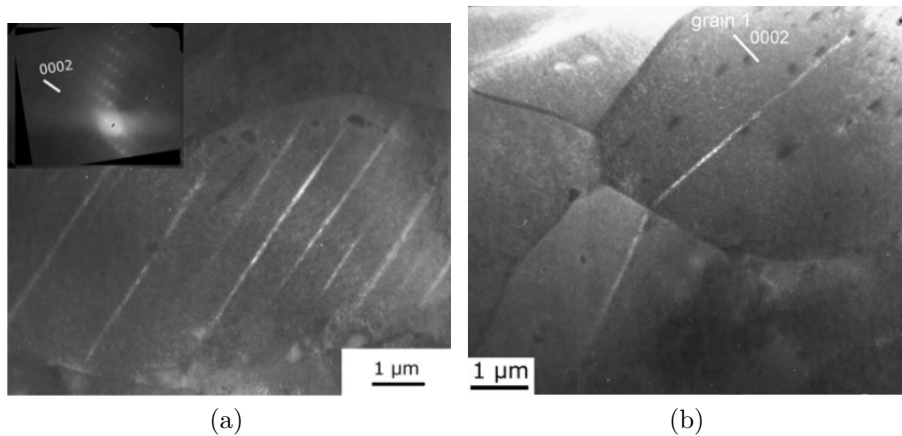
Figure 2.20 – TEM observations of (a) Basal channels and (b) propagation of a basal channel at a grain boundary in a neutron irradiated Zr alloy (fluence $0.6 \times 10^{25}\,\mathrm{n\,m^{-2}}$) after tensile strain. (Onimus, Bechade, and Gilbon (2012))

2 µm to 3 µm. Sharp (1972) has found clear bands width of 100 nm to 230 nm as shown on fig. 2.21, with an average spacing of 2 µm in irradiated copper single crystals (fluence $1 \times 10^{18}\,\mathrm{n\,m^{-2}}$), a value slightly decreased in copper alloy single crystals for which spacing is found to be around 1.2 µm (Sharp (1974)). This study also highlights the increase of the mean channel width in copper alloys to a mean value of 240 nm. T. Byun, N. Hashimoto, Farrell, et al. (2006) have found a mean channel width of 100 nm for a mean spacing of 1 µm in a 316 SA austenitic stainless steels after neutron irradiation up to 6.9 dpa. Sauzay, Bavard, and Karlsen (2010) found a similar mean spacing in a 316L allow neutron irradiated to 0.16 dpa, but found a lower width range: 20 nm to 60 nm.
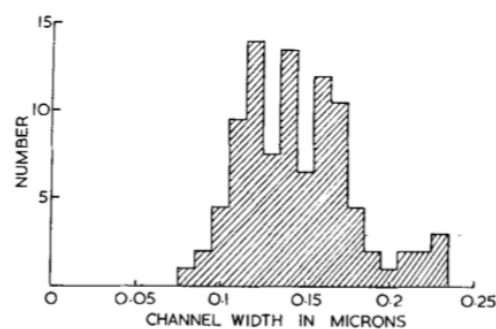
Figure 2.21 – Width distribution of clear channels in irradiated Copper single crystals after 10% tensile elongation (Sharp (1972))

Correlation with plastic slip

Besides characterizing their geometry, the large aforementioned literature on clear bands has delivered strong evidence indicating that they are induced by plastic slip, and are in fact very intense slip bands.

First, in all work cited above, clear channels are always found to be parallel to active slip planes of the crystal. On fig. 2.22 can be seen a clear channel parallel to a {110} plane in a bcc iron (Luppo et al. (2000)), and several channels parallel to a {111} plane in a Copper single crystal (Sharp (1974)). Clear bands in Zirconium alloys are found to be parallel to the basal or prismatic planes (Onimus, Bechade, and Gilbon (2012); Onimus, Monnet, et al. (2004); Peterson (1982)), and {111} planes in fcc austenitic stainless steels (T. Byun, N. Hashimoto, Farrell, et al. (2006); Sauzay, Bavard, and Karlsen (2010)). Onimus, Monnet, et al. (2004) have carried a systematic comparison of basal slip systems Schmid factor, and the occurence of basal channeling in a significant number of grains in their TEM samples. Their results, displayed on fig. 2.23, clearly show a strong correlation between a high basal Schmid factor and basal channeling. The same authors presented similar conclusions in another study (Onimus, Bechade, and Gilbon (2012)). Thus, there is a strong correlation between active slip systems planes and the orientation of clear bands in all irradiated metals.

(a)   (b)
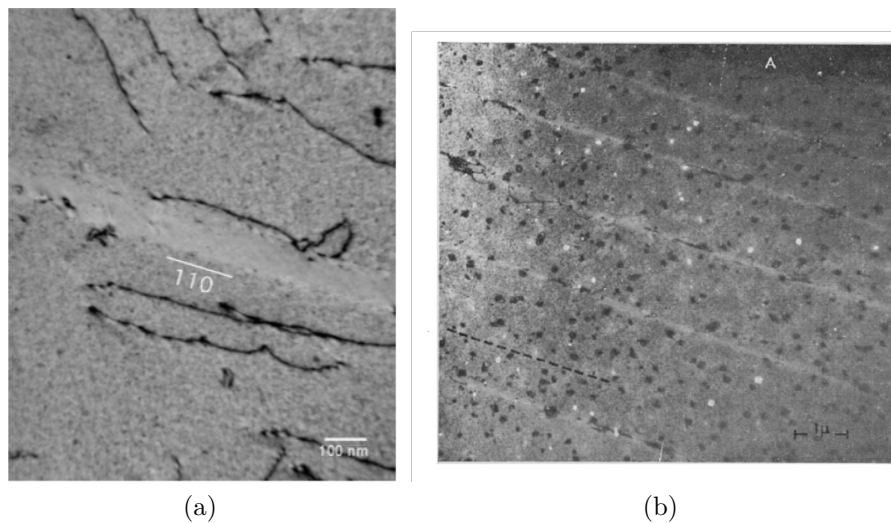
Figure 2.22 – (a) Defect free channel in a deformed proton-irradiated Fe-12Cr alloy (Luppo et al. (2000)). (b): Clear bands observed in a Copper alloy single crystal (Sharp (1974))

Besides, many observations of clear channels intersecting various objects demonstrate that these intersection induced large steps on them. A few examples
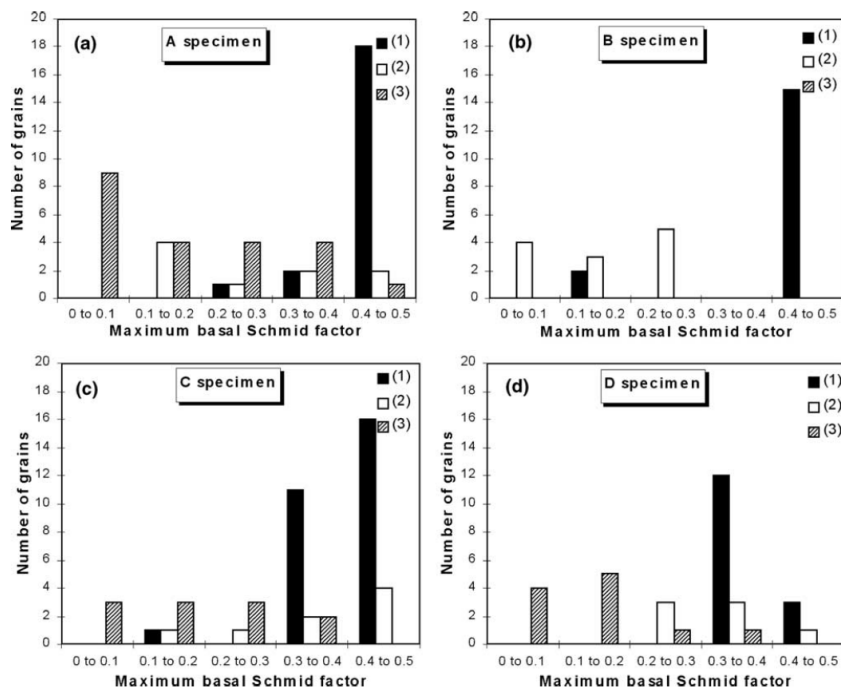
Figure 2.23 – Number of grains exhibiting channeling vs Schmid Factor observed with TEM in various samples ((1) grains with basal channels, (2) grains without basal channels, (3) grains without basal plane reachable in the TEM sample, thus their absence cannot be confirmed) Onimus, Monnet, et al. (2004)

are shown on fig. 2.24. On image (a), one channel is found intersecting two others as well as a dislocation in austenitic SS (Sauzay, Bavard, and Karlsen (2010)). At each intersection, a similar step in the direction of the channel is clearly observable. The authors have measured the step sizes of the order of the channel width (40 nm to 80 nm) indicating that the intersecting channel has induced a local straining of 100% for these objects. Similar steps are visible in the Copper single crystal studied by Sharp (1972) on image (c), which demonstrates that clear channels ending on a surface induce the formation of a strong step. Measurements of steps height yields strain level of the order of 170%. Again, similar straining of an annealing twin intersected by clear bands in an irradiated OFHC-Cu alloy (D.J. Edwards, B.N. Singh, and Bilde-Sørensen (2005)) are displayed on image (d). In addition, (Tucker, M. S. Wechsler, and Ohr (1969)) have provided images of observable dislocation tangles at channel intersections (b), proving that they glide in clear channels. Finally, recent works (Miura et al. (2009); Nishioka et al. (2008)) have directly shown that coarse surface slip steps that formed on their irradiated stainless steel samples are in fact clear channels that have reached the free surface, as illustrated on fig. 2.25.

To summarize, objects or free surfaces intersected by clear bands are highly strained, creating high steps in the direction of the Burgers vectors of the slip planes that are parallel to the bands, up to more than 100% local deformation. All of these observations clearly indicate that clear bands are intense plastic slip localization bands.

Slip localization

Several authors studied the evolution of the characteristics of these surface steps with the irradiation dose. The results of Jiao and Was (2010) and Fukuya et al. (2008) on austenitic stainless steels, presented on fig. 2.26 show that surface step spacing increases with irradiation, as well as surface height. Similar measurements have been obtained by Gupta, Hure, B. Tanguy, Laffont, M.-C. Lafont, et al. (2016); Gupta, Hure, B. Tanguy, Laffont, M.-C Lafont, et al. (2018), and by Sharp (1972) on Copper single crystals. Similar observations have been reported by Nishioka et al. (2008). Their observations reveal an increase in clear channels spacing when comparing deformed irradiated stainless steel up to 35 dpa to a less irradiated one (4 dpa).

Recently, using the high resolution DIC technique mentioned in section 2.1.2, Thomas et al. (2019) have been able to fully quantify the enhanced localization induced by irradiation on the surface of a proton irradiated Zircaloy-4 sample. Their results, displayed on fig. 2.27 show a rather homogeneous distribution
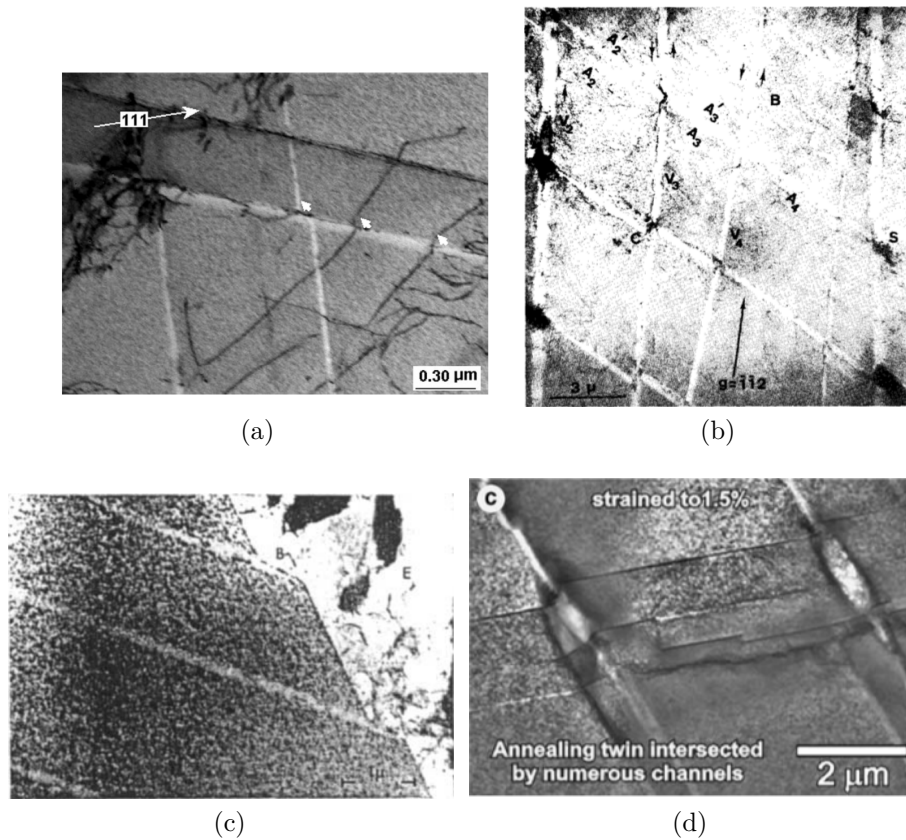
Figure 2.24 – (a) Dislocation and channels showing typical displacement steps at intersection with other channels in irradiated stainless steel (Sauzay, Bavard, and Karlsen (2010)) (b): Dislocation tangles and steps at channel intersections in irradiated Niobium (Tucker, M. S. Wechsler, and Ohr (1969)) (c): Observation of clear channels and associated surface slip steps in irradiated Copper single crystals (Sharp (1972)) (d): Annealing twin crossed by clear channels inducing strong slip steps in a OFHC-Cu irradiated alloy (D.J. Edwards, B.N. Singh, and Bilde-Sørensen (2005))
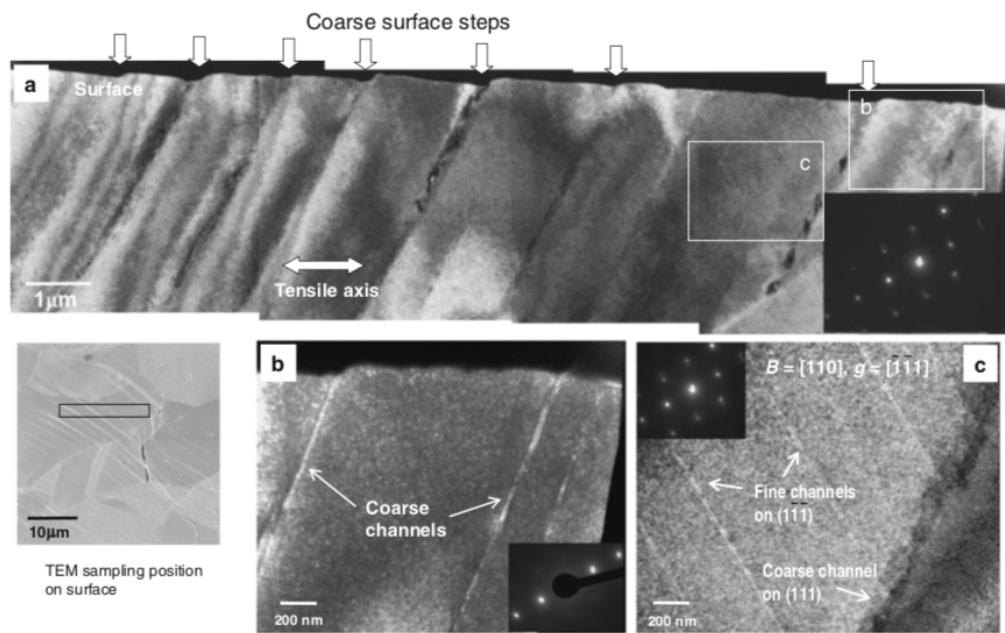
Figure 2.25 – Near surface post-deformation (13 %) microstructure of a 35-dpa neutron irradiated stainless steel specimen showing clear channels inducing surface steps (Nishioka et al. (2008))

of shear strain in the non-irradiated sample whereas intense slip lines, parallel to prismatic planes traces, where observed in most grains of the irradiated sample. They have measured a mean spacing of slip bands around 100 nm to 250 nm in the non-irradiated sample, while it appears several times higher for the irradiated one. Similarly to the measures of step heights by Jiao and Was (2010), they found a strong increase in shear intensity within the slip bands. They have shown that the ratio between the 99.99th percentile and the 0.01th percentile value of shear strain is 7 times higher in the irradiated region than the non-irradiated one.
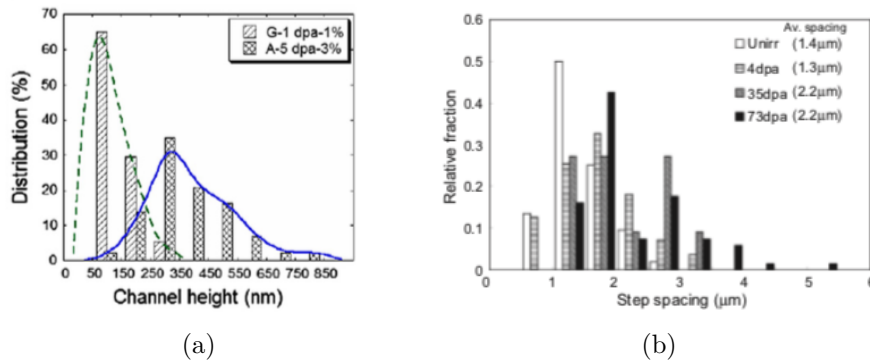
Figure 2.26 – (a) Distribution of step height in two austenitic stainless steels irradiated (with protons) strained to 1 and 3% showing increasing step height with dose (Jiao and Was (2010)) (b): Distribution of step spacing in cold work SUS316 stainless steel for various neutron irradiation doses after 2-3 % deformation (Fukuya et al. (2008))

On the other hand, among all the works studying clear channels cited above, none has mentioned significant signs of plastic activity in irradiated metals, outside of clear channels. Moreover, this fact has been specifically verified and confirmed by D.J. Edwards, B.N. Singh, and Bilde-Sørensen (2005) in irradiated Copper alloys. Onimus, Monnet, et al. (2004) have estimated the volume fraction of clear bands in their TEM samples to be around 2%, for an overall plastic strain of 0.5%. On the basis of this estimation, deformation levels of the order of 25% in clear channel would be sufficient to account for all macroscopic plastic strain. This hypothesis, considering the previously mentioned level of strain measured in clear bands, is highly probable.

Finally, it is important to mention that this phenomenon is an intra-granular localization phenomenon, and is not directly associated to macroscopic yield nor macroscopic localization. Indeed, Onimus, Monnet, et al. (2004) observation of cleared channels have been carried out on thin foils obtained from macroscopically homogeneously deformed areas, at very low levels of plastic strain
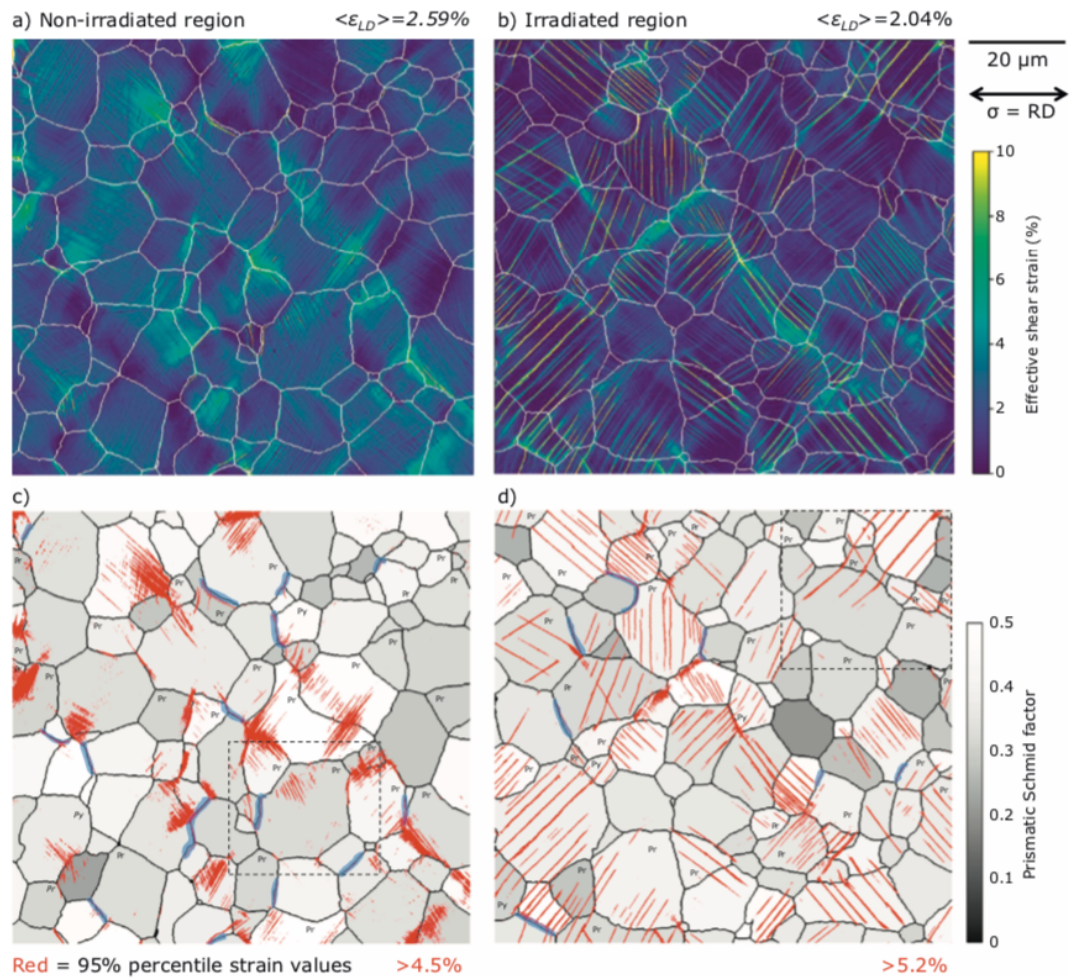
Figure 2.27 – Effective shear strain maps and associated skeleton maps of 95th percentile of effective shear strain for a proton irradiated Zircaloy-4 (0.13 dpa) (Thomas et al. (2019))

($< 0.5\%$). K. Field, M. N. Gussev, and J. Busby (2014) have observed them in a sample mildly deformed (0.8%) in austenitic stainless steels. Similarly, M. Gussev, K. G. Field, and J. T. Busby (2015) has observed dislocation channeling already at stress levels of the order of 65% of the yield stress in homogeneously deformed regions in austenitic stainless steels, similarly to D.J. Edwards, B.N. Singh, and Bilde-Sørensen (2005) results for irradiated Copper. The latter study also reported observation of clear channels for all strain ranges in specimens tested to failure.

Conditions for slip localization

Clear bands observations condition are consistent with their slip localization band nature. Indeed, they are mainly observed for high tests temperature. Takeo Onchi, Kayano, and Yasuhiro Higashiguchi (1980) reported observation of clear channels in irradiated Zr in the the range 473 K to 608 K for the testing temperature, but not below this value. Hashimoto et al. (2000) also reports formation of clear channels for a test temperature of 350 °C in irradiated austenitic stainless steels whereas at 60 °C the main deformation mode observed is twinning. They also found that at 350 °C, twinning is dominant for high strain rate tests, while channeling is the main mode for low strain rates. Similar results were obtained by (Victoria et al. (2000)) and Nishioka et al. (2008). As plastic deformation is a thermally activated mechanism, this dependence on temperature supports again the link between clear channels and plastic slip. Besides, Sharp (1974) has shown that the presence of hardening alloying particles that are strong obstacles to slip significantly affects slip localization by reducing step height and slip line spacing. In addition to temperature, all phenomena and microstructural features opposing to plastic slip have thus the potential to preclude or mitigate channeling.

Figure 2.28 shows a localization mode map for irradiated stainless steels in the true stress/dose space, revealing that twinning and channeling are associated to similar levels of activation stresses, with channeling being dominant at high irradiation doses. High irradiation doses are correlated to high densities of irradiation induced defects. Jiao and Was (2010) have found that the increase of dislocation loop density in austenitic stainless steels significantly increases the occurence of dislocation channeling, and in general, channeling is observed for irradiation doses close to saturation doses of the irradiation induced defects indicating a clear relation between these two features. However, Jiao and Was (2010) also demonstrated that the presence of Helium bubbles within the microstructure, produced by He ions irradiation, strongly mitigates the degree of strain localization. In these samples, they have observed a similar density of helium bubbles inside clear channels as in the surrounding matrix. In these conditions, they also observed the apparition of twinning as a significant competing deformation mode. Similar observations have

been made by E. Lee et al. (2001); Miura et al. (2009). Moreover, Sharp (1974) has conducted tensile tests on irradiated Cu-Al 4% alloys for which interstitial solute atoms have a strong binding effect, and found no formation of clear channels within them.
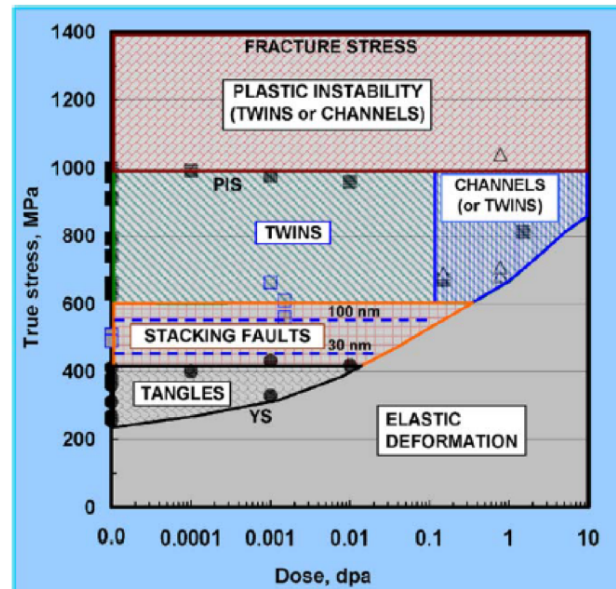
Figure 2.28 – Deformation mode map for 316 and 316 NL stainless steels (T. Byun, N. Hashimoto, and Farell (2006))

Thus, and as highlighted by T. Byun, N. Hashimoto, and Farell (2006); T. S. Byun and Naoyuki Hashimoto (2006), formation of clear channels is highly dependent on the density of irradiation induced defects, but also on their nature. Indeed, observation of cavities, dislocation tangles, or particles within clear channels is associated to a lower localization intensity. This suggests that channeling can be precluded by the presence of non-removable defects. In contrast, it underlines the central role played by the annihilation of removable defects such as SFTs or dislocation loops in the formation of clear channels, which will be the focus of section 2.2.5.

This is supported by the observation of a similar defect-free channel formation mechanism, correlated to intense slip bands, in quench-hardened gold or aluminium single crystal (Bapna and Meshii (1974); Mori and Meshii (1969)), both materials possessing respectively a high density of quench-induced SFTs and dislocation loops. A similar mechanism is observed in ω-enriched Ti-Nb-based gum metals where ω-particles depleted channel are correlated to surface slip localization bands (Lai, Tasan, and Raabe (2015)).

2.2.5   Dislocation channeling mechanism

The presence of defect free channels in deformed irradiated metals and their evident link with plastic slip suggest that these defects could be annihilated by dislocation glide. Hirsh (1976); M. Wechsler (1973) have synthesized the various possible mechanisms involved in the annihilation of Frank loops by dislocation glide. Dislocation loops are either glissile or faulted. However faulted loops can be unfaulted by a dislocation, turning them into glissile defects. Thus, the stress field induced by a gliding dislocation could cause the dislocation loop to glide along its cylinder, and be dragged by the dislocation. In this process, the loop can encounter another loop of opposite Burgers vector and thus be annihilated. Alternatively, when the Burgers vector of the dislocation and the loop are identical, the loop can be incorporated in the dislocation.

All these mechanisms result in the sweeping of loops induced by the glide of dislocations. As irradiation defects are pinning obstacles for dislocations, they glide more easily in the zone behind the dislocation that has been depleted from its defects, promoting further plastic slip in this area (fig. 2.29). Dislocation glide is thus channeled in this areas. This mechanism is called the dislocation channeling mechanism and is the key physical process identified as the cause of clear bands formation. As a result, clear bands are often called dislocation channels. Similar mechanisms exist for SFTs in low SFE FCC crystals.
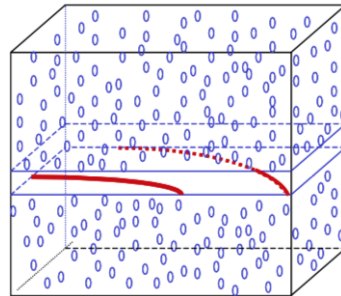
Figure 2.29 – Schematic representation of dislocation channeling. Two dislocations (red) clearing a plane from irradiation induced dislocation loops (blue)

Therefore, understanding the mechanisms of dislocation-defect interactions is a central issue for understanding and modeling slip localization in irradiated metals. By reviewing all the possible interactions between basal and prismatic dislocations with prismatic loops in Zr alloys, Onimus, Monnet, et al. (2004) have been able to determine that dislocation-loop junctions are all glissile for basal dislocation whereas only 2 out of 3 possible junctions are sessile for prismatic

dislocations. This explains well the less frequent formation of prismatic channels in Zirconium alloys. Recent in situ TEM observation have evidenced these mechanisms in Zirconium (Drouet et al. (2016); Onimus, Dupuy, and Mompiou (2012)), Copper (J. S. Robach et al. (2003)), or quenched-hardened copper and gold J. Robach et al. (2006).

These mechanisms are extensively studied with low-scale simulations techniques, such as dislocation dynamics or molecular dynamics. Atomistic simulations of David Rodney (2005) have shown that mechanisms such as absorption, drag or transformation of the defects can be caused by dislocation glide, but also demonstrated the formation of pinning junctions accounting for the hardening effect of loops and SFTs. J. S. Robach et al. (2003); J. Robach et al. (2006) have also been able to reproduce the annihilation mechanism observed in TEM in-situ testing with molecular dynamics simulations. These atomistic studies are used to construct dislocation-defect annihilation interaction laws that are then introduced into discrete dislocation dynamics codes. The resulting simulations have been able to reproduce the formation of clear channels for a large variety of materials and defects types (Arsenlis, Rhee, et al. (2012); Cui, Po, and Nasr M. Ghoniem (2018); Drouet et al. (2016); N. M. Ghoniem et al. (2001); Gururaj, Robertson, and Fivel (2015); Nogaret et al. (2008)).

Detailed description of such studies is beyond the scope of the present work. However it must be mentioned that it is a very active and important part of the research carried out to understand the multi-scale behavior of irradiated materials. Indeed, atomistic and dislocation scale observations and simulations provide essentials mechanisms and quantities to build up continuum models of slip localization.

2.3   Continuum modeling of the mechanical behavior of irradiated metals

Understanding the irradiation induced effects on the mechanical behavior of metals, presented in the last section, is crucial for the prediction of the integrity of structural parts in the reactor core. Modeling occupies a central place in their design, and thus significant efforts have been made for the modeling of the irradiation induced effects on metals. As this work lies in the continuity of these efforts, a review of the state of the art in this field is presented in this section.

2.3.1 Radiation-induced hardening

In section 2.2 we have clearly evidenced the link between the evolution of radiation induced hardening and of irradiation induced defect microstructure. Two approches have been proposed in order to model the increase in critical shear stress to activate plastic flow induced by these defects: the Dispersed Barrier Hardening and the Cascade Induced Source Hardening models, presented hereafter.

Dispersed Barrier Hardening (DBH)

As discussed in section 2.2.5, dislocations and defects can interact and form sessile junctions that have a strong dislocation pinning power. Moreover, long range dislocation-defects interactions can also induce forces resisting to the motion of dislocations. DBH is the most used model to account for their subsequent hardening effect (Hirsh (1976); Odette and Frey (1979)).

It consists in considering the defect population as evenly distributed rigid obstacles to dislocation glide. These obstacles pin the dislocations, which unpin only after reaching a specific curvature angle. Estimating the force to apply on the dislocation to yield this curvature angle allows to estimate the needed increase in shear stress. In classical isotropic elastic hardening theories, it is expressed as follows:

$$\tau = \alpha b \mu \frac{1}{l} \tag{2.5}$$

with b the Burgers vector of the pinned dislocation, μ the shear modulus, l the average distance between rigid obstacles and α is the so-called obstacle strength, which is linked to the minimal curvature angle needed to unpin the dislocation. In the case of irradiation induced defects, this mean distance is estimated by the inverse of $\sqrt{Nd}$ where N is the defect density and d the defect typical size. The dispersed barrier hardening model predicts then the following irradiation induced hardening:

$$\tau = \alpha b \mu \sqrt{Nd} \tag{2.6}$$

This model is the most widely used to reproduce irradiation induced hardening, as it provides a good agreement with experimental measurements. Typical value of α for dislocation loops are comprised between 0.2 and 0.8, depending of the type of junctions formed (Onimus and Bechade (2009); Pokor, Brechet, Dubuisson, Massoud, and Averty (2004)).

Cascad Induced Source Hardening (CISH)

An alternative theory exists to predict irradiation induced hardening. Blewitt et al. (1960) proposed that it is caused by dislocation anchoring by a Cottrell atmosphere of defects induced by displacement cascades. This idea is supported by observation of decorated dislocations in irradiated metals, as shown on fig. 2.30.

B.N. Singh, Foreman, and Trinkhaus (1997); Trinkaus, B.N. Singh, and Foreman (1997); Trinkhaus, B.N. Singh, and Foreman (1997) followed this idea and proposed the CISH model. Based on atomistic simulations, they have shown that dislocation acts as sinks attracting point defects clusters (black dots, small loops and SFTs) within a "stand-off" distance y from their core. The diffusion processes and this mechanism are then responsible for a much higher defect density within the "stand-off" distance, leading to the decoration and subsequent hardening of Frank-Read sources. They estimated the shear stress needed to unpin the dislocation from its defect atmosphere with the following expression:

$$\tau \approx \frac{\mu}{10} \left(\frac{b}{l}\right) \left(\frac{d}{y}\right)^2 \tag{2.7}$$

with d the defect diameter, l their characteristic spacing, b the Burgers vector of the dislocation and μ the shear modulus. Unpinned dislocations will then behave as very active F-R sources and emit a high number of dislocation, leading to the rapid clearing of irradiation induced defects in their plane. This brutal effect is often denoted as a "dislocation avalanche".
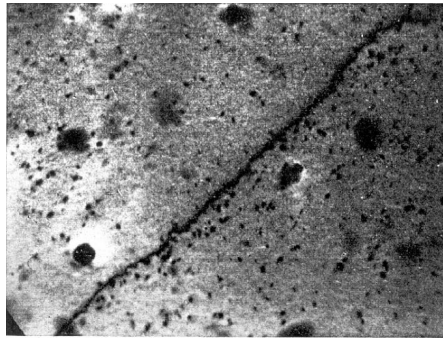
Figure 2.30 – Decorated dislocation by an atmosphere of small interstitial loops in neutron irradiated Copper (Makin (1964))

Both models are supported by observations and numerical simulations, and considering the variety of crystal structures and defects encountered in irradiated metals, they both have an important role to play in interpreting irradiation induced

hardening and associated softening mechanisms. Evaluation of their pertinence and associated parameters values (stand-off distance, obstacle strength) has been studied through atomistic and dislocation dynamics simulations (Cui, Po, and Nasr M. Ghoniem (2018); N. M. Ghoniem et al. (2001); Khraishi et al. (2002); D. Rodney, G. Martin, and Y. Brechet (2001); Sun et al. (2000)) and is still an open question.

2.3.2   Multiscale models for irradiated metal modeling

Based on these elementary hardening mechanisms, many crystal plasticity models have been developed to simulate the behavior of irradiated metals. They almost all rely on the association of the DBH model in conjunction with evolution equations of defect densities depending on plastic slip, that are based on the homogenization of the physical mechanisms of dislocation-defects interactions.

This modeling approach has been first proposed by Arsenlis, Wirth, and Rhee (2004). They proposed a finite strain isotropic plasticity model for irradiated copper combining dislocation-density based hardening and the DBH model, yielding a yield stress expressed as follow:

$$\sigma_y = \mu b \sqrt{\alpha \rho_d + \beta N d} \tag{2.8}$$

where ρ_d is the dislocation density, α the obstacle strength associated to dislocation forest hardening, N and d are respectively the density and mean size of irradiation induced SFTs, and β is the associated obstacle strength, and is a function of d. Following atomistic simulations demonstrating the shearing of SFTs into smaller ones by dislocations, they have derived, under the hypothesis of constant defects density, the following equation for SFTs density evolution :

$$\dot{N} = \frac{3}{2} N \underline{\dot{\varepsilon}}^p \tag{2.9}$$

$$\dot{d} = -\frac{1}{2} d \underline{\dot{\varepsilon}}^p \tag{2.10}$$

where $\underline{\varepsilon}^p$ is the plastic strain. This framework allows to model explicitly a specific dose by setting the initial density and size of defects, according to microstructural observations. They have been able to successfully reproduce the increase in yield stress and the progressive decrease of work hardening of irradiated copper alloys with increasing irradiated dose. They also evidenced that the model predicts a critical density for which initial yield point is followed by a macroscopic softening phase, in agreement with experiments.

Following the propositions of Pokor, Averty, et al. (2004); D. Rodney, G. Martin, and Y. Brechet (2001), Onimus and Bechade (2009) have proposed a similar formulation, extended to crystal plasticity, to model prismatic loop sweeping by basal dislocations in irradiated Zr alloys. They derived the following loop density evolution relation:

$$\dot{\rho_l} = -\frac{H}{b}\rho_l \left[\sum_{s \in B} |\dot{\gamma}^s|\right] \tag{2.11}$$

where $\rho_l = Nd$ with N and d respectively the loop density and size, H being the capture distance of loop by dislocations, and $\dot{\gamma}^s$ the plastic slip rate on the slip system s. This equation governs the decrease of loop density with increasing plastic slip. The sum indicates that all three system of the basal plane participate to the sweeping of dislocation. Associated to an increase in critical resolved shear stress given by eq. (2.6), it induces the local softening associated to the dislocation channeling mechanism. Again, their simulations are able to capture the increase in yield strength and softening regime induced by the increase in initial defect density.

This approach has then been successively refined by several authors. Krishna, Zamiri, and De (2010) introduced in this formulation a capture probability, acknowledging from atomistic studies that non all interactions with gliding dislocations lead to the sweeping of defects. Barton, Arsenlis, and Marian (2013) have included the anisotropy of dislocation sweeping and hardening through a tensorial irradiation damage density to model the dependence of dislocation-defects interactions on the orientation of their respective planes in bcc irradiated metals. This approach has been enriched with the capture probability modeling of Krishna, Zamiri, and De (2010), by Xiao et al. (2015) for irradiated FCC crystals, in particular copper. Finally, Patra and McDowell (2012) have proposed a very rich formulation of this framework aiming at modeling the behavior of irradiated BCC metals for a wide range of phenomenon: hardening, strain softening, cross-slip, creep and recovery. They include internal variables such as the density of each family of dislocations loops, but also of irradiation induced interstitial and vacancies, dislocation densities, which are involved in equations modeling defects creation and annihilation by dislocations, dislocation climbing, point defect absorption induced loop growth or classical multiplication of network dislocations. Their very rich modeling framework involve a high number of material parameters. They derive their value on the base of DD or MD simulations, or through mechanical behavior identification.

Recently, a model combining the approach mentioned above and a modeling of the dislocation avalanche effect has been proposed (Han (2012)). In this

model, the evolution of critical resolved shear stress with slip is given by:

$$\tau_c^s = \tau_0^s + \mu b \sqrt{\sum_u a^{su} \rho_d^u} + \mu(\alpha_l b_l) \sqrt{\sum_p d_l \rho_l} + \tau_a \exp{-\frac{|\gamma^s|}{\gamma_0}} \tag{2.12}$$

where b_d and ρ_d are respectively the magnitude of Burgers vector and density of dislocation, b_d, d_l and ρ_d the Burgers vector, size and density of dislocation loops, α_l the obstacle strength of loop and a is the hardening matrix of the crystal. The exponential decay term has been added to model the effect of dislocation avalanche predicted by the CISH model, where τ_a represented the additional shear stress needed to unpin dislocation from their defect atmosphere, and γ_0 is a paramter controlling softening speed. Adding this term was found necessary by Han (2012) in order to obtain satisfying initial hardening and strain softening in irradiated austenitic stainless steels simulations.

Using this model with finite element tensile simulations of a polycrystalline aggregate, Shawish, B. Tanguy, and Hure (2016) have identified the parameters for various irradiation doses on the base of the curves established by Pokor, Averty, et al. (2004) (fig. 2.12). They showed that the model prediction are in very good agreement with the experimental stress-strain curves, as shown on fig. 2.31. Identification yielded an increase of α_l with dose from 0.236 at 0.8 dpa to 0.518 at 13 dpa, as well as for τ_a which goes from 57 MPa at 2 dpa to 98 MPa at 13 dpa.
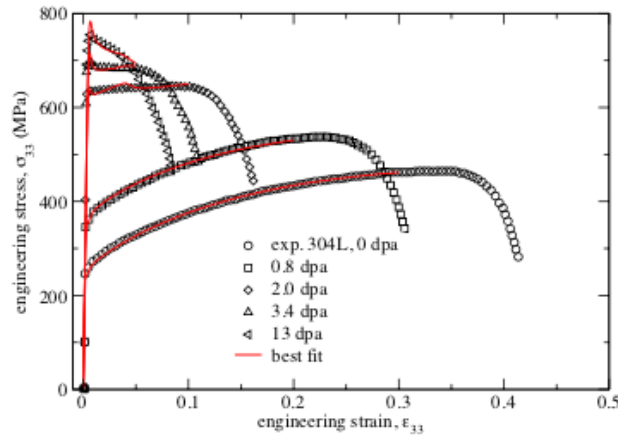
Figure 2.31 – Measured and calibrated tensile curves simulated for a 128 grains polycrystal for 304 stainless steel (Shawish, B. Tanguy, and Hure (2016))

2.3.3   Slip localization modeling

The crystal plasticity models of irradiated metals presented in the last section all allow to reproduce a strongly softening local behavior, as long as initial density and size of irradiation induced defect are sufficiently high. As a result, they should yield plastic slip localization when used within continuum polycrystalline simulations. Naturally, some of the authors that contributed to their developments have also investigated their prediction of strain localization in numerical simulations. Patra and McDowell (2016) have also used a simplified version of their rich irradiated bcc constitutive model (mentioned above, Patra and McDowell (2012)) to produce similar two dimensional simulations of strain localization in a more realistic Voronoi tessellation based polycrystal.

Using a model close to the one presented in Onimus and Bechade (2009) , Mora (2005) has conducted finite element simulation of ideal hexagonal grains deforming through a single in-plane slip system per grain.

(a)   (b)
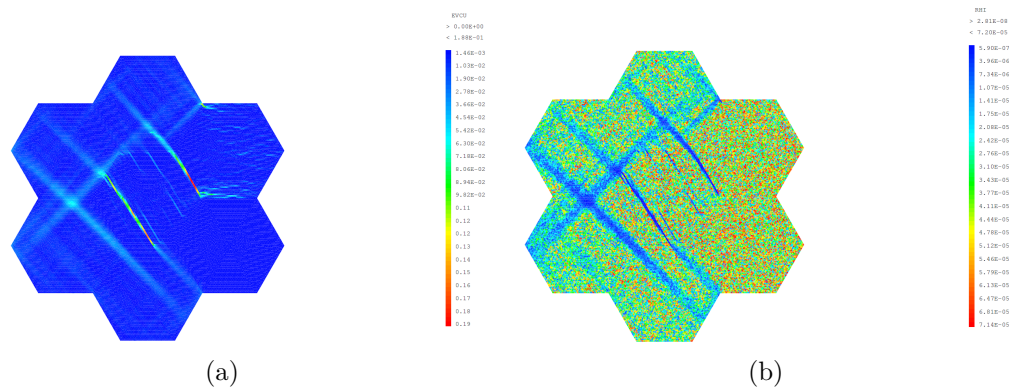
Figure 2.32 – Strain (a) and loop density (b) fields simulated after 1.4% tensile strain (Mora (2005))

Using a phenomenological linear softening model for irradiated Zr alloys, Erinosho and Dunne (2015) have explored with finite element simulations the influence of basal and prismatic softening on the mechanical behavior and the strain localization in three dimensional polycrystals with ideal cubic grains. Barton, Arsenlis, and Marian (2013) applied their model on a more representative 3D polycrystalline aggregate, and finally, Hure et al. (2016) simulated the model combining DBH and CISH developed by Han (2012) to simulate a realistic polycrystalline wire microstructure coming from diffraction contrast tomography data.

The methodology followed in these works is always the same: FE simula-
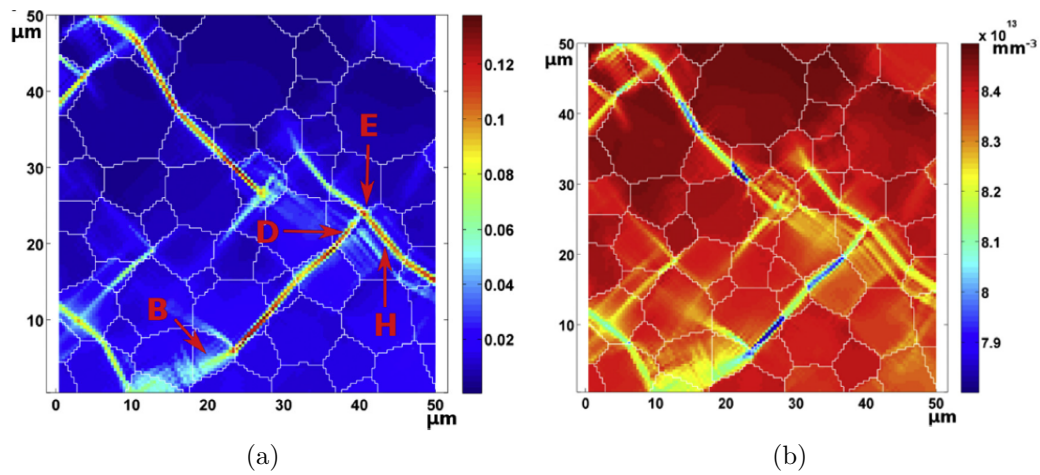
Figure 2.33 – Distribution of Von Mises effective inelastic strain (a) and averaged dislocation loop number density (b) after loading to 2% tensile strain, simulated with an irradiated bcc steel model (Patra and McDowell (2016))
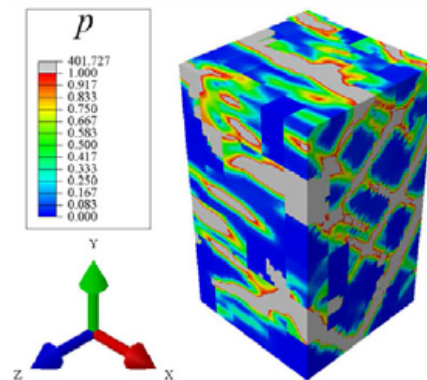
Figure 2.34 – Cumulated plastic strain field obtained after 10 traction-compression cycles on a textured model irradiated Zr polycrystal (Erinosho and Dunne (2015))

(a)

(b)
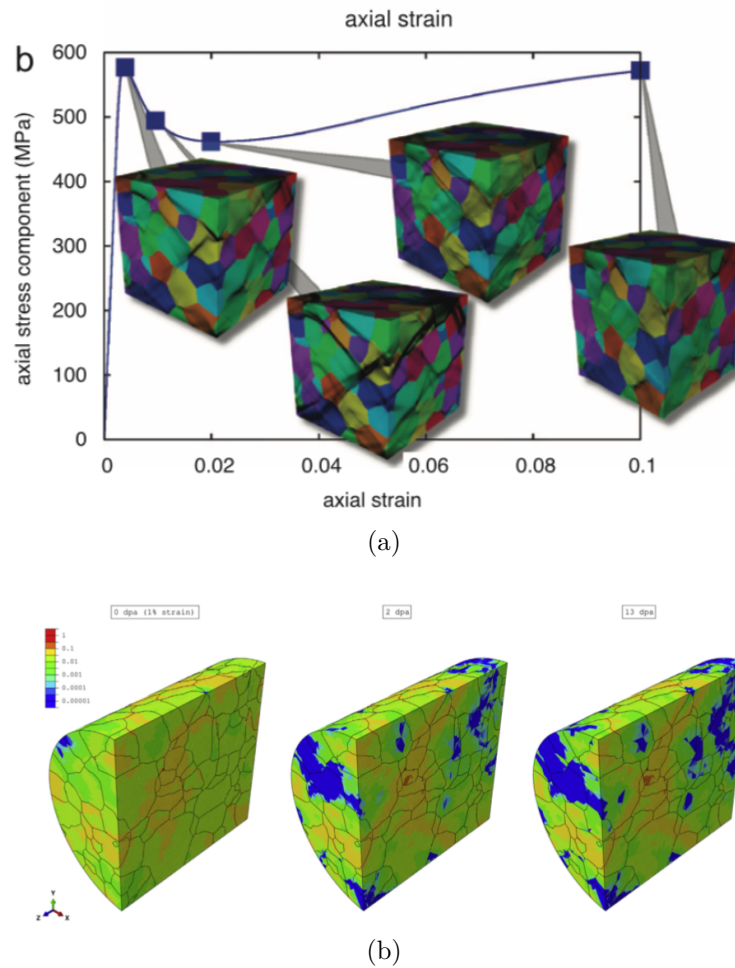
Figure 2.35 – (a): FE response to 10% strain a an irradiated model Copper alloy (Barton, Arsenlis, and Marian (2013)). (b): Cumulated slip simulated on the interior of an irradiated austenitic stainless steel polycrystal for 3 modeled irradiation doses Hure et al. (2016)

tions on the polycrystalline unit cell is used to calibrate the model parameters by fitting the results on an experimental strain-stress curve relevant for the simulated material. The simulated mechanical fields are observed a posteriori to study slip localization. The slip deformation fields obtained by these authors have many features in common. Some of their results are reproduced on figs. 2.32 to 2.35.

Most of these works show that polycrystalline modeling associated to a physically based model of dislocation channeling allows to obtain a very good agreement with experimentally observed stress-strained curves. Moreover, all of these authors observe strong plastic slip localization in their simulations, associated to a pronounced yield drop on the macroscopic curve. It is clear from the observation of figs. 2.32 and 2.33 that high plastic slip localization areas are associated to a strong drop in local defect density, evidencing the pertinence of the modeling of dislocation channeling to reproduce strain localization.

However, a closer look reveals features that are in contradiction with observation of clear bands. First, Mora (2005) (fig. 2.32) found crossing localization bands in several grains. Considering that they modeled only one slip system per grain, it is evident that one of these bands is not parallel to the active slip system. Similar observations can be drawn from the fields presented by Patra and McDowell (2016) (fig. 2.33), though the authors do not mention this issue. Furthermore, they used a full three dimensional description of bcc slip systems in a two dimensional simulation under generalized plane strain conditions, rendering interpretation of their simulated bands orientation questionnable. As established in section 2.2 , clear bands have very specific orientation features, and are clearly parallel to slip planes. This points out the discrepancy between the simulated bands presented in these works and the true nature of clear bands.

Secondly, all of these simulations rely on idealized microstructures and/or low mesh resolution, of the order of the tenth of the grain size at most. Yet, typical clear bands width is two order of magnitude below the grain size, and phenomena such as channel transmission at grain boundary are highly dependent on the grain microstructure geometry. Thus, the unit cells used in these works are too crude to accurately reproduce dislocation channeling at the relevant scale.

Then, their results show generally only one intense localization band per grain, correlated to triple junctions or grain boundaries. These intense bands quickly coalesce over the all unit cell to form a macroscopic localization band. This is typically observed on fig. 2.35-(a) and fig. 2.33-(a). This is not in agreement with the observations of dislocation channeling where generally several channels per grains are found, and can be observed in macroscopically homogeneously deformed zones.

Finally, softening crystal plasticity causes classical mesh dependence which is not discussed by these authors, but should render the prediction of these models for the width, number and intensity of the simulated localization bands highly mesh dependent. It must be noted, that recent advances in modeling irradiated single crystals have formulated strain gradient micromorphic plasticity models, in order to regularize slip localization bands (Ling et al. (2018); Scherer et al. (2019)).

2.4 FFT-based homogenization and the AMITEX_FFTP solver

In this section we present a review of the literature on the recent class of numerical homogenization method commonly called FFT-based homogenization methods, that will be the core of all numerical simulations of this thesis. After a presentation of the theoretical basis of the method, its historical developments are presented in two parts, the first being dedicated to their first introduction by Moulinec and Suquet (1998), and the second to all the developments that have followed during the past twenty years. It is followed by a brief reminder of the classical framework for the mechanical behavior modeling of non-linear materials and the associated UMAT formalism. This review is indispensable to the presentation of the solver AMITEX_FFTP, that occupies the last part of this section. Indeed, it is a high-performance solver for the homogenization of periodic non-linear materials relying on a FFT-based scheme including some of the recent advances in the field. As it is the main simulation tool used in this work, its algorithmic and computational structure will strongly impact the developments involved in this thesis, and therefore will be described in details.

2.4.1 Theoretical foundations of FFT based-homogenization methods

FFT-based solvers have been introduced in the context of homogenization of heterogenous materials mechanical behavior. In order to introduce them, we first consider the problem of the periodic homogenization of an heterogeneous elastic media, consisting in a periodic domain Ω submitted to a mean strain state $\underline{\underline{E}}$ and

characterized by its heterogeneous elasticity tensor $\underline{\underline{\Lambda}}(\boldsymbol{x})$. It is written as follow:

$$
\begin{cases}
\quad \boldsymbol{u}(\boldsymbol{x}) = \underline{E} \cdot \boldsymbol{x} + \boldsymbol{u}'(\boldsymbol{x}) & \forall \boldsymbol{x} \in \Omega, \quad \boldsymbol{u}' \# \partial\Omega \\
\quad \underline{\sigma}(\boldsymbol{x}) = \underline{\underline{\Lambda}}(\boldsymbol{x}) : \underline{\varepsilon}(\boldsymbol{x}) & \forall \boldsymbol{x} \in \Omega, \quad \underline{\sigma} \cdot \boldsymbol{n} - \#\partial\Omega \\
\operatorname{div}\left(\underline{\sigma}(\boldsymbol{x})\right) = 0 & \forall \boldsymbol{x} \in \Omega,
\end{cases}
\tag{2.13}
$$

where $\#\partial\Omega$ and $-\#\partial\Omega$ means respectively periodicity and anti-periodicity over $\partial\Omega$, and $\underline{E}$ is a symmetric constant strain tensor. In order to solve this problem, an auxiliary problem is introduced. This problem is the periodic homogenization of an homogeneous linear elastic media characterized by its elasticity tensor $\underline{\underline{\Lambda}}^0$, with an arbitrary polarization field $\underline{\tau}(\boldsymbol{x})$:

$$
\begin{cases}
\quad \boldsymbol{u}(\boldsymbol{x}) = \underline{E} \cdot \boldsymbol{x} + \boldsymbol{u}'(\boldsymbol{x}) & \forall \boldsymbol{x} \in \Omega, \quad \boldsymbol{u}' \# \partial\Omega \\
\quad \underline{\sigma}(\boldsymbol{x}) = \underline{\underline{\Lambda}}^0 : \underline{\varepsilon}(\boldsymbol{x}) + \underline{\tau}(\boldsymbol{x}) & \forall \boldsymbol{x} \in \Omega, \quad \underline{\sigma} \cdot \boldsymbol{n} - \#\partial\Omega \\
\operatorname{div}\left(\underline{\sigma}(\boldsymbol{x})\right) = 0 & \forall \boldsymbol{x} \in \Omega,
\end{cases}
\tag{2.14}
$$

These equations are then expressed in the Fourier space (when not used in subscripts, j is the pure imaginary unit). Taking the Fourier transform of the first equation yields:

$$
\hat{\varepsilon}_{ij}(\boldsymbol{\xi}) = \tfrac{1}{2}\left(\hat{u}'_{i,j} + \hat{u}'_{j,i}\right) = \tfrac{j}{2}\left(\xi_j \hat{u}'_i + \xi_i \hat{u}'_j\right)
\tag{2.15}
$$

$$
\hat{\varepsilon}_{ij}(0) = E_{ij}
\tag{2.16}
$$

which can be introduced in the Fourier transform of the two other equations:

$$
\hat{\sigma}_{ij}(\boldsymbol{\xi}) = j\Lambda^0_{ijkl}\xi_l\hat{u}'_k + \hat{\tau}_{ij}
\tag{2.17}
$$

$$
j\xi_j\hat{\sigma}_{ij} = 0
\tag{2.18}
$$

Combining eqs. (2.17) and (2.18), we get:

$$
\Lambda^0_{ijkl}\xi_h\xi_j\hat{u}'_k = j\hat{\tau}_{ij}\xi_j
$$

We then introduce the inverse $\underline{N}^0$ of the acoustic tensor associated to $\underline{\underline{\Lambda}}^0$: $\underline{N} = \left(\Lambda^0_{ijkl}\xi_l\xi_j\right)^{-1}$, and using the symmetry of $\underline{\tau}$, we can derive the expression of $\hat{u}_k$:

$$
\hat{u}'_k = j\hat{N}^0_{ki}\hat{\tau}_{ij}\xi_j = \frac{j}{2}\left[\hat{N}^0_{ki}\xi_j + \hat{N}^0_{kj}\xi_i\right]\hat{\tau}_{ij}
\tag{2.19}
$$

eq. (2.19) allows to write the expressions of $\hat{u}_{k,h}$ and subsequently $\hat{\varepsilon}_{kh}$:

$$\hat{u}'_{k,h} = j\hat{u}'_k\xi_h = -\frac{1}{2}\left[\hat{N}^0_{ki}\xi_j\xi_h + \hat{N}^0_{kj}\xi_i\xi_h\right]\hat{\tau}_{ij} \tag{2.20}$$

$$\hat{\varepsilon}'_{kh} = \frac{1}{2}\left[j\hat{u}'_k\xi_h + j\hat{u}'_h\xi_k\right]$$
$$= -\frac{1}{4}\left[\hat{N}^0_{ki}\xi_j\xi_h + \hat{N}^0_{kj}\xi_i\xi_h + \hat{N}^0_{hi}\xi_j\xi_k + \hat{N}^0_{hj}\xi_i\xi_k\right]\hat{\tau}_{ij} \tag{2.21}$$

which establishes the expression in Fourier space of the Green operator $\underline{\underline{\Gamma}}^0$ and its symmetric counterpart $\underline{\underline{\Gamma}}^{\diamond 0}$, defined such that $\hat{u}'_{k,h} = -\hat{\Gamma}^0_{khij}\hat{\tau}_{ij}$ and $\hat{\varepsilon}'_{kh} = -\hat{\Gamma}^{\diamond 0}_{khij}\hat{\tau}_{ij}$ and expressed as follow:

$$\hat{\Gamma}^0_{khij} = \frac{1}{2}\left[\hat{N}^0_{ki}\xi_j\xi_h + \hat{N}^0_{kj}\xi_i\xi_h\right] \tag{2.22}$$

$$\hat{\Gamma}^{\diamond 0}_{khij} = \frac{1}{4}\left[\hat{N}^0_{ki}\xi_j\xi_h + \hat{N}^0_{kj}\xi_i\xi_h + \hat{N}^0_{hi}\xi_j\xi_k + \hat{N}^0_{hj}\xi_i\xi_k\right] \tag{2.23}$$

Finally, we can write the solution of the problem 2.14 in real space:

$$\underline{\varepsilon}(\boldsymbol{x}) = \underline{E} - \underline{\underline{\Gamma}}^{\diamond 0} * \underline{\tau} \tag{2.24}$$

and in Fourier space:

$$\underline{\hat{\varepsilon}}(\boldsymbol{\xi}) = -\underline{\underline{\hat{\Gamma}}}^{\diamond 0} : \underline{\hat{\tau}} \tag{2.25}$$
$$\underline{\hat{\varepsilon}}(0) = \underline{E} \tag{2.26}$$

In order to use this auxiliary problem to solve 2.13, the latter can be written as follow:

$$\begin{cases} \boldsymbol{u}(\boldsymbol{x}) = \underline{E}\cdot\boldsymbol{x} + \boldsymbol{u}'(\boldsymbol{x}) & \forall \boldsymbol{x}\in\Omega, \quad \boldsymbol{u}'\#\partial\Omega \\ \underline{\sigma}(\boldsymbol{x}) = \underline{\underline{\Lambda}}^0 : \underline{\varepsilon}(\boldsymbol{x}) + \underline{\tau}(\boldsymbol{x}) & \forall \boldsymbol{x}\in\Omega, \quad \underline{\sigma}\cdot\boldsymbol{n} - \#\partial\Omega \\ \underline{\tau}(\boldsymbol{x}) = \left[\underline{\underline{\Lambda}}(\boldsymbol{x}) - \underline{\underline{\Lambda}}^0\right] : \underline{\varepsilon}(\boldsymbol{x}) & \forall \boldsymbol{x}\in\Omega, \\ \mathrm{div}\left(\underline{\sigma}(\boldsymbol{x})\right) = 0 & \forall \boldsymbol{x}\in\Omega, \end{cases} \tag{2.27}$$

which, according to the resolution of 2.14, admits the following solution:

$$\boxed{\underline{\varepsilon}(\boldsymbol{x}) = \underline{E} - \underline{\underline{\Gamma}}^{\diamond 0} * \left(\left[\underline{\underline{\Lambda}}(\boldsymbol{x}) - \underline{\underline{\Lambda}}^0\right] : \underline{\varepsilon}(\boldsymbol{x})\right)} \tag{2.28}$$

The homogeneous linear elastic media introduced in 2.13 to write 2.27 through its elasticity tensor $\underline{\underline{\Lambda}}^0$ is referred to as *the reference media* or *the reference material*.

eq. (2.28) is called the *periodic Lippmann-Schwinger equation*, and where $*$ denotes the convolution operator. A detailed lecture on the derivation of this equation and associated theoretical background on heterogeneous material can be found in Kröner (1972).

The extension of this framework to non-linear materials is rather straight forward. It consists in replacing the equation $\underline{\sigma}(\boldsymbol{x}) = \underline{\underline{\Lambda}}(\boldsymbol{x}) : \underline{\varepsilon}(\boldsymbol{x})$ in 2.13 by a non-linear constitutive relation symbolically written

$$\underline{\sigma}(\boldsymbol{x}) = \mathcal{F}(\underline{\varepsilon}(\boldsymbol{x})) \tag{2.29}$$

(this formulation is simplified for the sake of readability, the concept of non-linear constitutive relation is detailed in a more consistent manner further, in section 2.4.4). In this case, the original problem under the form 2.27 writes:

$$\begin{cases} \boldsymbol{u}(\boldsymbol{x}) = \underline{\boldsymbol{E}} \cdot \boldsymbol{x} + \boldsymbol{u}'(\boldsymbol{x}) & \forall \boldsymbol{x} \in \Omega, \quad \boldsymbol{u}' \# \partial\Omega \\ \underline{\sigma}^k(\boldsymbol{x}) = \underline{\underline{\Lambda}}^0 : \underline{\varepsilon}(\boldsymbol{x}) + \underline{\tau}(\boldsymbol{x}) & \forall \boldsymbol{x} \in \Omega, \quad \underline{\sigma} \cdot \boldsymbol{n} - \# \partial\Omega \\ \underline{\tau}(\boldsymbol{x}) = \mathcal{F}(\underline{\varepsilon}(\boldsymbol{x})) - \underline{\underline{\Lambda}}^0 : \underline{\varepsilon}(\boldsymbol{x}) & \forall \boldsymbol{x} \in \Omega, \\ \mathrm{div}\,(\underline{\sigma}(\boldsymbol{x})) = 0 & \forall \boldsymbol{x} \in \Omega, \end{cases} \tag{2.30}$$

whose solution is given by eq. (2.24).

The Lippmann-Schwinger equation can also be established for finite strain periodic homogenization. We directly formulate the generic non linear problem, postulating the existence of a constitutive relation between the displacement gradient $\boldsymbol{\nabla u}$ and the Boussinesq stress tensor $\underline{\boldsymbol{S}}$. In this case, the original problem to solve, written with respect to the Lagrangian coordinates, is:

$$\begin{cases} \boldsymbol{u}(\boldsymbol{X}) = \overline{\boldsymbol{\nabla u}} \cdot \boldsymbol{X} + \boldsymbol{u}'(\boldsymbol{X}) & \forall \boldsymbol{x} \in \Omega, \quad \boldsymbol{u}' \# \partial\Omega \\ \underline{\boldsymbol{S}}(\boldsymbol{X}) = \underline{\underline{\Lambda}}^0 : \boldsymbol{\nabla u}(\boldsymbol{X}) + \underline{\tau}(\boldsymbol{X}) & \forall \boldsymbol{x} \in \Omega, \quad \underline{\boldsymbol{S}} \cdot \boldsymbol{N} - \# \partial\Omega \\ \underline{\tau}(\boldsymbol{X}) = \mathcal{F}(\underline{\boldsymbol{F}}(\boldsymbol{X})) - \underline{\underline{\Lambda}}^0 : \boldsymbol{\nabla u}(\boldsymbol{X}) & \forall \boldsymbol{x} \in \Omega, \\ \mathrm{div}\,(\underline{\boldsymbol{S}}(\boldsymbol{X})) = 0 & \forall \boldsymbol{x} \in \Omega, \end{cases} \tag{2.31}$$

where $\overline{\boldsymbol{\nabla u}}$ is the imposed mean displacement gradient and is generally non symmetric. Following exactly the steps detailed above for the small strains formulation, it can be shown that the solution is given by:

$$\boxed{\boldsymbol{\nabla u}(\boldsymbol{X}) = \overline{\boldsymbol{\nabla u}} - \underline{\underline{\Gamma}}^0 * \left(\boldsymbol{\nabla u}(\underline{\boldsymbol{F}}(\boldsymbol{X})) - \underline{\underline{\Lambda}}^0 : \boldsymbol{\nabla u}(\boldsymbol{X}) \right)} \tag{2.32}$$

where the non symmetric Green operator $\underline{\underline{\Gamma}}^0$ of eq. (2.22) intervenes.

2.4.2 Resolution of the Lippmann-Schwinger equation: the basic scheme

Moulinec and Suquet (1998) have proposed to solve eq. (2.28) with an iterative fix-point algorithm scheme that takes advantage of the structure of this equation both in the real space and in the Fourier space. They proposed to solve iteratively the following equations:

$$\begin{cases} \underline{\boldsymbol{\tau}}^k(\boldsymbol{x}) = \left[\underline{\underline{\boldsymbol{\Delta}}}(\boldsymbol{x}) - \underline{\underline{\boldsymbol{\Delta}}}^0 \right] : \underline{\boldsymbol{\varepsilon}}^k(\boldsymbol{x}), & \forall \boldsymbol{x} \in \Omega & (2.33) \\ \underline{\boldsymbol{\varepsilon}}^{k+1}(\boldsymbol{x}) = \underline{\boldsymbol{E}} - \underline{\underline{\boldsymbol{\Gamma}}}^{\diamond 0} * \underline{\boldsymbol{\tau}}^k, & \forall \boldsymbol{x} \in \Omega & (2.34) \end{cases}$$

where superscript k denotes the value of the variables at iteration k. These two equations are solved alternatively until the resulting $\underline{\boldsymbol{\sigma}}^k$ is compatible. The application of $\underline{\underline{\boldsymbol{\Gamma}}}^{\diamond 0}$ generates compatible strain fields. Though, the crucial aspect of the proposed scheme relies in the computation of eq. (2.34) in Fourier space, where the non-local convolution operator becomes a purely local tensorial product, and the mean value of $\underline{\boldsymbol{\varepsilon}}$ can be easily prescribed by setting the value of its Fourier transform for the null frequency. The two equations of the fix point algorithm then become:

$$\begin{cases} \underline{\boldsymbol{\tau}}^k(\boldsymbol{x}) = \left[\underline{\underline{\boldsymbol{\Delta}}}(\boldsymbol{x}) - \underline{\underline{\boldsymbol{\Delta}}}^0 \right] : \underline{\boldsymbol{\varepsilon}}^k(\boldsymbol{x}) \, \forall \boldsymbol{x} \in \Omega & (2.35) \\ \underline{\hat{\boldsymbol{\varepsilon}}}^{k+1}(\boldsymbol{\xi}) = \underline{\underline{\hat{\boldsymbol{\Gamma}}}}^{\diamond 0} : \underline{\hat{\boldsymbol{\tau}}}^k, & \forall \boldsymbol{\xi} \neq 0, \, \underline{\hat{\boldsymbol{\varepsilon}}}^{k+1}(0) = E & (2.36) \end{cases}$$

The complete description of their numerical scheme, now commonly called the *basic scheme*, can be found in Moulinec and Suquet (1998). In practice, the reference media is chosen isotropic linear, and in this case the explicit expression of $\underline{\underline{\boldsymbol{\Gamma}}}^0$ and $\underline{\underline{\boldsymbol{\Gamma}}}^{\diamond 0}$ in function of the Lamé coefficients λ^0 and μ^0 is available, and given in Moulinec and Suquet (1998).

This particular formulation of the algorithm renders it easy to implement, and very convenient for a parallel implementation. Moreover, it does not need the construction nor inversion of a stiffness matrix as in finite elements, and is also a mesh-free technique, allowing to operate directly on microstructure images. Besides, the method can benefit from the performances of modern FFT packages, optimized for parallel computing, allowing for a very efficient computation of the discrete Fourier transform. They also presented a straightforward non-linear extension of the scheme, as it consists in substituting eq. (2.35) the incremental counterpart of eq. (2.29):

$$\underline{\boldsymbol{\tau}}^k(\boldsymbol{x}) = \mathcal{F}\left(\underline{\boldsymbol{\varepsilon}}^k(\boldsymbol{x}) \right) - \underline{\underline{\boldsymbol{\Delta}}}^0 : \underline{\boldsymbol{\varepsilon}}^k(\boldsymbol{x}) \, \forall \boldsymbol{x} \in \Omega \tag{2.37}$$

which also corresponds to the incremental formulation of 2.30. They have shown that this simulation technique is very efficient, and outperforms standard FEM codes used in the same context of periodic homogenization problems.

However, the basic scheme as proposed initially suffers from significant drawbacks:

1. The rate of convergence of the algorithm strongly depends on the Lamé coefficients λ^0 and μ^0 of the reference material. Moulinec and Suquet (1998) provide the expression of the coefficient yielding the best rate of convergence. They correspond to the mean between their maximal and minimal value over the periodic domain Ω:

$$\lambda^0 = \frac{1}{2}\Big(\inf_{\boldsymbol{x}\in\Omega} \lambda(\boldsymbol{x}) + \sup_{\boldsymbol{x}\in\Omega} \lambda(\boldsymbol{x}) \Big) \tag{2.38}$$

$$\mu^0 = \frac{1}{2}\Big(\inf_{\boldsymbol{x}\in\Omega} \mu(\boldsymbol{x}) + \sup_{\boldsymbol{x}\in\Omega} \mu(\boldsymbol{x}) \Big) \tag{2.39}$$

2. The rate of convergence increases linearly with the maximal elastic contrast between the phases contained within the periodic domain Ω as illustrated on fig. 2.38. Convergence is no more ensured for an infinite contrast (*i.e.* in the presence of voids or rigid reinforcements).

3. The simulated fields are polluted by spurious oscillations, often viewed as a manifestation of the Gibbs phenomenon.

Additionally, note that they proposed a formulation to apply mean stress or mixed loadings.
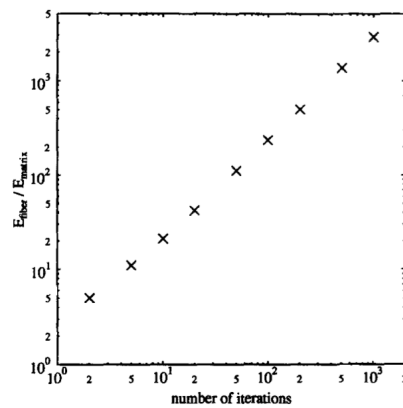
Figure 2.36 – Influence of elastic contrast on the convergence of the basic scheme (Moulinec and Suquet (1998))

2.4.3   Evolutions of the basic scheme

Algorithm improvements

Since their apparition twenty years from now, FFT-based homogenization methods have experienced extensive developments, mainly aimed at extending their scope to a large variety of situations, and solving the main issues of the basic scheme. D. Eyre and Milton (1999) have shown that the basic scheme is equivalent to solving equation eq. (2.28) by approximating the left term by its truncated Neumann expansion, to an order equivalent to the number of iterations before convergence, and shown that the rate of convergence is proportional to the contrast of the eigenvalues of this operator, which are directly related to the material elastic contrast. These results explain the second drawback of the method. By rewriting the problem with a polarization based formulation, they have shown that this new fix-point operator yields a rate of convergence that increases only with the square root of the material elastic contrast. This scheme is known as the *accelerated scheme.*

Similarly, on the base on the fix-point algorithm, Michel, Moulinec, and Suquet (2001) developed an augmented Lagrangian formulation solved with Usawa's algorithm, allowing the extension of the method to infinite contrasts. It has been further extended to small and finite strain elasto-viscoplasticity: Eisenlohr et al. (2013); R. A. Lebensohn, Kanjarla, and Eisenlohr (2012) demonstrated the superior efficiency of spectral methods over finite elements for the considered problems of homogenization of elasto-viscoplastic polycrystalline aggregates with this algorithm.

In parallel, other works have explored alternative iterative resolutions of eq. (2.28) that do not rely on a fix point algorithm. Initially, J. Zeman et al. (2010) and Brisard and Dormieux (2010), have proposed to use Krylov solvers, *i.e.* the conjugated gradient and biconjugate gradient algorithm. They have both shown that this method result in a much faster convergence and an algorithm able to take on infinite contrast materials. Lionel Gélébart and Mondon-Cancel (2013) and have extended it to generic non-linear material behaviors. Using the Conjugate Gradient FFT-based solver embedded in a Newton-Rapshon algorithm solvers, they demonstrated the faster convergence with respect to other schemes, and a reduce sensitivity to the choice of the reference material and contrast of this algorithm (see fig. 2.37). Finally, Kabel, Böhlke, and Schneider (2014), have adapted this approach to hyperelastic materials. Later on, N. Mishra, Vondřejc, and Jan Zeman (2016) have analyzed all mentioned schemes in the light of a similar variational framework and have shown that the Conjugated Gradient scheme has the best performances for solving the linear heterogeneous Lippmann-Schwinger equation.
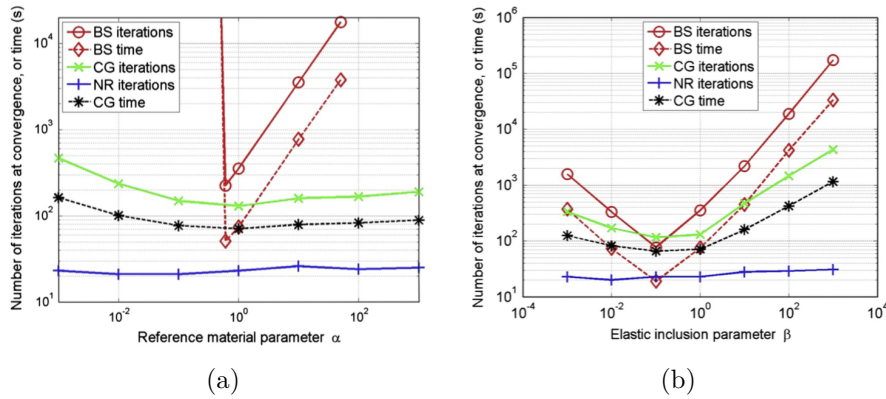
Figure 2.37 – Comparison of the sensitivity to the choice of reference material (a) and material contrast (b) of a incremental generic Newton-Rapshon / Conjugated Gradient based scheme (NR-CG) to the basic scheme (BS) (Lionel Gélébart and Mondon-Cancel (2013))

Green Operator computation improvements

The basic scheme relies on a collocation method for the evaluation of the discrete Green operator: it is computed from a truncated Fourier series of the continuous Green operator. J. Zeman et al. (2010) have proposed to discretize it by the trigonometric collocation method to form a linear system. Their algorithm exhibit no more dependance of the convergence rate on the choice of the reference material, and an increase proportional to the square root of the material contrast, as for the accelerated scheme. Simultaneously, Brisard and Dormieux (2010) have chosen to solve the initial problem by minimizing the variational counterpart of the Lippmann-Schwinger equation, based on the energy principle of Hashin and Shtrikman (Hashin and Shtrikman (1962)). The minimization procedure also relies on extensive use of the FFT algorithm and the application of a discrete Green operator in Fourier space. They derived from this approach a polarization based formulation and shown that it is well-posed for any contrast, including infinite ones.

Taking the analysis further, Brisard and Dormieux (2012) have shown that both the basic-scheme and their Hashin-Shtrikman scheme are two different discretization of the minimization problem. They demonstrated that the basic scheme collocation method is only an asymptotically consistent discretization of the problem. In practice, for any finite resolution, the discretization is non-consistent in the sens that the Green operator value on the approximation space (the discretized space) is only approximated by the truncated Fourier series. Conversely, their

energy-based scheme defines a consistent Green operator, as its exact value on the discretization space of voxel-wise constant fields is used, resulting in a much better approximation for the same resolution, however at a higher computational cost. The use of this modified Green operator also resulted in the suppression of spurious oscillations, showing that what is commonly attributed to the Gibbs phenomenon is due to the non-consistent discretization of the Green operator. The main counterpart of this approach is that the results are dependent on the choice of reference material. They have additionally proposed a filtered-consistent Green operator as a compromise between the two previous ones.

Following a similar idea, Willot (2015) has derived a discrete formulation of the basic-scheme Green operator. It is based on the use of intrinsic expression of finite difference operators in Fourier space. It consists in replacing in eq. (2.23) the terms of the form $\hat{N}_{hi}^0 \xi_j \xi_k$, that are equivalent to the Fourier transform of $N_{hi,jk}^0$, by $\hat{N}_{hi}^0 \xi_j^* \xi_k^*$ where the $\xi_j^* = j\sin(\xi_j)$ are modified frequencies that represented the action in Fourier space of a centered finite difference scheme. This is again an example of consistent discretization of the original problem, in the sense introduced by Brisard and Dormieux (2012). The results show improved convergence rate, and an improved solution characterized by the suppression of spurious oscillations, especially within sharp contrast interfaces.

Recently, Schneider, Merkert, and Kabel (2017) have adapted the framework of FFT-based homogenization to a new type of discretization: trilinear hexahedral finite element on a regular grid. As a result, their numerical scheme, equivalent to finite element formulation, does not suffer from the limitations observed in the previously proposed discretization: it converges for porous media and leads to solution fields without spurious oscillations, while preserving the main advantages of the basic scheme. It shows enhanced efficiency compared to the other schemes, as shown on fig. 2.38. Moreover, they have shown that the so-called "rotated" Finite Difference (FD) based Green Operator (Willot (2015)) is equivalent to a hexahedral finite elements with reduced integration discretization. Their study, together with a formulation of these methods within a variational framework (Brisard and Dormieux (2012); N. Mishra, Vondřejc, and Jan Zeman (2016)) show that the remaining spurious oscillations observed with FE or FD based Green Operators are a feature of the quality of the chosen discretization space as for FEM methods.

To conclude, the evolutions of the iterative algorithm used to solve the Lippmann-Schwinger equation improve the convergence rate of FFT-based solvers and reduce their sensitivity to elastic contrast, without affecting the solution. On the contrary, the evolutions of the discretization formulation, *i.e.* the computation of the Green Operator, improve the quality of the solution and as a result, also
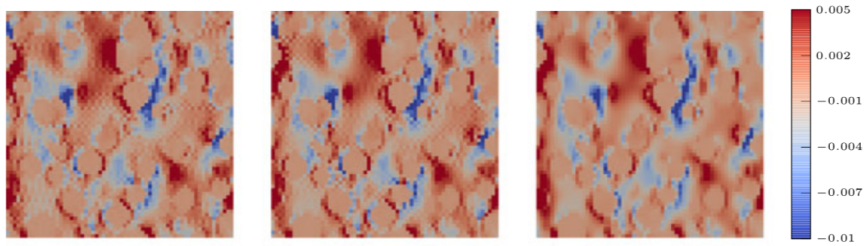
Figure 2.38 – Solution fields for a multi-sphere RVE, basic scheme (left), Willot scheme (middle), linear hexahedral elements (right) (Schneider, Merkert, and Kabel (2017))

improve the convergence rate. In addition, they remove the dependence on the choice of the reference material.

2.4.4 Non Linear material behavior modeling and the UMAT formalism

As exposed in section 2.4.2, FFT-based methods have been, since their first introduction by Moulinec and Suquet (1998), a tool to investigate the local and macroscopic response of non-linear periodic heterogeneous materials. The simulation of the non-linear behavior of materials is a well-established branch of mechanics. The aim of this paragraph is to recall its fundamentals, on which rely the UMAT formalism which is central for the solver AMITEX_FFTP, as well as for the development of composite voxel models presented in chap. 5.

The central notion for the modeling of the mechanical behavior of materials is the concept of constitutive relation. In the general case of non-linear material undergoing irreversible deformation processes, it is the mathematical relation between the stress state of a material and the history of its states. The history can be reduced to the knowledge of the transformation $\boldsymbol{x}(t) = \Phi(\boldsymbol{X}, t)$ that maps the original configuration of the material to its configuration at all instants t. Besides, important assumptions are classically added for the form of constitutive equations:

1. the principle of local state states that the behavior at a given point $\boldsymbol{X}$ depends only on variables defined on the same point, and not on the surrounding domain.

2. the objectivity principle states that the behavior does not depend on the observer. A consequence of this principle is that time cannot be explicitly used in the relation.

3. the constitutive relations must possess the same symmetry properties as the material.

All these principles can be summarized by the following relation:

$$\underline{\sigma}(\boldsymbol{x},t) = \underset{0 \leq \tau \leq t}{\mathcal{F}} \left\{ \Phi(\boldsymbol{X},\tau), \frac{\partial \Phi}{\partial \boldsymbol{X}}(\boldsymbol{X},\tau), \ldots, \frac{\partial^n \Phi}{\partial \boldsymbol{X}^n}(\boldsymbol{X},\tau) \right\} \tag{2.40}$$

This relation states that the chosen stress measure (here the Cauchy stress) depends on the transformation of the material and its gradients up to the order of derivation n. n denotes the order of the theory. We restrict in this to theories up to the second order, that represent the vast majority of the existing theories. It must be noted though that first order theories are the most used for a very large class of material behaviors. In addition, as the formulation as a history functional of eq. (2.40) is not easy to manipulate, it is advantageously replaced by the concept of internal state variables.

A set of internal variables, denoted $\boldsymbol{\alpha}$, whose value depend on the history of the material are defined. The constitutive relation becomes a functional of the different gradients of the transformation and of these internal variables, suppressing the dependence on the whole local history of the material. In addition, the specific behavior of a material is also characterized by a set of material constants $\boldsymbol{C}$ that differentiate it from other materials having the same class of behavior (for instance, stiff of soft elastic materials have the same class of behavior but not the same stress-strain response).

This writes, by including the dependance on $\Phi(\boldsymbol{X},\tau)$ in the variable $\boldsymbol{x}$:

$$\underline{\sigma}(\boldsymbol{x},t) = \mathcal{F} \left\{ \underline{\boldsymbol{F}}(\boldsymbol{x},t), \frac{\partial F}{\partial \boldsymbol{X}}(\boldsymbol{x},t), \boldsymbol{\alpha}(\boldsymbol{x},t), \boldsymbol{C} \right\} \tag{2.41}$$

Depending on the modeling choices, the form of constitutive relation can be written for a different stress measure than the Cauchy stress, in the framework of small strain, replacing $\underline{\boldsymbol{F}}$ and its gradients by the infinitesimal strain tensor $\underline{\boldsymbol{\varepsilon}}$, or include a dependence on the temperature, which has been omitted here to simplify the presentation. In practice, these relations consist in non-linear ordinary differential equation systems that are in practice impossible to solve for all t. For this reason, the simulation of the behavior of non-linear materials classically relies on a time discretization, and computes the relation 2.41 at each time step under its incremental form. Its general formulation for an integration between time steps

t and $t + \Delta t$ writes:

$$\left(\underline{\underline{\sigma}}^{t+\Delta t}, \boldsymbol{\alpha}^{t+\Delta t} \right) = \mathcal{F} \left\{ \underline{\underline{F}}^{t+\Delta t}, \underline{\underline{F}}^{t}, \frac{\partial F^{t}}{\partial \boldsymbol{X}}, \underline{\underline{\sigma}}^{t}, \boldsymbol{\alpha}^{t}, \Delta t, \boldsymbol{C} \right\} \tag{2.42}$$

eq. (2.42) are often derived from evolution equation for $\underline{\underline{\sigma}}$ and $\boldsymbol{\alpha}$ taking the form $\underline{\dot{\underline{\sigma}}} = \mathcal{F}(\cdots)$ and $\dot{\boldsymbol{\alpha}} = \mathcal{G}(\cdots)$ with the same dependancies as eq. (2.41). The latter are then classically approximated with a Runge-Kutta or a θ method discretization scheme to a relation of the form eq. (2.42). They are solved at each Gauss point in FEM simulations, or at each grid point in Fourier based schemes. A detailed description of this branch of the mechanics of materials is found in Besson et al. (2010).

This mathematical framework is generic and encompasses almost all constitutive relations used in numerical simulations. As a result, the UMAT formalism[1]has emerged as a standard computational structure for constitutive relations simulation: constitutive relations are implemented in a UMAT fortran subroutine, which is an executable program with a fixed set of inputs and outputs, adapted for the implementation of relations of the form of eq. (2.42). The compatibility of ABAQUS, CAST3M and AMITEX_FFTP with this formalism makes it possible to use a single implementation of a constitutive relation within them. Similarly, a simulation code compatible with the UMAT formalism is guaranteed to be generic, *i.e.* able to simulate the behavior of virtually any type of material.

2.4.5 AMITEX_FFTP

The solver AMITEX_FFTP has been developed at SRMA in order to build, from the advances of FFT-based simulation methods, a robust, generic and massively parallel tool for the computation of local and homogenized response of non-linear periodic materials, able to make the most of the recently available supercomputers.

It relies on:

1. A fix-point algorithm based on the formulation of the basic scheme of Moulinec and Suquet (1998) both for small and finite strain frameworks.
2. A modified Green operator based on discrete differential operators which is equivalent to Willot (2015) modified Green operator. The AMITEX_FFTP solver results are then, as shown by Schneider, Merkert, and Kabel (2017),

---

[1]A complete description of the UMAT formalism can be found on the website of the code CAST3M: http://www-cast3m.cea.fr/index.php?page=sources&source=umat

strictly equivalent to a finite element solution with a regular grid of linear hexahedral elements with reduced integration.

3. The basic scheme is accelerated with Anderson's acceleration technique (Anderson (1965)).

4. Compatibility with the UMAT formalism.

5. A parallel distributed memory structure relying on the efficient 2decomp library for domain decomposition and associated FFT algorithm.

6. A simple user interface that handles the translation of the input data to the distributed memory structure.

Anderson (1965) acceleration technique, is a linear algebra method used to accelerate iterative solvers. This technique consist in saving four pairs of residual and associated solutions (R^k, d^k) $k = 0, 1, 2, 3$, and used them to construct a subspace of both the residual and solution space. It is used for instance in the non-linear problem solving procedure of the FEM solver CAST3M. A detailed description of its implementation is given in Yang Chen et al. (2019). In AMITEX_FFTP, this acceleration procedure is applied every 3 iterations of the fix-point algorithm to the pair $\left(\left[\underline{\underline{\varepsilon}}^k - \underline{\underline{\varepsilon}}^{k-1} \right], \underline{\underline{\varepsilon}}^k \right)$ to compute the accelerated solution $\underline{\underline{\varepsilon}}_*^k$ for small strain, and to $\left(\left[\nabla u^k - \nabla u^{k-1} \right], \nabla u^k \right)$ to compute ∇u_*^k for finite strain.

Anderson's acceleration is easy to implement and reduces the dependence of convergence rate to elastic contrast. More importantly, it strongly improves the algorithm convergence rate even for non-linear material behaviors without needing to compute a tangent behavior. Used together with the modified Green operator, it makes the simulation with infinite contrast possible and quite efficient. Its only drawback is that it requires to store 3 additional fields pair.

For small strains, the use of the modified Green operator suppresses the dependence on the choice of the reference material, and improves the quality of the solution fields (strong reduction of spurious oscillations).

Thanks to the compatibility with the UMAT formalism, it is a fully versatile solver able to simulate virtually any kind of periodic microstructure.

As a result of this particular features, AMITEX_FFTP is a very efficient and robust FFT-based solver that largely outperforms standard FEM codes (used in the context of periodic homogenization problems), that is usable both on personnel computers as well as high performance computing facilities.

The detailed algorithm implemented in the solver is given on fig. 2.39. The convergence criterion for the algorithm is the equilibrium condition: simulated stress fields must be divergence free in the absence of body forces. In Fourier, this

condition is written for small (2.43) and finite (2.44) strain formulations:

$$\frac{\overline{||j\boldsymbol{\xi}_* \hat{\underline{\boldsymbol{\sigma}}}(\boldsymbol{\xi})||_2}}{\overline{||\hat{\underline{\boldsymbol{\sigma}}}(0)||_2}} \leq \eta \tag{2.43}$$

$$\frac{\overline{||j\boldsymbol{\xi}_* \hat{\underline{\boldsymbol{S}}}(\boldsymbol{\xi})||_2}}{\overline{||\hat{\underline{\boldsymbol{S}}}(0)||_2}} \leq \eta \tag{2.44}$$

where η is the tolerance of the algorithm. Note that the linear extrapolation used for the initial guess is an important feature to improve the convergence of the algorithm.

Time step : $t \longrightarrow t + \Delta t$

$$\text{INPUT} \left(\varepsilon^{t+\Delta t}, \varepsilon^t, \sigma^t, \alpha^t \right) \longrightarrow \left(\sigma^{t+\Delta t}, \alpha^{t+\Delta t} \right) \text{ OUTPUT}$$

$$\text{INPUT} \left(\nabla u^{t+\delta t}, \nabla u^t, \sigma^t, S^t, \alpha^t \right) \longrightarrow \left(\sigma^{t+\Delta t}, S^{t+\Delta t}, \alpha^{t+\Delta t} \right) \text{ OUTPUT}$$

- **Initial guess :** $\varepsilon^0 = \epsilon^t + \dfrac{\Delta_t}{\Delta_{t-1}} \left(\varepsilon^t - \varepsilon^{t-\Delta t} \right)$ $\qquad \nabla u^0 = \nabla u^t + \dfrac{\Delta_t}{\Delta_{t-1}} \left(\nabla u^t - \nabla u^{t-\Delta t} \right)$

$$\left(\sigma^0, \alpha^0 \right) = \mathcal{F} \left(\varepsilon^0, \varepsilon^t, \sigma^t, \alpha^t, C, \Delta t \right) \qquad \left(\sigma^0, \alpha^0 \right) = \mathcal{F} \left(F^0, F^t, \sigma^t, \alpha^t, C, \Delta t \right)$$

$$S^0 = \det(F^0) \sigma^0 F^{0^{-T}}$$

- **Fix-point algorithm : iteration k**

  1. *Convergence test*

  2. *Compute polarization*

     $$\tau^k = \sigma^k - \Lambda^0 : \varepsilon^k \qquad\qquad\qquad \tau^k = S^k - \Lambda^0 : \nabla u^k$$

  3. *Real space to Fourier space*

     $$\hat{\tau}^k = FFT(\tau^k) \qquad\qquad\qquad\qquad \hat{\tau}^k = FFT(\tau^k)$$

  4. *Apply Green operator*

     $$\hat{\varepsilon}^{k+1} = -\Gamma^{\diamond 0} : \hat{\tau}^k, \quad \hat{\varepsilon}^{k+1}(0) = E^{k+1} \qquad \hat{\nabla u}^{k+1} = -\Gamma^0 : \hat{\tau}^k, \quad \hat{\nabla u}^{k+1}(0) = \bar{\nabla} u^{k+1}$$

  5. *Fourier space to Real space*

     $$\varepsilon^{k+1} = FFT^{-1} \left(\hat{\varepsilon}^{k+1} \right) \qquad\qquad\qquad \nabla u^{k+1} = FFT^{-1} \left(\hat{\nabla u}^{k+1} \right)$$

  6. *Anderson's acceleration*

     $$\text{save} \left(\varepsilon^{k+1} - \varepsilon^k, \varepsilon^{k+1} \right) \qquad\qquad \text{save} \left(\nabla u^{k+1} - \nabla u^k, \nabla u^{k+1} \right)$$
     $$\text{if } k \equiv 0[3] \ \varepsilon^{k+1} = \varepsilon_*^{k+1} \qquad\qquad \text{if } k \equiv 0[3] \ \nabla u^{k+1} = \nabla u_*^{k+1}$$
     $$\text{save} \left(\varepsilon_*^{k+1} - \varepsilon^k, \varepsilon^{k+1} \right) \qquad\qquad \text{save} \left(\nabla u_*^{k+1} - \nabla u^k, \nabla u^{k+1} \right)$$

  7. *Constitutive relation*

     $$\left(\sigma^{k+1}, \alpha^{k+1} \right) = \mathcal{F} \left(\varepsilon^{k+1}, \varepsilon^t, \sigma^t, \alpha^t, C, \Delta t \right) \quad \left(\sigma^{k+1}, \alpha^{k+1} \right) = \mathcal{F} \left(F^{k+1}, F^t, \sigma^t, \alpha^t, C, \Delta t \right)$$

     $$S^{k+1} = \det(F^{k+1}) \sigma^0 F^{k+1^{-T}}$$

Figure 2.39 – Algorithm of the iterative FFT based scheme of AMITEX_FFTP for both small (black) and finite (blue) strain formulation

2.5 Synthesis and conclusions

This bibliographic review presented the elements allowing to analyze the behavior of irradiated metals in terms of elementary intragranular localization modes of plastic slip. This analysis allows to link the simulation of the mechanical behavior of irradiated metals to fundamental challenges regarding simulation of elementary slip processes in polycrystals. The learnings of this bibliographic study are synthesized hereafter, together with guidelines that they suggest for the present

work.

The detailed observation of intragranular plastic localization reveals that plastic slip in metals is intrinsically localized. Its elementary deformation process is the formation of slip bands in which shear deformation is much higher than the macroscopic shear accommodated by the grains, and separated by regions showing no sign of plastic slip. The lamellar nature of this process is induced by local softening mechanisms influencing the motion of dislocations at the slip plane scale.

In this light, the increased localization of plastic slip observed in irradiated metals appears as an intensification of the intrinsic characteristics of plastic slip. This is correlated to local highly softening mechanisms, linked to dislocation channeling. This process, which involves the clearing of irradiation induced defects is characterized by the formation of so-called clear bands. The review of their characteristics and repeated correlations to surface slip steps clearly reveals their nature. They can be characterized with no ambiguity as very intense slip bands, in the sense of the intragranular plastic localization mode presented in section 2.1. This implies that clear bands not kink bands.

In the end, the deformation process of irradiated metals appear to be an extreme case of the classical plastic processes of metals, but not different in nature. Hence, simulating slip localization in irradiated metals, more specifically, the formation of clear bands, is fundamentally dependent on the ability to simulate the intrinsic intragranular localization of plastic slip in polycrystals.

Intense slip bands can induce high local strain levels able to initiate void coalescence, or strong stress concentrations at grain boundaries, even for low overall strain levels. This issue is even more critical for irradiated metals where the extreme localization is associated to a strong loss of ductility, and connected to the Irradiation Assisted Stress Corrosion Cracking (IASCC) phenomenon. Therefore, accurately simulation of the formation of slip bands appears crucial for the prediction of ductile or inter-granular fracture of these materials.

Yet, bifurcation analysis indicates that classical crystal plasticity models, widely used for the numerical simulation of such phenomenons, are not able to properly discriminate slip from kink bands, at least at the bifurcation point. This analysis is generally overlooked in the literature of crystal plasticity simulations. In particular, it is never mentioned within dislocation channeling simulation studies, though most works seem to predict the formation of kink bands as clear channels. As slip and kink bands are very different in nature, this could be a crucial shortcoming of classical crystal plasticity, advocating for the use of generalized continuum based models.

We believe that addressing these fundamental and general issues are a

necessary step towards a better understanding of irradiated metals behavior. This provides important guidelines for this work.

First, the necessary study of the general relation between classical crystal plasticity models and the corresponding simulated intragranular localization modes that they predict.

Second, on the basis of the results, moving towards generalized crystal plasticity in order to develop more realistic models aimed at the simulation of the elementary slip processes at the continuum scale in polycrystals.

Third, exploring the explicit modeling of slip bands as an alternative solution to study directly the consequences of intragranular slip localization.

The recent developments of field measurements provide a very rich multi scale description of the elementary process of plasticity in polycrystals, and have been successfully applied to irradiated metals. They show that numerical models should be validated not only on the basis of predicted macroscopic behavior, as it is the case for most irradiated metals studies, but also by achieving a high fidelity of the predicted fields with these measurements, at subgrain scales. **This highlights the need for very high resolution simulations, and the development of field processing methods allowing for a direct comparison between experimental measures and numerically predicted fields.**

The use of FFT-based solver seems then a natural choice for this study. In particular the solver AMITEX_FFTP, coupled with supercomputing facilities, opens the way for high resolution comparison between numerical simulations and field measurements. The two main assets of this solver are its highly parallel implementation, and its generic structure, designed for the simulation of a wide range of physical and mechanical problems. Its development is of central importance for the numerical simulation research at SRMA, and could be useful to the whole material science community. Hence, a final guideline for this work is that **all numerical developments needed to improve numerical simulation of strain localization should be implemented in AMITEX_FFTP in the most possible generic way, and preserve its high parallelization.**

PREDICTION OF SLIP AND KINK BANDING WITH CLASSICAL CRYSTAL PLASTICITY

Chapter Outline

Résumé en français

Dans ce chapitre, nous proposons une nouvelle approche pour étudier la localisation de la déformation plastique dans les polycristaux. Elle s'appuie sur l'analyse systématique de la nature des bandes de localisation simulées, associée à une quantification de leurs caractéristiques physiques. Trois méthodes différentes pour identifier les bandes et les caractériser ont été proposées et comparées. Nous avons conduit une étude théorique simple, au sein du formalisme de la plasticité cristalline classique, qui met en évidence le lien entre la cinématique des bandes en genou et la rotation du réseau cristallin qui se produit en leur sein, et fournit une estimation de l'angle associé.

Nous avons démontré que l'utilisation de l'angle de rotation du réseau comme mesure pour distinguer les bandes de glissement des bandes en genou est une méthode très efficace pour produire des cartes précises des modes de localisation, pour des simulations polycristallines tridimensionnels réalistes avec des structures cristallines complexes. Puisqu'elle s'appuie sur un seuillage des champs de rotation de réseau et de déformation plastique, issus des simulations FFT, cette méthode est simple à mettre en œuvre.

Néanmoins, cette méthode n'utilisant pas comme critère la définition explicite des bandes de glissement ou des bandes en genou, une méthode alternative basée sur des critères géométriques a également été mise en œuvre. Elle permet également d'identifier efficacement la nature des bandes de localisation, mais s'est avérée un peu moins fiable que la première. De plus, reposant sur une méthode spectrale de traitement d'image permettant la segmentation de bandes parallèle au sein d'images binaires, sa mise en œuvre est complexe et n'a été effectuée que pour les images bidimensionnelles.

Ces méthodes ont été utilisées pour étudier la formation des bandes de localisation de la déformation plastique induite par les modèles formulés dans le cadre de la plasticité cristalline classique adoucissante, à partir de simulations FFT 2D et 3D à très haute résolution, rendues possibles par l'utilisation du solveur AMITEX_FFTP. La caractérisation quantitative des populations de bandes a mis en évidence une évolution post-bifurcation distincte des bandes de glissement et des bandes en genou simulées. En raison du durcissement induit par la rotation, les bandes en genou ont tendance à s'élargir à mesure que le chargement augmente. D'autre part, ces caractéristiques, de même que leur fraction volumique sont moins sensibles à la dépendance au maillage et à l'intensité de l'adoucissement. Ces indicateurs quantitatifs montrent également que la quantité de bandes de glissement et de bandes en genou se formant dans les simulations sont similaires.

En accord avec l'analyse de bifurcation d'Asaro et Rice, nous avons montré que les modes de localisation que sont les bandes de glissement ou en genou sont deux modes de bifurcation strictement équivalents pour les simulations polycristallines basées sur les équations de la plasticité cristalline classique adoucissante et des polycristaux aux grains initialement homogènes. De ce fait, dans le cadre de ces équations, seuls les effets de structure jouent un rôle sur la sélection des mode de localisation se formant dans les polycristaux, ce qui induit systématiquement la formation de quantités similaires des deux types de bandes au sein des simulations réalisées dans ce cadre.

Le travail présenté dans ce chapitre démontre que :

- L'analyse de la nature et des caractéristiques physique des bandes de localisation obtenues lors de l'étude de la localisation intra-granulaire de la déformation plastique par des simulations polycristallines, est fondamentale pour évaluer correctement la validité des modèles de plasticité cristalline, à travers la confrontation des résultats aux natures et caractéristiques des bandes observées dans la réalité.

- Les modèles classiques de plasticité cristalline prédisent systématiquement une quantité comparable de bandes de glissement et de bandes en genou, car ce sont deux modes de bifurcation strictement équivalents dans ce cadre, en accord avec l'analyse d'Asaro et Rice.

- Les bandes de glissement sont le principal mode de déformation observé dans les métaux adoucissant, tels que les alliages hypertrempés ou les métaux irradiés, au sein desquels les bandes en genou n'ont pas été observées. Par conséquent, les modèles classiques de plasticité cristalline sont fondamentalement incapables de simuler fidèlement la localisation de la déformation dans ces matériaux.

3.1   Introduction

As seen in chap. 2, Asaro and Rice (1977) bifurcation analysis shows that slip and kink bands arise as equivalent bifurcation modes of CCP equations from a homogeneous state, despite their distinct physical nature. Hence, assessing their ability to correctly predict slips and kinks formation should be a central concern for the simulation of intragranular plastic slip localization modes. Yet, this problem has been largely overlooked in the literature, leaving no clear answer to this question. In an effort to address these shortcomings, this chapter presents a study dedicated to a general characterization of the potential of softening CCP models for the simulation of slip and kink bands formation in polycrystals.

To this end, this study relies on two principal tools. First, a generic softening CCP model is implemented within AMITEX_FFTP, and is used to produce high resolution three dimensional polycrystalline simulations. Second, three original processing strategies have been developed to analyze the field outputs of the FFT simulations. They allow to build localization mode maps and quantitative/statistical indicators to identify and characterize simulated slip and kink band populations. The first two parts of this chapter, sections 3.2 and 3.3, are dedicated to the presentation of these elements.

Then, we present in section 3.4 the application of these processing methods to the characterization of the localization band populations predicted by the generic model on realistic and high resolution polycrystalline unit cells, for various crystal structures and material parameters. This leads, after a brief evaluation of the pertinence of the processing methods, to a discussion of the origin of slip and kink bands formation with CCP, which highlights its fundamental limitations. In addition, a comparison of our results with a simulation of a state of the art physics based model of irradiated austenitic stainless steel is given to confirm the conclusions obtained with the simple and generic CCP model.

3.2   Crystal plasticity model

Asaro and Rice (1977) have shown in their theoretical study that the onset of slip localization is only determined by the value of the equivalent tangent modulus of the material. For this reason, we believe that a generic constitutive model that allows to reproduce a softening or hardening behavior with only a few parameters is sufficient to study the process of slip and kink band formation within classical crystal plasticity simulations. Besides, this approach avoids any unnecessary material complexity in order to focus on the link between softening/hardening rate and
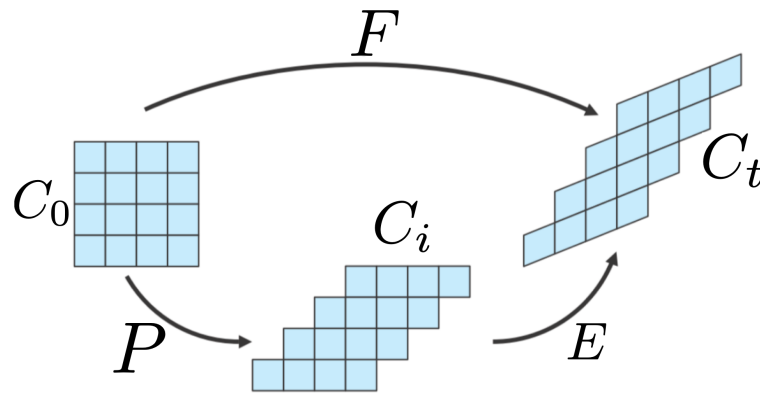
Figure 3.1 – Multiplicative decomposition of transformation gradient: initial C_0, isoclinic C_i and current C_t configurations

intragranular slip localization.

This constitutive model is described in this section. Kinematics and constitutive equations are detailed 3.2.1 and 3.2.2, followed by the description of the numerical integration procedure in section 3.2.3.

3.2.1 Crystal plasticity kinematics

The crystal plasticity formulation is based on the classical multiplicative decomposition of the deformation gradient tensor $\underline{F}$ into its elastic part $\underline{E}$ and its plastic part $\underline{P}$ (Mandel 1973):

$$\underline{F} = \underline{E} \cdot \underline{P}$$

where $\underline{P}$ maps the reference configuration C_0 to the isoclinic stress-free local configuration C_i, where crystal lattice orientation is unchanged with respect to the reference configuration, and $\underline{E}$ maps the intermediate local configuration into the deformed configuration (or current configuration) C_t, describing crystal lattice distortion and rotation (fig. 3.1). The mass densities of the material with respect to C_t and C_i are noted respectively ρ and ρ_i. This decomposition leads to an additive partition of the velocity gradient $\underline{L} = \dot{\underline{F}} \cdot \underline{F}^{-1}$:

$$\underline{L} = (\dot{\underline{E} \cdot \underline{P}})(\underline{E} \cdot \underline{P})^{-1} = \left(\dot{\underline{E}} \cdot \underline{P} + \underline{E} \cdot \dot{\underline{P}}\right)\left(\underline{P}^{-1} \cdot \underline{E}\right) = \dot{\underline{E}} \cdot \underline{E}^{-1} + \underline{E} \cdot \dot{\underline{P}} \cdot \underline{P}^{-1}\underline{E}^{-1}$$

$$\underline{L} = \underline{L}^e + \underline{E} \cdot \underline{L}^p \cdot \underline{E} \tag{3.1}$$

The plastic deformation is induced by isochoric glide, therefore:

$$J^p = \det(\underline{P}) = 1 \quad \text{and} \quad J^e = \det(\underline{E}) = J = \det(\underline{F}) \tag{3.2}$$

After some calculation (detailed in appendix B.1.1), the internal power mass density of the material can be written:

$$p_i^m = \frac{1}{\rho_i} \left[\underline{\Pi}^e : \dot{\underline{\mathcal{E}}}^e + \underline{\Pi}^M : \underline{L}^p \right] \tag{3.3}$$

where $\underline{\Pi}^e$ and $\underline{\Pi}^M$ are respectively the second Piola-Kirchhoff and Mandel stress tensors with respect to the $\underline{E}$, defined on C_i by:

$$\underline{\Pi}^e = J^e \underline{E}^{-1} \cdot \underline{\sigma} \cdot \underline{E}^{-T} \tag{3.4}$$

$$\underline{\Pi}^M = J^e \underline{E}^T \cdot \underline{\sigma} \cdot \underline{E}^{-T} \tag{3.5}$$

and where $\underline{\sigma}$ the Cauchy stress tensor; and $\underline{\mathcal{E}}^e$ is the Green-Lagrange elastic strain tensor, defined by:

$$\underline{\mathcal{E}}^e = \frac{1}{2} \left(\underline{E}^T \cdot \underline{E} - \underline{1} \right) \tag{3.6}$$

The plastic velocity gradient $\underline{L}^p = \dot{\underline{P}} \cdot \underline{P}^{-1}$ is then determined by the shearing rate of the N_s material slip systems, characterized by their slip plane normal direction $\boldsymbol{n}^s$ and glide direction $\boldsymbol{m}^s$ through the relation:

$$\underline{L}^p = \sum_s^N \dot{\gamma}^s \underline{\boldsymbol{\mu}}^s \tag{3.7}$$

where $\underline{\boldsymbol{\mu}}^s = \boldsymbol{m}^s \otimes \boldsymbol{n}^s$ is the Schmid orientation tensor of slip system s. This kinematical framework allows to distinguish between the transformation of material and crystal lattice directions. The latter are indeed transformed by the elastic part of the transformation characterized by $\underline{E}$. Consequently, the elastic rotation $\underline{R}^e$, defined through the polar decomposition of $\underline{E}$, given by:

$$\underline{E} = \underline{R}^e \cdot \underline{U}^e \tag{3.8}$$

characterizes the rotation of the crystal lattice directions, and the corresponding angle θ can be computed with eq. (3.9). Additionally, we introduce two scalar measures of the plastic slip intensity, the effective cumulative plastic strain p, defined through eq. (3.10), and the cumulative plastic slip on slip system s, γ_{cum}^s,

defined through eq. (3.11).

$$\theta = \arccos\left(\frac{1}{2}(\text{tr}(\underline{\boldsymbol{R}}^e) - 1)\right) \tag{3.9}$$

$$p = \int_0^t \sqrt{\underline{\boldsymbol{L}}^p : \underline{\boldsymbol{L}}^p} \, dt \tag{3.10}$$

$$\gamma_{cum}^s = \int_0^t |\dot{\gamma}^s| \, dt \tag{3.11}$$

where t denotes the time variable.

3.2.2   Constitutive equations

We introduce the Helmholtz free energy mass density ψ. Under isothermal conditions, the Clausius-Duhem inequality with respect to C_i is written as:

$$p_i^m - \dot{\psi} \geq 0 \tag{3.12}$$

Using eqs. (3.3) and (3.7), and multiplying by ρ_i, it becomes:

$$\underline{\boldsymbol{\Pi}}^e : \dot{\underline{\boldsymbol{\mathcal{E}}}}^e + \sum_{s=1}^N \tau^s \dot{\gamma}^s - \rho_i \dot{\psi} \geq 0 \tag{3.13}$$

where $\tau^s = \underline{\boldsymbol{\Pi}}^M : \underline{\boldsymbol{\mu}}^s$ is the resolved shear stress on slip system s. Assuming that ψ is a function of the elastic Green-Lagrange strain and of the cumulative plastic slip on each slip system: $\psi = \psi(\underline{\boldsymbol{\mathcal{E}}}^e, \gamma_{cum}^s)$, the following constitutive equations are chosen:

$$\underline{\boldsymbol{\Pi}}^e = \rho_i \frac{\partial \psi}{\partial \underline{\boldsymbol{\mathcal{E}}}^e} = \underline{\underline{\boldsymbol{\Lambda}}} : \underline{\boldsymbol{\mathcal{E}}}^e \tag{3.14}$$

$$\dot{\gamma}^s = \text{sign}(\tau^s)\left\langle \frac{|\tau^s| - \tau_c^s}{K} \right\rangle^n \tag{3.15}$$

$$\tau_c^s = \tau_0^s - \Delta\tau^s\left[1 - \exp\left(-\frac{\gamma_{cum}^s}{\gamma_0^s}\right)\right] + H^s\gamma_{cum}^s \tag{3.16}$$

eq. (3.14) describes the linear elasticity of the crystal through its elastic moduli tensor $\underline{\underline{\boldsymbol{\Lambda}}}$. eq. (3.15) is the flow rule giving the plastic slip rate on each slip system, where τ_c^s denotes the critical resolved shear stress on slip system and $\langle a \rangle$ denotes the positive part of a. Finally, eq. (3.16) describes the evolution equation of the critical resolved shear stress. The detailed thermodynamically consistent derivation

of these equations is given in appendix B.1.2.

The behavior is characterized by $2 + 4N_s$ material coefficients, where N_s is the number of distinct slip system families, in addition to elastic constants: n and K are respectively the exponent and coefficient of the Norton flow-rule, τ_0^s is the initial critical shear stress of slip system s, $\Delta\tau^s$ and γ_0^s are the parameters controlling the softening intensity and rate, and finally H^s is the linear hardening modulus.

It is important to note that the exponential softening term used eq. (3.16) is representative of the softening rate derived from physically based models for irradiated metals. Indeed it can be shown that in the case of a single slip system, combining the equations used to account for the hardening effect of irradiation induced crystal defects on the one hand, and the evolution equations modeling the sweeping of these defects on the other hand, yields an exponential softening of the critical resolved shear stress. A proof is provided in appendix B.1.3.

3.2.3   Numerical integration

In order to completely determine the material state, the constitutive equation must be solved for each γ^s and the elastic deformation gradient $\underline{E}$. The choice has been made to use $\underline{\mathcal{E}}^e$ as the integration variable for the elastic strain state, as simplifies the equation system and reduces its size by 3 ($\underline{E}$ has 9 independent components, $\underline{\mathcal{E}}^e$ only 6). In addition, the Cauchy stress $\underline{\sigma}$ must be computed. This integration procedure can be formally written as follow, from time step t to time $t + \Delta t$:

$$\{\underline{\sigma}_t, \gamma_t^s, \underline{\mathcal{E}}_t^e\} \rightarrow \boxed{\text{integration procedure}} \rightarrow \{\underline{\sigma}_{t+\Delta t}, \gamma_{t+\Delta t}^s, \underline{\mathcal{E}}_{t+\Delta t}^e\}$$

where Δt is the time increment value. For the integration procedure, the internal variables and Cauchy stress value at previous time step, indicated by subscript t, are known. The value of the imposed transformation gradient at the end of the time step $\underline{F}_{t+\Delta t}$ is known, and the equation are solved for the value of Cauchy stress and internal variables at the end of the time increment, indicated by subscript $t + \Delta t$. To solve the constitutive and kinematical equations, the implicit Newton's method is used. It consists in solving a system of residual equations formally written as:

$$\{\Delta v - \Delta t \dot{v}(t + \Delta t) = 0$$

where v represent the integration variables. The flow rule (eq. (3.15)) is easily linearized under this form. For the elastic strain increment residual equation, following the work of Weber and Anand (1990), we use an implicit estimate of

$\underline{\boldsymbol{P}}$ at the end of time increment to evaluate $\underline{\boldsymbol{E}}_{t+\Delta t}$. This method, detailed in appendix B.1.4, yields the following approximation for $\underline{\boldsymbol{E}}_{t+\Delta t}$:

$$\underline{\boldsymbol{E}}_{t+\Delta t} = \underline{\boldsymbol{F}}_{t+\Delta t} \cdot \underline{\boldsymbol{P}}_t^{-1} \cdot \left[\mathbf{1} - \sum_{s=1}^{N} \Delta\gamma^s \underline{\boldsymbol{\mu}}^s\right] \tag{3.17}$$

Finally, dropping the subscript $t+\Delta t$ to simplify the notation, the following system of equation must be solved for γ^s and $\underline{\boldsymbol{\mathcal{E}}}^e$:

$$\begin{cases} R_{\mathcal{E}^e} = \Delta\underline{\boldsymbol{\mathcal{E}}}^e + \underline{\boldsymbol{\mathcal{E}}}^e - \underline{\boldsymbol{\mathcal{E}}}^* + \sum_{s=1}^{N}\left[\Delta\gamma^s\left(\underline{\boldsymbol{C}}^* \cdot \underline{\boldsymbol{\mu}}^s\right)\right] = 0 \\[2mm] R_{\gamma^s} = \Delta\gamma^s - \Delta t\, \mathrm{sign}(\tau^s)\left\langle \dfrac{|\tau^s| - \tau_c^s}{K} \right\rangle^n = 0 \qquad 1 \le s \le N \end{cases} \tag{3.18}$$

where $\underline{\boldsymbol{\mathcal{E}}}^*$ and $\underline{\boldsymbol{C}}^* = \underline{\boldsymbol{E}}^{*T} \cdot \underline{\boldsymbol{E}}^*$ are respectively the Green-Lagrange strain tensor and the right Cauchy-Green deformation tensor associated to $\underline{\boldsymbol{E}}^* = \underline{\boldsymbol{F}}_{t+\Delta t} \cdot \underline{\boldsymbol{P}}_t^{-1}$. Additionally, the values of τ^s and τ_c are computed at each iteration with the relation $\tau^s = \underline{\underline{\boldsymbol{\Pi}}}^M : \underline{\boldsymbol{\mu}}^s$ and eq. (3.16).

This non linear system of equations has been implemented within the Mfront code generator (Helfer et al. 2015). This software automatically generates a UMAT subroutine implementing a resolution of the system with the Newton-Raphson algorithm, which consists in the following iterative algorithm, written in symbolic notation:

$$\begin{cases} \mathcal{J}_R^k(v^k) \cdot \Delta v^{k+1} = -R^k(v^k) \\[2mm] v^{k+1} = v^k + \Delta v^{k+1} \end{cases} \tag{3.19}$$

v^k, $R^k(v^k)$ and $\mathcal{J}_R^k$ denote respectively the value of the solution, the residual equations and of the Jacobian matrix of the eq. (3.18) system, at the step k of the algorithm. The system is solved for the increment Δv^{k+1} at each time step, then used to update the solution v of the system. Mfront provides the possibility of evaluating numerically the Jacobian matrix, allowing a robust and easy implementation of the resolution procedure. However, in order to speed-up the algorithm, the exact expression of the Jacobian matrix (see eq. (3.20)) has been implemented.

$$\mathcal{J}_R = \begin{bmatrix} \dfrac{\partial R_{\mathcal{E}^e}}{\partial \mathcal{E}^e} & \dfrac{\partial R_{\mathcal{E}^e}}{\partial \Delta\gamma^j} \\[2mm] \dfrac{\partial R_{\gamma^s}}{\partial \mathcal{E}^e} & \dfrac{\partial R_{\gamma^s}}{\partial \Delta\gamma^j} \end{bmatrix} \tag{3.20}$$

The detailed calculation of its terms is provided in appendix B.1.4.

3.3   Slip and kink localization modes analysis

Intragranular slip localization bands are typically one or two orders of magnitude below the grain size. Hence, characterizing the potential of CCP for the prediction of slip and kink banding must rely on high resolution representative polycrystalline simulations. They involve three dimensional mechanical fields containing a high number of slip localization bands, whose characteristics and nature should be meticulously analyzed. In that respect, producing a systematic analysis of localization bands is a central issue in the study of intragranular localization bands in polycrystalline simulations.

This section presents original post processing strategies developed during the present PhD thesis in order to to identify localization bands in mechanical fields and determine their nature. First, a preliminary analytical study of slip and kink banding is presented in order to highlight the physical measure that can be used to distinguish them. Then, a simple threshold based methodology exploiting this difference to obtain a segmentation of slip and kink bands maps is proposed. An alternative approach based on geometrical criteria and image processing is detailed after. Finally, the last section presents a complementary method relying on slip profiles processing, aimed at extracting statistical information to characterize localization bands.

3.3.1   Slip and kink banding: preliminary analytical modeling

As discussed in section 2.1, two of the central characteristics that distinguish slip and kink bands are the orientation of the band with respect to the slip system directions, and the presence of noticeable lattice rotation that is characteristic of kinks. We will show here that a very simple modeling of an intragranular slip localization band within the framework of classical crystal plasticity can capture this feature.

We approximate a plastic slip localization band as an elasto-plastic bidimensional layer embedded between two rigid layers and submitted to a pure shear sollicitation (fig. 3.2). The following assumptions are made to simplifiy the problem. In the case of the slip band:

1. We consider an infinite localization band: the problem is then independent of the x_m coordinate.

(a) slip band   (b) kink band
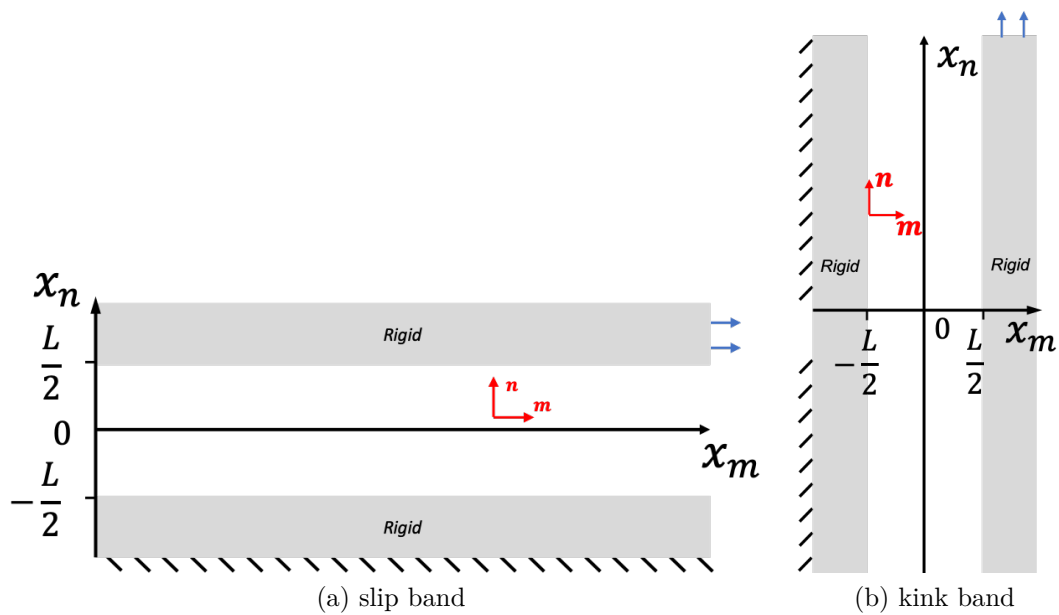
Figure 3.2 – Schematic modeling of the local shearing of a crystal within a slip localization band for a slip band (a) and a kink band (b). The central phase is elasto-plastic and deforms through a singe slip system, whose orientation is indicated in red.

2. The localization band undergoes pure shear:

$$\boldsymbol{u} = u(x_n)\boldsymbol{m} \tag{3.21}$$

3. the localization band must accommodate a mean shear strain $\bar{\gamma}$. This is equivalent to the boundary conditions:

$$u(-\tfrac{L}{2}) = 0 \quad \text{and} \quad u(\tfrac{L}{2}) = \bar{\gamma}L \tag{3.22}$$

4. The central phase has a perfectly plastic behavior with only one active slip system. The yield condition is:

$$\tau = \tau_c \tag{3.23}$$

5. The elastic behavior is linear isotropic, expressed with Lame coefficient (λ, μ) is:

$$\underline{\boldsymbol{\Pi}}^e = \lambda \operatorname{tr}(\underline{\boldsymbol{\mathcal{E}}}^e)\underline{\boldsymbol{1}} + 2\mu\underline{\boldsymbol{\mathcal{E}}}^e \tag{3.24}$$

For the case of the kink band, the assumptions are the same but the directions $\boldsymbol{m}$ and $\boldsymbol{n}$ are inverted.

Considering, as illustrated by the examples of section 2.1.2, that localization bands often have a homogeneous aspect along their length, the first three assumptions are a reasonable approximation of their kinematics far from their ends. The two last assumptions are made to simplify calculations. Neglecting elastic strain outside of the localization band justifies the assumptions of the rigid layer bounding it. Indeed, in most crystals, elastic constants are much higher than the critical shear stress, yielding small elastic strains. This problem is solved for the particular cases of the slip and the kink band. The detailed calculations are provided in appendix B.1.5, only the results are mentioned here.

In both cases, homogeneous fields in the band are the solution of the problem and the slip field is given by $\gamma \simeq \bar{\gamma}$. For the slip band, the elastic deformation gradients is $\underline{\boldsymbol{E}} \approx \underline{\boldsymbol{1}}$, showing that far from their tips, the formation of slip bands tends to cause no elastic strain, and thus no rotation of the crystal lattice. On the other hand, for the kink band, the elastic deformation gradient is:

$$\underline{\boldsymbol{E}} \approx \begin{pmatrix} 1 & \gamma \\ -\gamma & 1 \end{pmatrix} \tag{3.25}$$

eq. (3.25), combined with eq. (3.9) allows to compute the crystal lattice rotation angle inside the kink band. It is given by $\theta = \arcsin(\frac{-\gamma}{\sqrt{1+\gamma^2}})$, which, when $\bar{\gamma} \approx \gamma$ is

small, reduces to:

$$\boxed{|\theta| \approx |\gamma| \approx \bar{\gamma}} \tag{3.26}$$

This rather crude modeling shows that the crystal plasticity equations associated to the geometrical definition of slip and kink bands is sufficient to predict lattice rotation occurring within kink bands.

The approximation $|\theta| \approx |\gamma| \approx \bar{\gamma}$ indicates that for small deformations, the lattice rotation angle in kink bands evolves linearly with plastic slip. It provides an interesting estimation of the lattice rotation angle within kink bands: the magnitude of the crystalline rotation is roughly equal to the mean shear strain accommodated by the band.

Moreover, it shows that lattice rotation is the key output of our generic crystal plasticity model to look at in order to differentiate slip and kink bands if one does not want to rely on geometrical criterions. This important result is the cornerstone of the first strategy proposed to identify and classify slip localization bands populations in simulations results, presented in the next section.

3.3.2 Lattice rotation based strategy

In order to identify localization bands, we use the cumulative effective plastic strain field p (eq. (3.10)) as a measure of local slip intensity, and the lattice rotation angle field θ (eq. (3.9)) as a measure of the local intensity of lattice rotation. They are then used to define L and R, indicator functions respectively of slip localization and high lattice rotation areas, by the relations:

$$L(\boldsymbol{X}) = \mathcal{H}(p(\boldsymbol{X}) - \bar{p} \cdot \Phi_L) \tag{3.27}$$
$$R(\boldsymbol{X}) = \mathcal{H}(\theta(\boldsymbol{X}) - \bar{\theta} \cdot \Phi_R) \tag{3.28}$$

where $\mathcal{H}$ is the Heaviside step function and $\boldsymbol{X}$ is the material point coordinate vector. They indicate regions where fields p and θ are above a level defined by their mean value $\bar{p}$ and $\bar{\theta}$ over the whole unit cell, multiplied by suitably chosen relative thresholds, Φ_L and Φ_R respectively.

Therefore L maps plastic strain localization areas that are expected to be, according to Asaro and Rice (1977), the slip and kink bands. The results of the preliminary study suggests a practical definition of kink bands in simulation results as areas exhibiting both intense plastic slip and high lattice rotation, that is $L(\boldsymbol{X}) = 1$ and $R(\boldsymbol{X}) = 1$. We then assume that localization areas without intense

lattice rotation are slip bands. Hence, slip and kink bands indicator functions, S and K, are given by:

$$K(\boldsymbol{X}) = L(\boldsymbol{X}) \cdot R(\boldsymbol{X}) \tag{3.29}$$

$$S(\boldsymbol{X}) = L(\boldsymbol{X}) - K(\boldsymbol{X}) \tag{3.30}$$

and can be plotted simultaneously to evidence localization modes. Finally, these functions are used to determine for the slip and kink bands population, volume fractions, f_S and f_K, and mean value of equivalent plastic strain, $\bar{p}_S$ and $\bar{p}_K$, as follows:

$$\bar{p}_K = \frac{1}{f_K V} \int_\Omega K(\boldsymbol{X}) p(\boldsymbol{X}) \boldsymbol{dX} \tag{3.31}$$

$$\bar{p}_S = \frac{1}{f_S V} \int_\Omega S(\boldsymbol{X}) p(\boldsymbol{X}) \boldsymbol{dX} \tag{3.32}$$

This processing strategy, has the advantage of being very simple, and straightforward to apply in the context of FFT based simulations. Indeed, FFT based solvers handle mechanical fields in the form of 3D images, very well suited for the computation of the indicator functions and associated quantities defined above.

3.3.3   Image processing and morphology based strategy

The occurence of lattice rotation within kink bands is only a consequence of their kinematics and not a proper definition. Thus, using it as the only criterion to distinguish slip and kink bands could lead to identify a slip band crossing a high lattice rotation area, as a kink band. Besides, the strategy described in section 3.3.2 does not includes geometrical criterions for the definition of L, which is hoped to be exclusively composed of band-shaped regions. These considerations emphasize the need for an identification method based on geometric criteria. Additionally, it will be used to verify the results of the threshold based strategy.

This section presents the image processing method that we developed for the geometrical identification of slip and kink bands. This work was made possible thanks to a contribution of Dr. Frank Nguyen, who developed the spectral separation method. Starting from the binary image of the field $L(\boldsymbol{X})$, this image processing method is required to:

- Identify band-shaped objects, *i.e.* thin objects and segment them individually.

- Determine the orientation of each identified band-shaped object and compare

to the crystal slip planes orientations to determine its slip or kink nature.

The main challenge is then the segmentation of the band-shaped object populations with a different orientation, that could be crossing each other. A spectral method has been chosen to achieve this operation. It is indeed possible in Fourier space to identify the dominant orientations of elongated objects in a binary image. The principles of this processing technique are briefly explained here, but a very detailed description is given in appendix C.1.

fig. 3.3 shows a binary image (a) of many overlapping lines segments that are oriented along three specific direction. On (b), which shows the DFT of the image, three main lines crossing the origin corresponding to the three fundamental frequencies of each of the line segments orientations, rotated from $\frac{\pi}{2}$. Detection of these lines delivers easily the orientation of the bands in the original image.

(a)   (b)   (c)

Angle (°)

(d)
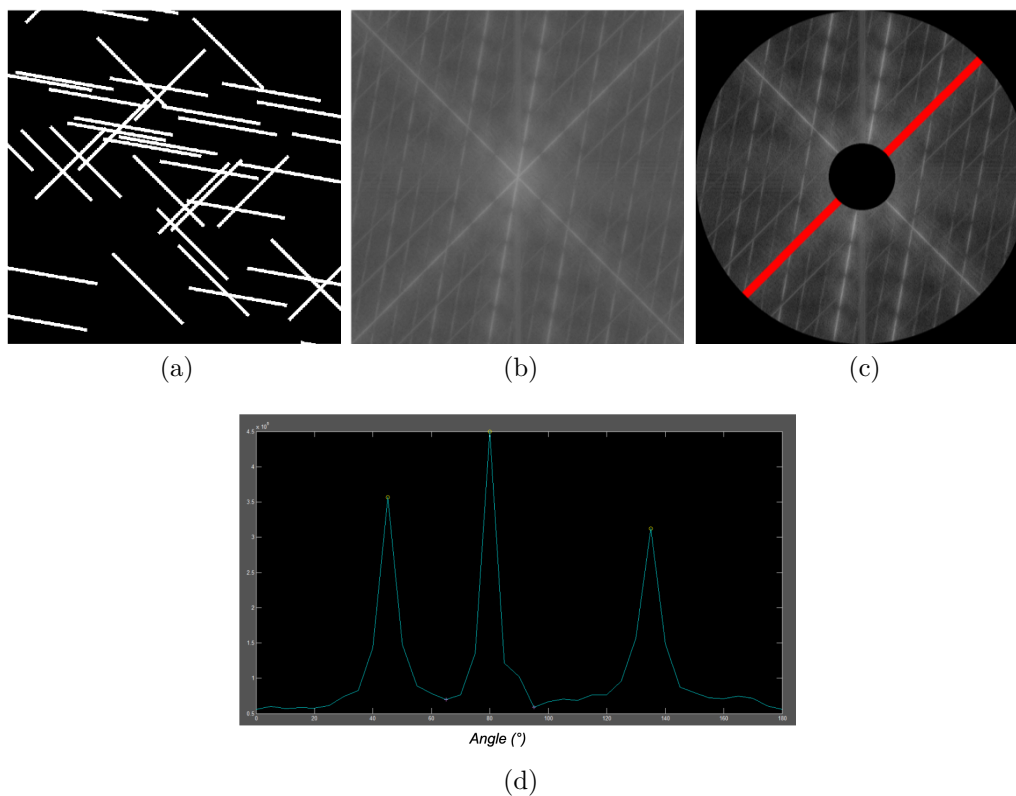
Figure 3.3 – Different steps of the spectral segmentation of line segment populations in a binary image. (a) binary image containing 3 different line segments families with the same orientation, (b) DFT of (a), (c) Highlight of one angular sector in the filtered frequency domain (d) Computed spectral angular density (images provided by F. Nguyen image processing course)

(a)   (b)
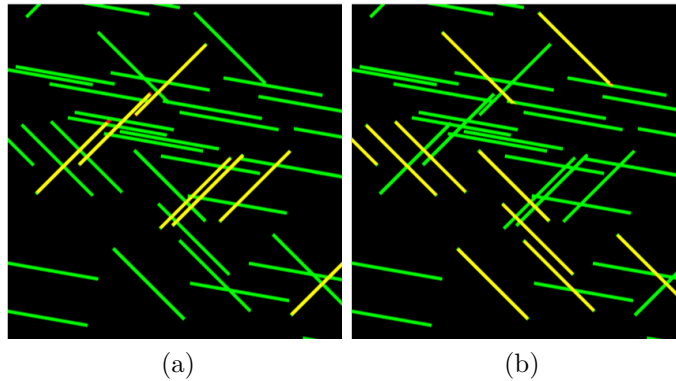
Figure 3.4 – Segmentation of two out of the three line segment families of fig. 3.3 (images provided by F. Nguyen image processing course)

The method consists in calculating the energy norm of each angular sector of the spectrum, as illustrated in (c), to obtain a curve describing the spectral angular density of the image. The maximums of this curve indicate the orientation of each band family in the image. By applying the inverse discrete Fourier transform of each of these identified sectors, an image containing only the corresponding line segments can be reconstructed, which allow for the segmentation of the different line segments in the image, that are displayed on fig. 3.4.

This spectral separation method is applied grain per grain on the localization indicator L. The reconstructed image of each band family in the grain is segmented to find connected objects with a high aspect ratio (*i.e.* bands) and determine their orientation angle. If the latter is consistent with a kink or a slip band, they are added to associated indicator functions. S and K are thus constructed grain per grain and assembled. It has been implemented only for two dimensional images during this work. A summary of this process is given on figure fig. 3.5, where the different steps of the method are illustrated on a binary image extracted from one of the simulations of this study.

3.3.4   Slip profiles processing

With a view to establishing statistical data on localization bands, each band should be properly identified and characterized. In that respect, the field processing methods presented above suffer some limitations.

First, as localization bands intersect, a high number among them will be cut into more than one object in the segmentation process. Reconstructing the bands from these fragments would requires a complex algorithm. Besides, the
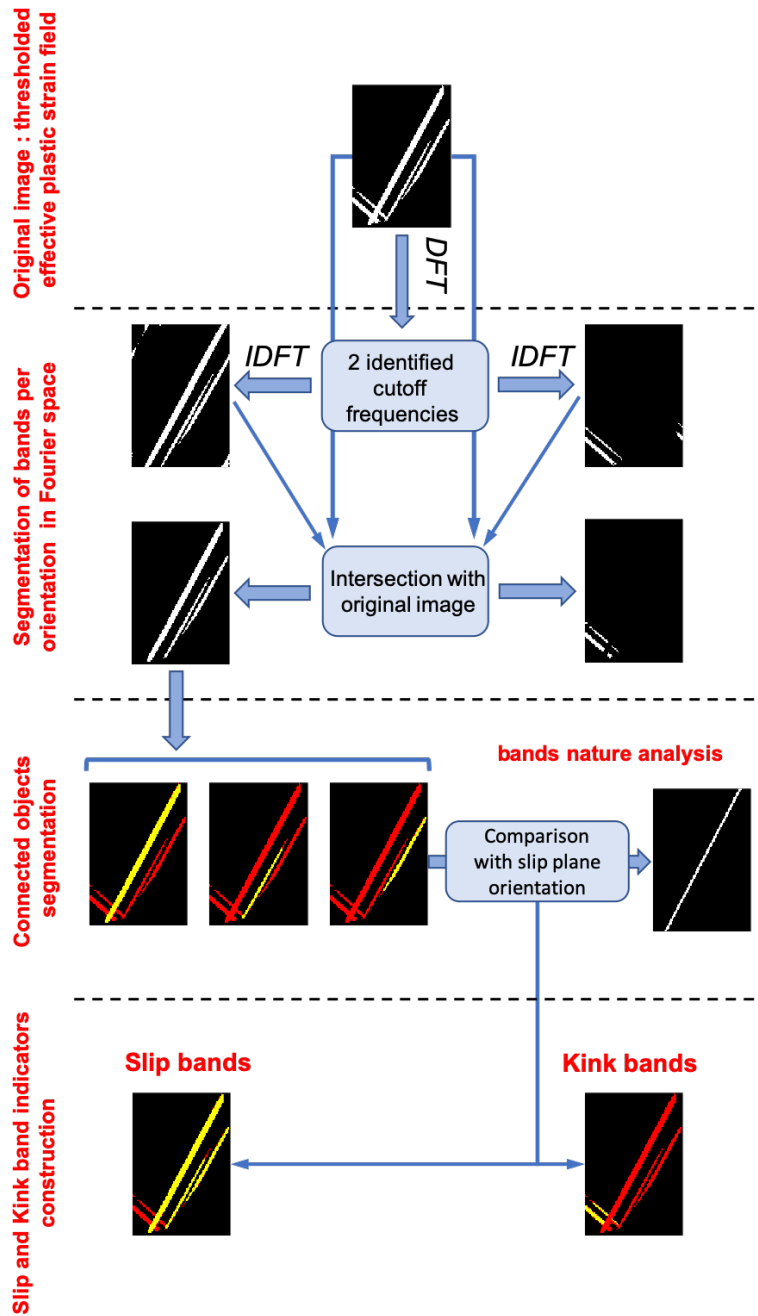
Figure 3.5 – Illustration of the second slip and kink band analysis strategy. DFT and IDFT denote discrete Fourier transform and its inverse. The identified objects at each step are displayed in yellow

superposition of post-processing algorithm layers would require a careful study of the influence that they have on the following processing layer, resulting in a complex process and a loss of reliability. Having independent processing methods seems a more cautious approach. If these independent methods can measure similar quantities, their comparison allow for a richer and more robust analysis.

Therefore, an additional and independent quantitative analysis method has been developed to provide statistical data on band populations from polycrystalline simulations field results. It consists in extracting for each slip variable field γ^s, one slip profile in the direction $\boldsymbol{n}^s$ and one in the direction $\boldsymbol{m}^s$, for each grain. They are interpolated starting from the grain barycenter. The two profiles are then processed to find their maximums, which will coincide with slip bands for the first profile, and kink bands for the second. This is illustrated on the diagram of fig. 3.6.
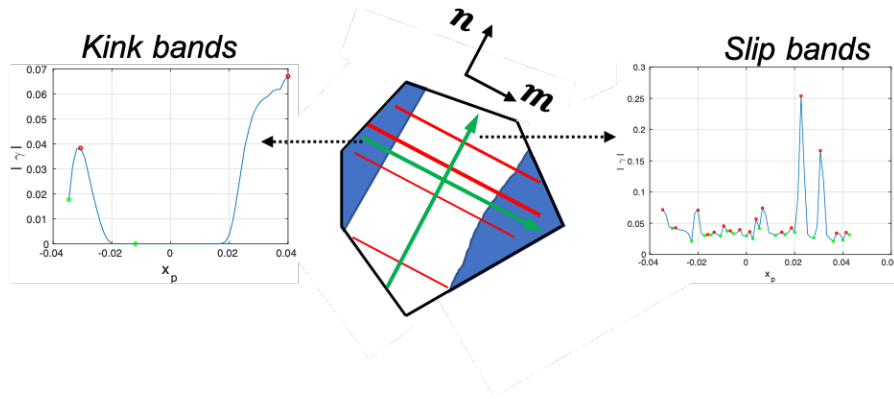
Figure 3.6 – Slip profiles interpolated in a grain in the glide direction and the normal to slip plan direction of the considered slip system. Slip bands are represented in red and kink bands in blue in the schematic grain.
Note that the two displayed profiles have been processed from real simulations but are not extracted from the same case. They are displayed together here for illustration purposes only.

From these profiles, the magnitude, the number and the location of the peaks can be identified, providing statistical data over the number of bands of each family, their intensity and the mean distance between bands. Besides, an approximation of the width is approximated by the distance between the roots of a parabolic function interpolating the peak. fig. 3.7 provides an illustration of the determination of such quantities in the slip profiles.

In practice, the peak detection is composed of several processing steps ensuring that:

1. peaks values below a certain threshold $\overline{p} \cdot \Phi_L$ are not retained
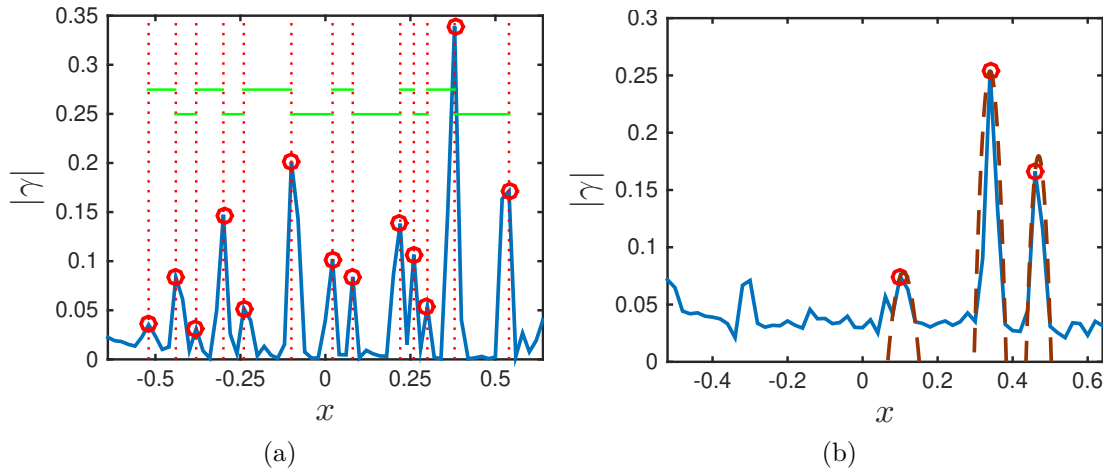
Figure 3.7 – (a) Determination of the distances (green lines) between the localization bands in a slip profile. (b) Interpolation of peaks with a parabolic function to estimate band widths (brown curves)

2. peaks that have a small height are not retained in order to avoid considering small fluctuations of the slip profile as localization bands. The peak height is defined as the difference between his value et the value of the higher minimum of the slip profile that is next to the peak.

The threshold $\bar{p} \cdot \Phi_L$ is the same as the one used to define the slip localization indicator L, presented in the first strategy section. All the distances that are obtained from this algorithm are normalized with respect to the mean grain size of the polycrystalline unit cell. A detailed description of the algorithm implemented for this strategy is given in appendix C.2. This strategy has been implemented only for crystal structures with a single slip plane in this work. The presence of several slip planes would require additional treatments as several slip systems could participate to the formation of a localization band on the same plane.

3.4   Results

3.4.1   Simulations description

Two types of polycrystalline microstructures have been generated using voxelized periodic Voronoi tessellations:

- 2D periodic unit cells (1 voxel thick in the $\boldsymbol{e}_1$ direction) containing 225 grains

K	n	E	ν	τ_0	$\Delta\tau$	γ_0	H
$10\,\mathrm{MPa\ s^{-n}}$	15	$100\,\mathrm{GPa}$	0.3	$100\,\mathrm{MPa}$	$20\,\mathrm{MPa}$	0.1	$0\,\mathrm{MPa}$

Table 3.1 – Material parameters used for all simulations (see eqs. (3.14) to (3.16))

(15^2). Because of x_1 direction periodicity, this is equivalent to 3D infinite columnar grains in the $\boldsymbol{e}_1$ direction, also equivalent to a 2D modeling under generalized plane strain hypothesis. One "in plane" slip system is modeled within each grain leaving all slip plane normals and glide directions in the ($\boldsymbol{e}_2, \boldsymbol{e}_3$) plane. Each grain is assigned a random 2D orientation.

- 3D periodic unit cells consisting of 64 grains (4^3) with random grain orientations. In order to assess results variability, 9 realizations of these random microstructures have been employed, as well as a 512 grains (8^3) random aggregate. Simulations have been carried out using the 12 FCC slip systems $\{111\} < 110 >$, their 12 BCC counterparts $\{110\} < 111 >$ or the 3 basal HCP slip systems $\{0001\} < 1\bar{2}10 >$.

Unless otherwise stated, grid resolution has been chosen so that mean grain size is resolved by 50 voxels. Thus, 2D and 3D simulations contain in average respectively 2500 and 125000 voxels per grain.

In addition to periodic boundary conditions, tensile loading is applied in the $\boldsymbol{e}_3$ direction by prescribing the mean value of the corresponding component of the displacement gradient $\underline{\boldsymbol{H}} = \underline{\boldsymbol{F}} - \underline{\boldsymbol{1}}$ at a constant strain rate of $10^{-5}\ s^{-1}$. A constant strain increments of $10^{-5}\ s^{-1}$ is used for the time discretization. Mean values of all other components of engineering stress ($\underline{\boldsymbol{S}}$) are prescribed to zero.

Constitutive model parameters used in all simulations, unless otherwise stated, are listed in table 3.1. All simulations feature isotropic linear elasticity. Norton law coefficients n and K values are chosen in order to limit rate dependence while preserving numerical convergence. As simulated crystal systems have only one family of equivalent slip systems, superscript s on flow rule parameter is omitted in the rest of this chapter. The single slip system softening behavior and simulated macroscopic mechanical behavior for 2D, 3D FCC and 3D BCC polycrystals are plotted on fig. 3.8 for this set of material parameters which involves 20% maximum softening of the critical resolved shear stress on each slip system.

3.4.2 Identification of slip and kink bands

fig. 3.9 (a) shows equivalent plastic strain and lattice rotation fields simulated for the 2D microstructure after 1% overall elongation. Clear networks
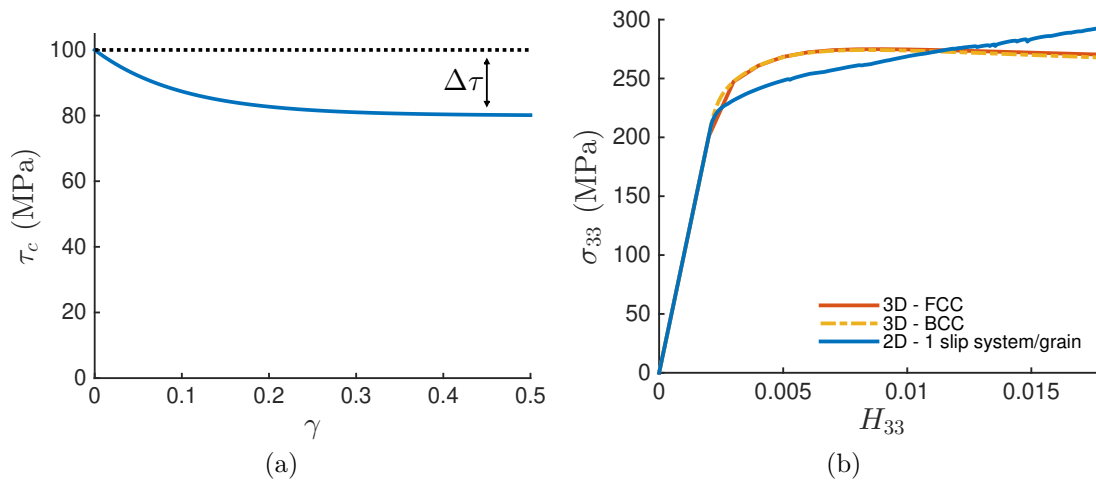
Figure 3.8 – Critical resolved shear stress evolution curve used for most simulations (a), and associated macroscopic stress-strain responses for different polycrystalline simulations (b) (FCC and BCC curves are almost superimposed)

of intragranular slip localization bands have formed as well as intense lattice rotation bands. Indicator functions S and K of slip/kink bands are computed from these fields as defined in eqs. (3.29) and (3.30). They are plotted respectively in red/blue and superimposed to the microstructure (grain boundaries) in order to build the associated localization mode map (b). In addition, slip planes traces are superposed to compare the detected slip and kink band orientations to the crystallographic slip planes. The zoomed view (c) clearly demonstrates that all red/blue bands are respectively parallel/perpendicular to a slip plane, which validates our detection procedure. Figure 3.11 shows similar results for a 3D simulation of a FCC polycrystal. A systematic study of the predicted bands nature with respect to slip planes confirms that the identification process is valid for all of detected bands.

Figure 3.10 presents a comparison of the maps obtained with the first and the second strategy developed to construct the slip and kink indicator fields. The two maps are very similar. The map (b) obtained with the image processing based strategy lacks of some segments with respect to the one obtained with the lattice rotation based strategy (a). However, localization modes identification is perfectly consistent between the two. This is an additional validation of the results of the first strategy.

Thresholds values in eqs. (3.27) and (3.28) have been tuned by hand to obtain optimal maps. Too low values of Φ_D leads to detection of more homogeneously deformed area whereas too high values leads to the detection of only a few

(a)

(b)   (c)
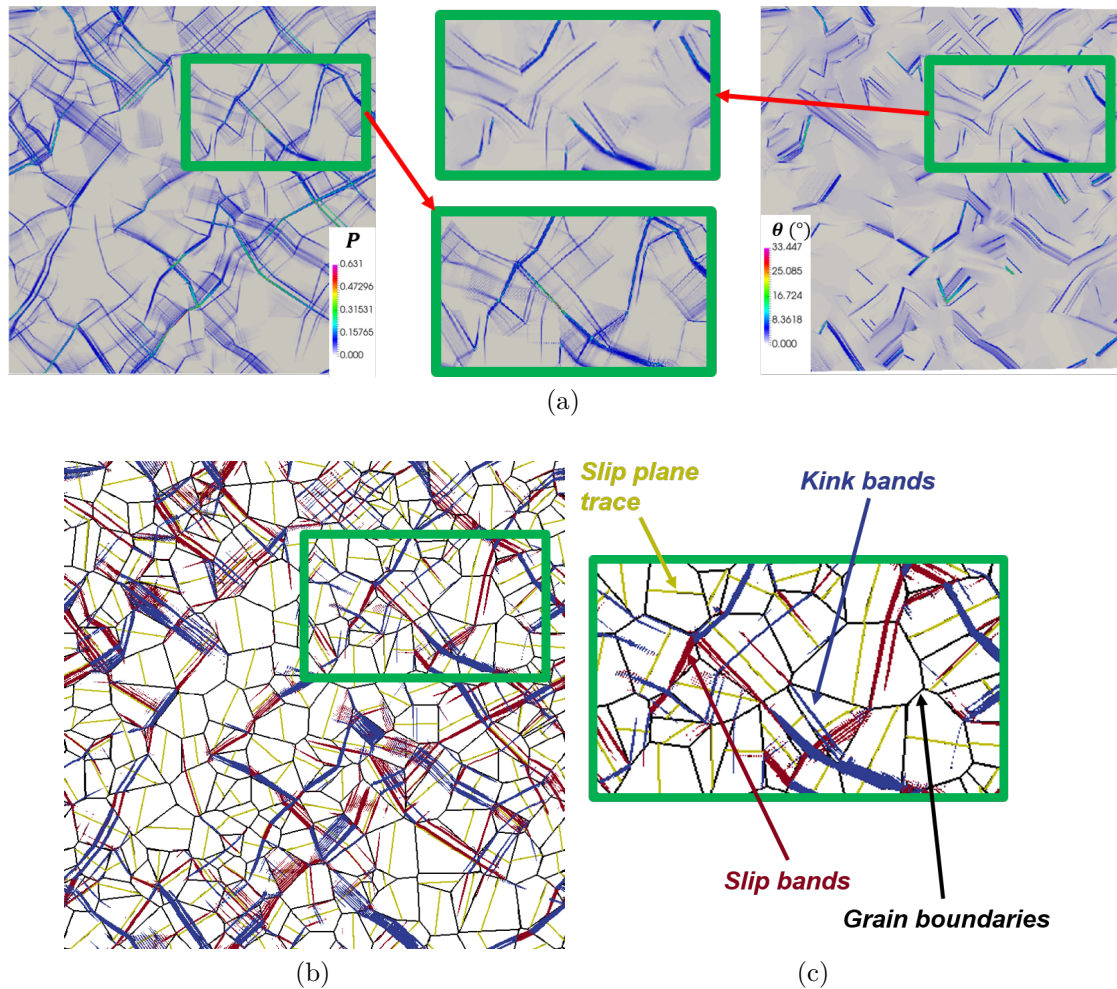
Figure 3.9 – Equivalent plastic strain and lattice rotation angle (a) fields for the 2D polycrystal (1 in-plane slip system) after 1% overall strain. Localization map computed with the lattice rotation based strategy (b). Slip (red) and kink (blue) bands are always respectively parallel/orthogonal to a slip plane (yellow) as illustrated by the zoom at the green-surrounded region (c). Grain boundaries are represented by black lines. Grid resolution: 750x750 voxels
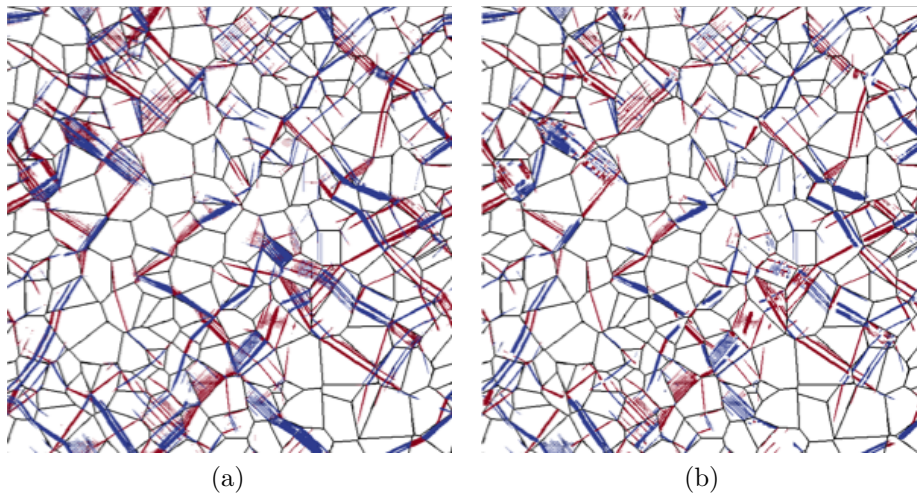
Figure 3.10 – Comparison of the localization maps obtained with the lattice rotation based (a) and the image processing based (b) strategy. Grid resolution: 750x750 voxels
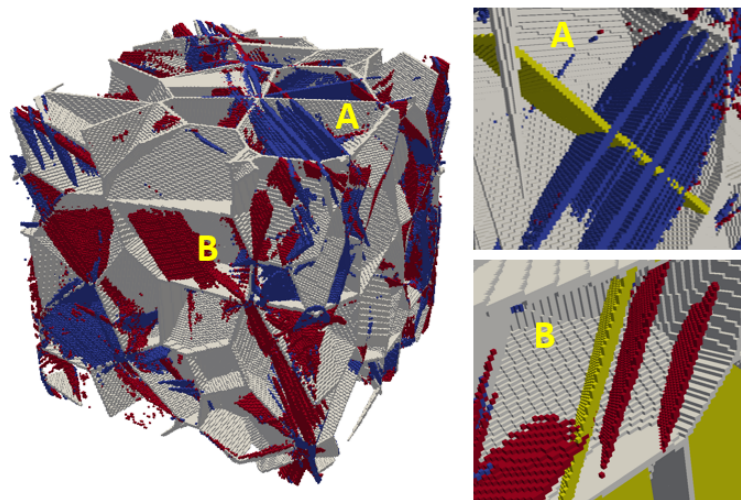
Figure 3.11 – Localization map built for a FCC 3D polycrystal after 1% overall strain showing slip/kink bands (red/blue) and grain boundaries (grey). Activated slip plane (yellow) is plotted on the zooms on A and B marked grains. The A grain contains a series of kink bands orthogonal to the activated slip plane. The B grain contains 2 slip bands parallel to the activated slip plane. Grid resolution: 200x200x200 voxels

localization bands. Best compromise has been achieved for $\Phi_D = 3$. Φ_R is then chosen to obtain best optimal band separation. Too high values lead to identification of kinks exhibiting too low lattice rotation as slips. Besides, regions with a slight inhomogeneous deformation can also have a moderate local lattice rotation and a slip band crossing them would be identified as a kink for too low values of Φ_R. Optimal results have been obtained for $\Phi_R = 2$. Thresholds values do not have a strong impact on qualitative analysis of localization maps. However they have a stronger influence on bands volume fraction and mean plastic strain estimation. Yet using the same set of threshold values to analyze different simulations allows for a relative comparison of these quantities that provides qualitative insights on strain localization properties, as presented in the following sections. Choice of thresholds for the second strategy are discussed in appendix C.1.

3.4.3   Grid resolution influence on slip and kink bands

fig. 3.12 shows the evolution of slip and kink band volume fractions and mean plastic strain after 1% total elongation, for 2D simulations, as a function of the spatial resolution. When increasing grid resolution, slip and kink bands volume fraction decreases when computed with the first strategy decreases while it slightly increases for kinks and is stable for slips with the second strategy. Conversely, for both methods, the average strain level within slips and kinks increases. Observation of associated maps show that the global thickness of bands decreases with increased resolution. This explains the augmentation of bands volume fraction computed with the second strategy as it is more efficient with finer objects. Therefore, the results of the first strategy seems more consistent.

Softening material behavior is known to induce numerical instabilities leading to such mesh dependence. However, results show that kink bands properties are less sensitive to grid resolution. Associated localization maps illustrate this trend: when increasing grid resolution the slip bands thickness decreases while their number increases. In contrast kink band patterns are more similar in the three maps.

To conclude, increasing spatial resolution decreases band thickness, and increase their number and intensity.

3.4.4   Softening influence on slip and kink bands

fig. 3.13 (a-b) presents the evolution of slip/kink volume fractions and mean plastic strain after 1% total elongation when varying the maximum softening level

(a)   (b)
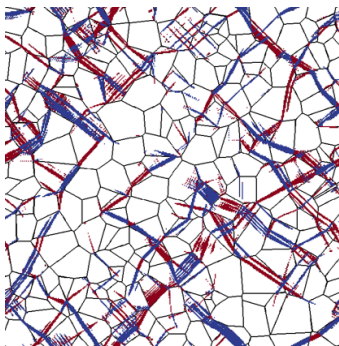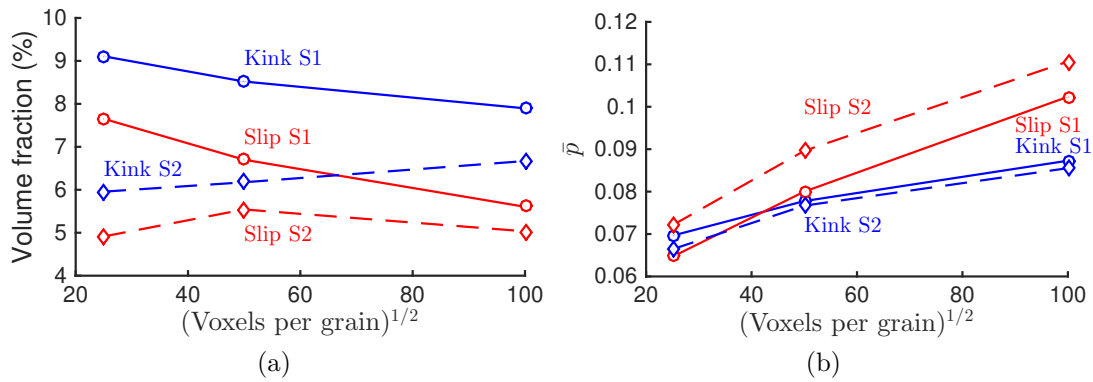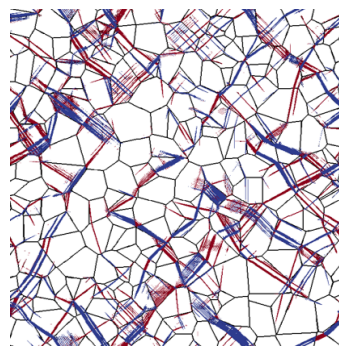
(c) 25^2 voxels per grain   (d) 50^2 voxels per grain   (e) 100^2 voxels per grain
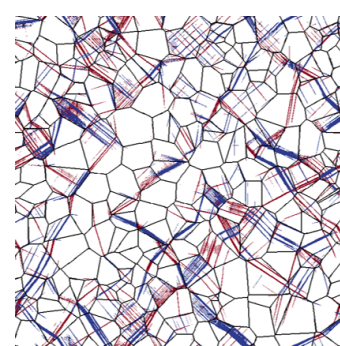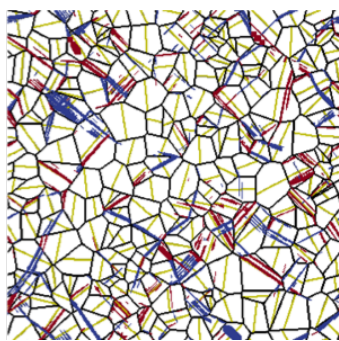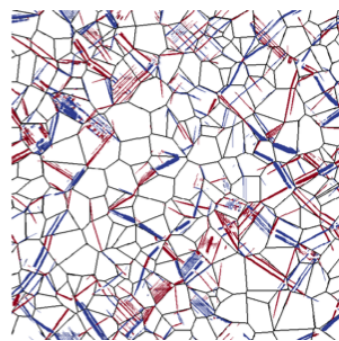
(f) 25^2 voxels per grain   (g) 50^2 voxels per grain   (h) 100^2 voxels per grain
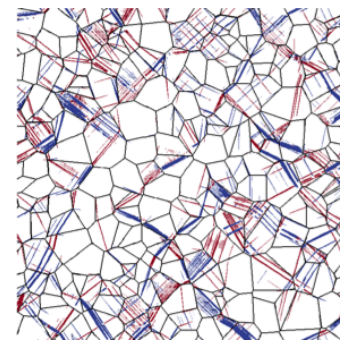
Figure 3.12 – Influence of grid resolution on slip and kink bands volume fraction (a) and mean equivalent plastic strain (b) for the 2D polycrystal after 1% overall strain. S1/S2 : first/second field processing strategies. localization maps obtained (c - e): with S1 (f-h): with S2

$\Delta\tau$ for 2D simulations, with a resolution of 50^2 voxels per grain. The observation of associated maps (fig. 3.13 (c-f)) induces observations similar to those of section 3.4.3: the results are consistent between the two strategies for the bands mean strain level, but not for volume fraction evolution. The two maps are closer when the overall aspects of bands is thinner, as in the case $\Delta\tau = 40\,\mathrm{MPa}$.

Increasing $\Delta\tau$ causes bands volume fraction to decrease, slightly more for slip bands, according to strategy 1, while strategy 2 results seem to indicated a roughly constant volume fraction. Quantifications obtained with the third strategy, shown on fig. 3.14 show that the relative increase in the number of bands (a) is lower than the relative decrease of the bands mean width (b), which is consistent with the trend yielded by the first post-processing strategy. Besides, fig. 3.14-(a-b) show strikingly close values of the quantitative indicators for kink and slip bands, for all value of the softening parameter.

The mean plastic strain level increases with softening intensity for both populations but increase is steeper for slip bands, for all three strategies (fig. 3.13-a,fig. 3.14-c). Associated localization maps fig. 3.13 (e-f) show that softening decreases band thickness and increases their number, with a stronger influence on slip band patterns. This trend is confirmed by the observation of the slip and kink band width distribution on fig. 3.15, obtained with the third strategy.

To conclude, increasing softening intensity yields a higher number of thinner and more intense localization bands, with a more pronounced influence on slip bands than kink bands. These results are similar to the one obtained for the sensitivity to spatial resolution.

3.4.5 Strain-rate sensitivity

Strain localization phenomenon can occur for a large range of temperatures, or can be associated to local adiabatic heating. This change in temperature will affect material viscosity and could potentially have an influence of strain localization patterns or intensity. To investigate this effect, a complementary study of the impact of strain-rate sensitivity on slip and kink bands has been carried out. Strain-rate sensitivity is essentially dependent on the Norton exponent n in the flow rule eq. (3.15).

Simulations with various values of n in a range going from $n = 2$ to $n = 50$ have been conducted. The results show that the only noticeable effect is that an increased strain-rate sensitivity (low value of n) leads to a small increase of the bands volume fraction, observed with both field processing methods (fig. 3.16). The evolution of the number of bands, their mean width and intensity obtained

(a)   (b)

(c) $\Delta\tau = 5$ MPa   (d) $\Delta\tau = 40$ MPa

(e) $\Delta\tau = 5$ MPa   (f) $\Delta\tau = 40$ MPa
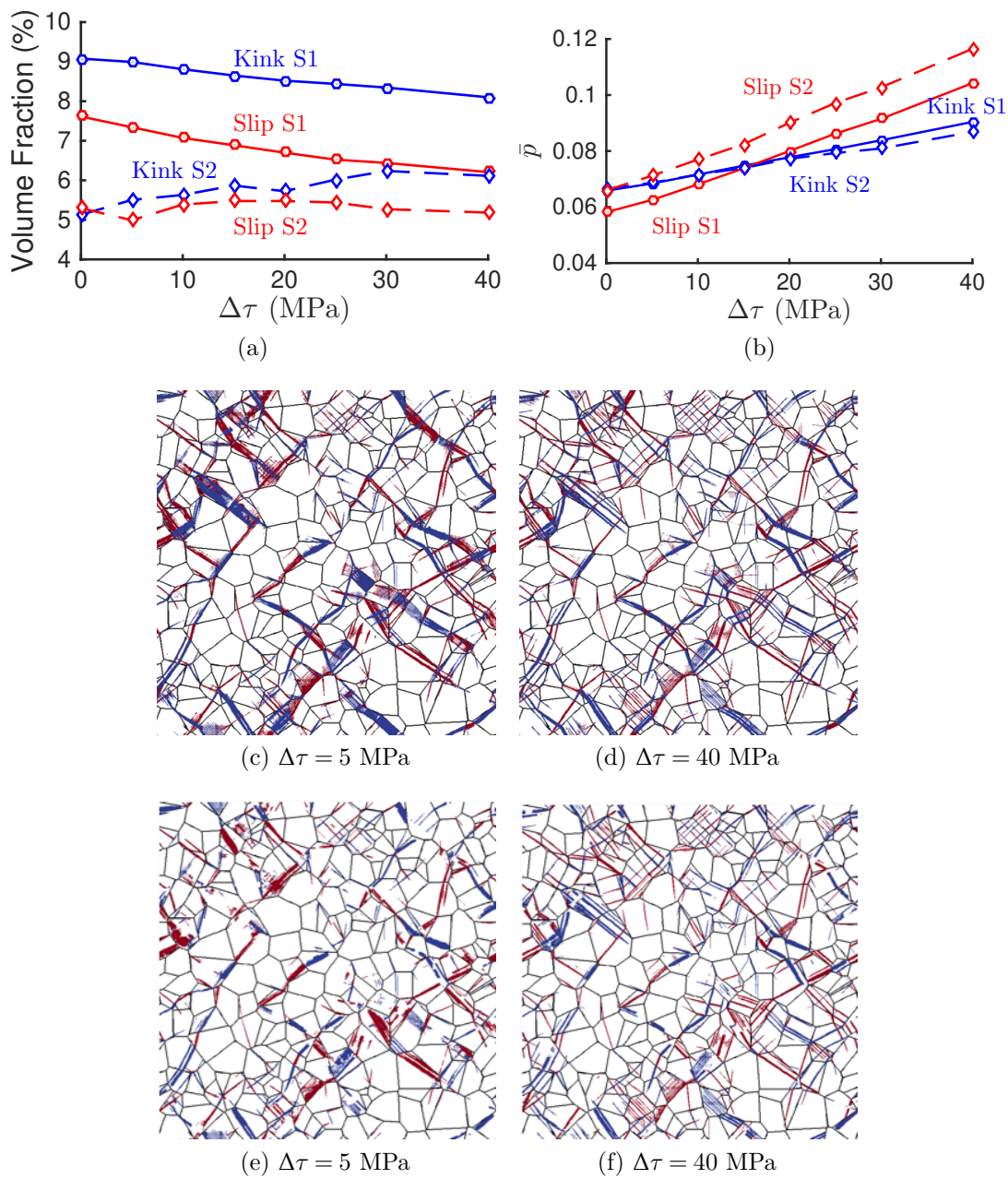
Figure 3.13 – Evolution of slip/kink bands volume fraction (a) and mean equivalent plastic strain (b) with $\Delta\tau$ for the 2D polycrystal after 1% overall strain. S1/S2 : first/second field processing strategies. Localization maps for 2 values of $\Delta\tau$ obtained (c-d) with S1 (e-f) with S2. Grid resolution: 750x750 voxels.
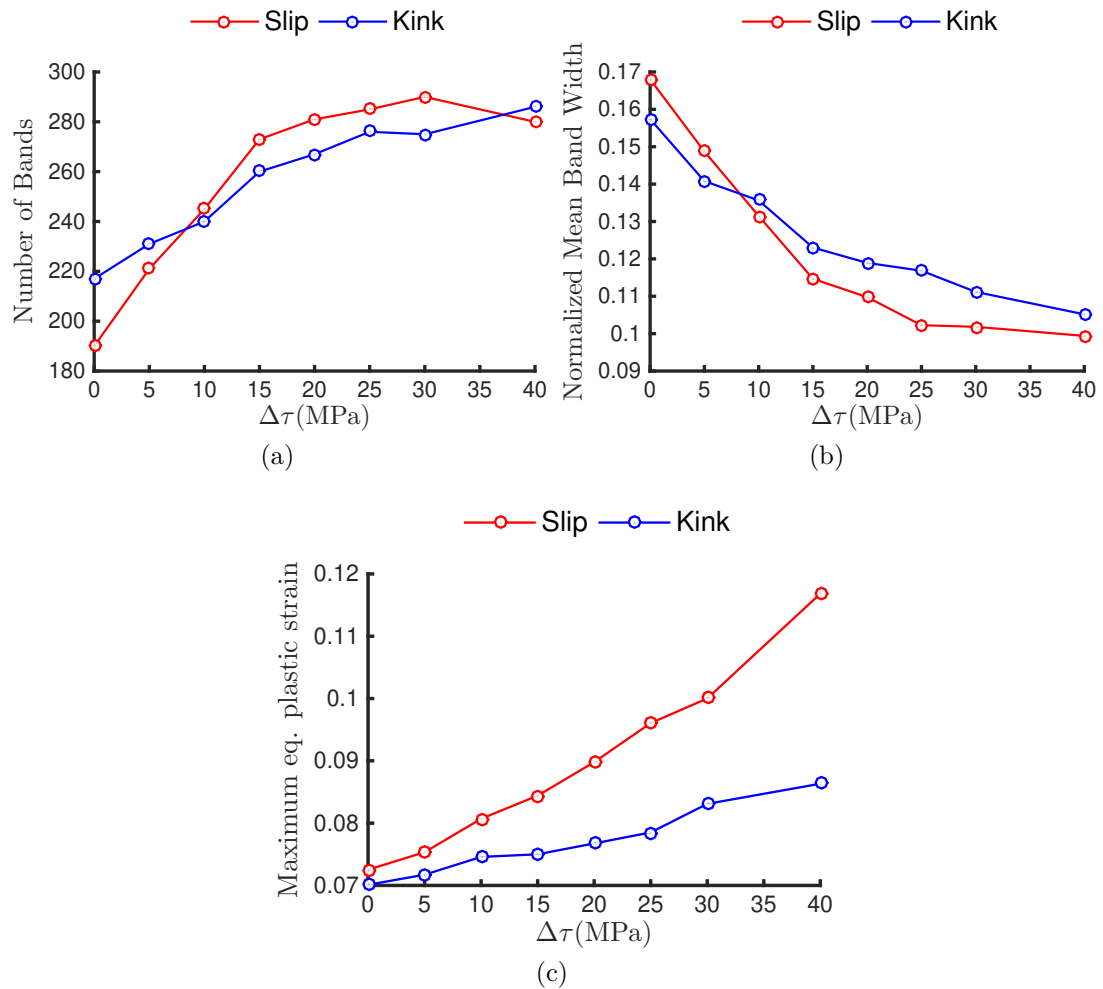
Figure 3.14 – Evolution of slip/kink band number (a), mean width (b) and maximum cumulated plastic strain (c) with softening intensity for the 2D polycrystal after 1% overall strain.

(a)   (b)
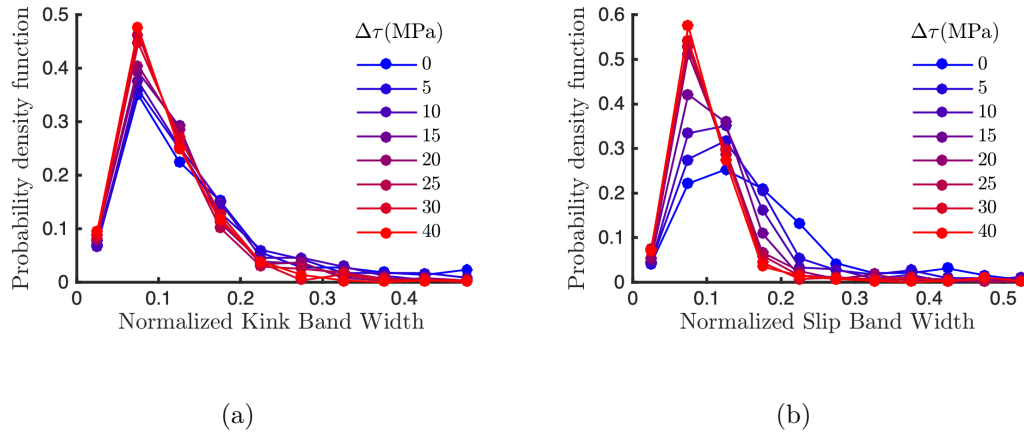
Figure 3.15 – Evolution of kink (a) and slip (b) band width distribution with softening intensity for the 2D polycrystal after 1% overall strain.

from the third processing strategy is shown on fig. 3.17. They show a clear but limited (less than 15%) increase of the bands number when n is decreasing from $n = 10$, associated to a relatively smaller decrease in bands mean width, which is consistent with the evolution of the band volume fractions. The value $n = 10$ seems to separate two regimes in which the evolution of the localization with n is reversed, but the variations remain very small for $n > 10$. Once again, the number of slip and kink bands are comparable.

Besides that, in the range of values that we studied (from n=2 to n=50), the localization pattern and band intensity is unchanged when n varies, as can be seen on the figures and localization maps (maps (a) is obtained for n=2, (b) for n=50).

To sum up, the strain rate sensitivity, in the strain rate and coefficients range tested here, does not have a significant impact on slip localization.

3.4.6 Strain localization with a hardening behavior

Asaro and Rice (1977) predicted in their bifurcation analysis that slip and kink banding can occur even for a strain-hardening material. They showed that if geometrical softening can overcome material hardening, plastic strain will
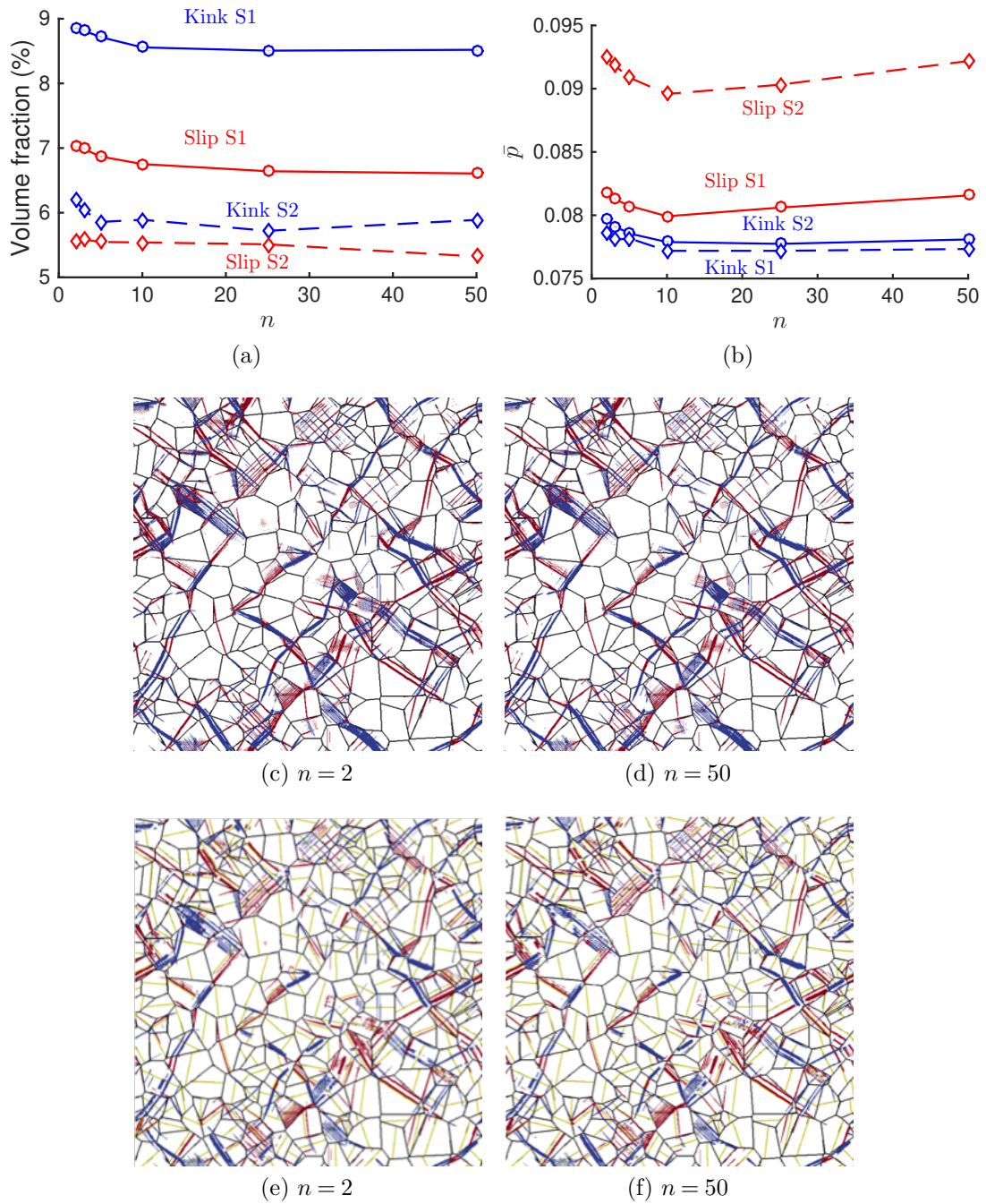
Figure 3.16 – Evolution of slip/kink bands volume fraction (a) and mean equivalent plastic strain (b) with Norton exponent n for the 2D polycrystal after 1% overall strain. Associated localization pattern obtained with: (c-d) the first strategy, (e-f) the second strategy. Yellow lines represent slip planes. Grid resolution: 750x750 voxels.
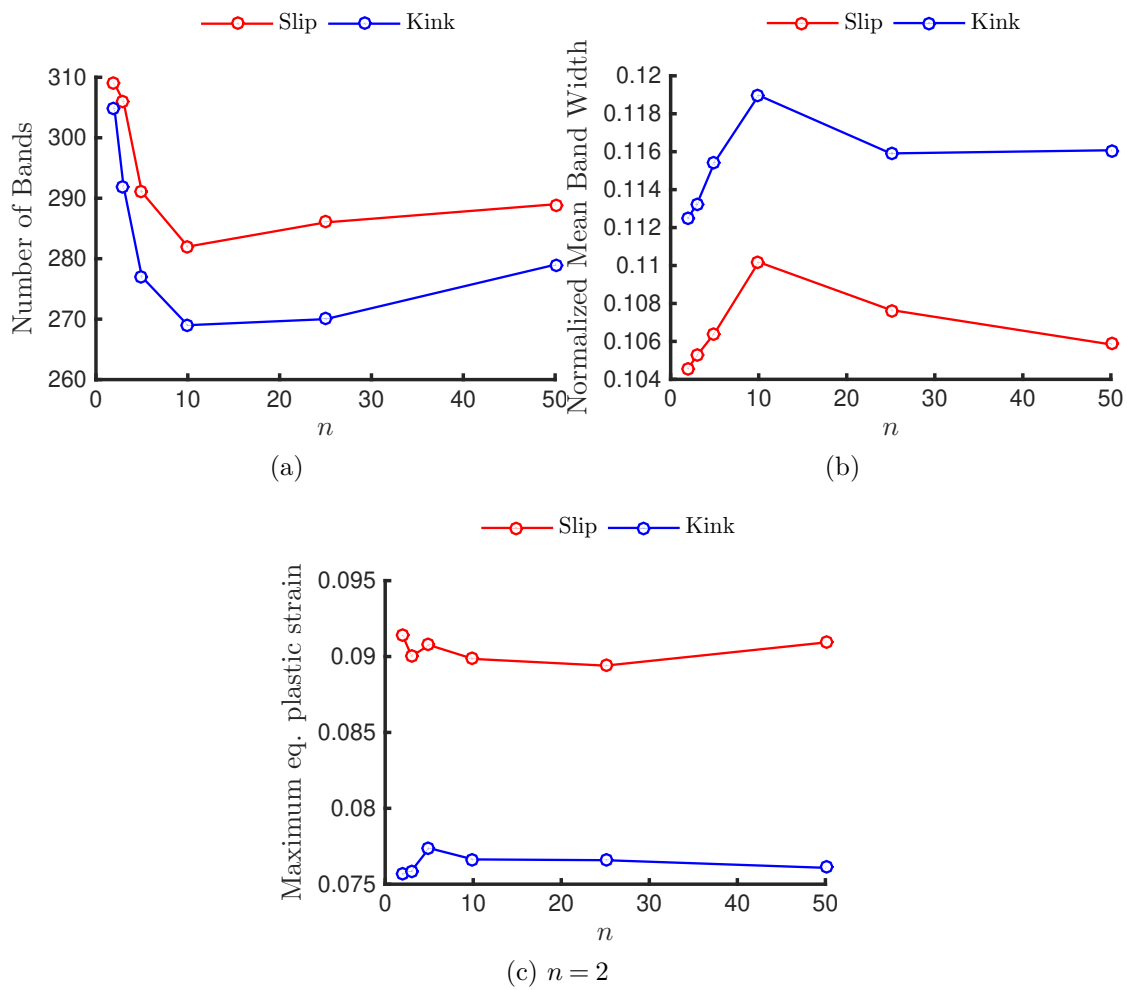
Figure 3.17 – Evolution of band number (a), mean width and maximum plastic strain (c) with Norton exponent n for the 2D polycrystal after 1% overall strain.

localize into a slip or a kink band. With a view to investigate if our localization modes analysis can evidence strain localization in this case, a simulation has been conducted with the 2D polycrystalline unit cell, the material coefficients of table 3.1, except $\Delta\tau$, in order to model a purely linear hardening material by setting $\Delta\tau = 0$ MPa. A small hardening modulus has been chosen, $H = 40$ MPa, in order to allow geometrical softening to quickly overcome hardening.

As predicted by Asaro and Rice, we observe strain localization in our simulation, as shown on fig. 3.18. Localization bands are logically thicker than in the purely softening simulations (fig. 3.13), but the same localization pattern is observed. The same grains exhibit the same localization modes in the softening and the slightly hardening simulations.
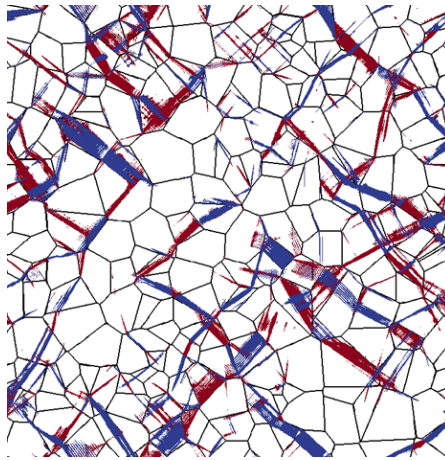
Figure 3.18 – Localization map obtained (lattice rotation based strategy) for the 2D polycrystal for 1% overall strain after a purely hardening simulation: $H = 40$ MPa, $\Delta\tau = 0$ MPa. Grid resolution: 750x750 voxels.

3.4.7   Comparison between 2D and 3D simulations

As mentioned in section 3.3, the second and third processing strategies have only been implemented for respectively 2D images, and crystal structures containing only one slip plane. Therefore, the results for 3D microstructures (50^3 voxels per grain in average, *i.e.* 200^3 voxels) presented in the following only rely on the first processing strategy.

fig. 3.19 and fig. 3.20 show the evolution of slip/kink band volume fractions and mean plastic strain level with increasing loading for a 2D simulation (with a single slip system per grain) and a 3D simulation of a FCC polycrystal. In both

simulations, the volume fraction grows more quickly for kinks than slip bands. 2D localization map snapshots on fig. 3.19 (a) show that kink bands volume fraction increases mainly because of widening of existing bands whereas increase in slip bands volume fraction is mostly due to new bands formation. Conversely the difference in slip/kink band thickness observed on 3D localization map snapshots is smaller fig. 3.19 (b). On the other hand, fig. 3.20 evidences that slip/kink mean plastic strain levels are almost identical in the two cases .

3.4.8 Sensitivity to simulated Volume Element

The results presented in previous sections reveal large proportions of kinks in simulated localization band networks. In order to find out if these proportions are due to the specific microstructure of the unit cell, 9 random realizations of 64 grains and one of 512 grains 3D polycrystals have been generated to characterize the variability of simulated localization bands populations with both the randomness and size of the unit-cell. fig. 3.21 presents the evolution of slip/kink bands volume fraction with increasing loading. It is found that for the 64 grains unit cell the standard deviation of simulated band volume fractions is generally smaller than the difference between slip and kink bands volume fractions. Results of the 512 grains aggregate simulation are contained within the error bars, very close to the mean value of the 9x64 grains simulations. Besides, similar localization networks are observed on 64 and 512 grains simulations localization maps. It follows that a single 64 grains volume element may be sufficient to draw a qualitative analysis of slip/kink bands populations for these cubic crystals, while a quantitative study requires whether to perform multiple simulations or to increase the size of the unit cell (both strategies providing consistent results).

3.5 Discussion

3.5.1 Bands analysis strategies

The results presented in section 3.4.2 clearly show that both the lattice rotation and image processing based strategy allow to construct a localization mode maps with no errors in the localization bands nature identification. As the geometrical criterion used for the second method are more selective than the simple threshold based strategy used in the first approach, a significant part of the localization indicator field L is cut off the localization map. However for all bands detected by these two independent methods, a perfect agreement on the nature

(a)

(b)
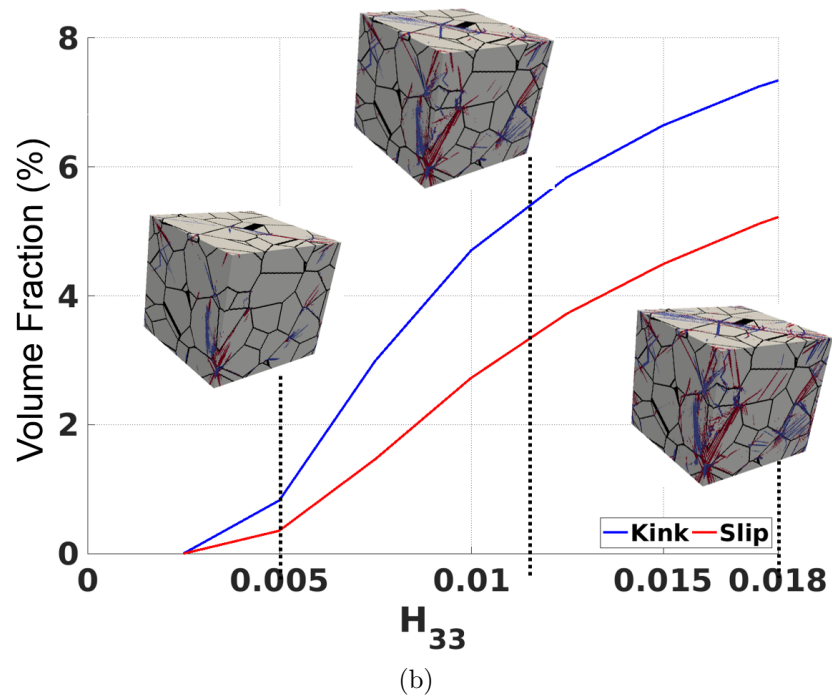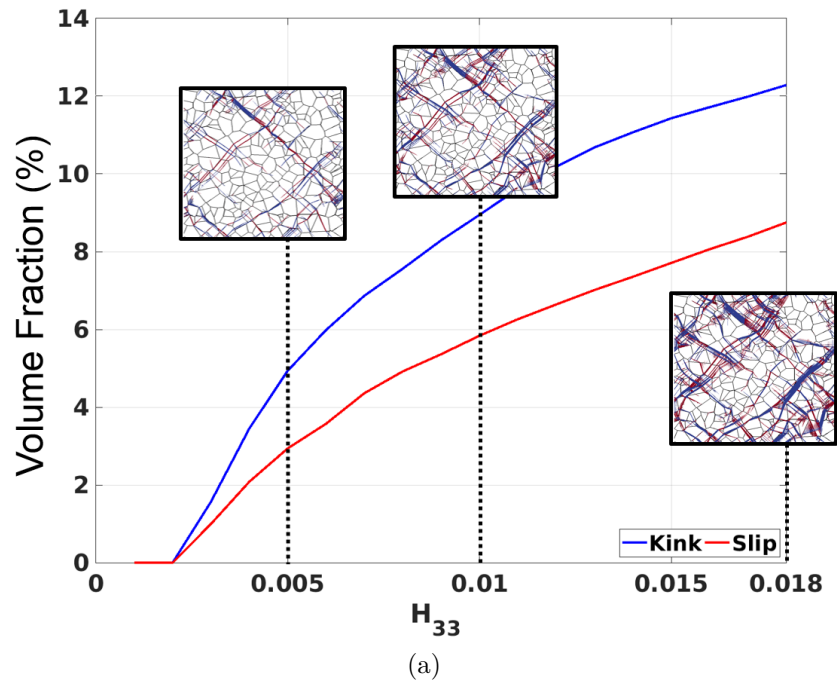
Figure 3.19 – Evolution of slip/kink band volume fraction for the 2D simulation (a) and a FCC 3D polycrystal (b), with snapshots of associated localization maps.
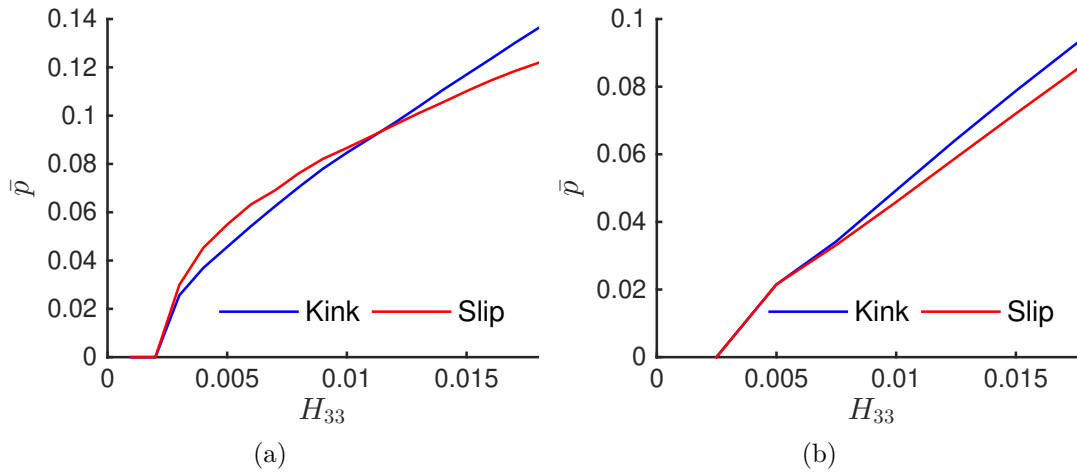
Figure 3.20 – Evolution of slip/kink band mean equivalent plastic strain for the 2D (a) and a FCC 3D 64 grain polycrystal (b)

of localization bands is found. The predicted nature is always consistent with the observation of the band orientation with respect to the slip plane.

In the light of the results presented in sections 3.4.3 to 3.4.6, results obtained with the image processing strategy shows a degree of uncertainty in the quantification of bands volume fractions that can preclude the analysis of the sensitivity to material parameters. Although it is clear that the algorithm implemented for this work is still basic and should be improved, this imprecision might be an intrinsic limitation to this kind of approach. Indeed, in polycrystals, bands formation, widening, and crossing lead to very complex patterns in the localization field L, that depends itself on the threshold Φ_D. These patterns are very sensitive to the value of the material parameters, the grid resolution etc... which renders cumbersome the identification of bands with image processing to a very high degree of precision.

Conversely, figures of sections 3.4.3 to 3.4.6 show that the first and third strategy predictions are always consistent, both with respect to each other and with the observation of localization maps. Their predictions are then more reliable.

This show that the lattice rotation based strategy is very effective at analyzing slip localization modes for classical crystal plasticity models. In addition, this method is straight-forward to implement, and is directly effective for 3D simulations as well, for which direct observation of bands orientation is cumbersome, and geometrically based image processing more involved.
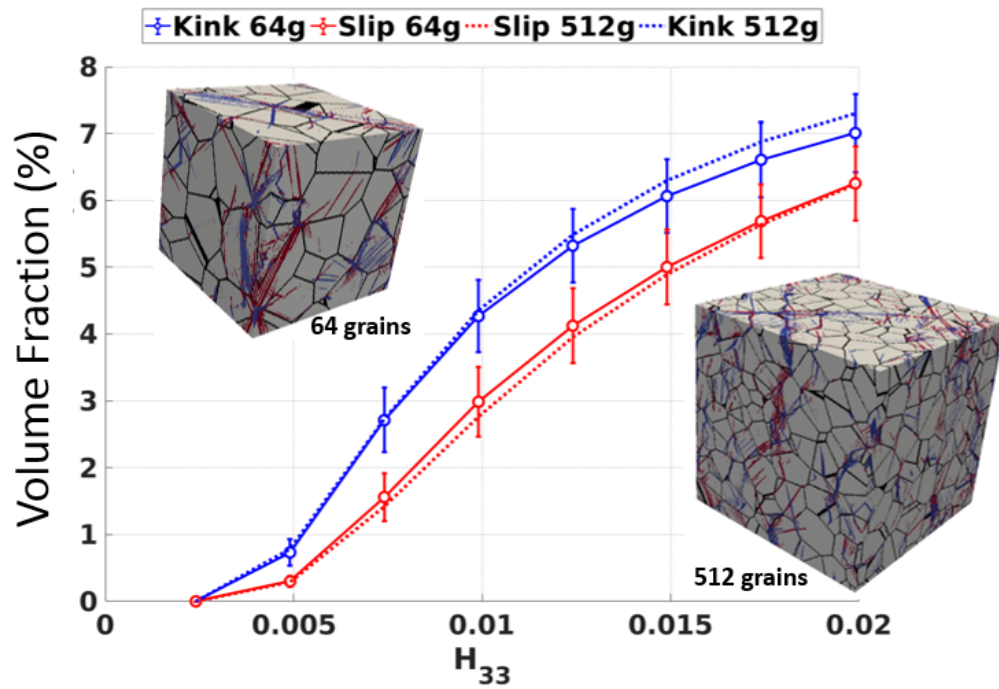
Figure 3.21 – Slip/kink bands volume fraction evolution with loading in FCC polycrystal. Plotted value is the mean of 9 realizations of a 64 grains random Voronoi aggregate, error bars indicating standard deviation of the 9 simulations. Results for the 512 grains random Voronoi aggregate are plotted in dashed-lines. Associated localization maps show localization at 2% overall strain in one 64 grains polycrystal and in the 512 grains one.

3.5.2   Lattice rotation and kink bands

Another interesting point is the analytical prediction of lattice rotation in kink bands (section 3.3.1). We found that the rotation angle value in radians is close to the mean local shear strain accommodated by the kink band, for small shear deformation: $\theta \approx \bar{\gamma}$. The fields γ and θ and the corresponding profiles extracted from one grain exhibiting kinks in our simulation, shown on fig. 3.22, show a very good agreement with it.
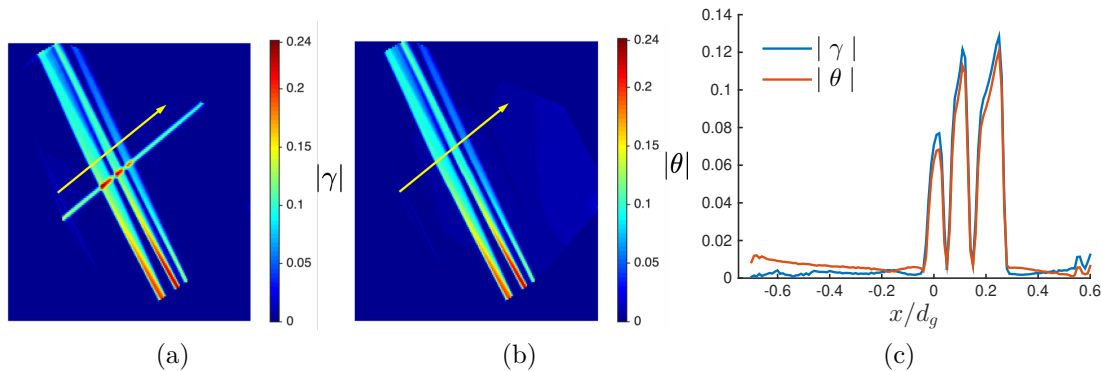
Figure 3.22 – (a) Slip field and (b) lattice rotation angle field (b) of a single grain showing three kink bands and one slip band. (c) Slip and lattice rotation profile along the yellow arrow. x/d_g is the normalized coordinate along the profile (with respect to grain size)

This result also seems consistent with the observation of the kink band like areas reported in the work of Gioacchino and Fonseca (2015), and discussed in section 2.1.2. In fact, as can be seen on fig. 2.5-(b), the lattice rotation in this area (denoted P2) is between 0.10 and 0.15 radians. The same area in the shear strain map (a) show a mean value also around 0.10 and 0.15. This shows a reasonable agreement with the approximation $\theta \approx \bar{\gamma}$. This may provide an additional criterion to identify kink bands in field measurements at small strains.

Besides, our results show that lattice rotation has an impact on kink bands characteristics: it can lead the Schmid factor to be locally decreased (or the reverse) and hinder further slip, resulting in lattice rotation induced hardening. This mechanism opposes to material softening and can explain why kink bands population exhibit a lower mesh size dependance, and sensitivity to softening intensity than slip bands. This difference seem to be less pronounced for three dimensional simulations. It could be explained by geometrical reasons: the same amount of lattice rotation induces lower variations of Schmid factor in three dimensional simulations compared to the 2D simulations where all directions involved in Schmid factor calculations

(glide direction, slip plane normal and loading directions) are coplanar.

3.5.3 Localization bands formation in crystal plasticity simulations

Asaro and Rice (1977) have shown that both slip and kink bands arise as the two possible bifurcation modes for elasto-plastic single crystals undergoing single slip at large strains. They defined this two modes as slip localization planes respectively orthogonal to glide plane normal direction $\boldsymbol{m}$ (slip bands) and glide direction $\boldsymbol{m}$ (kink bands). In the case of strain-softening crystals, their analysis shows that both modes become simultaneously possible at incipient plasticity. Incipient plasticity always occurs at small strain in metallic materials and in these conditions small strain formulation of crystal plasticity equations are valid to describe material behavior. In the small strain framework, resolved shear stress τ^s on slip system s and plastic strain are computed as follow:

$$\tau^s = \underline{\boldsymbol{\sigma}} \cdot \underline{\overset{\circ}{\boldsymbol{\mu}}}^s \tag{3.33}$$

$$\dot{\varepsilon}_p = \sum_{s=1}^{N_s} \dot{\gamma}^s \underline{\overset{\circ}{\boldsymbol{\mu}}}^s \tag{3.34}$$

The Cauchy stress $\underline{\boldsymbol{\sigma}}$ and $\underline{\overset{\circ}{\boldsymbol{\mu}}}^s = \frac{1}{2}(\boldsymbol{m} \otimes \boldsymbol{n} + \boldsymbol{n} \otimes \boldsymbol{m})$ being symmetric tensors, $\boldsymbol{m}$ and $\boldsymbol{n}$ play a perfectly symmetric role in eq. (3.33): inverting them leaves the equation unchanged. This consideration implies that kink and slip bifurcation modes are strictly equivalent at incipient plasticity with respect to the constitutive equations. It follows that structural effects, i.e. grain to grain plastic strain incompatibilities will govern the selection of slip or kink localization modes.

In order to provide an illustration of this property, two simulations have been carried out using the same grain geometry, grain orientations and material coefficients, but using two distinct crystal slip systems: the 12 FCC $\{111\} < 110 >$ slip systems and the 12 BCC $\{110\} < 111 >$ slip systems. The latter are indeed obtained by switching slip planes normals and glide directions of the FCC slip systems, thus according to Asaro and Rice analysis the potential localizations planes are the same in both polycrystals. The two identical microstructures induce identical structural effects and thus should activate the same localization planes at incipient plasticity. Simulations results clearly illustrate this point: in corresponding localization maps, shown on fig. 3.23, most of FCC slip (resp. kink) bands have a kink (resp. slip) counterpart for the BCC crystal structure. Then, finite strain kinematics leads to distinct evolutions of slip and kink bands because of rotation induced hardening, discussed in previous sections. It explains why the

two localization maps are not strictly equivalent after applying 1% overall tensile strain.

(a) FCC   (b) BCC
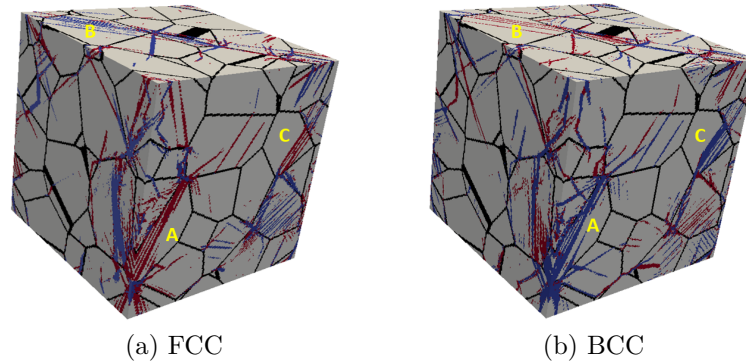
Figure 3.23 – Localization maps of 3D polycrystals after loading to 1% strain with (a): 12 FCC slip systems {111}[110] and (b) 12 BCC slip systems {110}[111], with identical geometry and grains orientations. Grains marked A,B and C illustrate the almost identical band structure, with FCC slip banding (resp. kink) corresponding to BCC kink banding (resp. slip). 200x200x200 voxels

With the view to investigating the influence of structural effects on slip/kink band formation a simulation has been carried out for a HCP crystal considering only the 3 basal slip systems $\{0001\} < 1\bar{2}10 >$. In that case the distribution of available localization planes is then strongly anisotropic and should be more influenced by structural effects than in more isotropic cases such as cubic crystals. Indeed, the only potential plane for slip band formation in each grain is the basal plane, whereas kink banding, in prismatic planes offer 3 times more planes to accommodate grain to grain plastic incompatibilities. fig. 3.24-a shows that kink bands volume fraction is approximately two times higher than slip band volume fraction, whereas the two quantities are much closer for the FCC crystals (fig. 3.21). Associated localization map (fig. 3.24-c) shows that localization occurs mainly at grain boundary triple lines from which kink bands seem to emerge more often than slip bands.

Triple lines grain boundary induce strong stress concentrations due to grain to grain incompatibilities. They are likely to trigger strain localization in some or all of the neighboring grains. Thus this structural effect will promote localization paths that extend over at least 2 grains and cross grain boundaries close to triple lines. Considering that, geometrically there are three distinct kink planes against only one slip plane, the probability to form such transgranular localization paths with kink bands is higher. This could explain why the gap between slip and kink bands volume fractions is higher in the case of the simulated HCP crystal.

(a)

(b)

(c)
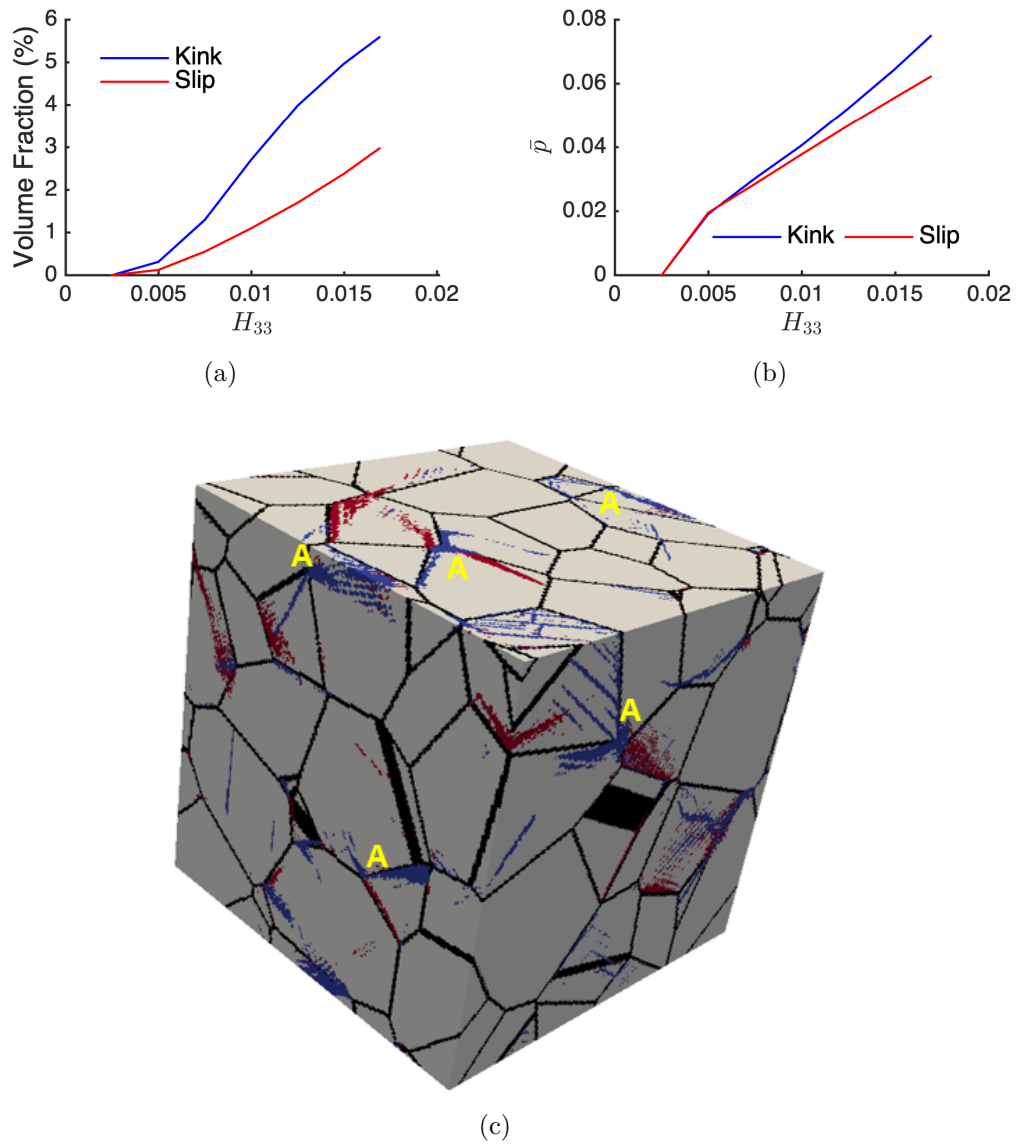
Figure 3.24 – Slip/kink bands volume fraction evolution (a) and mean equivalent plastic strain (b) for a 64 grains random HCP polycrystal. Zones marked A in the associated localization map after 1% overall strain (c) show that localization occurs generally at triple grain boundary junctions mostly through kink banding.

It is also interesting to note that in this case the intensity of kink bands is slightly higher and shows a steeper growth compared to slip bands after approximately 1.5 % strain (fig. 3.24-b), which is not observed for the FCC structure (with the same set of material coefficients, microstructure and grid resolution). This suggest that the strong anisotropy of the crystal favors kink bands as the main plastic deformation mode.

3.5.4 General validity of the bands formation mechanism for classical crystal plasticity models

This study is based on a simple generic softening constitutive model. However, strain localization in crystals is strongly dependent on factors such as strain hardening, strain-rate sensitivity, the complex interactions between dislocations of different slip systems, and of dislocations with other crystal defects. All those can be accounted for in the classical crystal plasticity (CCP) framework through the formulation of the constitutive equations that govern material behavior. The purpose of this section is to demonstrate that the bands formation mechanisms, resulting in comparable amounts of slip and kink bands, and revealed by our generic analysis, is also valid for more complex physics-based models.

Our generic model allows to study the impact of varying the softening/hardening rate and strain-rate sensitivity affecting each slip system independently. Simulations obtained for various softening intensity are described in section 3.4.4, for a small hardening behavior in section 3.4.6 and in section 3.4.5 for different material strain-rate sensitivity. All show very similar localization pattern: the constitutive behavior has an influence on the number, the thickness and the intensity of the bands but not on the localization modes observed in the grains.

Multi-scale CCP models encompass the complex interactions mechanisms between dislocations of various slip systems, and crystal defects, that yield a more realistic softening behavior. Despite this complexity, once softening occurs, slip should localize indifferently through slip or kink banding in order to best accommodate strain. Then, the relative amount of simulated kink and slip bands should remain unchanged.

In order to verify this prediction, we have carried out a simulation using a physics-based state of the art model of irradiated austenitic stainless steel, described in Hure et al. (2016). It features the modeling of the dislocation density on each slip of the twelve slip systems, the density of each of the four family of defect loops, a detailed modeling of the dislocation/dislocation and dislocation/loops interactions. It accounts for the annihilation of loops by gliding dislocation, yielding strong

softening on several slip systems.

We have reported in fig. 3.25 the results of this simulation and one carried out with our generic softening model, with same loading and FCC microstructure. Careful comparison of both localization maps reveals that the band pattern obtained with the state of the art model (a) encompasses the one obtained with the generic model (b). It proves that the same structural effects yield the same localization modes in the same grains even for two very different CPP models. The band pattern is more complex but it is clear on the map (a) that the relative amount of kink and slip bands is roughly the same than in map (b). The higher number of bands obtained with the irradiated austenitic steel model could be do to the impact of the interactions terms accounting for self and latent hardening, promoting the formation of new localization bands once the first have formed, but this remains an opened question.

This investigation confirms the validity of the localization modes formation mechanism discussed in section 3.5.3 for all set of constitutive equations relying on softening CCP. They can strongly affect the characteristics of the bands (number, thickness, intensity) but do not affect the selection of slip or kink banding, which are only determined by the crystal structure and structural effects. Thus, despite being detailed description of physical mechanisms, CCP will systematically induce formation of comparable amounts of slip and kink bands.

Asaro and Rice's analysis relies on the study of a bifurcation occuring in an homogeneous single crystal continuum. Hence, our results numerically confirm and extend Asaro and Rice's analytical results for such CCP polycrystalline simulations.

(a)   (b)
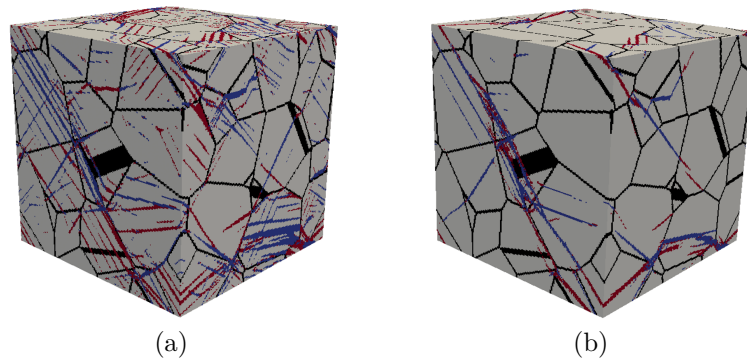
Figure 3.25 – Localization maps of FC 3D polycrystals after loading to 1% strain obtained with a state of the art crystal plasticity model of austenitic stainless steel Hure et al. (2016) (a) and the generic model with strong softening ($\Delta\tau = 50$ MPa) (b). 200x200x200 voxels

3.5.5 Critical assessment of classical crystal plasticity models use for strain localization simulation

R. Lebensohn et al. (2009) carried out crystal plasticity simulations of ice HCP polycrystals deforming mainly through basal slip. As in our HCP simulation, they note significant occurrence of intense kink bands in their results which is also in agreement with reported observations of kink bands in ice Montagnat et al. (2011); Wilson, Burg, and Mitchell (1986). Flouriot et al. Flouriot et al. (2003) have noted kink bands formation in crack-tip field simulations in a FCC crystal that are similar to those observed with crack-tip field measurements in ductile crystals Kysar and Briant (2002). As in this two situations, kink bands observations are mostly reported where strong strain incompatibilities arise such as crack-tip fields, compression of HCP single crystals Hagihara, Mayama, et al. (2016) or deformation of strongly anisotropic HCP polycrystals Hagihara, Okamoto, et al. (2016); Montagnat et al. (2011); Wilson, Burg, and Mitchell (1986) mainly deforming through basal slip. In those cases, crystal plasticity models appears to be well-suited to simulate their formation.

However, the case of irradiated Zirconium polycrystals provides a good example to also highlight their limitations. They are HCP crystals deforming mainly through basal slip and could exhibit formation of kink bands, like ice polycrystals, because of this slip anisotropy. On the contrary, deformed Zr polycrystal observations reveal only very intense slip bands, associated to dislocation channeling, a strongly softening mechanism, while kink bands have never been reported yet Fournier et al. (2009); Onimus, Monnet, et al. (2004). Thus, kink band formation in polycrystals could be the result of a competition between structural effects and microscopic mechanisms that cannot be accounted for within the classical crystal plasticity framework.

Indeed, slip and kink localization modes are strictly equivalent in these models from the constitutive law perspective. Yet considering associated dislocation mechanisms, both modes are very different: indeed, slip bands formation involves only a few very active dislocation sources located in close slip planes whereas kink band formation involves the activation of a considerably larger number of sources aligned along the direction normal to the slip plane. Hence, the two modes are not equivalent regarding dislocation mechanisms. For materials exhibiting strong softening mechanisms, dislocation emission from already active sources is promoted over the activation of new sources and thus kink bands formation should be unlikely. Kink bands are indeed never reported in observations of deformed irradiated or quench-hardened metals, that undergo such softening mechanisms (dislocation channeling), where slip localization seems to occur only through intense slip bands.

Yet, fig. 3.25 clearly shows that a state of the art physics based model for an austenitic stainless steel predicts the formation of a large amount of kink bands. Consequently classical crystal plasticity models appear to be fundamentally unable to reproduce accurately localization bands formation in these materials. fig. 3.25

3.6   Conclusions

We proposed a new approach to study localized deformation at incipient plasticity in polycrystals. It relies on the systematic nature and quantitative analysis of the simulated localization bands. Three different methods to identify the bands and characterize them have been proposed and compared. A simple theoretical study has evidenced the link between kink bands kinematics and the formation of lattice rotation, and provided an estimation of the associated angle. It has been shown that using lattice rotation to distinguish slip and kink bands is very effective at producing accurate localization modes maps, for bidimensional simulations as well as realistic three dimensional polycrystals with complex crystal systems. As it relies on the segmentation of lattice rotation and plastic strain fields, it is straightforward to implement. An alternative method based on a more consistent geometrical criterion has also been successfully implemented, but has proven to be a slightly less reliable than the former.

In this study, 2D and 3D simulations with a high spatial resolution were required, which was made possible with the use of the parallel FFT code AMITEX_FFTP.

Quantitative characterization of the band populations have highlighted the distinct mechanical characteristics of simulated slip and kink bands. Because of rotation induced hardening, kink bands tend to widen with increasing loading, and their volume fraction and mean strain level are less sensitive to mesh dependence and softening magnitude. Besides, these quantitative indicators explicitly show that the amount of slip and kink bands produced in the simulations are similar.

In agreement with Asaro and Rice's bifurcation analysis, we showed that slip or kink bands localization modes are strictly equivalent for polycrystalline simulations assuming initially homogeneous grains and softening classical crystal plasticity constitutive equations. These equations can only account for structure effects on plastic localization mode formation, which translate into a large amount of kink bands in all simulations of softening polycrystals. Consequently, this work demonstrates that:

- Identification of localization modes when simulating intragranular strain localization is fundamental in order to properly assess the validity of crystal

plasticity models, by means of comparison with experimental characterization of bands nature.

- Classical crystal plasticity models, systematically predict comparable amount of slip and kink bands, as they are two equivalent strain localization modes within this framework, in agreement with Asaro and Rice's analysis.

- Slip banding is largely the main deformation mode observed in locally softening metals, such as hyper-quenched metals or irradiated metals in which kink bands are not reported. Hence, classical crystal plasticity models are fundamentally unable to accurately simulate strain localization in such materials.

As a result, in order to accurately simulate intragranular strain localization at the continuum scale in softening metals, physical mechanisms introducing a distinction between kink or slip banding need to be accounted for with more complex plasticity theories, which is the subject of the next chapter.

PREDICTION OF SLIP AND KINK BANDING WITH STRAIN GRADIENT CRYSTAL PLASTICITY

Chapter Outline

Résumé en français

Pour surmonter les limites de la plasticité cristalline classique, mis en évidence au chapitre précédent, nous avons étudié la formation des modes de localisation intra-granulaires induits par un modèle de plasticité à gradient basé sur la théorie de Gurtin (2002). Dans ce cadre théorique, la prise en compte explicite par un terme énergétique de la courbure du réseau cristaillin, permet d'introduire une distinction physique entre bandes en genou, et bandes de glissement. En effet, le tenseur de Nye, utilisé dans l'énergie libre du crystal pour ce terme, doit être nul dans les bandes de glissement, mais ne l'est pas dans les bandes en genou. Ainsi, ce modèle doit fortement affecter la formation des bandes en genou, sans affecter celle des bandes de glissement.

Par rapport à la première implémentation FFT de ce modèle, réalisée par R. A. Lebensohn and Needleman (2016), notre travail a exploré l'influence du choix des opérateurs de dérivation sur la formation des bandes de localisation et a permis de déterminer un opérateur pour le double rotationnel intervenant dans ce modèle, permettant d'obtenir un calcul de courbure et de contrainte interne plus

correct sur les deux types de bandes de localisation. Nous avons également mis en évidence des façons plus cohérentes de mettre en œuvre les conditions aux limites, avec un impact important sur la prédiction du durcissement induit par les GND, notamment sur la dépendance au maillage. Par ailleurs, notre implémentation a été validée sur plusieurs solutions analytiques. Enfin, réalisée dans le contexte d'un code massivement parallèle, elle a permis de réaliser de nombreuses simulations avec des millions de voxels et des structures cristallines réalistes, nécessaires à l'étude de la localisation intra-granulaire du glissement plastique.

Notre travail démontre que, tout comme la plasticité formulée pour un milieu de Cosserat, ce modèle basé sur le tenseur de Nye peut résoudre les défauts des modèles de plasticité cristalline classique concernant les modes de localisation intra-granulaire. L'étude quantitative des populations de bandes de glissement et en genou simulées, a clairement mis en évidence les fortes différence dans leur mécanisme de formation induites par ce modèle. Ainsi, il en résulte que les bandes en genoux sont beaucoup moins nombreuses et plus larges que les bandes de glissement. Ces caractéristiques, ainsi que leur apparente formation sous la forme d'une succession dense de bandes de glissement successives, sont cohérentes avec les observations expérimentales des bandes en genou. Les prédictions du modèle sont également en accord qualitatif avec la caractérisation récente par des mesures de champs de la localisation de la déformation plastique dans divers polycristaux. Cela montre que les modèles de plasticité à gradient, basés sur la courbure de réseau, offrent un cadre prometteur pour modéliser les mécanismes élémentaires de la plasticité à l'échelle intra-granulaire dans le cadre de la mécanique des milieux continus.

Ce type de modèle promet également des progrès vis-à-vis de la simulation de la formation de bandes claires dans les métaux irradiés, car il favorise la formation de réseaux de bandes constitués de bandes de glissement intenses lors de simulation fortement adoucissantes, contrairement aux modèles de plasticité cristalline classique, pour lesquels de nombreuses bandes en genou intenses se forment également. Par conséquent, les modèles de de l'état de l'art pour les métaux irradiés basées sur des équations modélisant les interactions entre les dislocations et les défauts induits par l'irradiation devraient être reformulés dans le cadre de la plasticité à gradient pour prédire fidèlement la nature des bandes claires. Nos résultats montrent également que le problème de la dépendance au maillage des bandes de glissement n'a pas été résolu par cette formulation. Par conséquent, une longueur caractéristique supplémentaire visant à régulariser la largeur des bandes de glissement devrait être ajoutée dans de futurs travaux pour espérer une modélisation cohérente de la formation des bandes claires.

Enfin, les travaux présentés dans ce chapitre sont largement impliqués dans

l'extension du champ d'application de AMITEX_FFTP à la résolution par des méthodes spectrales d'équations de champ couplées à un problème d'homogénéisation périodique des matériaux. Ces développements génériques ont préservé son implémentation massivement parallèle ainsi que son interface utilisateur générique et simple d'utilisation. Il en est résulté une nouvelle version du solveur qui permet aux utilisateurs d'implémenter facilement pratiquement tous les types de problèmes couplés.

4.1   Introduction

We have evidenced in chap. 3 the shortcomings of CCP for the simulation of intragranular slip localization modes. As pointed out by Forest (1998), the lattice curvature induced by kink bands is a crucial difference with slip bands that should be accounted for by the constitutive modeling to obtain a more accurate modeling of their formation. His work has shown that the use of Cosserat plasticity breaks the equivalence of slip and kink modes in Asaro and Rice (1977) bifurcation analysis and can postpone or even preclude the formation of kink bands in single crystals simulations, due to the additional elastic energy stored for the formation of lattice curvature.

Another way to account for it is known from the work of (Nye 1953), that has linked lattice curvature to the dislocation density tensor $\underline{\boldsymbol{\alpha}}$. Gurtin (2002) has proposed a strain gradient plasticity theory that accounts for $\underline{\boldsymbol{\alpha}}$ in the crystal energy density. It has been mainly used to study grain size hardening effects in polycrystals (see for instance Cordero, Forest, and Busso (2012)). However, these studies never focused on the precise characterization of its influence on intragranular slip localization modes.

Besides, the recent developments of FFT-based solver have opened their scope to the general class of problems involving the coupled resolution of continuum mechanics and one or more additional field equations. FFT-based implementation of such models have been published in the field of phase field modeling by Y. Chen et al. (2019), the Field Dislocation Mechanics by Berbenni et al. (2014); Brenner et al. (2014); Djaka et al. (2019) and recently by R. A. Lebensohn and Needleman (2016) for the strain gradient plasticity model proposed by Gurtin (2002). Their development open the way for wide modeling possibilities that are of the highest interest for the developments of the AMITEX_FFTP solver.

This chapter presents a work aimed at pursuing these two goals. A generic extension of the AMITEX_FFTP solver has been implemented in order to solve virtually any type of problem involving the coupling of one or more field equations

with the classical FFT-based resolution of periodic mechanical homogenization. It allowed to implement a strain gradient crystal plasticity model based on Gurtin (2002) theory, that have been used to conduct a systematic study of its prediction of slip localization modes, similar to the one realized for CCP in chap. 3. It relies on analytical, and numerical predictions of the model for single and polycrystalline unit cells.

The chapter is organized as follow: first the non-local theory and the derived constitutive model are described, as well as analytical solution for the problem of ideal slip and kink band modeling. Then the generic developments introduced in the AMITEX_FFTP solver are presented, before going into the specific details of the strain gradient plasticity model FFT implementation, and its numerical validation. Finally, we present the results of high resolution simulations of single crystals and polycrystals, analyzed in the light of the localization modes analysis strategies developed in chap. 3. The chapter is concluded by a discussion on the results and the perspectives opened by this work.

4.2   Strain gradient crystal plasticity model

4.2.1   Dislocation density tensor

In the following paragraph, capital letters notation refer to tensors defined on the initial configuration of the body Ω or differential operators with respect to Lagrangian coordinates. Differential operators used in the rest of this chapter are defined in appendix A.3.

In continuum mechanics, the deformation gradient tensor $\underline{F}$ is a compatible field. This implies that its curl must vanish:

$$\underline{F} = \underline{1} + \operatorname{grad} \boldsymbol{u} \quad \Rightarrow \operatorname{Curl} \underline{F} = 0 \tag{4.1}$$

However, the two tensors $\underline{E}$ and $\underline{P}$ used in crystal plasticity kinematics based on the multiplicative decomposition of $\underline{F}$ ($\underline{F} = \underline{E} \cdot \underline{P}$, section 3.2.1) are not required to be compatible, and thus their curl should not vanish in general. A consequence of this property is the "closure failure": a contour integral of an oriented contour transformed by one of these tensors does not vanish. For instance, for an oriented surface $\mathcal{S}$ with closed contour $\mathcal{L}$ and normal vector $\boldsymbol{n}$ of the current configuration:

$$\boldsymbol{B} = \oint_{\mathcal{L}} \underline{E}^{-1} \cdot \boldsymbol{dx} = -\int_{\mathcal{S}} \operatorname{curl}(\underline{E}^{-1}) \cdot \boldsymbol{n} dS \tag{4.2}$$

where we have used the Stokes theorem (eq. (A.24)). The Burgers vector of a dislocation, is essentially defined as the net opening displacement of a closed contour $\mathcal{L}$obtained when introducing a dislocation passing through the surface $\mathcal{S}$ defined by this contour. By analogy, the vector $\boldsymbol{B}$ of eq. (4.2) can be considered as the continuum net Burgers vector for the contour $\mathcal{L}$. From there, the term on the right hand side can be seen as the count of the contribution of all geometrically necessary dislocations passing through $\mathcal{S}$, leading to the definition of the dislocation density tensor:

$$\underline{\boldsymbol{\alpha}} = -\operatorname{curl}(\underline{\boldsymbol{E}}^{-1}) \tag{4.3}$$

$$\boldsymbol{B} = \int_{\mathcal{S}} \underline{\boldsymbol{\alpha}} \cdot \boldsymbol{n} dS \tag{4.4}$$

By writing eq. (4.2) with respect to the initial configuration C_0, $\underline{\boldsymbol{\alpha}}$ can be linked to the curl of the plastic part of deformation gradient tensor.

$$\begin{aligned} \boldsymbol{B} &= \oint_{\mathcal{L}} \underline{\boldsymbol{E}}^{-1} \cdot \boldsymbol{dx} = \oint_{\mathcal{L}_0} \underline{\boldsymbol{E}}^{-1} \cdot \underline{\boldsymbol{F}} \cdot \boldsymbol{dX} = \oint_{\mathcal{L}_0} \underline{\boldsymbol{P}} \boldsymbol{dX} = -\int_{\mathcal{S}_0} \operatorname{Curl}(\underline{\boldsymbol{P}}) \cdot \boldsymbol{N} dS \\ &= -\int_{\mathcal{S}} \operatorname{Curl}(\underline{\boldsymbol{P}}) \cdot J^{-1} \underline{\boldsymbol{F}}^T \boldsymbol{n} ds \end{aligned} \tag{4.5}$$

Hence:

$$\underline{\boldsymbol{\alpha}} = -\frac{1}{J^e} \operatorname{Curl}(\underline{\boldsymbol{P}}) \cdot \underline{\boldsymbol{F}}^T \tag{4.6}$$

where $J^e = \det(\underline{\boldsymbol{E}})$

We recall that, in the case of a single active slip system with glide and normal to slip system directions denoted by $\boldsymbol{m}$ and $\boldsymbol{n}$, we have:

$$\underline{\boldsymbol{P}} = \underline{\boldsymbol{1}} + \gamma \boldsymbol{m} \otimes \boldsymbol{n} \tag{4.7}$$

which yields the expression of $\operatorname{Curl}(\underline{\boldsymbol{P}})$:

$$\operatorname{Curl}(\underline{\boldsymbol{P}}) = \epsilon_{jms} P_{im,s} \boldsymbol{e}_i \otimes \boldsymbol{e}_j \tag{4.8}$$

After injecting eq. (4.7) into eq. (4.8), we get, writing in the base $(\boldsymbol{m}, \boldsymbol{n}, \boldsymbol{e}_3 = \boldsymbol{m} \times \boldsymbol{n})$:

$$\operatorname{Curl}(\underline{\boldsymbol{P}}) = \gamma_{,3} \boldsymbol{m} \otimes \boldsymbol{m} - \gamma_{,m} \boldsymbol{m} \otimes \boldsymbol{e}_3 \tag{4.9}$$

Slip and kink bands can be viewed far from their ends as homogeneous

with respect to their in-plane coordinates. Thus, slip bands will be homogeneous in the directions $\boldsymbol{m}$ and $\boldsymbol{e}_3$, and kink bands in the directions $\boldsymbol{n}$ and $\boldsymbol{e}_3$. It follows then from eq. (4.9), that $\underline{\boldsymbol{\alpha}} = 0$ in slip bands whereas $\underline{\boldsymbol{\alpha}} \neq 0$ in kink bands, as the term $\gamma_{,3}$ does not vanish. Another way to look at this property is to consider Nye's formula (Nye (1953)):

$$\underline{\boldsymbol{\alpha}} = \underline{\boldsymbol{\kappa}}^T - \mathrm{tr}(\underline{\boldsymbol{\kappa}})\underline{\boldsymbol{1}} \tag{4.10}$$

which links $\underline{\boldsymbol{\alpha}}$ to the lattice curvature tensor $\underline{\boldsymbol{\kappa}}$, in the context of small strains, which is defined as the gradient of the axial vector associated to the lattice rotation tensor. This relation shows the direct link between the concentration of GND and the curvature of the crystal lattice. As discussed in chaps. 2 and 3, kink band formation involves lattice curvature, which is not the case for slip bands in general.

4.2.2   Nye tensor based model

The considerations established in section 4.2.1, evidence that accouting for an energy stored by the geometrically necessary dislocations (or by lattice curvature) introduces a physical difference between the formation of slip and kink bands. Similarly to the contribution of curvature to elastic energy in Cosserat crystal plasticity models (Forest (1998)), this will add an additional energetic cost for the formation of kink bands, and should favor plastic strain localization through slip banding.

Hence, we propose to use a strain gradient plasticity model which includes the full curl of the plastic part of the deformation gradient, which has been initially proposed by Gurtin (2002), to investigate the influence of accounting for the energy stored by GND on intragranular slip localization.

Kinematics

We restrict our study to small strain theory. All body configuration are considered identical, as well as Lagrangian and Eulerian coordinates. In this context, the multiplicative decomposition of deformation gradient $\underline{\boldsymbol{F}}$ becomes an additive decomposition of the displacement gradient $\underline{\boldsymbol{H}}$:

$$\underline{\boldsymbol{F}} = \underline{\boldsymbol{1}} + \underline{\boldsymbol{H}} = \underline{\boldsymbol{1}} + \underline{\boldsymbol{H}}^e + \underline{\boldsymbol{H}}^p \tag{4.11}$$

where $\underline{\boldsymbol{H}}^p$ and $\underline{\boldsymbol{H}}^e$ are the elastic and plastic parts of the displacement gradient. The plastic deformation rate is determined by the shearing rate of the N_s material slip systems, characterized by their slip plane normal direction $\boldsymbol{n}^s$ and glide direction

$\boldsymbol{m}^s$ through the relation::

$$\dot{\underline{\boldsymbol{H}}}^p = \sum_{s}^{N} \dot{\gamma}^s \underline{\boldsymbol{\mu}}^s \tag{4.12}$$

where $\underline{\boldsymbol{\mu}}^s = \boldsymbol{m}^s \otimes \boldsymbol{n}^s$ is the Schmid orientation tensor of slip system s. The elastic strain tensor $\underline{\boldsymbol{\varepsilon}}^e$ is defined as the symmetric part of $\underline{\boldsymbol{H}}^e$:

$$\underline{\boldsymbol{\varepsilon}}^e = \frac{1}{2}(\underline{\boldsymbol{H}}^{eT} + \underline{\boldsymbol{H}}^e) \tag{4.13}$$

In this context, the compatibility of $\underline{\boldsymbol{F}}$ yields:

$$\mathrm{curl}(\underline{\boldsymbol{F}}) = \mathrm{curl}(\underline{\boldsymbol{H}}) = \mathrm{curl}(\underline{\boldsymbol{H}}^e + \underline{\boldsymbol{H}}^p) = 0 \Rightarrow \mathrm{curl}(\underline{\boldsymbol{H}}^e) = -\mathrm{curl}(\underline{\boldsymbol{H}}^p) \tag{4.14}$$

Moreover, we have:

$$\underline{\boldsymbol{E}} = \underline{\boldsymbol{1}} + \underline{\boldsymbol{H}}^e \Rightarrow \underline{\boldsymbol{E}}^{-1} \approx \underline{\boldsymbol{1}} - \underline{\boldsymbol{H}}^e \tag{4.15}$$

Thus, combining eqs. (4.3), (4.14) and (4.15) we get:

$$\underline{\boldsymbol{\alpha}} = -\mathrm{curl}(\underline{\boldsymbol{E}}^{-1}) = \mathrm{curl}(\underline{\boldsymbol{H}}^e) = -\mathrm{curl}(\underline{\boldsymbol{H}}^p) \tag{4.16}$$

Again, we define the effective cumulative plastic strain p through eq. (4.18), the lattice rotation angle θ through eq. (4.17) and the cumulative plastic slip on slip system s, γ_{cum}^s, through eq. (4.19).

$$\theta = \arccos\left(\frac{1}{2}(\mathrm{tr}(\underline{\boldsymbol{R}}^e) - 1)\right) \tag{4.17}$$

$$p = \int_0^t \sqrt{\dot{\underline{\boldsymbol{H}}}^p : \dot{\underline{\boldsymbol{H}}}^p}\, dt \tag{4.18}$$

$$\gamma_{cum}^s = \int_0^t |\dot{\gamma}^s|\, dt \tag{4.19}$$

where $\underline{\boldsymbol{R}}^e$ is the rotation tensor in the polar decomposition of $\underline{\boldsymbol{E}}$:

$$\underline{\boldsymbol{E}} = \underline{\boldsymbol{1}} + \underline{\boldsymbol{H}}^e = \underline{\boldsymbol{R}}^e \cdot \underline{\boldsymbol{U}}^e \tag{4.20}$$

Balance equations

We consider a generalized continuum whose internal power density p^i and the contact power density p^c take the following form:

$$p_i = \underline{\sigma} : \dot{\underline{H}} + \underline{s} : \dot{\underline{H}}^p + \underline{M} : \mathrm{curl}\left(\dot{\underline{H}}^p\right) \tag{4.21}$$

$$p_c = \boldsymbol{t} : \dot{\boldsymbol{u}} + \underline{\boldsymbol{m}} : \dot{\underline{H}}^p \tag{4.22}$$

$\underline{s}$, work-conjugated to $\underline{H}^p$, is the micro-stress tensor, and $\underline{M}$, work-conjugated to $\mathrm{curl}(\underline{H}^p)$, is the double stress tensor, or generalized stress tensor. $\boldsymbol{t}$ is the classical traction vector and $\underline{\boldsymbol{m}}$ the double-traction vector or generalized traction vector. In the absence of external body forces and inertial forces, the principle of virtual power (detailed calculation in appendix B.2.1) yields the following balance equations, that hold over the whole body:

$$\mathrm{div}(\underline{\sigma}) = 0 \qquad \sigma_{ij,j} = 0 \tag{4.23}$$

$$\mathrm{curl}(\underline{M}) + \underline{s} = 0 \qquad \epsilon_{jkl}M_{ik,l} + s_{ij} = 0 \tag{4.24}$$

They are completed by the following boundary conditions:

$$\boldsymbol{t} = \underline{\sigma} \cdot \boldsymbol{n} \qquad t_i = \sigma_{ij}n_j \tag{4.25}$$

$$\underline{\boldsymbol{m}} = \underline{M} \cdot \underline{\epsilon} \cdot \boldsymbol{n} \qquad m_{ij} = M_{ik}\epsilon_{kjl}n_l \tag{4.26}$$

Cermelli and Gurtin (2002); Gurtin (2002) proposed an expression of simple higher order boundary conditions corresponding to a vanishing power of the generalized stresses working on slip gradients on the boundary $\mathcal{S}$. Following the same approach, analogous interface conditions can be derived for this model relying on $\mathrm{curl}(\underline{H}^p)$.

1. The *micro-clamped* or *microhard* boundary condition implies that plastic deformation vanishes on the interface:

$$\underline{H}^p(\boldsymbol{X}) = 0 \quad \forall \boldsymbol{x} \in \mathcal{S} \tag{4.27}$$

2. The *microfree* boundary condition implies that the generalized traction vanishes on the interface $\mathcal{S}$:

$$\underline{\boldsymbol{m}}(\boldsymbol{x}) = \underline{M}(\boldsymbol{x}) \cdot \underline{\epsilon} \cdot \boldsymbol{n} = 0 \quad \forall \boldsymbol{x} \in \mathcal{S} \tag{4.28}$$

The first one is the hardest possible boundary condition, it forbids the crossing of the interface by dislocations. The second one is the softest, opposing no resistance

to the flux of dislocations through the boundary. The specific form of interface condition that can be imposed on grain boundaries in our implementation is discussed later on, in section 4.4.2.

Constitutive modeling

As in section 3.2.2, we introduce the Helmholtz free energy density ψ, which is considered as a function of the elastic strain, of $\mathrm{curl}(\underline{\boldsymbol{H}}^p)$ and of the cumulative plastic slip on each slip system. It is assumed that the work associated to elastic deformation and to $\mathrm{curl}\left(\dot{\underline{\boldsymbol{H}}}^p\right)$ are non dissipative processes, and are associated to a simple quadratic potentiel in ψ, such that:

$$\rho\psi\left(\underline{\boldsymbol{\varepsilon}}^e, \mathrm{curl}(\underline{\boldsymbol{H}}^p), \gamma_{cum}^s\right) = \frac{1}{2}\underline{\boldsymbol{\varepsilon}}^e : \underline{\underline{\boldsymbol{\Lambda}}} : \underline{\boldsymbol{\varepsilon}}^e + \frac{1}{2}A\,\mathrm{curl}(\underline{\boldsymbol{H}}^p) : \mathrm{curl}(\underline{\boldsymbol{H}}^p) + \rho\psi^\star(\gamma_{cum}^s) \quad (4.29)$$

where A is a non-local modulus with the dimension of a stress multiplied by a squared length. In principle, a fourth order tensor of higher order moduli should be introduced, but for simplicity, a single modulus is introduced here as in Gurtin (2002). Then, classical thermodynamic arguments yield the constitutive relations:

$$\underline{\boldsymbol{\sigma}} = \underline{\underline{\boldsymbol{\Lambda}}} : \underline{\boldsymbol{\varepsilon}}^e \quad (4.30)$$

$$\underline{\boldsymbol{M}} = A\,\mathrm{curl}(\underline{\boldsymbol{H}}^p) \quad (4.31)$$

Combining the balance equation eq. (4.24) and eq. (4.31), we get:

$$\underline{\boldsymbol{s}} = -A\,\mathrm{curl}(\mathrm{curl}(\underline{\boldsymbol{H}}^p)) \quad (4.32)$$

Then, after introducing the notations: $\tau^s = \underline{\boldsymbol{\sigma}} : \underline{\boldsymbol{\mu}}^s$ and the backstress, $\chi^s = -\underline{\boldsymbol{s}} : \underline{\boldsymbol{\mu}}^s$ on slip system s, the model can be completed with the flow rule and the equation governing the evolution of the critical resolved shear stress:

$$\dot{\gamma}^s = \mathrm{sign}(\tau^s - \chi^s)\left\langle \frac{|\tau^s - \chi^s| - \tau_c^s}{K}\right\rangle^n \quad (4.33)$$

$$\tau_c^s = \tau_0^s - \Delta\tau^s\left[1 - \exp\left(-\frac{\gamma_{cum}^s}{\gamma_0^s}\right)\right] + H^s\gamma_{cum}^s \quad (4.34)$$

The details of the thermodynamically consistent derivation of eqs. (4.24), (4.30) and (4.32) to (4.34) is provided in appendix B.2.2.

Single slip case

We consider now the specific case of a crystal with only one active slip system, with glide direction $\boldsymbol{m}$ and normal to slip plane $\boldsymbol{n}$, and use the following base attached to this slip system: $(\boldsymbol{m}, \boldsymbol{n}, \boldsymbol{e}_3)$. When considering a vanishing initial plastic deformation, eq. (4.12) becomes:

$$\dot{\underline{\boldsymbol{H}}}^p = \dot{\gamma}\underline{\boldsymbol{\mu}} \qquad \Rightarrow \qquad \underline{\boldsymbol{H}}^p = \gamma\underline{\boldsymbol{\mu}} \tag{4.35}$$

From this, we have:

$$\mathrm{curl}(\underline{\boldsymbol{H}}^p) = \epsilon_{jms}H^p_{im,s}\boldsymbol{e}_i \otimes \boldsymbol{e}_j \tag{4.36}$$

$$\mathrm{curl}(\underline{\boldsymbol{H}}^p) = \gamma_{,3}\boldsymbol{m} \otimes \boldsymbol{m} - \gamma_{,m}\boldsymbol{m} \otimes \boldsymbol{e}_3 \tag{4.37}$$

and:

$$\mathrm{curl}\left(\mathrm{curl}\left(\underline{\boldsymbol{H}}^p\right)\right) = \epsilon_{jms}\epsilon_{mlr}H^p_{il,rs}\boldsymbol{e}_i \otimes \boldsymbol{e}_j \tag{4.38}$$

$$\mathrm{curl}\left(\mathrm{curl}\left(\underline{\boldsymbol{H}}^p\right)\right) = \gamma_{,mn}\boldsymbol{m} \otimes \boldsymbol{m} + \gamma_{,3n}\boldsymbol{m} \otimes \boldsymbol{e}_3 - (\gamma_{,mm} + \gamma_{,33})\boldsymbol{m} \otimes \boldsymbol{n} \tag{4.39}$$

which yields the expressions of $\underline{\boldsymbol{\alpha}}$, $\underline{\boldsymbol{s}}$ and $\underline{\boldsymbol{M}}$:

$$\underline{\boldsymbol{\alpha}} = -\left[\gamma_{,3}\boldsymbol{m} \otimes \boldsymbol{m} - \gamma_{,m}\boldsymbol{m} \otimes \boldsymbol{e}_3\right] \tag{4.40}$$

$$\underline{\boldsymbol{M}} = A\left[\gamma_{,3}\boldsymbol{m} \otimes \boldsymbol{m} - \gamma_{,m}\boldsymbol{m} \otimes \boldsymbol{e}_3\right] \tag{4.41}$$

$$\underline{\boldsymbol{s}} = -A\left[\gamma_{,mn}\boldsymbol{m} \otimes \boldsymbol{m} + \gamma_{,3n}\boldsymbol{m} \otimes \boldsymbol{e}_3 - (\gamma_{,mm} + \gamma_{,33})\boldsymbol{m} \otimes \boldsymbol{n}\right] \tag{4.42}$$

and the yield function of slip system s becomes:

$$f^s(\tau^s - \chi^s, \tau^s_c) = \ |\tau^s + \left(\underline{\boldsymbol{s}} : \underline{\boldsymbol{\mu}}\right)| - \tau^s_c = \ |\tau^s + A\left(\gamma_{,mm} + \gamma_{,33}\right)| - \tau^s_c \tag{4.43}$$

4.2.3 Choice of higher order coefficients and links with dislocation theory

The backstress χ^s that arises on each slip system corresponds to the resisting forces on gliding dislocation due to the energy stored in dislocation pile-ups, and is expressed as:

$$\chi^s = \underline{\boldsymbol{s}} : \underline{\boldsymbol{\mu}}^s = -A\left(\mathrm{curl}\left(\mathrm{curl}\left(\underline{\boldsymbol{H}}^p\right)\right) : \underline{\boldsymbol{\mu}}^s\right) \tag{4.44}$$

Following R. A. Lebensohn and Needleman (2016), we chose to decompose the higher order modulus as follow: $A = \lambda^2\pi_0$. λ has the dimension of a length and π_0

of a stress. In the single slip case, eq. (4.44), becomes

$$\chi^s = \underline{s} : \underline{\mu}^s = -\lambda^2 \pi_0 \left(\gamma_{,mm} + \gamma_{,33} \right) \tag{4.45}$$

At this point, we introduce l_p, the characteristic length of variation of the field γ, and $\bar{x}_1 = \frac{x_m}{l_p}$ and $\bar{x}_3 = \frac{x_3}{l_p}$ the associated dimensionless coordinates. Introducing them in eq. (4.45) and eq. (4.43), assuming a monotonic evolution and a perfectly plastic behavior, the yield condition can be written:

$$\tau^s + \left(\frac{\lambda}{l_p} \right)^2 \pi_0 \left[\frac{\partial^2 \gamma}{\partial \bar{x}_m^2} + \frac{\partial^2 \gamma}{\partial \bar{x}_3^2} \right] - \tau_0 = 0 \tag{4.46}$$

where τ_0 is the critical shear stress of the defect-free crystal.

The Nye tensor can be decomposed according to the canonical dislocation dyads decomposition (see Arsenlis and Parks 1999; Gurtin 2002; Kubin et al. 1992):

$$\underline{\alpha} = \rho_\odot \boldsymbol{m} \otimes \boldsymbol{m} + \rho_\vdash \boldsymbol{m} \otimes \boldsymbol{e}_3$$

where $\rho_\odot$ and $\rho_\vdash$ are respectively the density of screw and edge geometrically necessary dislocations for the slip system s. Here we have $\underline{\alpha} = - \left[\gamma_{,3} \, \boldsymbol{m} \otimes \boldsymbol{m} - \gamma_{,m} \, \boldsymbol{m} \otimes \boldsymbol{e}_3 \right]$, which after identification of the terms yields $\rho_\odot = -\gamma_{,3}$ and $\rho_\vdash = \gamma_{,m}$. Therefore, the differential term in eq. (4.46) can be written:

$$\frac{\partial^2 \gamma}{\partial \bar{x}_m^2} + \frac{\partial^2 \gamma}{\partial \bar{x}_3^2} = \frac{\partial \rho_\vdash}{\partial \bar{x}_m} - \frac{\partial \rho_\odot}{\partial \bar{x}_3}$$

A schematic representation of a square pile-up in the slip plane on fig. 4.1 shows that $\frac{\partial \rho_\vdash}{\partial \bar{x}_m}$ and $\frac{\partial \rho_\odot}{\partial \bar{x}_3}$ always have opposite signs for a given orientation of dislocation loops, when following the blue arrows and accounting for dislocations sign and positive or negative orientation with respect to $\bar{x}_3$ and $\bar{x}_m$. Consequently, the sum $\frac{\partial^2 \gamma}{\partial \bar{x}_m^2} + \frac{\partial^2 \gamma}{\partial \bar{x}_3^2}$ represents the local variation of in-plane dislocation lines density with respect to the chosen length scale. It will be denoted in the following by the notation $\frac{\partial \bar{\rho}}{\partial \bar{x}}$.

This allows to discuss the physical meaning of λ and π_0 in relation to the spatial variations of the GND at the considered length scale, through two distinct cases:

1. $\lambda = l_p \quad \Rightarrow \quad |\chi| \approx \pi_0 \frac{\partial \bar{\rho}}{\partial \bar{x}}$:
   Here, π_0 appears as the backstress induced on the slip system by a unit variation of $\frac{\partial \bar{\rho}}{\partial \bar{x}}$ within the characteristic length.
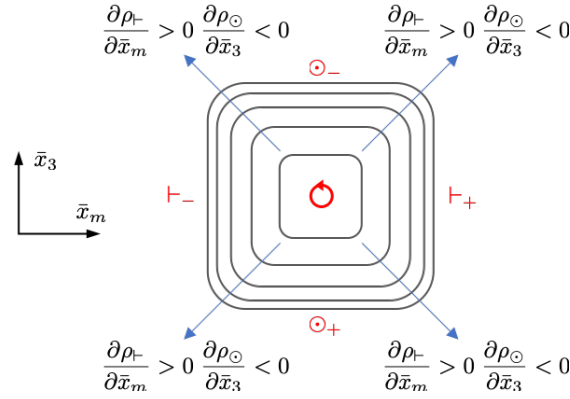
Figure 4.1 – Schematic illustration of the evolution of screw and edge dislocation density in the slip system plane for a square dislocation pile-up. Dislocation lines orientation is indicated by the red loop.

2. $\pi_0 = \tau_0 \quad \Rightarrow \quad \tau \approx \tau_0 \left[1 - \left(\frac{\lambda}{l_p} \right)^2 \frac{\partial \bar{\rho}}{\partial \bar{x}} \right]$:

Here, the backstress can be seen as the change in the crystal yield strength induced by GND. For unit variations of $\frac{\partial \bar{\rho}}{\partial \bar{x}}$, it will be negligible for $l_p \gg \lambda$. On the contrary, for $l_p \approx \lambda$, respectively $l_p \ll \lambda$, these variations will be of the order of τ_0, respectively much larger. In other words, λ indicates the length scale below which normalized variations of the GND density have a significant strengthening effect.

It can be concluded that λ is the length scale indicating the characteristic size of dislocation pile-ups that have a strengthening effect of the order of π_0. With a view to build physical multi-scale plasticity models, this analysis calls for the determination of this material constants through dislocation theory analysis.

Indeed, from the pioneering work of Eshelby, Frank, and Nabarro (1951), the discrete dislocation theory provide a framework to compute the length and associated stress-field of dislocation pile-ups in linear isotropic elastic mediums and simple situations. The recent developments of continuum dislocation theory (Akarapu and Hirth (2013); X. Chen et al. (2019); Y. Chen et al. (2019); D. Kochmann and Le (2008); X. Zhang (2017)) and field dislocation mechanics (Berbenni et al. (2014); Djaka et al. (2019)) open the scope of such analysis to three dimensional pile-ups in anisotropic medium. However, this is beyond the scope of the present work.

Our FFT polycrystalline simulations involve two characteristic length scales: the size of a voxel ∂x, and the mean grain size l_g. Hence, l_p will be comprised between them. Moreover, eq. (4.34) shows that the characteristic stresses can be of the order of τ_0 or H, as in practice the value of $\Delta \tau$ is of the order of τ_0. For

these reason, the value of λ and π_0 will be chosen as follows for the numerical simulations:

1. π_0 will be chosen equal to τ_0 for simulations with a perfectly plastic or strain softening behavior, and of the order of H for strain hardening behavior.

2. λ will have values in the range: $10^{-1} \cdot dx < \lambda < l_g$ in order to study the evolution of the non linear term influence on the result with respect to this characteristic length scale.

4.2.4   Application to analytical modeling of slip and kink banding

We now apply the model to the analytical modeling of slip and kink banding presented in section 3.3.1, consisting in an elastoplastic layer submitted to a pure shear loading, undergoing single slip, and embedded in two rigid layers. The reader in referred for the schematic representation of the model fig. 3.2 for the description of the coordinate system and the disposition of rigid and elasto-plastic phase. We consider here additionally a hardening modulus H, that can be either negative, positive or null, instead of perfect plasticity. The yield condition is then:

$$\underline{\sigma} : \underline{\mu} = \tau = \tau_0 + H\gamma_{cum} \tag{4.47}$$

The detailed hypothesis, calculation as well as the discussion of well-suited boundary conditions is provided in appendix B.2.3. Only the results are presented here.

Slip band

In agreement with the discussion of section 4.2.1, the calculation shows that ideal slip bands do not induce the formation of GND and associated backstress. As in section 3.3.1, homogeneous fields are a solution to the problem for $H \geq 0$. $H \leq 0$, according to Asaro and Rice 1977, yields plastic instability and result in plastic slip localization, forming a slip band, whose width is indeterminate.

Kink band

In the case of the kink band, because of the non vanishing backstress, the slip field is govern by the following equation:

$$\gamma_{,mm} - \frac{1}{\lambda_0^2}\gamma + \frac{1}{\lambda_0^2}\frac{\tau - \tau_0}{H} = 0 \tag{4.48}$$

with $\lambda_0 = \lambda\sqrt{\frac{\pi_0}{H}}$. The solution of this equation depends on the value of H. It has been computed as well as the corresponding expression of τ in appendix B.2.3, for the three cases $H > 0$, $H < 0$ and $H = 0$, but only the two first are presented here.

1. **Case** $H > 0$:

$$\gamma(x_m) = \frac{\tau - \tau_0}{H}\left[1 - \frac{\cosh\left(\frac{x_m}{\lambda_0}\right)}{\cosh\left(\frac{L}{2\lambda_0}\right)}\right] \tag{4.49}$$

2. **Case** $H < 0$:

$$\gamma(x_m) = \frac{\tau - \tau_0}{H}\left[1 + \cos\left(\frac{2\pi x_m}{\lambda_0'}\right)\right] \tag{4.50}$$

with $\lambda_0' = 2\pi\lambda\sqrt{\frac{\pi_0}{|H|}}$.

These solutions highlight the characteristic length scales over which γ varies: λ_0 and λ_0'. By setting $\pi_0 = |H|$ they become:

$$\lambda_0 = \lambda \tag{4.51}$$
$$\lambda_0' = 2\pi\lambda \tag{4.52}$$

Hence, in this case, λ will be the parameter that controls the size of the region in which the GND density will vary, and of the kink band width in the softening case.

For the softening case, we see that contrary to slip bands, kink bands will form with a sinusoidal profile and a well defined width. In practice, as in chap. 3, we are interested in the influence of the value of the softening parameter $\Delta\tau$ on slip localization, and its variations are chosen as a fraction of the initial yield strength of the slip system τ_0, such that $\Delta\tau = \eta\tau_0, 0 < \eta < 1$. With the exponential term used in the model, it can be shown (Scherer et al. 2019) that the localization problem is equivalent to the softening problem with H being the tangent modulus H' of the softening curve. After eq. (4.34), we have $|H'| = \frac{\Delta\tau}{\gamma_0}$. Thus, with the choices $\pi_0 = \tau_0$ and $\Delta\tau = \eta\tau_0$, kink band width should be approximately:

$$\omega_b \approx 2\pi\lambda\sqrt{\frac{\gamma_0}{\eta}} \tag{4.53}$$

It depends on both the softening rate through γ_0 and softening intensity through η, and on the intrinsic material length scale λ.

The solutions obtained here will be used for the validation of the numerical implementation of the model, presented in the next section.

4.3 Generic implementation of coupled problems resolution in the AMITEX_FFTP solver

As mentioned in the introduction, the resolution of the model presented in section 4.2 is a specific case of the general problem of the coupled resolution of classical continuum mechanics coupled with one or more additional field equations. This section presents the developments that we implemented in the solver AMITEX_FFTP to extend its scope to this class of problems, in the framework of Fourier transform based methods.

The focus is first put on the practical resolution of the additional field equations involved in these models. Then, the aforementioned developments introduced in AMITEX_FFTP are depicted.

4.3.1 Resolution of the non-local equation with FFT-based methods

The numerical resolution of non local mechanics or coupled problems requires the resolution, in addition to the equations of classical mechanics, of additional field equations under the form of partial differential equations. The terms of these equations are written as the application of a specific differential operator to a field involved in the equation. In Fourier space, the calculation of differential operators becomes a simple tensorial product. Thus, the resolution is reduced to the computation of the different differential terms eventually coupled with an iterative method to reach the solution if several equations must be verified simultaneously, exactly as for the resolution of the Lippmann-Schwinger equation.

However, following a collocation method, the discrete approximation of the Fourier transform of derivatives has proven to be the origin of spurious oscillations in the computed solution fields observed with FFT-based solvers. This has already been discussed in section 2.4.3 regarding the discrete Green-operator used in the basic-scheme (Moulinec and Suquet 1998), which led to the development of the modified discrete Green operator by Willot (2015) (built on a Finite-Differences approximation). It is the operator used in the AMITEX_FFTPcode. The issue and the solution is the same concerning the resolution of other types of PDE. Indeed, Berbenni et al. (2014); R. A. Lebensohn and Needleman (2016) have shown that the use of Finite-Differences based Fourier differential operator is very efficient at suppressing spurious oscillations occurring when using the classical discrete approximation of the Fourier transform derivative.

The notation used in the following is defined in appendix A.4. For a given

field f, the Fourier transform of its derivatives $f_{,i}$, $f_{,ii}$ or $f_{,ij}$ is given by the classical relations:

$$\hat{f}_{,i} = j\xi_i^\star \hat{f} \tag{4.54}$$

$$\hat{f}_{,ii} = -(\xi_i^\star)^2 \hat{f} \tag{4.55}$$

$$\hat{f}_{,ij} = -\xi_j^\star \xi_i^\star \hat{f} \tag{4.56}$$

where $\xi_i^\star$ is the i-th coordinate in the continuous Fourier space $\hat{\Omega}$ and j the complex unit. The discrete approximation of the Fourier transform derivative consists in replacing $\xi_i^\star$ by the discrete Fourier frequency ξ_i:

$$\hat{f}_{,i}(k_1, k_2, k_3) = j\xi_i \hat{f}(k_1, k_2, k_3) \tag{4.57}$$

$$\hat{f}_{,ii}(k_1, k_2, k_3) = -(\xi_i)^2 \hat{f}(k_1, k_2, k_3) \tag{4.58}$$

$$\hat{f}_{,ij}(k_1, k_2, k_3) = -\xi_j \xi_i \hat{f}(k_1, k_2, k_3) \tag{4.59}$$

The Finite-Differences based Fourier differentiation consists in replacing ξ_i by a modified frequency ξ_i^* that stems from the calculation of the Fourier transform of an intrinsic differential operator for the considered discretization grid, so that:

$$\hat{f}_{,i}(k_1, k_2, k_3) = j\xi_i^* \hat{f}(k_1, k_2, k_3) \tag{4.60}$$

$$\hat{f}_{,ii}(k_1, k_2, k_3) = \xi_{ii}^* \hat{f}(k_1, k_2, k_3) \tag{4.61}$$

$$\hat{f}_{,ij}(k_1, k_2, k_3) = \xi_{ij}^* \hat{f}(k_1, k_2, k_3) \tag{4.62}$$

In the works of Berbenni et al. (2014); R. A. Lebensohn and Needleman (2016), this is done for a 27-voxel centered finite difference approximation of first and second order derivatives, which yields the modified frequencies presented in table 4.1. The detailed expression of the finite difference operators and the calculations that allow to derive the modified frequencies are presented in appendix A.5.

Differentiation operators using these frequencies together with the modified frequencies involved in the definition of the modified Green operator (see section 2.4) have been implemented in AMITEX_FFTP. They are defined as follow:

$$\partial_i^* \left(\hat{f} \right) = j\xi_i^* \hat{f}(k_1, k_2, k_3) \quad \partial_i^\circ \left(\hat{f} \right) = j\xi_i^\circ \hat{f}(k_1, k_2, k_3) \tag{4.63}$$

$$\partial_{ii}^* \left(\hat{f} \right) = \xi_{ii}^* \hat{f}(k_1, k_2, k_3) \quad \partial_{ii}^\circ \left(\hat{f} \right) = \xi_{ii}^\circ \hat{f}(k_1, k_2, k_3) \tag{4.64}$$

$$\partial_{ij}^* \left(\hat{f} \right) = \xi_{ij}^* \hat{f}(k_1, k_2, k_3) \quad \partial_{ij}^\circ \left(\hat{f} \right) = \xi_{ij}^\circ \hat{f}(k_1, k_2, k_3) \tag{4.65}$$

where the superscript $\circ$ denotes the differentiation operators based on the Willot discrete Green operator frequencies. They have been implemented to be applied

Classical discrete approximation of FFT Derivative	27-voxels centered finite difference approximation
$\xi_i = \frac{\pi(2k_i - N_i)}{N_i}$	$\xi_i^* = \frac{1}{dx_i}\sin(2\pi\xi_i)$
$-\xi_i^2$	$\xi_{ii}^* = \frac{2}{dx_i^2}\Big[\cos(2\pi\xi_i) - 1\Big]$
$-\xi_i\xi_j$	$\xi_{ij}^* = \frac{2}{dx_i dx_j}\Big[\cos\left(2\pi\left[\xi_i + \xi_j\right]\right)$ $-\cos\left(2\pi\left[\xi_i - \xi_j\right]\right)\Big]$

Table 4.1 – Modified derivation frequencies for the 9-voxel centered finite difference approximation of first and second order derivatives. dx_i denotes the size of the voxels in the direction $\boldsymbol{e}_i$

through a fully parallel computation on the distributed memory field variables handled by AMITEX_FFTP. From these elementary operators, the more complex tensor analysis operators are constructed. For instance, the scalar laplacian, curl and double curl operators based on the 9-voxels centered finite differences are constructed as follow:

$$\triangle^*\left(\hat{a}\right) = \partial_{ii}^*\left(a\right) \tag{4.66}$$

$$\mathrm{curl}^*\left(\underline{\hat{\boldsymbol{A}}}\right) = \epsilon_{jms}\partial_s^*\left(\hat{A}_{im}\right)\boldsymbol{e}_i \otimes \boldsymbol{e}_j \tag{4.67}$$

$$\mathrm{curlcurl}^*\left(\underline{\hat{\boldsymbol{A}}}\right) = \epsilon_{jms}\epsilon_{mlr}\partial_{rs}^*\left(\hat{A}_{il}\right)\boldsymbol{e}_i \otimes \boldsymbol{e}_j \tag{4.68}$$

As a result any PDE calculation can now be easily implemented within the solver.

4.3.2 Generic implementation in AMITEX_FFTP

In addition to the implementation of the intrinsic DFT differentiation operators, significant developments have been introduced in the code AMITEX_FFTP in order to be able to handle a large variety of field equations coupled with continuum mechanics homogenization. The theoretical formulation of the classical non-linear periodic homogenization problem in continuum mechanics as been detailed in section 2.4.1 (eq. (2.30)). For the needs of the current discussion, we will formerly rewrite this problem in the framework of small strains as finding the

solution of the functional $\mathcal{S}$:

$$\mathcal{S}\left(\underline{\boldsymbol{\varepsilon}},\underline{\boldsymbol{\sigma}},\boldsymbol{\alpha},C\right)=0 \tag{4.69}$$

where $\boldsymbol{\alpha}$ and C are respectively the internal variables and material coefficients involved in the constitutive relations of the problem.

We consider now an arbitrary number of field variables denoted by $\boldsymbol{\phi}(\boldsymbol{x})$, that are solution to other field equations, depending on another set of internal variables $\boldsymbol{\beta}(\boldsymbol{x})$ and coefficients C'. This second problem is formally written as follow:

$$\mathcal{G}\left(\boldsymbol{\phi},\boldsymbol{\beta},C'\right)=0 \tag{4.70}$$

where $\mathcal{G}$ denotes an arbitrary number of field equations (PDE).

Let us now consider the case where the two problems are coupled. In this case, the mechanical problem $\mathcal{S}$ has an additional dependence on the field variables $\boldsymbol{\phi}(\boldsymbol{x})$, and the second problem depends possibly on the mechanical fields. The new problem arising is equivalent to the solution of:

$$\begin{cases} \mathcal{S}\left(\underline{\boldsymbol{\varepsilon}},\underline{\boldsymbol{\sigma}},\left(\boldsymbol{\alpha},\boldsymbol{\phi}\right),C\right)=0 \\ \mathcal{G}\left(\boldsymbol{\phi},\boldsymbol{\beta},C',\underline{\boldsymbol{\varepsilon}},\underline{\boldsymbol{\sigma}}\right)=0 \end{cases} \tag{4.71}$$

The developments introduced in AMITEX_FFTP to solve this type of problem relies on a non-intrusive coupling. The resolution of the problem $\mathcal{S}$ is already the core of the solver, and the previously presented principles and intrinsic differential operators constitute a development environment that allows for an easy implementation of a solver for problem $\mathcal{G}$. With this paradigm, $\boldsymbol{\phi}(\boldsymbol{x})$ can be viewed as additional internal variables included in the mechanical problem. The development challenges are then the coordination of the two resolution procedures and the transfer of the relevant fields between them, while keeping the distributed memory structure of the code, and the versatile user interface.

Two algorithms that preserve a non intrusive coupling have been implemented. They are presented on figs. 4.2 and 4.3. The first one is fully explicit: at each time step, each problem is solved one after another until reaching its own convergence criterion, and then transmits its results to the other resolution procedure. The other one is a pseudo implicit coupling. It consists in solving the problem $\mathcal{G}$ for each iteration of the resolution algorithm of $\mathcal{S}$. Thus, the constitutive equations are always solved with an updated solution of $\mathcal{G}$. However it is not fully implicit as $\mathcal{G}$ is solved with non equilibrated mechanical fields at each iteration.

Time step : $t \longrightarrow t + \Delta t$

    INPUT $\left(\varepsilon^{t+\Delta t}, \varepsilon^t, \sigma^t, \Phi^t, \alpha^t, \beta^t \right) \longrightarrow \left(\sigma^{t+\Delta t}, \Phi^{t+\Delta t} \alpha^{t+\Delta t}, \beta^{t+\Delta t} \right)$ OUTPUT

- **Initial guess :** $\varepsilon^0 = \epsilon^t + \dfrac{\Delta_t}{\Delta_{t-1}} \left(\varepsilon^t - \varepsilon^{t-\Delta t} \right)$

  $$\left(\sigma^0, \alpha^0 \right) = \mathcal{F} \left(\varepsilon^0, \varepsilon^t, \sigma^t, \alpha^t, \Phi^t, C, \Delta t \right)$$

- **Fix-point algorithm : iteration k**

  1. *Convergence test*

  2. *Compute polarization*
     $$\tau^k = \sigma^k - \Lambda^0 : \varepsilon^k$$

  3. *Real space to Fourier space*
     $$\hat{\tau}^k = FFT(\tau^k)$$

  4. *Apply Green operator*
     $$\hat{\varepsilon}^{k+1} = -\Gamma^{\diamond 0} : \hat{\tau}^k, \quad \hat{\varepsilon}^{k+1}(0) = E^{k+1}$$

  5. *Fourier space to Real space*
     $$\varepsilon^{k+1} = FFT^{-1} \left(\hat{\varepsilon}^{k+1} \right)$$

  6. *Anderson's acceleration*
     $$\text{save} \left(\varepsilon^{k+1} - \varepsilon^k, \varepsilon^{k+1} \right)$$
     $$\text{if } k \equiv 0[3] \; \varepsilon^{k+1} = \varepsilon_*^{k+1}$$
     $$\text{save} \left(\varepsilon_*^{k+1} - \varepsilon^k, \varepsilon^{k+1} \right)$$

  7. *Constitutive relation*
     $$\left(\sigma^{k+1}, \alpha^{k+1} \right) = \mathcal{F} \left(\varepsilon^{k+1}, \varepsilon^t, \sigma^t, \alpha^t, \Phi^t, C, \Delta t \right)$$

- **Solve additional field equation for** $\left(\Phi^{t+\Delta t}, \beta^{t+\Delta t} \right)$

  $$\left(\Phi^{t+\Delta t}, \beta^{t+\Delta t} \right) = \mathcal{G} \left(\Phi^t, \beta^t, C', \sigma^{t+\Delta t}, \varepsilon^{t+\Delta t}, \Delta t \right)$$

Figure 4.2 – Fully explicit coupling resolution of the periodic non-linear homogenization problem and the field equation $\mathcal{G}$ implemented in AMITEX_FFTP

In addition, developments have been carried out in order to adapt the memory structure of the code and the user interface to facilitate the implementation of such problems. The specific details of these developments will not be discussed as they are too far from the focus of this document.

They resulted in a new version of AMITEX_FFTP, in which users only have to implement the resolution of the field equations $\mathcal{G}$ with the differential operators presented in section 4.3.1, and choose one of the aforementioned coupling algorithms. All the fields involved are automatically introduced in the distributed memory structure, and the communications between the two resolution procedures are also automatically handled by the code.

Time step : $t \longrightarrow t + \Delta t$

INPUT $\left(\varepsilon^{t+\Delta t}, \varepsilon^t, \sigma^t, \Phi^t, \alpha^t, \beta^t\right) \longrightarrow \left(\sigma^{t+\Delta t}, \Phi^{t+\Delta t} \alpha^{t+\Delta t}, \beta^{t+\Delta t}\right)$ OUTPUT

- **Initial guess :** $\varepsilon^0 = \epsilon^t + \dfrac{\Delta_t}{\Delta_{t-1}} \left(\varepsilon^t - \varepsilon^{t-\Delta t}\right)$

  $$\left(\sigma^0, \alpha^0\right) = \mathcal{F}\left(\varepsilon^0, \varepsilon^t, \sigma^t, \alpha^t, \Phi^t, C, \Delta t\right)$$

- **Fix-point algorithm : iteration k**

  1. Convergence test

  2. Compute polarization
     $$\tau^k = \sigma^k - \Lambda^0 : \varepsilon^k$$

  3. Real space to Fourier space
     $$\hat{\tau}^k = FFT(\tau^k)$$

  4. Apply Green operator
     $$\hat{\varepsilon}^{k+1} = -\Gamma^{\diamond 0} : \hat{\tau}^k, \quad \hat{\varepsilon}^{k+1}(0) = E^{k+1}$$

  5. Fourier space to Real space
     $$\varepsilon^{k+1} = FFT^{-1}\left(\hat{\varepsilon}^{k+1}\right)$$

  6. Anderson's acceleration
     save $\left(\varepsilon^{k+1} - \varepsilon^k, \varepsilon^{k+1}\right)$
     if $k \equiv 0[3]\ \varepsilon^{k+1} = \varepsilon_*^{k+1}$
     save $\left(\varepsilon_*^{k+1} - \varepsilon^k, \varepsilon^{k+1}\right)$

  7. Constitutive relation
     $$\left(\sigma^{k+1}, \alpha^{k+1}\right) = \mathcal{F}\left(\varepsilon^{k+1}, \varepsilon^t, \sigma^t, \alpha^t, \Phi^k, C, \Delta t\right)$$

  8. Solve field equation for $\left(\Phi^{k+1}, \beta^{k+1}\right)$
     $$\left(\Phi^{k+1}, \beta^{k+1}\right) = \mathcal{G}\left(\Phi^t, \beta^t, C', \sigma^{k+1}, \varepsilon^{k+1}, \Delta t\right)$$

Figure 4.3 – Pseudo explicit coupling resolution of the periodic non-linear homogenization problem and the field equation $\mathcal{G}$ implemented in AMITEX_FFTP

This new framework, applied in the present PhD thesis to strain gradient plasticity, has recently been extended to easily implement a large variety of coupling such as the damage phase field implementation proposed by Y. Chen et al. (2019). Work is still in progress to introduce in this generic framework the coupling of AMITEX_FFTP with the Micromegas discrete dislocation dynamics code (developed by F. Boioli), the coupling with the martensite phase field transformation model of Kochman (developed by J. Boisse, Université de Lorraine), and finally, an implementation of a Field Dislocation Mechanics model in collaboration with S. Berbenni and J. Genée.

4.4 Implementation of the strain gradient plasticity model

4.4.1 Algorithms

The strain gradient plasticity model presented in section 4.2 has been implemented within the generic framework depicted in the previous section. In this particular case, the problem $\mathcal{G}$ reduces to eq. (4.32) that can be directly computed in Fourier space, with the application of the operator eq. (4.68). The field variable $\boldsymbol{\phi}(\boldsymbol{x})$ is therefore the microstress tensor $\underline{\boldsymbol{s}}$, and no specific internal variable $\boldsymbol{\beta}(\boldsymbol{x})$ is needed in this case. The non-local set of coefficient C' is composed of the two parameters λ and π_0, as we believe this distinction to be more physically relevant. However, only one higher order modulus could be sufficient.

Though, the algorithm has one specificity compared to the generic formulations presented above. Indeed, in order to properly model the differences between slip and kink bands, dependence on the non symmetric displacement gradient $\underline{\boldsymbol{H}} = \nabla \boldsymbol{u}$ and its plastic and elastic parts $\underline{\boldsymbol{H}}^p$ and $\underline{\boldsymbol{H}}^e$ is mandatory. Therefore, the algorithm has been reformulated in order to use $\underline{\boldsymbol{H}} = \nabla \boldsymbol{u}$ as the main variable while maintaining the small strain framework. One consequence is that the non symmetric Green Operator $\underline{\underline{\boldsymbol{\Gamma}}}^0$ intervenes in the algorithm, and no more the symmetric Green Operator $\underline{\underline{\boldsymbol{\Gamma}}}^{\diamond 0}$. This variable shift also concerns Anderson's acceleration technique. The two versions of the algorithm, respectively fully explicit and pseudo implicit, are depicted in figs. 4.4 and 4.5.

4.4.2 Practical imposition of grain boundary interface conditions

In this work, the main focus is put on polycrystalline simulations of strain localization, which raises the question of the non-local interface conditions to consider at grain boundaries and associated implementation. This matter is discussed in the present paragraph.

Cermelli and Gurtin (2002) have derived generalized constitutive modeling of grain boundaries consistent with the present theory and allowing for grain boundary energy and dissipation modeling. They can be formulated within a variational framework opening the way for their practical implementation. However, they require the explicit modeling of the geometry of grain boundary surfaces.

Handling explicit interface conditions on the interior of the periodic unit-cell with spectral methods is a complex issue and still an open problem. They may be imposed through a penalty method but this would require the use of an

Time step : $t \longrightarrow t + \Delta t$

INPUT $\left(\nabla u^{t+\Delta t}, \nabla u^t, \sigma^t, s^t, \alpha^t\right) \longrightarrow \left(\sigma^{t+\Delta t}, s^{t+\Delta t}\alpha^{t+\Delta t}\right)$ OUTPUT

- **Initial guess :** $\nabla u^0 = \nabla u^t + \dfrac{\Delta_t}{\Delta_{t-1}}\left(\nabla u^t - \nabla u^{t-\Delta t}\right) \quad \left(\sigma^0, \alpha^0\right) = \mathcal{F}\left(\nabla u^0, \nabla u^t, \sigma^t, \alpha^t, s^t, C, \Delta t\right)$

- **Fix-point algorithm : iteration k**

  1. *Convergence test* $\quad\quad\quad\quad\quad \dfrac{\overline{||j\xi_* \hat{\sigma}_0^k||_2}}{||\hat{\sigma}_0^k||_2} \leq \eta$

  2. *Compute polarization* $\quad\quad\quad \tau^k = \sigma^k - \Lambda^0 : \frac{1}{2}\left(\nabla u^k + (\nabla u^k)^T\right)$

  3. *Real space to Fourier space* $\quad \hat{\tau}^k = FFT(\tau^k)$

  4. *Apply Green operator* $\quad\quad\quad \hat{\nabla u}^{k+1} = -\Gamma^0 : \hat{\tau}^k, \quad \hat{\nabla u}^{k+1}(0) = E^{k+1}$

  5. *Fourier space to Real space* $\quad \nabla u^{k+1} = FFT^{-1}\left(\hat{\nabla u}^{k+1}\right)$

  6. *Anderson's acceleration* $\quad\quad\quad$ save $\left(\nabla u^{k+1} - \nabla u^k, \nabla u^{k+1}\right)$

     $\quad\quad\quad\quad\quad\quad\quad\quad\quad\quad\quad\quad\quad$ if $k \equiv 0[3]$ $\nabla u^{k+1} = \nabla u_*^{k+1}$

     $\quad\quad\quad\quad\quad\quad\quad\quad\quad\quad\quad\quad\quad\quad\quad$ save $\left(\nabla u_*^{k+1} - \nabla u^k, \nabla u^{k+1}\right)$

  7. *Constitutive relation* $\quad\quad\quad \left(\sigma^{k+1}, \alpha^{k+1}\right) = \mathcal{F}\left(\nabla u^{k+1}, \nabla u^t, \sigma^t, \alpha^t, s^t, C, \Delta t\right)$

- **Solve microstress equation** $\quad s_{ij}^{t+\Delta t} = -\lambda^2 \pi_0 \epsilon_{jms}\epsilon_{mlr}H_{il,rs}^{p,t+\Delta t}$

Figure 4.4 – Fully explicit coupling resolution of the periodic non-linear homogenization problem and the field equation $\mathcal{G}$ implemented in AMITEX_FFTP

augmented Lagrangian scheme to solve the problem, which is not compatible with the adopted formulation for the resolution of the problem. R. A. Lebensohn and Needleman (2016) have proposed a way to enforce the simple micro-clamped or micro-hard condition. By setting a very high critical shear stress for grain boundary voxels, they ensured that no slip would develop within them, which is consistent with the boundary condition.

This method is used in the present work to enforce the microhard, as well a the microfree interface conditions at grains boundaries. We denote by Ω_{GB} (see fig. 4.6 for a practical illustration) the set of voxels that are in contact with a grain boundary. The two conditions are implemented as follow:

Microhard-1 grain boundaries

$$\tau_c^s(\boldsymbol{x}) = 10^5 \tau_0^s \qquad \forall \boldsymbol{x} \in \Omega_{GB} \tag{4.72}$$

Time step : $t \longrightarrow t + \Delta t$
INPUT $\left(\nabla u^{t+\Delta t}, \nabla u^t, \sigma^t, s^t, \alpha^t\right) \longrightarrow \left(\sigma^{t+\Delta t}, s^{t+\Delta t}\alpha^{t+\Delta t}\right)$ OUTPUT

- **Initial guess :** $\quad \nabla u^0 = \nabla u^t + \dfrac{\Delta_t}{\Delta_{t-1}}\left(\nabla u^t - \nabla u^{t-\Delta t}\right) \quad (\sigma^0, \alpha^0) = \mathcal{F}\left(\nabla u^0, \nabla u^t, \sigma^t, \alpha^t, s^t, C, \Delta t\right)$

- **Fix-point algorithm : iteration k**

  1. *Convergence test* $\qquad \dfrac{\overline{||j\xi_*\hat{\sigma}_0^k||_2}}{||\hat{\sigma}_0^k||_2} \leq \eta$

  2. *Compute polarization* $\qquad \tau^k = \sigma^k - \Lambda^0 : \frac{1}{2}\left(\nabla u^k + (\nabla u^k)^T\right)$

  3. *Real space to Fourier space* $\quad \hat{\tau}^k = FFT(\tau^k)$

  4. *Apply Green operator* $\qquad \hat{\nabla u}^{k+1} = -\Gamma^0 : \hat{\tau}^k, \quad \hat{\nabla u}^{k+1}(0) = E^{k+1}$

  5. *Fourier space to Real space* $\quad \nabla u^{k+1} = FFT^{-1}\left(\hat{\nabla u}^{k+1}\right)$

  6. *Anderson's acceleration* $\qquad \text{save}\left(\nabla u^{k+1} - \nabla u^k, \nabla u^{k+1}\right)$
     $\qquad \text{if } k \equiv 0[3] \; \nabla u^{k+1} = \nabla u_*^{k+1}$
     $\qquad \text{save}\left(\nabla u_*^{k+1} - \nabla u^k, \nabla u^{k+1}\right)$

  7. *Constitutive relation* $\qquad \left(\sigma^{k+1}, \alpha^{k+1}\right) = \mathcal{F}\left(\nabla u^{k+1}, \nabla u^t, \sigma^t, \alpha^t, s^k, C, \Delta t\right)$

  8. *Solve microstress equation* $\qquad s_{ij}^{k+1} = -\lambda^2 \pi_0 \epsilon_{jms}\epsilon_{mlr}H_{il,rs}^{p,k+1}$

Figure 4.5 – Pseudo explicit coupling resolution of the periodic non-linear homogenization problem and the field equation $\mathcal{G}$ implemented in AMITEX_FFTP

this condition is exactly equivalent to the one implemented by R. A. Lebensohn and Needleman (2016).

Microfree grain boundaries

$$\lambda(\boldsymbol{x}) = 0 \qquad \forall \boldsymbol{x} \in \Omega_{GB} \tag{4.73}$$

As $\underline{\boldsymbol{M}} = \lambda^2\pi_0 \operatorname{curl}\left(\underline{\boldsymbol{H}}^p\right)$, the condition $\lambda(\boldsymbol{x}) = 0$ implies that $\underline{\boldsymbol{m}}(\boldsymbol{x}) = \underline{\boldsymbol{M}}(\boldsymbol{x}) \cdot \underline{\boldsymbol{\epsilon}} \cdot \boldsymbol{n} = 0$, enforcing the microfree boundary condition.

Despite their very straight forward implementation, these methods are not very satisfying as they rely on the specification of the constitutive behavior of entire voxels. Therefore, they are enforced on a sub volume and not a surface. To circumvent this problem, we propose here two additional types of boundary conditions that do not need to modify the behavior of a material subvolume, but
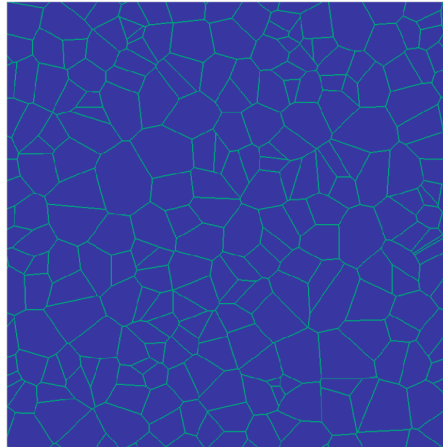
Figure 4.6 – Grain boundary voxels on which are enforced the microhard 1 and microfree boundary conditions (the set Ω_{GB}) are represented in light blue for a 2D polycrystalline unit cell

solely rely on the practical implementation of the differential operators.

Within our implementation, the microstress $\underline{s}$ is calculated through eq. (4.32), restituted here:

$$\underline{s} = -\lambda^2 \pi_0 \operatorname{curl}(\operatorname{curl}(\underline{\boldsymbol{H}}^p))$$

As this expression is derived from the combination of the constitutive equations and the balance equations, the verification of the generalized balance equation eq. (4.24) is ensured over the whole domain on which has been carried out the computation of the expression 4.32. Hence, the conditions satisfied by the voxelized interfaces derive from the form of the field $\underline{\boldsymbol{H}}^p$ passed to the differentiation operator.

In particular, it implies that the boundary condition eq. (4.26), *i.e.* the continuity of $\underline{\boldsymbol{m}}$ is ensured over this domain. In practice, eq. (4.32) is calculated in Fourier space over the whole grid, encompassing entirely the simulated periodic domain. Thus, the resolution of the problem with no particular conditions specified for grain boundary voxels constitutes the **Continuity condition at grain boundaries for $\underline{\boldsymbol{m}}$**.

A similar method is proposed to enforce the micro-hard grain boundary condition. The idea relies on a partition of the polycrystalline simulation domain Ω in M subsets of non connected grains Ω_i. A field $\underline{\boldsymbol{H}}_i^p$ is then constructed for each subset as the restriction of $\underline{\boldsymbol{H}}^p(\boldsymbol{x})$ to the subset and complemented by zeros,

which is formally written:

$$\begin{cases} \underline{\boldsymbol{H}}_i^p(\boldsymbol{x}) = \underline{\boldsymbol{H}}^p(\boldsymbol{x}) & \forall \boldsymbol{x} \in \Omega_i \\ \underline{\boldsymbol{H}}_i^p(\boldsymbol{x}) = 0 & \forall \boldsymbol{x} \notin \Omega_i \end{cases} \tag{4.74}$$

Instead of the direct evaluation of eq. (4.32), we propose to evaluate this expression for each $\underline{\boldsymbol{H}}_i^p$ and sum the results in order to construct the final microstress (eq. (4.75)). This process ensures that the balance equations are verified within each grain. However the computed back stresses will be consistent with a $\underline{\boldsymbol{H}}^p$ field vanishing at the boundary of each grain. We denote this interface condition the microhard-2 boundary condition:

Microhard-2 grain boundaries

$$\underline{\boldsymbol{s}}(\boldsymbol{x}) = -\lambda^2 \pi_0 \sum_{i=1}^{M} \mathbb{I}_{\Omega_i}(\boldsymbol{x}) \operatorname{curl}\left(\operatorname{curl}\left(\underline{\boldsymbol{H}}_i^p(\boldsymbol{x})\right)\right) \tag{4.75}$$

where $\mathbb{I}_{\Omega_i}$ is the indicator function of the set Ω_i.

As the continuity and microhard-2 conditions do not rely on the specification of a condition for a volume, they are believed to be more consistent and less voxel size dependent.

It must be noted though, that the microhard-2 condition is more computationally expensive, as it requires M evaluations of the non local equation. In order to mitigate this increased cost, the smallest partition of Ω in non-connected grains subsets should be used, which ultimately reduces to a map coloring problem. A specific algorithm has been developed to this end and is presented in appendix D.1. An example of such partition of the unit cell can be seen on fig. 4.7.

4.4.3   Numerical integration of constitutive equations

The set of constitutive equations are integrated with the implicit Newton's method, following the procedure described in section 3.2.3. The integration variables are the elastic strain tensor $\underline{\boldsymbol{\varepsilon}}^e$ and the slip variable on each slip system γ^s. At each time increment, the following non-linear system of residual equations is solved:

$$\begin{cases} R_{\underline{\boldsymbol{\varepsilon}}^e} = \Delta \underline{\boldsymbol{\varepsilon}}^e + \sum_{s=1}^{N} \left[\Delta \gamma^s \underline{\mathring{\boldsymbol{\mu}}}^s \right] - \Delta \underline{\boldsymbol{\varepsilon}} = 0 \\ R_{\gamma^s} = \Delta \gamma^s - \Delta t \operatorname{sign}(\tau^s - \chi^s) \left\langle \dfrac{|\tau^s - \chi^s| - \tau_c^s}{K} \right\rangle^n = 0 \qquad 1 \le s \le N \end{cases} \tag{4.76}$$
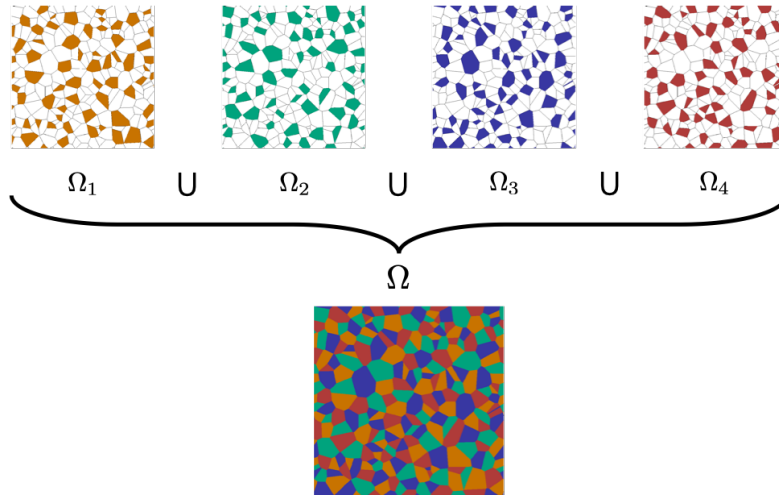
Figure 4.7 – Partition of a 2D polycrystalline unit cell in 4 non-connected grains subsets used to apply the microhard-2 grain boundary condition

Additionally, the values of τ^s and τ_c are computed at each iteration with the relation $\tau^s = \underline{\sigma} : \underline{\mu}^s$ and eq. (4.34).

Detailed calculation of the Jacobian matrix terms are given in appendix B.2.4. Note that, consistent with the coupling formulation, the backstress terms χ^s remains constant during this integration procedure.

4.4.4   Numerical validation

The validity of our implementation is validated through the simulation of two analytical results. The first is taken from Cordero, Gaubert, et al. (2010). It models a unidimensional bi-crystal configuration with one elastic phase and one perfectly plastic phase under single slip, aligned with the slip direction and submitted to a shear loading. The solution is a parabolic slip profile analogous to the one derived in appendix B.2.3 for the kink band with $H = 0$. The results are presented on fig. 4.8, and show a convergence with grid resolution of the numerical results towards analytical solution. The very small discrepancy cannot be further reduced with increasing resolution and could be due to the non exactly equivalent boundary conditions as in the analytical case, induced by the regular discretization. It is also caused by the viscoplastic formulation of the numerical model. Increasing n and decreasing K reduces the discrepancy, up to a limit where the algorithm does not converge anymore. Figure 4.8 shows the results obtained with $n = 100$ and $K = 0.5\,\mathrm{MPa}$, for $\tau_0 = 10\,\mathrm{MPa}$.
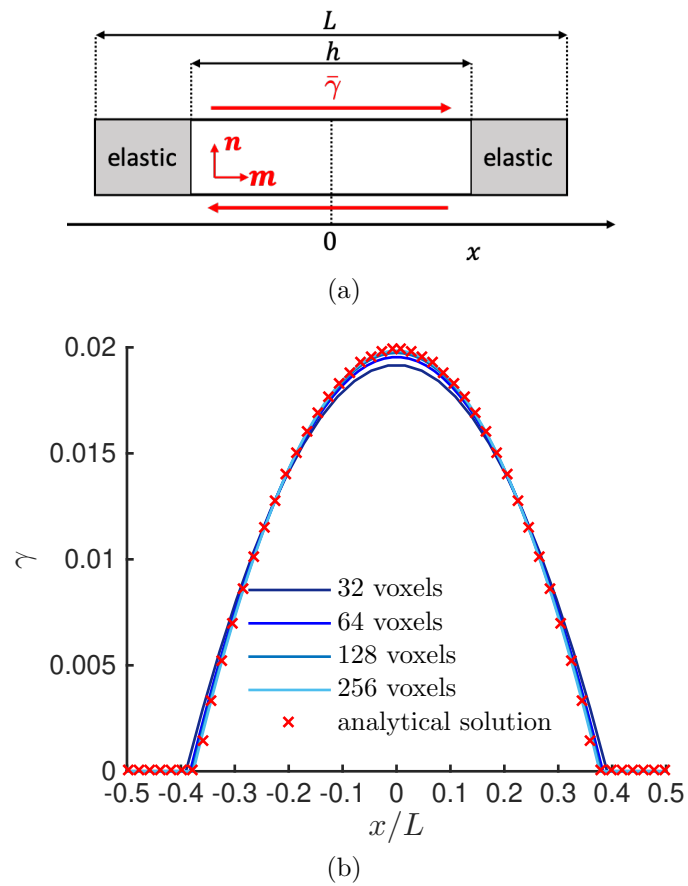
Figure 4.8 – (a): Schematic representation of the elastic-plastic bi-crystal problem presented in Cordero, Gaubert, et al. (2010) and comparison of the simulated curve with analytical solution (b) in the case $\frac{h}{L} = \frac{4}{5}$ and $\bar{\gamma} = 0.01$

The second is the case of the ideal slip and kink band modeling, presented in section 4.2.4, in the case $H =1000$ MPa. The geometrical description of this case is provided on fig. 3.2-(b). Other parameter values are: $n = 100$, $K =0.5$ MPa, $\tau_0 =10$ MPa, $\pi_0 = H$, $\mu =38.6$ GPa. In order to compare the purely local to the non-local formulation, 2 values of λ are tested: $\lambda = 0$ and $\frac{\lambda}{L} = \frac{1}{20} = 0.05$. Results are displayed on fig. 4.9, and show a very good agreement between analytical and numerical solutions. Results show that local and non-local formulation coincide for the slip band, as predicted in section 4.2.4.
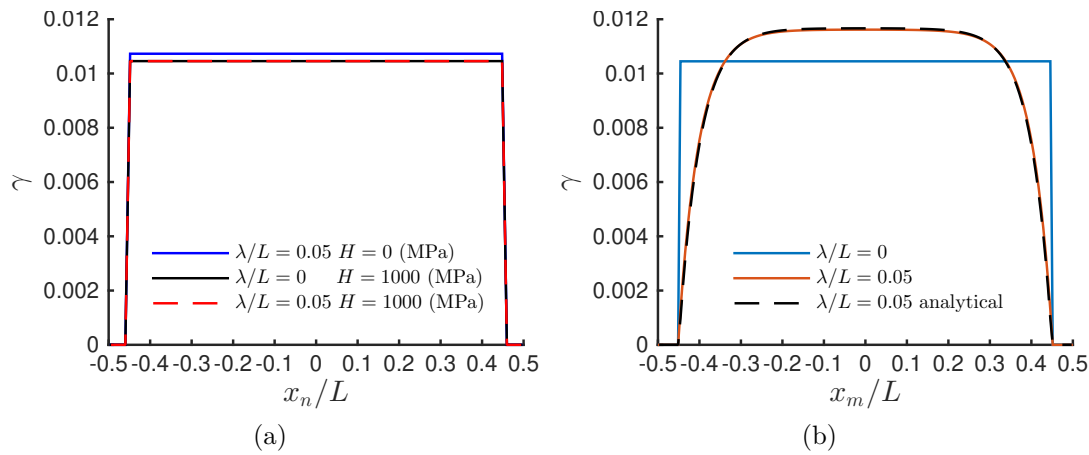
Figure 4.9 – Ideal slip (a) and kink (b) band simulation for $H =10$ MPa. Comparison of the results for vanishing ($\lambda = 0$) vs. non-zero ($\frac{\lambda}{L} = \frac{1}{20}$) gradient effects (grid resolution: $\frac{\partial x}{L} = \frac{1}{80}$)

4.4.5 Numerical analysis: choice of differentiation operator for the backstress calculation

The central idea that motivates the use of this model is the formation of a high GND density within kink bands contrary to slip bands. This is reflected by the expressions of Nye and microstress tensors, eqs. (4.40) and (4.42), that vanish in theory for slip bands but not for kink bands, as discussed in section 4.2.1. It is then crucial to verify that their numerical approximation preserves that property. This is the aim of this paragraph.

Slip and kink bands in softening CCP are sharp discontinuities of the slip field. They are therefore characterized by large variations of this field within one voxel. The formulation of the finite differences used to compute eqs. (4.40) and (4.42) will thus have a very strong influence on slip and kink band edges. In

fact, it is shown through an analytical bidimensional analysis in appendix B.2.5, that the calculation of $\underline{\boldsymbol{\alpha}}$ with the 9-voxels centered finite difference operator of eq. (4.67) preserves this property only for slip systems with $\boldsymbol{m}$ and $\boldsymbol{n}$ aligned with the directions of the discretization grid, or rotated of 45 degrees with respect to it. Moreover, it is shown that the operator of eq. (4.68), if used to compute $\underline{\boldsymbol{s}}$ preserves it only for aligned slip systems, and introduces a backstress on slip bands rotated of 45 degrees with respect to the grid.

For all other orientations it is shown that an intrinsic error is inevitable in the computation, and is larger for the double curl calculation. Error means a non zero value of $\underline{\boldsymbol{\alpha}}$ and $\underline{\boldsymbol{s}}$ within slip bands. Figure 4.10 shows the application of both operators to an artificially constructed field $\underline{\boldsymbol{H}}^p$ containing two crossing bands, a slip and a kink, shown on (a). It is clear that the value of $\underline{\boldsymbol{\alpha}}$ computed with curl* (b) is non zero on the slip band, but one order of magnitude smaller than for the kink band. On the contrary, the output of curlcurl* (c) results in close values for the slip and the kink backstresses.

(a) H_{23}^p (b) curl$^*(\underline{\boldsymbol{H}}^p)_{13}/L$ (c) curlcurl$^*(\underline{\boldsymbol{H}}^p)_{22}/L^2$
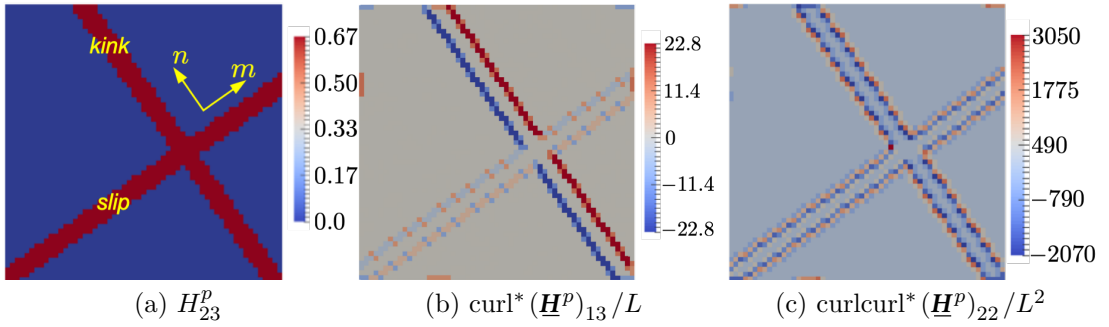
Figure 4.10 – One component of the fields $\text{curl}(\underline{\boldsymbol{H}}^p)$ (b) and $\text{curlcurl}(\underline{\boldsymbol{H}}^p)$ (c) for a constructed $\underline{\boldsymbol{H}}^p$ field representing one slip and one kink band crossing (a). The slip variable γ is 1 in the bands and 0 outside. L is the unit cell size.

This consideration led us to propose an alternative way to compute eq. (4.42), with a double application of the Finite-Difference based simple curl operator. This corresponds to a centered finite difference operator involving voxels in an octahedron of 3 voxels side. It is shown in appendix B.2.5 that it yields a larger difference in order of magnitude between slip and kink bands backstresses. We denote this operator curl2, which is expressed as follow:

$$\text{curl2}^*\left(\underline{\hat{\boldsymbol{A}}}\right) = \epsilon_{jms}\partial_s^*\left(\epsilon_{mlr}\partial_r^*\left(\hat{A}_{il}\right)\right)\boldsymbol{e}_i \otimes \boldsymbol{e}_j \tag{4.77}$$

This operator is applied to the constructed $\underline{\boldsymbol{H}}^p$ field, and compared also to the operator curl2° which is the double curl operator based on the differentiation

frequencies defined for the Willot Green operator (see section 2.4). Figure 4.11 shows that the order of magnitude of the slip band backstress is strongly reduced compared to the operator curlcurl* (fig. 4.11-(c)) in both cases. However, the operator curl2* is better than curl2°.

(a) $\mathrm{curl}2^*\,(\underline{\underline{H}}^p)_{22}/L^2$ (b) $\mathrm{curlcurl}^\circ\,(\underline{\underline{H}}^p)_{22}/L^2$
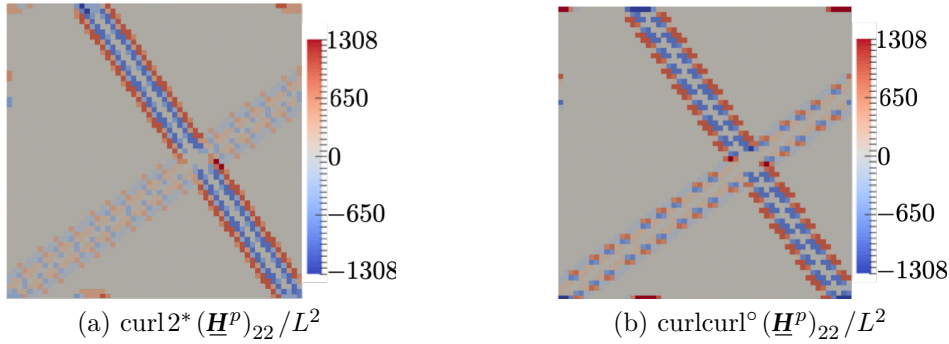
Figure 4.11 – Computed double curl of $\underline{\underline{H}}^p$ field representing one slip and one kink band crossing, for the operators $\mathrm{curl}2^*$ (a) and $\mathrm{curlcurl}^\circ$ (b). L is the unit cell size.

The implications of this operator choice on the formation of slip and kink bands will be illustrated by single crystals simulation in the next section. But we can already conclude from this numerical experiment which confirms the calculations carried out in appendix B.2.5, that the best suited approach in order to limit the formation of kink bands without affecting slips seems to be to compute $\underline{s}$ with $\mathrm{curl}2^*$.

4.5 Simulation of slip localization in single crystals

The influence of the Nye tensor based model on slip localization is first studied on single crystal simulations. This section presents the results aiming at evidencing the influence of material parameters, interface conditions and numerical aspects on slip/kink banding and stress-strain response.

Before describing the details of the simulations, we give a few considerations about the two proposed algorithms. Because of the significant softening and associated instability involved in our simulations, very small strain increments between 10^{-5} and 10^{-6} are needed to allow for the convergence of the numerical integration of the constitutive equations. For these particularly small increments the problem becomes almost linear and only 1 iteration of the fix-point algorithm is needed to reach convergence. In this cases, both explicit and pseudo-implicit algorithms are strictly equivalent. However, at incipient plasticity, when localization

is triggered, a few iterations are required to solve the problem and we observe the same issue reported in R. A. Lebensohn and Needleman (2016): the pseudo implicit formulation (fig. 4.5) of the algorithm is unstable and does not converge. **For this reason, all calculations have been carried out with the fully explicit algorithm** (fig. 4.4).

4.5.1 Simulation of ideal kink and slip banding

The case of ideal slip and kink band for a softening behavior, studied analytically in section 4.2.4 is simulated here, to serve both as a supplementary numerical validation and to study how the model predicts kink bands formation. We recall that L is the width of the elasto-plastic layer submitted to a shear loading and comprised between two rigid layers, and that the analytical solution is given by eq. (4.50). Once again, the reader is referred to fig. 3.2 for the description of the coordinate system and the disposition of rigid and elasto-plastic phase.

The overall displacement gradient is prescribed to impose a shear loading to the unit cell:

$$\underline{\boldsymbol{H}} = \bar{\gamma} \boldsymbol{n} \otimes \boldsymbol{m} \tag{4.78}$$

Grid resolution is set so that $\frac{L}{\partial x} = 360$, where ∂x is the voxel size.

Material coefficients detailed in section 4.4.4 are used here, except for $H = 0\,\text{MPa}$ and $\pi_0 = \tau_0$. In the present case we use the exponential softening law eq. (4.34), with varying values of the relative amount of softening $\eta = \frac{\Delta \tau}{\tau_0}$, and $\gamma_0 = 0.2$. We only examine the case $\frac{\lambda}{L} = \frac{1}{20} = 0.05$. In this cases, as the slip system directions are aligned with the grid directions, the curlcurl* operator is used to compute the backstress. An imperfection has been placed at the center voxel of the simulated unit cell to trigger slip localization, for which the initial critical shear stress is $\tau_0' = 0.99\tau_0$. Simulated slip and lattice rotation angle profiles in the vertical $\boldsymbol{m}$ direction are displayed on fig. 4.12 as well as the associated fields on fig. 4.13.

As predicted in section 4.2.4, no effect of the non-local term is observed in the slip band case. For all tested values, results are similar to fig. 4.12-(a): as for the purely local modeling, slip localizes on a band of a single voxel width.

For the kink band case, contrary to the analytical predictions, the slip field (fig. 4.13-(a-d)) is not homogeneous with respect to the horizontal direction. The kink band is found partially (cases $\eta = 0.05$ and $\eta = 0.1$) or completely ($\eta = 0.2$) composed of intense slip bands having a width and spacing of one voxel. The intensity of the slip bands increases with the intensity of softening. In addition,

(a) $\eta = 0.2$

(b) $\eta = 0.2$

(c) $\eta = 0.1$ and $\eta = 0.2$
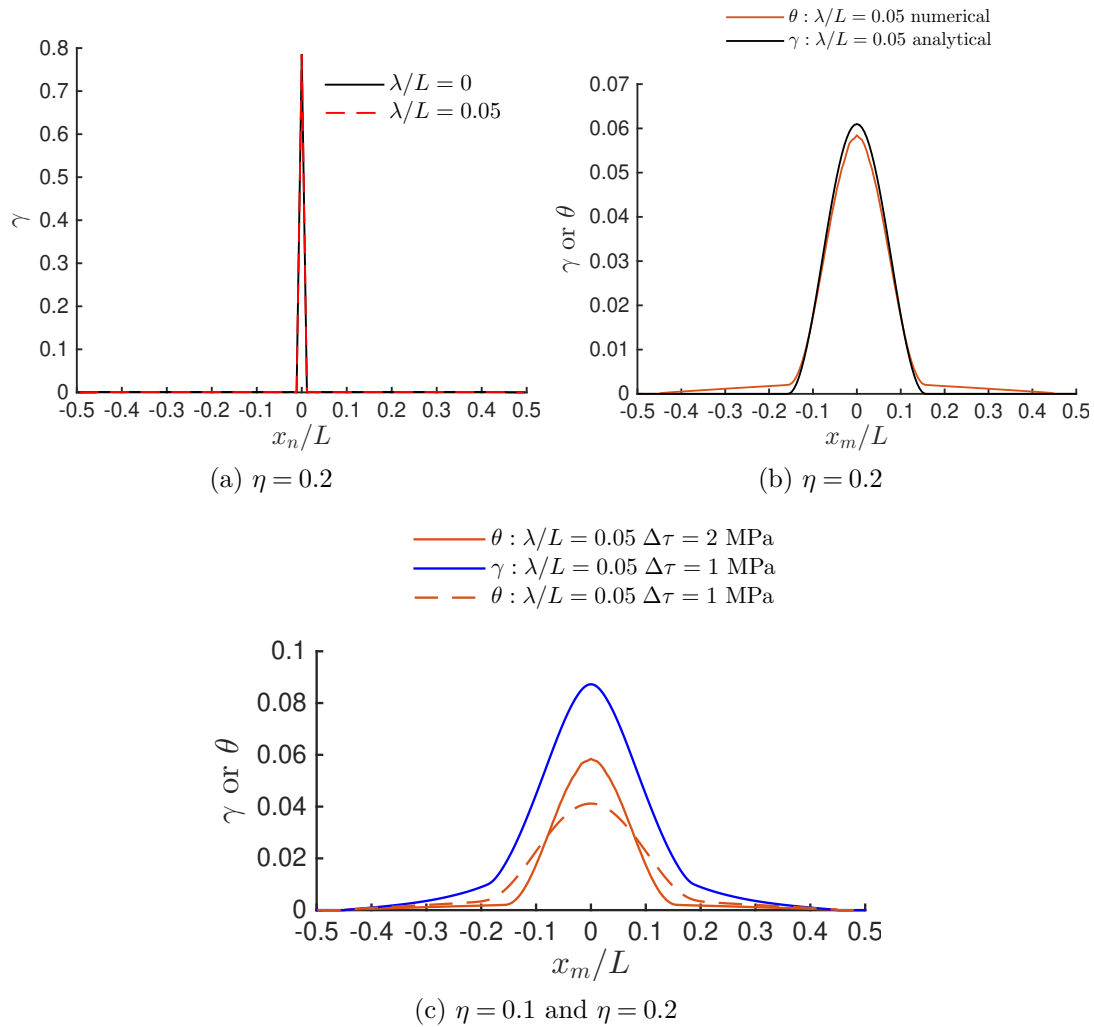
Figure 4.12 – Simulation of ideal slip (a) and kink (b-c) bands for a softening behavior. On (c): two lattice rotation angle profiles are plotted for two softening intensities. The slip profile (in blue) is plotted from the field displayed in fig. 4.13-(b) at the center of the kink band.

(a) $\eta = 0.05$

(b) $\eta = 0.1$

(c) $\eta = 0.2$

(d) $\eta = 0.2$

(e) $\eta = 0.2$

(f) $\eta = 0.2$
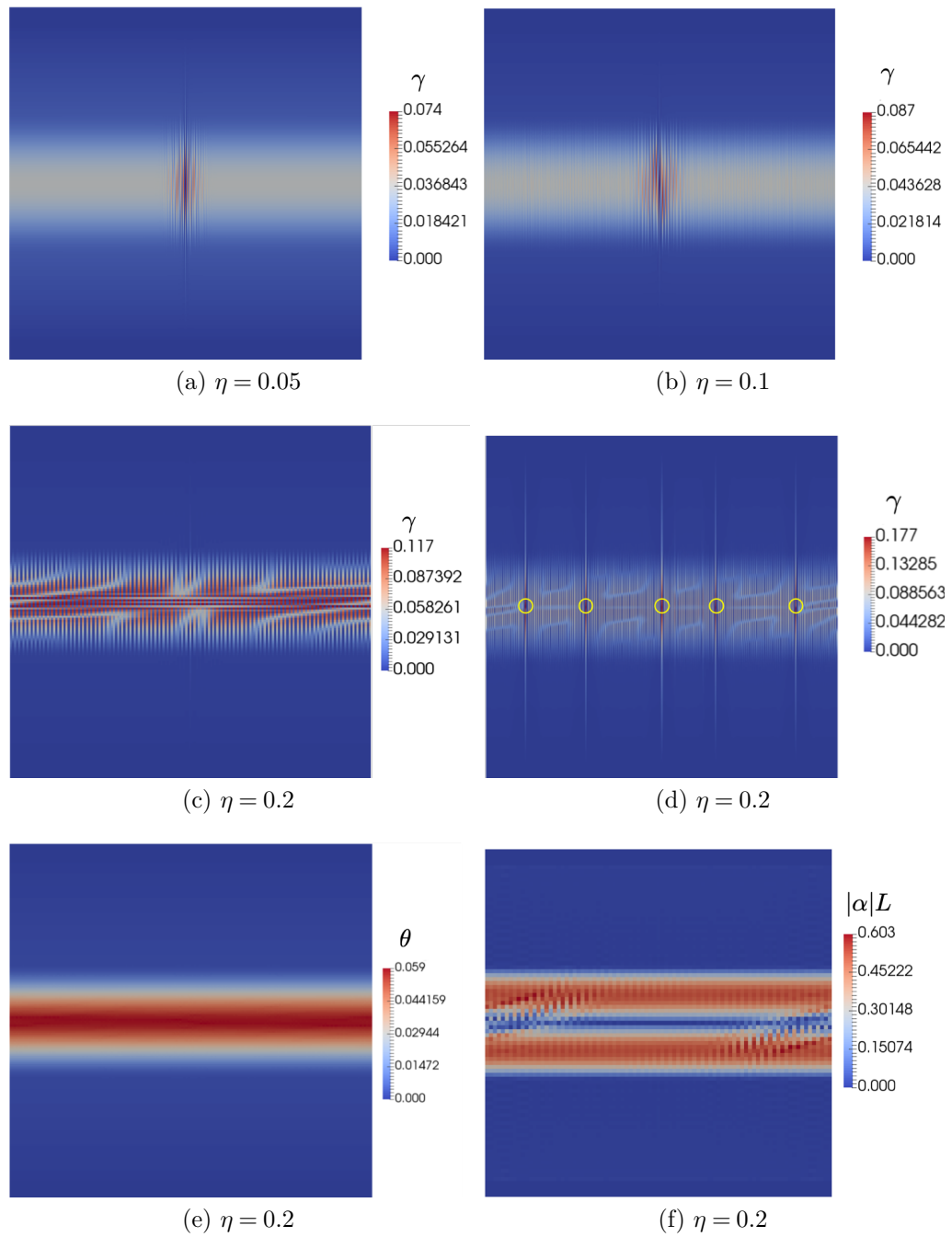
Figure 4.13 – Simulated ideal kink bands slip fields (a-d), lattice rotation angle field (e) and normalized Nye tensor's norm (f). (d) has been simulated with 5 initial weak points on the central horizontal line

complex patterns can be seen in the case $\eta = 0.2$. Conversely, the lattice rotation angle field of fig. 4.13-(e) is homogeneous. The normalized Nye tensor's norm field show clearly the two walls of GND induced by the formation of the kink band. They are relatively homogeneous as well.

Recalling from section 3.3.1 that for a kink band at small strains $\theta \approx \gamma$, the rotation angle is used to validate the simulated profile of the slip band, with respect to the analytically solution (eq. (4.50)). Figure 4.12-(b) shows a very good agreement with numerical results. The small discrepancy can be explained by the short stage of homogeneous deformation phase of the cell before bifurcation, whereas bifurcation is assumed to occur immediately at plastic yield for the analytical calculation.

Figure 4.12-(c) shows the comparison of the aforementioned profile with the case $\eta = 0.1$. When comparing the rotation angle profiles, it appears that the band narrows when increasing softening, in agreement with section 4.2.4. The analytically derived value of the band width is given by eq. (4.53). When computed for the problem values it yields $\frac{\omega_b}{L} = 0.31$ in the case $\eta = 0.2$ and $\frac{\omega_b}{L} = 0.44$ in the case $\eta = 0.1$, which is in good agreement with the widths observed on fig. 4.12-(c). The blue curve is the slip profile obtained in the central slip band, which has a largely higher value than the associated lattice rotation angle.

In order to test the influence on the imperfection introduced on this phenomenon, the case $\eta = 0.2$ has been simulated with 5 randomly placed imperfections along the symmetry line of the cell. As shown on fig. 4.13-(d), the decomposition in slip bands still holds. However, 5 more intense bands are observed at the imperfection locations, circled in yellow. The intensity of the other bands is decreased compared to the single weakness case $\eta = 0.2$ case on fig. 4.13-(c).

4.5.2   Slip and kink banding in an infinite single crystal

We now study a periodic homogeneous single crystal square domain, with an imperfection at its center. The slip system is rotated at 45 degrees from the grid directions in order to test the influence of the differentiation operator, case for which the backstress ratio discrepancy is maximal as discussed in section 4.4.5. Material parameters are unchanged, with $\eta = 0.2$. The length of the periodic cell is denoted L. The square unit cell is discretized by 21x21 pixels and submitted to a tension loading in the vertical direction, up to 1% strain, with all other components of the stress tensor prescribed to 0.

We consider first a purely local simulation: $\frac{\lambda}{L} = 0$. The equivalent plastic strain field is shown on fig. 4.14-(a), with the indication of the glide direction $\boldsymbol{m}$

and normal to slip plane direction $\boldsymbol{n}$. The plasticity is confined into two localization bands of width 1 voxel, one being a slip band, the other one being a kink band. The corresponding double curl fields computed with curlcurl* and curl2* operators are shown on (b) and (c). They clearly show that when increasing $\frac{\lambda}{L}$, a backstresses of the same order of magnitude will appear on both bands for the curlcurl* operator while for the curl2* operator, only the kink band will be affected, as it should be.

| (a) | (b) | (c) |
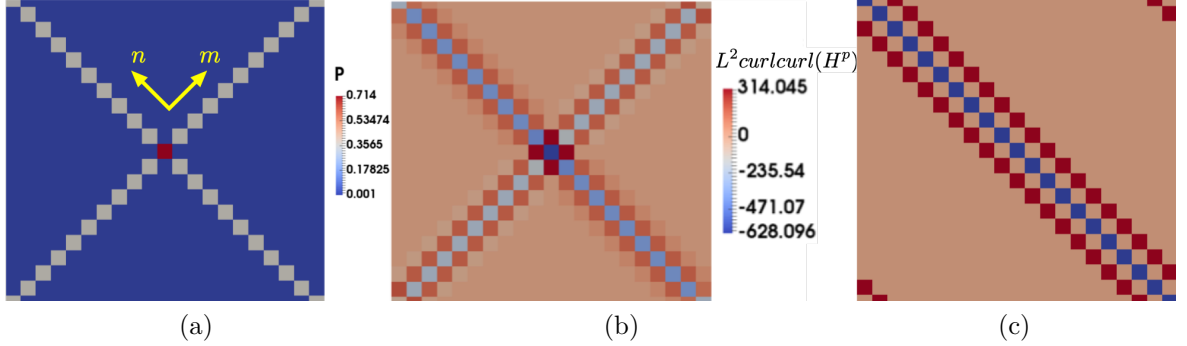
Figure 4.14 – Equivalent plastic strain field (a) and associated curlcurl$(\boldsymbol{H}^p)$ fields calculated with the curlcurl* (b) and the curl2* (c) operators for an infinite periodic single crystal domain ($\frac{\lambda}{L} = 0$). L is the length of the periodic unit cell.

Figure 4.15 displays the equivalent plastic strain fields obtained with $\frac{\lambda}{L} = 0.05$ (a-b) and $\frac{\lambda}{L} = 0.1$ (c-d). Results show that the kink band does not form, all the slip localizes in the slip band. In line with the observed double curled fields of fig. 4.14, the slip band intensity and width for the case where the curlcurl* operator is used depend on the value of the non local parameter. When $\frac{\lambda}{L}$ doubles, the width of the slip band doubles and its intensity is decreased, as would be expected for a kink band. On the contrary, the slip band intensity and width are completely independent of $\frac{\lambda}{L}$ when curl2* is used: slip is localized in a one-voxel thick band. This confirms the choice of this operator as the best suited for the numerical simulations.

4.5.3 Slip and kink banding for a single crystal plate under generalized plane strain

Finally, we consider a bi-dimensional single crystal unit cell in which free edges are introduced, represented on fig. 4.16. Relaxing periodic boundary conditions is achieved by including in the unit cell one layer of elastic voxels with vanishing elastic coefficients on each side of the cell. Periodic boundary conditions are imposed on top and bottom edges, and in the out of plane direction (resulting

(a) curlcurl*   (b) curl2*   (c) curlcurl*   (d) curl2*
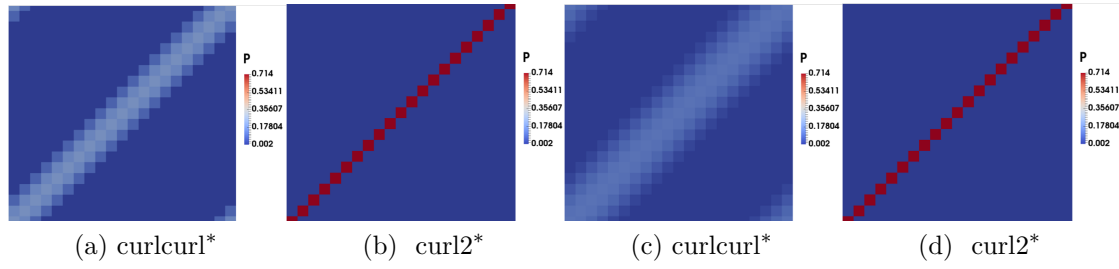
Figure 4.15 – Equivalent plastic strain field simulated at 1% tensile strain for $\frac{\lambda}{L} = 0.05$ (a-b) and $\frac{\lambda}{L} = 0.1$ (c-d) with the two double curl operators curl2* and curlcurl*.

in a generalized plane strain state. The unit cell is submitted to a tensile loading in the vertical direction, up to 1% strain, with all other components of stress prescribed to 0. Material coefficients detailed in section 4.4.4 are used except for: $\tau_0 = 100$ MPa, $\gamma_0 = 0.05$ and $\eta = 0.2$.

The unique slip system orientation with respect to grid axes is defined by the angle β, drawn on the diagram. Finally, we denote L the width of the plate in the horizontal direction. The height of the cell is $4L$. The grid resolution corresponds to 81 voxels along the width L. Again, an imperfection is added to trigger localization at the center, and $\frac{\lambda}{L}$ is the parameter controlling non local effects. The curl2* operator is systematically used to compute the backstresses.

In the following, CCP denote the simulations computed with $\lambda = 0$.

Starting with CCP, it is observed that this time only one localization mode is observed. According to Asaro and Rice's analysis, both slip and kink band could form in this situation. However, in the competition between the two, the shortest band will determine which one will form, depending thus on the orientation of the slip system: $\beta \geq \frac{\pi}{4}$ will yield a kink band while $\beta \leq \frac{\pi}{4}$ will result in a slip band. This is illustrated on fig. 4.17-(a and b). The slip band case corresponds to $\beta = 35°$ and the kink to $\beta = 55°$. On (c) and (d) the normalized GND density tensor norm is displayed, showing that almost no GND is found within the slip band, while the kink is bounded by two high GND density bands, as shown on the zoomed view in fig. 4.18-(b).

The observation of a zoomed view of the slip band on fig. 4.18-(a) reveals that a non zero GND density is observed near the free edges. This is due to the application of the curl* operator to the whole cell, including the two empty voxel layers where $\underline{\boldsymbol{H}}^p$ is set to 0. This corresponds to the application of *microhard2* condition (see section 4.4.2), on free edges. Alternatively, setting $\frac{\lambda}{L} = 0$ on the two
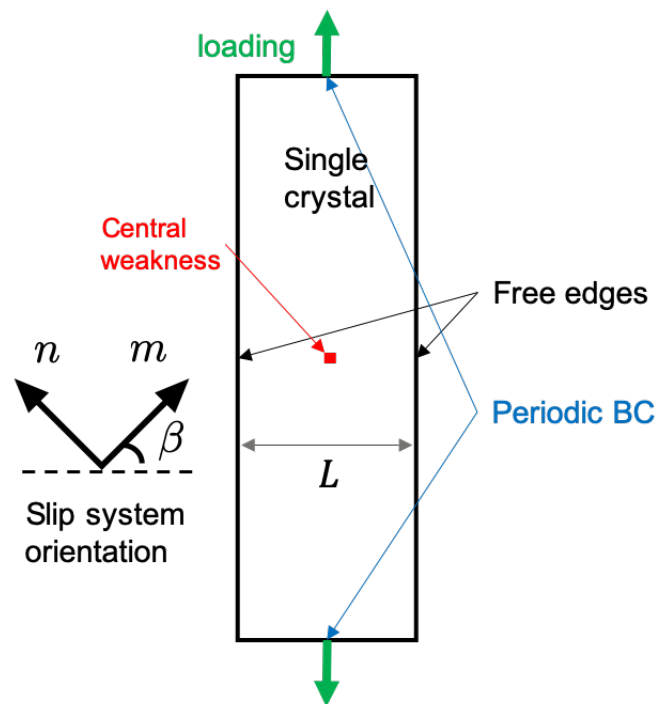
Figure 4.16 – Schematic representation of the simulated single crystal structure

(a) slip, $\beta = 35°$ (b) kink, $\beta = 55°$ (c) kink, $\beta = 55°$ (d) slip, $\beta = 35°$
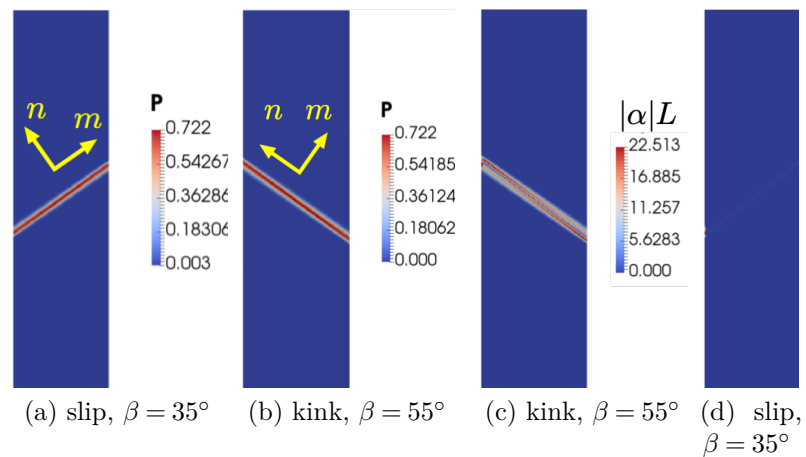
Figure 4.17 – Equivalent plastic strain field (a-b) and associated normalized Nye tensor's norm fields (c-d) for $\frac{\lambda}{L} = 0$.
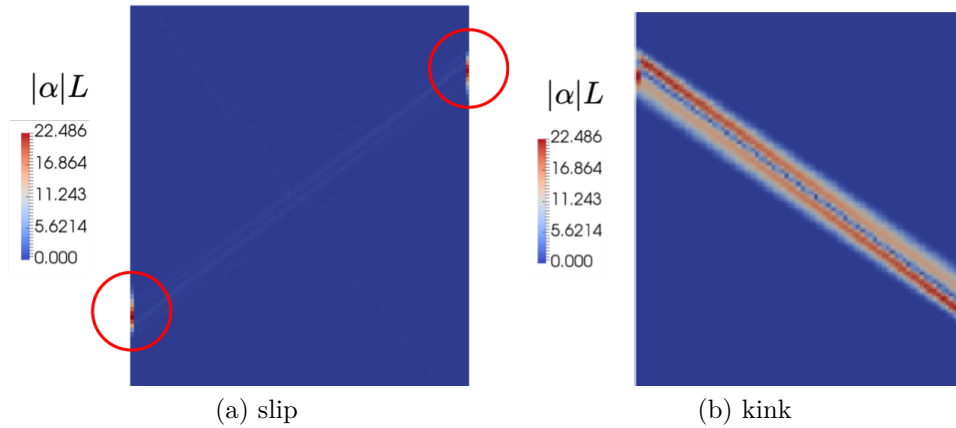
Figure 4.18 – Zoomed view on the normalized Nye tensor's norm fields for: (a) the slip band case revealing non zero GND density at the intersection of the band with the free edges, (b) the kink band case, revealing two dislocation walls bounding the band.

layers of crystal voxels in contact with the edges to impose the *microfree* boundary condition (BC) at the free edges.

Killing Kink bands

The influence of the non-local term is studied here. Simulations computed with $\frac{\lambda}{L} = 0.05$ and the two non-local BC are displayed on fig. 4.19, for the case $\beta = 55°$ which yields a kink band in the CCP case. Results show that the kink band no longer forms, similarly as in the infinite single crystal case. It is replaced by a slip band for all values of λ higher or equal to the voxel size dx. Thus, the study of the effects of the impact of the non-local term for the different boundary conditions and grid resolutions is carried only on slip bands.

Non local coefficient influence

We investigate here the influence of the ratio $\frac{\lambda}{L}$ on the results, for $\beta = 35°$ that yields a slip band for the purely local case. It is shown on fig. 4.20 (a) that the non-local coefficient has no influence on the stress-strain curve when using the microfree condition. Conversely, it has a hardening effect proportional to $\frac{\lambda}{L}$ when using the microhard condition, with a slope of $94\,\text{MPa}$ per unit length (L).

Moreover, the profile of the simulated localization bands in the normal to slip direction have been studied in both cases, and are displayed on fig. 4.21. They

(a) microhard2   (b) microfree
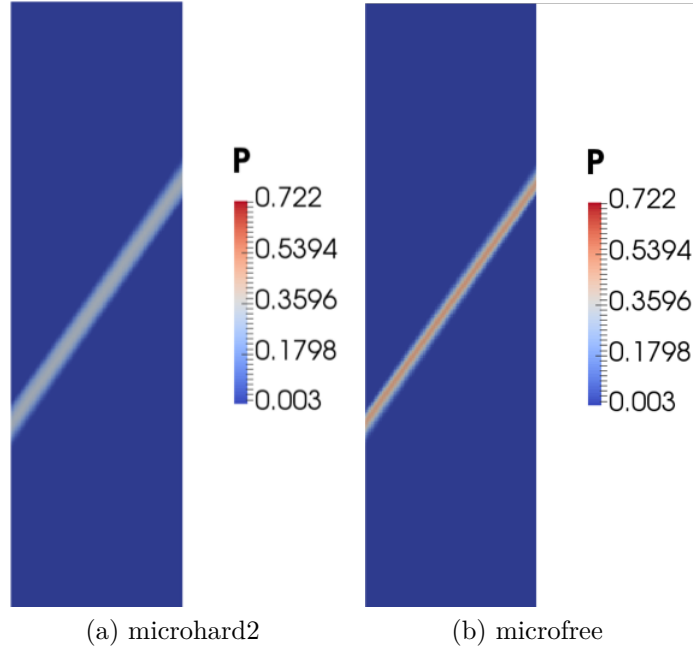
Figure 4.19 – Equivalent plastic strain field (a-b) for $\frac{\lambda}{L} = 0.05$ and $\beta = 55°$. Grid resolution: $\frac{L}{\partial x} = 81$

reveal that increasing $\frac{\lambda}{L}$ slightly reduces the intensity of the band when using the microfree condition (a), but does not affect its width. This influence is attributed to the numerical approximations in the calculation of the backstress (see section 4.4.5). However, when using the microhard condition, a linear increase of the band width with $\frac{\lambda}{L}$ is observed, as shown in figures (b) and (c), with slope of the normalized band width of 3.25. This value is surprisingly close to the approximate theoretical value of kink band width with the values of η and γ_0 used in this calculation which is $\omega_b = \lambda\pi$.

Influence of grid resolution

We now investigate the effect of grid resolution, with $\beta = 35°$. It is shown on fig. 4.22 that increasing the resolution delays the plastic instability and shortens the softening regime for both BC. A slight increase in the stress at 1% strain is observed with increasing resolution for the microhard condition, whereas it is not dependent of resolution with the microfree condition. Note that the increase because hardening effects occur within the localization band which represent a small fraction of the unit cell.

(a) microfree

(b) microhard2

(c)
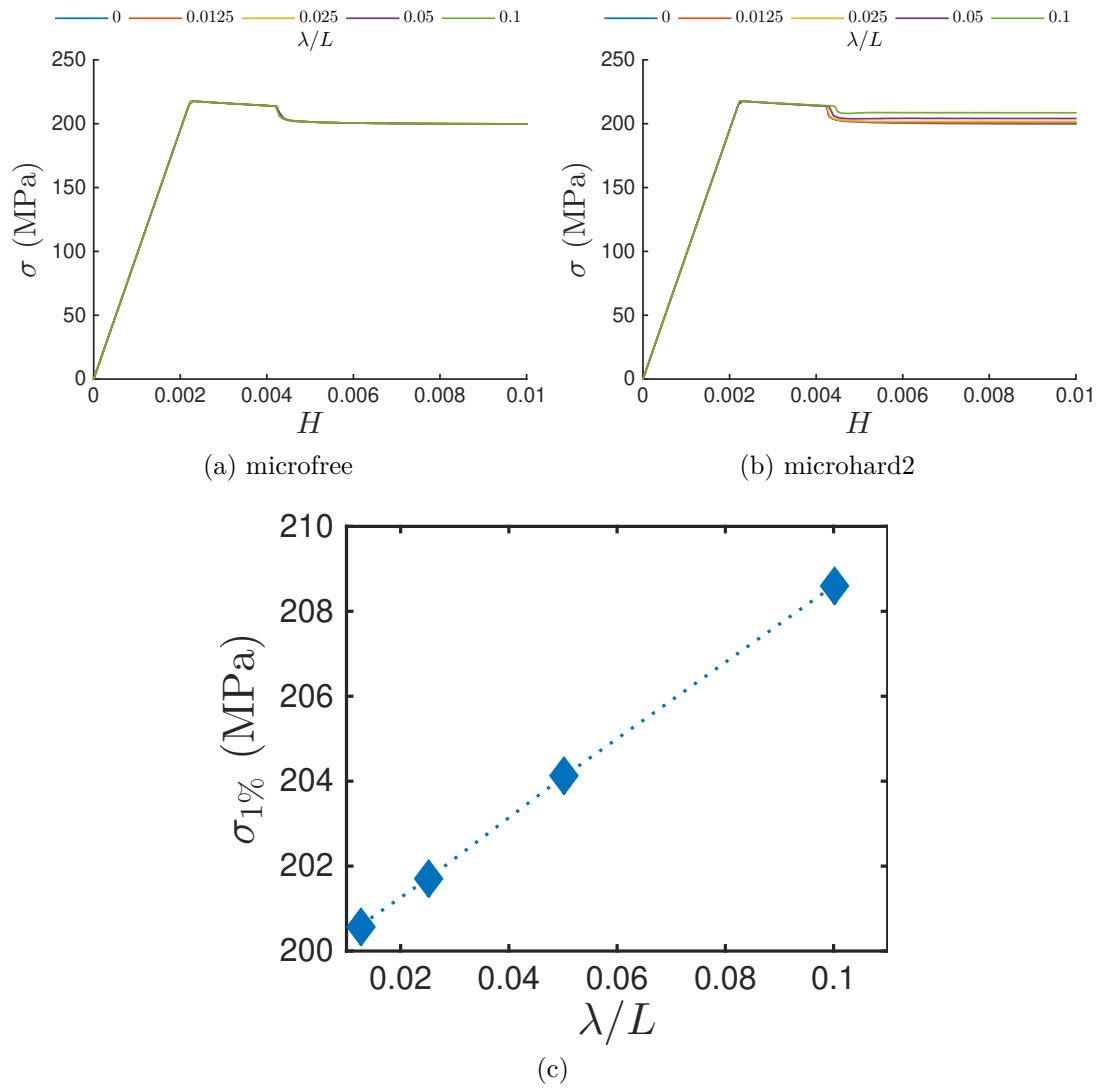
Figure 4.20 – Stress-strain curve for the microfree (a) and microhard2 (b) BC for various values of $\frac{\lambda}{L}$. (c): evolution of the stress value at 1% strain for the microhard BC.
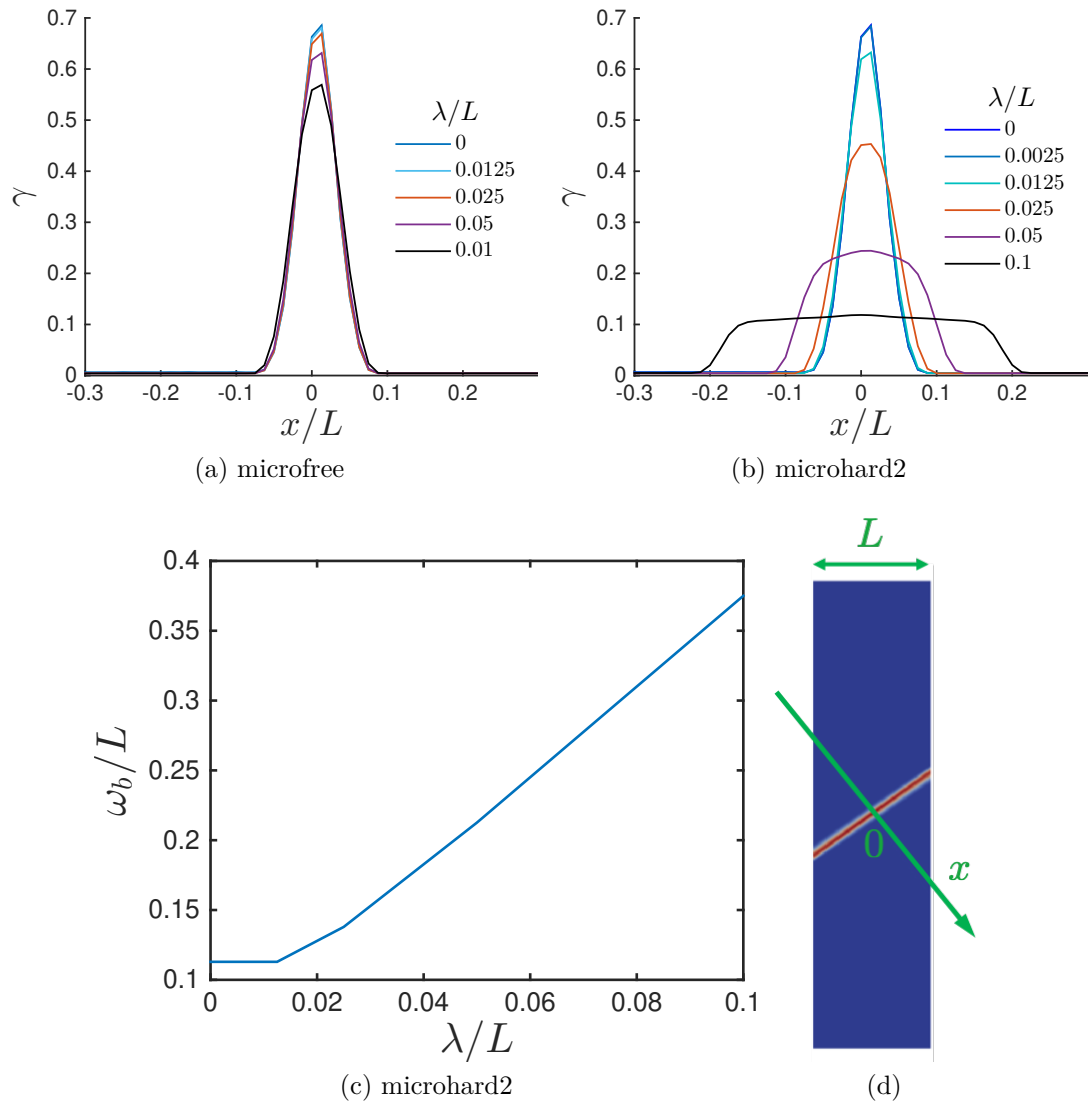
Figure 4.21 – (a-b): Slip profiles in the direction normal to the localization band for various value of $\frac{\lambda}{L}$. (c): evolution of the normalized band width with $\frac{\lambda}{L}$ in the microhard case ($\eta = 0.1 \rightarrow \Delta\tau = 20\,\text{MPa}$). (d): schematic representation of the slip profile location: it is interpolated on the green arrow.
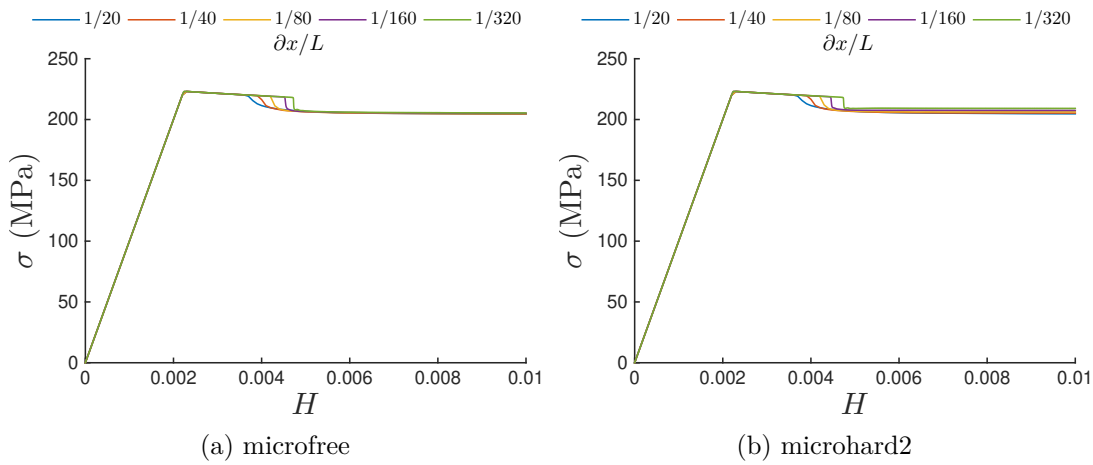
Figure 4.22 – Stress-strain curves for the microfree (a) and microhard2 (b) edge condition for increasing resolution ($\frac{\partial x}{L}$, number of voxels in the width of the cell).

The observation of slip profiles on fig. 4.23 reveals that when using the microfree edge condition, increasing the resolution leads to increased slip localization: the intensity of the band rises, and its width decreases. This is similar to the behavior os slip bands observed with CCP and is consistent with the fact that this SGP model little affects slip bands. For the microhard edge condition, the band width converges towards a stable value. The band intensity rises while the width decreases to convergence, however when the latter is reached, increasing the resolution leads to a decrease in band intensity.

4.5.4   Discussion

Before moving forward to polycrystalline unit cell simulations, we discuss here a few useful conclusions drawn from this series of single crystal simulations.

Influence of non-local term on slip and kink banding

The first question discussed is how the non-local backstress affects the competition between slip and kink banding. Two particular cases arise in this study.

The first one is the case where a kink band is forced to form, studied here with the ideal kink band modeling. According to the analytical modeling, kink bands should be regularized by this model. This property, which is of classical use
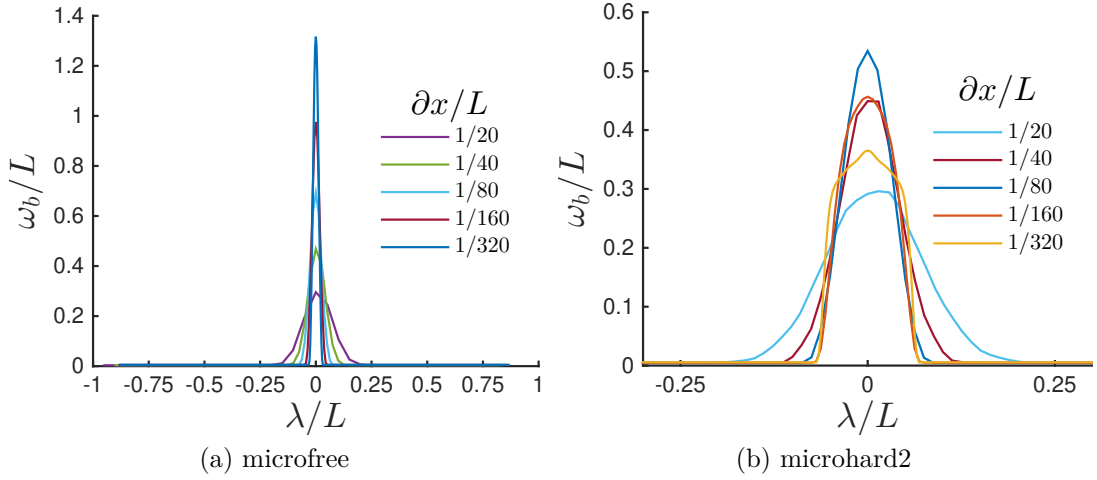
Figure 4.23 – Slip profile in the direction normal to the localization band for various resolutions ($\frac{\partial x}{L}$)

in softening gradient plasticity, implies that the localization bands should have a finite width. This holds true here if we consider kink bands as lattice rotation bands, as shown by fig. 4.13-(e) and fig. 4.12-(b). The width of the rotation angle localization bands are indeed finite, and consistent with the analytical modeling.

Yet, regarding the plastic slip field, the conclusion is different. The band is not homogeneous anymore as it should be induced by the cell geometry and loading symmetry. This symmetry breaking caused by the decomposition of the kink in successive slip bands separated by one voxel is enhanced by the increase of softening intensity. This suggests the occurrence of a plastic instability. Hence, kink band slip fields seem unstable. This scenario could be the one of a double bifurcation, that will be examined further in the final discussion section.

The simulation carried out with 5 weak points highlights the fact that when this second bifurcation is triggered on specific points, slip localization concentrates in slip bands nucleated at these points. This particular field (fig. 4.13-(d)) provides interesting insight into what could happen in a kink band forming in a polycrystal. Microstructure induced stress concentrations will play the triggering role of the weak points and could induce the decomposition of kinks in a few intense slip bands.

A second scenario arise when both slip and kink bands are possible localization modes, illustrated by the single crystal plate simulations. In this case, the best-suited mode to accommodate strain in the structure forms, as discussed in the previous chapter. **In the following, we refer to structure effects as the**

selection of a localization mode (slip or kink) by the energy minimization of the structure.

In this case, our results show that the non-local effects interfere with this structural competition, and systematically lead to the formation of the slip band over the kink band. This proves that the energy penalty that is given to kink band formation by this model favors slip banding over kink banding.

Influence of Boundary condition

We discuss here the effect of the BC chosen for the free edges on slip bands. As illustrated on fig. 4.18, for slip bands the backstress will develop only at the edges. Thus the microfree edge condition induces gradient effects only on the bulk part of the localization band. In this case, the classical instability of the localization band with grid refinement is observed, along with no hardening effect. From this, it can be concluded that the small value of backstress on slip bands induced by the curl2* operator (see section 4.4.5) are sufficiently small to avoid the unwanted regularization of slip bands.

Conversely, the microhard condition leads to the widening of slip bands that form with a width proportional to the material intrinsic length scale (λ), as well as a macroscopic hardening also proportional to it. This shows that boundary effects can strongly affect the characteristics of slip bands when accounted for.

4.6 Simulation of slip localization in polycrystals

We come now to the main study of this chapter, and finally address the problem of intragranular slip localization in polycrystals. We will present a systematic study of intragranular localization bands similar to the one presented in chap. 3 and compare their results in order to characterize the improvements obtained from the use of the strain gradient plasticity model with respect to CCP, in the view of the simulation of intragranular localization bands in softening polycrystals.

The simulations presented in this section are divided in two sets: bi-dimensional and three-dimensional simulations. The bi-dimensional simulations are analyzed extensively with the various processing strategies presented in chap. 3, in order to fully characterize qualitative and quantitative effects of the non-local term, the sensitivity to softening intensity, and grain boundary interface conditions, on slip and kink banding. Then, three-dimensional simulations, are qualitatively

K	n	E	ν	τ_0	$\Delta\tau$	γ_0	H	π_0
$10\,\text{MPa}\ \text{s}^{-n}$	15	$100\,\text{GPa}$	0.3	$100\,\text{MPa}$	$20\,\text{MPa}$	0.1	$0\,\text{MPa}$	$100\,\text{MPa}$

Table 4.2 – Material parameters used for polycrystalline simulations of the Nye tensor based model

analyzed in the light of the findings of two-dimensional simulations.

4.6.1   Description of Simulations

The polycrystalline cells used in this study are the same as the ones presented in section 3.4.1. Constitutive model parameters used in all simulations unless otherwise stated are listed in table 4.2. All simulations feature isotropic linear elasticity. Norton law coefficients n and K values are chosen in order to limit rate dependence while preserving numerical convergence. As simulated crystal systems have only one family of slip systems, superscript s on flow rule parameter is omitted in the rest of this chapter.

The characteristic stress π_0 is chosen so that $\pi_0 = \tau_0$. Thus the parameter controlling gradient effects is the ratio between the material intrinsic length scale λ and the microstructure characteristic length d_g, the mean grain size. **In the following simulations with $\lambda = 0$ will be referred to as CCP results, and with $\lambda > 0$ as SGP results.**

Unless otherwise stated grid resolution has been chosen so that each voxel contains $50^2 = 2500$ voxels in average. It is defined as the ratio between mean grain size and voxel size $\frac{d_g}{\partial x}$, where ∂x is the voxel size (here $\frac{d_g}{\partial x} = 50$).

In all simulations, unit cells are submitted to a simple tension loading in the $\boldsymbol{e}_3$ direction, up to 1 % strain, at a speed of $1 \times 10^{-5}\,\text{s}^{-1}$. Unless specified otherwise, the continuity of $\underline{\boldsymbol{m}}$ condition at grain boundaries is used.

4.6.2   Preliminary results

We provide here a few preliminary numerical results, obtained on the 225 grains 2D microstructure with one slip plane per grain. First, as all simulations rely on a purely explicit coupling algorithm, convergence with respect to the time discretization is verified. Figure 4.24 shows the stress-train curve obtained with $\frac{\lambda}{d_g} = 0.2$ when computing the simulation with 1000 or 10000 time increments, corresponding to 10^{-5} and 10^{-6} strain increments. A perfect superposition of the curves can be observed, indicating a converged simulation with respect to time
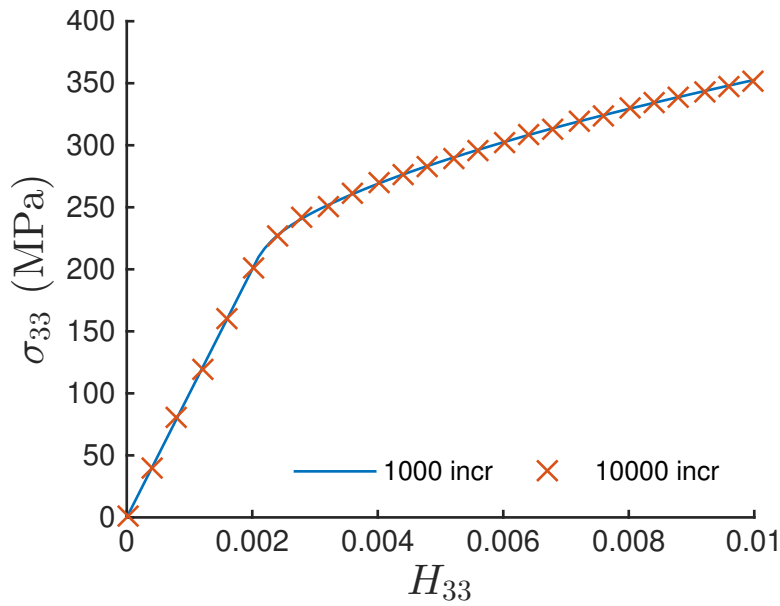
Figure 4.24 – Verification of the convergence of the time discretization for the explicit integration algorithm (225 grain 2D polycrystal)

discretization. Thus, simulations are carried out with 10^{-5} strain increments in the following.

Second, we highlight a central result regarding the application of the processing strategies to the strain gradient model. Chap. 3 has demonstrated the efficiency of the lattice rotation based strategy for slip and kink band analysis in CCP simulations. Yet, the results of section 4.5.1, especially fig. 4.13-(d), show examples of formation of intense slip bands inside an intense lattice rotation band. Hence, the fundamental property of CCP allowing to discriminate bands with their associated lattice rotation field is lost with the strain gradient plasticity model, because of kink bands instability. For this reason, only the image processing and peak analysis based strategies are used in the following analyses.

4.6.3 Bi-dimensional polycrystalline simulations

We describe in this part, the simulations carried out on the bi-dimensional polycrystalline unit cell of 64 (*i.e.* 160 000 voxels) or 225 (*i.e.* 562 500 voxels) grains with a unique in plane slip system. The study focuses on induced hardening effects and the systematic analysis of slip and kink bands populations produced in the grains.

GND induced hardening

Strain gradient plasticity models are classically used to study hardening grain size effects in polycrystals. R. A. Lebensohn and Needleman (2016) have proposed the first FFT-based implementation of a $\mathrm{curl}(\boldsymbol{H}^p)$ based model, and provided a few illustrative examples of their capability to predict size effect. However, their results only rely on the microhard-1 grain boundary condition and a hardening crystal plasticity law. Thus, before the study of gradient effects on slip localization, we propose to apply our implementation to extend this analysis of GND induced hardening effects with a FFT-based implementation, in the case of locally softening plasticity. A particular focus is put on the evaluation of the influence of the various grain boundary conditions.

Figure 4.25 shows the various stress-strain curves obtained for $0 \leq \frac{\lambda}{d_g} \leq 0.2$ and $\frac{d_g}{\partial x} = 50$. As in the CCP case (see chap. 3), even though the local behavior of the crystal is softening, the overall behavior of this polycrystal with one slip system per grain is hardening. All curves have the same yield stress, completely overlap in the incipient plasticity regime but diverge during plastic flow. Results show that no hardening effect is observed for $\frac{\lambda}{d_g} < \frac{\partial x}{d_g}$. Indeed, the two curves obtained with $\frac{\lambda}{d_g} = 0$ and $\frac{\lambda}{d_g} = 0.01$, which corresponds to a material length scale smaller than the voxel size, are superimposed. For higher values, the final stress increases with $\frac{\lambda}{d_g}$.

In the particular case of $\frac{\lambda}{d_g} = 0.2$, fig. 4.26-(a) shows a comparison of the stress-strain curves corresponding to the four BC presented in section 4.4.2, enforced at grain boundaries. As expected, the two microhard conditions predicts the strongest response, while the microfree yields the softer. The continuity condition yields an intermediate prediction of gradient hardening effects. The curves reveal that the microhard-1 condition is significantly harder than the microhard-2 condition.

As discussed in section 4.4.2, because it does not prescribe the condition on a sub volume, the microhard-2 condition is expected to be less grid dependent than the microhard-1. This property is investigated in fig. 4.26-(b). Results clearly show than the microhard-1 condition induces much larger variations than the microhard-2 when varying grid resolution. Besides, they vary in opposite directions: when grid refinement increases, the microhard-1 condition gets softer, while the microhard-2 gets harder. Both conditions seem to converge towards the same curve, but a more refined grid should be used to confirm this fact. Additionally, the microhard-2 condition clearly shows a faster convergence. The continuity and microfree conditions results are very similar to those of the microhard-2 condition. Microfree boundary condition appears to induce the smaller voxel size dependence.
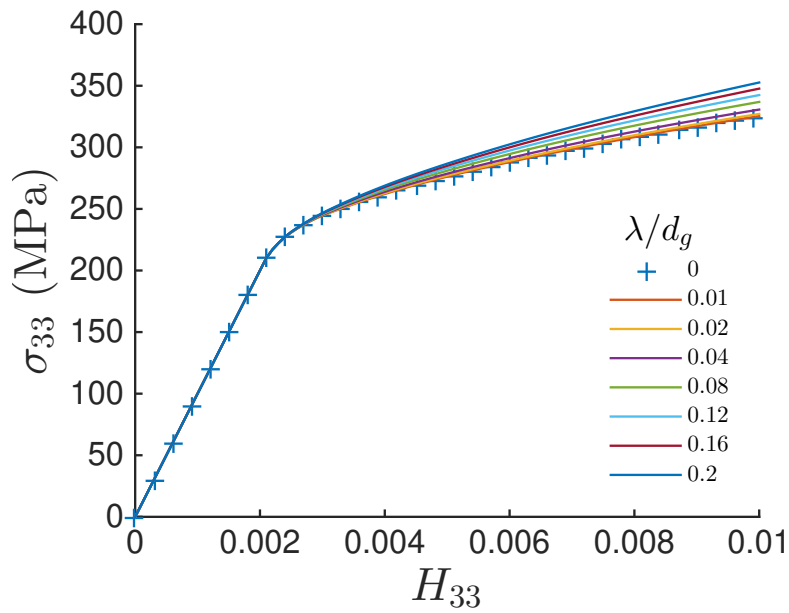
Figure 4.25 – Stress-strain curves for various values of $\frac{\lambda}{d_g}$ and $\frac{d_g}{\partial x} = 50$ with continuity condition enforced at grain boundaries

Finally, the increase observed in the overall stress at 1% overall strain is plotted for the three condition microfree, continuity and microhard-2 in function of $\frac{\lambda}{d_g}$ on fig. 4.27. For $\frac{\lambda}{d_g} \geq 0.04$, the hardening effect can be approximated by a linear function of $\frac{\lambda}{d_g}$. The highest slope is obtained with the microhard condition, the softest with the microfree condition, and the continuity condition yields an intermediate slope.

Influence of higher order parameters on slip and kink banding

Here, we study the influence of gradient effects on the formation of slip and kink bands. Figure 4.28 show the localization maps produced for various values of $\frac{\lambda}{d_g}$, from 0 to 0.4. The map obtained for CCP ($\frac{\lambda}{d_g} = 0$) is very similar to the maps studied in chap. 3. It shows a large amount of both slip and kink bands, with no particular distinction between them. When $\frac{\lambda}{d_g}$ increases, the number of visible kink band rapidly decreases. Only a few thick kink bands remain visible. Conversely, slip band population is little affected by the increase of the gradient term.

The observation of the associated equivalent plastic strain and lattice rotation angle fields on fig. 4.29 confirms that highly localized kink bands are

(a) All BC

(b) Microhard

(c) Continuity

(d) Microfree
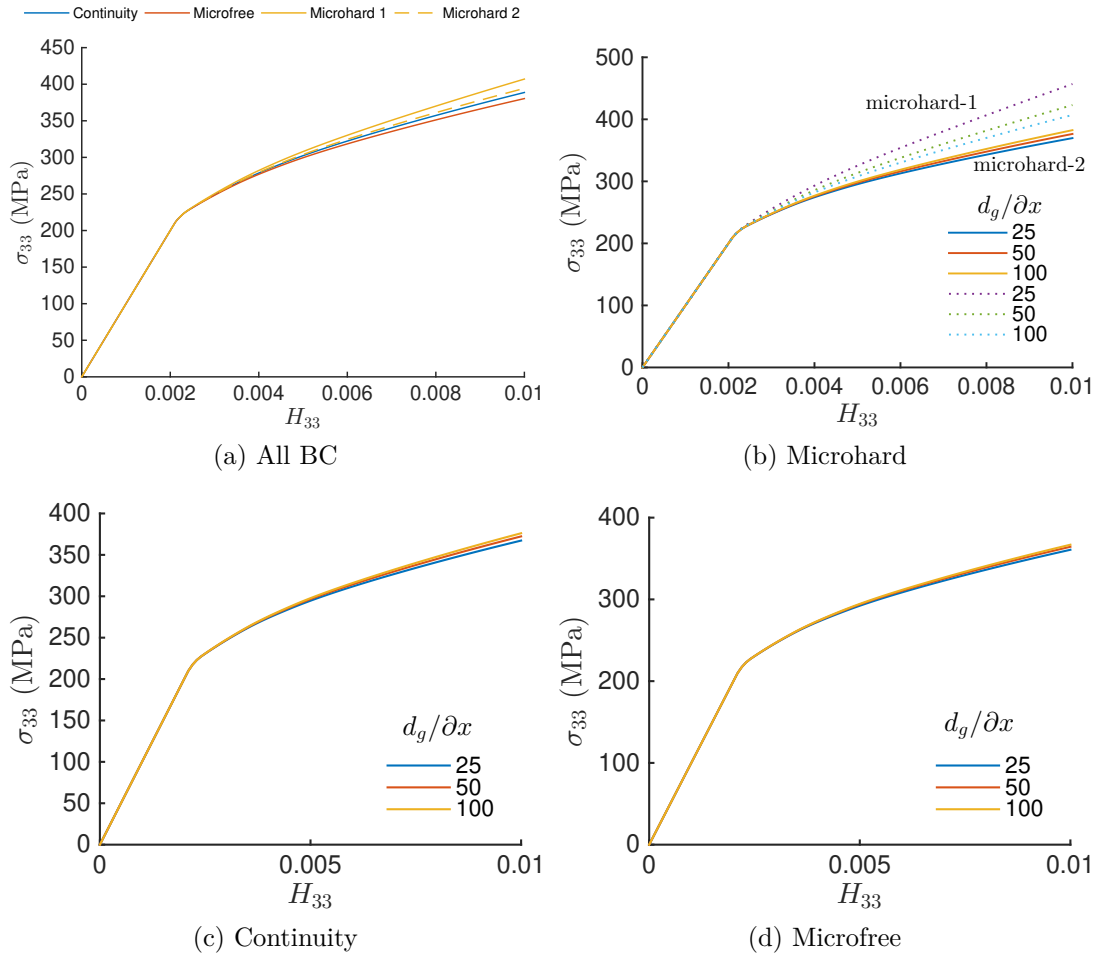
Figure 4.26 – (a): Comparison of the stress-strain curves for various grain boundary condition with $\frac{\lambda}{d_g} = 0.2$ and $\frac{d_g}{\partial x} = 50$. (b-d): Comparison of the stress-strain curves for various resolution between the two implementations of the microhard boundary condition ((b), dotted lines correspond to the microhard-1 condition, the full lines to the microhard-2 condition), for the continuity of $\underline{\boldsymbol{m}}$ condition (c), and for the microfree condition (d).
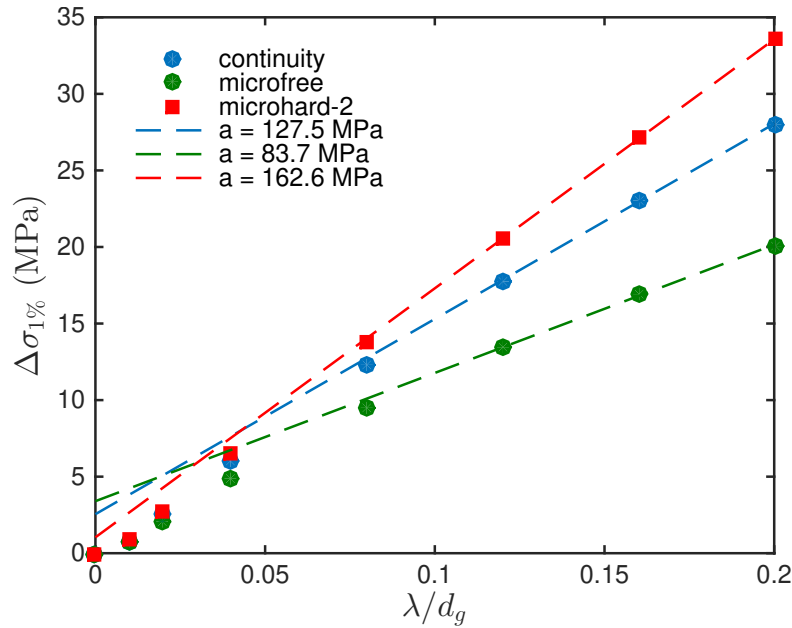
Figure 4.27 – Comparison of the increase of overall stress at 1 % strain in function of $\frac{\lambda}{d_g}$ for various grain boundary conditions and and $\frac{d_g}{\partial x} = 50$ (225 grain 2D polycrystal). $\Delta\underline{\sigma}_f = \underline{\sigma}(\frac{\lambda}{d_g}) - \underline{\sigma}(\lambda = 0, H = 0.01)$.

suppressed in the case $\frac{\lambda}{d_g} = 0.2$. Sharp slip bands are still observed but are less intense than with CCP. Moreover, the overall intensity of slip localization is lower when the gradient term is non-zero. In particular, the kink banding areas of the field (a) are replaced by thick and homogeneous areas of moderate slip. Careful examination of the field (b) reveals also that in some of these areas, the decomposition of kink bands in a series of successive and very close slip bands exhibited in section 4.5.1 can be observed.

The comparison of the lattice rotation angle field shows that the same grains experience lattice curvature in both cases. However, with CCP, the field is composed of many thin bands of very intense rotation, whereas in the SGP, only one or rarely two rotation bands are found. They are significantly wider, and much less intense, with locally a rotation about 4-5 times lower.

The quantitative analysis of these localization bands populations is presented on figs. 4.30 and 4.31. Figure 4.30-(a) and fig. 4.31-(a) confirm the previous observation: the computed number of kink bands as well as their volume fraction, equivalent to their slip band counterpart for CCP results, strongly decreases when $\frac{\lambda}{d_g}$ increases. The number of kink bands is divided by 10 when $\frac{\lambda}{d_g}$ goes from 0 to 0.4, while the number of slip bands is only slightly reduced. However, their volume

(a) $\frac{\lambda}{d_g} = 0$

(b) $\frac{\lambda}{d_g} = 0.08$

(c) $\frac{\lambda}{d_g} = 0.2$

(d) $\frac{\lambda}{d_g} = 0.4$
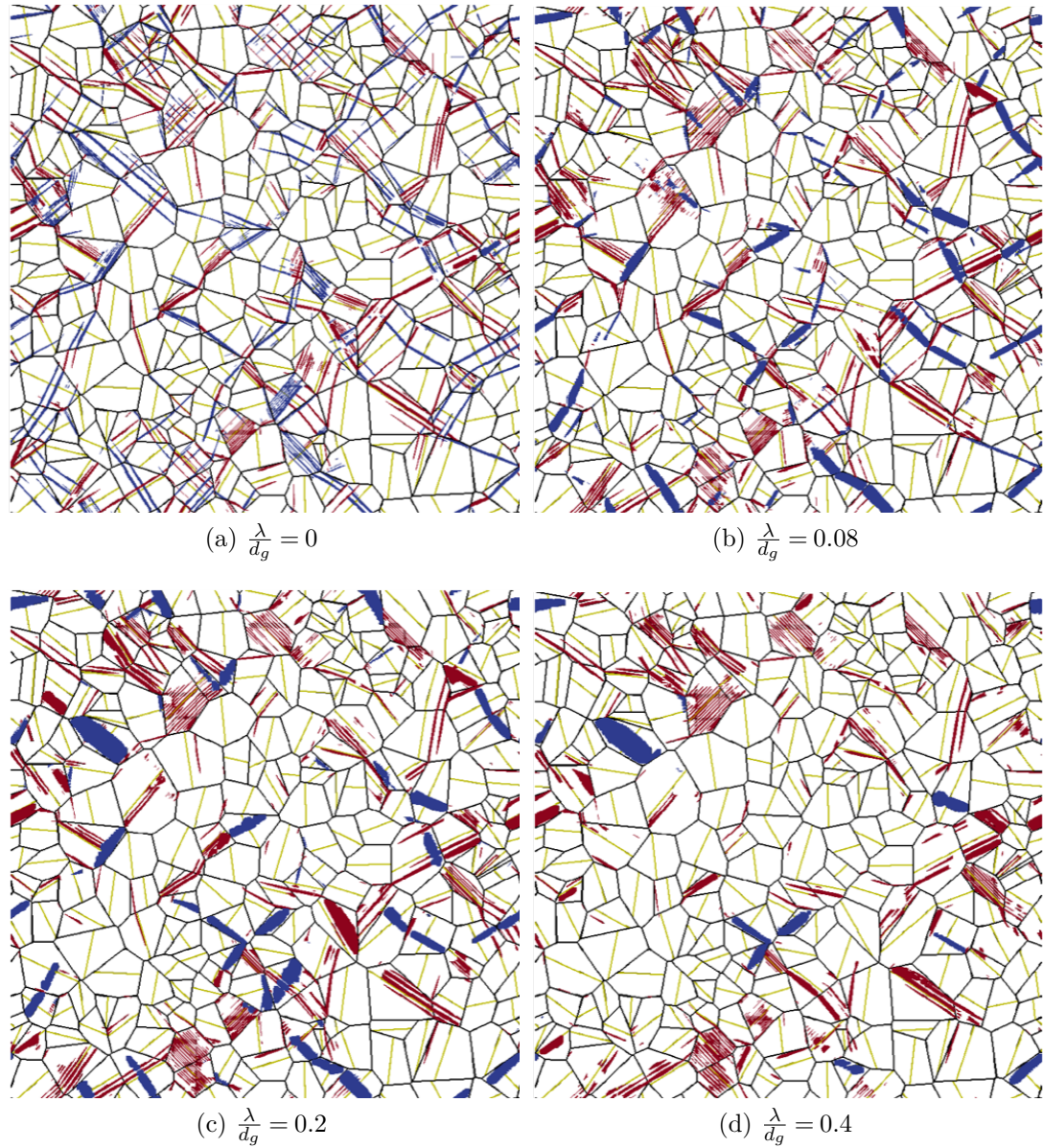
Figure 4.28 – Localization maps constructed with the second processing strategy of chap. 3 for various values of $\frac{\lambda}{d_g}$ and for $\frac{d_g}{\partial x} = 50$ (225 grain 2D polycrystal), showing slip (red) and kink (blue) bands populations. Slip planes are displayed in yellow.

(a) $\frac{\lambda}{d_g} = 0$ (b) $\frac{\lambda}{d_g} = 0.2$

(c) $\frac{\lambda}{d_g} = 0.0$ (d) $\frac{\lambda}{d_g} = 0.2$
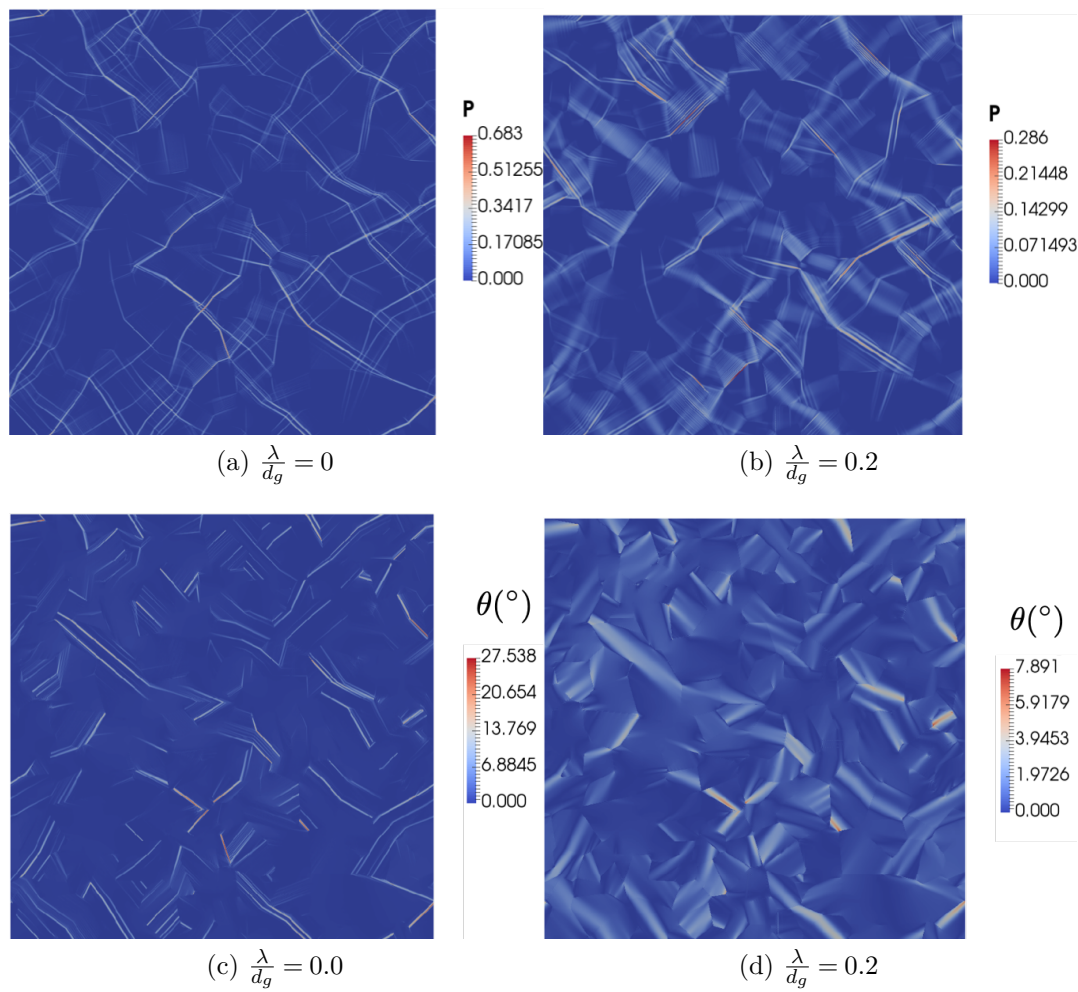
Figure 4.29 – Equivalent plastic strain (a-b) and lattice rotation angle (c-d) fields for various values of $\frac{\lambda}{d_g}$ and for $\frac{d_g}{\partial x} = 50$ (225 grain 2D polycrystal).

fraction is divided by approximately 4, because of the compensation induced by the widening of remaining kink bands, which is clearly shown on fig. 4.31-(b). It also confirms the little influence on slip band width of the higher order term, already observed for the microfree single crystal structures (section 4.5.3).

On the other hand, fig. 4.30-(b) and fig. 4.31-(c) confirms the overall drop of the intensity of slip localization induced by gradient effects. This decrease is non-linear and gradually slower. Finally, fig. 4.31-(d) evidences the little influence of the gradient effects on the mean distance between slip bands, consistently with the observation of localization maps. On the contrary, it strongly increases for kink bands, up to a saturation value of $1.5d_g$. As d_g is the mean grain size, this shows that the grains exhibiting two rotation bands are larger than the average grain size [1]. This is to put in relation with the theoretical width of kink bands predicted by eq. (4.53), which in this case is approximately the average grain size: $\frac{\omega_b}{d_g} \approx 0.9$ for $\frac{\lambda}{d_g} = 0.2$ and superior for $\frac{\lambda}{d_g} \geq 0.3$, which is the saturation value.

To conclude, all quantitative indicators shown on figs. 4.30 and 4.31 for $\frac{\lambda}{d_g} = 0$ are almost identical for slip and kink bands but exhibit an increasing gap as $\frac{\lambda}{d_g}$ increases.
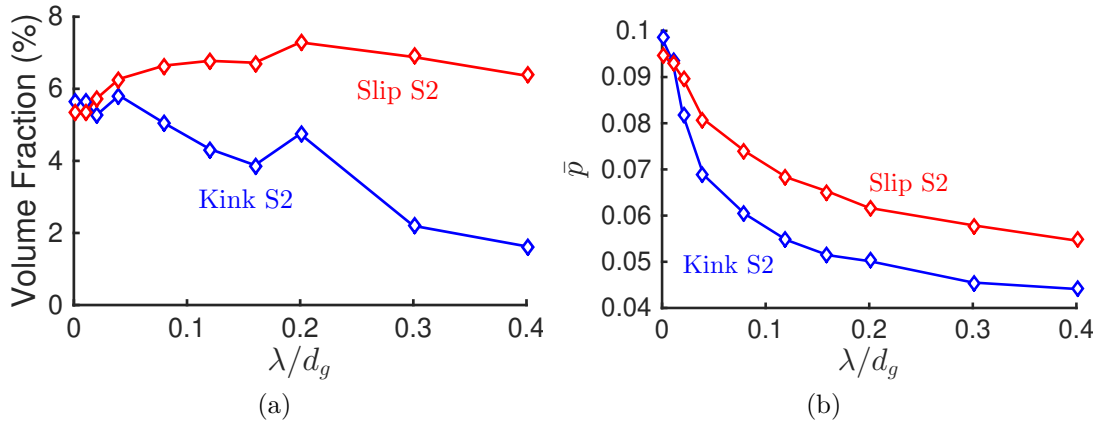
Figure 4.30 – Evolution of bands volume fraction (a) and mean plastic strain (b) with $\frac{\lambda}{d_g}$ and for $\frac{d_g}{\partial x} = 50$ (225 grain 2D polycrystal), computed with the second processing strategy of chap. 3.

---

[1] note that if only one band is found in the grain, no band spacing is computed
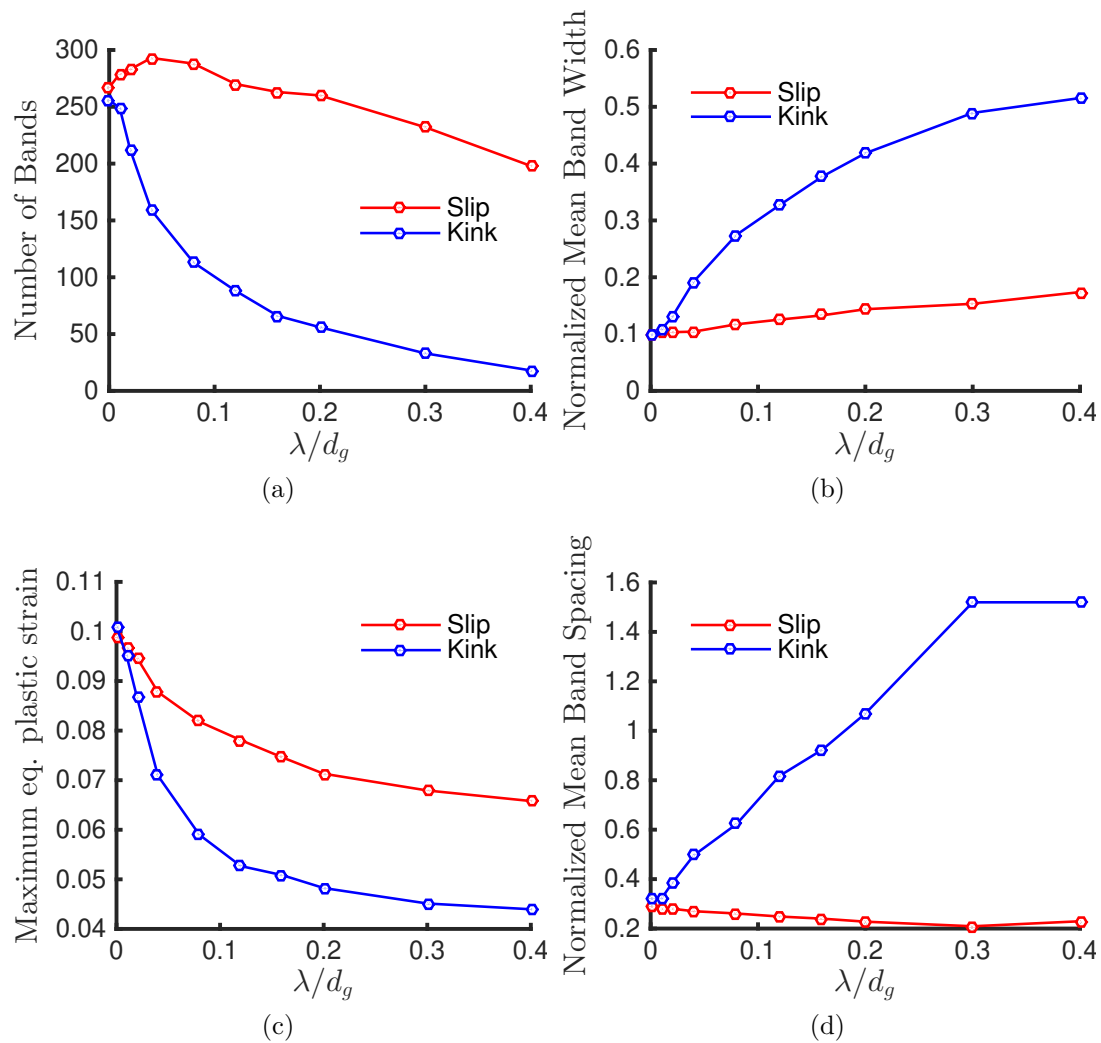
Figure 4.31 – Evolution of band number (a), mean width (b), maximum plastic strain (c) and mean spacing (d) with $\frac{\lambda}{d_g}$, computed with the slip profile based analysis strategy.

Grain boundary condition influence on slip and kink banding

After investigating above their influence on GND induced hardening, we study now the influence of grain boundary conditions on intragranular localization bands formation. Figure 4.32 shows the localization maps obtained with the three conditions (microfree, continuity and microhard2) for $\frac{\lambda}{d_g} = 0.2$. The three localization maps do not show large differences. The same grains exhibit the same localization modes, indicating the weak influence of grain boundary condition on intragranular localization band networks.

An investigation of a few quantitative indicators of localization band populations, computed with the slip profile analysis strategy is presented in fig. 4.33. Overall, it confirms the weak influence of the boundary conditions on band populations.

Grid resolution influence

The influence of grid resolution on localization band networks is now investigated. In this paragraph, results are obtained with a 64 grains polycrystal. Material parameters are unchanged, and the characteristic length is set to $\frac{\lambda}{d_g} = 0.2$. Figure 4.34 shows the computed localization maps (a-c), effective plastic strain (d-f) and lattice rotation angle (g-i) fields computed for three increasing resolutions. They reveal that slip band formation is highly influenced by grid resolution: as grid refinement increases, the number of slip bands rapidly increases, as well as their intensity, visible on the effective plastic strain fields. On the contrary, kink bands populations does not seem affected by the variation of grid resolution. In particular, fields (g-i) show that lattice rotation field is regularized and completely independent of the grid resolution.

The examination of three quantitative indicators computed with the slip profile analysis strategy confirm the results of the image processing based localization maps. They are displayed on fig. 4.35, and clearly show that the number of slip bands (a) is proportional to the grid resolution, and their width (b) inversely proportional. On the contrary, kink bands number and width is clearly stable for the three grid resolutions. The proportional (resp. inversely proportional) evolution of slip bands number (resp. width) is the signature of the classical numerical instability induced by softening behaviors, indicating that slip bands are not regularized by the model, despite the intrinsic errors induced by the finite difference evaluation of the back-stress.

This also shows that the spacing between slip bands will be directly controlled by the grid resolution. Figure 4.35-(c) shows the probability density

(a) microfree

(b) continuity

(c) microhard-2
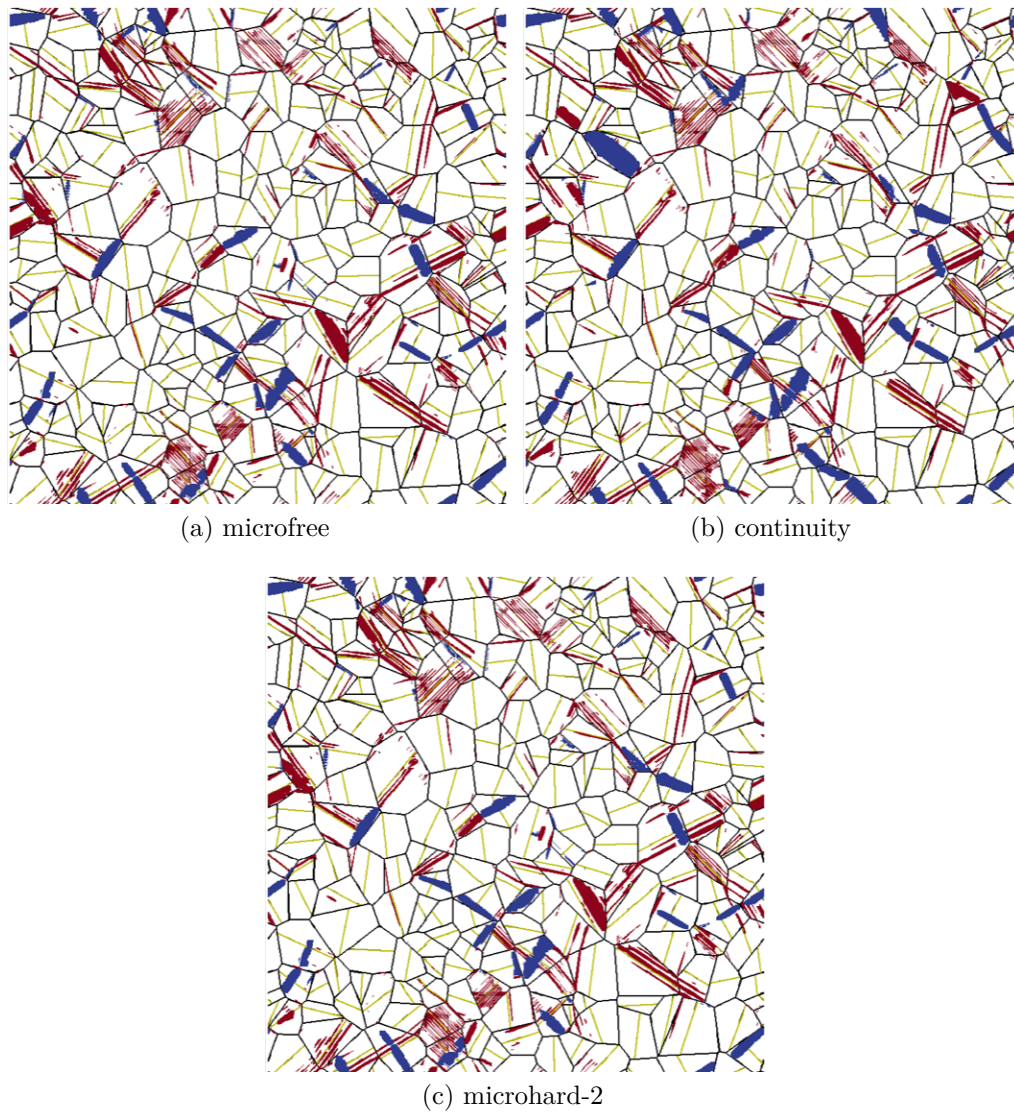
Figure 4.32 – Localization maps constructed with the second processing strategy of chap. 3 for the three grain boundary conditions with $\frac{\lambda}{d_g} = 0.2$ and for $\frac{d_g}{\partial x} = 50$ (225 grain 2D polycrystal).
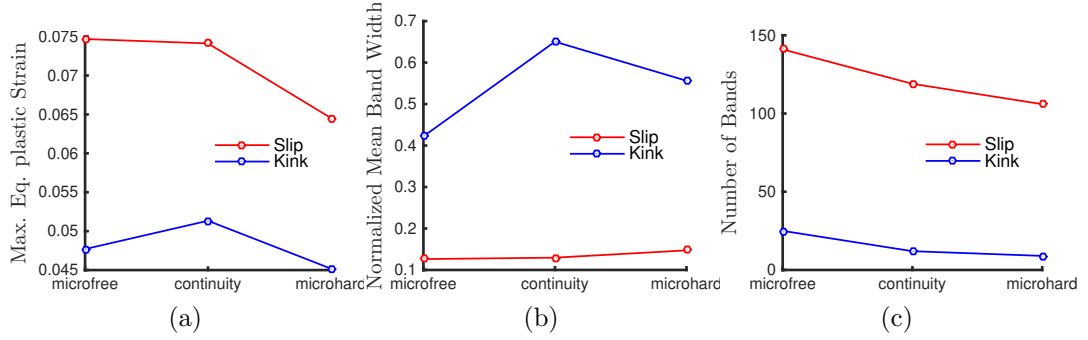
Figure 4.33 – Evolution of bands mean maximum plastic strain, width and number for various grain boundary condition with $\frac{\lambda}{d_g} = 0.2$. Band width is normalized with respect to mean grain size d_g

function of slip bands spacing computed for the three resolutions. The distribution clearly shifts towards the voxel size as the number of voxels increases, confirming the dependence of slip band spacing on grid resolution.

In addition, it has already be shown on fig. 4.26 that grid resolution has only a small influence on the macroscopic behavior for the considered resolution, for all types of boundary conditions, to the exception of the use of microhard-1.

Influence of softening intensity on slip and kink banding

In this paragraph, we study the influence of softening intensity on slip localization. Simulations are carried out on the 225 grains unit cell, with $\frac{\lambda}{d_g} = 0.2$ and the continuity condition at grain boundaries. Softening intensity is controlled with $\Delta\tau = \eta\tau_0$.

Figure 4.36 presents the localization maps obtained for increasing values of η, up to 0.5 (*i.e.* a maximum of 50% local softening). They illustrate the very strong impact of softening intensity on localization network. As it increases, the number of slip bands strongly increases, and they appear thinner. Kink bands seem slightly thinner with a strong softening. However, the most striking fact is the decomposition of a few large kink bands into a succession of intense slip bands when softening is increased, which reminds us of the results presented in section 4.5.1. The quantitative indicators computed with these localization maps are shown on fig. 4.37. They confirm the visual analysis of localization maps. Figure 4.37-(a) shows that after an significant decrease that could correspond to the decomposition of the larger kinks, their volume fraction remains stable when increasing η. Their mean equivalent plastic strain (b) increases at the same time. On the contrary, the

(a) $\frac{\partial x}{d_g} = 0.04$ (b) $\frac{\partial x}{d_g} = 0.02$ (c) $\frac{\partial x}{d_g} = 0.01$

(d) $\frac{\partial x}{d_g} = 0.04$ (e) $\frac{\partial x}{d_g} = 0.02$ (f) $\frac{\partial x}{d_g} = 0.01$

(g) $\frac{\partial x}{d_g} = 0.04$ (h) $\frac{\partial x}{d_g} = 0.02$ (i) $\frac{\partial x}{d_g} = 0.01$
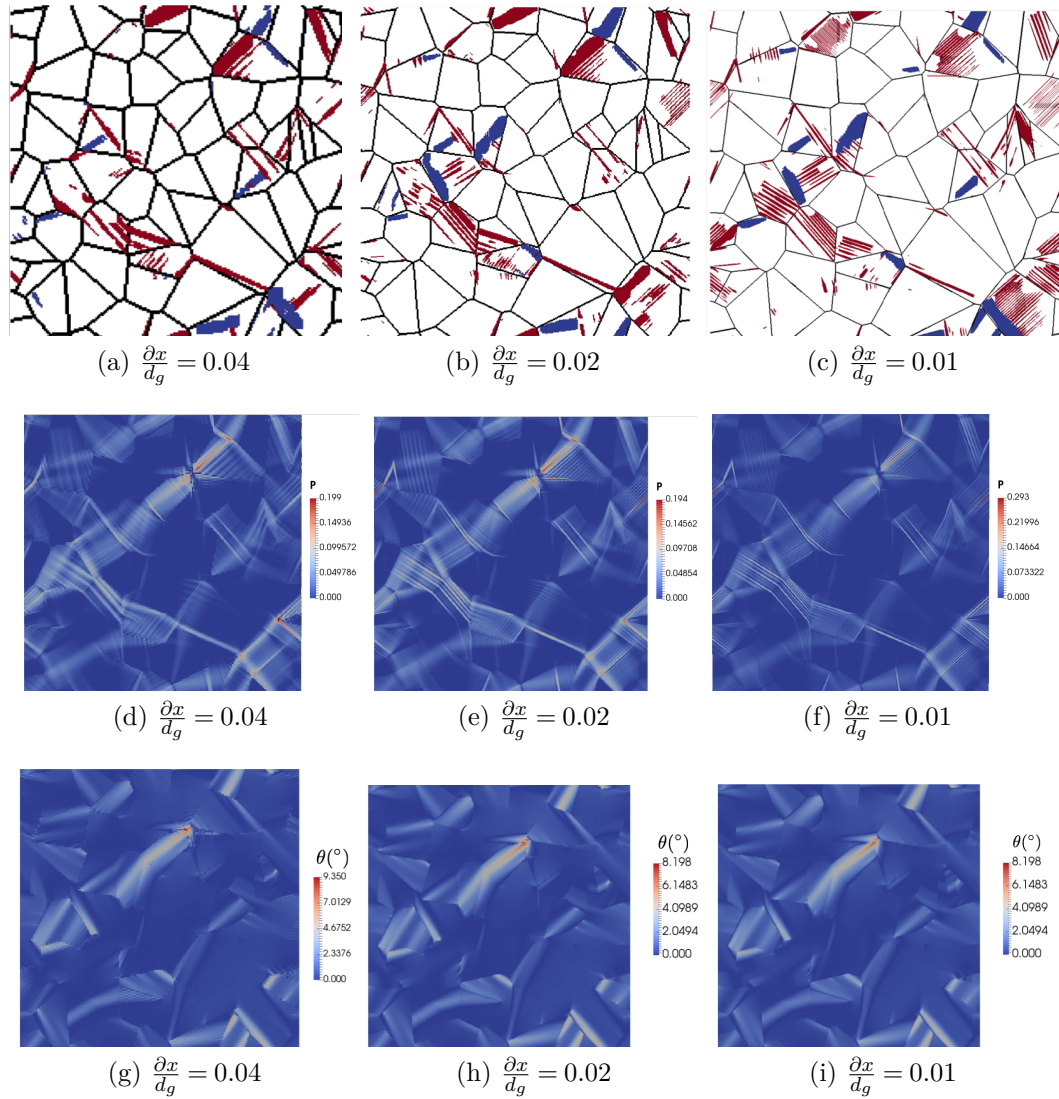
Figure 4.34 – Localization maps (a-c), equivalent plastic strain (d-f) and lattice rotation angle (g-i) fields for $\frac{\lambda}{d_g} = 0.2$ various resolution, described here by the ratio $\frac{\partial x}{d_g}$ for indicative comparison with $\frac{\lambda}{d_g}$. 64 grain polycrystal
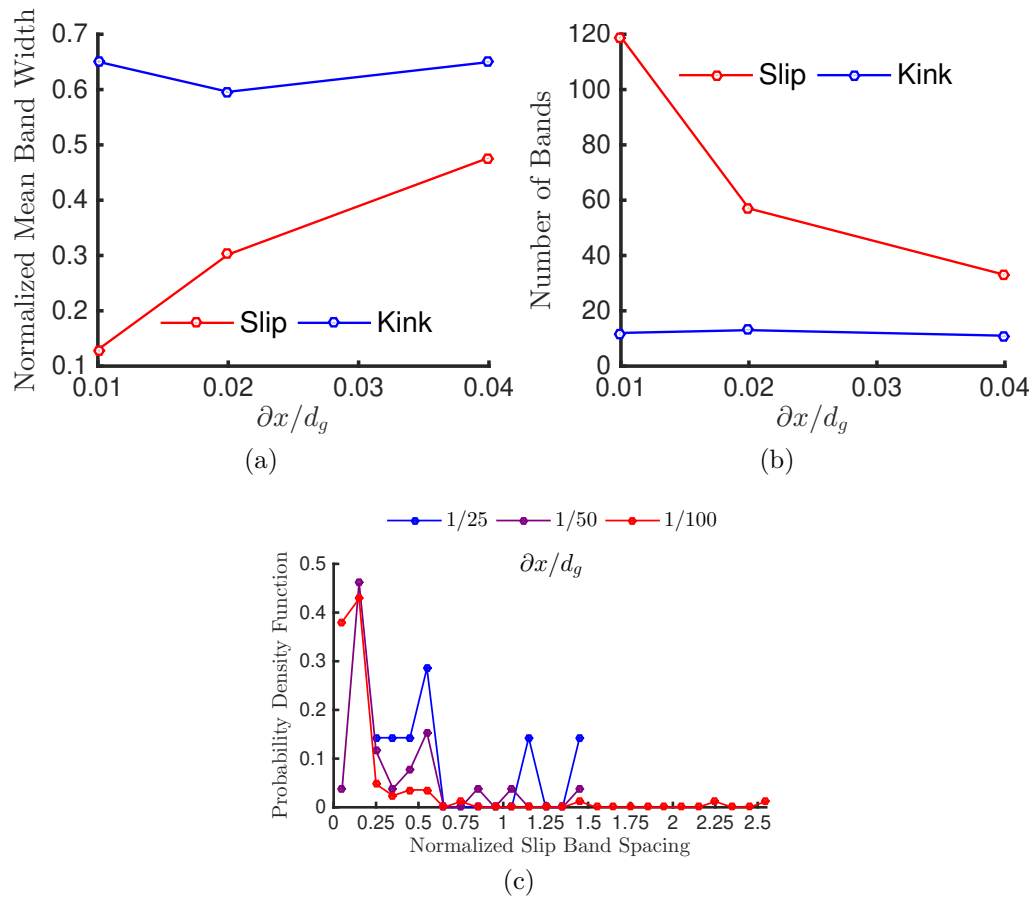
Figure 4.35 – Evolution of bands number (a), mean width normalized by the mean grain size (b), and slip band spacing distribution (c) for various resolutions (number of voxel per grain: $\frac{d_g}{\partial x}$). 64 grain polycrystal

slip band volume fraction increases by 50% from $\eta = 0$ to $\eta = 0.5$, and their mean equivalent plastic strain is almost doubled.

(a) $\eta = 0$ (b) $\eta = 0.3$ (c) $\eta = 0.5$
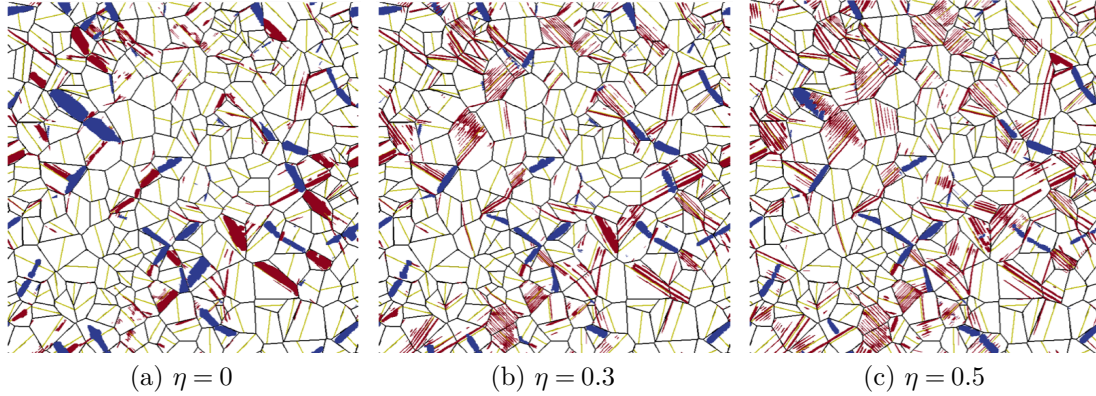
Figure 4.36 – Localization maps obtained for various softening intensities. $\frac{\lambda}{d_g} = 0.2$ and $\frac{d_g}{\partial x} = 50$ (225 grain 2D polycrystal)
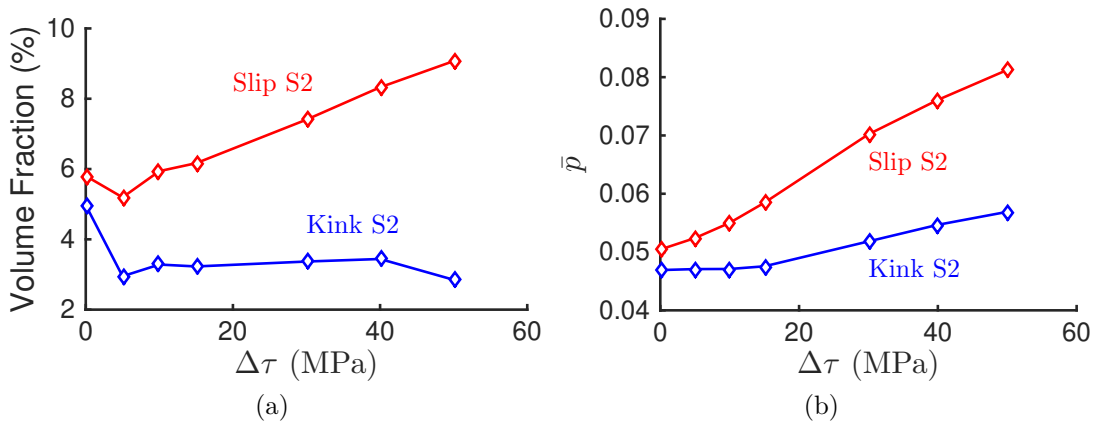
Figure 4.37 – Band volume fractions (a) and mean plastic strain (b) associated to localization maps of fig. 4.36.

Once again, quantitative indicators obtained from slip profile analysis are presented to complement the study of the localization maps in fig. 4.38. The number of kink bands (a) is completely independent of the softening intensity whereas the slip band number is multiplied by three as η goes from 0 to 0.5. The mean band spacing curve (b) reveals that kink band spacing remains stable around the mean grain size d_g, indicating that grains with more than one kink band are larger than the average. On the contrary slip band spacing decreases with increasing

$\Delta\tau$, and saturates around $\Delta\tau = 15$ MPa. A decrease in band slip band spacing indicates than areas with a relatively homogeneous plastic deformation decompose into successive slip bands.

Figure 4.38-(c-d) show the evolution of slip and kink band width distributions. The slip band width distribution clearly shifts to the left of the diagram when increasing softening, indicating a significant global decrease of all slip band width, with a peak around 2-4 voxel-wide slip bands (the used resolution verifies $\frac{\partial x}{d_g} = 0.02$, hence 2-4 correspond to a 0.04-0.08 normalized width consistent with the observed peak). Kink band width distribution also shifts toward the left when softening increasing, but the effect is much weaker than for the slip band width distribution. The theoretical value given by the analytical prediction of kink band width is $\omega_b \approx 2\pi\lambda\sqrt{\frac{\gamma_0}{\eta}}$, which predicts $\omega_b \approx 0.56 \cdot d_g$ when the peak of the distribution is observed around 0.4. This value is lower than the theoretical prediction of ideal kink banding, but of the right order of magnitude.

Comparison of macroscopically equivalent CCP and SGP simulations

The previous studies have highlighted two opposite effects on the intensity of strain localization. A stronger gradient effect induced by increasing $\frac{\lambda}{d_g}$ reduces localization intensity and yields a harder overall behavior, while increasing the softening parameter $\Delta\tau$ results in the opposite. On the other hand, strong gradient effects drastically reduce the number and the intensity of kink bands. Besides, these bands remain unstable and increasing softening intensity amplifies their decomposition into slip bands.

Therefore, the two effects can be combined to compensate the hardening effect of the gradient term with an increased softening, in order to maintain the overall stress-strain relation close to the CCP behavior. In this process, the combined reduction of the number of kink bands and their increased decomposition should result in a drastic reduction of their population. This question of central interest for the present work is studied in this section. It consists in the comparison of 2 cases:

1. CCP: $\frac{\lambda}{d_g} = 0$ and the rest of the material parameters indicated in table 4.2.
2. SGP: $\frac{\lambda}{d_g} = 0.3$, $\Delta\tau = 50$ MPa and $\gamma_0 = 0.05$.

Figure 4.39 shows the stress strain curves of this two cases, and an additional curve corresponding to the coefficients of the CCP case with $\frac{\lambda}{d_g} = 0.3$. This last curve shows the global hardening induced by the gradient effects, which is then compensated in case 2 by the increase of softening speed γ_0 and intensity $\Delta\tau$. It is clear that the curves of cases 1 and 2 almost overlap. They are macroscopically
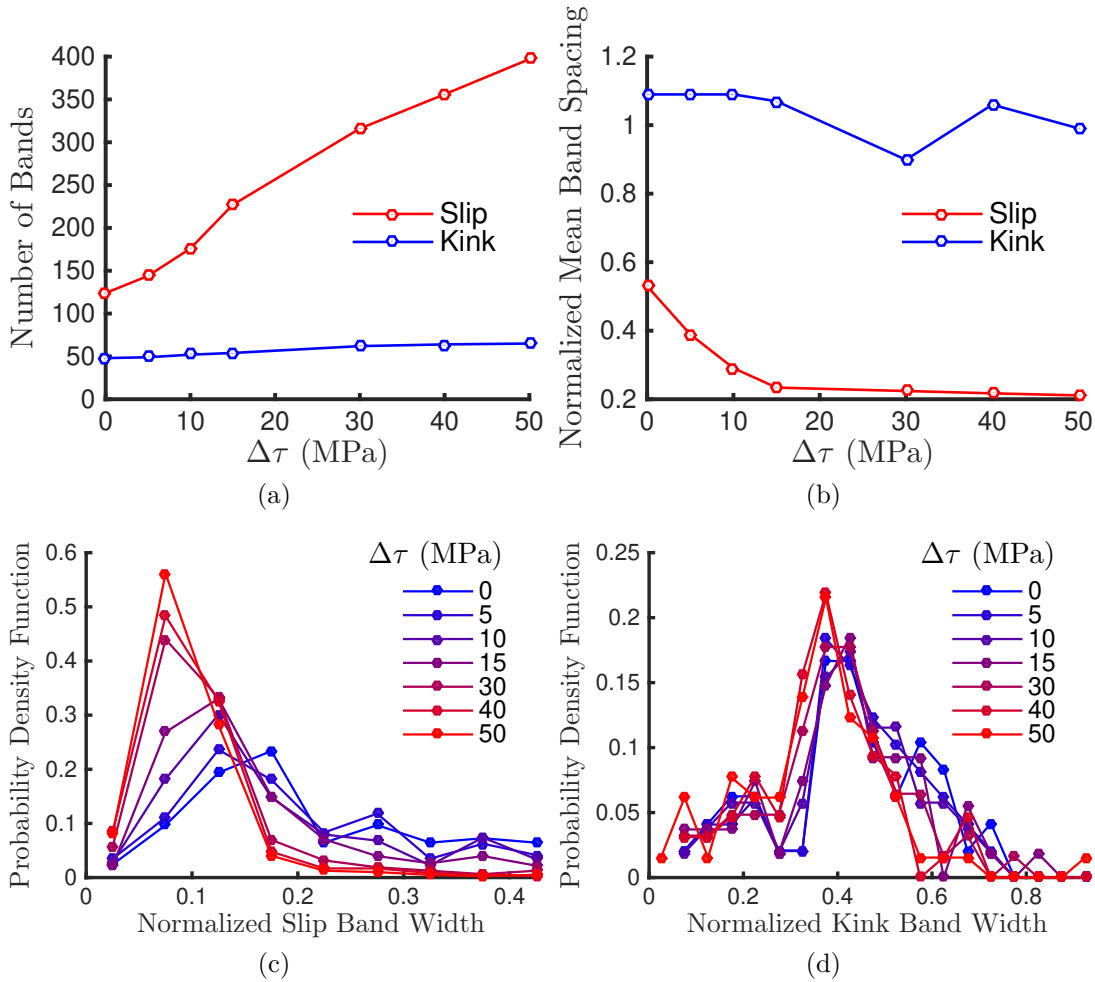
Figure 4.38 – Evolution of band number (a), normalized mean spacing with respect to average grain size (b), and probability density functions of band width for slip (c) and kink (d) bands, with respect to softening intensity. $\frac{\lambda}{d_g} = 0.2$ and $\frac{d_g}{\partial x} = 50$ (225 grain 2D polycrystal)
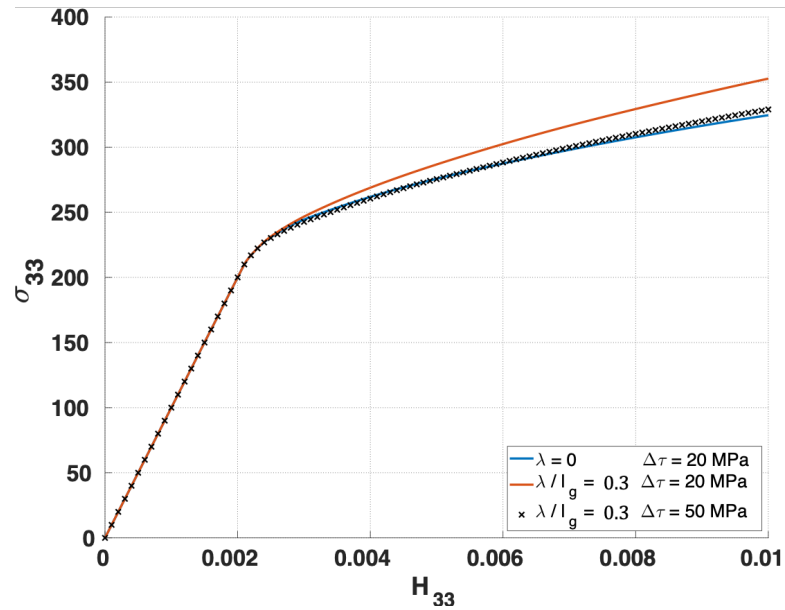
Figure 4.39 – Stress-strain curves for three different set of coefficients showing macroscopically equivalent curves. $\frac{d_g}{\partial x} = 50$ (225 grain 2D polycrystal).

equivalent.

We present in fig. 4.40 a quantitative analysis of both cases obtained with the slip profile processing based strategy. For CCP, the three quantitative indicators that are the distributions of the number of bands per grain, of the maximum plastic strain per band and normalized band width are highly similar for slip and kink bands populations. This is the signature of the strict equivalence of slip and kink modes for CCP, evidenced in chap. 3. On the contrary, the distributions of these indicators for SGP reveal significant differences between slip and kink bands populations. As expected, it these indicators show that kink band drastically less numerous, less intense and wider in the SGP case whereas slip bands are more numerous with an intensity and width that is little affected.

It is clear on the equivalent plastic strain and lattice rotation fields on fig. 4.41 that the distribution of plastic strain/lattice rotation at the intergranular scale is similar in both simulations. Plastic slip/rotation is intense in the same grains, and the intergranular localization networks are similar. However, large differences between CCP and SGP are observed at the the intragranular scale: intense kink bands of CCP are replaced by a diffuse kink band which is often decomposed into a dense succession of intense slip bands with SGP.

With CCP, intense localization areas with very high lattice rotation are found whereas with SGP lattice rotation is more diffuse and locally much lower.
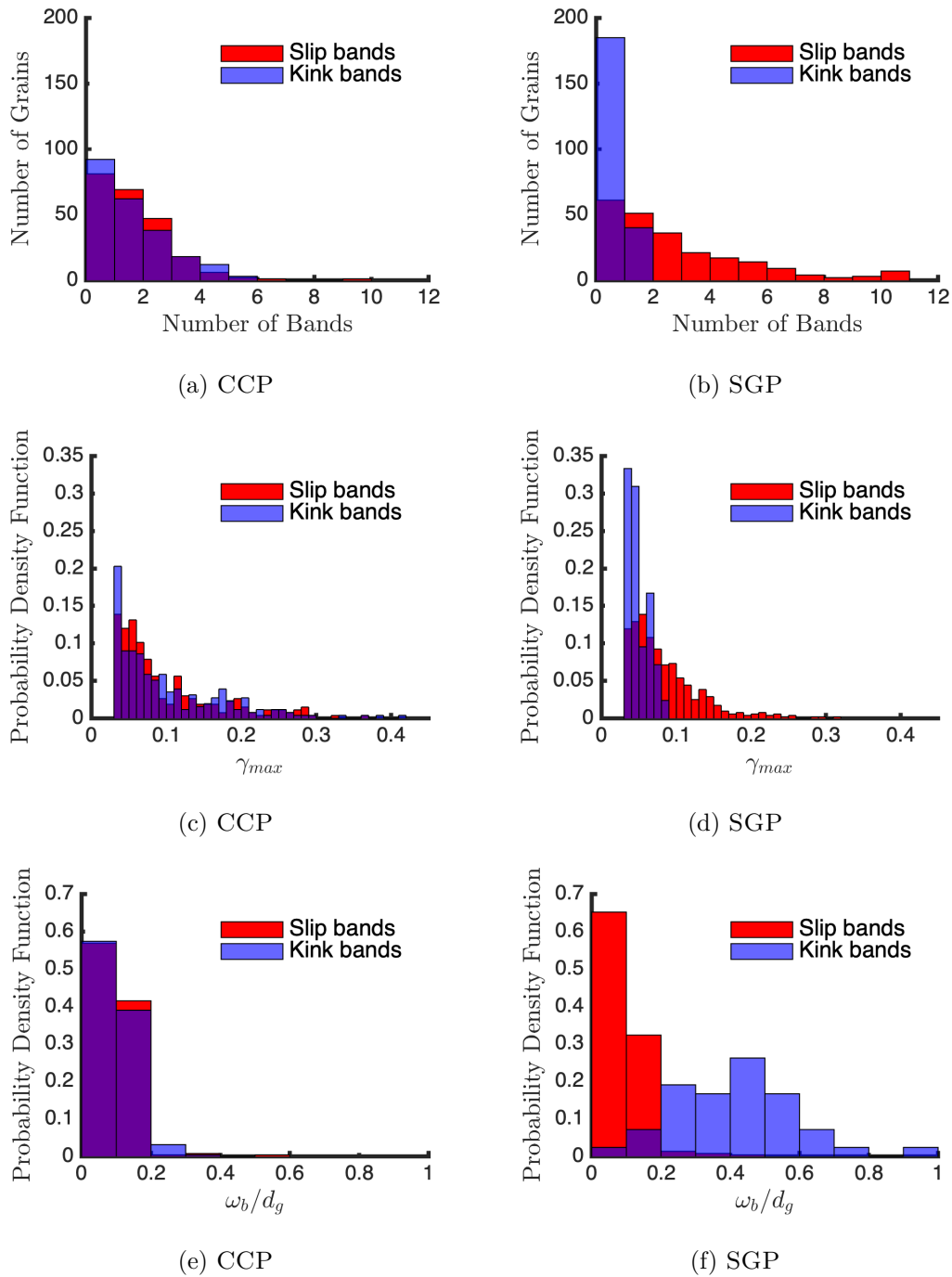
Figure 4.40 – Comparison of band number per grain (a-b), and probability density functions of bands maximum plastic strain (c-d) and width (e-f), for the macroscopically equivalent CCP and SGP cases. $\frac{d_g}{\partial x} = 50$ (225 grain 2D polycrystal).
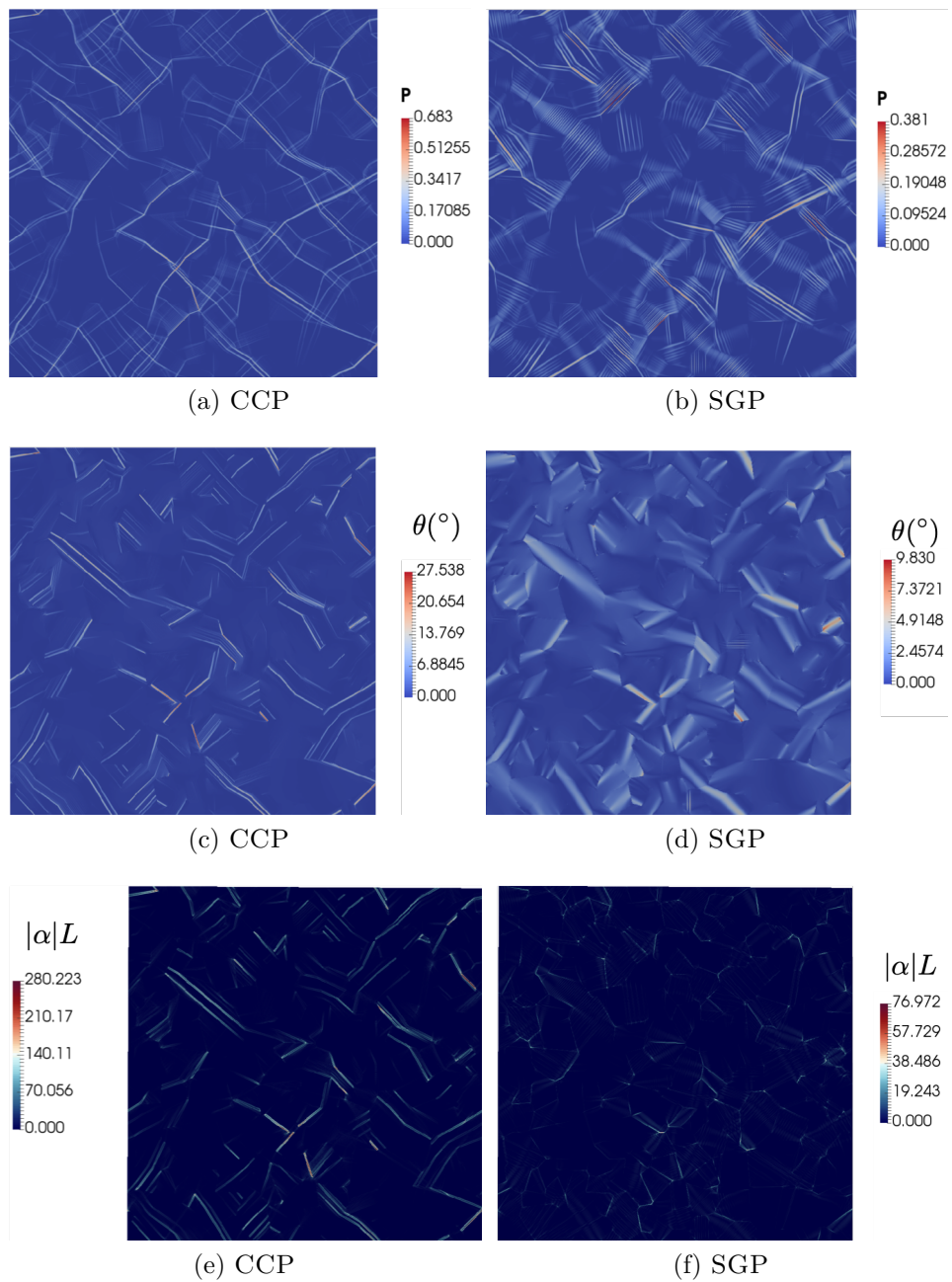
Figure 4.41 – Equivalent plastic strain (a-b), lattice rotation angle (c-d) and normalized Nye tensor's norm (e-f) fields comparison between the macroscopically equivalent CCP and SGP cases. $\frac{d_g}{\partial x} = 50$ (225 grain 2D polycrystal).

On the other hand, high GND density (figures (e-f)) is strongly correlated to kink bands with CCP whereas it clearly concentrates on grain boundaries and is significantly reduced in the SGP case.

4.6.4 Three-dimensional polycrystalline simulations

We apply now the model to three dimensional polycrystals with cubic and hexagonal crystal structures, in order to provide qualitative observations of the model predictions for localization band patterns.

Comparison between CFC and BCC crystal structures

First, the comparison of the two symmetric crystal structures that are the 12 FCC $\{111\} < 110 >$ slip systems and the 12 BCC $\{110\} < 111 >$ slip systems is resumed. Its study in section 3.5.3 has highlighted their equivalence with CCP: they involve the same microstructure, grain orientations resulting in identical structure effects in the sense defined in section 4.5.4, *i.e.* the selection of the localization modes that minimize the energy of the polycrystalline structure. As a result, CCP yield the same band pattern, with the difference that slip and kink are inverted in the two patterns. Hence, it is usefull to study the influence of gradient effects on two bands patterns where slips and kink play a symmetric role.

Therefore, this comparison is used to investigate how structure effects influence localization band patterns in three dimensional polycrystals with many slip systems in function of the nature of the band composing the pattern. However, it is not aimed to provide general insights into the formation of slip localization and GND density patterns in cubic crystal structures.

In the following, we compare macroscopically equivalent behaviors, similarly to the last bi-dimensional case study presented in the last paragraph:

1. CCP: $\frac{\lambda}{d_g} = 0$ and the rest of the material parameters of table 4.2.

2. SGP: $\frac{\lambda}{d_g} = 0.2$, $\Delta\tau = 50\,\mathrm{MPa}$.

for both crystal structures. The macroscopically equivalent stress-strain curves are displayed on fig. 4.42. They show an overall behavior of the polycrystal close to perfect plasticity on the simulated strain range, obtained with $\Delta\tau = 50\,\mathrm{MPa}$. Again the case $\frac{\lambda}{d_g} = 0.2$ with unchanged softening intensity is shown to highlight the compensation of gradient hardening effects by increased softening.

An internal section of the simulated fields is presented for both CCP and SGP, and both crystal structures on fig. 4.43. The plastic strain fields of CCP (a)
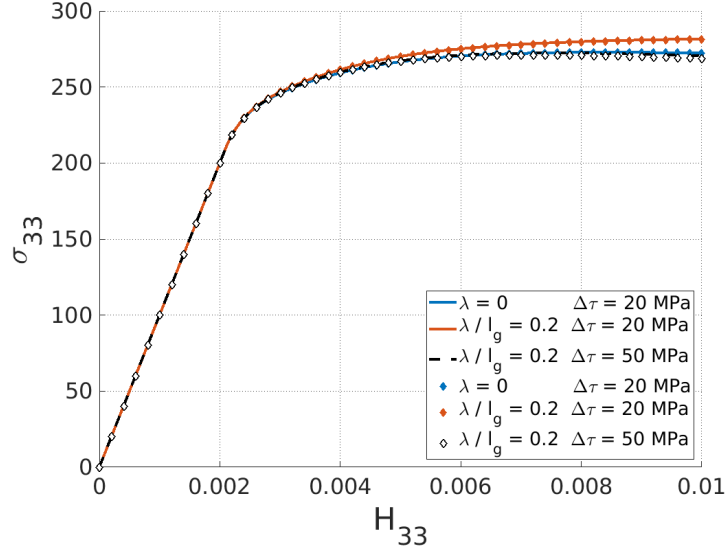
Figure 4.42 – Stress-strain curves for three different set of coefficients showing CCP and SGP macroscopically equivalent curves, for both BCC and CFC crystal structures with 12 slip systems. BCC results are denoted by diamond points. $\frac{l_g}{\partial x} = 50$, 64 grain polycrystal (8 million voxels)

are strictly identical for the two crystal structures. Contrary to the finite strain comparison of chap. 3 , the small strain CCP renders the two structures perfectly equivalent for all the simulation, not only at incipient plasticity.

Many grains contain one intense localization band, that are connected through grain boundaries forming a transgranular network. Three branches composed of the most intense connected (at grain boundaries) localization bands, circled in red in the figures, constitute the core of the network. Their formation is controlled by structure effects, and indicate the intergranular deformation path that is best suited to minimize the polycrystal energy during deformation.

The intense bands observed on the lattice rotation angle fields (b-c) reveal the location of kink bands in the two networks. In the BCC case (c), intense rotation bands are mostly located outside of the circled areas, and coincide with intense slip localization bands (*i.e.* kink bands). Obviously it is the opposite for the CFC band network that is mostly composed of intense rotation bands inside these areas. Hence, this specific microstructure accommodates strain mostly through kink banding in the CFC case, and slip banding in the FCC case. As a result, gradient effects are expected to influence more the development of the FCC localization band pattern than the BCC one.

(a) CCP CFC=BCC   (b) CCP CFC   (c) CCP BCC

(d) BCC SGP   (e) BCC SGP

(f) CFC SGP   (g) CFC SGP
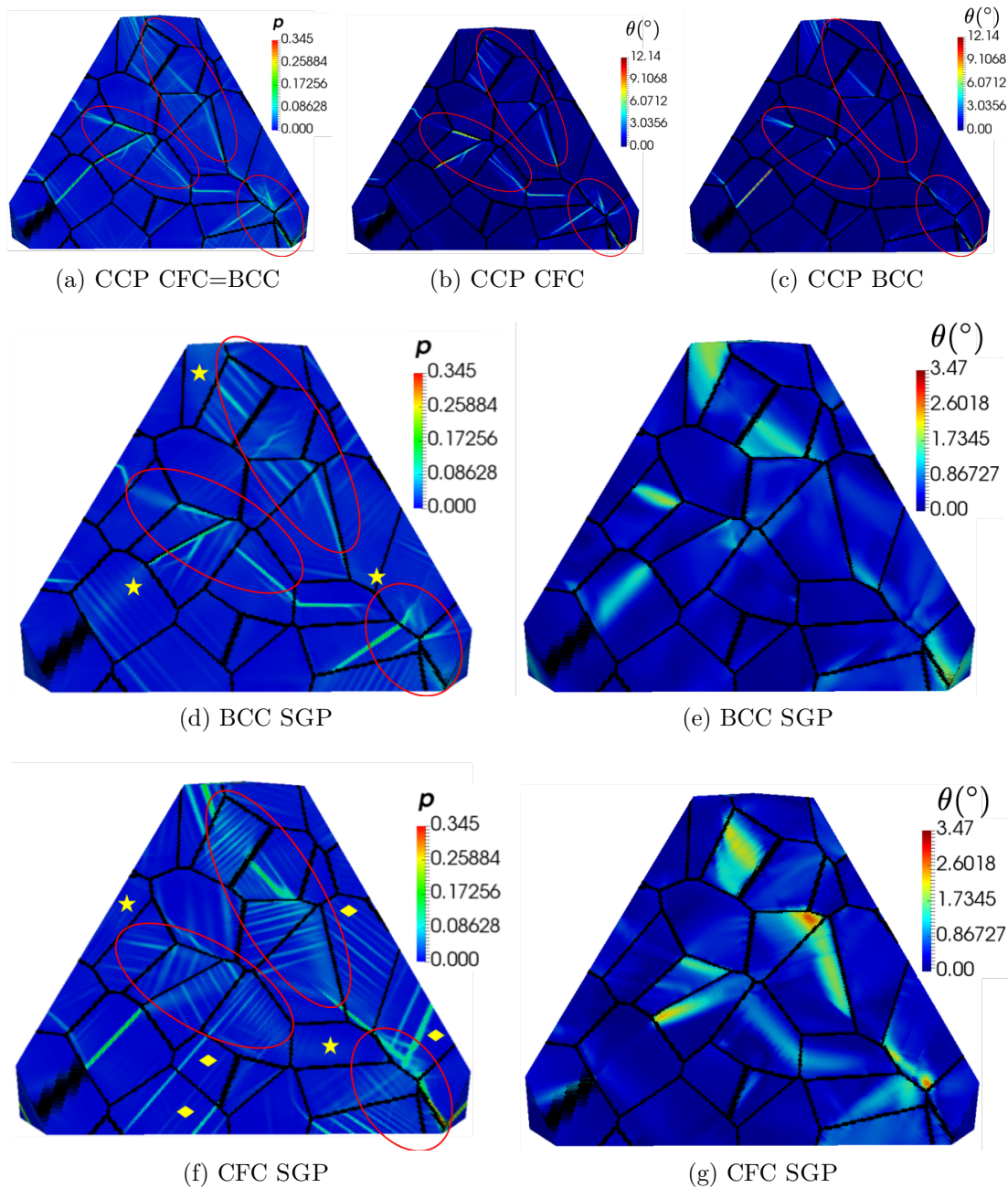
Figure 4.43 – Equivalent plastic strain and lattice rotation angle fields comparison between CCP (a) for which BCC and CFC crystal structures are equivalent, and the SGP BCC (c-d) and SGP CFC (e-f) cases. $\frac{l_g}{\partial x} = 50$, 64 grain polycrystal (8 million voxels)

This expectation is in agreement with the macroscopically equivalent SGP equivalent plastic deformation fields, shown on figures (d) and (f): indeed, the BCC localization network is mostly composed of same slip bands in the circled areas found in the CCP BCC simulation. On the other hand, the few kink bands found in CCP are strongly attenuated in the SGP simulation. They are indicated by the grains marked with a yellow star.

On the contrary, the CFC localization band network is strongly modified by the gradient effects, as illustrated by figure (f). Most of the intense kink bands constituting the core of the network in CCP (circled areas) have been decomposed into relatively intense successive slip bands. On the other hand, the slip bands of CCP network have become more intense. These strong modifications appear related to other changes in the network. Indeed, the formation of these slip bands not found in the CCP network has led to the development of new slip transmission paths. The grains plastically activated by this mechanism are indicated on figure (f) by a yellow diamond.

Moreover, a few grains undergoing kink banding in CCP do not show signs of plastic activity in SGP. They are marked with a yellow star. It is interesting to note that these grains have neighbours that undergo strong slip activity only in SGP, suggesting that the strain accommodated by these vanishing kink bands predicted by CCP is now accommodated by neighboring grains. These areas lie outside of the main deformation path, and are thus region where structure effects are lighter than in the circled areas. Hence, this shows that gradient effects modify the result of the competition between slip and kinks, to the favor of slip bands, where structure effects are weak in the polycrystal.

Overall, it must also be noted that, as for the bidimensional simulations, the distribution of lattice rotation at the intergranular scale is similar in both crystal structures for CCP and SGP. Once again, rotation bands predicted by SGP are wider and less intense.

HCP crystal structure

Finally, we present a similar study on a HCP crystal structure, considering only the basal slip systems. This crystal structure, already studied and discussed in section 3.5.3, is representative of strongly anisotropic hexagonal crystal such as ice. It can also be regarded as a model material to study basal channeling in irradiated Zirconium alloys.

Like in the cubic case, this study presents the comparison of CCP and SGP macroscopically equivalent cases, identical to those used for the cubic crystal
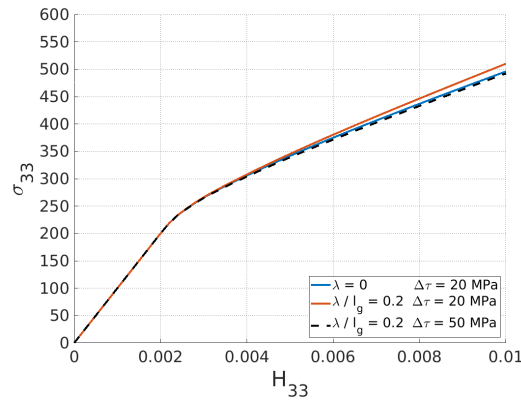
Figure 4.44 – Stress-strain curves for three different set of coefficients showing CCP and SGP macroscopically equivalent curves, for the HCP crystal structure with only basal slip accounted for. $\frac{l_g}{\partial x} = 50$, 64 grain polycrystal (8 million voxels)

structures study. The comparison of the obtained stress-strain curves is shown on fig. 4.44. Again the case $\frac{\lambda}{d_g} = 0.2$ with unchanged softening intensity is shown to highlight the compensation of gradient hardening effects by increased softening.

An internal section of the simulated fields is presented for both CCP and SGP cases on fig. 4.45. In agreement with the arguments presented in section 3.5.3, the plastic strain (a) and lattice rotation (c) fields simulated with CCP show many intense kink bands. A few intense slip bands are found too but they are less numerous. Some of these bands are indicated on figure (a).

Again, in this case, the macroscopically equivalent SGP case exhibit a significantly different plastic strain field at the intragranular scale (c) compared to CCP. Numerous and rather intense successive slip bands formed in all the plastically deformed grains. Most of the strong kink bands are no more noticeable. Moreover, several examples of slip transmission at grain boundaries are now clearly noticeable, for instace in the area highlighted by the red circle. In fact, this slip transmission mode appears more significant than the localization transmission/initiation at triple junctions in this case.

The two lattice rotation fields (b-d) show once again a similar global distribution of lattice rotation, but more diffuse in the SGP case. The GND density field (normalized by the unit cell size L) (e) show that intense kink bands and associated triple junctions are the areas containing most GND in CCP. Conversely, in the SGP case (f), high GND density is found exclusively on grain boundaries. No specific concentration of GND is found on triple junctions.
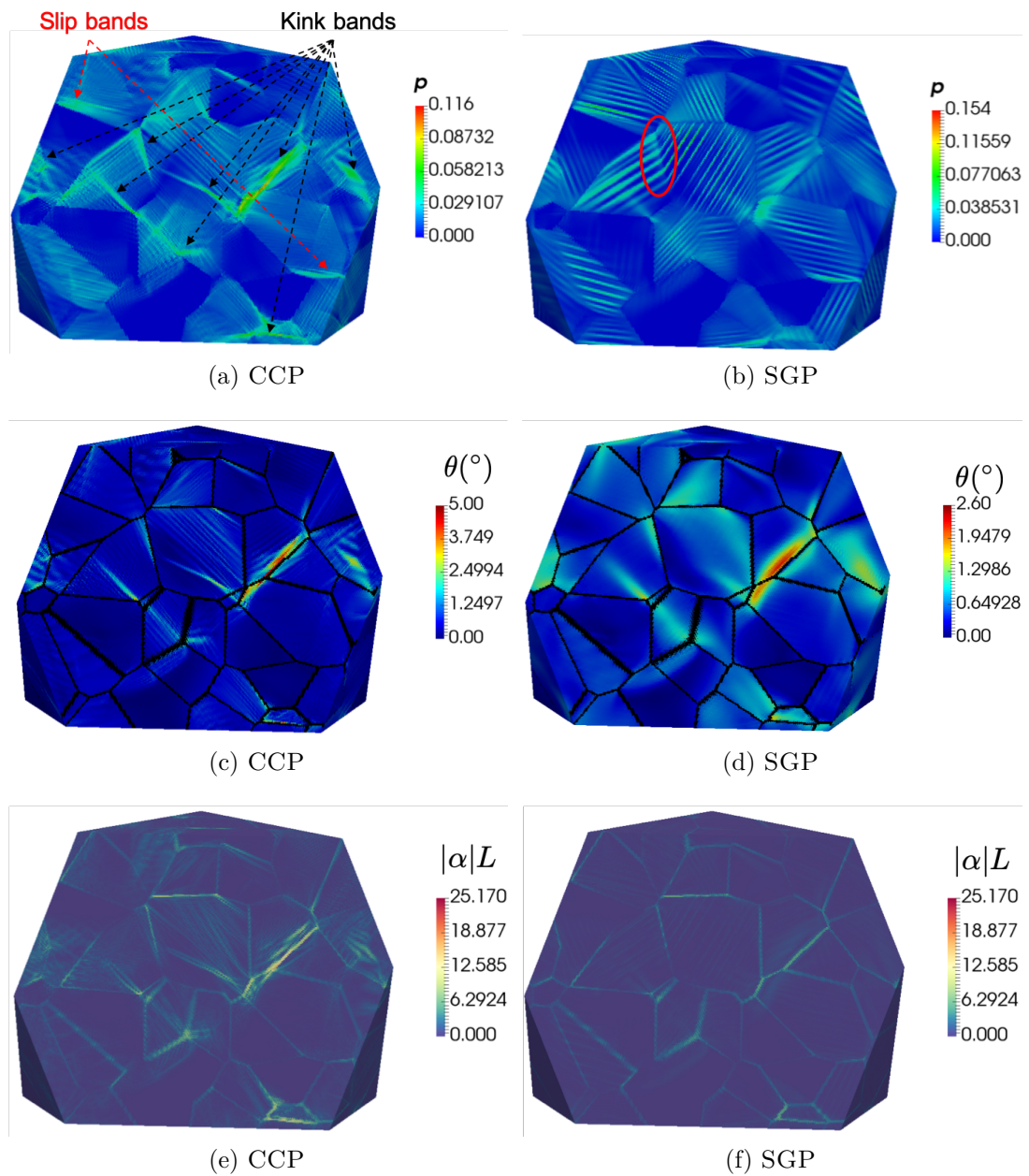
Figure 4.45 – Equivalent plastic strain (a-b) lattice rotation angle (c-d) and normalized Nye tensor's norm (e-f) fields comparison between CCP and SGP macroscopically equivalent cases for the HCP crystal structure with only basal slip accounted for. $\frac{l_g}{\partial x} = 50$, 64 grain polycrystal (8 million voxels)

4.7   Discussion

4.7.1   Numerical implementation of SGP plasticity

Differential operators

This study shows that the curl2∗ operator is the best suited for the application of this strain gradient plasticity model to intragranular slip localization. In spite of the intrinsic error inducing the computation of a non zero backstress in slip bands evidenced in appendix B.2.5, our single crystal and polycrystalline simulations show that slip band width and formation is very little affected by the gradient effects. Though, it comes with the drawback of being less local (*i.e.* double curl at a voxel depends on the value of the fields over a larger area) than the 27-voxels centered Finite-Differences operator introduced by Berbenni et al. (2014) for the computation of elastic distorsions in Field Dislocation Mechanics problems. However, our results have shown that this 27-voxels centered operator causes a strong regularization of slip bands, precluding its use to simulate intragranular localization bands.

However, the present work leaves room for improvement of the differential operator used to compute $\mathrm{curlcurl}(\underline{\boldsymbol{H}}^p)$, in order to find a more local differentiation formulation that correctly predicts vanishing backstresses on slip bands.

Algorithm

The simulations presented in this work suffers from convergence issues in the following cases:

1. for $\lambda \geq l_p$ or L (the relevant length scale of the crystal structure)
2. for a high softening intensity
3. for high resolutions

The difficulties observed with the two last cases are not surprising as they both intensify the instabilities induced by the softening behavior. The first one can be understood from the discussion of section 4.2.3. It establishes that when π_0 is set equal to the relevant stress regarding the yield condition (H or τ_0), a value of $\frac{\lambda}{l_g} \gg 1$ induces variations of the backstress much larger than the relevant stress, for unitary variations of the slip curvature. In these conditions, small variations of the slip field will induce very large evolution of the yield condition from one time step to another, rendering the integration of constitutive equations cumbersome.

These convergence issues always affect the integration of constitutive

equations at plastic yield. The only way to allow for convergence is to reduce the time increment. As a result, the macroscopic problems becomes almost linear and only one iteration of the FFT solver is generally needed. Thus, introducing an implicit scheme is not expected to speed-up convergence for strongly softening simulations, in the case of a non intrusive coupling between non local equations and FFT-based homogenization.

Boundary conditions

Our results demonstrate that enforcing conditions over a sub-volume around grain boundaries to enforce interface conditions should be avoided in general to implement boundary conditions with FFT-based solvers. They induce a stronger mesh dependence, and a slower convergence of the results. On the contrary, our methods based on the modification of the field processed by the differentiation operator is more efficient. It is important to note that even when using a polycrystal coloring algorithm to optimize the underlying partition of the unit cell, they involve a higher computational cost. However, compared to the computational time spent in the integration of constitutive equations, this loss is negligible.

Unfortunately, this application of this technique for the microfree boundary condition is not straightforward. Indeed, if constructing a field padded with zeros to enforce the zero plastic deformation condition is easy, how to construct one inducing a vanishing $\mathrm{curl}(\underline{\boldsymbol{H}}^p)$ at grain boundaries is an open question. Alternatively, penalty methods could be used to enforce this condition, but they would require a modification of our algorithm to switch from fix-point iterations to a Lagrangian based scheme.

In addition, Panteghini and Bardella (2018) pointed out that a consistent implementation of Dirichlet higher order boundary condition involved in this model requires that not all the components of the plastic strain should be considered as nodal degrees of freedom. Consequently, they developed a H(curl) Finite Element formulation of this model, that solves this issue. Building a FFT-based solver equivalent to this H(curl) FE formulation could provide an effective way of properly applying the microfree condition, as well as more complex grain boundary modeling. In addition, specific spectral differentiation operators should be developed for this, and could be more effective than the finite difference operator used in this work.

An alternative method to avoid the delicate issue of imposing conditions on surfaces in FFT-based solver could be modeling thick grain boundaries (for instance with a phase-field based approach: Ask et al. (2018)), with a specific material behavior. To define such constitutive behaviors, the thermodynamical

framework proposed by Cermelli and Gurtin (2002) to model grain boundaries could be used.

4.7.2 Intragranular localization modes modeling

Stability analysis

In this section, we analyze the results obtained for the ideal kink band modeling in the light of Asaro and Rice's bifurcation analysis.

The solution found in section 4.2.4 for the ideal kink banding modeling with the strain gradient plasticity model in the softening case, is given, after a first bifurcation, by eq. (4.50), reproduced here:

$$\gamma(x_m) = \frac{\tau - \tau_0}{H} \left[1 + \cos\left(\frac{2\pi x_m}{\lambda_0'} \right) \right]$$

Taking the time derivative of this equation yields:

$$\dot{\gamma} = \frac{\dot{\tau}}{H} \left[1 + \cos\left(\frac{2\pi x_m}{\lambda_0'} \right) \right] \tag{4.79}$$

which can be written:

$$\dot{\tau} = \frac{H}{\left[1 + \cos\left(\frac{2\pi x_m}{\lambda_0'} \right) \right]} \dot{\gamma} \tag{4.80}$$

The factor of γ in the right hand side can be viewed as the effective linear hardening modulus in the kink band in this SGP framework, expressed as:

$$H_{eq} = \frac{H}{\left[1 + \cos\left(\frac{2\pi x_m}{\lambda_0'} \right) \right]} \tag{4.81}$$

It is dependent on the position inside de band. We can then write:

$$\dot{\tau} = H_{eq}\dot{\gamma}$$
$$\underline{\dot{\sigma}} : \underline{\mu} = H_{eq}\dot{\gamma}$$
$$\underline{\underline{\Delta}} : \underline{\dot{\varepsilon}}^e : \underline{\mu} = H_{eq}\dot{\gamma}$$
$$\underline{\underline{\Delta}} : (\underline{\dot{\varepsilon}} - \underline{\dot{\varepsilon}}^p) : \underline{\mu} = H_{eq}\dot{\gamma}$$
$$\underline{\underline{\Delta}} : \left(\underline{\dot{\varepsilon}} - \underline{\mu}\dot{\gamma} \right) : \underline{\mu} = H_{eq}\dot{\gamma} \tag{4.82}$$

After factorization, eq. (4.82) yields:

$$\dot{\gamma} = \frac{\underline{\boldsymbol{\mu}} : \underline{\underline{\boldsymbol{\Lambda}}} : \underline{\dot{\boldsymbol{\varepsilon}}}}{H_{eq} + \underline{\boldsymbol{\mu}} : \underline{\underline{\boldsymbol{\Lambda}}} : \underline{\boldsymbol{\mu}}} \tag{4.83}$$

We can finally derive the constitutive tangent modulus. The elasticity law gives:

$$\underline{\dot{\boldsymbol{\sigma}}} = \underline{\underline{\boldsymbol{\Lambda}}} : \underline{\dot{\boldsymbol{\varepsilon}}}^e$$
$$= \underline{\underline{\boldsymbol{\Lambda}}} : \left(\underline{\dot{\boldsymbol{\varepsilon}}} - \underline{\boldsymbol{\mu}} \dot{\gamma} \right)$$

This, expression, after substituting eq. (4.83) and some factorization, yields the tangent modulus $\underline{\underline{\boldsymbol{L}}}$ expression:

$$\underline{\dot{\boldsymbol{\sigma}}} = \left[\underline{\underline{\boldsymbol{\Lambda}}} - \frac{\left(\underline{\underline{\boldsymbol{\Lambda}}} : \underline{\boldsymbol{\mu}} \right) \otimes \left(\underline{\boldsymbol{\mu}} : \underline{\underline{\boldsymbol{\Lambda}}} \right)}{H_{eq} + \underline{\boldsymbol{\mu}} : \underline{\underline{\boldsymbol{\Lambda}}} : \underline{\boldsymbol{\mu}}} \right] : \underline{\dot{\boldsymbol{\varepsilon}}} = \underline{\underline{\boldsymbol{L}}} : \underline{\dot{\boldsymbol{\varepsilon}}} \tag{4.84}$$

As described in section 2.1.3, slip localization can occur as a discontinuity through planar area of normal $\boldsymbol{n}$ if the acoustic tensor $(\boldsymbol{n} \cdot \underline{\underline{\boldsymbol{L}}} \cdot \boldsymbol{n})$ becomes singular. Equation (4.84) shows that the acoustic tensor that arises in the present case is exactly the same as the one considered by Asaro and Rice (1977). Hence their results can be applied here.

Equation (4.81) shows that, despite the GND induced hardening, the equivalent linear hardening modulus in the kink band will still be negative everywhere in the kink band. According to Asaro and Rice's analysis, it implies that the behavior is unstable, and should lead to a second bifurcation: a slip or a kink band. This could explains the observation of unstable kink bands within our simulations of ideal kink banding in section 4.5.1.

In addition the non local modeling imposes the continuity of $\underline{\boldsymbol{m}}$. In particular, this implies in the present case the continuity $\gamma_{,m}$ and a fortiori of $\gamma(x_m)$. For this reason, an additional kink discontinuity cannot be formed after this second bifurcation, leaving only slip band formation as available bifurcation mode. This could explain the decomposition of kinks in successive slip bands, observed throughout our simulations.

Furthermore, we recall that in these small strain conditions, $|\gamma| \approx |\theta|$ for ideal kink bands, and that as slip bands do not create lattice rotation far from obstacles. Yet, it turns out that lattice rotation fields do not show any signs of the slip bands, and closely verifies the equation governing analytically predicted slip field, eq. (4.50), which does not contain slip bands. This suggests that the second

bifurcation could lead to an additive decomposition of the slip field into a mean field value $\gamma^0(x_m)$ that would verify eq. (4.50) and accommodate the mean shear strain prescribed to the kink band, and an heterogenous fluctuation $\gamma^\star(x_m, x_m)$ that would be composed of slip bands, inducing no lattice rotation.

Of course, this idea is only a qualitative analysis based on insights obtained from a first order continuum bifurcation analysis argument. It should be clarified by conducting a proper bifurcation analysis for the generalized continuum considered in this chapter.

In conclusion, according to this argument, this model predicts that in the presence softening, kink bands form as stable lattice rotation bands that accommodate the mean shear strain locally imposed to the band, through the formation of a dense slip band superposition. This analysis is remarkably close to the interpretation of their field measurements proposed by Gioacchino and Fonseca (2015) (see section 2.1.2). They suggested that the strong lattice rotation shown in the kink band like area is due to a locally high density of slip bands. Hess and Barrett (1949), based on observation of kink band formation in Zn crystals, also proposed a formation mechanisms, represented in fig. 4.46, based on the emission of dislocation in successive slip bands that align themselves along two planes perpendicular to the glide direction, forming dislocation walls which delimit the kink band.
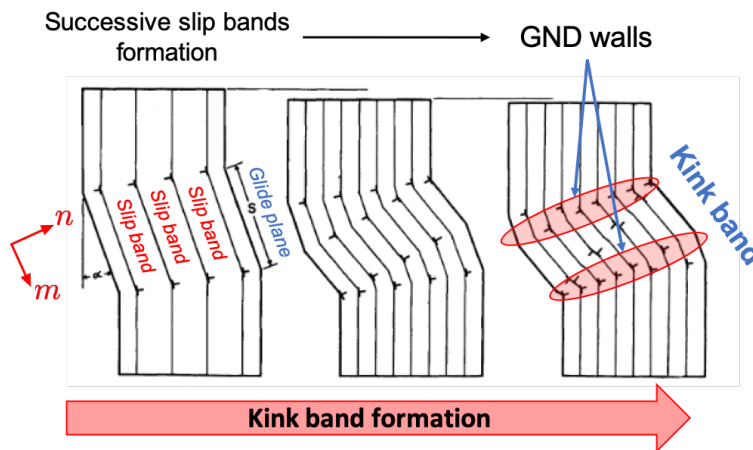
Figure 4.46 – Schematic representation of a kink band formation, after Hess and Barrett (1949)

We believe that these considerations show that the physical picture of kink band formation predicted by this model is in good agreement with observations.

Competition between slip and kink banding

As highlighted by our results, the SGP model affects the competition between slip and kink bands in two possible ways for a locally softening modeling. The first case has been observed in the three dimensional BCC simulation, as well as for single crystal plates. In these situations, structure effects are weak, which means that the additional energy that would be required to switch from slip to kink banding (or the opposite depending on the best structurally suited mode) is low. When, in the SGP framework, the additional energy stored in high GND density associated to kink bands is higher than the later, gradient effects control the competition between slip and kink banding, which result in slip bands formation.

On the contrary, in the FCC simulation as well as 2D simulations with a single slip system, the kink bands observed in the local case are all maintained in the SGP simulations. In those cases, kink bands are essential to the formation of the intergranular localization network. Most likely the additional energy stored in the structure that would be require to replace those kinks with slips is higher than the energy stored in kink bands GND walls. Hence, kink bands are forced to form, however under the form of a dense successive slip band pattern. Hence, this model still predicts the formation of kink bands when structural effects are sufficiently strong to overcome the energetic cost of lattice curvature formation.

Overall, our polycrystalline simulations show that softening strain gradient plasticity based on the energetic contribution of GND yields the formation of numerous slip bands as the primary slip localization modes. Other forms of slip localization such as transgranular localization bands networks or kink bands form through the transmission or accumulation of slip bands. The plastic strain and lattice rotation fields predicted by the SGP model in our macroscopically equivalent comparisons (figs. 4.41, 4.43 and 4.45) are qualitatively in good agreement with the field measurements of deformed polycrystals presented in section 2.1.2 (figs. 2.5 and 2.6). In conclusion, it proves to be a very promising framework for the accurate simulation of intragranular slip localization in polycrystals.

Material length scale and kink bands

A consequence of these predictions is that, if π_0 and λ are considered as intrinsic crystal properties, then it implies that kink band width also is an intrinsic material property. Therefore, according to this model, it should be the same for various order of magnitude of the grain size. It also implies that kink bands would not form in grains smaller than their characteristic width. This could explain why the majority of kink bands have been reported in the literature for single crystals

experiments, or polycrystals with large grain sizes.

For instance in ice, kink bands are reported with a width ranging from 0.1 mm to 1 mm in polycrystals with a mean grain size around 10 mm (Mansuy, Philip, and Meyssonier (2001); Montagnat et al. (2011); Wilson, Burg, and Mitchell (1986)). Our strongly anisotropic HCP crystal structure simulation (fig. 4.45) provides an interesting comparison case. The purely local simulation can be interpreted as a polycrystal with a grain size much larger than the kink band characteristic width. As a result, many intense kink bands are observed, specifically triggered at triple junctions, like in these large grain ice polycrystals. On the contrary, when accounting for an intrinsic length of the order of the grain size, only a few mild kink bands are formed. Investigation of the formation of kink bands in polycrystalline ice with grain sizes smaller or equal to the characteristic width of observed kinks could provide key insights into the physical validity of this modeling approach. Of course, similar experiments could be imagined with others anisotropic crystals dominated by basal slip (Mg, Zn, Ti...).

This model also predicts that kink band width is intrinsically linked to hardening size effects. Thus, a strong consequence of these predictions could be that grain size effects and associated moduli could be investigated through the characterization of kink bands characteristics, or the characterization of kink band like rotation areas as exhibited in the work of Gioacchino and Fonseca (2015) (see section 2.1.2).

4.7.3 Consequences for irradiation induced strain localization modeling

The simulations of three dimensional cubic and hexagonal crystal structures (figs. 4.43 and 4.45) show that a significantly softening modeling with strong non local effects leads to localization bands networks exclusively composed of intense slip bands. This was the original purpose of all the work presented in the present chapter. In that respect, this modeling approach is a step forward towards the modeling of clear bands formation in irradiated metals. Indeed, as demonstrated in chap. 3, the current state of the art models predict the formation of kink clear channels, whereas all clear channels reported in the literature have clearly the characteristics of intense slip bands.

The natural follow up of these developments would be to formulate the constitutive equations developed to account at the continuum scale for the interactions between dislocation and irradiation induced defects (presented in section 2.3.2) in the framework of this strain gradient plasticity theory. In addition,

it strongly encourages a change in material coefficients identification process. Indeed, our macroscopically equivalent solutions show that different models (in our case, CCP and SGP) can predict the same overall behavior of the polycrystalline unit cell, but strongly different local fields. Considering the crucial consequences of dislocation channeling at the local scale (intergranular or ductile fracture), we believe that the identification criterion should involve the comparison of local fields to field measurements in irradiated deformed metals, as in the work of Thomas et al. (2019).

In the absence of such data, the identification process should at least include criteria on quantitative indicators reflecting the local characteristics of the predicted fields. For instance, the processing methods that we developed in chap. 3 allow to compute the number, the width, the spacing, or the volume fraction of slip localization bands. This values could be compared to TEM observations of clear channels characteristics or measured volume fraction (see Onimus, Monnet, et al. (2004)). As shown by our macroscopically equivalent simulations, identifying the coefficients under the constraint of minimizing kink band volume fraction or number would yield a high value for higher order coefficients, and consequently a higher value for the parameters responsible for softening. These parameters can be the magnitude of dislocation avalanches induced softening, the obstacle strength of irradiation induced defects, the frequency associated to the annihilation of defects by gliding dislocations, that are often identified only from the macroscopic stress-strain curve. The identification process that we propose here would certainly have strong consequences of their values, and thus could change our physical understanding of irradiated materials. Additionally, this raises the complex question of the dependence of size effects on the irradiation dose, for which very little experimental data exists.

In addition, it must be mentioned that slip band instability due to softening is still an issue attached to the present modeling. It results in a decreasing slip band spacing when increasing softening intensity, which is not in agreement with the enhanced slip band spacing with increasing dose observed in irradiated metals. Thus, regularizing slip bands with another length scale appears mandatory to achieve a proper modeling of clear channels.

4.8   Conclusions

To overcome the shortcomings of CCP, we have implemented a strain gradient plasticity model based on Gurtin (2002) theory. With respect to the first FFT implementation of R. A. Lebensohn and Needleman (2016), our work has

explored the influence of the choice of the derivation operators on slip localization bands formation and allowed to determine a more consistent double curl operator for the numerical implementation of this model. We also evidenced more consistent ways to implement boundary conditions, with a strong impact on the prediction of GND induced hardening. Moreover, it has been validated on several analytical solutions. Finally, our parallel implementation has allowed to run many simulations with millions of voxels and realistic crystal structures, required to study intragranular slip localization.

In addition, our work demonstrates that, similarly to Cosserat plasticity, this Nye tensor based model can solve the shortcoming of CCP models regarding slip localization modes. The quantitative study of the simulated slip and kink bands populations clearly evidenced the strong difference in their formation induced by this model. Kink bands are found to be much less numerous and wider than slips. These features, along with their decomposition in successive slip bands is consistent with experimental observations of kink bands. The predictions of the model are also in qualitatively good agreement with recent field characterization of intragranular localization in polycrystals. This shows that softening SGP models are a promising way to model the formation of slip bands in metals, which are thought to be the result of softening mechanisms at the dislocation scale.

This type of model is also a progress for achieving the simulation of clear bands formation in irradiated metals, as it strongly favors intense slip bands over kinks for strongly softening crystals, contrary to CCP models. Hence, the state of the art models relying on constitutive equations modeling the interactions between dislocation and irradiation induced defects, should be reformulated within this strain gradient framework. However, the meh dependence of slip bands has not been solved by this work. Therefore, an additional length scale aimed at regularizing slip bands width should be added in future works to hope for a consistent modeling of clear bands formation.

Finally, this work raises questions about the identification of material parameters for irradiated metal models. First, the question of the dependence of higher order moduli on the irradiation dose is open. This could be explored through the observation of grain size effect evolution with irradiation dose for various irradiated crystals. Second, we have shown that macroscopically equivalent stress-strain curves can be associated to very different local fields, which brings up the problem of the development of consistent model identification techniques based on comparison of simulations with field measurements. The quantitative indicators computed by the field processing strategies developed during this thesis could provide a starting point to attempt such identification.

Finally, the work presented in this chapter is largely involved in the

extension of the scope of AMITEX_FFTP to the resolution with spectral methods of field equations coupled with continuum mechanics homogenization. This generic developments have preserved its highly parallel implementation and its versatile user interface. This resulted in a new version of the solver that enables users to easily implement virtually any type of coupled problems.

CHAPTER 5

EXPLICIT SLIP BANDS MODELING WITH COMPOSITE VOXELS

Chapter Outline

205

Résumé en français

Les résultats du chap. 4 constituent un premier pas vers une simulation fidèle des bandes claires, permettant d'éviter la formation de bandes en genou hautement localisées non-physiques qui se forment avec les modèles de plasticité cristalline classique. Cependant, à l'heure actuelle, ils ne permettent pas encore d'obtenir une modélisation physiquement représentative de la localisation intra-granulaire du glissement plastique. En effet, notre cadre de plasticité à gradient ne permet pas de contrôler la largeur des bandes de glissement ni leur espacement. Au contraire, ces caractéristiques peuvent être facilement prises en compte lorsqu'on modélise explicitement (c'est-à-dire géométriquement) des bandes de glissement. Il s'agit d'une approche plus pragmatique visant à mieux comprendre l'effet d'une localisation accrue sur le comportement mécanique des métaux irradiés, parallèlement au développement à long terme de modèles physiquement représentatifs dans le cadre de la plasticité à gradient.

Cependant, des simulations polycristallines réalistes de bandes claires sont difficiles à réaliser d'un point de vue informatique. En effet, la largeur typique des bandes claires étant cent fois inférieure à la taille de grain typique des alliages de l'industrie nucléaire, la taille des voxels à utiliser dans les simulations FFT doit être au moins égale ou inférieure, nécessitant des millions d'éléments par grain. La simulation d'un nombre représentatif de grains avec prise en compte explicite des bandes claires a donc un coût de calcul colossal.

Afin de limiter l'impact du temps de calcul sur les simulations, des modèles voxel composites ont été implémentés dans le solveur AMITEX_FFTP, et entièrement intégrés à son implémentation parallèle et son interface utilisateur. Ces développements permettent d'améliorer considérablement les performances du solveur pour la simulation de microstructures complexes avec de nombreuses interfaces, comme les matériaux composites chargés d'inclusion ou les fibres (Charière, Marano, and Gélébart (2020)), mais également pour la prise en compte des interfaces entre de nombreuses bandes de glissement intra-granulaires et la matrice cristalline qui les contient. Par ailleurs, les modèles implémentés au cours de ce travail, de par leur formulation générique et non-linéaire, constituent une base pour l'extension future des modèles voxel composites mis en œuvre dans le solveur AMITEX_FFTP au cadre des déformations finies.

Nous avons montré que les voxels composites multi-couche permettent d'améliorer les performances de la modélisation avec prise en compte explicite des bandes de glissement dans les simulations polycristallines, diminuant d'un facteur 4 la résolution nécessaire à l'obtention d'une solution convergé par rapport à des simulations classiques, sans voxels composites. Cela nous a permis de réaliser des

simulations de cellules polycristallines tridimensionnelles avec des résolutions très élevées, pour décrire avec précision des réseaux de bandes claires potentielles aux dimensions réalistes, et issues d'une famille de plans de glissement. Dans le futur, cette approche devra être étendue pour prendre en compte plus d'une famille de plans de glissement par grain, ce qui soulève certaines difficultés dans la définition des voxels composites associés aux interfaces de plusieurs bandes de glissement. En particulier, le modèle multi-couche ne peut pas être correctement défini dans ce contexte, et ne semble plus physiquement pertinent.

Enfin, nous avons illustré une application potentielle de cette approche, en montrant qu'elle permet de simuler certaines conséquences de la canalisation basale dans les alliages de Zr texturés irradiés, utilisés pour les tubes de gainage du combustible dans l'industrie nucléaire. L'accroissement de la localisation du glissement plastique induite par l'irradiation est explicitement prise en compte par l'augmentation de l'espacement des bandes de glissement potentielle modélisées. Nos résultats montrent qu'elle induit un écrouissage cinématique global et des concentrations de contraintes aux joints de grains qui croissent avec la localisation de la déformation. Ces résultats de simulations ont nécessité des simulations à très haute résolution, très exigeantes en temps de calcul, et n'auraient pas pu être obtenus sans l'utilisation de voxels composites couplés à une implémentation parallèle efficace comme celle du solveur AMITEX_FFTP.

5.1 Introduction

The results of chap. 4 provide a first step toward the accurate simulation of clear channels, as they allow to preclude the formation of the non physical "slip band like" highly localized kink bands that form with CCP models. However, at the present time, they are not yet suitable to achieve a representative physics-based modeling of the consequences of intragranular slip localization. Indeed, our SGP framework does not allow to control the slip band width nor their spacing. On the contrary, these features can be easily accounted for when explicitly (*i.e.* geometrically) modeling slip bands. This represents a more pragmatic approach aimed at gaining insight into the effect of increased localization on the mechanical behavior of irradiated metals, in parallel to the long-term development of physically representative models.

M. Zhang et al. (2010) have modeled slip band formation in the α phase of duplex Ti-6Al-4V by prescribing a band pattern of fixed width and spacing where the material can soften. This model qualitatively reproduced the slip band behavior observed from an experiment at various strain levels. Meanwhile, a similar

approach has been applied to simulate the consequence of clear channel formation in irradiated austenitic steels by Sauzay, Bavard, and Karlsen (2010). They have explicitly modeled one or two clear channels between a free surface and a grain boundary within a FE mesh, embedded in a hard matrix, to study the evolution with channels width and spacing of the surface slip step and stress on grain boundary. Their results show slip step levels that are in agreement with observations and have evidenced that slip band width is the most influential parameter on both quantities.

However, these studies are both restricted to planar simulations with plane strain/stress conditions, and a small number of grains. Realistic polycrystalline simulations of clear channels in irradiated metals are more challenging from a computational point of view. Indeed, as typical width of clear bands is one hundred time lower than usual grain size in nuclear industry alloys, the size of elements should be at least equal or smaller, requiring millions of elements per grain. Hence simulating a representative number of grains comes with a colossal computational cost.

In this context, such simulation are hardly affordable even with classical FFT solvers. To get around this issue, the use of composite voxels seems a promising approach. Recently introduced (Gélébart and Ouaki (2015); Kabel, Merkert, and Schneider (2015)), they allow to replace the constitutive behavior of a voxel crossed by an interface with a homogenized behavior accounting for the phases within it and possibly some geometrical information regarding their arrangement in the voxel. These works have shown that they strongly increase both the accuracy of the calculated effective properties and the local quality of the strain and stress fields. As a result, they allow to achieve the same degree of precision as classical FFT based methods with a reduced resolution, and should be of prime interest for explicit slip band modeling which involves a high number of interfaces within the unit cell simulation.

In this chapter, we follow this idea to propose a first step towards the accurate explicit modeling of clear channels in irradiated metals. First, we present generic non-linear composite voxel models implemented in the code AMI-TEX_FFTP. Then, we apply them to explicit slip band modeling in polycrystals and show that composite voxels allow a significant increase in efficiency. Finally, this framework is applied to a simplified model to study the influence of slip localization in textured irradiated Zr alloys used in the nuclear industry, with a specific focus on slip localization induced kinematic hardening and grain boundary stress concentrations. All the applications presented in this chapter rely on perfect plasticity, in order to avoid numerical convergence difficulties associated to softening to build this Proof of Concept model. In addition, it allows isolate

the effect of slip band distribution on the mechanical behavior from material point hardening/softening influence.

5.2   Generic composite voxel models

5.2.1   Composite voxels

FFT-based solver operate on voxelwise constant fields defined on regular grids. At each iteration, the stress field over each voxel $\underline{\sigma}(\boldsymbol{x})$ must be evaluated in order to build the polarization field $\underline{\tau}(\boldsymbol{x})$ as follow:

$$\underline{\tau}(\boldsymbol{x}) = \underline{\sigma}(\boldsymbol{x}) - \underline{\underline{\Lambda}}^0 : \underline{\varepsilon}(\boldsymbol{x}) \; \forall \boldsymbol{x} \in \Omega \tag{5.1}$$

$$\text{with:} \underline{\sigma}(\boldsymbol{x}) = \mathcal{F}\left(\underline{\varepsilon}^k(\boldsymbol{x})\right) \tag{5.2}$$

When simulating non-linear materials, this process requires the integration of the constitutive relation $\mathcal{F}$ of the material phase lying in the voxel. However, when the voxel is crossed by one or more interfaces (see fig. 5.1), this choice is no longer unique. In this case, most FFT-based solver evaluate the constitutive relation of the phase lying at the center of the voxel, resulting in a poor description of the microstructure close to interfaces. Alternatively, more sophisticated choices for the constitutive relation have been proposed by Gélébart and Ouaki (2015); Kabel, Merkert, and Schneider (2015), and called composite voxels (CV). In practice they are homogenization rules for the global behavior of the voxel, allowing to account for the different phases and their distribution in the voxel.
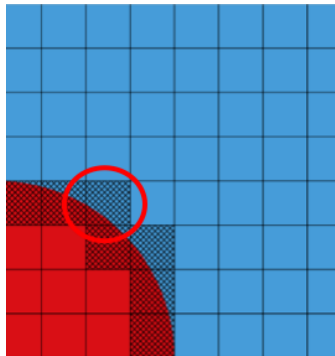
Figure 5.1 – Regular grid discretization of a circular inclusion (in red) showing the voxels crossed by the interface (one is highlighted by the red circle) that can be modeled as composite voxels.

5.2.2 Generic composite voxel models in the small strain framework

Following the notations and definitions of section 2.4.4, in the small strain framework, CV models can be seen as a constitutive relation $\mathcal{F}_{CV}$ linking the stress over the voxel to: the strain, the volume fraction f_i and the constitutive relation of its constitutive phases $\mathcal{F}_i$ (eq. (5.5)). This relation involves internal variables $\boldsymbol{\alpha}_{CV}$ and coefficients $\boldsymbol{C}_{CV}$ that are specific to the chosen homogenization rule $\mathcal{H}$. Each phase composing the voxel has its own mechanical stress and strain state: $\underline{\boldsymbol{\sigma}}_i, \underline{\boldsymbol{\varepsilon}}_i$.

These relations must be verified under the classical constraint that the mean over the voxel of these local states $\underline{\boldsymbol{\sigma}}_i, \underline{\boldsymbol{\varepsilon}}_i$ is equal to the global mechanical state of the voxel: $\underline{\boldsymbol{\sigma}}_{CV}, \underline{\boldsymbol{\varepsilon}}_{CV}$ (given by eqs. (5.3) and (5.4) for phase-wise homogeneous local states). Hence, a CV model containing N_ϕ phases can be written formally as the following set of equations:

$$
\begin{cases}
\underline{\boldsymbol{\sigma}}_{CV} = \sum_{i=1}^{N_\phi} f_i \underline{\boldsymbol{\sigma}}_i & (5.3) \\[2ex]
\underline{\boldsymbol{\varepsilon}}_{CV} = \sum_{i=1}^{N_\phi} f_i \underline{\boldsymbol{\varepsilon}}_i & (5.4) \\[2ex]
\underline{\boldsymbol{\sigma}}_i = \mathcal{F}\left\{ \underline{\boldsymbol{\varepsilon}}_i, \boldsymbol{\alpha}_i, \boldsymbol{C}_i \right\} \qquad \forall i/1 \leq i \leq N_\phi & (5.5) \\[2ex]
\mathcal{H}\left\{ \underline{\boldsymbol{\sigma}}_{CV}, \underline{\boldsymbol{\varepsilon}}_{CV}, \underline{\boldsymbol{\sigma}}_1, \ldots, \underline{\boldsymbol{\sigma}}_{N_\phi}, \underline{\boldsymbol{\varepsilon}}_1, \ldots, \underline{\boldsymbol{\varepsilon}}_{N_\phi}, \boldsymbol{\alpha}_{CV}, \boldsymbol{C}_{CV} \right\} = 0 & (5.6)
\end{cases}
$$

Defining a composite voxel model consists then in proposing a specific homogenization rule $\mathcal{H}$, and its associated internal variables and coefficients $\boldsymbol{\alpha}_{CV}$ and $\boldsymbol{C}_{CV}$. We have considered three different rules in our work, following Gélébart and Ouaki (2015); Kabel, Merkert, and Schneider (2015). They are described below.

Voigt Composite Voxels

In Voigt CV, $\mathcal{H}$ is replaced with the Voigt approximation: the strain state is supposed to be homogeneous in the voxel, which implies:

$$
\underline{\boldsymbol{\varepsilon}}_i = \underline{\boldsymbol{\varepsilon}}_{CV} \qquad \forall i/1 \leq i \leq N_\phi \tag{5.7}
$$

The constraint defined by eq. (5.4) is then automatically verified. All the local strain states $\underline{\boldsymbol{\varepsilon}}_i$ are known and thus also all stress states $\underline{\boldsymbol{\sigma}}_i$ through the constitutive

relations (eq. (5.5)). Finally the macroscopic stress state can be evaluated using eq. (5.3). No specific coefficients $\boldsymbol{C}_{CV}$ are required, and the relevant internal variables describing the mechanical state of each phase are the local stress states $\boldsymbol{\alpha}_{CV} = \left\{ \underline{\boldsymbol{\sigma}}_1, \ldots, \underline{\boldsymbol{\sigma}}_{N_\phi} \right\}$.

Voigt approximation provides the stiffest bound for the composite voxel constitutive relation.

Reuss Composite Voxels

In Reuss CV, $\mathcal{H}$ is replaced with the Reuss approximation: the stress state is supposed to be homogeneous in the voxel, which implies:

$$\underline{\boldsymbol{\sigma}}_i = \underline{\boldsymbol{\sigma}}_{CV} \qquad \forall i / 1 \le i \le N_\phi \tag{5.8}$$

The constraint defined by eq. (5.3) is then automatically verified. To find the solution, the non-linear system of eq. (5.5) must be solved for the $\underline{\boldsymbol{\varepsilon}}_i$ under the constraint of eq. (5.4). No specific coefficients $\boldsymbol{C}_{CV}$ are required, and the relevant internal variables describing the mechanical state of each phase are the local strain states $\boldsymbol{\alpha}_{CV} = \left\{ \underline{\boldsymbol{\varepsilon}}_1, \ldots, \underline{\boldsymbol{\varepsilon}}_{N_\phi} \right\}$.

Reuss approximation provides the softer bound for the composite voxel constitutive relation.

Laminate Composite Voxels

Laminate CV consist in a linear approximation of the interface between phases, which is assumed to be a plane $\mathcal{P}$ with normal direction $\boldsymbol{N}$, as illustrated on fig. 5.2. The voxel is supposed to behave as an infinite laminate material. The solution of this classical mechanical problem are phasewise constant fields, that must verify the following relation:

$$\underline{\boldsymbol{\sigma}}_{CV}^N = \underline{\boldsymbol{\sigma}}_i^N \qquad \forall i / 1 \le i \le N_\phi \tag{5.9}$$
$$\underline{\boldsymbol{\varepsilon}}_{CV}^{\mathcal{P}} = \underline{\boldsymbol{\varepsilon}}_i^{\mathcal{P}} \qquad \forall i / 1 \le i \le N_\phi \tag{5.10}$$

Superscripts N and $\mathcal{P}$ denote respectively the normal and in-plane part (3 components each) of a tensor with respect to the plane $\mathcal{P}$ (see appendix A.2 for a complete description of this notation). Equation (5.9) states that the local stress fields must verify the continuity of the traction vector at the interface between the phases, and eq. (5.10) states that local strain fields must induce a compatible deformation at both sides of each planar interface. To find the solution, the non-linear system of

eq. (5.5) must be solved for the $\underline{\boldsymbol{\varepsilon}}_i^N$ under the constraint of eqs. (5.4) and (5.10). eq. (5.3) is then used to compute $\underline{\boldsymbol{\sigma}}_{CV}$.

In this case, the coefficients associated to the homogenization rule are $\boldsymbol{C}_{CV} = \boldsymbol{N}$, and the relevant internal variables describing the mechanical state of each phase are the local normal strain and planar stress states $\boldsymbol{\alpha}_{CV} = \left\{ \underline{\boldsymbol{\varepsilon}}_1^N, \ldots, \underline{\boldsymbol{\varepsilon}}_{N_\phi}^N, \underline{\boldsymbol{\sigma}}_1^{\mathcal{P}}, \ldots, \underline{\boldsymbol{\sigma}}_{N_\phi}^{\mathcal{P}} \right\}$.
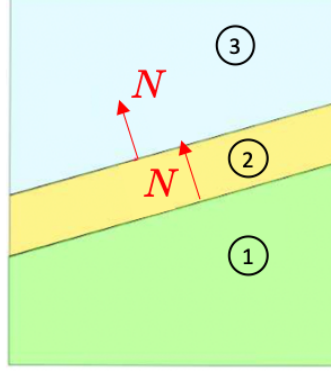
Figure 5.2 – Schematic representation of a 3-phases Laminate composite voxel with $\boldsymbol{N}$ the normal direction to the planar interface between phases.

5.2.3 Numerical resolution

We describe here the generic algorithm structure that has been implemented in AMITEX_FFTP for the resolution of CV models, in the small strain framework, for any arbitrary number of constitutive phases having any non-linear behavior.

As described in section 2.4.4 (eq. (2.42)), the constitutive relations are integrated with an incremental formulation at each time step, for a prescribed strain increment, to compute the stress increment. In order to simplify notations, we drop here the subscripts t and $t+\Delta t$ used in section 2.4.4, and denote by $(\underline{\boldsymbol{\sigma}}_{CV}, \underline{\boldsymbol{\varepsilon}}_{CV})$ and $\Delta\underline{\boldsymbol{\sigma}}_{CV}, \Delta\underline{\boldsymbol{\varepsilon}}_{CV}$ the initial mechanical state and its incremental evolution for the CV, and $(\underline{\boldsymbol{\sigma}}_i, \underline{\boldsymbol{\varepsilon}}_i)$ and $\Delta\underline{\boldsymbol{\sigma}}_i, \Delta\underline{\boldsymbol{\varepsilon}}_i$ the corresponding quantities for the phases contained within the CV.

The generic definition of a CV model given by eqs. (5.3) to (5.6) allows to define a generic procedure for the numerical resolution of these equations in incremental form. The solution of the CV model is obtain when eqs. (5.5) and (5.6) are solved for all the $\Delta\underline{\boldsymbol{\varepsilon}}_i$. In practice, as $\Delta\underline{\boldsymbol{\varepsilon}}_{CV}$ is prescribed, eq. (5.4) allows to

reduce by one the number of unkowns $\underline{\boldsymbol{\varepsilon}}_i$. eq. (5.5) allows to compute the $\Delta\underline{\boldsymbol{\sigma}}_i$ when the solution is found and eq. (5.4) to compute $\Delta\underline{\boldsymbol{\sigma}}_{CV}$.

Solving the problem requires then the solution a the non-linear system of the form: $\mathcal{H}(\Delta\underline{\boldsymbol{\varepsilon}}_1,\ldots,\Delta\underline{\boldsymbol{\varepsilon}}_{N_\phi-1}) = 0$. We chose to use iterative Newton-like methods to solve it. They consist in computing, at each iteration k:

$$\Delta\underline{\boldsymbol{\varepsilon}}_i^k = \Delta\underline{\boldsymbol{\varepsilon}}_i^{k-1} + \partial\Delta\underline{\boldsymbol{\varepsilon}}_i^k \tag{5.11}$$
$$\mathcal{L}^k : \partial\Delta\underline{\boldsymbol{\varepsilon}}_i^k = -\mathcal{H}(\Delta\underline{\boldsymbol{\varepsilon}}_i^{k-1}) \tag{5.12}$$

until eq. (5.6) is verified to the precision η: $\mathcal{H}(\Delta\underline{\boldsymbol{\varepsilon}}_i^k) < \eta$. The choice of $\mathcal{L}^k$ defines the iterative Newton-like method. If it is chosen to be equal to the Jacobian of $\mathcal{H}$ then this procedure is the Newton-Rapshon algorithm. This choices will be detailed in the following, as well as the specific forms of $\mathcal{H}$ for the three CV models of section 5.2.2.

In addition, the convergence acceleration technique used in AMITEX_FFTP for the fix-point algorithm (section 2.4.5) is also applied to the pair $\left(\Delta\underline{\boldsymbol{\varepsilon}}_i^k, \mathcal{H}(\Delta\underline{\boldsymbol{\varepsilon}}_i^k)\right)$, as well as the linear extrapolation from previous increment values of the initial guess $\Delta\underline{\boldsymbol{\varepsilon}}_i^0$ (see fig. 2.39). Finally, note that strain and stress tensors are handled in Voigt notation in AMITEX_FFTP and are thus 6 component vectors.

Voigt Composites Voxels

For Voigt CV, $\mathcal{H}$ is defined by eq. (5.7). By prescribing $\Delta\underline{\boldsymbol{\varepsilon}}_{CV}$ and the $\Delta\underline{\boldsymbol{\varepsilon}}_i$ all be prescribed equal, it is automatically verified. No iterative resolution is then needed in this case. After prescribing the strain increments, eqs. (5.3) and (5.5) are used to compute directly the solution.

Reuss Composite Voxels

For Reuss CV, $\mathcal{H}$ is defined by eq. (5.8). The solution coincide then with the equality of all the stress states $\underline{\boldsymbol{\sigma}}_i + \Delta\underline{\boldsymbol{\sigma}}_i$ ($\forall i/1 \le i \le N_\phi$). $\mathcal{H}$ can then by written as $N_{phi} - 1$ tensorial equations:

$$\mathcal{H}_i = \underline{\boldsymbol{\sigma}}_{i+1} - \underline{\boldsymbol{\sigma}}_1 \qquad \forall i/1 \le i \le N_\phi - 1 \tag{5.13}$$

Equation (5.4) allow to reduce the number of variables in **??** by writting:

$$\Delta\underline{\boldsymbol{\varepsilon}}_1 = \frac{1}{f_1}\left[\Delta\underline{\boldsymbol{\varepsilon}}_{CV} - \sum_{i=2}^{N_\phi} f_i \Delta\underline{\boldsymbol{\varepsilon}}_i\right] \tag{5.14}$$

Using eq. (5.14), eq. (5.13) can be rewritted as:

$$\mathcal{H}_i = \underline{\boldsymbol{\sigma}}_{i+1}(\Delta\underline{\boldsymbol{\varepsilon}}_{i+1}) - \underline{\boldsymbol{\sigma}}_1 \left(\frac{1}{f_1} \left[\Delta\underline{\boldsymbol{\varepsilon}}_{CV} - \sum_{i=2}^{N_\phi} f_i \Delta\underline{\boldsymbol{\varepsilon}}_i \right] \right) \qquad \forall i/1 \leq i \leq N_\phi - 1 \tag{5.15}$$

Hence, eq. (5.15) defines a non-linear system of $6(N_\phi - 1)$ equations.

Finally, with eq. (5.15) we get an expression of the form

$$\mathcal{H}(\Delta\underline{\boldsymbol{\varepsilon}}_2, \ldots, \Delta\underline{\boldsymbol{\varepsilon}}_{N_\phi}) = 0$$

that characterizes the solution of the Reuss CV model. Its Jacobian matrix is expressed in block notation as:

$$d\mathcal{H} = \begin{bmatrix} d\mathcal{H}_{11} & \cdots & d\mathcal{H}_{1N_\phi} \\ \vdots & \ddots & \vdots \\ d\mathcal{H}_{N_\phi 1} & \cdots & d\mathcal{H}_{N_\phi N_\phi} \end{bmatrix} \tag{5.16}$$

where the $d\mathcal{H}_{ij}$ are 6x6 square matrices given by:

$$d\mathcal{H}_{ij} = \frac{\partial \mathcal{H}_i}{\partial \Delta\underline{\boldsymbol{\varepsilon}}_j} = \delta_{ij} \frac{\partial \Delta\underline{\boldsymbol{\sigma}}_{j+1}}{\partial \Delta\underline{\boldsymbol{\varepsilon}}_{j+1}} + \frac{f_{j+1}}{f_1} \frac{\partial \Delta\underline{\boldsymbol{\sigma}}_1}{\partial \Delta\underline{\boldsymbol{\varepsilon}}_1} \tag{5.17}$$
$$\forall i/1 \leq i \leq N_\phi - 1, \quad \forall j/1 \leq i \leq N_\phi - 1$$

This problem is solved with the Newton-like iterative method described in eqs. (5.11) and (5.12). The tangent operator is chosen constant and equivalent to the one obtained in the case where all constitutive phases of the CV are isotropic linear elastic. Its components are computed as follow:

$$\mathcal{L}_{ij} = \delta_{ij} \underline{\underline{\boldsymbol{\Delta}}}^{j+1} + \frac{f_{j+1}}{f_1} \underline{\underline{\boldsymbol{\Delta}}}^1 \tag{5.18}$$

The $\underline{\underline{\boldsymbol{\Delta}}}^j$ are the equivalent elastic moduli tensor of the constitutive phases of the CV. They can be defined by the classical Lamé coefficient or with E and ν, Young's modulus and Poisson's ratio. This choice is classically called a quasi-Newton method. As mentioned previously, the Quasi-Newton method is accelerated by a Anderson's acceleration technique. The Newton-Raphson method has not been implemented yet for the Reuss CV model.

Laminate Composite Voxels

As shown by eqs. (5.9) and (5.10), the laminate CV model is similar to a combination Voigt CV model restricted to the in-plane part of the strain states, and to Reuss CV restricted to normal components of the strain states. Hence, the in-plane part of the strain states $\Delta\underline{\varepsilon}_i^{\mathcal{P}}$ are directly prescribed. The problem can then be solved exactly as for Reuss CV, but only for the normal part of the strain increments $\Delta\underline{\varepsilon}_i^N$. Hence, the non-linear system to solve is written:

$$\mathcal{H}_i = \underline{\sigma}_{i+1}^N(\Delta\underline{\varepsilon}_{i+1}^N) - \underline{\sigma}_1^N\left(\frac{1}{f_1}\left[\Delta\underline{\varepsilon}_{CV}^N - \sum_{i=2}^{N_\phi} f_i\Delta\underline{\varepsilon}_i^N\right]\right) \qquad \forall i/1 \le i \le N_\phi - 1 \tag{5.19}$$

It is a non-linear system of $3(N_\phi - 1)$ equations, with a jacobian defined by:

$$d\mathcal{H}_{ij} = \frac{\partial\mathcal{H}_i}{\partial\Delta\underline{\varepsilon}_j^N} = \delta_{ij}\frac{\partial\Delta\underline{\sigma}_{j+1}^N}{\partial\Delta\underline{\varepsilon}_{j+1}^N} + \frac{f_{j+1}}{f_1}\frac{\partial\Delta\underline{\sigma}_1^N}{\partial\Delta\underline{\varepsilon}_1^N} \tag{5.20}$$

Numerically, the tensors $\Delta\underline{\sigma}_j^N$ and $\Delta\underline{\varepsilon}_j^N$ $\forall j$ (that have only 3 independent components each) are handled as 3 components vectors. Hence, in this case, $d\mathcal{H}_{ij}$ is a 3x3 matrix. The tangent operator $\frac{\partial\Delta\underline{\sigma}_i^N}{\partial\Delta\underline{\varepsilon}_j^N}$ is obtained by computing the 6x6 matrix $\frac{\partial\Delta\underline{\sigma}_i}{\partial\Delta\underline{\varepsilon}_j}$ in the interface basis (see appendix A.2):

$$\left\{(\boldsymbol{N}\otimes\boldsymbol{N}), (\boldsymbol{T}_1\otimes\boldsymbol{T}_1), (\boldsymbol{T}_2\otimes\boldsymbol{T}_2), \frac{1}{2}\left[(\boldsymbol{N}\otimes\boldsymbol{T}_1) + (\boldsymbol{T}_1\otimes\boldsymbol{N})\right],\right.$$

$$\left.\frac{1}{2}\left[(\boldsymbol{N}\otimes\boldsymbol{T}_2) + (\boldsymbol{T}_2\otimes\boldsymbol{N})\right], \frac{1}{2}\left[(\boldsymbol{T}_1\otimes\boldsymbol{T}_2) + (\boldsymbol{T}_2\otimes\boldsymbol{T}_1)\right],\right\}$$

and restricting it to the 3 columns and 3 lines associated to the normal components:

$$\left\{(\boldsymbol{N}\otimes\boldsymbol{N}), \frac{1}{2}\left[(\boldsymbol{N}\otimes\boldsymbol{T}_1) + (\boldsymbol{T}_1\otimes\boldsymbol{N})\right], \frac{1}{2}\left[(\boldsymbol{N}\otimes\boldsymbol{T}_2) + (\boldsymbol{T}_2\otimes\boldsymbol{N})\right]\right\}$$

Three choices of tangent operator have been implemented:

1. $\mathcal{L}^{NR} = d\mathcal{H}$, this choice is the Newton-Raphson method. In this case eq. (5.20) is explicitly computed from its analytical formula, for each component of the tangent operator.

2. $\mathcal{L}^{num} = d\mathcal{H}^{num}$, where $d\mathcal{H}^{num}$ is a numerical approximation of $d\mathcal{H}$, computed

as follow:

$$dH_{ij}^{num} = \frac{\mathcal{H}_i(\ldots, \Delta\underline{\underline{\varepsilon}}_j^N + \epsilon, \ldots) - \mathcal{H}_i(\ldots, \Delta\underline{\underline{\varepsilon}}_j^N, \ldots)}{\epsilon} \tag{5.21}$$

where ϵ is a perturbation that is small compared to $\Delta\underline{\underline{\varepsilon}}_j$. This choice is a numerical approximation of the Newton-Raphson method.

3. $\mathcal{L}^0$, the constant isotropic linear elastic tangent operator similar to the one described for Reuss CV, corresponding to a Quasi-Newton method. Its components are computed as follows:

$$\mathcal{L}_{ij} = \delta_{ij}\underline{\underline{\mathbf{\Delta}}}_N^{j+1} + \frac{f_{j+1}}{f_1}\underline{\underline{\mathbf{\Delta}}}_N^1 \tag{5.22}$$

where $\underline{\underline{\mathbf{\Delta}}}_N^j$ are the equivalent elastic moduli tensors of the constitutive phases of the CV restricted to the 3 columns and 3 lines associated to the normal components of the tensors, as detailed above for the true tangent operator.

Generic implementation

All the CV models presented here have been formulated in a complete non-intrusive fashion with respect to the constitutive relations of each phase, and can include as many constitutive phases as necessary. Moreover, in AMITEX_FFTP, the implemented evaluation of these relations is done through the call of a UMAT subroutine, exactly as for homogeneous voxels (see section 2.4.5). As a result, these CV models can be evaluated with virtually any type of material behavior for the constitutive phases, and thus do not restrict the scope of applications of the solver, in particular for non-linear materials. In addition, the UMAT formalism allows to provide the tangent operator $\frac{\partial\Delta\underline{\underline{\sigma}}_i}{\partial\Delta\underline{\underline{\varepsilon}}_i}$ of the constitutive relations of each phase, which enables to construct the true tangent operator of the Newton-Raphson method.

Besides, the developments introduced in AMITEX_FFTP allow to build a distributed memory description of all composite voxels from standard user input data by only specifying the geometrical description of these composite voxels. Indeed, in AMITEX_FFTP, a voxelized unit-cell is described as follow:

- a "material" consists in a set of voxels with the same constitutive law
- a "zone" consists in a set of voxels of a "material", that have the same coefficients for this constitutive law

This geometrical description is provided by two three-dimensional fields input (VTK format), and is used to build the distributed memory structure of the code. An important constraint for the introduction of CV models in AMITEX_FFTP was to

build the CV description from this original unit cell description without CV, as an overlayer. Thus, CV input data must consist in the specification of CV positions, as well as the number of the "material" and "zone" to which each of its phases relate, in order to enable the code to search in the original description the information needed to build CV. However, some of this information can be located in another part of the distributed memory structure than the one containing the composite voxel. To this end, a specific communication procedure had to be developed in order to allow the communication of these informations.

As a result, CV models can be virtually added to any simulation in AMITEX_FFTP, by specifying the geometrical description of CV as well as their composition, without modifying the original input data and having CV voxels well integrated to the distributed memory structure. Hence, it maintains the performance of the massively parallel implementation of the solver as well as its generic user interface.

Validation and performances

The numerical implementation of the various CV models have been validated on analytical isotropic linear elastic solutions, as well as non-linear material behaviors by comparing its predictions to an infinite laminate unit-cell simulated with AMITEX_FFTP for a resolution sufficient to obtained a converged solution. The results show that:

- As shown by other authors (Gélébart and Ouaki (2015); Kabel, Fink, and Schneider (2017); Kabel, Merkert, and Schneider (2015); Kabel, Ospald, and Schneider (2016)) composite voxels enhance the convergence of the FFT based method, and improve the quality of local fields.

- The laminate composite voxels show the best overall performances but is less pertinent when the elastic contrast between phases becomes large ($> 10^3$).

- The Newton-Raphson method yields the best performances for the convergence of Laminate CV algorithms. However it requires the explicit expression of the tangent operator for each phase behavior.

- For strongly non-linear behaviors, the quasi-Newton method (with Anderson's acceleration technique) convergence becomes difficult, while the numerical approximation of the Newton-Raphson method does not. Both methods do not require the explicit expression of the tangent operator for each phase.

- For moderate non-linear behaviors, the quasi-Newton method (with Anderson's acceleration technique) is faster than the numerical approximation of Newton-Rapshon method.

The detail of these simulations is not provided as they are not central for the subject of explicit slip band modeling. The reader is referred to the work presented in Charière, Marano, and Gélébart (2020), where these developments have been used to simulate hollow glass thin microspheres/polypropylene composites, for an application of these developments that confirms the trend listed above.

5.3   Efficient simulations of intragranular slip bands

Explicit slip bands modeling for polycrystalline simulations involve the explicit consideration of many interfaces at small scales that are hardly described by a regular grid. Hence, composite voxels are expected to be particularly well suited to enhance the performances of this modeling approach. In this section, we present the application of our CV models to this problem.

5.3.1   Explicit slip band modeling with Composite Voxels

Similarly to M. Zhang et al. (2010), we consider in a polycrystalline unit cell, generated with a Voronoi tessellation, a distribution of equally spaced bands of constant width that are parallel to the slip systems of each grain. As a first step, we consider only a single slip plane per grain, with normal direction $\boldsymbol{n}$, defining 3 slip systems rotated from 120° relatively to each other. This is equivalent to the basal slip system family of hexagonal crystals. The band width is noted ω_b, the band spacing d_b, the mean grain size d_g and the voxel size ∂x. As a result, the average number of bands per grain is $N_b = \frac{d_g}{d_b}$ and the average bands volume fraction is $f_b = \frac{\omega_b}{d_b}$.

As shown on the planar schematic of fig. 5.3, each potential slip band is defined by 2 planes crossing the discretization grid, with normal direction $\boldsymbol{n}$. Each voxel lying entirely between the two planes is given a plastic behavior, and each voxel lying entirely outside is given an isotropic linear elastic behavior. Each voxel crossed by one of these planes is defined as a composite voxel composed of the plastic and the elastic phase. The volume fraction of each phase is computed within each of these voxel. Figure 5.4 shows the three steps of generation of a polycrystalline unit cell with this method: the polycrystalline unit cell with homogeneous grains
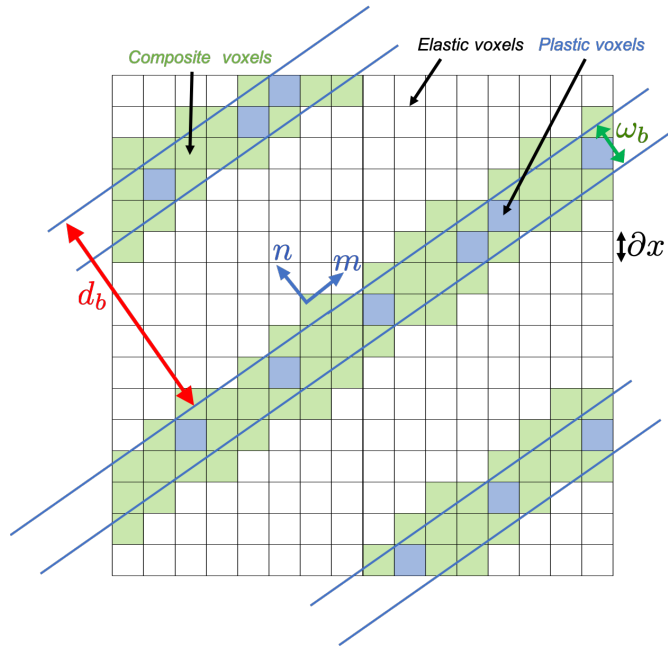
Figure 5.3 – Planar representation of potential slip bands of fixed width ω_b and spacing d_b on a regular grid with homogeneous and composite voxels, for a single slip system defined by its glide and normal to slip plane directions $\boldsymbol{m}$ and $\boldsymbol{n}$.

(a), the addition of plastic voxels representing the slip bands (b) and the addition of composite voxels to resolve exactly the interfaces of the bands (c).
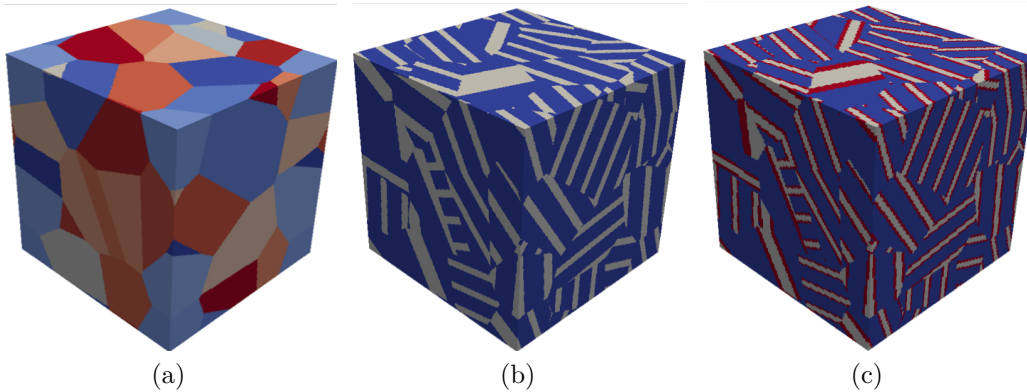
Figure 5.4 – 27 grains polycrystalline unit cell ($240^3 \approx 14$ million voxels) with one family of potential slip bands modeled: $N_b = 3$, $\frac{\omega_b}{d_g} = \frac{1}{10}$.
(a) Voronoi tessellation defining the grains, (b) unit cell with elastic (blue) and plastic (gray) voxels, (c) unit cell with addition of composite voxels (red).

5.3.2   Results

In order to study the gain obtained when using composite voxel models, simulations have been carried out on the two microstructures shown on fig. 5.5. The constitutive modeling chosen for the plastic phase is a simple perfectly plastic crystal plasticity model with a Norton flow rule, summarized by eqs. (5.23) to (5.27):

$$\underline{\varepsilon} = \underline{\varepsilon}^e + \underline{\varepsilon}^p \tag{5.23}$$

$$\underline{\sigma} = \underline{\underline{\Lambda}} : \underline{\varepsilon}^e \tag{5.24}$$

$$\underline{\varepsilon}^p = \sum_{s=1}^{N} \gamma^s \underline{\overset{\diamond}{\mu}}^s \tag{5.25}$$

$$\dot{\gamma}^s = \text{sign}(\tau^s) \left\langle \frac{|\tau^s| - \tau_c}{K} \right\rangle^n \tag{5.26}$$

$$\tau^s = \underline{\sigma} : \underline{\overset{\diamond}{\mu}}^s \tag{5.27}$$

The critical resolved shear stress $\tau_c = 100\,\text{MPa}$ is constant and the Norton flow rule coefficients $n = 20$ and $K = 10\,\text{MPa s}^{1/\text{n}}$ are chosen so that the behavior is almost rate-independent. The elastic moduli tensor is chosen isotropic linear elastic with Young's modulus $E = 1 \times 10^5\,\text{MPa}$ and Poisson's ratio $\nu = 0.3$. The elastic phase has the same elastic behavior as the plastic phase.

In practice, these relations are implemented in a UMAT subroutine using the Mfront code generator and solved with an implicit Newton-Raphson method. It has already been presented in section 3.2.3 and is thus not detailed further here. This implementation allows to compute the tangent operator of the constitutive relation $\frac{\partial \Delta \underline{\sigma}}{\partial \Delta \underline{\varepsilon}}$. It is used to apply the true Newton-Raphson method for the resolution of laminate CV models (section 5.2.2) in the following, whereas Reuss CV are solved using the quasi-Newton method (with convergence acceleration).

The unit cell is submitted to a mean tensile strain loading in the direction $\boldsymbol{e}_3$ up to $\underline{\varepsilon}_{33} = 0.01$. All other components of the mean stress tensor are prescribed to zero. The simulation is carried out with strain increments of 10^{-5}, at a strain rate of $1 \times 10^{-5}\,\text{s}^{-1}$.

The different CV models presented in the last section are tried out, and compared to the case where only homogeneous voxels are considered. The relevant resolution is defined as the ratio between the band width and the voxel size $r = \frac{\omega_b}{\partial x}$. The simulations are carried out for various resolution verifying $r^P = 2^P \cdot r^0$, where P is the grid refinement coefficient, and $r^0 = 0.5$ is the initial resolution. The convergence of $\underline{\sigma}_f = \underline{\sigma}_{33}(\underline{\varepsilon}_{33} = 0.01)$, the computed final macroscopic stress in the tensile direction, is studied. Two different error indicators are used to quantify its
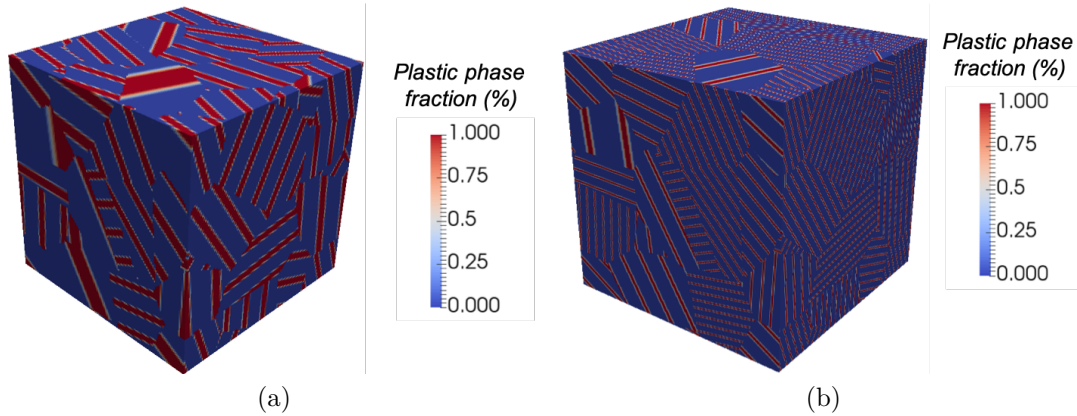
Figure 5.5 – Plastic phase volume fraction for two different potential slip band pattern generated (27 grains polycrystalline unit cell), with $\frac{\omega_b}{\partial x} = 2$.
(a) $\frac{\omega_b}{d_g} = \frac{1}{3}$, 3 bands per grain in average, (b) $\frac{\omega_b}{d_g} = \frac{1}{50}$, 10 bands per grain in average. 0% indicates elastic voxels, 1% plastic voxels, and a value in between indicates composite voxels.

evolution with grid refinement:

$$E_{cv}(P) = \frac{\boldsymbol{\sigma}_f(P) - \boldsymbol{\sigma}_f(P-1)}{\boldsymbol{\sigma}_f(P-1)} \tag{5.28}$$

$$E_{rel}\left(\frac{\omega_b}{\partial x}, \boldsymbol{\sigma}^{ref}\right) = \frac{\boldsymbol{\sigma}_f\left(\frac{\omega_b}{\partial x}\right) - \boldsymbol{\sigma}^{ref}}{\boldsymbol{\sigma}^{ref}} \tag{5.29}$$

$E_{cv}(P)$ is the relative gap between the solution obtained for a given resolution and a two times higher resolution. A low value of $E_{cv}(K)$ indicates that the solution is converged with respect to grid resolution. E_{rel} is the relative error compared to a reference value $\boldsymbol{\sigma}^{ref}$ (which will be defined later), it evaluates the precision of a given simulation with respect to the reference value.

Figure 5.6 presents the evolution of E_{cv} for the two microstructures with grid refinement on (a-b). They show that laminate CV yield the best convergence for the final stress value. Their convergence is even better when modeling thin bands (b), when for other models E_{cv} does not diminish with grid refinement in this case, indicating a slow convergence. Reuss CV model could not converge unless $\frac{\omega_b}{\partial x} \geq 4$, and only for strain increments of 10^{-6} resulting in much longer simulations than all other models. This is certainly due to the use of the quasi-Newton method instead of the Newton-Raphson method. For this reason their results are not plotted on figure (b). Figure 5.6 -(c) shows a comparison of the stress-strain curves

obtained without CV and with laminate CV for all resolutions. It shows that both models converge towards the same solution, and highlights the faster convergence of the model relying on laminate CV.
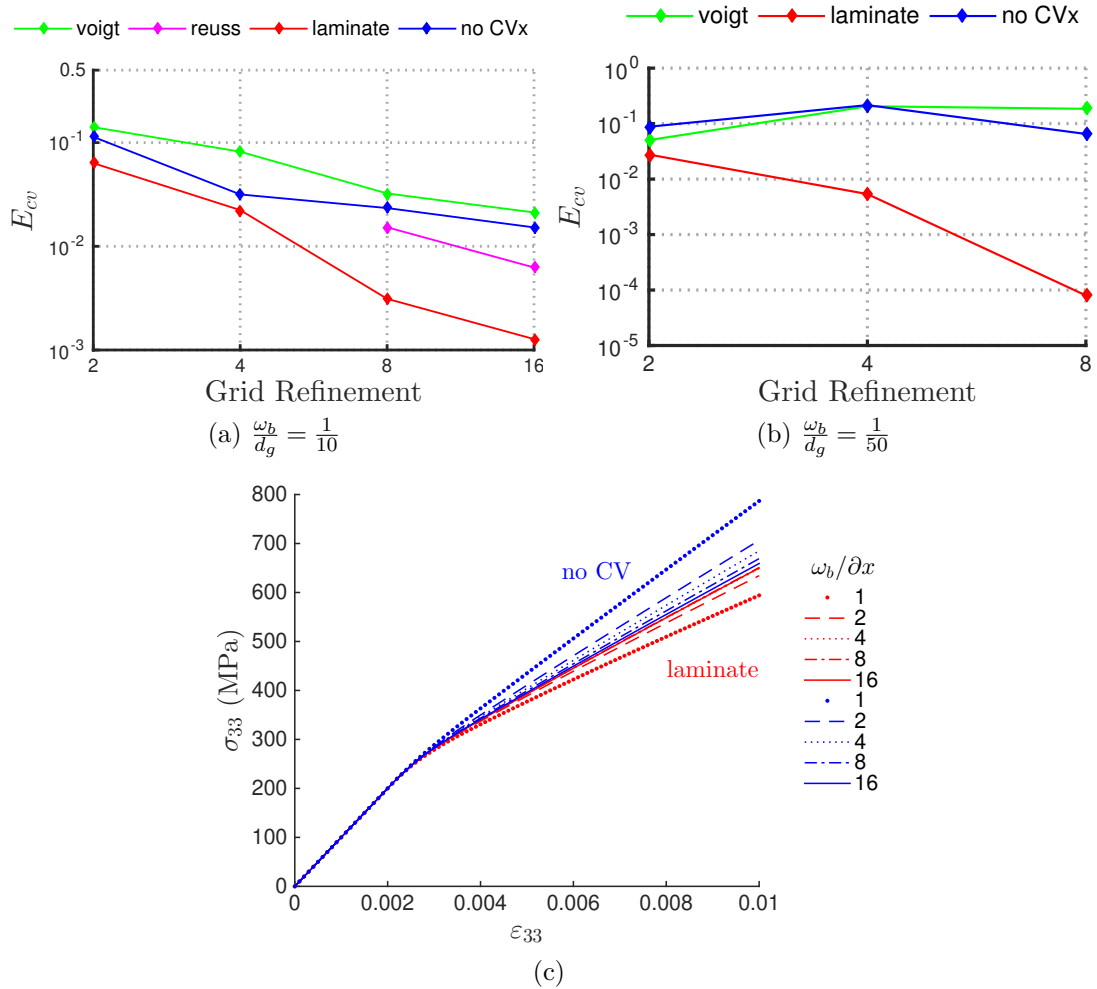
Figure 5.6 – Evolution of convergence error with grid refinement (2^K) for the case (a) $\frac{\omega_b}{d_g} = \frac{1}{10}$, 3 bands per grain in average and (b) $\frac{\omega_b}{d_g} = \frac{1}{50}$, 10 bands per grain in average. Simulated stress-strain curve (c) for the first case without composite voxels (no CV) and with laminate composite voxels.

The value obtained with Laminate CV can then be defined as the best converged solution, and is chosen as the reference value to evaluate E_{rel} as indicated by eq. (5.29). Figure 5.7 shows the results obtained for the two band patterns. It appears that laminate voxels allow to get the same precision than other models with a resolution 4 to 8 times lower, which corresponds to 64 to 512 times less

voxels. With $\frac{\omega_b}{\partial x} = 1$, the error is only of a few percent with laminate CV. It also shows that Reuss or Voigt CV models lead to less precise simulation than the model without composite voxels.

Figure 5.8 presents the evolution of the mean strain level in the plastic phase with $\frac{\omega_b}{\partial x}$ (*i.e.* inside the slip bands, the mean computation accounts for both homogeneous plastic voxels as well as plastic phase volume fraction inside CV). Here again, the model with laminate CV converge faster that the other to predict this quantity, and seem to yield a good prediction for $\frac{\omega_b}{\partial x} = 2$.

(a)   (b)
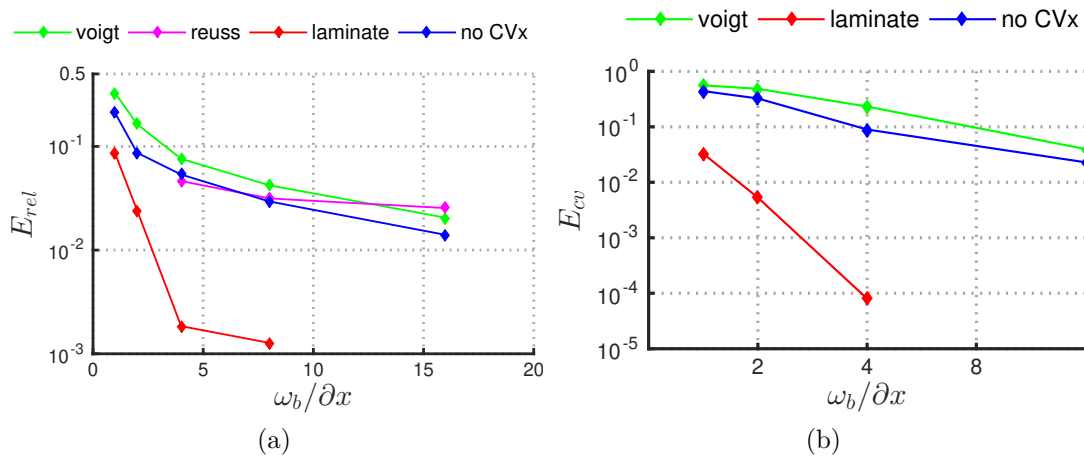
Figure 5.7 – Evolution of the relative error with respect to the converged solution (with laminate composite voxels) with increasing resolution.
(a) $\frac{\omega_b}{d_g} = \frac{1}{10}$, 3 bands per grain in average and (b) $\frac{\omega_b}{d_g} = \frac{1}{50}$, 10 bands per grain in average

These simulations have been carried out with the supercomputer Cobalt (from the Centre de Calcul Recherche et Technologie of CEA) on 1000 cores. The evolution of E_{rel} with computational time is shown on fig. 5.9. It shows that the use of laminate CV allows to reduce the computational time to obtain a precision lower that 1% compared to all other models.

All these results confirm that laminate CV strongly enhance the efficiency of explicit slip band modeling in polycrystalline simulations with FFT based solvers. The gain is even higher when modeling very thin slip bands compared to the grain size, which is of prime interest for the modeling of clear channels in irradiated metals. On the other hand, other CV models, namely Reuss and Voigt CV, deteriorate the solution compared to a modeling without CV.

The observation of the simulated Von Mises equivalent strain fields, shown on fig. 5.10, reveals that when the number of voxels inside slip bands becomes
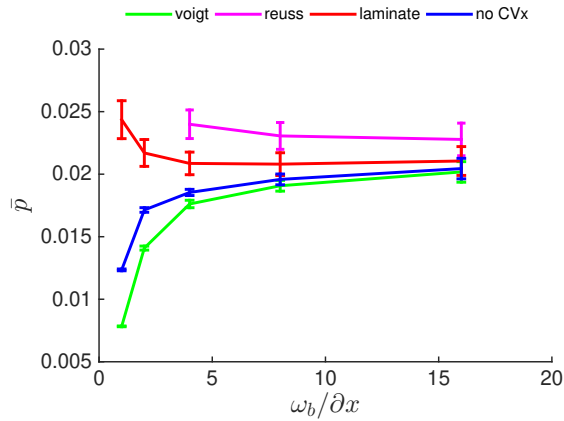
Figure 5.8 – Evolution of the mean cumulated plastic strain in the plastic phase with increasing resolution in the case $\frac{\omega_b}{d_g} = \frac{1}{10}$, 3 bands per grain in average. Error bars represent the standard deviation over the plastic phase (including homogeneous and composite voxels)
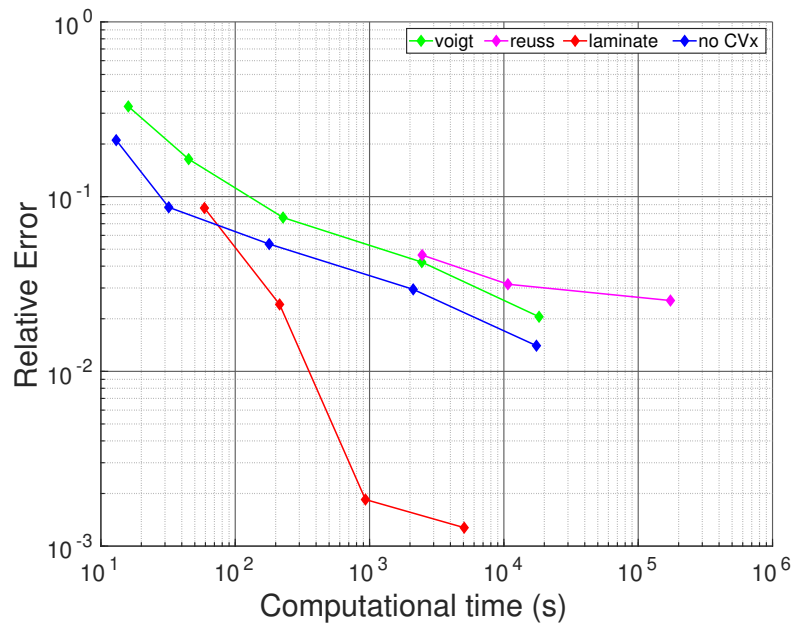
Figure 5.9 – Evolution of the relative error with respect to the converged solution (with laminate composite voxels) in function of the computational time on 1000 cores (2.4 GHz and 4.6 Go RAM per core) on the supercomputer Cobalt. From left to right the points correspond for each curve to the following number of voxels: $30^3, 60^3, 120^3, 240^3, 480^3$. The reference value is the simulation computed with laminate CV with 480^3 voxels, not plotted on the figure. The $30^3, 60^3$ Reuss CV simulations have not converged and are not plotted either.

larger than 4, deformation tends to localize on the band boundaries, which is not consistent with physical slip bands that have a rather homogeneous aspect along their width (see section 2.1.2). This artifact is most likely due to the plastic instability predicted by Asaro and Rice's bifurcation analysis (Asaro and Rice (1977)) for a perfectly plastic behavior inducing the formation of slip bands inside the explicitly modeled potential slip bands. This issue could be precluded in this case by using a small hardening modulus in the constitutive modeling. Fortunately, as shown above, laminate CV allow to obtain an accurate global solution for $1 \leq \frac{\omega_b}{\partial x} \leq 4$ as well as smooth deformation fields inside the bands, even for very thin slip bands, as shown on figure (d).

(a) $\frac{\omega_b}{\partial x} = 4$ (b) $\frac{\omega_b}{\partial x} = 8$ (c) $\frac{\omega_b}{\partial x} = 16$

(d) $\frac{\omega_b}{\partial x} = 4$
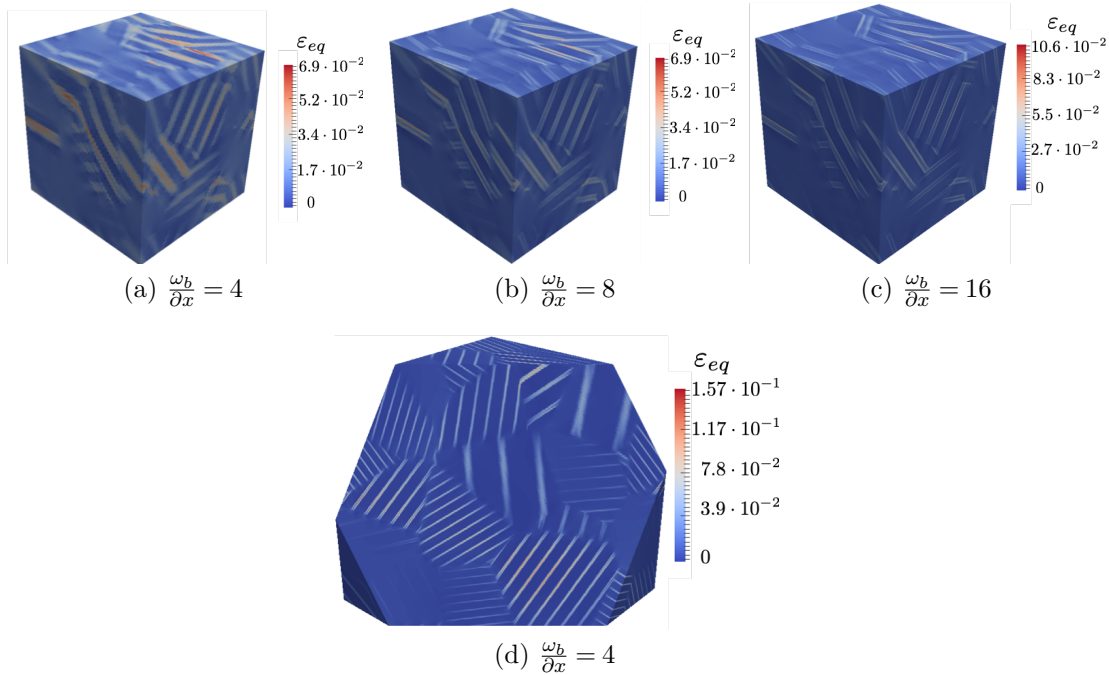
Figure 5.10 – (a-c) Equivalent strain fields for the 27 grains polycrystalline unit cell with 3 potential slip bands ($\frac{\omega_b}{d_g} = \frac{1}{10}$) per grain in average with laminate CV. (d) Internal view of an equivalent strain field for the unit cell with 10 potential slip bands ($\frac{\omega_b}{d_g} = \frac{1}{50}$) per grain in average with laminate CV.

5.4 Application: simplified modeling of slip localization in textured irradiated Zirconium

      The results of the last section have shown that the efficient implementation of AMITEX_FFTP coupled with the use of laminate CV allows to achieve accurate simulations of three-dimensional polycrystal models accounting for explicit potential slip bands, with a width that can be as small as two orders of magnitude lower than the considered grain size. Hence, this framework allows the explicit modeling of clear channels in irradiated metals in realistic polycrystalline simulations.

   As a first step towards this direction, we propose in this section a simplified modeling of textured irradiated Zr alloys used for cladding tubes in the nuclear industry. In particular, we study the ability of this modeling approach to reproduce the increased Bauschinger effect observed in irradiated Zr by Wisner, Reynolds, and Adamson (1994), and attributed by Luft (1991) and Onimus and Bechade (2009) to the strain incompatibilities generated by clear channels formation. Moreover, we study the predicted evolution of the grain boundary normal stress distribution with increasing slip localization. If this question is not really relevant for Zr alloys, these quantities are thought to be a good indicator to build an intergranular crack initiation criterion for the prediction of IASCC observed in irradiated stainless steels (Hure et al. (2016)).

5.4.1 Simplified modeling of irradiated textured Zr

Crystallographic Texture

      The texture of cold-rolled recrystallized Zr alloys used for cladding tubes has been studied experimentally by Pawlik (1986) and consists in a majority of grains having their <c> axis at an angle ±30° of the radial direction of the tubes, in the plane defined by the radial direction and the transverse direction (TD). This plane is orthogonal to the rolling direction (RD).

      From these results, a representative orientation distribution density function has been built and used to generate a file of 1×10^5 grain orientations that is representative of the texture (Onimus and L. Gélébart (2018)). In order to generate a representative polycrystalline unit cells of this material, a random set of orientations is drawn from this file.

      To ensure that this set of orientations is a good approximation of the reference 1×10^5 grains texture, the Kearns anisotropy factor is used. It is defined as the resolved volume fraction of <a> or <c> poles in a specific direction of the

sample (Fong (2013); Kearns (1965)). For a given direction $\boldsymbol{d}$, denoting by θ_i the angle between the $<c>$ axis of each grain with $\boldsymbol{d}$, the Kearns factor K_d of $<c>$ axis in direction $\boldsymbol{d}$ is given by:

$$K_d = \sum_i f_i \cos^2(\theta_i) \tag{5.30}$$

where the f_i are the volume fraction of each grain with respect to the aggregate.

For each orientation set drawn from the reference file, the Kearns factors for all directions of the cartesian basis $\boldsymbol{e}_1, \boldsymbol{e}_2, \boldsymbol{e}_3$ for the $<c>$ axis are computed, and compared to the factors of the 1×10^5 grains texture. If the relative distance in quadratic norm of the vectors containing the 3 factors is higher than 0.1%, the orientation set is rejected and a new one is drawn. This procedure allows to have small orientation sets that are more representative of the anisotropy of the considered material, as shown on fig. 5.11.
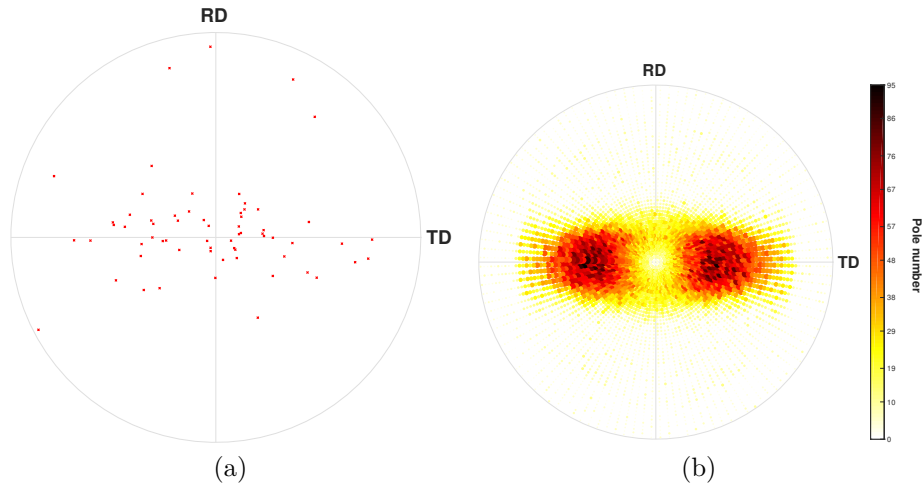
Figure 5.11 – $<c>$ Pole figure obtained for a random 64 grains texture (a) with equivalent Kearns factors than the reference texture for 100000 grains (b). TD: transverse direction, RD: rolling direction

Unit cell: explicit modeling of potential slip bands

As shown by observations (T. Onchi, Kanayo, and Y. Higashiguchi (1977); Onimus, J. L. Béchade, and Gilbon (2012); Onimus, Monnet, et al. (2004)), irradiated Zr alloys strained along the TD mainly deform through basal channeling. Thus, as a first approximation, we model in the following only basal slip systems. As a result, only one family of potential slip bands is prescribed in each grain,

following the method presented in section 5.3.

Two types of potential slip band patterns are generated within a 64 grains polycrystalline aggregate with a representative texture. First, a set of pattern with a fixed potential slip band volume fraction (20%) and varying number of bands is generated. When reducing the number of slip bands per grain, band width rises as well as band spacing. This set of patterns allows to isolate the effect of the repartition of the slip bands constituting the plastic phase from the effect of a varying plastic phase volume fraction, and thus evidences the pure effect of slip localization. A second set of patterns is generated with an increasing number of bands of fixed width, $\frac{\omega_b}{d_g} = \frac{1}{100}$, which is the typical order of the ratio between grain size ($\sim5\,\mu\text{m}$ to $10\,\mu\text{m}$) and clear channel width ($\sim40\,\text{nm}$ to $100\,\text{nm}$) observed in irradiated Zr alloys. A few examples are shown on fig. 5.12.

Grid resolution is set to 100^3 voxels per grain in average, in order to stay above the convergence limit of laminate CV that is $\frac{\omega_b}{\partial x} = 1$. Thus all simulations presented below involve 64 millions voxels.

(a) 3 bands per grain						(b) 15 bands per grain

(c) 3 bands per grain						(d) 20 bands per grain
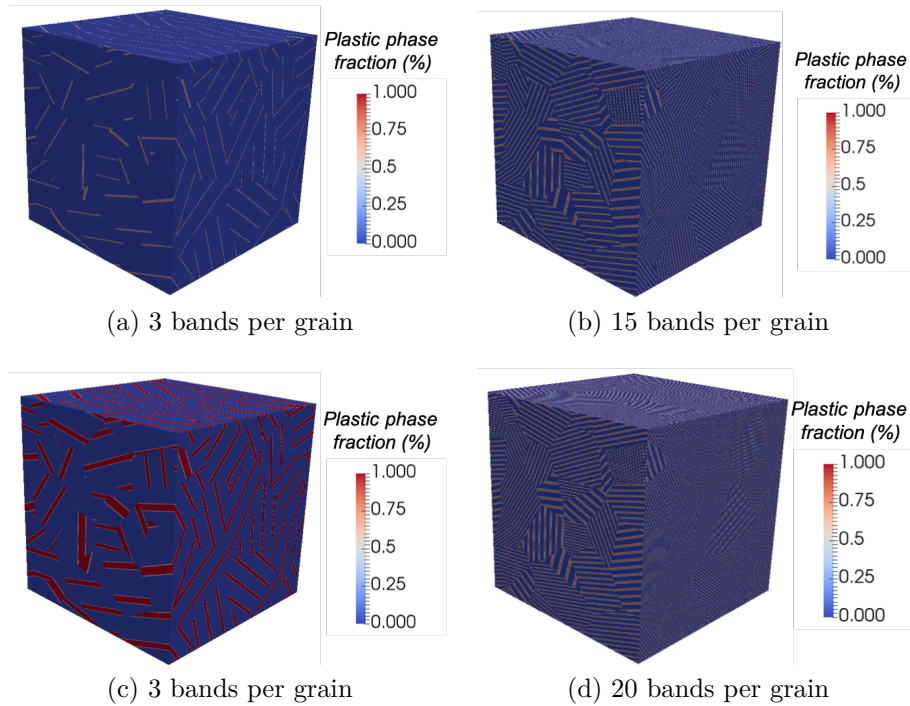
Figure 5.12 – 64 grains polycrystalline unit cells ($400^3 = 64$ million voxels) with potential basal slip bands with Zr cladding tubes texture.
(a-b): thin bands (width of the order of basal clear channel width: $\frac{\omega_b}{d_g} = \frac{1}{100}$),
(c-d): band volume fraction of 20% with varying number of bands N_b ($\omega_b = \frac{0.2}{N_b}$).

Material behavior

The constitutive modeling is identical to the one presented in section 5.3 (eqs. (5.23) to (5.27)). The chosen critical shear stress is the typical value of unirradiated Zr basal slip systems: $\tau_c = 80\,$MPa (after Onimus and Bechade (2009)), which amounts to considering potential slip bands as clear channels completely depleted from irradiation induced defects. Hence, this model cannot capture the irradiation induced hardening, and can only simulate the influence of geometrical characteristics of clear channels on the mechanical behavior after the annihilation of all irradiation induced defects.

As elasticity could have an influence on the long range stresses induced by clear channels responsible for the strong Bauschinger effect observed in irradiated Zr alloys, the complete anisotropic hexagonal elasticity tensor of Zr alloys (Onimus and L. Gélébart (2018)) is modeled. It is defined by the following elastic moduli:

- $E_a = 70\,028\,$MPa is the Young modulus along direction <a>

- $E_c = 110\,354\,$MPa is the Young modulus along direction <c>

- $G_a = 22\,900\,$MPa is the shear modulus in basal plane

- $G_{ac} = 27\,000\,$MPa is the shear modulus in (<a>,<c>) planes

- $\nu_a = 0.203$ is the Poisson coefficient in basal plane

- $\nu_{ac} = 0.529$ is the Poisson coefficient in (<a>,<c>) planes

5.4.2   Slip localization induced kinematic hardening

The model presented above is simulated for tension-compression loading along the TD, to study the evolution of hardening with the geometrical characteristics of the potential slip band patterns. As the plastic behavior is perfectly plastic, only kinematic hardening due to strain incompatibilities that must be elastically accommodated is expected. This is confirmed by fig. 5.13-(a), which displays the stress-strain curve for one of these simulations with 3 cycles of increasing amplitude. It shows that the cycles are perfectly superimposed, and that the elastic domain remains of the same size for the three amplitudes. Figure (b) shows that the superior and inferior parts (*i.e.* the loading and unloading parts) of the cycles are perfectly symmetric.

The yield points are found by detecting the first point in the elastic domains where the slope of the curve deviate of more than 5% from the Young
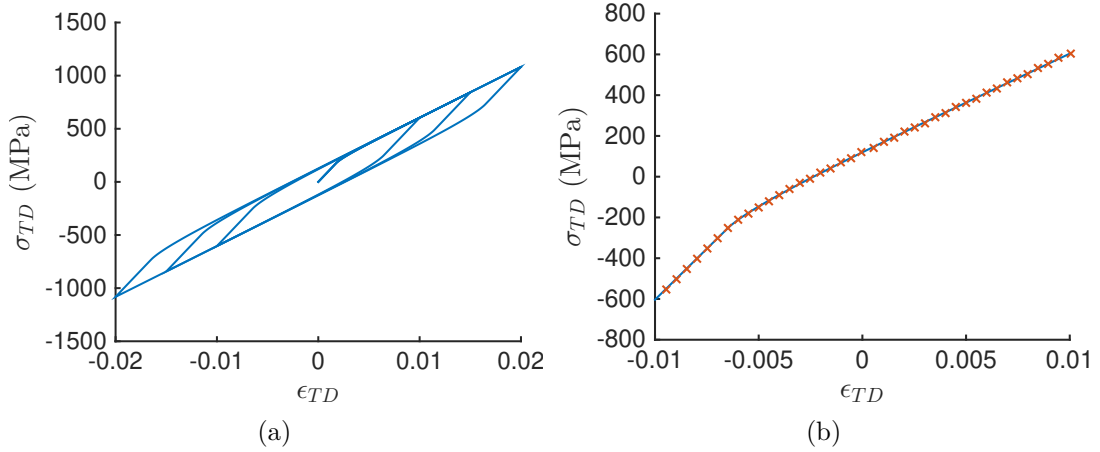
Figure 5.13 – (a): Stress-strain curve for three tension-compression cycles to $\pm 1\%$, $\pm 2\%$ and $\pm 3\%$ strain in transverse direction (TD), for a 64 grains textured polycrystal with 3 potential slip bands per grain ($\frac{\omega_b}{d_g} = \frac{1}{100}$, $400^3 = 64$ million voxels). (b) Superimposition of the first compression and tension branches of (a) after a mirror symmetry.

modulus in TD. This allows to compute the yield stress, and the size of the elastic domain in the unloading phase, from which are computed the linear R and kinematic X part of hardening. The evolution of these quantities is studied for loading-unloading tensile test up to 1% strain in TD, with different potential slip band patterns, and for a 100% polycrystal, for which the plastic behavior is affected to all voxels.

Results are shown in fig. 5.14 for the set of pattern with a varying number of bands of fixed width ($\frac{\omega_b}{d_g} = \frac{1}{100}$). They confirm that no isotropic hardening is predicted by this modeling approach. It predicts a strong increase in kinematic hardening when the number of bands is decreasing. The results obtained with 20 potential slip bands per grain in average are rather close to the 100% plastic polycrystal (*i.e.* homogeneous plastic grains). On the other hand, 3 potential slip bands per grain in average, which is close to the average number of clear channels observed in irradiated Zr alloys (Onimus, Monnet, et al. (2004)), the hardening is ~60% higher than for the 100% plastic polycrystal. Note that even the case of the 100% plastic polycrystal predicts a strong kinematic hardening.

Figure 5.14 present similar results for the set of pattern with a fixed potential slip bands volume fraction (20%) and varying number of bands. Again, the kinematic hardening increases when decreasing bands number (*i.e.* increasing band spacing), although the increase is lower than in the case of fig. 5.14. This is
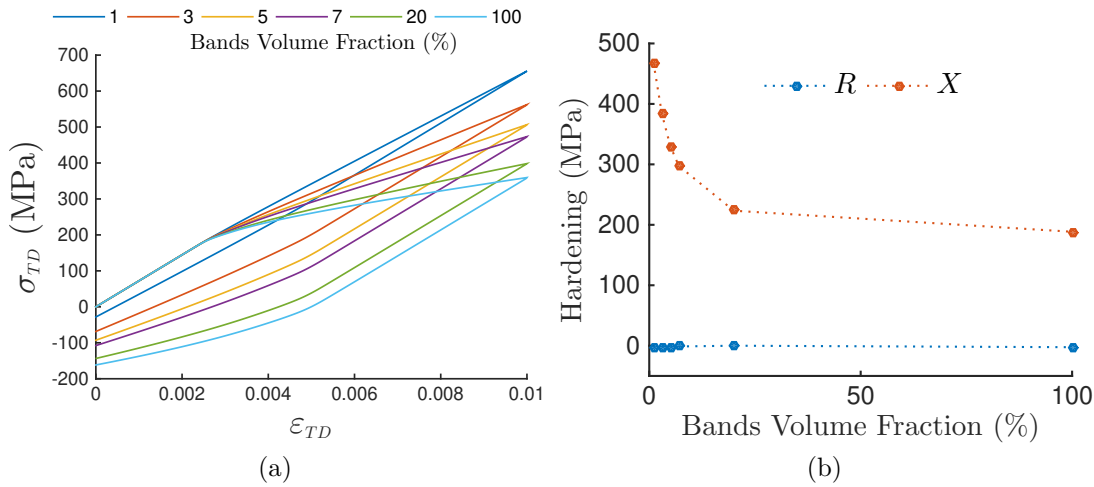
Figure 5.14 – (a): Stress-strain curve for a loading-unloading tensile test ($\pm$ 1% strain in TD) and evolution of Kinematic and Linear hardening values (b) for various band volume fractions with fixed band width: $\frac{\omega_b}{d_g} = \frac{1}{100}$.

easily explained by the fact that for the same band number, this set of patterns has a higher band volume fraction (20%), resulting in a softer behavior. However, this result shows that even with the same volume fraction of plastic phase, the geometrical characteristics of the slip band pattern has still a strong influence on kinematic hardening.
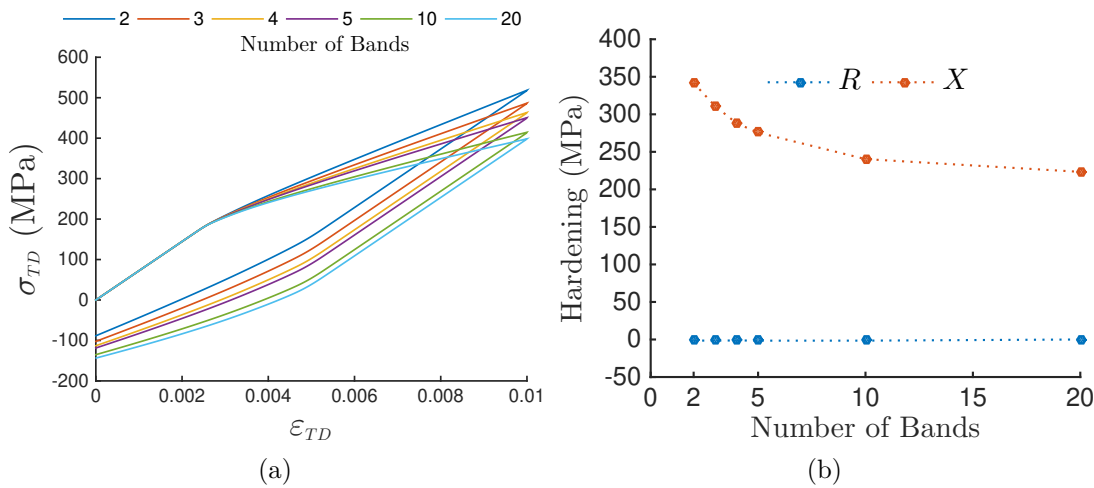
Figure 5.15 – (a): Stress-strain curve for a loading-unloading tensile test (1% strain in TD) and evolution of Kinematic and Linear hardening values (b) for various number of bands with fixed volume fraction $f_b = 0.2$.

In conclusion, this modeling approach predicts a strong increase of kinematic hardening for increased slip localization, understood as the increase of slip band spacing, which is qualitatively consistent with the stronger Bauschinger effect observed on irradiated textured Zr alloys than for non irradiated ones.

5.4.3   Evolution of grain boundary normal stresses with slip localization

The stress fields computed at 1% tensile strain with the previously described simulations have been processed in order to compute the grain boundary normal stress distribution. The Voronoi tessellation used to generate the polycrystalline unit cell provides the exact definition of the planes forming the grain facets: their position and their normal vector $\mathbf{N}_i$. From this information, grain boundary voxels lying on each facet can be detected, and the grain boundary normal stress is evaluated by computing $\mathbf{N}_i \cdot \underline{\boldsymbol{\sigma}} \cdot \mathbf{N}_i$. In addition, $\underline{\boldsymbol{\sigma}}_{95\%}$, the 95th grain boundary normal stress percentile is computed from the distribution, as the upper tail is the relevant part of the curve used to build intergranular cracking criterions (Hure et al. (2016)).

Figure 5.16 shows the evolution of the grain boundary normal stress distribution and $\underline{\boldsymbol{\sigma}}_{95\%}$ for the set of pattern with a varying number of bands of fixed width representative of clear channel width ($\frac{\omega_b}{d_g} = \frac{1}{100}$). It reveals (a) that when increasing slip localization, the grain boundary normal stress distribution becomes less symmetric and spreads towards the high tensile stress values. This is confirmed by the evolution of $\underline{\boldsymbol{\sigma}}_{95\%}$ (b), that increases when reducing the number of bands. The distributions are relatively close and smooth in the cases with 3,5,7 and 20 bands per grain (3,5,7 and 20% bands volume fraction), whereas the single band per grain case is associated to a more irregular distribution, showing a significantly higher occurrence of high traction stress on grain boundaries. On the contrary, the distribution for homogeneous plastic grains is the smoothest and shows a significantly lower occurence of high traction stress on grain boundaries.

Figure 5.17 shows the evolution of the grain boundary normal stress distribution and $\underline{\boldsymbol{\sigma}}_{95\%}$ for the set of pattern with a fixed potential slip band volume fraction (20%) and varying number of bands. It showis a similar evolution to the previously studied set of patterns. Note that the results indicated by the 20% plastic phase case for the first set of band patterns and the 20 bands per grain case in the second correspond to the same simulation. In Figure 5.16-(a), and in Figure 5.17-(b), the curves corresponding to 3 to 10 bands per grain are rather close to the distribution corresponding to 20 bands per grain, and show similar evolution with number of bands. This demonstrates, surprisingly, that the results
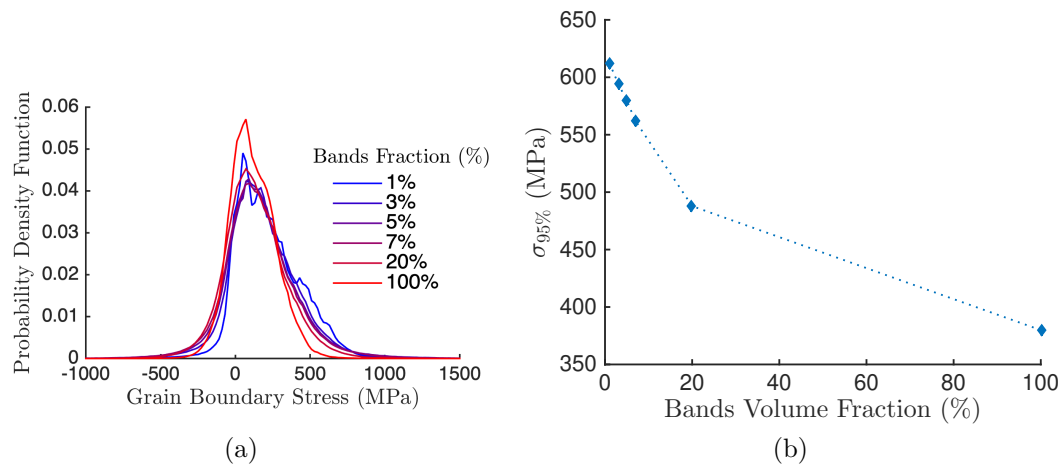
Figure 5.16 – Grain boundary stress distribution at 1% tensile strain in TD (a) and evolution of its 95th percentile (b) for various band volume fractions with fixed band width: $\frac{\omega_b}{d_g} = \frac{1}{100}$.
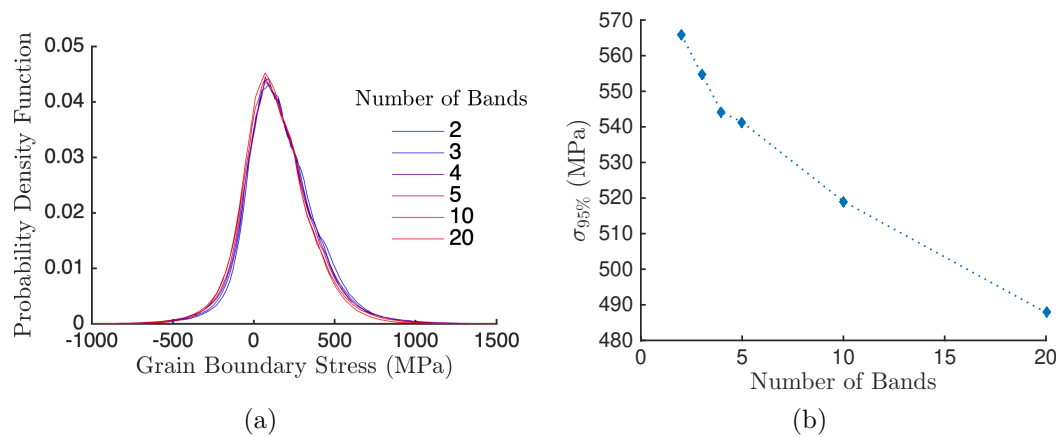
Figure 5.17 – Grain boundary stress distribution at 1% tensile strain in TD (a) and evolution of its 95th percentile (b) for various number of bands with fixed volume fraction $f_b = 0.2$.

obtained for the second set of patterns are very similar to the first for a similar number of bands.

$$\frac{\omega_b}{d_g} = \frac{1}{100}, \ N_b = 1 \qquad \frac{\omega_b}{d_g} = \frac{1}{100}, \ N_b = 7 \qquad \frac{\omega_b}{d_g} = \frac{1}{100}, \ N_b = 20$$

$$f_b = 20\%, \ N_b = 2 \qquad f_b = 20\%, \ N_b = 4 \qquad f_b = 20\%, \ N_b = 10$$
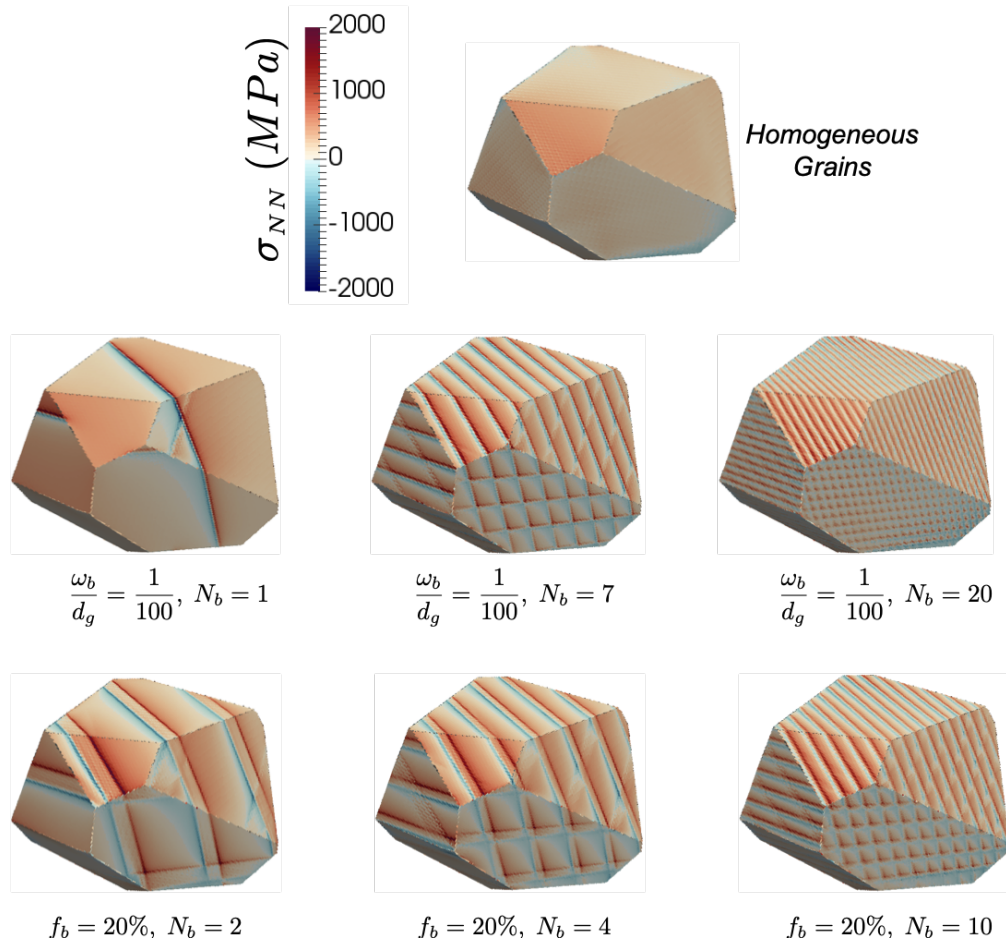
Figure 5.18 – Grain boundary normal stress fields on a grain in the polycrystal, for various band width ω_b and number of bands N_b. (in all cases: $\frac{d_g}{\partial x} = \frac{1}{100}$ *i.e.* 64 millions voxels)

Figures 5.18 and 5.19 presents the associated normal stress fields on the surface of two grains of the polycrystalline microstructure, for various cases from the two sets of patterns. Clear stress concentration corresponding at slip band tips can be observed in all cases, except for the homogeneous grains case, which is not surprising. In both grains, normal stress concentrations are stronger when the degree of localization is higher (*i.e.* with a lower number of bands), which is consistent with the results presented on figs. 5.16 and 5.17.

The fields obtained in the case of a single band per grain show that stress concentrations are very high on some facets of the grain, whereas none are found
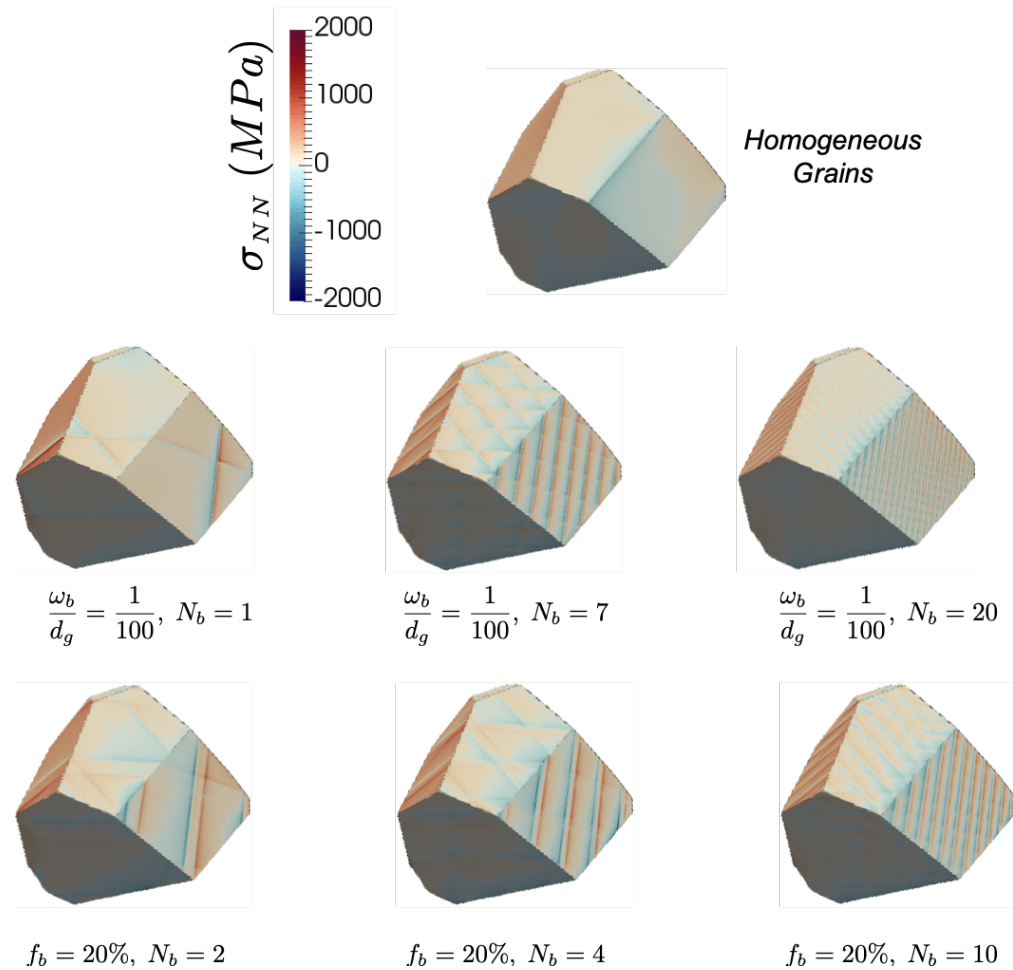
Figure 5.19 – Grain boundary normal stress fields on a grain in the polycrystal, for various band width ω_b and number of bands N_b. (in all cases: $\frac{d_g}{\partial x} = \frac{1}{100}$ $i.e.$ 64 millions voxels)

for other facets, meaning that no slip bands intersects them. This explains the irregular aspect of the associated distribution, shown on fig. 5.16-(a). Besides, very smooth fields with no stress concentrations are observed on the grain facets in the homogeneous grain case, explaining the smooth aspect of the associated distribution as well as its low value for high stresses.

These fields also explain why normal stress distributions are close for the two bands patterns. Indeed, they show that the cases with 20% bands volume fraction and a low number of bands are associated to similar normal stress concentrations in terms of value and width.

These simulations highlight the ability of this modeling approach to predict increased stress concentrations on grain boundaries induced by slip localization. They have required 1 to 6 hours of calculation for each on the Cobalt supercomputer with 4000 cores. Note that when using more usual computational ressources the computational time on 100-200 cores would have been comprised between one and five days, which remains reasonable. Overall, this demonstrates that a parallel implementation is mandatory to achieve such simulations.

5.4.4　Discussion

Kink band free simulations ?

One goal of this modeling approach was to suppress the "slip band like" kink bands predicted by CCP. Indeed, they appear on fig. 5.20-(c) where the Von Mises strain field obtained for homogeneous grains show intense kink bands in the areas circled in red. As expected, when prescribing a low number of bands per grain, the material deforms mostly through intense slip banding, as illustrated on fig. 5.20-(a), and those area undergo no significant deformation. However, when increasing the number of bands to 20 potential bands per grain, the slip bands are more intense inside these areas, tending to reform the deformation paths leading to kink formation in the homogeneous grains case. As in the previous chapter, this shows that the kink bands that are required by strong structure effects can be formed through a dense succession of slip bands. This should encourage the extension of this modeling framework to finite strain in order to study if these areas also exhibit lattice rotation.

Overall, these results suggest that kink bands cannot form when only a few distant slip planes can be activated within the grains. This is the case in irradiated metals because of the dislocation channeling mechanism, inducing the formation of one or a few intense slip bands (the clear channels) in plastically deformed grains, and where no kink bands are observed. Hence, this modeling

framework, when accounting for a low number of potential slip bands per grain (≤ 10) appears well adapted to the modeling of irradiated metals.

(a) 3 bands per grain

(b) 20 bands per grain

(c) Homogeneous grains
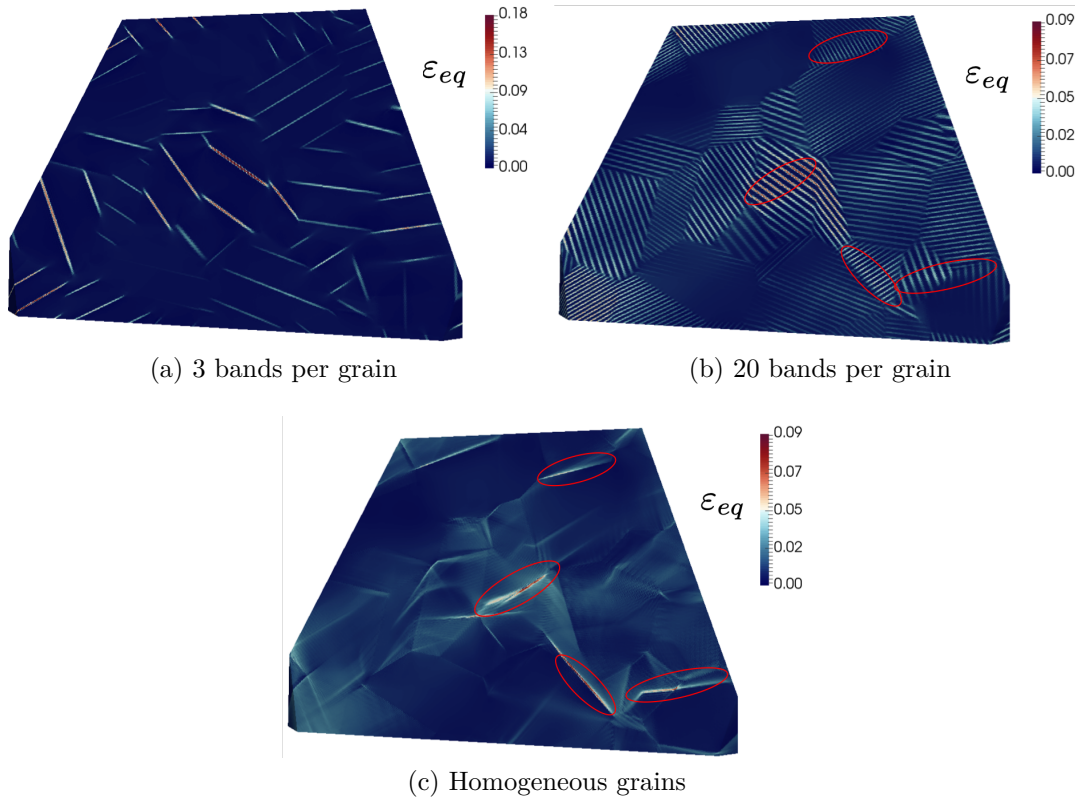
Figure 5.20 – Internal section of equivalent stress fields at 1% tensile strain in TD for various number of bands with with fixed band width: $\frac{\omega_b}{d_g} = \frac{1}{100}$ (a-b) and for homogenous plastic grains (c) (64 millions voxels)

Slip localization induced kinematic hardening

As evidenced by these results, accounting explicitly for localized slip has a very strong impact on the simulated behavior of a polycrystalline unit cells. In fact, it predicts a strong Bauschinger effect when prescribing a low number of potential slip bands per grain. As illustrated by fig. 5.21, this effect is due to both the reduction of the plastic phase volume fraction and stress concentrations. Indeed, it is clear on the Von-Mises stress field (a) of the case with 3 thin bands per grain ($\frac{\omega_b}{d_g} = \frac{1}{100}$) that the mean level of strain in each grain is higher than when using 20 bands per grain (b) or homogeneous grains (c), which is due to a higher mean level of elastic strain, induced by the lower plastic phase volume fraction. Besides, the

same field (a) show strong stress concentrations at band tips which can extend rather far in the bulk of the grains for some of them. This shows that localized slip can induce long range stress concentrations at grain boundaries participating in the increase of the observed Bauschinger effect.

Figure 5.21-(d-f) show the Von Mises strain and stress fields of the case with 20 potential slip bands per grain ($\frac{\omega_b}{d_g} = \frac{1}{100}$). An interesting phenomenon can be observed in the areas circled in purple: they show significant slip transmission at three grain boundaries on the strain field (d), which are not associated with significant stress concentration on the stress field (f), whereas the grain boundaries without slip transmission exhibit stress concentrations. This phenomenon should reduce strain incompatibilities and thus mitigate kinematic hardening, and could explain while kinematic hardening predicted in the 20 potential bands per grain case is close to the homogeneous grain cases. This could be an effect of the specific texture used here, which favors the occurence of similarly oriented slip planes in neighboring grains.

Moreover, when compared to homogeneous grain simulations, this strong localization induced effect on the stress-strain curve is obtained without any changes of the material parameters describing the behavior of the plastic phase (this even without changing its volume fraction). This implies that, when using the same constitutive behavior at the voxel scale and for the same macroscopic stress-strain curve, model identification would yield largely different material coefficients than for simulations with homogeneous grains. For instance, reproducing the high Bauschinger effect that our perfectly plastic model predicted for low number of bands would require to add a strong additional kinematic hardening term in homogeneous grain simulations, to phenomenologically account for strain incompatibilities induced by slip localization. However, this would come with a locally hardening behavior and thus produce no slip localization. On the contrary, explicit slip band modeling allows to directly account for these structure effects, and needs only local hardening/softening mechanisms to be accounted for by local constitutive relations.

Grain boundary normal stress concentrations

As mentioned in section 5.4.3, the normal stress distribution on grain boundaries are similar (figs. 5.16 and 5.17), as well as the stress concentrations on grain facets (figs. 5.18 and 5.19) when using the same number of bands for the two set of patterns. Yet, this result is surprising as they correspond to a different band width: broader bands should induce more diffuse and less intense stress concentrations. This is most likely an artefact of this modeling approach,

(a) 3 bands per grain

(b) 20 bands per grain

(c) Homogeneous grains

(d) 20 bands per grain
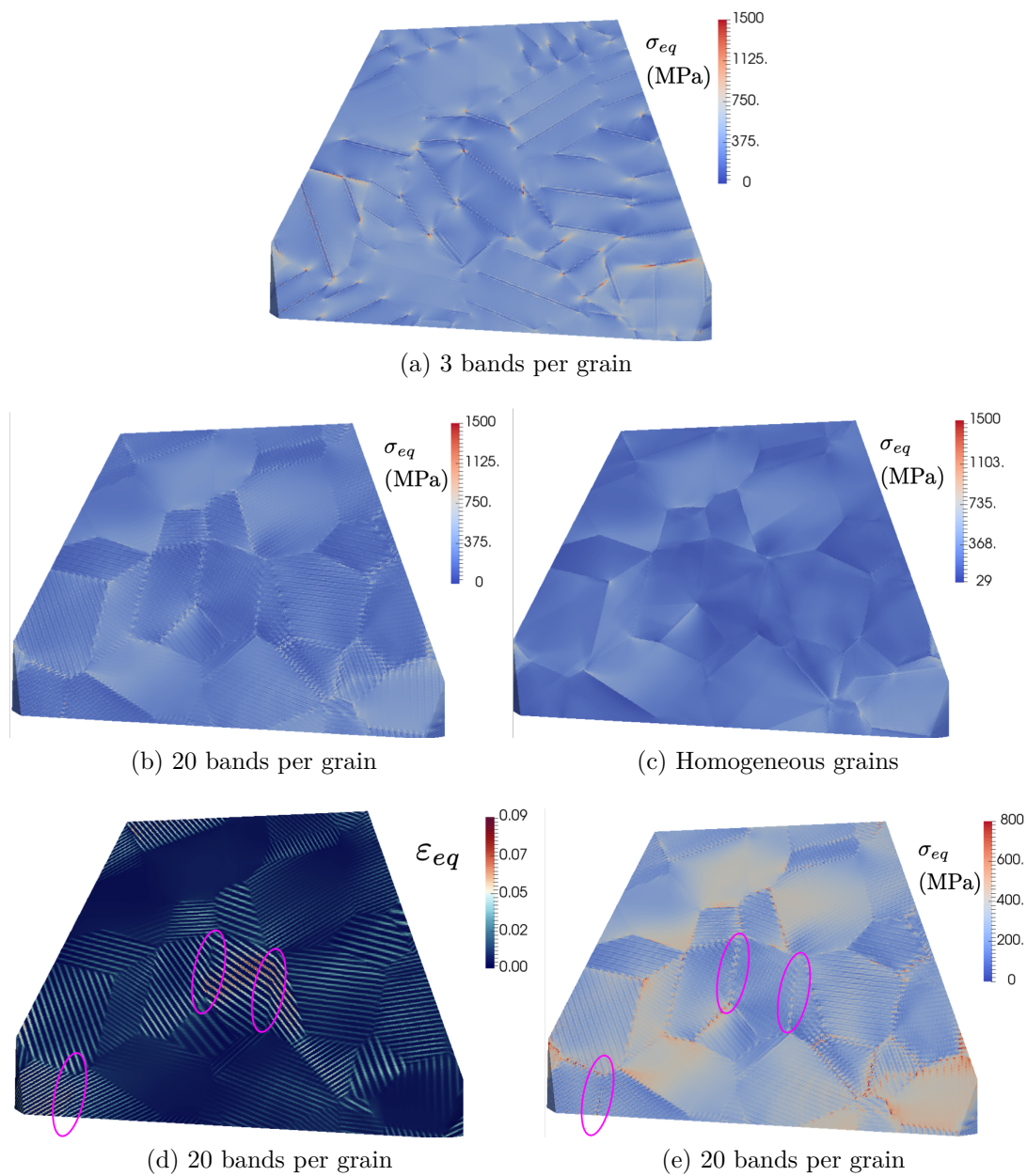
(e) 20 bands per grain

Figure 5.21 – Internal section of equivalent stress fields (a-c) at 1% tensile strain in TD for two different number of bands per grain, and homogenous plastic grains. (d-e) strain and stress fields for the 20 bands per grain case. $\frac{\omega_b}{d_g} = \frac{1}{100}$ (64 millions voxels)

linked to the issue presented in fig. 5.10: when modeling thick bands, because of the instability of perfect plasticity, slip localizes in two intense slip bands of approximately one voxel width (with $\frac{\partial x}{d_g} = \frac{1}{100}$) located on each boundary of the band. As a result, these simulations have thinner localization bands that the one geometrically prescribed, which explain why they induce similar normal stress concentrations as the simulation where very thin bands are prescribed ($\frac{\omega_b}{d_g} = \frac{1}{100}$). This phenomenon is indeed observed on our simulations for the set of pattern with fixed bands volume fraction (20%), for low number of bands (*i.e.* broader bands), as shown on fig. 5.22.
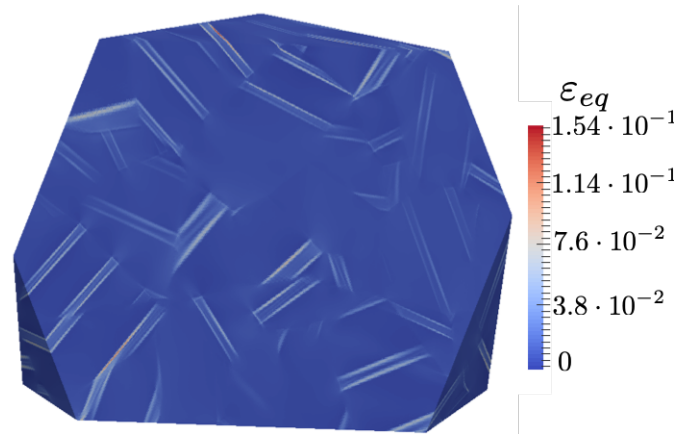
Figure 5.22 – Internal section of equivalent strain field at 1% tensile strain in TD for a 20% bands volume fraction and 2 bands per grain: $\frac{\omega_b}{d_g} = \frac{1}{10}$ (64 millions voxels)

Representativity of the results

Finally, it must be mentioned that the results presented here have been obtained for only one aggregate and one texture. Although they provide an interesting qualitative insight into the possibilities opened by this modeling approach, they are certainly not statistically representative of the behavior of our model material. Assessing this representativity should be mandatory for future studies aiming at obtaining quantitatively representative results.

5.5 Conclusions and future prospects

Generic composite voxel models have been implemented in the solver AMITEX_FFTP, and fully integrated to its parallel implementation and user

interface. These developments allow to considerably improve the performance of the solver for the simulation of complex microstructures with many interfaces, such as composite materials charged with inclusion or fibers (Charière, Marano, and Gélébart (2020)). They also provide a basis for the extension of composite voxel models implemented in AMITEX_FFTP to the finite strain framework, which is one of the future prosects of the present work.

We have shown that laminate composite voxels allows to enhance the performance of explicit slip band modeling in polycrystalline simulations. The problem size required to obtain a well converged solution is reduced by a factor of 64 to 512 for three dimensional simulations.This enabled us to apply this modeling approach to more realistic three-dimensional polycrystalline unit cells than previous attempts, and use very high resolutions with tens of million elements to precisely describe slip bands for width as low as two order of magnitude than the average grain size. In future works, this approach should be extended to slip band patterns including more than one slip plane family per grain, which raises some difficulties in the determination of composite voxels and associated volume fractions. In particular laminate CV cannot be properly defined at the intersection of two bands, and new choices must be explored in this case.

Finally, we have shown that this approach can be used to simulate some consequences of basal channeling in irradiated textured Zr alloys. The increased localized slip induced by irradiation is explicitly accounted for by increasing slip band spacing, resulting in a higher global kinematic hardening of the polycrystalline unit cell, and the increase of grain boundary stress concentrations. The efficient explicit slip band modeling with laminate CV allowed to consider slip bands 100 time thiner than the the average grain size, which is the relevant size for clear channels in irradiated Zr alloys. These high resolution simulations results could not have been obtained without an efficient parallel implementation provided by AMITEX_FFTP.

However, this work is still a proof of concept and the crude modeling of irradiated Zr alloys only provides a qualitative insight of the interest of this modeling approach. To obtain quantitative predictions of the local and overall behavior of such materials within this framework, many improvements should be introduced in this process. To name a few: the other slip systems should be accounted for by prismatic and possibly pyramidal families of slip bands, or the 12 FCC slip systems to model austenitic stainless steels, a realistic physics-based model of the plasticity of irradiated metals should be used in the plastic phase, the modeling could be extended to the finite strain framework and statistically representative aggregates should be simulated.

CHAPTER 6

CONCLUSIONS AND PERSPECTIVES

The present thesis has been dedicated to improving the numerical modeling of intragranular strain localization phenomena in irradiated polycrystals, as well as to adapt it to the rapid developments of high-performance material simulation, driven by the constant increase of the available computing power in research laboratories. In this context, one goal of this work was to carry out the required numerical developments in the efficient framework of FFT-based solvers, more specifically in the AMITEX_FFTP solver, whose massively parallel implementation and generic formulation allow to get the best out of sophisticated non-linear material behavior models and modern supercomputer facilities.

The problem of slip localization in irradiated metals has been replaced in the general context of intragranular slip localization in polycrystals, throughout the bibliographic review. It has emerged from it that, the enhanced plastic slip localization observed in irradiated metals appears as an extreme case magnifying the intrinsically localized nature of plastic slip. As a result, it has to be considered in the light of the two intragranular single slip localization modes: the slip bands and the kink bands. It has been concluded that the clear bands, that are the signature of slip localization in irradiated metals, are extremely intense slip bands, and should be modeled as such. However, this fundamental aspect for clear bands modeling has been overlooked in previous works. Yet, as slip and kink bands are very different localization modes, assessing the nature of the predicted intragranular localization modes is fundamental and has been the first focus of this work.

The investigation of this question led us to develop original field processing techniques allowing to evidence and quantitatively study the slip and kink band

243

populations within crystal plasticity simulations. Thanks to our efficient parallel implementation, they could be applied on high resolution polycrystalline simulations realized with a generic classical crystal plasticity model, that helped us to uncover a fundamental shortcoming of classical crystal plasticity regarding intragranular localization modes prediction. Indeed, our results have extended the prediction of a bifurcation analysis conducted 40 years ago by Asaro and Rice on uniform crystals, showing that slip and kink modes are completely equivalent at the bifurcation point in the context of softening crystal plasticity polycrystalline simulations. Hence, they systematically predict slip and kink bands with similar characteristics and in comparable amounts, which fundamentally precludes them to accurately simulate clear band formation in irradiated metals. As all existing irradiated metal models are formulated within this framework, this brought us to explore a more physically consistent framework to overcome this issue.

Building on the fact that the principal difference between slip and kink bands is the strong lattice curvature induced by the latter, we have explored the potential of a strain gradient plasticity model accounting for an energy contribution of geometrically necessary dislocations density for slip and kink banding prediction. To accomplish this, the implementation of AMITEX_FFTP has been extended to solve additional field equations coupled with the classical continuum mechanics periodic homogenization problem, while maintaining its highly parallel and generic formulation.

Thanks to these developments, we implemented the strain gradient plasticity model in the framework of FFT-based methods. Our work brought out a more consistent way to compute the differential operators involved in the model to avoid the unwanted numerical regularization of slip bands by spurious gradient effects, which is mandatory to accurately simulate intragranular slip localization. Additionally, we proposed a novel way to implement the classical higher order grain boundary conditions, that have proved to be less grid dependent than those proposed in the literature. This efficient implementation provides a solid basis to focus in the future on the formulation and implementation of more sophisticated grain boundary conditions in the context of FFT-based solvers. To this end, the composite voxel technique could be adapted to formulate specific composite voxel models to enforce these boundary conditions. This would however raise the challenging question of the definition of the derivatives of mechanical fields in the presence of composite voxels. Alternatively, thick grain boundaries with complex behaviors could be modeled as well. Those issues could be of central interest to study within continuum modeling the interaction of clear channels with grain boundaries.

A complete analytical and numerical study of the strain gradient plasticity

model have shown that it allows for a more physically consistent modeling of intragranular slip localization modes than classical crystal plasticity. In particular, we have discovered that it predicts the formation of kink bands as broad rotation bands composed of a dense succession of slip bands, which is strikingly similar to the characteristics of experimentally observed kink bands. We propose the hypothesis that this is linked to a double bifurcation phenomenon, that should be investigated by means of a rigorous bifurcation analysis to clarify this process.

In addition, this model also favors slip banding over kink banding because of the additional energetic cost of kink band formation due to the high geometrically necessary dislocation density that they involve. We have shown that, when accounting for strong gradient effects and high local softening, these two mechanisms allow to simulate localization band networks almost exclusively composed of very intense slip bands in realistic polycrystalline simulations. This is a decisive step towards an accurate modeling of clear channels in irradiated metals. In particular, we demonstrated that this framework can simulate a macroscopical behavior that is equivalent to one simulated with classical crystal plasticity while predicting physically more consistent fields. As this requires to account for a more intense softening, strain gradient plasticity based model will most likely lead to reconsider the value of the coefficients currently used to model dislocation channeling induced softening in current state of the art models for irradiated metals, that are formulated in the classical crystal plasticity framework.

Adapting these models to the strain gradient plasticity framework will be a delicate task. Indeed, we used in the present work a very simple quadratic potential involving only one higher order coefficient, which is most likely not the best suited formulation to match real irradiated materials behavior. Though, the most pressing issue is to fix the mesh dependence of slip bands by introducing a second length scale to regularize them.

In addition, future works will have to develop new model identification procedures that should include criteria ensuring that predicted localization bands are consistent with clear channels observations. The quantitative indicators computed from the field processing techniques developed during this thesis may prove to be helpful in this context. This also raises the question of which experimental data are to be used to identify the value of higher order moduli in irradiated metals? Lattice rotation fields measurements or studies of grain size hardening effects on irradiated metals could be considered to this end, or alternatively, multi-scale approaches relying on lower scales simulations (FDM, DDD or MD) could also provide insights on this matter.

The previously mentioned developments are long-term perspectives considering the amount of work that is still needed to achieve an accurate modeling

of clear channels. In order to propose an alternative way to numerically study slip localization influence on the mechanical behavior of irradiated metals, we enhanced an explicit slip band modeling approach, with the use of the composite voxel technique. This approach ensures that the modeled clear channels will never be kink bands, which is more physically consistent than classical crystal plasticity based approaches. Generic composite voxel models have been implemented in the solver AMITEX_FFTP, while preserving again its highly parallel implementation, resulting in a large increase of its efficiency for the simulation of complex microstructures containing many interfaces. It allowed us to carry out polycrystalline simulations with explicit slip bands of the pertinent dimension for clear channels modeling. We applied this modeling approach to a simple modeling of textured irradiated Zr alloys used for fuel cladding tubes, and showed that it allows to qualitatively account for the strong Bauschinger effect caused by slip localization that has been evidenced in irradiated Zr, as well as increased grain boundary stress concentrations. Once again, these results could not have been obtained without an efficient parallel implementation.

These developments have set the ground for more sophisticated models, accounting for realistic crystal structures, and material behaviors inside the explicitly modeled slip bands, for which no heavy developments of the solver AMITEX_FFTP are needed anymore, to the exception of the extension of composite voxel models to the finite strain framework, that is achievable in a very short-term perspective. These models could provide very interesting insight into the modeling of irradiated metals.

To conclude this thesis, the author hopes that this work will contribute to illustrate the central importance of the study of slip and kink bands formation to improve in general our understanding of crystal plasticity and plastic slip localization phenomenon.

Conclusions et Perspectives en français

La présente thèse a été dédiée à l'amélioration de la simulation numérique du phénomènes de localisation intra-granulaire de la déformation plastique dans les polycristaux irradiés, en s'appuyant sur le développement rapides de la simulation haute performance des matériaux issue de l'augmentation constante de la puissance de calcul disponible dans les laboratoires de recherche. Dans ce contexte, l'un des objectifs de ces travaux était de réaliser les développements numériques nécessaires à l'étude de ce problème physique au sein du solveur AMITEX_FFTP, basé sur les méthodes FFT pour l'homogénéisation périodique des matériaux, dont

l'implémentation massivement parallèle et la formulation générique permettent de tirer le meilleur parti des modèles sophistiqués de comportement non-linéaire des matériaux et des supercalculateurs modernes.

La revue bibliographique a permis de replacer la localisation du glissement plastique observée dans les métaux irradiés dans le contexte plus général de la localisation intra-granulaire du glissement dans les polycristaux. La forte localisation de la déformation plastique observée dans les métaux irradiés y apparaît comme un cas extrême, où de la nature intrinsèquement localisée du glissement plastique est exacerbée. Par conséquent, elle doit être considérée comme relevant des modes de localisation intra-granulaires du glissement (en glissement simple) : les bandes de glissement et les bandes en genou. Cette étude a permis de montrer que les bandes claires, qui sont la signature de la localisation du glissement dans les métaux irradiés, sont des bandes de glissement très intenses, et devraient être modélisées comme telles. Cependant, cet aspect fondamental a été négligé dans les travaux précédents. Or, les bandes de glissement et les bandes en genou étant des modes de localisation très différents, l'analyse des modes de localisation intra-granulaires obtenus dans les simulations est fondamentale et a été le premier objectif de ce travail.

L'étude de cette question nous a amenés à développer des techniques originales de traitement des champs mécaniques, permettant de mettre en évidence et d'étudier quantitativement les populations de bandes de glissements et en genou dans des simulations de plasticité cristalline. Grâce à notre implémentation parallèle, elles ont pu être appliquées à des simulations polycristallines à haute résolution sur des agrégats réalistes. Celles-ci nous ont permis d'étudier un modèle générique de plasticité cristalline classique adoucissant, et de mettre à jour une lacune fondamentale de ce cadre de modélisation vis-à-vis de la prédiction des modes de localisation intra-granulaire du glissement plastique. En effet, nos résultats ont étendu les résultats d'une analyse de bifurcation réalisée il y a 40 ans par Asaro et Rice sur des cristaux homogènes, démontrant que les bandes de glissement et en genou sont deux deux modes de bifurcation strictement équivalents du point de vue des équations de la plasticité cristalline classique. Par conséquent, les simulations polycristallines basées sur ces équations, prédisent systématiquement des bandes de glissement et en genou ayant des caractéristiques similaires et apparaissant en quantités comparables. Cette équivalence de ces deux modes de localisation dans les équations constitue une limite fondamentale de la plasticité cristalline classique, qui rend impossible de simuler fidèlement la formation des bandes de localisation intra-granulaires dans les polycristaux, et à fortiori les bandes claires dans les métaux irradiés. Etant donné que tous les modèles existants pour les métaux irradiés sont formulés dans ce cadre, il est ainsi nécessaire d'explorer un cadre physique plus adapté pour surmonter ce problème.

Partant du fait que la principale différence entre les bandes de glissement et les bandes en genou est la forte courbure du réseau cristallin induite par ces dernières, nous avons exploré le potentiel d'un modèle de plasticité à gradient prenant en compte une contribution purement énergétique du tenseur densité de dislocations, qui est intrinsèquement lié à la courbure de réseau. Pour pouvoir le simuler à l'aide des méthodes FFT, l'implémentation de AMITEX_FFTP a été étendue pour résoudre des problèmes décrits par un nombre arbitraire d'équations de champ couplées au problème d'homogénéisation périodique classique. Ces développements ont été effectués en maintenant la structure massivement parallèle et générique du code.

Nos travaux ont permis de mettre au point une formulation des opérateurs différentiels impliqués dans le modèle plus adaptés, afin d'éviter la régularisation numérique indésirable des bandes de glissement par des effets de gradients parasites, qui est obligatoire pour simuler avec précision la localisation intra-granulaire de glissement. De plus, nous avons proposé une implémentation nouvelle de certaines conditions d'interface aux joints de grains, qui se sont révélées moins dépendantes au maillage que celles proposées dans des travaux précédents.

Une étude analytique et numérique complète du modèle de plasticité du gradient de déformation a montré qu'il permet de capturer les caractéristiques physiques essentielles des modes de localisation intra-granulaires du glissement plastique. En particulier, nous avons découvert qu'il prédit la formation des bandes en genou sous la forme de bandes de rotation de réseau d'une épaisseur fixée par les paramètres du modèle, et formée d'une succession dense de bandes de glissement. Ces caractéristiques sont remarquablement similaires à celles observées expérimentalement sur les bandes en genou.

De plus, au sein de la compétition entre les deux modes de localisation intra-granulaires, ce modèle favorise la formation des bandes de glissement, en raison du coût énergétique supplémentaire de la courbure de réseau induite par la formation des bandes en genou. Nous avons montré que, en présence de forts effets de gradient et d'un adoucissement prononcé, ce modèle permet de simuler des réseaux de bandes presque exclusivement composés de bandes de glissement très intenses. Il s'agit d'une étape décisive vers une modélisation fidèle des bandes claires dans les métaux irradiés. En particulier, nous avons démontré que l'on peut simuler un comportement macroscopique équivalent à celui simulé avec un modèle de plasticité cristalline classique tout en prédisant des champs physiquement plus cohérents. Ces résultats suggèrent que les modèles basés sur la plasticité à gradient conduiront très probablement à reconsidérer la valeur des coefficients actuellement utilisés pour modéliser l'adoucissement induit par la canalisation des dislocations dans les modèles actuels pour les métaux irradiés, formulés dans le cadre classique

de la plasticité cristalline.

L'adaptation de ces modèles au cadre de la plasticité à gradient dans le futur soulève tout de même quelques problèmes. En effet, nous avons utilisé dans le présent travail un potentiel quadratique très simple n'impliquant qu'un seul coefficient supplémentaire, ce qui n'est probablement pas la formulation la mieux adaptée pour décrire le comportement réel des matériaux cristallins. Par ailleurs, il est également nécessaire de corriger la dépendance au maillage des bandes de glissement simulées en introduisant une deuxième longueur caractéristique pour les régulariser. De plus, il sera fondamental d'élaborer de nouvelles procédures d'identification des modèles qui devraient inclure des critères permettant de s'assurer que les bandes de localisation prévues correspondent aux observations de bandes claires réelles, en tenant compte de leur nature et leur caractéristiques physiques. Les indicateurs quantitatifs et techniques de traitement d'image développées au cours de cette thèse pourront s'avérer utiles dans ce contexte.

Néanmoins, les évolutions mentionnées restent des perspectives à long terme compte tenu de la quantité de travail qu'il reste à accomplir pour parvenir à une modélisation représentative. Afin de proposer une méthode alternative, utilisable en l'état pour étudier numériquement l'influence de la localisation du glissement sur le comportement mécanique des métaux irradiés, nous avons optimisé une approche fondée sur la prise en compte explicite des bandes de glissement, en utilisant des modèles de voxel composites. Cette approche garantit que les bandes claires modélisées ne seront jamais des bandes en genou, résolvant ainsi le problème des approches basées sur la plasticité cristalline cristalline seule. Des modèles voxel composites génériques ont été implémentés dans le solveur AMITEX_FFTP, tout en préservant son implémentation parallèle, ce qui a permis d'augmenter considérablement son efficacité pour la simulation de microstructures complexes contenant de nombreuses interfaces. Ceci nous a permis de réaliser des simulations polycristallines en prenant en compte explicitement des réseaux de bandes de glissement potentielles de la dimension pertinente pour la modélisation des bandes claires, tout en maintenant des temps de calculs acceptables. Nos simulations et les temps de calculs associés illustrent bien que sans les performances liées à l'utilisation de voxels composites et d'un code massivement parallèle, ce type de modélisation n'est pas envisageable à l'heure actuelle. Nous avons appliqué cette approche à une modélisation rudimentaire des alliages de Zr texturés irradiés utilisés pour les tubes de gainage de combustible, et montré qu'elle permet de capturer qualitativement l'accroissement de l'effet Bauschinger induit par la localisation de glissement, phénomène ayant été mis en évidence dans le Zr irradié, ainsi que l'accroissement des concentrations de contraintes aux joints de grains avec l'accentuation de la localisation.

Ces développements ouvrent la voie à des modèles plus sophistiqués et plus proches de réels métaux irradiés, en tenant compte de structures cristallines plus représentatives et de lois de comportement à l'intérieur des bandes de glissement modélisées explicitement plus réalistes. En effet, aucune de ces extensions ne nécessitera de développements importants à effectuer au sein du solveur AMI-TEX_FFTP, à l'exception de l'extension des modèles voxel composites au cadre des grandes déformations.

Akarapu, S. and J.P. Hirth (2013). "Dislocation pile-ups in stress gradients revisited". In: *Acta Materialia* 61.10, pp. 3621–3629. ISSN: 1359-6454. DOI: https://doi.org/10.1016/j.actamat.2013.02.049. URL: http://www.sciencedirect.com/science/article/pii/S1359645413001791.

Anderson, D.G. (1965). "Iterative procedures for nonlinear integral equations". In: *J. Assoc. Comput. Mach.* 12, pp. 547–560. DOI: 10.1145/321296.321305.

Arsenlis, A. and D. M. Parks (1999). "Crystallographic aspects of geometrically-necessary and statistically-stored dislocation density". In: *Acta Materiala* 47, pp. 1597–1611.

Arsenlis, A., M. Rhee, et al. (2012). "A dislocation dynamics study of the transition from homogeneous to heterogeneous deformation in irradiated body-centered cubic iron". In: *Acta Materialia* 60, pp. 3748–3757. DOI: 10.1016/j.actamat.2012.03.041.

Arsenlis, A., B. D. Wirth, and M. Rhee (2004). "Dislocation density-based constitutive model for the mechanical behaviour of irradiated Cu". In: *Philosophical Magazine* 84:34, pp. 3617–3635. DOI: 10.1080/14786430412331293531.

Asaro, R.J. and J.R. Rice (1977). "Strain localization in ductile single crystals". In: *Journal of the Mechanics and Physics of Solids* 25, pp. 309–338. DOI: 10.1016/0022-5096(77)90001-1.

Ask, Anna et al. (2018). "A Cosserat crystal plasticity and phase field theory for grain boundary migration". In: *Journal of the Mechanics and Physics of Solids* 115, pp. 167–194. ISSN: 0022-5096. DOI: https://doi.org/10.1016/j.jmps.2018.03.006. URL: http://www.sciencedirect.com/science/article/pii/S0022509617309018.

Bapna, M.MS and M. Meshii (1974). "Deformation of Quench-Hardened Gold Crystals". In: *Materials Science and Engineering* 16, pp. 181–191. DOI: https://doi.org/10.1016/0025-5416(74)90152-9.

Barton, N.R., A. Arsenlis, and J. Marian (2013). "A polycrystal plasticity model of strain localization in irradiated iron". In: *Journal of the Mechanics and Physics of Solids* 61, pp. 341–351. DOI: 10.1016/j.jmps.2012.10.009.

Berbenni, S. et al. (2014). "A numerical spectral appraoch for solving elasto-static field dislocation and g-disclination mechanics". In: *International Journal of Solids and Structures* 51, pp. 4157–4175. DOI: http://dx.doi.org/10.1016/j.ijsolstr.2014.08.009.

Besson, Jacques et al. (2010). *Non-Linear Mechanics of Materials*. Springer Netherlands. ISBN: 9789048133567. DOI: 10.1007/978-90-481-3356-7. URL: http://dx.doi.org/10.1007/978-90-481-3356-7.

Blewitt, T.H. et al. (1960). "Radiation hardening of copper single crystals". In: *Journal of Nuclear Materials* 4, pp. 277–298. DOI: 10.1016/0022-3115(60)90001-5.

Brechet, Y.J.M, G.R. Canova, and L.P. Kubin (1993). "Static versus propagative strain localisations". In: *Scripta Metallurgica et Materialia* 29, pp. 1165–1170. DOI: 10.1016/0956-716X(93)90103-Y.

Brenner, R. et al. (2014). "Numerical implementation of static Field Dislocation Mechanics theory for periodic media". In: *Philosophical Magazine* 94, pp. 1764–1787. DOI: https://doi.org/10.1080/14786435.2014.896081.

Brisard, S. and L. Dormieux (2010). "FFT-based methods for the mechanics of composites: A general variational framework". In: *Computational Materials Science* 49.3, pp. 663–671. ISSN: 0927-0256. DOI: https://doi.org/10.1016/j.commatsci.2010.06.009. URL: http://www.sciencedirect.com/science/article/pii/S0927025610003563.

— (2012). "Combining Galerkin approximation techniques with the principle of Hashin and Shtrikman to derive a new FFT-based numerical method for the homogenization of composites". In: *Computer Methods in Applied Mechanics and Engineering* 217, pp. 197–212. DOI: https://doi.org/10.1016/j.cma.2012.01.003.

Bruemmer, S.M et al. (1999). "Radiation-induced material changes and susceptibility to intergranular failure of light-water-reactor core internals". In: *Journal of Nuclear Materials* 274.3, pp. 299–314. ISSN: 0022-3115. DOI: https://doi.org/10.1016/S0022-3115(99)00075-6. URL: http://www.sciencedirect.com/science/article/pii/S0022311599000756.

Byun, T.S., N. Hashimoto, and K. Farell (2006). "Deformation mode map of irradiated 316 stainless steel in true stress-dose space". In: *Journal of Nuclear Materials* 351, pp. 303–315. DOI: 10.1016/j.jnucmat.2006.02.033.

Byun, T.S., N. Hashimoto, K. Farrell, et al. (2006). "Characteristics of microscopic strain localization in irradiated 316 stainless steels and pure vanadium". In:

Journal of Nuclear Materials 349, pp. 251–264. DOI: 10.1016/j.jnucmat.2005.10.011.

Byun, Thak Sang and Naoyuki Hashimoto (Jan. 2006). "Strain Localization in Irradiated Materials". In: *Nuclear Engineering and Technology* 38.

Cermelli, Paolo and Morton E. Gurtin (2002). "Geometrically necessary dislocations in viscoplastic single crystals and bicrystals undergoing small deformations". In: *International Journal of Solids and Structures* 39.26, pp. 6281–6309. ISSN: 0020-7683. DOI: https://doi.org/10.1016/S0020-7683(02)00491-2. URL: http://www.sciencedirect.com/science/article/pii/S0020768302004912.

Charière, R., A. Marano, and Gélébart (2020). "Use of composite voxels in FFT based elastic simulations of hollow glass microspheres/polypropylene composites". In: *International Journal of Solids and Structures* 182-183, pp. 1–14. ISSN: 0020-7683. DOI: https://doi.org/10.1016/j.ijsolstr.2019.08.002. URL: http://www.sciencedirect.com/science/article/pii/S0020768319303531.

Chen, Xiaolei et al. (2019). "Elastic fields due to dislocations in anisotropic bi- and tri-materials: Applications to discrete dislocation pile-ups at grain boundaries". In: *International Journal of Solids and Structures* 164, pp. 141–156. ISSN: 0020-7683. DOI: https://doi.org/10.1016/j.ijsolstr.2019.01.020. URL: http://www.sciencedirect.com/science/article/pii/S0020768319300411.

Chen, Y. et al. (June 2019). "A FFT solver for variational phase-field modeling of brittle fracture". In: *Computer Methods in Applied Mechanics and Engineering* 349.dzd, pp. 167–190. DOI: https://doi.org/10.1016/j.cma.2019.02.017.

Chen, Yang et al. (2019). "Analysis of the damage initiation in a SiC/SiC composite tube from a direct comparison between large-scale numerical simulation and synchrotron X-ray micro-computed tomography". In: *International Journal of Solids and Structures* 161, pp. 111–126. ISSN: 0020-7683. DOI: https://doi.org/10.1016/j.ijsolstr.2018.11.009. URL: http://www.sciencedirect.com/science/article/pii/S0020768318304554.

Chopra, O.K. and A.S. Rao (2011). "A review of irradiation effects on LWR core internal materials – IASCC susceptibility and crack growth rates of austenitic stainless steels". In: *Journal of Nuclear Materials* 409.3, pp. 235–256. ISSN: 0022-3115. DOI: https://doi.org/10.1016/j.jnucmat.2010.12.001. URL: http://www.sciencedirect.com/science/article/pii/S0022311510008147.

Churchman, A.T. (1955). "The yield phenomena, kink bands and geometric softening in titanium crystals". In: *Acta Metallurgica* 3, pp. 22–29. DOI: 10.1016/0001-6160(55)90006-7.

Cordero, N.M., S. Forest, and E. P. Busso (2012). "Generalised continuum modelling of grain size effects in polycrystals". In: *Comptes Rendus Mecanique* 340, pp. 261–274. DOI: 10.1016/j.crme.2012.02.009.

Cordero, N.M., A. Gaubert, et al. (2010). "Size effects in generalised continuum crystal plasticity for two-phase laminates". In: *Journal of the Mechanics and Physics of Solids* 58.11, pp. 1963–1994. ISSN: 0022-5096. DOI: https://doi.org/10.1016/j.jmps.2010.06.012. URL: http://www.sciencedirect.com/science/article/pii/S0022509610001286.

Crone, W.C. and T.W. Shield (2001). "Experimental study of the deformation near a notch tip in copper and copper-beryllium single crystals". In: *Journal of the Mechanics and Physics of Solids* 49, pp. 2819–2938. DOI: https://doi.org/10.1016/S0022-5096(01)00080-1.

Cui, Yinan, Giacomo Po, and Nasr M. Ghoniem (2018). "A coupled dislocation dynamics-continuum barrier field model with application to irradiated materials". In: *International Journal of Plasticity* 104, pp. 54–67. ISSN: 0749-6419. DOI: https://doi.org/10.1016/j.ijplas.2018.01.015. URL: http://www.sciencedirect.com/science/article/pii/S0749641917306964.

Djaka, K. et al. (2019). "A FFT-based numerical implementation of mesoscale field dislocation mechanics: Application to two-phase laminates". In: *International Journal of Solids and Structures* in press, in press. DOI: https://doi.org/10.1016/j.ijsolstr.2018.12.027.

Drouet, J. et al. (2016). "A direct comparison between in-situ transmission electron microscopy observations and Dislocation Dynamics simulations of interaction between dislocation and irradiation induced loop in a zirconium alloy". In: *Scripta Materialia* 119, pp. 71–75. ISSN: 1359-6462. DOI: https://doi.org/10.1016/j.scriptamat.2016.03.029. URL: http://www.sciencedirect.com/science/article/pii/S1359646216301142.

Edwards, D.J., B.N. Singh, and J.B. Bilde-Sørensen (2005). "Initiation and propagation of cleared channels in neutron-irradiated pure copper and a precipitation hardened CuCrZr alloy". In: *Journal of Nuclear Materials* 342.1, pp. 164–178. ISSN: 0022-3115. DOI: https://doi.org/10.1016/j.jnucmat.2005.04.001. URL: http://www.sciencedirect.com/science/article/pii/S002231150500187X.

Edwards, D.J, E.P Simonen, and S.M Bruemmer (2003). "Evolution of fine-scale defects in stainless steels neutron-irradiated at 275 °C". In: *Journal of Nuclear Materials* 317.1, pp. 13–31. ISSN: 0022-3115. DOI: https://doi.org/10.1016/S0022-3115(03)00002-3. URL: http://www.sciencedirect.com/science/article/pii/S0022311503000023.

Edwards, D.J, E.P Simonen, F.A Garner, et al. (2003). "Influence of irradiation temperature and dose gradients on the microstructural evolution in neutron-irradiated 316SS". In: *Journal of Nuclear Materials* 317.1, pp. 32–45. ISSN: 0022-3115. DOI: https://doi.org/10.1016/S0022-3115(03)00003-5. URL: http://www.sciencedirect.com/science/article/pii/S0022311503000035.

Eisenlohr, P. et al. (2013). "A spectral method solution to crystal elasto-viscoplasticity at finite strains". In: *International Journal of Plasticity* 46, pp. 37–53. DOI: http://dx.doi.org/10.1016/j.ijplas.2012.09.012.

Erinosho, T.O. and F.P.E. Dunne (2015). "Strain localization and failure in irradiated zircaloy with crystal plasticity". In: *International Journal of Plasticity* 71, pp. 170–194. DOI: 10.1016/j.ijplas.2015.05.008.

Eshelby, J.D., F.C. Frank, and F.R.N. Nabarro (Apr. 1951). "XLI. The equilibrium of linear arrays of dislocations." In: *The London, Edinburgh, and Dublin Philosophical Magazine and Journal of Science* 42.327, pp. 351–364. ISSN: 1941-5990. DOI: 10.1080/14786445108561060. URL: http://dx.doi.org/10.1080/14786445108561060.

Estrin, Y. and L.P. Kubin (1986). "Local strain hardening and nonuniformity of plastic deformation". In: *Acta Metallurgica* 34.12, pp. 2455–2464. ISSN: 0001-6160. DOI: https://doi.org/10.1016/0001-6160(86)90148-3. URL: http://www.sciencedirect.com/science/article/pii/0001616086901483.

Evrard, Pierre and Maxime Sauzay (2010). "Modelling of the effect of dislocation channel on intergranular microcrack nucleation in pre-irradiated austenitic stainless steels during low strain rate tensile loading". In: *Journal of Nuclear Materials* 405.2, pp. 83–94. ISSN: 0022-3115. DOI: https://doi.org/10.1016/j.jnucmat.2010.06.006. URL: http://www.sciencedirect.com/science/article/pii/S0022311510002473.

Eyre, D.J. and G.W. Milton (1999). "A fast numerical scheme for computing the response of composites using grid refinement". In: *The European Physical Journal / Applied Physics* 6, pp. 41–47. DOI: https://doi.org/10.1051/epjap:1999150.

Féron, D., E. Herms, and B. Tanguy (2012). "Behavior of stainless steels in pressurized water reactor primary circuits". In: *Journal of Nuclear Materials* 427.1, pp. 364–377. ISSN: 0022-3115. DOI: https://doi.org/10.1016/j.jnucmat.2012.03.034. URL: http://www.sciencedirect.com/science/article/pii/S0022311512001559.

Field, K.G., M. N. Gussev, and J.T. Busby (2014). "Microstructural characterization of deformation localization at small strains in a neutron-irradiated 304 stainless steel". In: *Journal of Nuclear Materials* 452, pp. 500–508. DOI: 10.1016/j.jnucmat.2014.05.053.

Flouriot, S. et al. (2003). "Strain localization at the crack tip in single crystal CT specimens under monotonous loading: 3D Finite Element analyses and application to nickel-base superalloys". In: *International Journal of Fracture* 124, pp. 44–77. DOI: 10.1023/B:FRAC.0000009300.70477.ba.

Fong, R.W.L. (2013). "Anisotropy factors from texture and mechanical strain in Zircaloy-4 fuel sheaths". In: *Journal of Nuclear Materials* 440.1, pp. 288–

297. ISSN: 0022-3115. DOI: https://doi.org/10.1016/j.jnucmat.2013.04.089. URL: http://www.sciencedirect.com/science/article/pii/S0022311513007083.

Forest, S. (1998). "Modeling slip, kink and shear banding in classical and generalized single crystal plasticity". In: *Acta Materialia* 46, pp. 3265–3281. DOI: 10.1016/S1359-6454(98)00012-3.

Fournier, L. et al. (2009). "Proton irradiation effect on microstructure, strain localization and iodine-induced stress corrosion cracking in Zircaloy-4". In: *Journal of Nuclear Materials* 384, pp. 38–47. DOI: 10.1016/j.jnucmat.2008.10.001.

Fukumoto, Ken-ichi, Masanari Sugiyama, and Hideki Matsui (2007). "Features of dislocation channeling in neutron-irradiated V–(Fe, Cr)–Ti alloy". In: *Journal of Nuclear Materials* 367-370. Proceedings of the Twelfth International Conference on Fusion Reactor Materials (ICFRM-12), pp. 829–833. ISSN: 0022-3115. DOI: https://doi.org/10.1016/j.jnucmat.2007.03.075. URL: http://www.sciencedirect.com/science/article/pii/S0022311507004941.

Fukuya, K. et al. (2008). "Fracture behavior of austenitic stainless steels irradiated in PWR". In: *Journal of Nuclear Materials* 378.2, pp. 211–219. ISSN: 0022-3115. DOI: https://doi.org/10.1016/j.jnucmat.2008.06.028. URL: http://www.sciencedirect.com/science/article/pii/S0022311508003553.

Gélébart, Lionel and Romain Mondon-Cancel (2013). "Non-linear extension of FFT-based methods accelerated by conjugate gradients to evaluate the mechanical behavior of composite materials". In: *Computational Materials Science* 77, pp. 430–439. ISSN: 0927-0256. DOI: https://doi.org/10.1016/j.commatsci.2013.04.046. URL: http://www.sciencedirect.com/science/article/pii/S0927025613002188.

Gélébart and F. Ouaki (2015). "Filtering material properties to improve FFT-based methods for numerical homogenization". In: *Journal of Computational Physics* 294, pp. 90–95. ISSN: 0021-9991. DOI: https://doi.org/10.1016/j.jcp.2015.03.048. URL: http://www.sciencedirect.com/science/article/pii/S002199911500203X.

Ghoniem, N. M. et al. (Nov. 2001). "On dislocation interaction with radiation-induced defect clusters and plastic flow localization in fcc metals". In: *Philosophical Magazine A* 81.11, pp. 2743–2764. ISSN: 1460-6992. DOI: 10.1080/01418610108216667. URL: http://dx.doi.org/10.1080/01418610108216667.

Gilman, J. J. (May 1954). "Mechanism of ortho kink-band formation in Compressed Zinc Monocrystals". In: *JOM* 6.5, pp. 621–629. ISSN: 1543-1851. DOI: 10.1007/bf03398884. URL: http://dx.doi.org/10.1007/BF03398884.

Gioacchino, Fabio di and João Quinta da Fonseca (2015). "An experimental study of the polycrystalline plasticity of austenitic stainless steel". In: *International Journal of Plasticity* 74, pp. 92–109. DOI: `10.1016/j.ijplas.2015.05.012`.

Griffiths, M. (1988). "A review of microstructure evolution in zirconium alloys during irradiation". In: *Journal of Nuclear Materials* 159, pp. 190–218. ISSN: 0022-3115. DOI: `https://doi.org/10.1016/0022-3115(88)90093-1`. URL: `http://www.sciencedirect.com/science/article/pii/0022311588900931`.

Gupta, J., J. Hure, B. Tanguy, L. Laffont, M.-C. Lafont, et al. (2016). "Evaluation of stress corrosion cracking of irradiated 304L stainless steel in PWR environment using heavy ion irradiation". In: *Journal of Nuclear Materials* 476, pp. 82–92. ISSN: 0022-3115. DOI: `https://doi.org/10.1016/j.jnucmat.2016.04.003`. URL: `http://www.sciencedirect.com/science/article/pii/S0022311516301179`.

— (2018). "Characterization of ion irradiation effects on the microstructure, hardness, deformation and crack initation behavior of austenitic stainless steel : Heavy ions vs protons". In: *Journal of Nuclear Materials* 501, pp. 45–58. DOI: `10.1016/j.jnucmat.2018.01.013`.

Gurtin, Morton E. (2002). "A gradient theory of single-crystal viscoplasticity that accounts for geometrically necessary dislocations". In: *Journal of the Mechanics and Physics of Solids* 50, pp. 5–32. DOI: `https://doi.org/10.1016/S0022-5096(01)00104-1`.

Gururaj, K., C. Robertson, and M. Fivel (Apr. 2015). "Channel formation and multiplication in irradiated FCC metals: a 3D dislocation dynamics investigation". In: *Philosophical Magazine* 95.12, pp. 1368–1389. ISSN: 1478-6443. DOI: `10.1080/14786435.2015.1029560`. URL: `http://dx.doi.org/10.1080/14786435.2015.1029560`.

Gussev, M.N., K. G. Field, and J. T. Busby (2015). "Deformation localization and dislocation channel dynamics in neutron-irradiated austenitic stainless steel". In: *Journal of Nuclear Materials* 460, pp. 139–152. DOI: `10.1016/j.jnucmat.2015.02.008`.

Hagihara, Koji, Tsuyoshi Mayama, et al. (2016). "Orientation dependence of the deformation kink band formation behavior in Zn single crystals". In: *International Journal of Plasticity* 77, pp. 174–191. DOI: `10.1016/j.ijplas.2015.10.005`.

Hagihara, Koji, Takuya Okamoto, et al. (2016). "Electron backscatter diffraction pattern analysis of the deformation band formed in the Mg-based long-period stacking ordered phase". In: *Scripta Materialia* 117, pp. 32–36. DOI: `10.1016/j.scriptamat.2016.02.016`.

Han, X. (2012). "Modélisation de la fragilisation due au gonflement dans les aciers inoxydables austénitiques irradiés". PhD thesis. Ecole Nationale Supérieure des Mines de Paris.

Hashimoto, N. et al. (2005). "Deformation microstructure of neutron-irradiated pure polycrystalline vanadium". In: *Journal of Nuclear Materials* 336, pp. 225–232. DOI: 10.1016/j.jnucmat.2004.09.017.

Hashimoto, N et al. (2000). "Deformation mechanisms in 316 stainless steel irradiated at 60°C and 330°C". In: *Journal of Nuclear Materials* 283-287. 9th Int. Conf. on Fusion Reactor Materials, pp. 528–534. ISSN: 0022-3115. DOI: https://doi.org/10.1016/S0022-3115(00)00087-8. URL: http://www.sciencedirect.com/science/article/pii/S0022311500000878.

Hashin, Z. and S. Shtrikman (1962). "On some variational principles in anisotropic and nonhomogeneous elasticity". In: *Journal of the Mechanics and Physics of Solids* 10.4, pp. 335–342. ISSN: 0022-5096. DOI: https://doi.org/10.1016/0022-5096(62)90004-2. URL: http://www.sciencedirect.com/science/article/pii/0022509662900042.

Hasson, D. F. et al. (Feb. 1974). "Radiation effects on the yield stress and dislocation channeling in neutron irradiated molybdenum". In: *Metallurgical Transactions* 5.2, pp. 371–379. ISSN: 1543-1916. DOI: 10.1007/bf02644104. URL: http://dx.doi.org/10.1007/BF02644104.

Helfer, Thomas et al. (2015). "Introducing the open-source MFront code generator: Application to mechanical behaviours and material knowledge management within the PLEIADES fuel element modelling platform". In: *Computer and Mathematics with Applications* 70, pp. 994–1023. DOI: https://doi.org/10.1016/j.camwa.2015.06.027.

Hess, J. B. and C. S. Barrett (Sept. 1949). "Structure and nature of kink bands in zinc". In: *JOM* 1.9, pp. 599–606. ISSN: 1543-1851. DOI: 10.1007/bf03398902. URL: http://dx.doi.org/10.1007/BF03398902.

Hirsh, P. (1976). "Point defect cluster hardening". In: *Point defect behaviour and duffusional processes, University of Bristol, 13-16 Septembrer, pp. 95-107.*

Hure, J. et al. (2016). "Intergranular stress distributions in polycrystalline aggregates". In: *Journal of Nuclear Materials* 476, pp. 231–242. DOI: 10.1016/j.jnucmat.2016.04.017.

Jaoul, Bernard (1964). *Etude de la plasticité et application aux métaux.* Les Presses - Mines ParisTech.

Jaoul, Par B. (1961). "Consolidation des polycristaux de fer et hypothèses sur l'origine du palier des courbes de traction". In: *Journal of the Mechanics and Physics of Solids* 9.2, pp. 69–90. ISSN: 0022-5096. DOI: https://doi.org/10.1016/0022-5096(61)90026-6. URL: http://www.sciencedirect.com/science/article/pii/0022509661900266.

Jaoul, Par B. and D. Gonzalez (1961). "Déformation plastique de monocristaux de fer". In: *Journal of the Mechanics and Physics of Solids* 9.1, pp. 16–38. ISSN: 0022-

5096. DOI: https://doi.org/10.1016/0022-5096(61)90036-9. URL: http://www.sciencedirect.com/science/article/pii/0022509661900369.

Jiao, Z., J.T. Busby, and G.S. Was (2007). "Deformation microstructure of proton-irradiated stainless steels". In: *Journal of Nuclear Materials* 361.2. TMS 2007:Wechsler Symposium, pp. 218–227. ISSN: 0022-3115. DOI: https://doi.org/10.1016/j.jnucmat.2006.12.012. URL: http://www.sciencedirect.com/science/article/pii/S0022311506006040.

Jiao, Z. and G.S. Was (2010). "The role of irradiated microstructure in the localized deformation of austenitic stainless steels". In: *Journal of Nuclear Materials* 407.1. Proceedings of the Symposium on Microstructural Processes in Irradiated Materials and on Reactor Pressure Vessel (RPV) Embrittlement and Fusion Materials: Measuring, Modeling and Managing Irradiation Effects, pp. 34–43. ISSN: 0022-3115. DOI: https://doi.org/10.1016/j.jnucmat.2010.07.006. URL: http://www.sciencedirect.com/science/article/pii/S0022311510002916.

— (2011). "Impact of localized deformation onIASCC in austenitic stainless steels". In: *Journal of Nuclear Materials* 408, pp. 246–256. DOI: 10.1016/j.jnucmat.2010.10.087.

Kabel, Matthias, Thomas Böhlke, and Matti Schneider (Oct. 2014). "Efficient fixed point and Newton–Krylov solvers for FFT-based homogenization of elasticity at large deformations". In: *Computational Mechanics* 54.6, pp. 1497–1514. ISSN: 1432-0924. DOI: 10.1007/s00466-014-1071-8. URL: http://dx.doi.org/10.1007/s00466-014-1071-8.

Kabel, Matthias, Andreas Fink, and Matti Schneider (2017). "The composite voxel technique for inelastic problems". In: *Computer Methods in Applied Mechanics and Engineering* 322, pp. 396–418. ISSN: 0045-7825. DOI: https://doi.org/10.1016/j.cma.2017.04.025. URL: http://www.sciencedirect.com/science/article/pii/S0045782516317881.

Kabel, Matthias, Dennis Merkert, and Matti Schneider (2015). "Use of composite voxels in FFT-based homogenization". In: *Computer Methods in Applied Mechanics and Engineering* 294, pp. 168–188. ISSN: 0045-7825. DOI: https://doi.org/10.1016/j.cma.2015.06.003. URL: http://www.sciencedirect.com/science/article/pii/S0045782515001954.

Kabel, Matthias, Felix Ospald, and Matti Schneider (2016). "A model order reduction method for computational homogenization at finite strains on regular grids using hyperelastic laminates to approximate interfaces". In: *Computer Methods in Applied Mechanics and Engineering* 309, pp. 476–496. ISSN: 0045-7825. DOI: https://doi.org/10.1016/j.cma.2016.06.021. URL: http://www.sciencedirect.com/science/article/pii/S0045782516306077.

Karlsen, Wade, Gonzalo Diego, and Bastian Devrient (2010). "Localized deformation as a key precursor to initiation of intergranular stress corrosion cracking of austenitic stainless steels employed in nuclear power plants". In: *Journal of Nuclear Materials* 406.1. FP6 IP PERFECT Project: Prediction of Irradiation Damage Effects in Reactor Components, pp. 138–151. ISSN: 0022-3115. DOI: https://doi.org/10.1016/j.jnucmat.2010.01.029. URL: http://www.sciencedirect.com/science/article/pii/S0022311510001297.

Kearns, J.J. (1965). "Thermal expansion and preferred orientation in Zircaloy". In: *LWBR Development Program.*

Khraishi, Tariq et al. (Apr. 2002). "Localized deformation and hardening in irradiated metals: Three-dimensional discrete dislocation dynamics simulations". In: *Metallurgical and Materials Transactions B* 33, pp. 285–296. DOI: 10.1007/s11663-002-0012-7.

Kimura, Yuichi, Ryo Ueta, and Kazuyuki Shizawa (2018). "Dislocation-based crystal plasticity FE analysis for kink band formation in Mg-based LPSO phase considering higher-order stress". In: *Procedia Manufacturing* 15, pp. 1825–1832. DOI: 10.1016/j.promfg.2018.07.208.

Klusemann, Benjamin and Dennis M. Kochmann (2014). "Microstructural pattern formation in finite-deformation single-slip crystal plasticity under cyclic loading: Relaxation vs. gradient plasticity". In: *Computer Methods in Applied Mechanics and Engineering* 278, pp. 765–793. ISSN: 0045-7825. DOI: https://doi.org/10.1016/j.cma.2014.05.015. URL: http://www.sciencedirect.com/science/article/pii/S0045782514001765.

Klusemann, Benjamin and Tuncay Yalçinkaya (2013). "Plastic deformation induced microstructure evolution through gradient enhanced crystal plasticity based on a non-convex Helmholtz energy". In: *International Journal of Plasticity* 48, pp. 168–188. ISSN: 0749-6419. DOI: https://doi.org/10.1016/j.ijplas.2013.02.012. URL: http://www.sciencedirect.com/science/article/pii/S0749641913000570.

Kochmann, D.M. and K.C. Le (2008). "Dislocation pile-ups in bicrystals within continuum dislocation theory". In: *International Journal of Plasticity* 24.11, pp. 2125–2147. ISSN: 0749-6419. DOI: https://doi.org/10.1016/j.ijplas.2008.03.007. URL: http://www.sciencedirect.com/science/article/pii/S0749641908000594.

Korbel, A. and P. Martin (1986). "Microscopic versus macroscopic aspect of shear bands deformation". In: *Acta Metallurgica* 34.10, pp. 1905–1909. ISSN: 0001-6160. DOI: https://doi.org/10.1016/0001-6160(86)90249-X. URL: http://www.sciencedirect.com/science/article/pii/000161608690249X.

— (1988). "Microstructural events of macroscopic strain localization in prestrained tensile specimens". In: *Acta Metallurgica* 36.9, pp. 2575–2586. ISSN: 0001-6160.

DOI: https://doi.org/10.1016/0001-6160(88)90202-7. URL: http://www.sciencedirect.com/science/article/pii/0001616088902027.

Krishna, Shree, Amir Zamiri, and Suvranu De (2010). "Dislocation and defect density-based micromechanical modeling of the mechanical behavior of FCC metals under neutron irradiation". In: *Philosophical Magazine* 90:30, pp. 4013–4025. DOI: 10.1080/14786435.2010.502150.

Kröner, E. (1972). *Statistical Continuum Mechanics*. Springer Verlag.

Kubin, L.P. et al. (1992). "Dislocation microstructures and plastic flow: a 3D simulation." In: *Solid State Phenomena* 23, pp. 455–472.

Kysar, Jeffrey W. and Clyde L. Briant (2002). "Crack tip deformation fields in ductile single crystals". In: *Acta Materialia* 50, pp. 2367–2380. DOI: 10.1016/S1359-6454(02)00070-8.

Lai, M.J., C.C. Tasan, and D. Raabe (2015). "Deformation mechanism of omega-enriched Ti–Nb-based gum metal : Dislocation channeling and deformation induced omega–beta transformation". In: *Acta Materialia* 100, pp. 290–300. DOI: http://dx.doi.org/10.1016/j.actamat.2015.08.047.

Lebensohn, R. A., A. K. Kanjarla, and P. Eisenlohr (2012). "An elasto-viscoplastic formulation based on fast Fourier transforms for the prediction of micromechanical fields in polycrystalline materials". In: *International Journal of Plasticity* 32-33, pp. 59–69. DOI: 10.1016/j.ijplas.2011.12.005.

Lebensohn, R. A. and A. Needleman (2016). "Numerical implementation of non-local polycrystal plasticity using fast Fourier transforms". In: *Journal of the Mechanics and Physics of Solids* 97, pp. 333–351. DOI: http://dx.doi.org/10.1016/j.jmps.2016.03.023.

Lebensohn, R.A. et al. (2009). "Modeling viscoplastic behavior and heterogeneous intracrystalline deformation of columnar ice polycrystals". In: *Acta Materialia* 57, pp. 1405–1415. DOI: 10.1016/j.actamat.2008.10.057.

Lee, E.H. et al. (2001). "Origin of hardening and deformation mechanisms in irradiated 316 LN austenitic stainless steel". In: *Journal of Nuclear Materials* 296.1. 4th Int. Workshop on Spallation Materials Technology, pp. 183–191. ISSN: 0022-3115. DOI: https://doi.org/10.1016/S0022-3115(01)00566-9. URL: http://www.sciencedirect.com/science/article/pii/S0022311501005669.

Ling, Chao et al. (2017). "Void growth and coalescence in triaxial stress fields in irradiated FCC single crystals". In: *Journal of Nuclear Materials* 492, pp. 157–170. DOI: 10.1016/j.jnucmat.2017.04.013.

— (2018). "A reduce d micromorphic single crystal plasticity model at finite deformations. Application to strain localization and void growth in ductile metals". In: *International Journal of Solids and Structures* 134, pp. 43–69. DOI: 10.1016/j.ijsolstr.2017.10.013.

Luft, A. (1991). "Microstructural processes of plastic instabilities in strengthened metals". In: *Progress in Materials Science* 35.2, pp. 97–204. ISSN: 0079-6425. DOI: https://doi.org/10.1016/0079-6425(91)90002-B. URL: http://www.sciencedirect.com/science/article/pii/007964259190002B.

Luppo, M.I et al. (2000). "Tensile properties and microstructure of 590 MeV proton-irradiated pure Fe and a Fe–Cr alloy". In: *Journal of Nuclear Materials* 283-287. 9th Int. Conf. on Fusion Reactor Materials, pp. 483–487. ISSN: 0022-3115. DOI: https://doi.org/10.1016/S0022-3115(00)00370-6. URL: http://www.sciencedirect.com/science/article/pii/S0022311500003706.

Mahajan, S. and B.L. Eyre (2017). "Formation of dislocation channels in neutron irradiated molybdenum". In: *Acta Materialia* 122, pp. 259–265. ISSN: 1359-6454. DOI: https://doi.org/10.1016/j.actamat.2016.09.029. URL: http://www.sciencedirect.com/science/article/pii/S1359645416307285.

Makin, M.J. (1964). "The longue-range forces between dislocation loops and dislocations". In: *Phil. Mag.* 10, pp. 695–711. DOI: 10.1080/14786436408228488.

Mandel, J. (1973). "Equations constitutives et directeurs dans les milieux plastiques et viscoplastiques". In: *International Journal of Solids and Structures* 9, pp. 725–740. DOI: 10.1016/0020-7683(73)90120-0.

Mansuy, P., A. Philip, and J. Meyssonier (2001). "Localization of deformation in polycrystalline ice". In: *J. Phys.* 11, pp. 267–274. DOI: http://dx.doi.org/10.1051/jp4:2001433.

McMurtrey, M.D. et al. (2014). "Strain localization at dislocation channel–grain boundary intersections in irradiated stainless steel". In: *International Journal of Plasticity* 56, pp. 219–231. ISSN: 0749-6419. DOI: https://doi.org/10.1016/j.ijplas.2014.01.001. URL: http://www.sciencedirect.com/science/article/pii/S0749641914000023.

Michel, J.C., H. Moulinec, and P. Suquet (2001). "A computational scheme for linear and non-linear composites with arbitrary phase contrast". In: *International journal for numerical methods in engineering* 52, pp. 139–160. DOI: 10.1002/nme.275.

Mishra, Nachiketa, Jaroslav Vondřejc, and Jan Zeman (2016). "A comparative study on low-memory iterative solvers for FFT-based homogenization of periodic media". In: *Journal of Computational Physics* 321, pp. 151–168. ISSN: 0021-9991. DOI: https://doi.org/10.1016/j.jcp.2016.05.041. URL: http://www.sciencedirect.com/science/article/pii/S0021999116301863.

Miura, Terumitsu et al. (2009). "Characterization of deformation structure in ion-irradiated stainless steels". In: *Journal of Nuclear Materials* 386-388. Fusion Reactor Materials, pp. 210–213. ISSN: 0022-3115. DOI: https://doi.org/10.1016/j.jnucmat.2008.12.093. URL: http://www.sciencedirect.com/science/article/pii/S002231150800843X.

Montagnat, Maurine et al. (2011). "Measurements and full-field predictions of deformation heterogeneities in ice". In: *Earth and Planetary Science Letters* 305, pp. 153–160. DOI: 10.1016/j.epsl.2011.02.050.

Mora, V. (2005). "Simulation par elements finis du phenomene de localisation dans les alliages de zirconium irradies". In: *Document Technique DMN* DMN/SRMA/LA2M/NT/2005-2732/A.

Mori, T. and M. Meshii (1969). "Plastic deformation of quench-hardened aluminium single crystals". In: *Acta Metallurgica* 17, pp. 167–175. DOI: 10.1016/0001-6160(69)90137-0.

Moulinec, H. and P. Suquet (1998). "A numerical method for computing the overall response of nonlinear composites with complex microstructure". In: *Comput. Methods Appl. Mech. Engrg.* 157, pp. 69–94. DOI: 10.1016/S0045-7825(97)00218-1.

Neuhäuser, H. (1983). "Dislocation in Solids". In: *ed. F.R.N. Nabarro. Holland Publishing Company* Vol. 6, pp. 319–440.

Nishioka, Hiromasa et al. (Apr. 2008). "Deformation Structure in Highly Irradiated Stainless Steels". In: *Journal of Nuclear Science and Technology* 45.4, pp. 274–287. ISSN: 1881-1248. DOI: 10.1080/18811248.2008.9711437. URL: http://dx.doi.org/10.1080/18811248.2008.9711437.

Nogaret, T. et al. (2008). "Clear-band formation simulated by dislocation dynamics: Role of helical turns and pile-ups". In: *Journal of Nuclear Materials* 380, pp. 22–29. DOI: 10.1016/j.jnucmat.2008.07.001.

Northwood, D.O. (1977). "Irradiation damage in zirconium and its alloys". In: *Atomix Energy Review* 15, pp. 547–610.

Northwood, D.O. et al. (1979). "Characterization of neutron irradiation damage in zirconium alloys — an international "round-robin" experiment". In: *Journal of Nuclear Materials* 79.2, pp. 379–394. ISSN: 0022-3115. DOI: https://doi.org/10.1016/0022-3115(79)90103-X. URL: http://www.sciencedirect.com/science/article/pii/002231157990103X.

Nye, J.F. (1953). "Some geometrical relations in dislocated crystal". In: *Acta Metallurgica* 1, pp. 153–162.

Odette, G.R. and D. Frey (1979). "Development of mechanical property correlation methodology for fusion environments". In: *Journal of Nuclear Materials* 85 - 86, pp. 817–822. DOI: 10.1016/0022-3115(79)90360-X.

Onchi, T., H. Kanayo, and Y. Higashiguchi (May 1977). "Effect of Neutron Irradiation on Deformation Behavior of Zirconium". In: *Journal of Nuclear Science and Technology* 14.5, pp. 359–369. ISSN: 1881-1248. DOI: 10.1080/18811248.1977.9730770. URL: http://dx.doi.org/10.1080/18811248.1977.9730770.

Onchi, Takeo, Hideo Kayano, and Yasuhiro Higashiguchi (1980). "The inhomogeneous deformation behaviour of neutron irradiated Zircaloy-2". In: *Journal of*

Nuclear Materials 88.2, pp. 226–235. ISSN: 0022-3115. DOI: https://doi.org/
10.1016/0022-3115(80)90278-0. URL: http://www.sciencedirect.com/
science/article/pii/0022311580902780.

ONCHI, Takeo et al. (Nov. 1980). "Effects of Temperature, Strain Rate, and
Specimen Orientation on Localized Plastic Deformation of Irradiated Zircaloy-
2". In: *Journal of Nuclear Science and Technology* 17.11, pp. 848–856. ISSN:
1881-1248. DOI: 10.1080/18811248.1980.9732664. URL: http://dx.doi.
org/10.1080/18811248.1980.9732664.

Onimus, F., J. L. Béchade, and D. Gilbon (Oct. 2012). "Experimental Analysis of
Slip Systems Activation in Neutron-Irradiated Zirconium Alloys and Comparison
with Polycrystalline Model Simulations". In: *Metallurgical and Materials Trans-
actions A* 44.S1, pp. 45–60. ISSN: 1543-1940. DOI: 10.1007/s11661-012-1463-3.
URL: http://dx.doi.org/10.1007/s11661-012-1463-3.

Onimus, F. and J.L. Bechade (2009). "A polycrystalline modeling of the mechan-
ical behavior of neutron irradiated zirconium alloys". In: *Journal of Nuclear
Materials* 384, pp. 163–174. DOI: 10.1016/j.jnucmat.2008.11.006.

Onimus, F., J.L. Bechade, and D. Gilbon (2012). "Experimental analysis of slip
systems activation in neutron-irradiated zirconium alloys and comparison with
polycrystalline model simulations". In: *The Mineral, Metals and Materials
Society and ASM International 2012.*

Onimus, F., J.L. Béchade, et al. (2006). "Investigation of neutron radiation effects
on the mechanical behavior of recrystallized zirconium alloys". In: *Journal of
Nuclear Materials* 358.2, pp. 176–189. ISSN: 0022-3115. DOI: https://doi.org/
10.1016/j.jnucmat.2006.07.005. URL: http://www.sciencedirect.com/
science/article/pii/S0022311506004016.

Onimus, F., L. Dupuy, and F. Mompiou (2012). "In situ TEM observations of
interactions between gliding dislocations and prismatic loops in Zr-ion irradiated
zirconium alloys". In: *Progress in Nuclear Energy* 57, pp. 77–85. DOI: 10.1016/
j.pnucene.2011.10.005.

Onimus, F. and L. Gélébart (2018). *Comparaison entre deux méthodes d'homogénéisation
des polycristaux en champ complet par FFT et champ moyen pour la prédiction
du comportement sous irradiation des alliages de zirconium.* Tech. rep. CEA -
DEN/DANS/DMN/SRMA/LA2M.

Onimus, F., I. Monnet, et al. (2004). "A statistical TEM investigation of dislocation
channeling mechanism in neutron irradiated zirconium alloys". In: *Journal of
Nuclear Materials* 328, pp. 165–179. DOI: 10.1016/j.jnucmat.2004.04.337.

OROWAN, E. (June 1942). "A TYPE OF PLASTIC DEFORMATION NEW IN
METALS". In: *Nature* 149.3788, pp. 643–644. ISSN: 1476-4687. DOI: 10.1038/
149643a0. URL: http://dx.doi.org/10.1038/149643a0.

Orozco-Caballero, Alberto et al. (2017). "How magnesium accommodates local deformation incompatibility: A high-resolution digital image correlation study". In: *Acta Materialia* 133, pp. 367–379. ISSN: 1359-6454. DOI: https://doi.org/10.1016/j.actamat.2017.05.040. URL: http://www.sciencedirect.com/science/article/pii/S1359645417304275.

Panteghini, Andrea and Lorenzo Bardella (2018). "On the role of higher-order conditions in distortion gradient plasticity". In: *Journal of the Mechanics and Physics of Solids* 118, pp. 293–321. ISSN: 0022-5096. DOI: https://doi.org/10.1016/j.jmps.2018.05.019. URL: http://www.sciencedirect.com/science/article/pii/S002250961830231X.

Patil, Swapnil D., R. Narasimhana, and Raja K. Mishra (2009). "Observation of kink shear bands in an aluminium single crystal fracture specimen". In: *Scripta MAterialia* 61, pp. 465–468. DOI: 10.1016/j.scriptamat.2009.04.043.

Patra, A. and D.L. McDowell (2012). "Crystal plasticity-based constitutive modelling of irradiated BCC structures". In: *Philosophical Magazine* 92:7, pp. 861–887. DOI: 10.1080/14786435.2011.634855.

— (2016). "Crystal plasticity investigation of the microstructural factors influencing dislocation channeling in a model irradiated bcc material". In: *Acta Materiala* 110, pp. 364–376. DOI: 10.1016/j.actamat.2016.03.041.

Pawlik, K. (1986). "Determination of the orientation distribution function from pole figures in arbitrarily defined cells". In: *physica status solidi (b)* 134.2, pp. 477–483. DOI: 10.1002/pssb.2221340205. eprint: https://onlinelibrary.wiley.com/doi/pdf/10.1002/pssb.2221340205. URL: https://onlinelibrary.wiley.com/doi/abs/10.1002/pssb.2221340205.

Peterson, K. (1982). "Evidence for basal or near-basal slip in irradiated zircaloy". In: *Journal of Nuclear Materials* 105, pp. 341–344. DOI: 10.1016/0022-3115(82)90394-4.

Pokor, C, X Averty, et al. (2004). "Effect of irradiation defects on the work hardening behavior". In: *Scripta Materialia* 50.5, pp. 597–600. ISSN: 1359-6462. DOI: https://doi.org/10.1016/j.scriptamat.2003.11.029. URL: http://www.sciencedirect.com/science/article/pii/S1359646203007590.

Pokor, C, Y Brechet, P Dubuisson, J.-P Massoud, and X Averty (2004). "Irradiation damage in 304 and 316 stainless steels: experimental investigation and modeling. Part II: Irradiation induced hardening". In: *Journal of Nuclear Materials* 326.1, pp. 30–37. ISSN: 0022-3115. DOI: https://doi.org/10.1016/j.jnucmat.2003.12.008. URL: http://www.sciencedirect.com/science/article/pii/S0022311503005361.

Pokor, C, Y Brechet, P Dubuisson, J.-P Massoud, and A Barbu (2004). "Irradiation damage in 304 and 316 stainless steels: experimental investigation and modeling. Part I: Evolution of the microstructure". In: *Journal of Nuclear Materials* 326.1,

pp. 19–29. ISSN: 0022-3115. DOI: https://doi.org/10.1016/j.jnucmat.2003.11.007. URL: http://www.sciencedirect.com/science/article/pii/S0022311503005129.

Proudhon, Henry, Nicolas Guéninchault, et al. (Oct. 2018). "Incipient Bulk Polycrystal Plasticity Observed by Synchrotron In-Situ Topotomography". In: *Materials* 11.10, p. 2018. ISSN: 1996-1944. DOI: 10.3390/ma11102018. URL: http://dx.doi.org/10.3390/ma11102018.

Proudhon, Henry, Jia Li, et al. (2016). "Coupling Diffraction Contrast Tomography with the Finite Element Method". In: *Advanced Engineering Materials* 18.6, pp. 903–912. DOI: 10.1002/adem.201500414. eprint: https://onlinelibrary.wiley.com/doi/pdf/10.1002/adem.201500414. URL: https://onlinelibrary.wiley.com/doi/abs/10.1002/adem.201500414.

Rice, J.R. (1976). "The localization of plastic deformation". In: *Theoretical and Applied Mechanics* 1, pp. 207–220.

Rieger, G.F. and D. Lee (1974). "Strength and ductility of neutron irradiated and textured Zy-2". In: *Zirconium in nuclear applications.* Ed. by American Society for Testing Materials ASTM STP 551, pp. 355–369.

Robach, J. S. et al. (Jan. 2003). "In-situ transmission electron microscopy observations and molecular dynamics simulations of dislocation-defect interactions in ion-irradiated copper". In: *Philosophical Magazine* 83.8, pp. 955–967. ISSN: 1478-6443. DOI: 10.1080/0141861031000065329. URL: http://dx.doi.org/10.1080/0141861031000065329.

Robach, J.S. et al. (2006). "Dynamic observations and atomistic simulations of dislocation–defect interactions in rapidly quenched copper and gold". In: *Acta Materialia* 54.6, pp. 1679–1690. ISSN: 1359-6454. DOI: https://doi.org/10.1016/j.actamat.2005.11.038. URL: http://www.sciencedirect.com/science/article/pii/S1359645405007366.

Rodney, D., G. Martin, and Y. Brechet (2001). "Irradiation hardening by interstitial loops : atomistic study and micromechanical model". In: *Material Science and Engineering* A309-310, pp. 198–202. DOI: 10.1016/S0921-5093(00)01723-8.

Rodney, David (2005). "Atomic-scale modeling of clear band formation in FCC metals". In: *Nuclear Instruments and Methods in Physics Research B* 225, pp. 100–110. DOI: 10.1016/j.nimb.2004.10.029.

Sauzay, Maxime, Karine Bavard, and Wade Karlsen (2010). "TEM observations and finite element modelling of channel deformation in pre-irradiated austenitic stainless steels – Interactions with free surfaces and grain boundaries". In: *Journal of Nuclear Materials* 406.1. FP6 IP PERFECT Project: Prediction of Irradiation Damage Effects in Reactor Components, pp. 152–165. ISSN: 0022-3115. DOI: https://doi.org/10.1016/j.jnucmat.2010.01.027. URL: http://www.sciencedirect.com/science/article/pii/S0022311510000838.

Scherer, J.M. et al. (2019). "Strain gradient crystal plasticity with evolving length scale : Application to voided irradiated materials". In: *European Journal of Mechanics / A Solids* 77. DOI: https://doi.org/10.1016/j.euromechsol.2019.04.003.

Schneider, Matti, Dennis Merkert, and Matthias Kabel (2017). "FFT-based homogenization for microstructures discretized by linear hexahedral elements". In: *International journal for numerical methods in engineering* 109, pp. 1461–1489. DOI: 10.1002/nme.5336.

Sharp, J.V. (1972a). "Correlation between cleared channels and surface slip steps in neutron irradiated copper crystals". In: *Radiation Effects* 14, pp. 71–75. DOI: 10.1080/00337577208230474.

— (1972b). "Deformation of neutron-irradiated copper single crystals". In: *Radiation Effects* 14, pp. 71–75. DOI: 10.1080/14786436708229258.

— (1974). "Deformation of neutron irradiated copper alloys". In: *Acta Metallurgica* 22, pp. 449–457. DOI: 10.1016/0001-6160(74)90097-2.

Shawish, S. El, B. Tanguy, and J. Hure (2016). "Macroscopic Validation of the Micromechanical Model for Neutron-Irradiated Stainless Steel". In: *25th International Conference Nuclear Energy for New Europe.*

Singh, B.N., J.H. Evans, et al. (1998). "Effects of neutron irradiation on microstructure and deformation behaviour of mono and polycrystalline molybdenum and its alloys". In: *Journal of Nuclear Materials* 258-263, pp. 865–872. DOI: 10.1016/S0022-3115(98)00259-1.

Singh, B.N., A.J.E. Foreman, and H. Trinkhaus (1997). "Radiation hardening revisited : role of intracascade clustering". In: *Journal of Nuclear Materials* 249, pp. 103–115. DOI: 10.1016/S0022-3115(97)00231-6.

Singh, B.N., N.M. Ghoniem, and H. Trinkaus (2002). "Experiment-based modelling of hardening and localized plasticity in metals irradiated under cascade damage conditions". In: *Journal of Nuclear Materials* 307-311, pp. 159–170. DOI: 10.1016/S0022-3115(02)01095-4.

Singh, B.N, D.J Edwards, and P Toft (2001). "Effect of neutron irradiation and post-irradiation annealing on microstructure and mechanical properties of OFHC-copper". In: *Journal of Nuclear Materials* 299.3, pp. 205–218. ISSN: 0022-3115. DOI: https://doi.org/10.1016/S0022-3115(01)00698-5. URL: http://www.sciencedirect.com/science/article/pii/S0022311501006985.

Singh, B.N, A Horsewell, and P Toft (1999). "Effects of neutron irradiation on microstructure and mechanical properties of pure iron". In: *Journal of Nuclear Materials* 271-272, pp. 97–101. ISSN: 0022-3115. DOI: https://doi.org/10.1016/S0022-3115(98)00767-3. URL: http://www.sciencedirect.com/science/article/pii/S0022311598007673.

Sugiyama, M., K. Fukumoto, and H. Matsui (2004). "Dislocation channel formation process in V-Cr-Ti alloys irradiated below 300°C". In: *Journal of Nuclear Materials* 329-333, pp. 467–471. DOI: `10.1016/j.jnucmat.2004.04.295`.

Sun, L.Z et al. (2000). "3D dislocation dynamics study of plastic instability in irradiated copper". In: *Journal of Nuclear Materials* 283-287. 9th Int. Conf. on Fusion Reactor Materials, pp. 741–745. ISSN: 0022-3115. DOI: `https://doi.org/10.1016/S0022-3115(00)00073-8`. URL: `http://www.sciencedirect.com/science/article/pii/S0022311500000738`.

Tanguy, Benoit, Faiza Sefta, and Pierre Joly (May 2015). "Le vieillissement des internes de cuve. Programme de recherche en support à la durée de fonctionnement des réacteurs REP". In: *Revue Générale Nucléaire* 3, pp. 56–63. ISSN: 0335-5004. DOI: `10.1051/rgn/20153056`. URL: `http://dx.doi.org/10.1051/rgn/20153056`.

Thomas, R. et al. (2019). "Characterisation of irradiation enhanced strain localisation in a zirconium alloy". In: *Materialia* 5, p. 100248. ISSN: 2589-1529. DOI: `https://doi.org/10.1016/j.mtla.2019.100248`. URL: `http://www.sciencedirect.com/science/article/pii/S2589152919300444`.

Torimaru, T. et al. (2010). "Fracture Toughness of Austenitic Stainless Steels after BWR Irradiation." In: *Symposium fontevraud7- Contribution of MAterials Investigations to Improve the Safety and Performance of LWRs.* A060-T02.

Trinkaus, H., B.N. Singh, and A.J.E. Foreman (1997). "Mechanisms for decoration of dislocations by small dislocation loops under cascade damage conditions". In: *Journal of Nuclear Materials* 249, pp. 91–102. DOI: `10.1016/S0022-3115(97)00230-4`.

Trinkhaus, H., B.N. Singh, and A.J.E. Foreman (1997). "Segregation of cascade induced interstitial loops at dislocations : possible effect on initiation of plastic deformation". In: *Journal of Nuclear Materials* 251, pp. 172–187. DOI: `10.1016/S0022-3115(97)00246-8`.

Tucker, R. P., M. S. Wechsler, and S. M. Ohr (Jan. 1969). "Dislocation Channeling in Neutron-Irradiated Niobium". In: *Journal of Applied Physics* 40.1, pp. 400–408. ISSN: 1089-7550. DOI: `10.1063/1.1657068`. URL: `http://dx.doi.org/10.1063/1.1657068`.

Victoria, M et al. (2000). "The microstructure and associated tensile properties of irradiated fcc and bcc metals". In: *Journal of Nuclear Materials* 276.1, pp. 114–122. ISSN: 0022-3115. DOI: `https://doi.org/10.1016/S0022-3115(99)00203-2`. URL: `http://www.sciencedirect.com/science/article/pii/S0022311599002032`.

Weber, G. and L. Anand (1990). "Finite deformation constitutive equations and a time integration procedure for isotropic hyperelastic-viscoplastic solids". In: *Computer Methods in Applied Mechanics and Engineering* 79, pp. 173–202.

Wechsler, M.S. (1973). "Dislocation channeling in irradiated and quenched metals, the inhomogeneity of plastic deformation". In: *ASM, Metals Park, Ohio.*

Willot, François (2015). "Fourier-based schemes for computing the mechanical response of composites with accurate local fields". In: *Comptes Rendus Mécanique* 343.3, pp. 232–245. ISSN: 1631-0721. DOI: https://doi.org/10.1016/j.crme.2014.12.005. URL: http://www.sciencedirect.com/science/article/pii/S1631072114002149.

Wilson, C.J.L, J.P. Burg, and J.C. Mitchell (1986). "The origin of kinks in polycrystalline ice". In: *Tectonophysics* 127, pp. 27–48. DOI: 10.1016/0040-1951(86)90077-6.

Wisner, SB, MB Reynolds, and RB Adamson (1994). "Fatigue Behavior of Irradiated and Unirradiated Zircaloy and Zirconium". In: *Zirconium in the Nuclear Industry: Tenth International Symposium*, pp. 499–499–22. DOI: 10.1520/stp15206s. URL: http://dx.doi.org/10.1520/STP15206S.

Xiao, X. et al. (2015). "A size-dependent tensorial plasticity model for FCC single crystals with irradiation". In: *International Journal of Plasticity* 65, pp. 152–167. DOI: 10.1016/j.ijplas.2014.09.004.

Yasuda, T., M. Nakatsuka, and K. Yamashita (1987). "Deformation and fracture properties of neutron-irradiated recrystallized Zircaloy-2 cladding under uniaxial tension". In: *Zirconium in the nuclear industry: 7th international symposium.* Ed. by ASTM. Vol. STP 939, pp. 734–747.

Zeman, J. et al. (2010). "Accelerating a FFT-based solver for numerical homogenization of periodic media by conjugate gradients". In: *Journal of Computational Physics* 229.21, pp. 8065–8071. DOI: https://doi.org/10.1016/j.jcp.2010.07.010.

Zhang, M. et al. (2010). "Simulation of slip band evolution in duplex Ti–6Al–4V". In: *Acta Materialia* 58.3, pp. 1087–1096. ISSN: 1359-6454. DOI: https://doi.org/10.1016/j.actamat.2009.10.025. URL: http://www.sciencedirect.com/science/article/pii/S1359645409007198.

Zhang, Xiaohan (2017). "A continuum model for dislocation pile-up problems". In: *Acta Materialia* 128, pp. 428–439. ISSN: 1359-6454. DOI: https://doi.org/10.1016/j.actamat.2017.01.057. URL: http://www.sciencedirect.com/science/article/pii/S1359645417300824.

Zinkle, S.J., P.J. Maziasz, and R.E. Stoller (1993). "Dose dependence of the microstructural evolution in neutron-irradiated austenitic stainless steel". In: *Journal of Nuclear Materials* 206.2, pp. 266–286. ISSN: 0022-3115. DOI: https://doi.org/10.1016/0022-3115(93)90128-L. URL: http://www.sciencedirect.com/science/article/pii/002231159390128L.

APPENDIX A

This first appendix provides the definition of the mathematical operators and formulas used throughout this document are listed in section.

Throughout this document, the points $\boldsymbol{M}$ of the Euclidean space are characterized by classical cartesian coordinates x_i: $\boldsymbol{M} = \boldsymbol{M}(x_i)$. The canonical basis vectors are defined as: $\boldsymbol{e}_i = \frac{\partial \boldsymbol{M}}{\partial x_i}$.

Unless explicitly stated, the Einstein summation convention is used in all tensorial expressions: summation over all values of repeated indexes is implied by this convention. For instance: $x_i y_i = \sum\limits_{i=1}^{3} x_i y_i$.

The symbol δ_{ij} denotes the Kronecker symbol.

A.1   Tensor operations

- **First order tensor product**:

$$\underline{C} = \boldsymbol{a} \otimes \boldsymbol{b} \qquad \rightarrow \qquad C_{ij} = a_i b_j$$

- **Second order tensors products**:

$$\underline{\underline{C}} = \underline{\boldsymbol{A}} \otimes \underline{\boldsymbol{B}} \qquad \rightarrow \qquad C_{ijkl} = A_{ij} B_{kl}$$
$$\underline{\underline{C}} = \underline{\boldsymbol{A}} \;\overline{\otimes}\; \underline{\boldsymbol{B}} \qquad \rightarrow \qquad C_{ijkl} = A_{il} B_{jk}$$
$$\underline{\underline{C}} = \underline{\boldsymbol{A}} \;\underline{\otimes}\; \underline{\boldsymbol{B}} \qquad \rightarrow \qquad C_{ijkl} = A_{ik} B_{jl}$$

271

- **Tensor contractions**:

$$
\begin{aligned}
c &= \boldsymbol{a} \cdot \boldsymbol{b} & \rightarrow \quad & c &&= a_i b_i \\
c &= \underline{\boldsymbol{A}} : \underline{\boldsymbol{B}} & \rightarrow \quad & c &&= A_{ij} B_{ij} \\
\boldsymbol{c} &= \underline{\boldsymbol{A}} \cdot \boldsymbol{b} & \rightarrow \quad & c_i &&= A_{ij} b_j \\
\boldsymbol{c} &= \boldsymbol{a} \cdot \underline{\boldsymbol{B}} & \rightarrow \quad & c_i &&= a_i B_{ij} \\
\underline{\boldsymbol{C}} &= \underline{\boldsymbol{A}} \cdot \underline{\boldsymbol{B}} & \rightarrow \quad & C_{ij} &&= A_{ik} B_{kj} \\
\underline{\boldsymbol{C}} &= \underline{\underline{\boldsymbol{A}}} : \underline{\boldsymbol{B}} & \rightarrow \quad & C_{ij} &&= A_{ijkl} B_{kl} \\
\underline{\boldsymbol{C}} &= \underline{\boldsymbol{A}} : \underline{\underline{\boldsymbol{B}}} & \rightarrow \quad & C_{ij} &&= A_{kl} B_{klij} \\
\underline{\underline{\boldsymbol{C}}} &= \underline{\underline{\boldsymbol{A}}} : \underline{\underline{\boldsymbol{B}}} & \rightarrow \quad & C_{ijkl} &&= A_{ijmn} B_{mnkl}
\end{aligned}
$$

Sometimes in the document, expression with a simple contracted product are noted without the central dot: $\underline{\boldsymbol{A}} \cdot \underline{\boldsymbol{B}} = \underline{\boldsymbol{A}}\underline{\boldsymbol{B}}$, in order to shorten long expression.

- **Levi-Civita permutation tensor**:

$$
\epsilon_{ijk} = \begin{cases} +1 & \text{if } (i,j,k) \text{ is an even permutation} \\ -1 & \text{if } (i,j,k) \text{ is an odd permutation} \\ 0 & \text{otherwise} \end{cases} \tag{A.1}
$$

$$
\epsilon_{ijk} = \epsilon_{jki} = \epsilon_{kij} \tag{A.2}
$$
$$
\epsilon_{ijk} = -\epsilon_{ikj} \tag{A.3}
$$
$$
\epsilon_{ijj} = 0 \tag{A.4}
$$

- **Cross product**:

$$
\boldsymbol{c} = \boldsymbol{a} \times \boldsymbol{b} = \underset{\sim}{\boldsymbol{\epsilon}} : (\boldsymbol{a} \otimes \boldsymbol{b}) = \epsilon_{ijk} a_j b_k \boldsymbol{e}_i = (\boldsymbol{a} \otimes \boldsymbol{b}) : \underset{\sim}{\boldsymbol{\epsilon}} = a_i b_j \epsilon_{ijk} \boldsymbol{e}_k
$$

- **Partial derivatives**:

$$
\frac{\partial \underline{\boldsymbol{A}} \cdot \underline{\boldsymbol{B}}}{\partial \underline{\boldsymbol{B}}} = \frac{\partial A_{im} B_{mj}}{\partial B_{kl}} = A_{im} \frac{\partial B_{mj}}{\partial B_{kl}} = A_{ik} \delta_{jl} = \boxed{\underline{\boldsymbol{A}} \otimes \underline{\boldsymbol{1}}}
$$

$$
\frac{\partial \underline{\boldsymbol{A}} \cdot \underline{\boldsymbol{B}}}{\partial \underline{\boldsymbol{A}}} = \frac{\partial A_{im} B_{mj}}{\partial A_{kl}} = B_{mj} \frac{\partial A_{im}}{\partial A_{kl}} = B_{lj} \delta_{ik} = \boxed{\underline{\boldsymbol{1}} \otimes \underline{\boldsymbol{B}}^T}
$$

$$\frac{\partial \underline{A}(\underline{C}) \cdot \underline{B}(\underline{C})}{\partial \underline{C}} = \frac{\partial A_{im} B_{mj}}{\partial C_{kl}} = \frac{\partial A_{im}}{\partial A_{pq}} B_{mj} \frac{\partial A_{pq}}{\partial C_{kl}} + A_{im} \frac{\partial B_{mj}}{\partial B_{pq}} \frac{\partial B_{pq}}{\partial C_{kl}}$$

$$= \delta_{ip} \delta_{mq} B_{mj} \frac{\partial A_{pq}}{\partial C_{kl}} + A_{im} \delta_{mp} \delta_{jq} \frac{\partial B_{pq}}{\partial C_{kl}} = \delta_{ip} B_{qj} \frac{\partial A_{pq}}{\partial C_{kl}} + A_{ip} \delta_{jq} \frac{\partial B_{pq}}{\partial C_{kl}}$$

$$= \boxed{(\underline{1} \otimes \underline{B}^T) : \frac{\partial \underline{A}}{\partial \underline{C}} + (\underline{1} \otimes \underline{A}) : \frac{\partial \underline{B}}{\partial \underline{C}}}$$

$$\frac{\partial \underline{A}^T}{\partial \underline{A}} = \frac{\partial A_{ji}}{\partial A_{kl}} = \delta_{jk} \delta_{il} = \boxed{\underline{1} \,\overline{\otimes}\, \underline{1}}$$

$$\frac{\partial \underline{A} : \underline{B}}{\partial \underline{A}} = \frac{\partial A_{ij} B_{ij}}{\partial A_{kl}} = \delta_{ik} \delta_{jl} B_{ij} = \boxed{\underline{B}}$$

A.2   Usefull tensors

- **Identity tensors**:

$$\underline{1} : \quad 1_{ij} \;\; = \delta_{ij} \tag{A.5}$$

$$\underline{\underline{1}} : \quad 1_{ijkl} = \frac{1}{2} \left(\delta_{ik} \delta_{jl} + \delta_{il} \delta_{jk} \right) \tag{A.6}$$

- **Projection tensors**:

  - Projectors $\underline{\underline{\mathcal{K}}}$ and $\underline{\underline{\mathcal{J}}}$ respectively on spherical and deviatoric part:

$$\underline{\underline{\mathcal{K}}} = \tfrac{1}{3} \underline{1} \otimes \underline{1} \tag{A.7}$$

$$\underline{\underline{\mathcal{J}}} = \underline{\underline{1}} - \underline{\underline{\mathcal{K}}} \tag{A.8}$$

  - Let $\mathcal{P}$, $\boldsymbol{N}$, and $(\boldsymbol{T}_1, \boldsymbol{T}_2)$ be respectively a plane, the normal to the plane direction unit vector, and two in-plane unit vectors, such that $(\boldsymbol{N}, \boldsymbol{T}_1, \boldsymbol{T}_2)$ forms a base.
    A second order tensor $\underline{A}$ can be decomposed into its in-plane part $\underline{A}^{\mathcal{P}}$ and its normal to the plane part $\underline{A}^N$, defined as follow:

$$\underline{A}^N = \underline{\underline{P}}^N : \underline{A} \tag{A.9}$$

$$\underline{A}^{\mathcal{P}} = \underline{\underline{P}}^{\mathcal{P}} : \underline{A} \tag{A.10}$$

    where the fourth order tensors $\underline{\underline{P}}^N$ and $\underline{\underline{P}}^{\mathcal{P}}$ are the projectors on respec-

tively the normal to the plane and in-plane tensors spaces for second order tensors, and are defined as follow:

$$
\begin{aligned}
\underline{\underline{P}}^N = {}& (\boldsymbol{N} \otimes \boldsymbol{N}) \otimes (\boldsymbol{N} \otimes \boldsymbol{N}) + (\boldsymbol{N} \otimes \boldsymbol{T}_1) \otimes (\boldsymbol{N} \otimes \boldsymbol{T}_1) \\
& + (\boldsymbol{N} \otimes \boldsymbol{T}_2) \otimes (\boldsymbol{N} \otimes \boldsymbol{T}_2) + (\boldsymbol{T}_1 \otimes \boldsymbol{N}) \otimes (\boldsymbol{T}_1 \otimes \boldsymbol{N}) \\
& + (\boldsymbol{T}_2 \otimes \boldsymbol{N}) \otimes (\boldsymbol{T}_2 \otimes \boldsymbol{N})
\end{aligned}
\tag{A.11}
$$

$$
\begin{aligned}
\underline{\underline{P}}^{\mathcal{P}} = {}& (\boldsymbol{T}_1 \otimes \boldsymbol{T}_1) \otimes (\boldsymbol{T}_1 \otimes \boldsymbol{T}_1) + (\boldsymbol{T}_2 \otimes \boldsymbol{T}_2) \otimes (\boldsymbol{T}_2 \otimes \boldsymbol{T}_2) \\
& + (\boldsymbol{T}_1 \otimes \boldsymbol{T}_2) \otimes (\boldsymbol{T}_1 \otimes \boldsymbol{T}_2) + (\boldsymbol{T}_2 \otimes \boldsymbol{T}_1) \otimes (\boldsymbol{T}_2 \otimes \boldsymbol{T}_1)
\end{aligned}
\tag{A.12}
$$

such that $\underline{\underline{P}}^{\mathcal{P}} = \underline{\underline{1}} - \underline{\underline{P}}^N$, and:

$$
\begin{aligned}
\underline{A}^N = {}& A_{NN}(\boldsymbol{N} \otimes \boldsymbol{N}) + A_{NT_1}(\boldsymbol{N} \otimes \boldsymbol{T}_1) + A_{NT_2}(\boldsymbol{N} \otimes \boldsymbol{T}_2) \\
& + A_{T_1 N}(\boldsymbol{T}_1 \otimes \boldsymbol{N}) + A_{T_2 N}(\boldsymbol{T}_2 \otimes \boldsymbol{N})
\end{aligned}
\tag{A.13}
$$

$$
\begin{aligned}
\underline{A}^{\mathcal{P}} = {}& A_{T_1 T_1}(\boldsymbol{T}_1 \otimes \boldsymbol{T}_1) + A_{T_2 T_2}(\boldsymbol{T}_2 \otimes \boldsymbol{T}_2) + A_{T_1}(\boldsymbol{T}_1 \otimes \boldsymbol{T}_2) \\
& + A_{T_2 T_1}(\boldsymbol{T}_2 \otimes \boldsymbol{T}_1)
\end{aligned}
\tag{A.14}
$$

A.3   Tensor Analysis

- **Differential operators**:

  Let $\boldsymbol{T} = T_{i_1 \cdots i_k}\, \boldsymbol{e}_{i_1} \otimes \cdots \otimes \boldsymbol{e}_{i_k}$ be a tensor field of arbitrary order k. Differential operators are then defined as follow:

  Gradient operator:

  $$
  \mathrm{grad}(\boldsymbol{T}) = T_{i_1 \cdots i_k, j}\, \boldsymbol{e}_{i_1} \otimes \cdots \otimes \boldsymbol{e}_{i_k} \otimes \boldsymbol{e}_{i_j}
  $$

  Divergence operator:

  $$
  \mathrm{div}(\boldsymbol{T}) = T_{i_1 \cdots i_{k-1}j, j}\, \boldsymbol{e}_{i1} \otimes \cdots \otimes \boldsymbol{e}_{i_{k-1}}
  $$

  Curl operator:

  $$
  \mathrm{curl}(\boldsymbol{T}) = \underline{\boldsymbol{\varepsilon}} : grad(\boldsymbol{T}) = \epsilon_{jms} T_{i_1 \cdots i_{k-1}m, s}\, \boldsymbol{e}_{i_1} \otimes \cdots \otimes \boldsymbol{e}_{i_{k-1}} \otimes \boldsymbol{e}_j
  $$

  The gradient operator increases the order of the tensor by one, the curl operator leaves it unchanged, and the divergence operator decreases it by one. Applied for scalar f, vector $\boldsymbol{u}$, and second order tensor fields $\underline{A}$, theses

formula lead to the particular expressions:

$$\text{grad}(f) = f_{,i}\boldsymbol{e}_i \tag{A.15}$$
$$\text{grad}(\boldsymbol{u}) = u_{i,j}\boldsymbol{e}_i \otimes \boldsymbol{e}_j \tag{A.16}$$
$$\text{grad}(\underline{\boldsymbol{A}}) = A_{ij,k}\boldsymbol{e}_i \otimes \boldsymbol{e}_j \otimes \boldsymbol{e}_k \tag{A.17}$$

$$\text{div}(\boldsymbol{u}) = u_{i,i} \tag{A.18}$$
$$\text{div}(\underline{\boldsymbol{A}}) = A_{ij,j}\boldsymbol{e}_i \tag{A.19}$$

$$\text{curl}(\boldsymbol{u}) = \epsilon_{kij}u_{i,j}\boldsymbol{e}_k \tag{A.20}$$
$$\text{curl}(\underline{\boldsymbol{A}}) = \epsilon_{jms}A_{im,s}\boldsymbol{e}_i \otimes \boldsymbol{e}_j \tag{A.21}$$

- **Formulas**:

  We recall here Stoke's formula, for a vector field $\boldsymbol{u}$ and an oriented surface $\mathcal{S}$ with unit normal vector $\boldsymbol{N}$ and border $\mathcal{L}$.

  Stoke's formula

$$\oint_{\mathcal{L}} u_i dl_i = -\epsilon_{kij}\int_{\mathcal{S}} u_{i,j}N_k dS \tag{A.22}$$

  From Stoke's formula can be derived the Stoke's theorem, which links the circulation of a tensor field around $\mathcal{L}$ to the flux of its curl through $\mathcal{S}$. Its exact expression derives from Stoke's formula and the adopted definition of the curl operator, and thus is not unique. Using the above definition, we get the Stoke's theorem for vector and second order tensor fields.

  Stoke's theorem

$$\oint_{\mathcal{L}} \boldsymbol{u} \cdot \boldsymbol{dl} = -\int_{\mathcal{S}} \text{curl}(\boldsymbol{u}) \cdot \boldsymbol{N} dS \tag{A.23}$$
$$\oint_{\mathcal{L}} \underline{\boldsymbol{A}} \cdot \boldsymbol{dl} = -\int_{\mathcal{S}} \text{curl}(\underline{\boldsymbol{A}}) \cdot \boldsymbol{N} dS \tag{A.24}$$

  We recall additionally the divergence theorem, for a vector or a second order tensor field, that links its flux over a surface $\mathcal{S}$ to the volume integral of its divergence.

Divergence theorem

$$\oint_{\mathcal{S}} \boldsymbol{u} \cdot \boldsymbol{N} \, dS = \int_{\mathcal{V}} \operatorname{div}(\boldsymbol{u}) \, dV \tag{A.25}$$

$$\oint_{\mathcal{S}} \underline{\boldsymbol{u}} \cdot \boldsymbol{N} \, dS = \int_{\mathcal{V}} \operatorname{div}(\underline{\boldsymbol{u}}) \, dV \tag{A.26}$$

A.4 Discrete Fourier transform

We consider a three dimensional domain Ω, discretized with a regular grid Ω_d, defined by the orthogonal unit vectors $\boldsymbol{e_1}$, $\boldsymbol{e_2}$ and $\boldsymbol{e_3}$ and whose points are characterized by an index triplet: $\boldsymbol{x} = \boldsymbol{x}(i_1, i_2, i_3)$, with $i_1 \in [\![0, N_1 - 1]\!]$, $i_2 \in [\![0, N_2 - 1]\!]$, $i_3 \in [\![0, N_3 - 1]\!]$. Let f be a scalar field defined over Ω_d such that:

$$f(i_1, i_2, i_3) = f(\boldsymbol{x}[i_1, i_2, i_3]) \tag{A.27}$$

The discrete Fourier transform of f is then defined by:

$$\begin{aligned}
\hat{f}(k_1, k_2, k_3) &= \sum_{i_1=0}^{N_1-1} \sum_{i_2=0}^{N_2-1} \sum_{i_3=0}^{N_3-1} f(i_1, i_2, i_3) e^{-j \frac{2\pi k_1 i_1}{N_1}} e^{-j \frac{2\pi k_2 i_2}{N_2}} e^{-j \frac{2\pi k_3 i_3}{N_3}} \\
\hat{f}(\xi_1, \xi_2, \xi_3) &= \sum_{i_1=0}^{N_1-1} \sum_{i_2=0}^{N_2-1} \sum_{i_3=0}^{N_3-1} f(i_1, i_2, i_3) e^{-j \xi_1 i_1} e^{-j \xi_2 i_2} e^{-j \xi_3 i_3}
\end{aligned} \tag{A.28}$$

with:

$$k_1 \in [\![0, N_1 - 1]\!], \ k_2 \in [\![0, N_2 - 1]\!], \ k_3 \in [\![0, N_3 - 1]\!]$$

$$\xi_1 \in [-\pi, \pi \frac{N_1 - 1}{N_1}], \ \xi_2 \in [-\pi, \pi \frac{N_2 - 1}{N_2}], \ \xi_3 \in [-\pi, \pi \frac{N_3 - 1}{N_3}]$$

where (ξ_1, ξ_2, ξ_3) and (k_1, k_2, k_3) are respectively the coordinates and associated index in the discrete Fourier space $\hat{\Omega}_d$, and j is the complex unity. They are linked by the relation:

$$\xi_i = \frac{2\pi \left(k_i - \frac{N_i}{2}\right)}{N_i} \tag{A.29}$$

The previous equation can be simplified using the vector notations: $\boldsymbol{\xi} = (\xi_1, \xi_2, \xi_3)$ and $\boldsymbol{x} = (i_1, i_2, i_3)$.

$$\hat{f}(\boldsymbol{\xi}) = \sum_{\boldsymbol{x}_i \in \Omega_d} f(\boldsymbol{x}_i) e^{-j\boldsymbol{\xi} \cdot \boldsymbol{x}_i} \tag{A.30}$$

Similarly the inverse discrete Fourier transform is defined as follow:

$$f(i_1, i_2, i_3) = \sum_{k_1=0}^{N_1-1} \sum_{k_2=0}^{N_2-1} \sum_{k_3=0}^{N_3-1} \hat{f}(k_1, k_2, k_3) \frac{1}{N_1 N_2 N_3} e^{j\frac{2\pi k_1 i_1}{N_1}} e^{j\frac{2\pi k_2 i_2}{N_2}} e^{j\frac{2\pi k_3 i_3}{N_3}}$$

$$f(\boldsymbol{x}) = \sum_{\boldsymbol{\xi}_i \in \hat{\Omega}_d} \hat{f}(\boldsymbol{\xi}_i) e^{j\boldsymbol{\xi}_i \cdot \boldsymbol{x}} \tag{A.31}$$

A.5 Intrinsic discrete Fourier 27-voxels centered Finite Differences frequencies

(a)　　　　　(b)
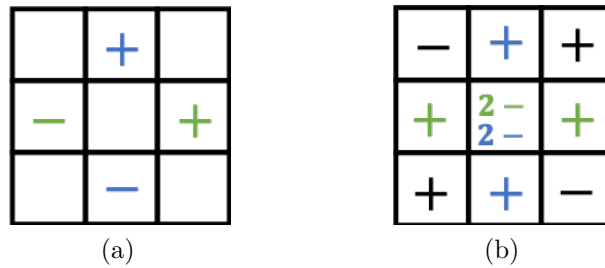
Figure A.1 – Schematization in 2D of the 27-voxels centered finite difference action scheme to compute derivatives on the central voxel. First order finite differences are represented in (a), second order in (b). Derivation along x_1 is represented in green, along x_2 in blue, crossed derivation in black.

We give here the detailed calculation that allow to retrieve the expression of the modified frequencies presented in table 4.1. First we give the expression of the 27-voxels centered Finite Differences operators used to define the discrete approximations of the first and second order derivatives of a field f, (illustrated on the diagram of fig. A.1). For the first order derivatives they are:

$$f_{,1}(i_1, i_2, i_3) = \frac{1}{2dx_1} [f(i_1 + 1, i_2, i_3) - f(i_1 - 1, i_2, i_3)] \tag{A.32}$$

$$f_{,2}(i_1, i_2, i_3) = \frac{1}{2dx_2} [f(i_1, i_2 + 1, i_3) - f(i_1, i_2 - 1, i_3)] \tag{A.33}$$

$$f_{,3}(i_1, i_2, i_3) = \frac{1}{2dx_3} \left[f(i_1, i_2, i_3 + 1) - f(i_1, i_2, i_3 - 1) \right] \tag{A.34}$$

$$\tag{A.35}$$

For the second order derivatives they are:

$$f_{,11}(i_1, i_2, i_3) = \frac{1}{dx_1^2} \left[f(i_1 + 1, i_2, i_3) - 2f(i_1, i_2, i_3) + f(i_1 - 1, i_2, i_3) \right] \tag{A.36}$$

$$f_{,22}(i_1, i_2, i_3) = \frac{1}{dx_2^2} \left[f(i_1, i_2 + 1, i_3) - 2f(i_1, i_2, i_3) + f(i_1, i_2 - 1, i_3) \right] \tag{A.37}$$

$$f_{,33}(i_1, i_2, i_3) = \frac{1}{dx_3^2} \left[f(i_1, i_2, i_3 + 1) - 2f(i_1, i_2, i_3) + f(i_1, i_2, i_3 - 1) \right] \tag{A.38}$$

$$\begin{aligned} f_{,12}(i_1, i_2, i_3) = \frac{1}{4dx_1 dx_2} &\left[f(i_1 + 1, i_2 + 1, i_3) - f(i_1 + 1, i_2 - 1, i_3) \right. \\ &\left. - f(i_1 - 1, i_2 + 1, i_3) + f(i_1 - 1, i_2 - 1, i_3) \right] \end{aligned} \tag{A.39}$$

$$\begin{aligned} f_{,13}(i_1, i_2, i_3) = \frac{1}{4dx_1 dx_3} &\left[f(i_1 + 1, i_2, i_3 + 1) - f(i_1 + 1, i_2 - 1, i_3 - 1) \right. \\ &\left. - f(i_1 - 1, i_2, i_3 + 1) + f(i_1 - 1, i_2, i_3 - 1) \right] \end{aligned}$$

$$\begin{aligned} f_{,23}(i_1, i_2, i_3) = \frac{1}{4dx_2 dx_3} &\left[f(i_1, i_2 + 1, i_3 + 1) - f(i_1, i_2 + 1, i_3 - 1) \right. \\ &\left. - f(i_1, i_2 - 1, i_3 + 1) + f(i_1, i_2 - 1, i_3 - 1) \right] \end{aligned} \tag{A.40}$$

Taking the Fourier transform of eq. (A.32), we get

$$\begin{aligned} \hat{f}_{,1}(k_1, k_2, k_3) =& \frac{1}{2dx_1} \left[\hat{f}(i_1 + 1, i_2, i_3) - \hat{f}(i_1 - 1, i_2, i_3) \right] \\ =& \frac{1}{2dx_1} \sum_{i_1=0}^{N_1-1} \sum_{i_2=0}^{N_2-1} \sum_{i_3=0}^{N_3-1} \left[f(i_1 + 1, i_2, i_3) - f(i_1 - 1, i_2, i_3) \right] e^{-j2\pi \left(\frac{k_1 i_1}{N_1} + \frac{k_2 i_2}{N_2} \frac{k_3 i_3}{N_3} \right)} \\ =& \frac{e^{j2\pi \frac{k_1}{N_1}}}{2dx_1} \sum_{i_1=0}^{N_1-1} \sum_{i_2=0}^{N_2-1} \sum_{i_3=0}^{N_3-1} f(i_1 + 1, i_2, i_3) e^{-j2\pi \left(\frac{k_1 (i_1+1)}{N_1} + \frac{k_2 i_2}{N_2} \frac{k_3 i_3}{N_3} \right)} \\ &- \frac{e^{-j2\pi \frac{k_1}{N_1}}}{2dx_1} \sum_{i_1=0}^{N_1-1} \sum_{i_2=0}^{N_2-1} \sum_{i_3=0}^{N_3-1} f(i_1 - 1, i_2, i_3) e^{-j2\pi \left(\frac{k_1 (i_1-1)}{N_1} + \frac{k_2 i_2}{N_2} \frac{k_3 i_3}{N_3} \right)} \end{aligned}$$

At this step, the following substitutions are made: $i_1' = i_1 + 1$ and $i_1'' = i_1 - 1$, we have:

$$\hat{f}_{,1}(k_1, k_2, k_3) = \frac{e^{j2\pi \frac{k_1}{N_1}}}{2dx_1} \sum_{i_1'=1}^{N_1} \sum_{i_2=0}^{N_2-1} \sum_{i_3=0}^{N_3-1} f(i_1', i_2, i_3) e^{-j2\pi \left(\frac{k_1 i_1'}{N_1} + \frac{k_2 i_2}{N_2} \frac{k_3 i_3}{N_3} \right)}$$

$$-\frac{e^{-j2\pi\frac{k_1}{N_1}}}{2dx_1}\sum_{i_1''=-1}^{N_1-2}\sum_{i_2=0}^{N_2-1}\sum_{i_3=0}^{N_3-1}f(i_1'',i_2,i_3)e^{-j2\pi\left(\frac{k_1i_1''}{N_1}+\frac{k_2i_2}{N_2}\frac{k_3i_3}{N_3}\right)}$$

$$=\frac{e^{j2\pi\frac{k_1}{N_1}}-e^{-j2\pi\frac{k_1}{N_1}}}{2dx_1}\sum_{i_1=0}^{N_1-1}\sum_{i_2=0}^{N_2-1}\sum_{i_3=0}^{N_3-1}f(i_1,i_2,i_3)e^{-j2\pi\left(\frac{k_1i_1}{N_1}+\frac{k_2i_2}{N_2}\frac{k_3i_3}{N_3}\right)}$$

$$=\frac{i}{dx_1}\sin\left(\frac{2\pi k_1}{N_1}\right)\hat{f}(k_1,k_2,k_3)$$

$$\hat{f}_{,1}(\xi_1,\xi_2,\xi_3)=\frac{i}{dx_1}\sin\left(2\pi\xi_1\right)\hat{f}\hat{f}_{,1}(\xi_1,\xi_2,\xi_3)$$

$$\hat{f}_{,1}=i\xi_1^*\hat{f}$$

which establishes the expression of the modified frequency ξ_1^*. Between the first and the second line of the previous calculation, we have used the fact that $e^{-2\pi j\frac{N_1k_1}{N_1}}=e^0$ and $e^{2\pi j\frac{k_1}{N_1}}=e^{-2\pi j\frac{(N_1-1)k_1}{N_1}}$. The calculation follows the same steps for the expression of ξ_2^* and ξ_3^*.

Now, taking the Fourier transform of eq. (A.39), we get

$$\hat{f}_{,11}(k_1,k_2,k_3)=\frac{1}{dx_1^2}\left[\hat{f}(i_1+1,i_2,i_3)-2\hat{f}(i_1,i_2,i_3)+\hat{f}(i_1-1,i_2,i_3)\right]$$

$$=\frac{1}{dx_1^2}\sum_{i_1=0}^{N_1-1}\sum_{i_2=0}^{N_2-1}\sum_{i_3=0}^{N_3-1}[f(i_1+1,i_2,i_3)-2f(i_1,i_2,i_3)$$

$$+f(i_1-1,i_2,i_3)]e^{-j2\pi\left(\frac{k_1i_1}{N_1}+\frac{k_2i_2}{N_2}\frac{k_3i_3}{N_3}\right)}$$

Then, using the same type of factorization in the exponential terms and substitution as the first calculation, we get

$$\hat{f}_{,11}(k_1,k_2,k_3)=\frac{1}{dx_1^2}\left[e^{j2\pi\frac{k_1}{N_1}}+e^{-j2\pi\frac{k_1}{N_1}}-2\right]\hat{f}(k_1,k_2,k_3)$$

$$=\frac{2}{dx_1^2}\left[\cos\left(\frac{2\pi k_1}{N_1}\right)-1\right]\hat{f}(i_1,i_2,i_3)$$

$$\hat{f}_{,11}(\xi_1,\xi_2,\xi_3)=\frac{2}{dx_1^2}\left[\cos\left(2\pi\xi_1\right)-1\right]\hat{f}\hat{f}_{,1}(\xi_1,\xi_2,\xi_3)$$

$$\hat{f}_{,11}=\xi_{,11}^*\hat{f}$$

which establishes the expression of the modified frequency $\xi_{,11}^*$. The calculation follows the same steps for the expression of $\xi_{,22}^*$ and $\xi_{,33}^*$. Finally, applying the same

steps to , we get

$$f_{,12}(k_1,k_2,k_3) = \frac{1}{4dx_1dx_2}\left[f(i_1+1,i_2+1,i_3) - f(i_1+1,i_2-1,i_3)\right.$$
$$\left. -f(i_1-1,i_2+1,i_3) + f(i_1-1,i_2-1,i_3)\right]$$
$$= \frac{1}{4dx_1dx_2}\sum_{i_1=0}^{N_1-1}\sum_{i_2=0}^{N_2-1}\sum_{i_3=0}^{N_3-1}\left[f(i_1+1,i_2+1,i_3) - f(i_1+1,i_2-1,i_3)\right.$$
$$\left. -f(i_1-1,i_2+1,i_3) + f(i_1-1,i_2-1,i_3)\right]$$
$$= \frac{1}{4dx_1dx_2}\left[e^{j2\pi\frac{k_1}{N_1}}e^{j2\pi\frac{k_2}{N_2}} + e^{-j2\pi\frac{k_1}{N_1}}e^{-j2\pi\frac{k_2}{N_2}}\right.$$
$$\left. -e^{j2\pi\frac{k_1}{N_1}}e^{-j2\pi\frac{k_2}{N_2}} - e^{-j2\pi\frac{k_1}{N_1}}e^{j2\pi\frac{k_2}{N_2}}\right]\hat{f}(k_1,k_2,k_3)$$
$$= \frac{1}{4dx_1dx_2}\left[2\cos\left[2\pi\left(\frac{k_1}{N_1}+\frac{k_2}{N_2}\right)\right]\right.$$
$$\left. -2\cos\left[2\pi\left(\frac{k_1}{N_1}-\frac{k_2}{N_2}\right)\right]\right]\hat{f}(k_1,k_2,k_3)$$
$$\hat{f}_{,12}(\xi_1,\xi_2,\xi_3) = \frac{1}{2dx_1dx_2}\left[\cos\left[2\pi\left(\xi_1+\xi_2\right)\right] - 2\cos\left[2\pi\left(\xi_1-\xi_2\right)\right]\right]\hat{f}(\xi_1,\xi_2,\xi_3)$$
$$\hat{f}_{,12} = \frac{1}{2dx_1dx_2}\xi_{,12}^*\hat{f}$$

which establishes the experssion of the modified frequency $\xi_{,12}^*$. The calculation follows the same steps for the expression of $\xi_{,13}^*$ and $\xi_{,23}^*$.

APPENDIX B

ANALYTICAL CALCULATIONS

This appendix presents the detailed calculations needed to establish the models described in chaps. 3 to 5 and their numerical implementations. Each section is dedicated to the calculations of one chapter of this work.

B.1 Calculations involved in the generic finite strain crystal plasticity model

This section details the calculations involved in chap. 3.

B.1.1 Internal power mass density calculation

The calculation of the internal power mass density of the material for the finite strain crystal plasticity kinematics given by eq. (3.3) in section 3.2.1 is detailed here. We recall that $\underline{L} = \dot{\underline{F}} \cdot \underline{F}^{-1} = \underline{L}^e + \underline{E} \cdot \underline{L}^p \cdot \underline{E}$. The internal power density of the material with respect to current configuration is: $p_i = \underline{\sigma} : \underline{D}$, where $\underline{D} = \overset{\circ}{\underline{L}}$ is the (symmetric) strain-rate tensor. Dividing by ρ and using the symmetry of $\underline{\sigma}$, we get the internal power mass density:

$$p_i^m = \frac{1}{\rho}\underline{\sigma} : \overset{\circ}{\underline{L}} = \frac{1}{\rho}\underline{\sigma} : \underline{L} = \frac{1}{\rho}\left[\underline{\sigma} : \underline{L}^e + \underline{\sigma} : \left(\underline{E} \cdot \underline{L}^p \cdot \underline{E}^{-1}\right)\right]$$

281

In order to express this power density on the intermediate configuration C_i, the following expression are used:

$$J^e = \frac{\rho_i}{\rho} \qquad \underline{\boldsymbol{\sigma}} = \frac{1}{J^e} \underline{\boldsymbol{E}} \cdot \underline{\boldsymbol{\Pi}}^e \cdot \underline{\boldsymbol{E}}^T$$

where $\underline{\boldsymbol{\Pi}}^e$ is the second Piola-Kirchoff stress tensor on the intermediate configuration, and $J^e = \det(\underline{\boldsymbol{E}})$. The power mass density can then be expressed as:

$$
\begin{aligned}
p_i^m &= \frac{1}{\rho_i} \left(\underline{\boldsymbol{E}} \cdot \underline{\boldsymbol{\Pi}}^e \cdot \underline{\boldsymbol{E}}^T \right) : \left(\underline{\dot{\boldsymbol{E}}} \cdot \underline{\boldsymbol{E}}^{-1} \right) + \frac{1}{\rho_i} J^e \underline{\boldsymbol{\sigma}} : \left(\underline{\boldsymbol{E}} \cdot \underline{\dot{\boldsymbol{P}}} \cdot \underline{\boldsymbol{P}}^{-1} \cdot \underline{\boldsymbol{E}}^{-1} \right) \\
&= \frac{1}{\rho_i} \left[E_{ik} \Pi_{kl}^e E_{jl} \dot{E}_{in} E_{nj}^{-1} + J^e \sigma_{ij} E_{ik} \dot{P}_{kl} P_{lm}^{-1} E_{mj}^{-1} \right] \\
&= \frac{1}{\rho_i} \left[\Pi_{kl}^e E_{ik} \dot{E}_{in} + \left(J^e E_{ki}^T \sigma_{ij} E_{mj}^{-T} \right) \dot{P}_{kl} P_{lm}^{-1} \right] \\
&= \frac{1}{\rho_i} \left[\underline{\boldsymbol{\Pi}}^e : \left(\underline{\boldsymbol{E}}^T \cdot \underline{\dot{\boldsymbol{E}}} \right) + \underline{\boldsymbol{\Pi}}^M : \left(\underline{\dot{\boldsymbol{P}}} \cdot \underline{\boldsymbol{P}}^{-1} \right) \right]
\end{aligned}
$$

where $\underline{\boldsymbol{\Pi}}^M = J^e \underline{\boldsymbol{E}}^T \cdot \underline{\boldsymbol{\sigma}} \cdot \underline{\boldsymbol{E}}^{-T}$ is the Mandel stress tensor. Then, considering that $\underline{\boldsymbol{\Pi}}^e$ is a symmetric tensor, that the Green-Lagrange strain rate tensor is:

$$\underline{\dot{\boldsymbol{\mathcal{E}}}}^e = \left(\underline{\boldsymbol{E}}^T \overset{\diamond}{\cdot} \underline{\dot{\boldsymbol{E}}} \right)$$

and identifying the plastic velocity gradient tensor $\underline{\boldsymbol{L}}^p$, we get:

$$\boxed{ p_i^m = \frac{1}{\rho_i} \left[\underline{\boldsymbol{\Pi}}^e : \underline{\dot{\boldsymbol{\mathcal{E}}}}^e + \underline{\boldsymbol{\Pi}}^M : \underline{\boldsymbol{L}}^p \right] } \tag{B.1}$$

B.1.2 Thermodynamically consistent derivation of constitutive equations

We present here the derivation of the constitutive equations for the finite strain crystal plasticity model presented in section 3.2.2.

We recall that ψ is the Helmholtz free energy mass density. Under isothermal conditions, the Clausius-Duhem inequality is written:

$$p_i^m - \dot{\psi} \geq 0 \tag{B.2}$$

We also recall that ψ is a function of the elastic Green-Lagrange strain and of the cumulative plastic slip on each slip system: $\psi = \psi(\underline{\boldsymbol{\mathcal{E}}}^e, \gamma_{cum}^s)$. Thus, using eq. (B.1),

$\underline{\boldsymbol{L}}^p = \sum\limits_{s}^{N} \dot{\gamma}^s \underline{\boldsymbol{\mu}}^s$ and multiplying it by ρ_i, the inequality becomes:

$$\boldsymbol{\Pi}^e : \underline{\dot{\boldsymbol{\mathcal{E}}}}^e + \sum_{s=1}^{N} \tau^s \dot{\gamma}^s - \rho_i \dot{\psi} \geq 0 \tag{B.3}$$

After differentiation of ψ, eq. (B.3) becomes:

$$\left(\boldsymbol{\Pi}^e - \rho_i \frac{\partial \psi}{\partial \underline{\boldsymbol{\mathcal{E}}}^e} \right) : \underline{\dot{\boldsymbol{\mathcal{E}}}}^e + \sum_{s=1}^{N} (\tau^s \dot{\gamma}^s - \tau_c^s \dot{\gamma}_{cum}^s) \geq 0 \tag{B.4}$$

where $\tau_c^s = \rho_i \frac{\partial \psi}{\partial \gamma_{cum}^s}$ is the thermodynamic force associated with γ_{cum}^s, and is the critical resolved shear stress on slip system s. As elastic deformation processes are non dissipative, the first term of eq. (B.3) must vanish. Assuming a classical quadratic potential for the elastic part of the free energy density, we get the relation that governs elasticity of the material:

$$\boxed{\boldsymbol{\Pi}^e = \rho_i \frac{\partial \psi}{\partial \underline{\boldsymbol{\mathcal{E}}}^e} = \underline{\boldsymbol{\Lambda}} : \underline{\boldsymbol{\mathcal{E}}}^e} \tag{B.5}$$

where $\underline{\boldsymbol{\Lambda}}$ is the elastic moduli fourth order tensor. Finally, the model is complemented by the equation of the critical resolved shear stress:

$$\boxed{\tau_c^s = \rho_i \frac{\partial \psi}{\partial \gamma_{cum}^s} = \tau_0^s - \Delta\tau^s \left[1 - \exp\left(-\frac{\gamma_{cum}^s}{\gamma_0^s} \right) \right] + H^s \gamma_{cum}^s} \tag{B.6}$$

With these choices, the residual dissipation is then:

$$\sum_{s=1}^{N} (\tau^s \dot{\gamma}^s - \tau_c^s \dot{\gamma}_{cum}^s) \geq 0 \tag{B.7}$$

We then introduce the dissipation potentials $\boldsymbol{\Omega}^s(\tau^s, \tau_c^s)$ defining the flow rule and the evolution equation of γ_{cum}^s for each slip system:

$$\dot{\gamma}^s = \frac{\partial \boldsymbol{\Omega}^s}{\partial \tau^s} \qquad \dot{\gamma}_{cum}^s = -\frac{\partial \boldsymbol{\Omega}^s}{\partial \tau_c^s} \tag{B.8}$$

It is assumed to depend on the Schmid yield function: $f^s(\tau^s, \tau_c^s) = |\tau^s| - \tau_c^s$ such that $\boldsymbol{\Omega}^s = \boldsymbol{\Omega}^s(f^s(\tau^s, \tau_c^s))$, so that:

$$\dot{\gamma}^s \quad = \text{sign}(\tau^s) \frac{\partial \boldsymbol{\Omega}^s}{\partial f^s} \tag{B.9}$$

$$\dot{\gamma}^s_{cum} = -\frac{\partial \boldsymbol{\Omega}^s}{\partial \tau^s_c} = \frac{\partial \boldsymbol{\Omega}^s}{\partial f^s} = |\dot{\gamma}^s| \tag{B.10}$$

It follows that, under the condition $\frac{\partial \boldsymbol{\Omega}^s}{\partial f^s} > 0$, eq. (B.7) is satisfied. A viscoplastic power law potential and associated flow rule (eq. (3.15)) compatible with these restrictions is chosen:

$$\boldsymbol{\Omega}^s(\tau^s, \tau^s_c) = \frac{K}{n+1}\left\langle \frac{f^s(\tau^s, \tau^s_c)}{K} \right\rangle^{n+1} = \frac{K}{n+1}\left\langle \frac{|\tau^s| - \tau^s_c}{K} \right\rangle^{n+1} \tag{B.11}$$

$$\boxed{\dot{\gamma}^s = \mathrm{sign}(\tau^s)\left\langle \frac{|\tau^s| - \tau^s_c}{K} \right\rangle^n} \tag{B.12}$$

B.1.3   Integration of softening equations used for dislocation channeling modeling

The purpose of this section is to relate the softening term of the generic crystal plasticity model used for the simulations of chap. 3 to the softening rate obtained with physics-based models for irradiated metals available in the literature Arsenlis, Wirth, and Rhee (2004); Barton, Arsenlis, and Marian (2013); Hure et al. (2016); Krishna, Zamiri, and De (2010); Ling et al. (2017); Onimus and Bechade (2009); Patra and McDowell (2012); Xiao et al. (2015).

They principally rely on two mechanisms. The first is the hardening effect of the irradiation induced defects in the crystal. The second is the dislocation channeling mechanism: gliding dislocation interactions with irradiation induced defects lead to the progressive annihilation of the defects and thus to a strong softening in the areas swept by many dislocations. The set of constitutive equations used by all these authors to model these two mechanisms have the same form, and reduces to an exponential decay law of the critical resolved shear stress, similar to (eq. (3.16)), when integrated in the case of single slip.

To illustrate this, we rely on the irradiated Zirconium model presented in Onimus and Bechade (2009). According to the dispersed barrier hardening model the increase in resolved shear stress due the radiation induced dislocation loops is expressed by:

$$\Delta \tau_c = \alpha \mu b \sqrt{Nd} \tag{B.13}$$

where μ is the shear modulus, N is the loop density, d is the loop diameter, b the loop Burgers vector and α the loop obstacle strength. The evolution of the loop

density is given by the equation:

$$\dot{\rho}_l = -k_B \rho_l \left[\sum_{s \in B} |\dot{\gamma}_s| \right] \tag{B.14}$$

where $\rho_l = Nd$, and $s \in B$ denotes the sum over slip systems of the basal plane. During the formation of a dislocation channel, it is reasonable to assume single slip conditions. eq. (B.14) then reduces to:

$$\dot{\rho}_l = -k_B \rho_l |\dot{\gamma}| \tag{B.15}$$

which yields after integration:

$$\rho_l = \rho_0 \exp(-k_B |\gamma|) \tag{B.16}$$

eq. (B.16) is then reintroduced in eq. (B.13) to yield the exponential decay of the critical resolved shear stress:

$$\Delta\tau_c = \alpha\mu b \sqrt{\rho_l} = \alpha\mu b \sqrt{\rho_0} \exp(\frac{-k_B |\gamma|}{2}) \tag{B.17}$$

B.1.4 Numerical integration of the generic crystal plasticity model

We present here the calculation involved in the numerical integration of the generic finite strain crystal plasticity model, presented in section 3.2.3.

Implicit approximation of the elastic strain tensor

Weber and Anand (1990) have shown that, for an equation of the form $\dot{y} = A(y) \cdot y$, the implicit operator:

$$y_{t+\Delta t} = \exp\left(\Delta t A(y_{t+\Delta t})\right) y_t$$

is a consistent first order approximation of the equation. The plastic velocity gradient tensor equation used within the finite strain crystal plasticity framework (eq. (3.7)) has the same form. Indeed, considering that $\underline{\underline{L}}^p = \underline{\underline{\dot{P}}} \cdot \underline{\underline{P}}^{-1}$, it can be written as follow:

$$\underline{\underline{\dot{P}}} = \left[\sum_{s=1}^{N} \dot{\gamma}^s{}_{t+\Delta t} \underline{\underline{\mu}}^s \right] \cdot \underline{\underline{P}}$$

has the same form. Therefore, Weber and Anand (1990) used it to construct the following implicite approximation of $\underline{\boldsymbol{P}}_{t+\Delta t}$:

$$\underline{\boldsymbol{P}}_{t+\Delta t} = \exp\left[\sum_{s=1}^{N} \Delta\gamma^s \underline{\boldsymbol{\mu}}^s\right] \cdot \underline{\boldsymbol{P}}_t \tag{B.18}$$

Using the multiplicative decomposition of the transformation gradient $\underline{\boldsymbol{F}} = \underline{\boldsymbol{E}} \cdot \underline{\boldsymbol{P}}$, allows to write:

$$\underline{\boldsymbol{E}}_{t+\Delta t} \cdot \underline{\boldsymbol{P}}_t^{-1} = \underline{\boldsymbol{E}}_{t+\Delta t} \cdot \underline{\boldsymbol{P}}_{t+\Delta t} \cdot \underline{\boldsymbol{P}}_t^{-1} \tag{B.19}$$

Using eq. (B.18), the implicit approximation of $\underline{\boldsymbol{P}}$ can be substituted in eq. (B.19):

$$\begin{aligned}
\underline{\boldsymbol{E}}_{t+\Delta t} \cdot \underline{\boldsymbol{P}}_t^{-1} &= \underline{\boldsymbol{E}}_{t+\Delta t} \cdot \underline{\boldsymbol{P}}_{t+\Delta t} \cdot \underline{\boldsymbol{P}}_t^{-1} \\
&= \underline{\boldsymbol{E}}_{t+\Delta t} \cdot \exp\left[\sum_{s=1}^{N} \Delta\gamma^s \underline{\boldsymbol{\mu}}^s\right] \cdot \underline{\boldsymbol{P}}_t \cdot \underline{\boldsymbol{P}}_t^{-1} \\
&= \underline{\boldsymbol{E}}_{t+\Delta t} \cdot \exp\left[\sum_{s=1}^{N} \Delta\gamma^s \underline{\boldsymbol{\mu}}^s\right]
\end{aligned}$$

which yields the following expression of $\underline{\boldsymbol{E}}_{t+\Delta t}$:

$$\underline{\boldsymbol{E}}_{t+\Delta t} = \underline{\boldsymbol{E}}_{t+\Delta t} \cdot \underline{\boldsymbol{P}}_t^{-1} \cdot \exp\left[-\sum_{s=1}^{N} \Delta\gamma^s \underline{\boldsymbol{\mu}}^s\right]$$

Finally, the exponential term is approximated by its first order development, and we get the final expression for the approximation of $\underline{\boldsymbol{E}}_{t+\Delta t}$:

$$\underline{\boldsymbol{E}}_{t+\Delta t} = \underline{\boldsymbol{E}}_{t+\Delta t} \cdot \underline{\boldsymbol{P}}_t^{-1} \cdot \left[\underline{\boldsymbol{1}} - \sum_{s=1}^{N} \Delta\gamma^s \underline{\boldsymbol{\mu}}^s\right] \tag{B.20}$$

Then, calculating the associated Green-Lagrange tensor we get:

$$\underline{\boldsymbol{\mathcal{E}}}_{t+\Delta t}^{e} = \frac{1}{2}\left[\underline{\boldsymbol{E}}_{t+\Delta t}^{*T}\cdot\underline{\boldsymbol{E}}_{t+\Delta t}^{*} - \underline{\boldsymbol{1}}\right]$$

$$= \frac{1}{2}\left[\left(\underline{\boldsymbol{F}}_{t+\Delta t}\underline{\boldsymbol{P}}_t^{-1}\left[\underline{\boldsymbol{1}} - \sum_{s=1}^{N}\Delta\gamma^s\underline{\boldsymbol{\mu}}^s\right]\right)^T\cdot\left(\underline{\boldsymbol{F}}_{t+\Delta t}\underline{\boldsymbol{P}}_t^{-1}\left[\underline{\boldsymbol{1}} - \sum_{s=1}^{N}\Delta\gamma^s\underline{\boldsymbol{\mu}}^s\right]\right) - \underline{\boldsymbol{1}}\right]$$

$$= \frac{1}{2}\left[\underline{\boldsymbol{E}}^{*T}\underline{\boldsymbol{E}}^{*} - \underline{\boldsymbol{1}} - 2\sum_{s=1}^{N}\Delta\gamma^s\left(\underline{\boldsymbol{E}}^{*T}\underline{\boldsymbol{E}}^{*}\right)\underline{\boldsymbol{\mu}}^s + \left(\sum_{s=1}^{N}\Delta\gamma^s\underline{\boldsymbol{\mu}}^s\right)^T\underline{\boldsymbol{E}}^{*T}\underline{\boldsymbol{E}}^{*}\left(\sum_{s=1}^{N}\Delta\gamma^s\underline{\boldsymbol{\mu}}^s\right)\right]$$

$$= \underline{\boldsymbol{\mathcal{E}}}^{*} - \sum_{s=1}^{N}\left[\Delta\gamma^s\left(\underline{\boldsymbol{C}}^{*}\cdot\underline{\boldsymbol{\mu}}^s\right)\right] + \frac{1}{2}\left[\left(\sum_{s=1}^{N}\Delta\gamma^s\underline{\boldsymbol{\mu}}^s\right)^T\underline{\boldsymbol{E}}^{*T}\underline{\boldsymbol{E}}^{*}\left(\sum_{s=1}^{N}\Delta\gamma^s\underline{\boldsymbol{\mu}}^s\right)\right]$$

where we used the notation $\underline{\boldsymbol{E}}^{*} = \underline{\boldsymbol{F}}_{t+\Delta t}\cdot\underline{\boldsymbol{P}}_t^{-1}$, $\underline{\boldsymbol{\mathcal{E}}}^{*} = \frac{1}{2}\left(\underline{\boldsymbol{E}}^{*T}\cdot\underline{\boldsymbol{E}}^{*} - \underline{\boldsymbol{1}}\right)$ and $\underline{\boldsymbol{C}} = \underline{\boldsymbol{E}}^{*T}\cdot\underline{\boldsymbol{E}}^{*}$. Neglecting order 2 terms in the previous expression finally yields the elastic strain residual equation:

$$R_{\mathcal{E}^e} = \Delta\underline{\boldsymbol{\mathcal{E}}}^{e} + \underline{\boldsymbol{\mathcal{E}}}^{e} - \underline{\boldsymbol{\mathcal{E}}}^{*} + \sum_{s=1}^{N}\left[\Delta\gamma^s\left(\underline{\boldsymbol{C}}^{*}\cdot\underline{\boldsymbol{\mu}}^s\right)\right] = 0$$

Jacobian matrix

We provide here the detailed calculation of the Jacobian matrix used to compute the Newton-Raphson algorithm (eq. (3.18)). It is recalled that, according to the definition of $\underline{\boldsymbol{E}}^{*} = \underline{\boldsymbol{F}}_{t+\Delta t}\cdot\underline{\boldsymbol{P}}_t^{-1}$, the tensors $\underline{\boldsymbol{\mathcal{E}}}^{*}$ and $\underline{\boldsymbol{C}}^{*}$ are constants during the Newton-Raphson algorithm.

- **Partial derivatives of the elastic strain residual equation** $R_{\mathcal{E}^e}$:

$$R_{\mathcal{E}^e} = \Delta\underline{\boldsymbol{\mathcal{E}}}^{e} + \underline{\boldsymbol{\mathcal{E}}}^{e} - \underline{\boldsymbol{\mathcal{E}}}^{*} + \sum_{s=1}^{N}\left[\Delta\gamma^s\left(\underline{\boldsymbol{C}}^{*}\cdot\underline{\boldsymbol{\mu}}^s\right)\right] = 0$$

  – With respect to $\Delta\underline{\boldsymbol{\mathcal{E}}}^{e}$:

$$\boxed{\frac{\partial R_{\mathcal{E}^e}}{\partial\Delta\underline{\boldsymbol{\mathcal{E}}}^{e}} = \underline{\boldsymbol{1}}} \tag{B.21}$$

  – With respect to $\Delta\gamma^j$:

$$\boxed{\frac{\partial R_{\mathcal{E}^e}}{\partial\Delta\gamma^j} = \underline{\boldsymbol{C}}^{*}\cdot\underline{\boldsymbol{\mu}}^j} \tag{B.22}$$

- **Partial derivatives of the slip residual equation** R_{γ^s}:

$$R_{\gamma^s} = \Delta\gamma^s - \Delta t \, \text{sign}(\tau^s) \left\langle \frac{|\tau^s| - \tau_c^s}{K} \right\rangle^n = 0$$

– With respect to $\Delta\underline{\boldsymbol{\mathcal{E}}}^e$:

$$\frac{\partial R_{\gamma^s}}{\partial \Delta\underline{\boldsymbol{\mathcal{E}}}^e} = -\Delta t \, \text{sign}(\tau^s) \, \text{sign}(\tau^s) \frac{n}{K} \left\langle \frac{|\tau^s| - \tau_c^s}{K} \right\rangle^{n-1} \frac{\partial \tau^s}{\partial \Delta\underline{\boldsymbol{\mathcal{E}}}^e}$$

$$= -\Delta t \frac{n}{K} \left\langle \frac{|\tau^s| - \tau_c^s}{K} \right\rangle^{n-1} \frac{\partial \left(\underline{\boldsymbol{\Pi}}^M : \underline{\boldsymbol{\mu}}^s \right)}{\partial \Delta\underline{\boldsymbol{\mathcal{E}}}^e}$$

$$= -\Delta t \frac{n}{K} \left\langle \frac{|\tau^s| - \tau_c^s}{K} \right\rangle^{n-1} \frac{\partial \left(\underline{\boldsymbol{\Pi}}^M : \underline{\boldsymbol{\mu}}^s \right)}{\partial \underline{\boldsymbol{\Pi}}^M} \frac{\partial \underline{\boldsymbol{\Pi}}^M}{\partial \Delta\underline{\boldsymbol{\mathcal{E}}}^e}$$

$$= -\Delta t \frac{n}{K} \left\langle \frac{|\tau^s| - \tau_c^s}{K} \right\rangle^{n-1} \underline{\boldsymbol{\mu}}^s : \frac{\partial \left(\underline{\boldsymbol{C}}^e \cdot \underline{\boldsymbol{\Pi}}^e \right)}{\partial \Delta\underline{\boldsymbol{\mathcal{E}}}^e}$$

$$= -\Delta t \frac{n}{K} \left\langle \frac{|\tau^s| - \tau_c^s}{K} \right\rangle^{n-1} \underline{\boldsymbol{\mu}}^s : \left[\left(\underline{\boldsymbol{1}} \,\underline{\otimes}\, \underline{\boldsymbol{\Pi}}^{eT} \right) : \frac{\partial \underline{\boldsymbol{C}}^e}{\partial \Delta\underline{\boldsymbol{\mathcal{E}}}^e} + \left(\underline{\boldsymbol{1}} \,\underline{\otimes}\, \underline{\boldsymbol{C}}^e \right) : \frac{\partial \underline{\boldsymbol{\Pi}}^e}{\partial \Delta\underline{\boldsymbol{\mathcal{E}}}^e} \right]$$

$$\frac{\partial \underline{\boldsymbol{C}}^e}{\partial \Delta\underline{\boldsymbol{\mathcal{E}}}^e} = \frac{\partial \left(2 \left[\underline{\boldsymbol{\mathcal{E}}}^e + \Delta\underline{\boldsymbol{\mathcal{E}}}^e \right] + \underline{\boldsymbol{1}} \right)}{\partial \Delta\underline{\boldsymbol{\mathcal{E}}}^e}$$

$$= 2 \cdot \underline{\underline{\boldsymbol{1}}}$$

$$\frac{\partial \underline{\boldsymbol{\Pi}}^e}{\partial \Delta\underline{\boldsymbol{\mathcal{E}}}^e} = \frac{\partial \underline{\underline{\boldsymbol{\Lambda}}} : \left(\underline{\boldsymbol{\mathcal{E}}}^e + \Delta\underline{\boldsymbol{\mathcal{E}}}^e \right)}{\partial \Delta\underline{\boldsymbol{\mathcal{E}}}^e}$$

$$= \underline{\underline{\boldsymbol{\Lambda}}}$$

$$\Rightarrow \boxed{ \frac{\partial R_{\gamma^s}}{\partial \Delta\underline{\boldsymbol{\mathcal{E}}}^e} = -\Delta t \frac{n}{K} \left\langle \frac{|\tau^s| - \tau_c^s}{K} \right\rangle^{n-1} \underline{\boldsymbol{\mu}}^s : \left[2 \left(\underline{\boldsymbol{1}} \,\underline{\otimes}\, \underline{\boldsymbol{\Pi}}^{eT} \right) + \left(\underline{\boldsymbol{1}} \,\underline{\otimes}\, \underline{\boldsymbol{C}}^e \right) : \underline{\underline{\boldsymbol{\Lambda}}} \right] }$$

$$(B.23)$$

– With respect to $\Delta\gamma^j$:

$$\frac{\partial R_{\gamma^s}}{\partial\Delta\gamma^j} = \delta_{sj} + \Delta t \operatorname{sign}(\tau^s)\frac{n}{K}\left\langle\frac{|\tau^s|-\tau_c^s}{K}\right\rangle^{n-1}\frac{\partial\tau_c^s}{\partial\Delta\gamma^j}$$

$$\frac{\partial\tau_c^s}{\partial\Delta\gamma^j} = \frac{\partial}{\partial\Delta\gamma^j}\left(\tau_0^s - \Delta\tau^s\left[1 - \exp\left(-\frac{\gamma_{cum}^s}{\gamma_0^s}\right)\right] + H^s\gamma_{cum}^s\right)$$
$$= \frac{\partial\gamma_{cum}^s}{\partial\Delta\gamma^j}\left[H^s - \frac{1}{\gamma_0^s}\exp\left(-\frac{\gamma_{cum}^s}{\gamma_0^s}\right)\right]$$

$$\frac{\partial\gamma_{cum}^s}{\partial\Delta\gamma^j} = \frac{\partial\gamma_{cum}^s}{\partial\Delta|\gamma^j|}\frac{\partial|\gamma^j|}{\partial\Delta\gamma^j} = \delta_{sj}\operatorname{sign}(\gamma^j)$$

$$\Rightarrow \boxed{\frac{\partial R_{\gamma^s}}{\partial\Delta\gamma^j} = \delta_{sj}\left(1 + \Delta t \operatorname{sign}(\tau^s\gamma^j)\frac{n}{K}\left\langle\frac{|\tau^s|-\tau_c^s}{K}\right\rangle^{n-1}\left[H^s - \frac{e^{-\frac{\gamma_{cum}^s}{\gamma_0^s}}}{\gamma_0^s}\right]\right)}$$

$$(B.24)$$

B.1.5   Analytical modeling of slip and kink banding with CCP

This section presents the resolution of the slip localization band modeling problem presented in section 3.3.1, for the specific case of a slip band and a kink band. We recall here the geometry on fig. B.1 and the assumptions of the problem.

We approximate a plastic slip localization band as an elasto-plastic bidimensional layer embedded between two rigid layers and submitted to a pure shear sollicitation (fig. B.1). The following assumptions are made to simplifiy the problem. In the case of the slip band:

1. We consider an infinite localization band: the problem is then independent of the x_m coordinate.
2. The localization band undergoes pure shear:

   $$\boldsymbol{u} = u(x_n)\boldsymbol{m}$$

3. the localization band must accommodate a mean shear strain $\bar\gamma$. This is
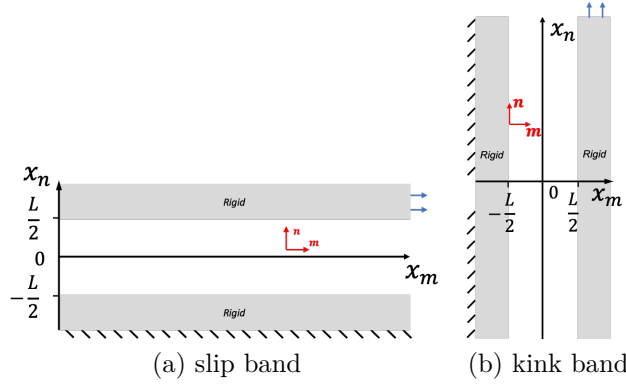
Figure B.1 – Schematic modeling of the local shearing of a crystal within a slip localization band for a slip band (a) and a kink band (b). The central phase is elasto-plastic and deforms through a singe slip system, whose orientation is indicated in red.

equivalent to the boundary conditions:

$$u(-\tfrac{L}{2}) = 0 \quad \text{and} \quad u(\tfrac{L}{2}) = \bar{\gamma}L$$

4. The central phase has a perfectly plastic behavior with only one active slip system, with $\boldsymbol{m}$ and $\boldsymbol{n}$ respectively the glide and normal to slip plane directions. The yield condition is:

$$\tau = \tau_c$$

5. The elastic behavior is linear isotropic, expressed with Lame coefficient (λ, μ) is:

$$\underline{\underline{\boldsymbol{\Pi}}}^e = \lambda \operatorname{tr}(\underline{\underline{\boldsymbol{\mathcal{E}}}}^e)\underline{\underline{\boldsymbol{1}}} + 2\mu\underline{\underline{\boldsymbol{\mathcal{E}}}}^e$$

For the case of the kink band, the assumptions are the same but the directions $\boldsymbol{m}$ and $\boldsymbol{n}$ are inverted.

Slip band

Geometrically, a slip band is defined as a plastic slip localization band perpendicular to the normal to slip plane direction (see fig. 3.2-(a)). Under these conditions and assumptions, the transformation gradient of the considered problem

is:

$$\underline{F} = \underline{1} + u_{,n} \boldsymbol{m} \otimes \boldsymbol{n} \tag{B.25}$$

Under single slip, with the condition $\underline{P}(t=0) = \underline{1}$, $\underline{L}^p = \dot{\underline{P}} \cdot \underline{P}^{-1} = \sum_s^N \dot{\gamma}^s \underline{\mu}^s$ yields:

$$\dot{\underline{P}} \qquad = (\dot{\gamma} \boldsymbol{m} \otimes \boldsymbol{n}) \cdot \underline{P} = \begin{pmatrix} \dot{\gamma} P_{nm} & \dot{\gamma} P_{nn} \\ 0 & 0 \end{pmatrix}$$

$$\dot{\underline{P}}(t=0) = \begin{pmatrix} 0 & \dot{\gamma} \\ 0 & 0 \end{pmatrix}$$

From this expression, we get: $P_{nn}(t) = 1$ and $P_{nm}(t) = 0$, which yields the following expression of $\underline{P}$ and its inverse:

$$\underline{P} = \underline{1} + \gamma \boldsymbol{m} \otimes \boldsymbol{n} \tag{B.26}$$
$$\underline{P}^{-1} = \underline{1} - \gamma \boldsymbol{m} \otimes \boldsymbol{n} \tag{B.27}$$

Using eq. (B.27) and the multiplicative decomposition of $\underline{F}$, we get:

$$\underline{E} = \underline{F} \cdot \underline{P}^{-1} = \begin{pmatrix} 1 & u_{,n} \\ 0 & 1 \end{pmatrix} \begin{pmatrix} 1 & -\gamma \\ 0 & 1 \end{pmatrix} = \begin{pmatrix} 1 & u_{,n} - \gamma \\ 0 & 1 \end{pmatrix} \tag{B.28}$$

and the associate Green-Lagrange elastic strain tensor:

$$\begin{aligned} \underline{\boldsymbol{\mathcal{E}}}^e &= \frac{1}{2} \left(\underline{E}^T \underline{E} - \underline{1} \right) = \frac{1}{2} \left\{ \begin{pmatrix} 1 & 0 \\ u_{,n} - \gamma & 1 \end{pmatrix} \begin{pmatrix} 1 & u_{,n} - \gamma \\ 0 & 1 \end{pmatrix} - \underline{1} \right\} \\ &= \frac{1}{2} \begin{pmatrix} 0 & u_{,n} - \gamma \\ u_{,n} - \gamma & (u_{,n} - \gamma)^2 \end{pmatrix} \end{aligned} \tag{B.29}$$

with the assumption of small elastic strain, we can neglect the quadratic terms in the expression of $\underline{\boldsymbol{\mathcal{E}}}^e$:

$$\underline{\boldsymbol{\mathcal{E}}}^e = \frac{1}{2} (u_{,n} - \gamma) [\boldsymbol{m} \otimes \boldsymbol{n} + \boldsymbol{n} \otimes \boldsymbol{m}] \tag{B.30}$$

Using the elasticity law eq. (B.25), the Piola stress tensor is:

$$\underline{\boldsymbol{\Pi}}^e = \mu (u_{,n} - \gamma) [\boldsymbol{m} \otimes \boldsymbol{n} + \boldsymbol{n} \otimes \boldsymbol{m}] \tag{B.31}$$

Besides, the Piola stress is related to Boussinesq stress by the following relation:

$$
\begin{aligned}
\underline{\mathbf{\Pi}}^e &= J^e \underline{\mathbf{E}}^{-1} \cdot \underline{\boldsymbol{\sigma}} \cdot \underline{\mathbf{E}}^{-T} = J^e \underline{\mathbf{E}}^{-1} \cdot \underline{\boldsymbol{\sigma}} \cdot \left(\underline{\mathbf{F}} \cdot \underline{\mathbf{P}}^{-1} \right)^{-T} = J^e \underline{\mathbf{E}}^{-1} \cdot \underline{\boldsymbol{\sigma}} \cdot \underline{\mathbf{F}}^{-T} \cdot \underline{\mathbf{P}}^{T} \\
&= \underline{\mathbf{E}}^{-1} \cdot \left(J^e \underline{\boldsymbol{\sigma}} \cdot \underline{\mathbf{F}}^{-T} \right) \cdot \underline{\mathbf{P}}^{T} = \underline{\mathbf{E}}^{-1} \cdot \underline{\mathbf{S}} \cdot \underline{\mathbf{P}}^{T}
\end{aligned}
\tag{B.32}
$$

Boussinesq stress is then given by:

$$
\begin{aligned}
\underline{\mathbf{S}} &= \underline{\mathbf{E}} \cdot \underline{\mathbf{\Pi}}^e \cdot \underline{\mathbf{P}}^{-T} \\
&= \begin{pmatrix} 1 & u_{,n} - \gamma \\ 0 & 1 \end{pmatrix} \begin{pmatrix} 0 & \mu\left(u_{,n} - \gamma\right) \\ \mu\left(u_{,n} - \gamma\right) & 0 \end{pmatrix} \begin{pmatrix} 1 & 0 \\ -\gamma & 1 \end{pmatrix} \\
&= \begin{pmatrix} \mu\left(u_{,n} - \gamma\right)^2 & \mu\left(u_{,n} - \gamma\right) \\ \mu\left(u_{,n} - \gamma\right) & 0 \end{pmatrix} \begin{pmatrix} 1 & 0 \\ -\gamma & 1 \end{pmatrix} \\
&= \begin{pmatrix} \mu\left(u_{,n} - \gamma\right)^2 - \mu\gamma\left(u_{,n} - \gamma\right) & \mu\left(u_{,n} - \gamma\right) \\ \mu\left(u_{,n} - \gamma\right) & 0 \end{pmatrix} \\
&\approx \begin{pmatrix} -\mu\gamma\left(u_{,n} - \gamma\right) & \mu\left(u_{,n} - \gamma\right) \\ \mu\left(u_{,n} - \gamma\right) & 0 \end{pmatrix} \\
&\approx \underline{\mathbf{\Pi}}^e - \mu\gamma\left(u_{,n} - \gamma\right) \boldsymbol{m} \otimes \boldsymbol{m}
\end{aligned}
\tag{B.33}
$$

As quadratic strain terms are neglected, the Mandel stress is approximately equal to the Piola stress:

$$
\begin{aligned}
\underline{\mathbf{\Pi}}^M &= \underline{\mathbf{C}}^e \cdot \underline{\mathbf{\Pi}}^e \\
&\approx \begin{pmatrix} 1 & u_{,n} - \gamma \\ u_{,n} - \gamma & 1 \end{pmatrix} \begin{pmatrix} 0 & \mu\left(u_{,n} - \gamma\right) \\ \mu\left(u_{,n} - \gamma\right) & 0 \end{pmatrix} \\
&= \begin{pmatrix} \mu\left(u_{,n} - \gamma\right)^2 & \mu\left(u_{,n} - \gamma\right) \\ \mu\left(u_{,n} - \gamma\right) & \mu\left(u_{,n} - \gamma\right)^2 \end{pmatrix} \approx \begin{pmatrix} 0 & \mu\left(u_{,n} - \gamma\right) \\ \mu\left(u_{,n} - \gamma\right) & 0 \end{pmatrix} \\
&\approx \underline{\mathbf{\Pi}}^e
\end{aligned}
\tag{B.34}
$$

The equilibrium equation $\mathrm{div}(\underline{\mathbf{S}}) = 0$, gives:

$$
\underline{\mathbf{S}}_{mn,n} = \underline{\mathbf{\Pi}}^e_{mn,n} = \tau_{,n} = 0
\tag{B.35}
$$

The resolved shear stress is therefore constant and thus, yield condition is achieved in the whole plastic phase:

$$
\tau = \underline{\mathbf{\Pi}}^M : (\boldsymbol{m} \otimes \boldsymbol{n}) = \underline{\mathbf{\Pi}}^e_{mn} = \mu\left(u_{,n} - \gamma\right) = \tau_c
\tag{B.36}
$$

This relation yields:

$$u_{,m} = \frac{\tau_c}{\mu} + \gamma \tag{B.37}$$

As mentioned above, typical value of the shear modulus and of critical resolved shear verify: $\frac{\tau_c}{\mu} \ll 1$. Finally, we get:

$$u_{,m} \approx \gamma \tag{B.38}$$

It is then straightforward to verify that the solution is the homogeneous plastic slip field $\gamma \simeq \bar{\gamma}$. The expression of the elastic part of the transformation gradient becomes:

$$\boxed{\underline{\underline{E}} \approx \underline{\underline{1}}} \tag{B.39}$$

Kink band

By contrast, a kink band is defined as a plastic slip localization band perpendicular to the glide direction (see fig. B.1-(a)), which yields the following expression of $\underline{\underline{F}}$:

$$\underline{\underline{F}} = \begin{pmatrix} 1 & 0 \\ u_{,m} & 1 \end{pmatrix} \tag{B.40}$$

$\underline{\underline{P}}$ and $\underline{\underline{P}}^{-1}$ are still defined by eqs. (B.26) and (B.27). Calculations of $\underline{\underline{E}}$ and $\underline{\underline{\mathcal{E}}}^e$ yields:

$$\underline{\underline{E}} = \underline{\underline{F}} \cdot \underline{\underline{P}}^{-1} = \begin{pmatrix} 1 & 0 \\ u_{,m} & 1 \end{pmatrix} \begin{pmatrix} 1 & -\gamma \\ 0 & 1 \end{pmatrix} = \begin{pmatrix} 1 & -\gamma \\ u_{,m} & 1 - \gamma u_{,m} \end{pmatrix} \tag{B.41}$$

$$\begin{aligned}
\underline{\underline{\mathcal{E}}}^e &= \frac{1}{2} \left(\underline{\underline{E}}^T \underline{\underline{E}} - \underline{\underline{1}} \right) = \frac{1}{2} \left\{ \begin{pmatrix} 1 & u_{,m} \\ -\gamma & 1 - \gamma u_{,m} \end{pmatrix} \begin{pmatrix} 1 & -\gamma \\ u_{,m} & 1 - \gamma u_{,m} \end{pmatrix} - \underline{\underline{1}} \right\} \\
&= \frac{1}{2} \begin{pmatrix} u_{,m}^2 & u_{,m} - \gamma(1 + u_{,m}^2) \\ u_{,m} - \gamma(1 + u_{,m}^2) & \gamma^2(1 + u_{,m}^2) - 2\gamma u_{,m} \end{pmatrix}
\end{aligned} \tag{B.42}$$

The small elastic strain hypothesis implies that $u_{,m}^2 \ll 1$, which provides a first simplification of eq. (B.42):

$$\underline{\underline{\mathcal{E}}}^e \approx \frac{1}{2}\begin{pmatrix} 0 & u_{,m} - \gamma \\ u_{,m} - \gamma & \gamma(\gamma - u_{,m}) - \gamma u_{,m} \end{pmatrix} \tag{B.43}$$

Then, applying it to non diagonal terms gives: $(u_{,m} - \gamma) \ll 1 \quad \Rightarrow u_{,m} \sim \gamma$. This implies that the term $\mathcal{E}_{nn}$ are of the order of $u_{,m}^2$ and can be neglected as well. In the end, we obtain the same Green-Lagrange elastic strain tensor as in the slip band case, and thus the same Piola stress tensor:

$$\underline{\underline{\mathcal{E}}}^e = \frac{1}{2}\left(u_{,m} - \gamma\right)\left[\boldsymbol{m} \otimes \boldsymbol{n} + \boldsymbol{n} \otimes \boldsymbol{m}\right] \tag{B.44}$$

$$\underline{\underline{\Pi}}^e = \mu\left(u_{,m} - \gamma\right)\left[\boldsymbol{m} \otimes \boldsymbol{n} + \boldsymbol{n} \otimes \boldsymbol{m}\right] \tag{B.45}$$

Calculating $\underline{\underline{\Pi}}^M$ and $\underline{\underline{S}}$ while neglecting quadratic terms yield also the same expression as in the case of the slip band: eq. (B.33) and eq. (B.34), and consequently the end of the calculation is identical. We have again $u_{,m} \approx \gamma$ and a homogeneous solution with $\gamma \simeq \bar{\gamma}$. However this time the expression of $\underline{\underline{E}}$ becomes:

$$\boxed{\underline{\underline{E}} \approx \begin{pmatrix} 1 & -\gamma \\ \gamma & 1 \end{pmatrix}} \tag{B.46}$$

It is evident that the skew symmetric part of $\underline{\underline{E}}$ is non zero, and thus the associated elastic rotation can be calculated. The elastic Cauchy-Green tensor is first computed:

$$\underline{\underline{C}}^e = \underline{\underline{E}}^T \cdot \underline{\underline{E}} = (1 + \gamma^2)\underline{\underline{1}} \tag{B.47}$$

The inverse of the elastic dilatation tensor $\underline{\underline{U}}^{e-1}$ is thus: $\underline{\underline{U}}^{e-1} = \frac{1}{\sqrt{1+\gamma^2}}\underline{\underline{1}}$, which yield the expression of the elastic rotation tensor:

$$\underline{\underline{R}}^e = \underline{\underline{E}} \cdot \underline{\underline{U}}^{e-1} = \begin{pmatrix} \frac{1}{\sqrt{1+\gamma^2}} & \frac{-\gamma}{\sqrt{1+\gamma^2}} \\ \frac{\gamma}{\sqrt{1+\gamma^2}} & \frac{1}{\sqrt{1+\gamma^2}} \end{pmatrix} \approx \begin{pmatrix} \cos(\theta) & -\sin(\theta) \\ \sin(\theta) & \cos(\theta) \end{pmatrix} \tag{B.48}$$

The lattice rotation angle is given by $\theta = \arcsin(\frac{-\gamma}{\sqrt{1+\gamma^2}})$. When γ is relatively small, we obtain the following approximation:

$$|\theta| = |\arcsin(\frac{\gamma}{\sqrt{1+\gamma^2}})| \approx |\arcsin(\gamma)|$$

$$|\theta| \approx |\gamma| \approx \bar{\gamma}$$

B.2 Calculations involved in the GND density tensor based model

This section details the calculations involved in chap. 4.

B.2.1 Principle of virtual power for the Nye tensor based model

We recall that for the considered generalized continuum, the internal power density p^i and the contact power density p^c take the following form:

$$p_i = \underline{\sigma} : \dot{\underline{H}} + \underline{s} : \dot{\underline{H}}^p + \underline{M} : \mathrm{curl}\left(\dot{\underline{H}}^p\right) \tag{B.49}$$

$$p_c = \boldsymbol{t} : \dot{\boldsymbol{u}} + \underline{\boldsymbol{m}} : \dot{\underline{H}}^p \tag{B.50}$$

$\underline{s}$, work-conjugated to $\underline{H}^p$, is the micro-stress tensor, and $\underline{M}$, work-conjugated to $\mathrm{curl}(\underline{H}^p)$, is the double stress tensor, or generalized stress tensor. $\boldsymbol{t}$ is the classical traction vector and $\underline{\boldsymbol{m}}$ the double-traction vector or generalized traction vector. From eq. (B.49), the total power of internal forces on a domain of volume $\mathcal{V}$ bounded by the surface $\mathcal{S}$ is:

$$
\begin{aligned}
P_i = \int_{\mathcal{V}} p_i dV &= \int_{\mathcal{V}} \left(\underline{\sigma} : \dot{\underline{H}} + \underline{s} : \dot{\underline{H}}^p + \underline{M} : \mathrm{curl}\left(\dot{\underline{H}}^p\right) \right) dV \\
&= \int_{\mathcal{V}} \left(\sigma_{ij}\dot{u}_{i,j} + s_{ij}\dot{H}^p_{ij} + M_{ij}\epsilon_{jkl}\dot{H}^p_{ik,l} \right) dV \\
&= \int_{\mathcal{V}} \left((\sigma_{ij}\dot{u}_i)_{,j} - \sigma_{ij,j}\dot{u}_i + s_{ij}\dot{H}^p_{ij} + (\epsilon_{jkl}M_{ij}\dot{H}^p_{ik})_{,l} - \epsilon_{jkl}M_{ij,l}\dot{H}^p_{ik} \right) dV
\end{aligned} \tag{B.51}
$$

after using the divergence theorem, we get:

$$= \oint_{\mathcal{S}} \left(\sigma_{ij}\dot{u}_i n_j + \epsilon_{jkl}M_{ij}\dot{H}^p_{ik}n_l \right) dS - \int_{\mathcal{V}} \left(\sigma_{ij,j}\dot{u}_i + (\epsilon_{jkl}M_{ij,l} - s_{ij})\dot{H}^p_{ik} \right) dV$$

From eq. (B.50), the total power of external contact forces is:

$$P_c = \oint_{\mathcal{S}} p_c dS = \oint_{\mathcal{S}} \left(\boldsymbol{t} : \dot{\boldsymbol{u}} + \underline{\boldsymbol{m}} : \dot{\underline{H}}^p \right) dS = \oint_{\mathcal{S}} \left(t_i \dot{u}_i + m_{ij}\dot{H}^p_{ij} \right) dS \tag{B.52}$$

In the absence of external body forces and inertial forces, the principle of virtual power states that, internal and external contact forces power are equal, for any admissible virtual motion $\dot{u}$ and $\dot{\underline{H}}^p$, and any domain $\mathcal{V}$ of the body. From classical variational arguments, considering the case $\dot{\underline{H}}^p = 0$ yield the first balance

equation eq. (B.53), and the case $\dot{u} = 0$ the second eq. (B.54).

$$\text{div}(\underline{\boldsymbol{\sigma}}) = 0 \qquad\qquad \sigma_{ij,j} = 0 \tag{B.53}$$

$$\text{curl}\,(\underline{\boldsymbol{M}}) + \underline{\boldsymbol{s}} = 0 \qquad \epsilon_{jkl} M_{ik,l} + s_{ij} = 0 \tag{B.54}$$

They are completed by the following boundary conditions:

$$\boldsymbol{t} = \underline{\boldsymbol{\sigma}} \cdot \boldsymbol{n} \qquad\qquad t_i = \sigma_{ij} n_j \tag{B.55}$$

$$\underline{\boldsymbol{m}} = \underline{\boldsymbol{M}} \cdot \underset{\approx}{\boldsymbol{\epsilon}} \cdot \boldsymbol{n} \qquad m_{ij} = M_{ik} \epsilon_{kjl} n_l \tag{B.56}$$

B.2.2 Thermodynamically consistent derivation of constitutive equations

We present here the derivation of the constitutive equations for the strain gradient crystal plasticity model presented in section 4.2.2. We recall the corresponding expression of Clausius-Duhem inequality:

$$p_i^v - \rho\dot{\psi} \geq 0$$

$$\underline{\boldsymbol{\sigma}} : \dot{\underline{\boldsymbol{H}}} + \underline{\boldsymbol{s}} : \dot{\underline{\boldsymbol{H}}}^p + \underline{\boldsymbol{M}} : \text{curl}\left(\dot{\underline{\boldsymbol{H}}}^p\right) - \rho\dot{\psi} \geq 0 \tag{B.57}$$

Using the symmetry of $\underline{\boldsymbol{\sigma}}$ and the decomposition of the displacement gradient, we can write:

$$\underline{\boldsymbol{\sigma}} : \dot{\underline{\boldsymbol{H}}} = \underline{\boldsymbol{\sigma}} : \left(\dot{\underline{\boldsymbol{H}}}^e + \dot{\underline{\boldsymbol{H}}}^p\right) = \underline{\boldsymbol{\sigma}} : \dot{\underline{\boldsymbol{H}}}^e + \underline{\boldsymbol{\sigma}} : \dot{\underline{\boldsymbol{H}}}^p = \underline{\boldsymbol{\sigma}} : \dot{\underline{\boldsymbol{\varepsilon}}}^e + \underline{\boldsymbol{\sigma}} : \dot{\underline{\boldsymbol{H}}}^p \tag{B.58}$$

We then assume that ψ is a function of the elastic strain, of $\text{curl}\,(\underline{\boldsymbol{H}}^p)$ and of the cumulative plastic slip on each slip system:

$$\psi = \psi\left(\underline{\boldsymbol{\varepsilon}}^e, \text{curl}\,(\underline{\boldsymbol{H}}^p), \gamma_{cum}^s\right)$$

After injecting eq. (B.58) in eq. (B.57) and some factorisation, we get:

$$\left(\underline{\boldsymbol{\sigma}} - \rho\frac{\partial\psi}{\partial\underline{\boldsymbol{\varepsilon}}^e}\right) : \dot{\underline{\boldsymbol{\varepsilon}}}^e + (\underline{\boldsymbol{\sigma}} + \underline{\boldsymbol{s}}) : \dot{\underline{\boldsymbol{H}}}^p + \left(\underline{\boldsymbol{M}} - \rho\frac{\partial\psi}{\partial\,\text{curl}\,(\underline{\boldsymbol{H}}^p)}\right) : \text{curl}\left(\dot{\underline{\boldsymbol{H}}}^p\right)$$
$$- \sum_{s=1}^{N} \rho\frac{\partial\psi}{\partial\gamma_{cum}^s}\dot{\gamma}_{cum}^s \geq 0 \tag{B.59}$$

It is assumed that the work associated to elastic deformation and to $\text{curl}\left(\dot{\underline{\boldsymbol{H}}}^p\right)$ are non dissipative processes. Therefore, the associated terms in eq. (B.59) must

vanish, which yields:

$$\underline{\boldsymbol{\sigma}} = \rho \frac{\partial \psi}{\partial \underline{\boldsymbol{\varepsilon}}^e}, \qquad \underline{\boldsymbol{M}} = \rho \frac{\partial \psi}{\partial \operatorname{curl}(\underline{\boldsymbol{H}}^p)} \tag{B.60}$$

A simple quadratic potential is considered for these non dissipative terms: the classical quadratic form represented by the Hooke tensor $\underline{\boldsymbol{\Lambda}}$ for the elastic energy, and a simple quadratic and isotropic form for the energy stored by GND. It is written:

$$\rho \psi = \frac{1}{2} \underline{\boldsymbol{\varepsilon}}^e : \underline{\boldsymbol{\Lambda}} : \underline{\boldsymbol{\varepsilon}}^e + \frac{1}{2} A \operatorname{curl}(\underline{\boldsymbol{H}}^p) : \operatorname{curl}(\underline{\boldsymbol{H}}^p) \tag{B.61}$$

which yield the constitutive relations

$$\boxed{\begin{aligned} \underline{\boldsymbol{\sigma}} &= \underline{\boldsymbol{\Lambda}} : \underline{\boldsymbol{\varepsilon}}^e \\ \underline{\boldsymbol{M}} &= A \operatorname{curl}(\underline{\boldsymbol{H}}^p) \end{aligned}} \tag{B.62} \tag{B.63}$$

Combining the balance equation eq. (4.24) and eq. (B.63), we get:

$$\boxed{\underline{\boldsymbol{s}} = -A \operatorname{curl}(\operatorname{curl}(\underline{\boldsymbol{H}}^p))} \tag{B.64}$$

Then, after introducing the notation: $\tau^s = \underline{\boldsymbol{\sigma}} : \underline{\boldsymbol{\mu}}^s$ and $\chi^s = -\underline{\boldsymbol{s}} : \underline{\boldsymbol{\mu}}^s$, and substituting eq. (4.12) in eq. (B.59), the residual dissipation is expressed as:

$$D = \sum_{s=1}^{N} [(\tau^s - \chi^s)\dot{\gamma}^s - \tau_c^s \dot{\gamma}_{cum}^s] \geq 0 \tag{B.65}$$

where $\tau_c^s = \rho_i \frac{\partial \psi}{\partial \gamma_{cum}^s}$ is the thermodynamic force associated with γ_{cum}^s. We then introduce the dissipation potentials $\boldsymbol{\Omega}^s(\tau^s - \chi^s, \tau_c^s)$ defining the flow rule and the evolution equation of γ_{cum}^s for each slip system:

$$\dot{\gamma}^s = \frac{\partial \boldsymbol{\Omega}^s}{\partial (\tau^s - \chi^s)} \qquad \dot{\gamma}_{cum}^s = -\frac{\partial \boldsymbol{\Omega}^s}{\partial \tau_c^s} \tag{B.66}$$

It is assumed to depend on the Schmid yield function: $f^s(\tau^s - \chi^s, \tau_c^s) = |\tau^s - \chi^s| - \tau_c^s$ such that $\boldsymbol{\Omega}^s = \boldsymbol{\Omega}^s(f^s(\tau^s, \tau_c^s))$, and that eq. (B.65) is satisfied under the condition $\frac{\partial \boldsymbol{\Omega}^s}{\partial f^s} > 0$. It is then defined exactly as in appendix B.1.2, which yields the flow rule and τ_c^s evolution equation:

$$\boxed{\dot{\gamma}^s = \text{sign}(\tau^s - \chi^s) \left\langle \frac{|\tau^s - \chi^s| - \tau_c^s}{K} \right\rangle^n} \tag{B.67}$$

$$\boxed{\tau_c^s = \tau_0^s - \Delta\tau^s \left[1 - \exp\left(-\frac{\gamma_{cum}^s}{\gamma_0^s} \right) \right] + H^s \gamma_{cum}^s} \tag{B.68}$$

B.2.3 Analytical modeling of slip and kink banding

(a) slip band   (b) kink band
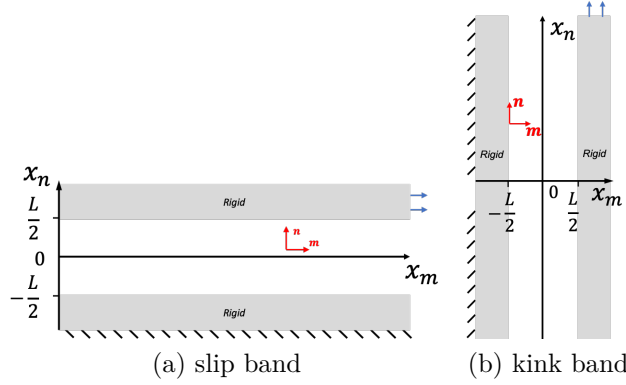
Figure B.2 – Schematic modeling of the local shearing of a crystal within a slip localization band for a slip band (a) and a kink band (b). The central phase is elasto-plastic and deforms through a singe slip system, whose orientation is indicated in red.

The analytical modeling of slip and kink banding is applied here with the strain gradient plasticity model. The geometrical modeling is recalled on the schematic of fig. B.2: a plastic slip localization band is approximated as an elasto-plastic bidimensional layer embedded between two rigid layers and submitted to a pure shear sollicitation.

We recall briefly the hypothesis, in the context of small perturbations, for the slip band case:

1. Unidimensional modeling, invariant with coordinate x_m and x_3. The localization undergoes pure shear so that:

$$\boldsymbol{u} = u(x_n)\boldsymbol{m}, \quad \underline{\boldsymbol{F}} = \underline{\boldsymbol{1}} + u_{,n}\boldsymbol{m} \otimes \boldsymbol{n} \Rightarrow \underline{\boldsymbol{H}} = u_{,n}\boldsymbol{m} \otimes \boldsymbol{n} \tag{B.69}$$

2. The rigid phases impose a mean shear strain $\bar{\gamma}$ to the localization band:

$$u_{(-\frac{L}{2})} = 0 \quad \text{and} \quad u_{(\frac{L}{2})} = \bar{\gamma}L \tag{B.70}$$

3. Plastic phase has one active slip system with slip direction and normal to slip system direction $\boldsymbol{m}$ and $\boldsymbol{n}$. We consider here additionally a hardening modulus H, that can be either negative, positive or null:

$$\underline{\boldsymbol{\sigma}} : \underline{\boldsymbol{\mu}} = |\tau| - \chi = \tau_0 + H\gamma_{cum} \tag{B.71}$$

4. Elastic behavior is linear isotropic:

$$\underline{\boldsymbol{\sigma}} = \lambda \operatorname{tr}(\underline{\boldsymbol{\varepsilon}}^e)\underline{\boldsymbol{1}} + 2\mu\underline{\boldsymbol{\varepsilon}}^e \tag{B.72}$$

As in in section 3.3.1, the hypothesis are the same for the kink band case with $\boldsymbol{m}$ and $\boldsymbol{n}$ directions inverted.

Slip band

We recall that the case of a slip band is the case where the glide direction is $\boldsymbol{m}$ and the normal to slip direction is $\boldsymbol{n}$. Equation (4.35): $\underline{\boldsymbol{H}}^p = \gamma\underline{\boldsymbol{\mu}}$, and eq. (B.69) yield the expression of $\underline{\boldsymbol{H}}^e$ and $\underline{\boldsymbol{\varepsilon}}^e$:

$$\underline{\boldsymbol{H}}^e = (u_{,n} - \gamma)\,\boldsymbol{m} \otimes \boldsymbol{n} \tag{B.73}$$

$$\underline{\boldsymbol{\varepsilon}}^e = \frac{1}{2}(u_{,n} - \gamma)(\boldsymbol{m} \otimes \boldsymbol{n} + \boldsymbol{n} \otimes \boldsymbol{m}) \tag{B.74}$$

Then using eq. (B.72) we get:

$$\underline{\boldsymbol{\sigma}} = \mu(u_{,n} - \gamma)(\boldsymbol{m} \otimes \boldsymbol{n} + \boldsymbol{n} \otimes \boldsymbol{m}) \tag{B.75}$$

From eqs. (4.42) and (4.45) we have immediately $\chi = 0$. The balance equation $\operatorname{div}(\underline{\boldsymbol{\sigma}}) = 0$ yields for a monotonic evolution of the slip variable (for which $\gamma_{cum} = \gamma$):

$$\sigma_{mn,n} = \tau_{,n} = 0 \tag{B.76}$$

Hence, the yield condition is verified everywhere in the band, and using $\chi = 0$, eqs. (B.71) and (B.75), it is expressed as:

$$\mu(u_{,n} - \gamma) = \tau_0 + H\gamma \tag{B.77}$$

As in section 3.3.1, it is easy to verify than homogeneous fields are a solution to the problem. However, for $H \leq 0$, according to Asaro and Rice 1977, yields plastic instability and result in plastic slip localization, forming a slip band, whose width is undetermined.

Kink band

In the case of the kink band we have:

$$\underline{\boldsymbol{H}} = u_{,m}\boldsymbol{n} \otimes \boldsymbol{m} \tag{B.78}$$

$$\underline{\boldsymbol{H}}^e = \underline{\boldsymbol{H}} - \underline{\boldsymbol{H}}^p = u_{,m}\boldsymbol{n} \otimes \boldsymbol{m} - \gamma\boldsymbol{m} \otimes \boldsymbol{n} \tag{B.79}$$

Thus, the expressions of $\underline{\boldsymbol{\varepsilon}}^e$, $\boldsymbol{\sigma}$ are also given by eqs. (B.74) and (B.75), but with $\boldsymbol{m}$ and $\boldsymbol{n}$ coordinates inverted. However, here eq. (4.45) becomes:

$$\chi = -\lambda^2 \pi_0 \gamma_{,mm} \tag{B.80}$$

After eq. (B.71), the yield condition becomes, for a monotonic evolution of the slip variable:

$$\tau - \chi = \tau + \lambda^2 \pi_0 \gamma_{,mm} = \tau_0 + H\gamma \tag{B.81}$$

The balance equation eq. (B.76) is still valid which implies that τ is constant. Thus from eq. (B.81), we get the differential equation governing the slip variable:

$$\gamma_{,mm} - \frac{H}{\lambda^2 \pi_0}\gamma + \frac{\tau - \tau_0}{\lambda^2 \pi_0} = 0 \tag{B.82}$$

$$\gamma_{,mm} - \frac{1}{\lambda_0^2}\gamma + \frac{1}{\lambda_0^2}\frac{\tau - \tau_0}{H} = 0 \tag{B.83}$$

with $\lambda_0 = \lambda\sqrt{\frac{\pi_0}{H}}$. The solution of this equation depends on the value of H, and the three cases $H > 0$, $H = 0$ and $H < 0$ must be discussed. Additional boundary condition for the plastic slip must also be considered for the problem to be well posed.

Considering the geometry of the modeled localization band (fig. 3.2), and the form of the equation, the symmetry of $\gamma(x_m)$ is the first condition to consider. The other boundary condition to consider is the interface condition at the rigid-platic interphase. Cordero, Gaubert, et al. (2010) have shown that with the curl$(\underline{\boldsymbol{H}}^p)$ based model, $\underline{\boldsymbol{m}}$ must exhibit a jump at plastic-elastic interfaces in order to allow non zero slip in the plastic phase. Thus, no condition is enforced at the boundary for $\underline{\boldsymbol{m}}$. The continuity of the plastic slip field requires the microhard

condition at the interface, as no plastic slip occurs in the rigid phase.

To sum up, γ must fulfill the two conditions:

1. $\gamma(\pm\frac{L}{2}) = 0$ (microhard BC)
2. $\gamma(x_m) = \gamma(-x_m)$ (symmetry condition)

The calculation for the three cases are briefly described in the following.

1. **Case** $H > 0$:
   The solution takes the form:

$$\gamma = \alpha \cosh\left(\frac{x_m}{\lambda_0}\right) + \beta \sinh\left(\frac{x_m}{\lambda_0}\right) + \frac{\tau - \tau_0}{H} \tag{B.84}$$

   From the symmetry of the problem follows $\beta = 0$. The plastic-rigid interface microhard condition yields:

$$\alpha = \frac{\tau_0 - \tau}{H \cosh\left(\frac{L}{2\lambda_0}\right)} \tag{B.85}$$

   Finally the solution is written:

$$\boxed{\gamma(x_m) = \frac{\tau - \tau_0}{H}\left[1 - \frac{\cosh\left(\frac{x_m}{\lambda_0}\right)}{\cosh\left(\frac{L}{2\lambda_0}\right)}\right]} \tag{B.86}$$

   We recall that the resolved shear stress, according to the expression of $\underline{\sigma}$ (eq. (B.75)), is given by:

$$\tau = \mu\left(u_{,m} - \gamma\right) \tag{B.87}$$

   According to the balance equation eq. (B.76), τ is constant over the localization band. Thus it is equal to its mean over the whole localization band, which writes:

$$\tau = \frac{1}{L}\int_{\frac{-L}{2}}^{\frac{L}{2}} \tau\, dx_m = \frac{1}{L}\int_{\frac{-L}{2}}^{\frac{L}{2}} \mu\left(u_{,n} - \gamma\right) dx_m = \frac{\mu}{L}\overline{u_{,n}} - \frac{\mu}{L}\int_{\frac{-L}{2}}^{\frac{L}{2}} \gamma(x_m) dx_m \tag{B.88}$$

   The imposed mean shear (eq. (B.70)) imposes that $\overline{u_{,n}} = \overline{\gamma}L$. Substituting it in eq. (B.88), we get:

$$\tau = \mu\overline{\gamma} - \frac{\mu}{L}\int_{\frac{-L}{2}}^{\frac{L}{2}} \gamma(x_m) dx_m \tag{B.89}$$

Substituting eq. (B.86), it yields:

$$
\begin{aligned}
\tau &= \mu\overline{\gamma} - \frac{\mu}{L}\int_{\frac{-L}{2}}^{\frac{L}{2}}\frac{\tau - \tau_0}{H}\left[1 - \frac{\cosh\left(\frac{x_m}{\lambda_0}\right)}{\cosh\left(\frac{L}{2\lambda_0}\right)}\right]dx_m \\
&= \mu\left(\overline{\gamma} - \frac{\tau - \tau_0}{H}\right) + \frac{\mu(\tau - \tau_0)}{HL\cosh\left(\frac{L}{2\lambda_0}\right)}2\lambda_0\sinh\left(\frac{L}{2\lambda_0}\right) \\
&= \mu\left[\overline{\gamma} + \frac{\tau - \tau_0}{H}\left(\frac{2\lambda_0}{L}\tanh\left(\frac{L}{2\lambda_0}\right) - 1\right)\right] \\
&= \mu\left[\overline{\gamma} + \frac{\tau - \tau_0}{K^1}\right]
\end{aligned}
$$

After writing $K_1 = \dfrac{H}{\frac{2\lambda_0}{L}\tanh\left(\frac{L}{2\lambda_0}\right) - 1}$ and some factorization we get:

$$
\tau\left(\frac{1}{\mu} - \frac{1}{K_1}\right) = \overline{\gamma} - \frac{\tau_0}{K_1} \quad \Rightarrow \tau = \frac{\overline{\gamma} - \frac{\tau_0}{K_1}}{\frac{1}{\mu} - \frac{1}{K_1}} \tag{B.90}
$$

2. **Case** $H = 0$:
   In this case eq. (B.82) takes the parabolic form

$$
\gamma_{,mm} = \frac{\tau_0 - \tau}{\lambda^2\pi_0} \tag{B.91}
$$

whose general solution is:

$$
\gamma = \left(\frac{\tau_0 - \tau}{2\lambda^2\pi_0}\right)x_m^2 + \alpha x_m + \beta \tag{B.92}
$$

From the symmetry condition follows that $\alpha = 0$, and from the boundary condition:

$$
\beta = -\left(\frac{\tau_0 - \tau}{2\lambda^2\pi_0}\right)(\frac{L}{2})^2 \tag{B.93}
$$

Finally the solution is written:

$$
\boxed{\gamma(x_m) = \left(\frac{\tau - \tau_0}{2\lambda^2\pi_0}\right)\left[\left(\frac{L}{2}\right)^2 - x_m^2\right]} \tag{B.94}
$$

We can now compute τ:

$$\tau = \mu\overline{\gamma} - \frac{\mu}{L}\int_{\frac{-L}{2}}^{\frac{L}{2}}\left(\frac{\tau - \tau_0}{2\lambda^2\pi_0}\right)\left[\left(\frac{L}{2}\right)^2 - x_m^2\right]dx_m$$

$$= \mu\overline{\gamma} - \frac{\mu}{L}\left(\frac{\tau - \tau_0}{2\lambda^2\pi_0}\right)\left[L\left(\frac{L}{2}\right)^2 - \frac{2}{3}\left(\frac{L}{2}\right)^3\right]$$

$$= \mu\overline{\gamma} - \frac{\mu(\tau - \tau_0)}{12\lambda^2\pi_0}L^2$$

After writing $K_2 = \frac{12\lambda^2\pi_0}{L^2}$ and factorization we get:

$$\tau\left(\frac{1}{\mu} + \frac{1}{K_2}\right) = \overline{\gamma} + \frac{\tau_0}{K_2} \quad \Rightarrow \tau = \frac{\overline{\gamma} + \frac{\tau_0}{K_2}}{\frac{1}{\mu} - + \frac{1}{K_2}} \tag{B.95}$$

3. **Case** $H < 0$:
   In this case eq. (B.83) is written under the new form:

$$\gamma_{,mm} + \frac{2\pi^2}{\lambda_0'}\gamma + \frac{2\pi^2}{\lambda_0'}\frac{\tau - \tau_0}{|H|} = 0 \tag{B.96}$$

where $\lambda_0' = 2\pi\lambda\sqrt{\frac{\pi_0}{|H|}}$. This equation admits general solutions of the form

$$\gamma = \alpha\cos\left(\frac{2\pi x_m}{\lambda_0'}\right) + \beta\sin\left(\frac{2\pi x_m}{\lambda_0'}\right) + \frac{\tau - \tau_0}{H} \tag{B.97}$$

The symmetry condition yields $\beta = 0$. As the hardening modulus is negative, the plastic slip instability should be reached at initial yield. Hence, we look for a localized solution, *i.e.* a solution where the plastic slip is non zero over a region of width ω_b. This time, the boundary of the band are inside the plastic phase, thus the condition of vanishing generalized traction can be applied. Hence, the boundary conditions become:

(a) $\gamma(\pm\frac{\omega_b}{2}) = 0$ (localized solution condition)

(b) $\underline{\boldsymbol{m}}(\pm\frac{\omega_b}{2}) = \underline{\boldsymbol{M}}(\pm\frac{\omega_b}{2})\cdot\underset{\sim}{\boldsymbol{\varepsilon}}\cdot\boldsymbol{n} = 0 \iff \gamma_{,n}(\pm\frac{\omega_b}{2}) = 0$ (vanishing generalized traction at the end of plastic zone)

these conditions yield:

$$\alpha = \frac{\tau - \tau_0}{H} \tag{B.98}$$

$$\omega_b = \lambda'_0 = 2\pi\lambda\sqrt{\frac{\pi_0}{|H|}} \tag{B.99}$$

Finally the solution is written:

$$\boxed{\gamma(x_m) = \frac{\tau - \tau_0}{H}\left[1 + \cos\left(\frac{2\pi x_m}{\lambda'_0}\right)\right]} \tag{B.100}$$

We can now compute τ:

$$\tau = \mu\overline{\gamma} - \frac{\mu}{L}\int_{\frac{-\omega_b}{2}}^{\frac{\omega_b}{2}} \frac{\tau - \tau_0}{H}\left[1 + \cos\left(\frac{2\pi x_m}{\lambda'_0}\right)\right] dx_m$$

$$= \mu\left(\overline{\gamma} - \frac{\omega_b(\tau - \tau_0)}{HL}\right)$$

As we have $\omega_b = \lambda'_0$, after writing $K_3 = \frac{LH}{\lambda'_0}$ and factorization we get:

$$\tau\left(\frac{1}{\mu} + \frac{1}{K_3}\right) = \overline{\gamma} + \frac{\tau_0}{K_3} \quad \Rightarrow \tau = \frac{\overline{\gamma} + \frac{\tau_0}{K_3}}{\frac{1}{\mu} + \frac{1}{K_3}} \tag{B.101}$$

It must be noted that these calculation are very similar to those presented in Scherer et al. (2019), where a single crystal under a pure shear solicitation with a micromorphic model based on the gradient of a cumulated slip variable is considered.

B.2.4 Jacobian matrix for the integration of constitutive equations with Newton's method

We provide here the detailed calculation of the Jacobian matrix used to compute the Newton-Raphson algorithm to solve eq. (4.76)). It is recalled that χ^s is constant during the algorithm iterations.

- **Partial derivatives of the elastic part of deformation gradient residual equation $R_{\underline{\varepsilon}^e}$:**

$$R_{\underline{\varepsilon}^e} = \Delta\underline{\varepsilon}^e + \sum_{s=1}^{N}\left[\Delta\gamma^s\mathring{\underline{\mu}}^s\right] - \Delta\underline{\varepsilon} = 0$$

– With respect to $\Delta\underline{\boldsymbol{\varepsilon}}$:

$$\boxed{\frac{\partial R_{\underline{\boldsymbol{\varepsilon}}^e}}{\partial\Delta\underline{\boldsymbol{\varepsilon}}^e} = \underline{\mathbf{1}}}$$

(B.102)

– With respect to $\Delta\gamma^j$:

$$\boxed{\frac{\partial R_{\underline{\boldsymbol{\varepsilon}}^e}}{\partial\Delta\gamma^j} = \overset{\diamond}{\underline{\boldsymbol{\mu}}}{}^{s,j}}$$

(B.103)

• **Partial derivatives of the slip residual equation R_{γ^s}:**

$$R_{\gamma^s} = \Delta\gamma^s - \Delta t\,\mathrm{sign}(\tau^s - \chi^s)\left\langle\frac{|\tau^s - \chi^s| - \tau_c^s}{K}\right\rangle^n = 0$$

– With respect to $\Delta\underline{\boldsymbol{\varepsilon}}^e$:

$$\frac{\partial R_{\gamma^s}}{\partial\Delta\underline{\boldsymbol{\varepsilon}}^e} = -\Delta t\,\mathrm{sign}(\tau^s - \chi^s)\,\mathrm{sign}(\tau^s - \chi^s)\frac{n}{K}\left\langle\frac{|\tau^s - \chi^s| - \tau_c^s}{K}\right\rangle^{n-1}\frac{\partial\tau^s}{\partial\Delta\underline{\boldsymbol{\varepsilon}}^e}$$

$$= -\Delta t\frac{n}{K}\left\langle\frac{|\tau^s - \chi^s| - \tau_c^s}{K}\right\rangle^{n-1}\frac{\partial\left(\underline{\boldsymbol{\sigma}} : \overset{\diamond}{\underline{\boldsymbol{\mu}}}{}^s\right)}{\partial\Delta\underline{\boldsymbol{\varepsilon}}^e}$$

$$= -\Delta t\frac{n}{K}\left\langle\frac{|\tau^s - \chi^s| - \tau_c^s}{K}\right\rangle^{n-1}\overset{\diamond}{\underline{\boldsymbol{\mu}}}{}^s : \frac{\partial(\underline{\boldsymbol{\Lambda}}\cdot\underline{\boldsymbol{\varepsilon}}^e)}{\partial\Delta\underline{\boldsymbol{\varepsilon}}^e}$$

$$\Rightarrow\boxed{\frac{\partial R_{\gamma^s}}{\partial\Delta\underline{\boldsymbol{\varepsilon}}^e} = -\Delta t\frac{n}{K}\left\langle\frac{|\tau^s - \chi^s| - \tau_c^s}{K}\right\rangle^{n-1}\overset{\diamond}{\underline{\boldsymbol{\mu}}}{}^s : \underline{\boldsymbol{\Lambda}}}$$

(B.104)

– With respect to $\Delta\gamma^j$:

$$\frac{\partial R_{\gamma^s}}{\partial\Delta\gamma^j} = \delta_{sj} + \Delta t\,\text{sign}(\tau^s - \chi^s)\frac{n}{K}\left\langle\frac{|\tau^s - \chi^s| - \tau_c^s}{K}\right\rangle^{n-1}\frac{\partial\tau_c^s}{\partial\Delta\gamma^j}$$

$$\frac{\partial\tau_c^s}{\partial\Delta\gamma^j} = \frac{\partial}{\partial\Delta\gamma^j}\left(\tau_0^s - \Delta\tau^s\left[1 - \exp\left(-\frac{\gamma_{cum}^s}{\gamma_0^s}\right)\right] + H^s\gamma_{cum}^s\right)$$
$$= \frac{\partial\gamma_{cum}^s}{\partial\Delta\gamma^j}\left[H^s - \frac{1}{\gamma_0^s}\exp\left(-\frac{\gamma_{cum}^s}{\gamma_0^s}\right)\right]$$

$$\frac{\partial\gamma_{cum}^s}{\partial\Delta\gamma^j} = \frac{\partial\gamma_{cum}^s}{\partial\Delta|\gamma^j|}\frac{\partial|\gamma^j|}{\partial\Delta\gamma^j} = \delta_{sj}\,\text{sign}(\gamma^j)$$

$$\Rightarrow \boxed{\begin{aligned}\frac{\partial R_{\gamma^s}}{\partial\Delta\gamma^j} &= \delta_{sj}\left(1 + \Delta t\,\text{sign}((\tau^s - \chi^s)\gamma^j)\frac{n}{K}\left\langle\frac{|\tau^s - \chi^s| - \tau_c^s}{K}\right\rangle^{n-1}\right.\\ &\qquad\left.\left[H^s - \frac{e^{-\frac{\gamma_{cum}^s}{\gamma_0^s}}}{\gamma_0^s}\right]\right)\end{aligned}}$$

$$(\text{B.105})$$
$$(\text{B.106})$$

B.2.5   Finite differentiation curl operators applied to slip and kink bands

Here, we apply the 27 voxel centered finite-differences formulas defined in appendix A.5 to the calculation of the curl and double curl of three particular cases of pixelized slip localization bands, shown in fig. B.3, before generalizing the results to all orientations. The examples are bi dimensional to simplify the calculation. The slip fields verifies $\gamma = \gamma^*$ inside the bands, and 0 outside. We recall that, in a bidimensional case, from eqs. (4.37) and (4.39) we have:

$$\text{curl}(\underline{\boldsymbol{H}}^p) = -\gamma_{,m}\boldsymbol{m}\otimes\boldsymbol{e}_3 \tag{B.107}$$
$$\text{curl}\left(\text{curl}(\underline{\boldsymbol{H}}^p)\right) = \gamma_{,mn}\boldsymbol{m}\otimes\boldsymbol{m} - \gamma_{,mm}\boldsymbol{m}\otimes\boldsymbol{n} \tag{B.108}$$

Besides, the directional derivatives in $\boldsymbol{m}$ and $\boldsymbol{n}$ directions of γ are defined as follow:

$$\gamma_{,m} = \gamma_{,1}n_2 - \gamma_{,2}n_1 \tag{B.109}$$
$$\gamma_{,mm} = \gamma_{,11}n_2^2 + \gamma_{,22}n_1^2 - 2\gamma_{,12}n_1n_2 \tag{B.110}$$
$$\gamma_{,mn} = n_1n_2(\gamma_{,11} - \gamma_{,22}) + \gamma_{,12}(n_2^2 - n_1^2) \tag{B.111}$$

where n_1 and n_2 are the components of $\boldsymbol{n}$. We consider square pixels of size dx.
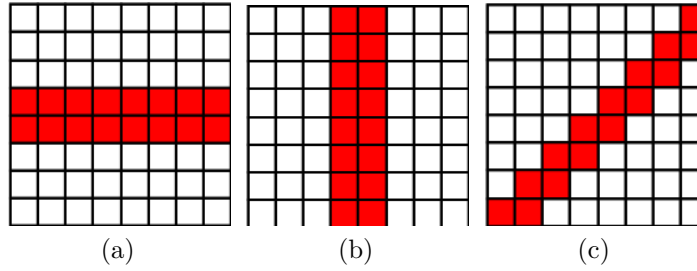
Figure B.3 – Schematization of pixelized fields of ideal localization bands. $\gamma = \gamma^*$ on red voxels, $\gamma = 0$ on white voxels. Horizontal band (a), vertical band (b), band rotated at 45 degrees with respect to discretization grid.

Horizontal band

In the case of the horizontal band (fig. B.3-(a)), we have:

$$\gamma_{,1} = 0$$
$$\gamma_{,2} = \pm\frac{\gamma^*}{2dx}$$
$$\gamma_{,11} = 0$$
$$\gamma_{,12} = 0$$
$$\gamma_{,22} = -\frac{\gamma^*}{dx^2}$$

Then, using eqs. (B.109) to (B.111) we obtain:

$$\gamma_{,m} = \pm\frac{n_1}{2dx}\gamma^*$$
$$\gamma_{,mm} = -\frac{n_1^2}{dx^2}\gamma^*$$
$$\gamma_{,mn} = \frac{n_1 n_2}{dx^2}\gamma^*$$

The case of the **slip band** corresponds to $n_1 = 0$ and $n_2 = 1$, which yields

$$\gamma_{,m} = 0$$

$$\gamma_{,mm} = 0$$
$$\gamma_{,mn} = 0$$

corresponding to $\underline{\boldsymbol{\alpha}} = 0$ and $\underline{\boldsymbol{s}} = 0$.

The case of the **kink band** corresponds to $n_1 = 1$ and $n_2 = 0$, which yields

$$\gamma_{,m} = \pm\frac{1}{2dx}\gamma^*$$
$$\gamma_{,mm} = -\frac{1}{dx^2}\gamma^*$$
$$\gamma_{,mn} = 0$$

corresponding to $\underline{\boldsymbol{\alpha}} \neq 0$ and $\underline{\boldsymbol{s}} \neq 0$.

In the case of a localization band associated to a slip system whose directions $\boldsymbol{m}$ and $\boldsymbol{n}$ are aligned with the grid directions, the 27 voxel centered finite-differences formulation of the model predicts no GND density (proportional to $\mathrm{curl}(\underline{\boldsymbol{H}}^p)$) nor backstress (proportional to $\mathrm{curl}(\mathrm{curl}(\underline{\boldsymbol{H}}^p))$) induced by slip bands, but non-zero values for kink bands.

Vertical band

The case of the vertical band is exactly identical to the previous one, with inverted indexes.

45 degrees rotated band

We consider now the case of a 45° rotated band with respect to the grid directions (fig. B.3-(b)). The action of the 27 voxel centered finite-differences formulation on the field $\underline{\boldsymbol{H}}^p$, in a bi dimensional field, for the two different types of voxels (from respectively upper and lower part of the band) of the band is represented on fig. B.4.

In this case we have:

$$\gamma_{,1} = \pm\frac{1}{2dx}\gamma^*$$
$$\gamma_{,2} = \pm\frac{1}{2dx}\gamma^*$$
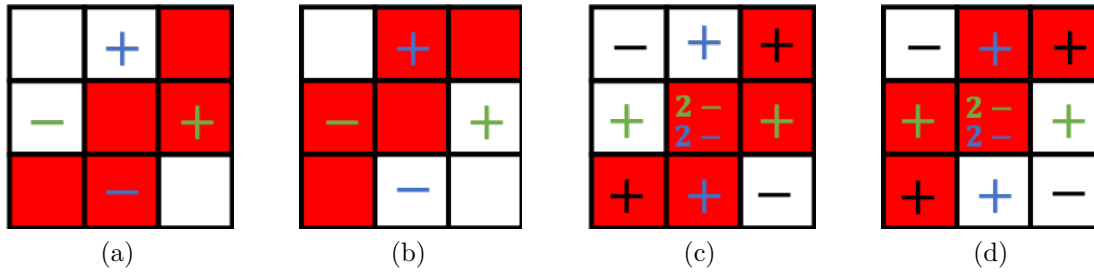
Figure B.4 – Schematization of 9-pixels centered finite difference action on the central voxel of a schematic localization band of width 2 voxels. $\gamma = \gamma^*$ on red voxels, $\gamma = 0$ on white voxels. First order finite differences are represented in (a-b), second order in (c-d). Derivation along x_1 is represented in green, along x_2 in blue, crossed derivation in black.

with $\gamma_{,1} = -\gamma_{,2}$

$$\gamma_{,11} = \gamma_{,22} = -\frac{1}{2dx^2}\gamma^*$$

$$\gamma_{,12} = \frac{1}{2dx^2}\gamma^*$$

Then, using eqs. (B.109) to (B.111) we obtain:

$$\gamma_{,m} = \pm\frac{n_1 + n_2}{2dx}\gamma^*$$

$$\gamma_{,mm} = -\frac{1 + n_1 n_2}{dx^2}\gamma^*$$

$$\gamma_{,mn} = -\frac{n_2^2 - n_1^2}{2dx^2}\gamma^*$$

The case of the **slip band** corresponds to $n_1 = -n_2 = -\frac{\sqrt{2}}{2}$, which yields

$$\gamma_{,m} = 0$$

$$\gamma_{,mm} = -\frac{1}{2dx}\gamma^*$$

$$\gamma_{,mn} = 0$$

corresponding to $\underline{\alpha} = 0$ and $\underline{s} \neq 0$.

The case of the **kink band** corresponds to $n_1 = n_2 = \frac{\sqrt{2}}{2}$, which yields

$$\gamma_{,m} = \pm \frac{\sqrt{2}}{2dx}\gamma^*$$
$$\gamma_{,mm} = -\frac{3}{2dx}\gamma^*$$
$$\gamma_{,mn} = 0$$

corresponding to $\underline{\alpha} \neq 0$ and $\underline{s} \neq 0$.

In the case of a localization band associated to a slip system whose directions $\boldsymbol{m}$ and $\boldsymbol{n}$ are rotated of 45 degrees from the grid axes, the 9 voxel centered finite-differences formulation of the model predicts no GND density induced by slip bands and a non-zero values for kink bands. However, it predicts a non zero backstress on the slip band ($\frac{1}{3}$ of the kink band backstress) which is in contradiction with analytical results.

Generic diagonal band

A pixelized 2 pixel width localization band associated to a slip system with an arbitrary orientation in the plane, is composed of segments of the three types of band segments studied previously, and illustrated on , for which the expressions of $\gamma_{,m}$, $\gamma_{,mm}$ and $\gamma_{,mn}$ are given above. We denote θ the angle indicating the inclination of the slip system with respect to the grid axes, so that $n_1 = -\sin(\theta), n_2 = \cos(\theta)$ for a slip band, and $n_1 = \cos(\theta), n_2 = \sin(\theta)$ for a kink band.

We then examine the case $0 \leq \theta \leq \frac{\pi}{4}$. If θ is close to $\frac{\pi}{4}$, then the band will be mostly composed of segments rotated of 45 degrees. Thus, in the case of a slip band we have:

$$|\gamma_{,m}|_s = |\frac{\cos(\theta) - \sin(\theta)}{2dx}\gamma^*|$$
$$|\gamma_{,mm}|_s = \frac{1 - \frac{\sin(2\theta)}{2}}{dx^2}\gamma^*$$

and in the case of the kink band:

$$|\gamma_{,m}|_k = |\frac{\cos(\theta) + \sin(\theta)}{2dx}\gamma^*|$$
$$|\gamma_{,mm}|_k = \frac{1 + \frac{\sin(2\theta)}{2}}{dx^2}\gamma^*$$

If θ is close to 0, then the band will be mostly composed of horizontal segments. Thus, in the case of a slip band we have:

$$|\gamma_{,m}|_s = |\frac{\sin(\theta)}{2dx}\gamma^*|$$
$$|\gamma_{,mm}|_s = \frac{\sin(\theta)^2}{dx^2}\gamma^*$$

and in the case of the kink band:

$$|\gamma_{,m}|_k = |\frac{\cos(\theta)}{2dx}\gamma^*|$$
$$|\gamma_{,mm}|_k = \frac{\cos(\theta)^2}{dx^2}\gamma^*$$

Thus, the backstress ratio between slip and kink band is:

$$\frac{|\gamma_{,mm}|_s}{|\gamma_{,mm}|_k} = \frac{|1 - \frac{\sin(2\theta)}{2}|}{|1 + \frac{\sin(2\theta)}{2}|} \qquad \text{close to ,} \theta = \frac{\pi}{4}$$
$$\frac{|\gamma_{,mm}|_s}{|\gamma_{,mm}|_k} = \frac{|\sin(\theta)^2|}{|\cos(\theta)^2|} \qquad \text{close to ,} \theta = 0$$

and between the two in the domain $0 \leq \theta \leq \frac{\pi}{4}$. Analogous expressions can be derived for the other quadrant $\frac{\pi}{4} \leq \theta \leq \frac{\pi}{2}$. It shows that the ratio is maximal for $\gamma_{,mm}$ when $\theta = \frac{\pi}{4}$ and tends toward $\frac{1}{3}$, when it tends towards 0 for the ratio of $\gamma_{,m}$.

This yield the idea of computing twice the curl with first order finite differences in order to benefit from this result in the worst case observed for the unwanted backstress on slip bands. By applying twice eq. (4.37) with the first order finite difference on 45 degrees segments, we get in order of magnitude for the slip and then kink case:

$$|(\gamma_{,m}),_m|_s = |\frac{\cos(\theta) - \sin(\theta)}{2dx}| \cdot |\gamma_{,m}| = |\frac{\cos(\theta) - \sin(\theta)}{2dx}|^2$$
$$|(\gamma_{,m}),_m|_k = |\frac{\cos(\theta) + \sin(\theta)}{2dx}| \cdot |\gamma_{,m}| = |\frac{\cos(\theta) + \sin(\theta)}{2dx}|^2$$

which yields a backstress ratio of:

$$\frac{|(\gamma_{,m}),_m|_s}{|(\gamma_{,m}),_m|_k} = \frac{|\cos(\theta) - \sin(\theta)|^2}{|\cos(\theta) + \sin(\theta)|^2} \qquad \text{close to ,} \theta = \frac{\pi}{4}$$

which tends towards 0 when θ is close to $\theta = \frac{\pi}{4}$. This calculation of the double curl of $\underline{\boldsymbol{H}}^p$ is then more adapted to our application aimed at limiting kink band formation without affecting slip bands.

APPENDIX C

SLIP AND KINK BAND ANALYSIS METHODS

This Appendix presents a detailed description of the processing strategies presented in sections 3.3.3 and 3.3.4, used to identify and analyze slip and kink bands formation in softening crystal plasticity polycrystalline simulations.

C.1 Discrete Fourier Transform and bands morphology based strategy

This section aims at providing mathematical and technical precisions on the second slip and kink bands analysis strategy, described in section 3.3.3. First, a study of the discrete Fourier transform of ideal elongated objects is presented, which will highlight useful properties for band population separation. Then, the method based on these properties, effectively used to separate bands with different orientations in a binary image is presented. Finally, other important processing steps for slip and kink band detection are detailed in the last part.

C.1.1 Mathematical foundation

Discrete Fourier transform of a band-shaped object

We consider a two dimensional regular grid, defined by the two orthogonal unit vectors $\boldsymbol{e_1}$ and $\boldsymbol{e_2}$, whose points are defined by:

$$\boldsymbol{x}(i_1,i_2) = \boldsymbol{x}^* + i_1 dx_1 \boldsymbol{e_1} + i_2 dx_2 \boldsymbol{e_2} = \boldsymbol{x}^* + x_1 \boldsymbol{e_1} + x_2 \boldsymbol{e_2} \quad i_1 \in [\![0, N_1-1]\!],\ i_2 \in [\![0, N_2-1]\!]$$

Let Ω_R be a rectangular region of the grid of width l and length L defined by:

$$\Omega_R = \left\{ \boldsymbol{X}(i_1,i_2) \mid i_1^0 < i_1 < i_1^f, i_2^0 < i_2 < i_2^f \right\}$$
$$\text{with } i_1^f - i_1^0 = l/dx_1, \quad i_2^f - i_2^0 = L/dx_2$$

Let $\mathbb{I}_{\Omega_R}$ be the indicator function of Ω_R. The calculation of its DFT gives:

$$\begin{aligned}
\hat{\mathbb{I}}_{\Omega_R}(\xi_1,\xi_2,\xi_3) &= \sum_{i_1=0}^{N_1-1} \sum_{i_2=0}^{N_2-1} \mathbb{I}_{\Omega_R}(i_1,i_2,i_3) e^{-j\xi_1 i_1} e^{-j\xi_2 i_2} \\
&= \sum_{i_1=i_1^0}^{i_1^f} \sum_{i_2=i_2^0}^{i_2^f} e^{-j\xi_1 i_1} e^{-j\xi_2 i_2} = \sum_{i_1=i_1^0}^{i_1^f} e^{-j\xi_1 i_1} \left[\sum_{i_2=i_2^0}^{i_2^f} e^{-j\xi_2 i_2} \right] \\
&= \sum_{i_1=i_1^0}^{i_1^f} e^{-j\xi_1 i_1} \left[\sum_{n=0}^{i_2^f-i_2^0} e^{-j\xi_2\left(i_2^0+n\right)} \right] = \sum_{i_1=i_1^0}^{i_1^f} e^{-j\xi_1 i_1} e^{-j\xi_2 i_2^0} \left[\sum_{n=0}^{i_2^f-i_2^0} e^{-j\xi_2 n} \right] \\
&= \sum_{i_1=i_1^0}^{i_1^f} e^{-j\xi_1 i_1} e^{-j\xi_2 i_2^0} \left[\frac{1-e^{-j\xi_2\left(i_2^f-i_2^0+1\right)}}{1-e^{-j\xi_2}} \right] \\
&= e^{-j\xi_2 i_2^0} \sum_{i_1=i_1^0}^{i_1^f} e^{-j\xi_1 i_1}\ \frac{e^{\frac{-j\xi_2\left(i_2^f-i_2^0+1\right)}{2}}}{e^{\frac{-j\xi_2}{2}}} \left[\frac{e^{\frac{j\xi_2\left(i_2^f-i_2^0+1\right)}{2}} - e^{\frac{-j\xi_2\left(i_2^f-i_2^0+1\right)}{2}}}{e^{\frac{j\xi_2}{2}} - e^{\frac{-j\xi_2}{2}}} \right] \\
&= e^{-j\xi_2 i_2^0} \sum_{i_1=i_1^0}^{i_1^f} e^{-j\xi_1 i_1} e^{\frac{-j\xi_2\left(i_2^f-i_2^0\right)}{2}} \frac{\sin\left[\frac{\xi_2\left(i_2^f-i_2^0\right)}{2}\right]}{\sin\left[\frac{\xi_2}{2}\right]} \\
&= e^{\frac{-j\xi_2\left(i_2^f+i_2^0\right)}{2}} \frac{\sin\left[\frac{\xi_2 L}{2dx_2}\right]}{\sin\left[\frac{\xi_2}{2}\right]} \sum_{i_1=i_1^0}^{i_1^f} e^{-j\xi_1 i_1}
\end{aligned}$$

$$\hat{\mathbb{I}}_{\Omega_R}(\xi_1,\xi_2,\xi_3) = e^{\frac{-j\xi_1\left(i_1^f+i_2^0\right)}{2}} e^{\frac{-j\xi_2\left(i_2^f+i_2^0\right)}{2}} \frac{\sin\left(\frac{\xi_1 l}{2dx_l}\right)\sin\left(\frac{\xi_2 L}{2dx_2}\right)}{\sin\left(\frac{\xi_1}{2}\right)\sin\left(\frac{\xi_2}{2}\right)} \tag{C.1}$$

Thus, we have:

$$|\hat{\mathbb{I}}_{\Omega_R}(\xi_1,\xi_2,\xi_3)| = \left|\frac{\sin\left(\frac{\xi_1 l}{2dx_l}\right)\sin\left(\frac{\xi_2 L}{2dx_2}\right)}{\sin\left(\frac{\xi_1}{2}\right)\sin\left(\frac{\xi_2}{2}\right)}\right| = |g(\xi_1,l/dx)\,g(\xi_2,L/dx)| \tag{C.2}$$

This expression shows that the modulus of the DFT of the indicator function of Ω_R has a central symmetry. The function $g(\xi,L/dx)$ is similar to the cardinal sine function. It has an central pic of magnitude 1 and its first zeros are located at $\xi = \pm\frac{2\pi dx}{L}$. The peak width is $\frac{4\pi dx}{L}$, corresponding to the index range $|k_i| \leq N_i\frac{dx}{L}$.

We see that $|\hat{\mathbb{I}}_{\Omega_R}(\xi_1,\xi_2,\xi_3)|$ will have a central spot with the same aspect ratio L/l than the the domain Ω_R in the real space, but rotated of 90 degrees. fig. C.1 shows two exemples of binary images containing a rectangular domain, their DFT calculated with Matlab FFT function, and the analytical field given by eq. (C.2).

Additionally, it can be noted that only the first term of eq. (C.1) depends on the position of the band-shaped object in the image, and has a modulus of 1. Thus the position of a band-shaped object will have no influence on the modulus of its Fourier transform.

Discrete Fourier transform of a rotated band-shaped object

We consider now the discrete Fourier transform of a rectangular domain Ω'_R obtain from Ω_R, through the rotation $\boldsymbol{\mathcal{R}}$, and we defined the rotated coordinates x'_i, associated to the rotated grid Ω' and the rotated frequencies ξ'_i, as follow:

$$\boldsymbol{x}' = \boldsymbol{\mathcal{R}}\cdot\boldsymbol{x} \tag{C.3}$$

Using the vector notation of the DFT (eq. (A.30)), and neglecting edge effects of the finite grid, we have:

$$\hat{\mathbb{I}}_{\Omega'_R}(\boldsymbol{\xi}') = \sum_{\boldsymbol{x}'_i\in\Omega'} \mathbb{I}_{\Omega'_R}(\boldsymbol{x}'_i)e^{-j\boldsymbol{\xi}'\cdot\boldsymbol{x}'_i} = \sum_{\boldsymbol{x}_i\in\Omega} \mathbb{I}_{\Omega'_R}(\boldsymbol{\mathcal{R}}\cdot\boldsymbol{x})e^{-j\boldsymbol{\xi}'\cdot\boldsymbol{\mathcal{R}}\cdot\boldsymbol{x}}$$

(a) binary image   (b) numerical DFT   (c) analytical DFT

(d) binary image   (e) numerical DFT   (f) analytical DFT
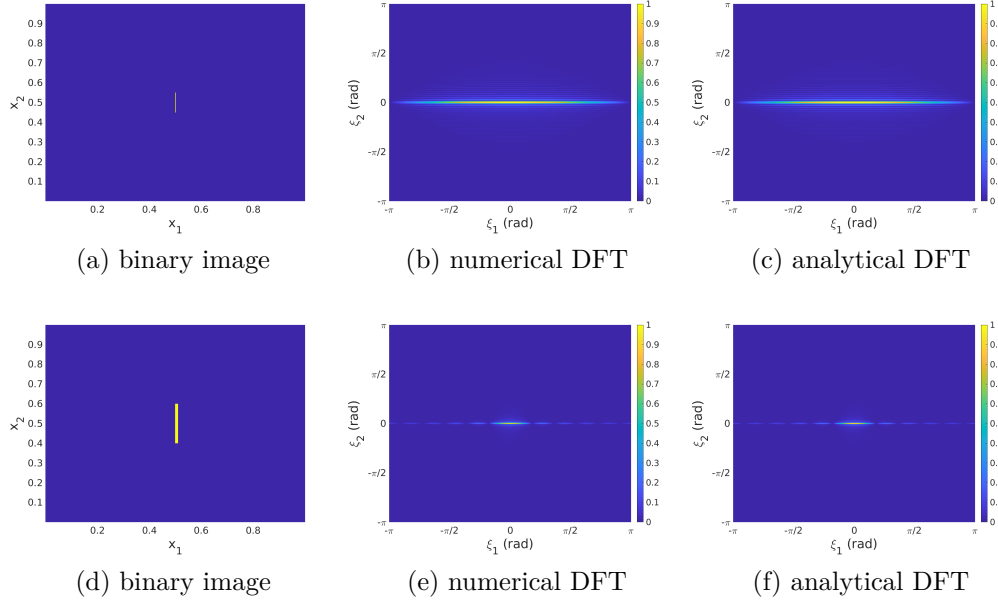
Figure C.1 – Exemples of the DFT of a binary rectangular domain for two different domains.

By definition, we have $\mathbb{I}_{\Omega'_R}(\boldsymbol{x}'_i) = \mathbb{I}_{\Omega_R}(\boldsymbol{x})$. Thus:

$$\hat{\mathbb{I}}_{\Omega'_R}(\boldsymbol{\xi}') = \sum_{\boldsymbol{x}_i \in \Omega} \mathbb{I}_{\Omega_R}(\boldsymbol{x}) e^{-j\left(\underline{\boldsymbol{\mathcal{R}}}^T \cdot \boldsymbol{\xi}'\right) \cdot \boldsymbol{x}}$$

Finally, introducing the variable change $\boldsymbol{\xi}' = \underline{\boldsymbol{\mathcal{R}}} \cdot \boldsymbol{\xi}$, we have:

$$\hat{\mathbb{I}}_{\Omega'_R}(\underline{\boldsymbol{\mathcal{R}}} \cdot \boldsymbol{\xi}) = \sum_{\boldsymbol{x}_i \in \Omega} \mathbb{I}_{\Omega_R}(\boldsymbol{x}) e^{-j\boldsymbol{\xi} \cdot \boldsymbol{x}} = \hat{\mathbb{I}}_{\Omega_R}(\boldsymbol{\xi}) \tag{C.4}$$

This result shows that the DFT of a rotated rectangular region is the DFT of the original region transformed by the same rotation, as illustrated on fig. C.2. The presence of harmonic frequencies due to edge effect is noticeable.

(a) binary image

(b) numerical DFT

(c) binary image

(d) numerical DFT
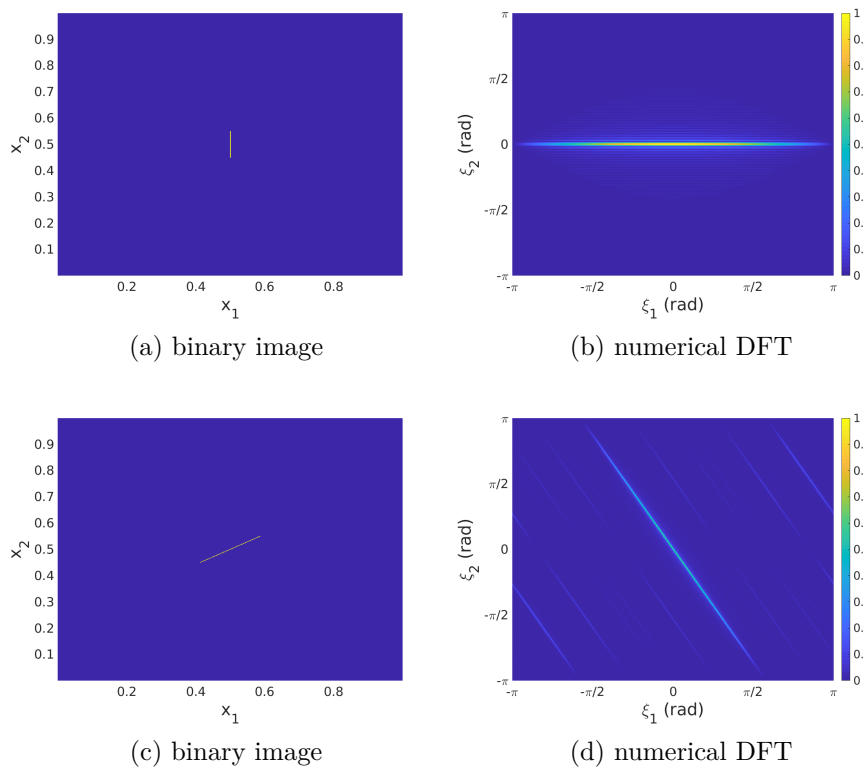
Figure C.2 – Exemples of the DFT of a rotated object with respect to the DFT of the original object. (a-b) : original object and it's DFT. (c-d): rotated object and its DFT rotated of the same angle

(a) binary image

(b) numerical DFT
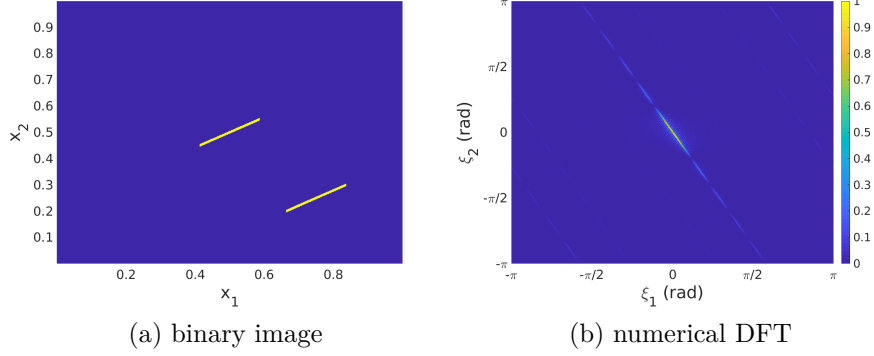
Figure C.3 – Exemples of the DFT of two identical objects separated by a translation.

Discrete Fourier transform of a band-shaped object and its translated copy

We now consider the DFT of the domain $\Omega_{RR'} = \Omega_R \cup \Omega'_R$, where Ω'_R is identical to Ω_R but translated of a vector $\boldsymbol{u} = (i_1^u, i_2^u)$, so that $\Omega_R \cap \Omega'_R = \emptyset$.

$$
\begin{aligned}
\hat{\mathbb{I}}_{\Omega_{RR'}}(\boldsymbol{\xi}) &= \sum_{\boldsymbol{x}_i \in \Omega} \left[\mathbb{I}_{\Omega_R}(\boldsymbol{x}_i) + \mathbb{I}_{\Omega'_R}(\boldsymbol{x}_i) \right] e^{-j\boldsymbol{\xi} \cdot \boldsymbol{x}_i} \\
&= \sum_{\boldsymbol{x}_i \in \Omega} \mathbb{I}_{\Omega_R}(\boldsymbol{x}_i) e^{-j\boldsymbol{\xi} \cdot \boldsymbol{x}_i} + \sum_{\boldsymbol{x}_i \in \Omega_R} \mathbb{I}_{\Omega'_R}(\boldsymbol{x}_i) e^{-j\boldsymbol{\xi} \cdot \boldsymbol{x}_i} \\
&= \sum_{\boldsymbol{x}_i \in \Omega} \mathbb{I}_{\Omega_R}(\boldsymbol{x}_i) e^{-j\boldsymbol{\xi} \cdot \boldsymbol{x}_i} + \sum_{\boldsymbol{x}_i \in \Omega_R} \mathbb{I}_{\Omega_R}(\boldsymbol{x}_i) e^{-j\boldsymbol{\xi} \cdot (\boldsymbol{x}_i + \boldsymbol{u})} \\
&= \left(1 + e^{-j\boldsymbol{\xi} \cdot \boldsymbol{u}} \right) \hat{\mathbb{I}}_{\Omega_R}(\boldsymbol{\xi}) = 2e^{-j\frac{\boldsymbol{\xi} \cdot \boldsymbol{u}}{2}} \cos\left(\frac{\boldsymbol{\xi} \cdot \boldsymbol{u}}{2} \right) \hat{\mathbb{I}}_{\Omega_R}(\boldsymbol{\xi})
\end{aligned}
$$

Taking the modulus of this expression, we get:

$$
\left| \hat{\mathbb{I}}_{\Omega_{RR'}}(\boldsymbol{\xi}) \right| = \left| \cos\left(\frac{\boldsymbol{\xi} \cdot \boldsymbol{u}}{2} \right) \right| \left| \hat{\mathbb{I}}_{\Omega_R}(\boldsymbol{\xi}) \right| \tag{C.5}
$$

Thus, the DFT of two identical objects separated by a translation of vector $\boldsymbol{u}$ is the DFT of one object modulated by a sinusoid in the direction of $\boldsymbol{u}$ and of period $\sim \frac{2\pi D}{\|\boldsymbol{u}\|}$ in Fourier space, where D is the dimension of the grid in the direction $\boldsymbol{u}$. This period is always bigger than the grid and thus the modulation is hardly noticeable on the scpeter, as can be seen on the exemple given in *fig. C.3*.

C.1.2 Application to image processing: spectral method for band separation

The results presented above show that, for a binary image containing one family of band-shaped objects with the same orientation and similar geometrical features, its discrete Fourier transform will be composed of a frequency band rotated of a right angle with respect to the bands orientation in the original image, with minor modulations due to the different positions and shapes of the bands. It also show that taking the inverse Fourier transform of this band will allow to reconstruct an image of the band-shaped objects.

When considering multiples band families, the DFT of the image will be the sum of the DFT of each of the band families in the image, each of them being non negligible in its associated frequency band. Each of these frequency band contains the information in the image relative to its associated object family, and can be used to reconstruct an image containing only this band object family. In principle, it is then possible to extract one band object family by taking the DFT of the original image, applying a filter that isolate this particular frequency band, and take finally the inverse DFT of the resulting filtered spectrum.

In practice, plastic slip intragranular localization is highly likely to occur forming bands along specific directions linked to the crystallography of the material. Thus the localization indicator function L presented in section 3.3.2, when restricted to a grain, will be a binary image composed of elongated objects oriented in one of these directions, and likely to cross each-other, similar to the images of ideal rectangular objects used for illustration in this section.

For this reason, the proposed spectral method allow to solve the issue raised in section 3.3.3, that is the separation of elongated objects crossing each other, in order to allow for proper segmentation of band-shaped objects in L. Each of the slip band localization orientations will have an associated frequency band in the DFT of L, $\hat{L}$. As these bands occupy all the radial extension of the frequency domain, an angular research method is well suited for their identification in Fourier space. The method consists in finding the angular directions that have the highest spectral density in $\hat{L}$, and then apply filtering and inverse Fourier transform.

In practice however, the bands intersect at the origin in Fourier space where they also achieve their maximum spectral density. Thus, the DFT of an image containing more than one family of bands will have a very dense central spot containing most of the spectrum energy, as illustrated on fig. C.4 (b). The intensity of this central spot can compromise the search for most dense angular sectors of the spectrum. To avoid this issue, low frequencies can be filtered with a radial cut-off in order to obtain a spectrum where the different frequency band are
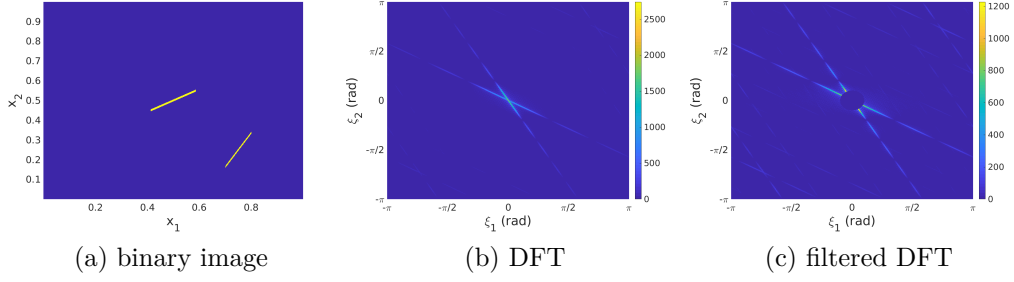
(a) binary image   (b) DFT   (c) filtered DFT

Figure C.4 – Exemples of the DFT of two different band-shaped objects. (a) original image, (b) its DFT and (c) its DFT with a radial cutoff of low-frequency.

(a)   (b)   (c)
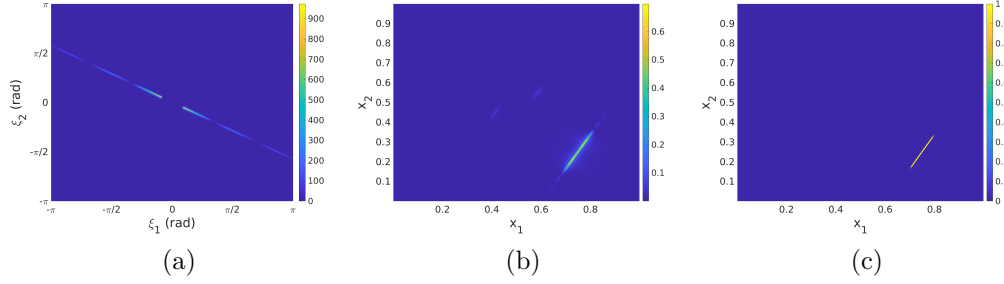
Figure C.5 – Exemples of the DFT of two different band-shaped objects. (a) original image, (b) its DFT and (c) its DFT with a radial cutoff of low-frequency.

well separated, as shown on fig. C.4 (c), and thus easily found with the angular search method.

The reconstruction process is illustrated on fig. C.5. (a) show one of the two frequency bands of fig. C.4 (c) identified after the angular search process. As shown on (b), the inverse DFT of this band frequency contains spurious noise of low magnitude, due to the loss of information associated to filtering, however the corresponding band of the original image is clearly visible. The final step for the reconstruction of a binary image containing only the desired objects, is to transform it into a binary image above a threshold This way we obtain a binary image indicating the region of the original image associated to the filtered frequency band. Finally, taking its intersection with the original image yields the desired reconstruction. The result of this process can be seen on fig. C.5 (c).

This spectral separation method is then used to construct grain per grain the slip and kink indicator fields. The main steps of the algorithm are:

1. In the binary image L, crop the region of a grain of the polycrystal

2. An image opening is applied to the field in the grain and is subtracted to the original image. This technique allows to eliminate objects without an elongated shape.

3. Apply the spectral separation method and extract the different images corresponding to the each maximum of the computed spectral angular density.

4. For each of these images:

   (a) Segmentation of connected objects

   (b) Elimination of objects with a low aspect ratio.

   (c) Comparison of the orientation of segmented objects with slip planes orientation. Parallel objects are added to the slip band indicator S and perpendicular objects are added to the kink band indicator K, and subtracted from the processed image.

5. If all bands have not been detected, repeat steps 3 and 4 on the remaining image

C.1.3   Algorithm details

This strategy has been implemented using the Matlab software/langage, in particular the Image Processing and signal Processing tool boxes which contain functions for the segmentation of connected objects in binary images, as well as their geometrical characterization. Determination of segmented objects aspect ratio and orientation is obtained through the function **regionprops** of the Matlab Image Processing Toolbox. This function evaluates a large set of geometrical properties of all the connected objects of its binary image argument, providing all the necessary information to select elongated object and sort them according to their orientation.

Image opening substraction

The spectral separation method of different families of band-shaped objects is efficient only if the processed image is mainly composed of such elongated objects. Otherwise the other objects will pollute its spectrum, in which the frequency bands will be hardly distinguishable. Hence, localization indicator fields must be processed to take out non elongated objects prior to the application of the spectral separation method. To this end, the image opening technique is employed.

Image opening consist in the succession of an erosion and a dilation of binary image by a structuring element. Exact description of these operations can be found in a mathematical morphology course and will not be detailed here. For
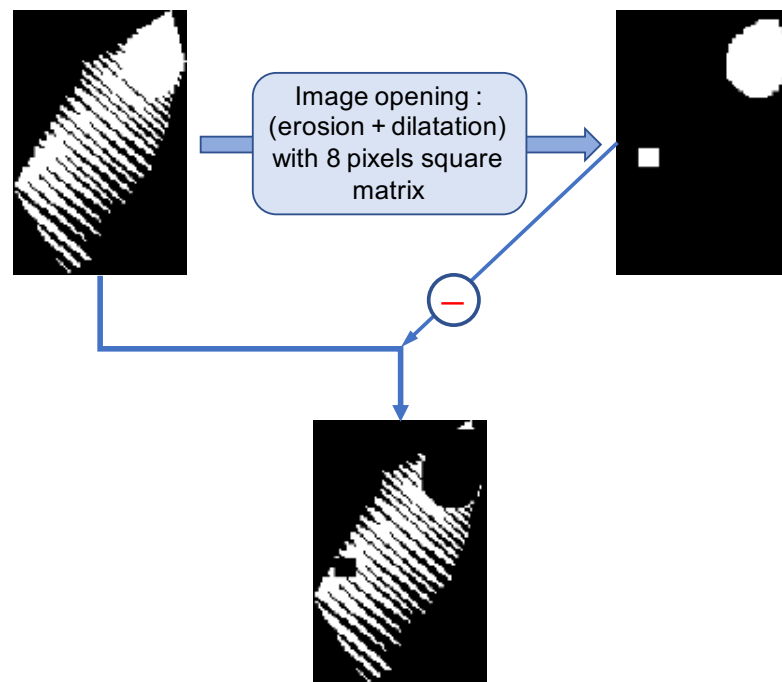
Figure C.6 – Elimination of non elongated objects from the *L* field of a grain by subtraction of the opening of original image. The reference element is a square matrix of size equivalent here to the fifth of the grain size.

the present work, it is sufficient to know that the erosion step removes objects that have a dimension that is smaller to the structuring element, while the dilatation step restores the shape of remaining objects. Using a square matrix of N pixels, this technique will remove objects that extend over N pixels or less in one direction, in particular all band-shaped objects that are thiner than N pixels. Thus, subtracting this image to the original one yield an image containing only objects that have at least one dimension smaller than N voxels, and is free of non band-shaped objects. This process is illustrated on fig. C.6.

Iterative search

After, the opening technique and spectral based reconstruction of a band family binary image, connected objects are segmented and classified according to their orientation. Several steps of processing can be required to find all the objects contained in the image, due to the loss of information associated to the spectral separation method. Thus at each step, the residual image of non classified objects is processed again with the spectral method and the segmentation and geometrical

(a) Algorithm first pass


(b) Algorithm second pass
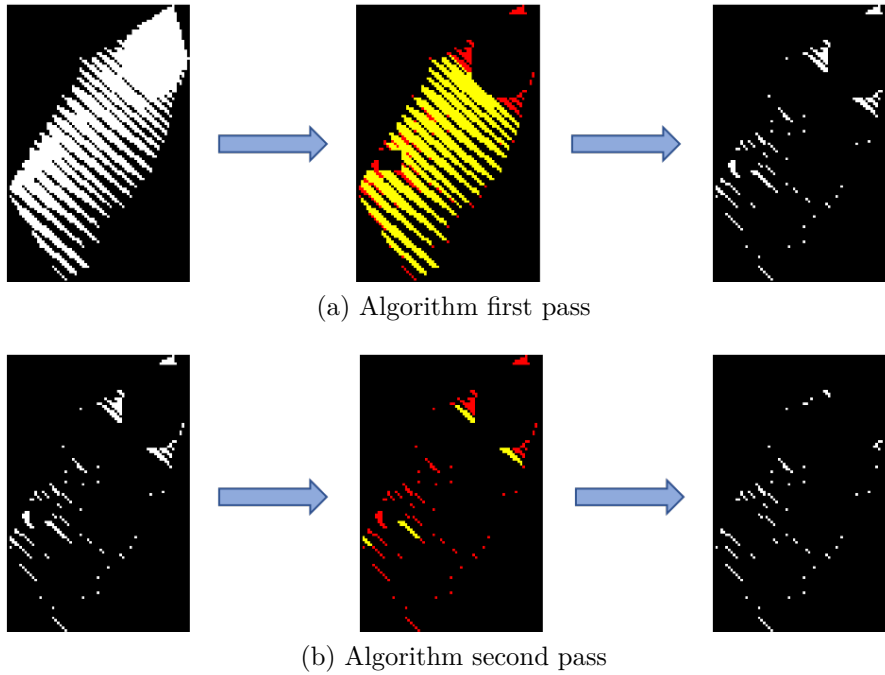
Figure C.7 – Two step of identification of slip bands in a grain's slip indicator function. Each step is composed of a spectral analysis of the image, and the segmentation and orientation based classification of connected objects. Left image are algorithm starting point, the central image shows in yellow the identified objects after the step, and the last image is the residual image with non processed objects

analysis. The process stops when no more objects are found or when the residual of the image contains less than percent of the original image.

C.1.4 Algorithm parameters

The algorithm that has been implemented to apply this analysis strategy require the following set of input parameters:

1. Φ_D: relative threshold for the construction of L from the effective plastic deformation field.

2. N_o: size of the square matrix use for the image opening subtraction step.

3. R_ξ: cutoff radius for low frequencies to filter $\hat{L}$

4. $\Delta\varphi$: angular discretization of Fourier space for the most dense frequency bands search

5. A_{min}: minimal aspect ratio required to consider segmented objects as localization bands and add them to slip and kink indicator functions. Aspect ratio is defined as the ratio between the longest dimension of the object and its shortest. It is an output of the function **regionprops** of the Matlab Image Processing Toolbox.

6. $\Delta\theta$: angular tolerance. This parameter is used for the classification of segmented objects. They are sorted as slip/kink bands if their evaluated orientation $\theta*$ verifies

$$\theta* \in \left[\theta^i - \Delta\theta, \theta^i + \Delta\theta\right]$$

where θ^i is one of the theoretical orientations of slip/kink bands of the grain, given by its crystallographic orientation.

R_ξ and $\Delta\varphi$ has been chosen after trying a range of value on a test polycrystalline simulation. The retained value for R_ξ has been chosen by progressively rising the threshold until the number of errors in the angular search of dense directions does not evolve any more. The value of $\Delta\varphi$ is chosen as the optimal compromised observed between the quality of reconstruction of band family images, and algorithm speed. $\Delta\theta$ is chosen equal to 8° as it is the uncertainty on the orientation of a discretized object of aspect ratio 3.5 is $\arctan\left(\frac{1}{3.5}\right) \approx 16°$. N_o, Φ_D and A_{min} are given values that seem reasonable to characterize localization bands.

All simulations treated with this algorithm in this document were processed with the same set of values for these parameters:

$\Phi_D = 3$	$N_o = \frac{l_g}{5}$	$R_\xi = 0.05\pi$	$\Delta\varphi = 5°$	$A_{min} = 3$	$\Delta\theta = 8°$

where l_g is the mean grain size of the polycrystal.

C.2   Slip profiles processing based strategy

This section provides a complete description of the signal processing algorithm used to obtain a statistical description of the localization bands populations in a polycrystalline simulation, presented in section 3.3.4. First the algorithm steps are described. Then, the issues linked to the use of a profile interpolated inside a localization band is discussed, as well as implemented solutions.

C.2.1   Peak detection algorithm

The extraction of slip profiles in each grain is done by:

1. Choosing a starting point $\boldsymbol{x}_0$ in the grain domain Ω_g.

2. From this starting point, generating the following sets of points:

$$\begin{aligned}
\mathbb{X}_{sl}^p &= \left\{ \boldsymbol{x}^k = \boldsymbol{x}_0 + kdl\boldsymbol{n}^s \mid k \in \mathbb{Z},\ \boldsymbol{x}^k \in \Omega_g \right\} \\
\mathbb{X}_{ki}^p &= \left\{ \boldsymbol{x}^k = \boldsymbol{x}_0 + kdl\boldsymbol{m}^s \mid k \in \mathbb{Z},\ \boldsymbol{x}^k \in \Omega_g \right\}
\end{aligned} \tag{C.6}$$

3. For each set of points in Ω_g, constructing a slip profile by interpolating the slip field obtain from FFT simulations at the points of the set:

$$\begin{aligned}
\mathbb{P}_{sl}^s &= \left\{ |\gamma^s(\boldsymbol{x}^k)| \mid k \in \mathbb{Z},\ \boldsymbol{x}^k \in \mathbb{X}_{sl}^p \right\} \\
\mathbb{P}_{ki}^s &= \left\{ |\gamma^s(\boldsymbol{x}^k)| \mid k \in \mathbb{Z},\ \boldsymbol{x}^k \in \mathbb{X}_{ki}^p \right\}
\end{aligned} \tag{C.7}$$

$\mathbb{X}_{sl}^p$ and $\mathbb{X}_{ki}^p$ denote respectively the set of points defining the slip band and kink band slip profiles. $\mathbb{P}_{sl}^s$ and $\mathbb{P}_{ki}^s$ denote respectively the value of interpolated slip profile along the slip band profile and the kink band profile.

The peak detection algorithm takes a slip profile, as defined in eq. (C.7), and returns two sets:

- A set of selected maxima and minima:

$$\mathbb{M} = \left\{ m_i^\pm \mid m_i^\pm \in \mathbb{P}_*^s,\ m_+^i \text{ is a maximum}, m_-^i \text{ is a minimum} \right\} \tag{C.8}$$

The actual set of maxima and minima obtained a the step k of the algorithm is noted $\mathbb{M}^k$.

- Its associated set of coordinates:

$$\mathbb{X}_\mathbb{M} = \left\{ \boldsymbol{x}^i \mid |\gamma^s(\boldsymbol{x}^i)| = m_i^\pm,\ \boldsymbol{x}^k \in \mathbb{X}_*^p \right\} \tag{C.9}$$

Identically, the set of coordinates obtained at the step k of the algorithm is noted $\mathbb{X}_\mathbb{M}^k$. x^i denotes the coordinate on the profile of the point $\boldsymbol{x}^i$ with respect to the starting point $\boldsymbol{x}^0$, i.e. $x^i = (\boldsymbol{x}^i - \boldsymbol{x}^0) \cdot \boldsymbol{d}$, where $\boldsymbol{d}$ is the direction of the profile unit vector.

After setting these notations, we can now described the algorithm steps:

<u>Step 1</u>: **Raw detection of all local maxima and minima**:
at each point where the sense of variation of the signal changes, the extrema

is stored in $\mathbb{M}^1$. Thus, this set is composed of a succession of maximum and minimum couples one after the other:

$$\mathbb{M}^1 = \left\{ \ldots, m_-^i, m_+^i, m_-^{i+1}, m_+^{i+1}, \ldots \right\}$$

Step 2: **Suppression of maximums/minimums below/above threshold** :
The elements of $\mathbb{M}^1$ are compared to the threshold $\Phi^* = \bar{p} \cdot \Phi_D$. The maxima that are under this value, and the minima that are above, are taken out of the set.

$$\mathbb{M}^2 = \mathbb{M}^1 \setminus \left[\left\{ m_+^i \,\middle|\, m_+^i < \Phi^*, \, m_+^i \in \mathbb{M}^1 \right\} \cup \left\{ m_-^i \,\middle|\, m_-^i > \Phi^*, \, m_-^i \in \mathbb{M}^1 \right\} \right]$$

This step allows this for this method to be consistent with the definition of the slip localization indicator function L of methods 1 and 2. Indeed, after this steps, the element of $\mathbb{X}_{\mathbb{M}}^2$ verify:

$$L(\boldsymbol{x}_i) = 1, \qquad \forall \boldsymbol{x}_i \in \mathbb{X}_{\mathbb{M}}^2$$

Step 3: **Fusion of consecutive maxima**:
In order to have to a non ambiguous definition of slip localization bands, they should be defined by a single maximum between two minimums of the slip profile. In this step, all the subsets of successive maxima in $\mathbb{M}^2$ are replaced by the barycenter of these maxima (for both maximum value and coordinate).

$$\left\{ m_+^i, m_+^{i+1}, \ldots, m_+^{i+r} \right\} \longmapsto m_+^{i*} = \frac{1}{r+1} \sum_{k=i}^{i+r} m_+^k$$

$$\left\{ \boldsymbol{x}^i, \boldsymbol{x}^{i+1}, \ldots, \boldsymbol{x}^{i+r} \right\} \longmapsto \boldsymbol{x}^{i*} = \frac{1}{r+1} \sum_{k=i}^{i+r} \boldsymbol{x}_+^k$$

Step 4: **Suppression of small peaks**:
A peak height is defined as the difference between a maximum and the next or previous minimum. Two heights can be computed for each peak. In this step, all peaks that have heights below the threshold $\frac{\Phi*}{4}$ are taken out of the set. This step is designed to suppress fluctuation peaks, that are small compared to the threshold. This step can be formally written:

$$\mathbb{M}^4 = \mathbb{M}^3 \setminus \left\{ m_+^i \,\middle|\, |m_+^i - m_-^{i\pm 1}| < \frac{\Phi*}{4}, \, m_+^i \in \mathbb{M}^3, m_-^{i+1} \in \mathbb{M}^3 \right\}$$

Step 5: **Fusion of consecutive minima**:
This step is similar to Step 3, but for the fusion of minima of the set $\mathbb{M}^4$. Successive minima are replaced by the minimum of these minima (for both maximum value and coordinate).

$$\left\{ m_-^i, m_-^{i+1}, \ldots, m_-^{i+r} \right\} \longmapsto m_-^{i*} = \min\left(m_-^i, m_-^{i+1}, \ldots, m_-^{i+r} \right)$$
$$\left\{ \boldsymbol{x}^i, \boldsymbol{x}^{i+1}, \ldots, \boldsymbol{x}^{i+r} \right\} \longmapsto \boldsymbol{x}^{i*} \text{ such that } |\gamma^s(\boldsymbol{x}^{i*})| = m_-^{i*}$$

At this stage, the obtain set $\mathbb{M}^5$ contains, as $\mathbb{M}^1$ a succession of maximum and minimum couples.

Step 6: **Definition of interpolation points for each peak**:
For each maxima m_+^i contained in $\mathbb{M}^5$, two interpolation points m_l^i and m_r^i are defined at the following profile coordinates:

$$x_l^i = \max\left(x_-^{i-1}, \max\left\{ x^j \, | |\gamma^s(\boldsymbol{x}^j)| < \Phi_0, \, x^j < x^i, \, \boldsymbol{x}^j \in \mathbb{X}_*^p \right\} \right)$$
$$x_r^i = \min\left(x_-^{i+1}, \min\left\{ x^j \, | |\gamma^s(\boldsymbol{x}^j)| < \Phi_0, \, x^j > x^i, \, \boldsymbol{x}^j \in \mathbb{X}_*^p \right\} \right)$$

m_l^i is the first point to the left of m_+^i to be below the value Φ_0, or the previous minimum if it closest. m_r^i has the same definition. The threshold is chosen so that: $\Phi_0 = \bar{p}$.

The three points $\{m_l^i, m_+^i, m_r^i\}$ are then interpolated by a parabola, in order to evaluate the peak width. It is approximated by the distance between the roots of the parabola. When one of the roots of the interpolating parabola is located outside the grain, the band width is computed as the distance between the other root and the grain boundary. Moreover, is a maximum is located on the grain boundary, only one interpolating point can be properly defined. In this case the other one is constructed by taking the symmetric of the first interpolation point with respect to m_+^i, as illustrated on fig. C.8.

Hence, in this method a localization band is approximated by a parabola passing through the peak and its two closest minimums, or the two closest points below the mean plastic strain in the polycrystalline cell, if they are closer. Step 6 is designed in order to avoid ambiguous definitions of interpolating points when the slip profile fluctuates at low values on both sides of the peak. Indeed, because of Step 5, minimum positions in this zone is not well defined and thus the threshold Φ^0 is used to define interpolating points. On the contrary, when the closest minima are above Φ^0, the threshold based definition is impossible and they should be chosen as interpolating points.
Finally, the result allow to construct the set of distances between the bands as
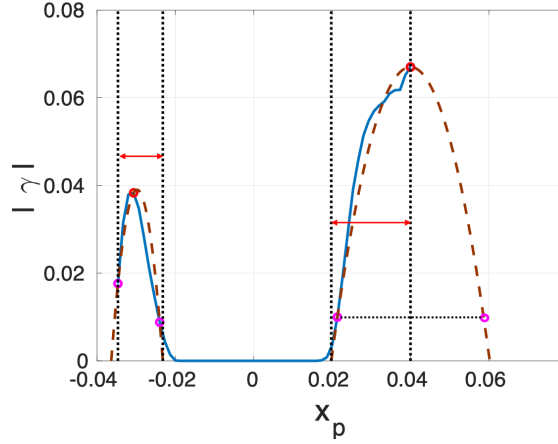
Figure C.8 – Evaluation of band width for peaks close to grain boundaries. The evaluated width are represented by the red double arrows, the position of the peaks by the red circles, the interpolation by the purple circles and the interpolating parabolas are the brown dashed curves.

follow:

$$\mathbb{D} = \left\{ \left| x^{i+1} - x^i \right| \mid x^i \in \mathbb{X}_{\mathbb{M}}^6 \right\}$$

All the steps of the algorithm are illustrated on fig. C.9.

C.2.2   Peak detection inside a localization band

The algorithm is design for slip profiles that have a mean value that is small compared to Φ^*. This is generally the cases in softening polycrystalline simulations. Indeed, slip tends to localize in intense bands while elsewhere the plastic activity is almost zero. However, it may occur that the slip profiles are interpolated inside or close to a localization band, and thus have a high mean value. In this case, Step 2 will lead to the suppression of most of the minima in the profile, and Step 3 will result in the undesired fusion of most of the maxima, leading to a wrong identification of localization band number, position, and width. To avoid it, when the mean slip level of the profile is high, the thresholds are adapted as follow:

$$\text{if} \, \overline{\mathbb{P}} > \frac{2\Phi^*}{3} \longrightarrow \left\{ \Phi^* = \Phi^\star = 1.25\overline{\mathbb{P}}, \quad \Phi_0 = \Phi_0^\star = 0.75\overline{\mathbb{P}} \right\} \tag{C.10}$$

where $\overline{\mathbb{P}}$ is the mean value of the slip profile.
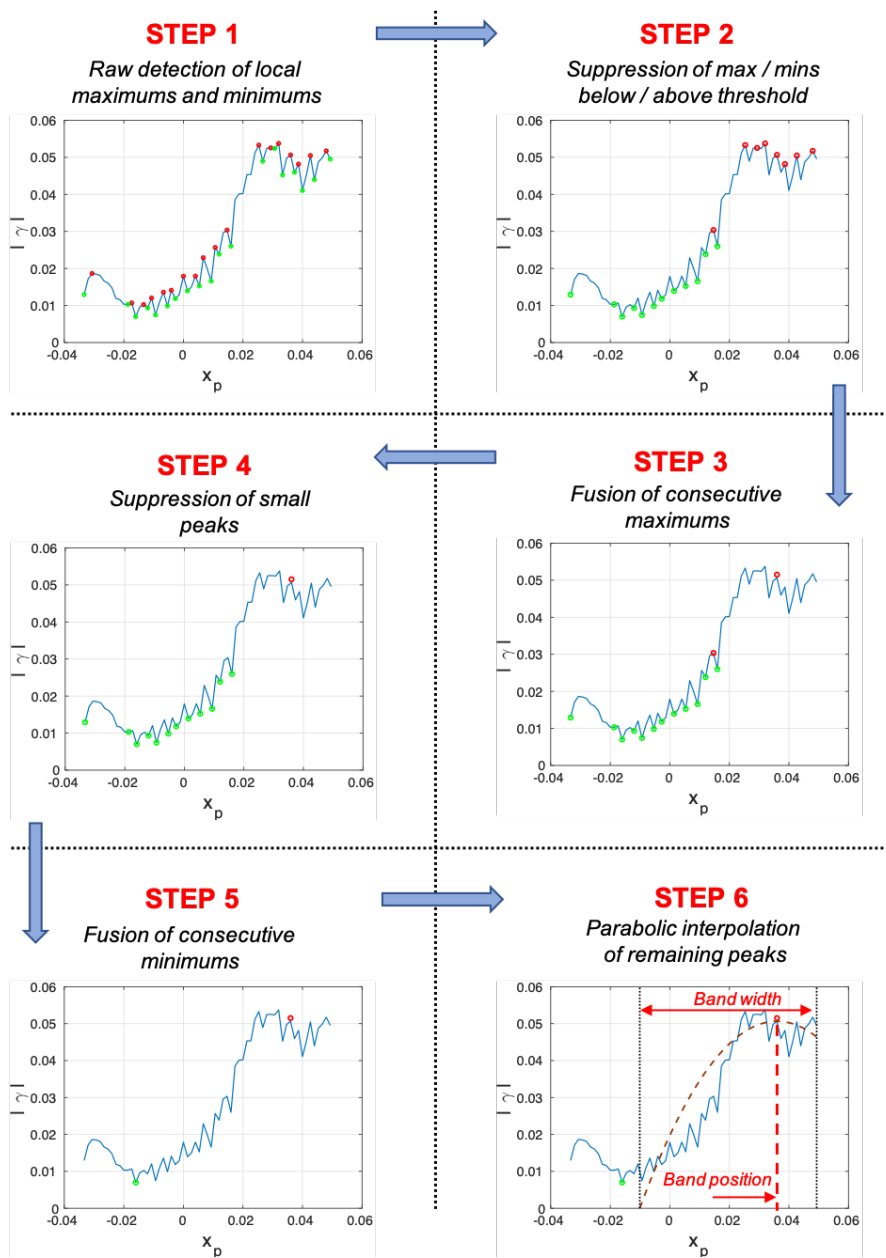
Figure C.9 – Overview of all the steps of the peak detection algorithm illustrated of a given slip profile.
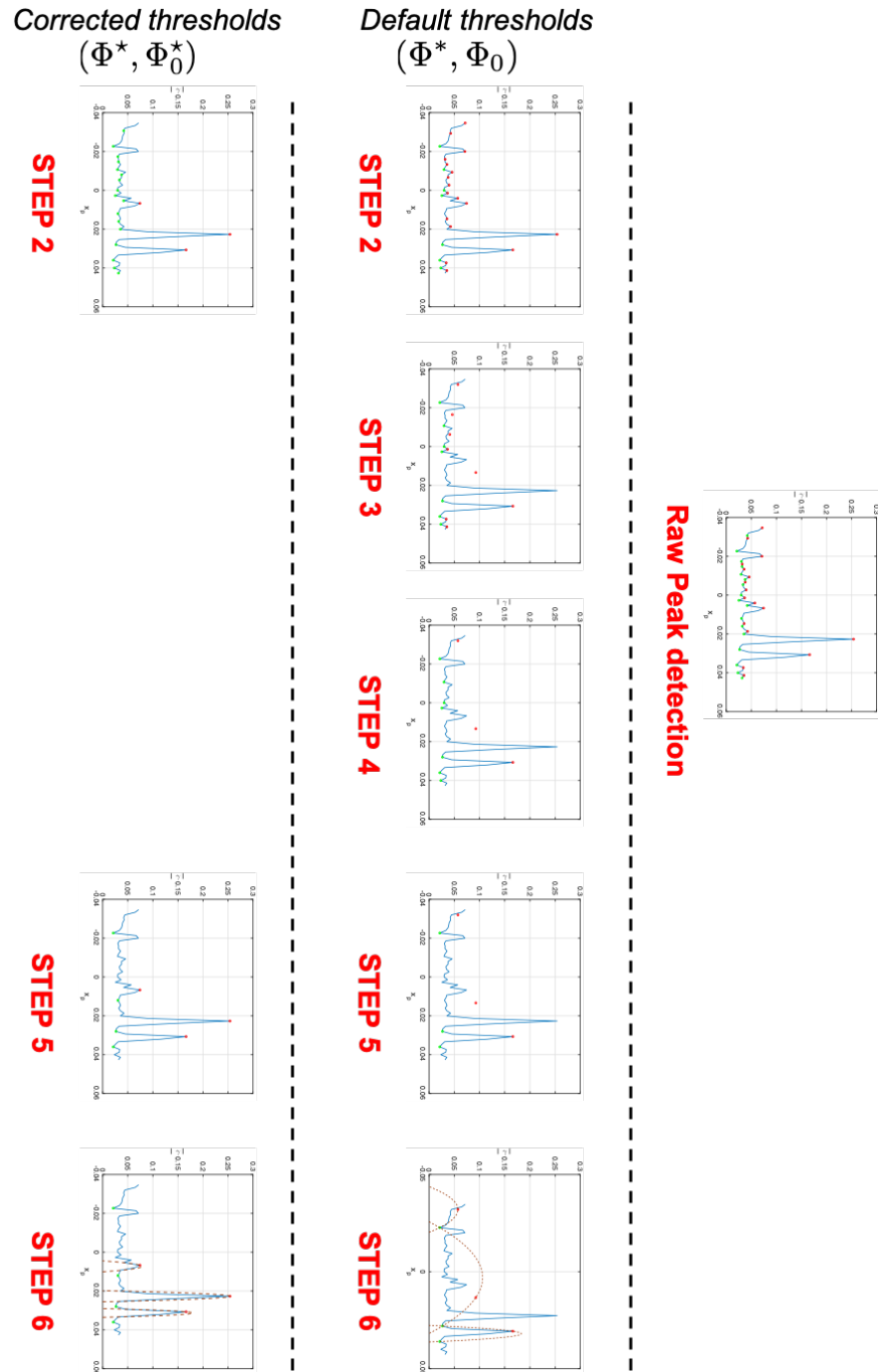
Figure C.10 – Comparison of the algorithm efficiency for the default thresholds (Φ^*, Φ_0) and the corrected thresholds $(\Phi^\star, \Phi_0^\star)$ in the case of a high mean value slip profile. Maxima are represented by the red circles, the minima by the green circles and the interpolating parabolas are the brown dashed curves.

APPENDIX D

POLYCRYSTAL COLORING ALGORITHM

We present here the algorithm implemented to search for an optimal coloring of a polycrystal.

D.1 Notation, definitions and four color theorem

This section provides the definitions and notation used to describe the coloring algorithm. Coloring problems are a branch of graph theory. For the sake of simplicity, mathematical objects involved in these problems are simplified and redefined for the specific context of polycrystal images coloring.

Definition. *We define a polycrystal $\mathcal{P}$ as a set of N grains G_i:*

$$\mathcal{P} = \left\{ \bigcup_{i=1}^{N} G_i \right\}$$

The grains are a partition of $\mathcal{P}$ into contiguous regions connected through edges, the grain boundaries.

Definition. *The neighborhood of the grain G_i in $\mathcal{P}$, $\mathcal{V}_i$, is the set of grains of $\mathcal{P}$ that are in contact with G_i, i.e that share a grain boundary with G_i.*

$$\mathcal{V}_i = \{ G_k \mid G_k \cup G_i \neq \varnothing,\ G_k \in \mathcal{P}, G_i \in \mathcal{P} \}$$

Definition. *A color palette $\mathcal{C}$ is a set of colors C_k:*

$$\mathcal{C} = \{C_k\}$$

Definition. *A coloring of $\mathcal{P}$ with the color palette $\mathcal{C}$ is the set of pairs composed of a grain of $\mathcal{P}$ and an associated color:*

$$\mathbb{C}(\mathcal{P},\mathcal{C}) = \{(G_i,C_i) \mid G_i \in \mathcal{P}, C_i \in \mathcal{C}\}$$

Definition. *$\mathbb{C}(\mathcal{P},\mathcal{C})$ is a **proper coloring** if each grain is associated to a color that is not associated to any of its neighbors, i.e. if:*

$$\{(G_i,C_i) \in \mathbb{C}(\mathcal{P},\mathcal{C}) \Rightarrow C_j \neq C_i \, , \forall G_j \in \mathcal{V}_i\}$$

Definition. *The order of the coloring $\mathbb{C}(\mathcal{P},\mathcal{C})$ is the number of colors used for the coloring, $\eta = \mathrm{card}(\mathcal{C})$. A k-colorable polycrystal is a polycrystal for which exists at least one proper coloring of order k.*

Definition. *The color palette used for the coloring of a subset $\mathcal{K}$ of $\mathcal{P}$, is noted $\mathcal{C}[\mathcal{K}]$. Thus, the color palette associated to the coloring of the neighbors of grain G_i is $\mathcal{C}[\mathcal{V}_i]$*

Definition. *A Kempe grain chain is a bichromatic set of connected grains. $\mathcal{K}(G_i,C_i,C_l)$ is the $(C_i,C_l) - $ Kempe chain of the grain G_i in $\mathcal{P}$. It is the maximal subset of connected grains of $\mathcal{P}$ containing G_i and only grains associated to the colors C_i and C_l.*

A schematic example of two Kempe chains is given on . From the definition of Kempe grain chains, it is clear that this sets are connected only with grains that are not colored with the two colors defining the chain. This implies that, the colors of the grains in a Kempe chain can be inverted while keeping the polycrystal properly colored.

Definition. *A Kempe grain chain inversion is the operation that inverts the colors of the grains of a particular Kempe chain. Formally, it can be written:*

$$(G_i,C_k) \longmapsto (G_i,C_l) \quad \forall (G_i,C_k) \in \mathcal{K}(G_k,C_k,C_l)$$
$$(G_i,C_l) \longmapsto (G_i,C_k) \quad \forall (G_i,C_l) \in \mathcal{K}(G_k,C_k,C_l)$$

Theorem 1 (Four color theorem 1)**.** *In graph theory, the four color theorem states that every planar graph is four-colorable.*
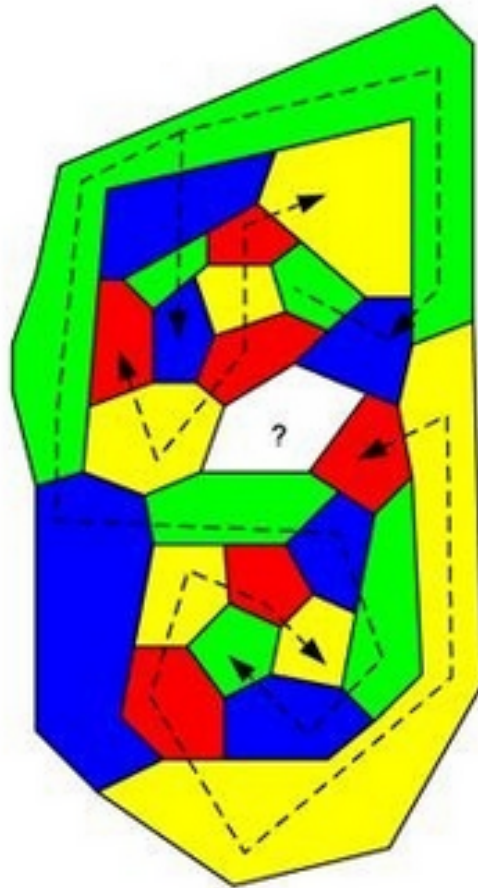
Figure D.1 – Schematic representation of a polycrystal coloring. The dotted lines represent Kempe chains associated to the color pairs blue-green, and yellow-red.

As a planar region divided into contiguous region that are considered adjacent if they share an edge is always equivalent to a planar graph, the theorem can be applied in the context of polycrystal coloring.

Theorem 2 (Four color theorem 2). *Every two dimensional polycrystal is four-colorable.*

D.2 Algorithm description

A polycrystal coloring algorithm is an algorithm that take an image of a polycrystal as input and returns one of its proper colorings. A secondary objective of the algorithm, is to return an optimal coloring of the polycrystal. Optimal coloring of a polycrystal is intended as finding a coloring with the lowest possible order.

To obtain optimal coloring of a N grain polycrystal $\mathcal{P}$, the first possibility is the so-called brute force algorithm. It consists in considering all the k-colorings of $\mathcal{P}$, and output any of the obtained proper colorings if at least one is found. If no proper coloring is obtained, repeat the operation for $k + 1$-colorings, and so on until a proper coloring is found. It has the advantage of finding every time an optimal coloring of the polycrystal, but has to explore N^k possibilites at each step. Then, this algorithm requires in average N^m coloring operations in order to find a proper coloring, if $\mathcal{P}$ is at least m colorable. This strategy is not very well suited for large polycrystals for which the number of possibilities rapidly explodes, before finding a proper coloring.

An alternative is a greedy algorithm. It consists in considering the grains in a specific order, and for each of them, assigning the first available color, adding one to the palette if needed. The available color are the one that have note already been used to color its neighbors. It has the advantage of finding every time a proper coloring, but not necessarily an optimal one. In fact, the order of the computed coloring is strongly dependent on the order in which the grains are colored.

The greedy algorithm has been chosen as the baseline strategy for the coloring algorithm developed here. In order to optimize the process, when the algorithm needs to add a new color to the color palette for a particular grain, the coloring is reconfigured in order to change the color of the neighboring grains to free one of the colors already in the palette. This operation is done by trying to find Kempe chains that contains only one neighbor of the considered grain. If such chains exist, they can be inverted. This result in a color change for the grain neighbor involved in this chain, which allows to use its former color for the considered grain.

The algorithm, written with the notation described in appendix D.1, is shown on fig. D.2

D.3   Results

fig. D.3 shows a two dimensional 225 grains polycrystal with an optimal coloring of 4 colors, obtain with this algorithm. The algorithm has been runed with $n_{max} = 1000$ iterations, and found 29 coloring of 4 colors, which gives a $\sim 3\%$ rate of success for the obtention of an optimal coloring. It means that an average of 30 attempt of greedy coloring must be made in order to find an optimal coloring. Compared to the $225^4 = 2\,562\,890\,625$ possibilities to explores with the brute force algorithm, it shows the efficiency of the chosen coloring method. Coloring attempts for a 64 grains two dimensional polycrystal have yielded a rate of success of 20%. Additionnally, the algorithm has been tested over a 64 grains three dimensional polycrystal, and has been able to find 8-colorings at the best after 1000 iterations. Note that the four color theorem is not valid for three dimensional polycrystals. Letting the algorithm run fore more iterations may allow it to find a better coloring, but the best one can be known for sure only after applying the brute force algorithm to completion.

While $l \leq n_{max}$ **construct coloring** $\mathbb{C}^l$

1. $l \rightarrow l + 1$

2. Generate a random permutation of the N grains σ_N^l

3. Initialize color palette : $\mathcal{C} = \{C_1\}$

4. Iterate for $i = \sigma^l(1)$ to $\sigma^l(N)$

    1. Construct available colors palette $: \mathcal{C}^*$

$$\mathcal{C}^* = \{C_k \mid C_k \notin \mathcal{C}\left[\mathcal{V}_i\right], \, C_k \in \mathcal{C}\}$$

    2. if $\mathcal{C}^* = \varnothing$:   *no available colors, reconfiguration attempt*

$$\forall \, (G_k, G_l) \in \mathcal{V}_i^2 \mid G_k \neq G_l \quad \longrightarrow \text{construct} : \mathcal{K}(G_k, C_k, C_l)$$

$$\left|\begin{array}{l} \text{if } G_l \notin \mathcal{K}(G_k, C_k, C_l) \quad \longrightarrow \text{invert } \mathcal{K}(G_k, C_k, C_l) \\ \qquad\qquad\qquad\qquad\qquad \longrightarrow C_i = C_l \\ \qquad\qquad\qquad\qquad\qquad \longrightarrow \text{next iteration} \end{array}\right.$$

      • Kempe chains inversion failure : create new color

$$\mathcal{C} \longrightarrow \{\mathcal{C}, C_{card(\mathcal{C})+1}\}$$
$$C_i = C_{card(\mathcal{C})+1}$$

    3. if $\mathcal{C}^* \neq \varnothing$

$$C_i = C_k \, , C_k \in \mathcal{C}^* \text{random choice}$$

5. if $\eta < card(\mathcal{C}) \longrightarrow$ store $\mathbb{C}^l, \eta = card(\mathcal{C})$

Figure D.2 – Improved greedy algorithm for polycrystal coloring
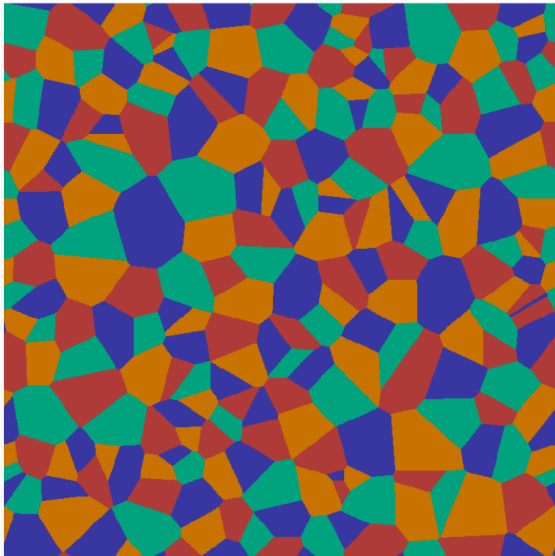
Figure D.3 – Two dimensional polycrystal image colored with four colors

RÉSUMÉ

Les polycristaux irradiés sont connus pour être le siège d'une intense localisation de la déformation plastique à l'échelle du grain, causant une diminution de leur ductilité ainsi qu'une sensibilité accrue à la corrosion sous contrainte. Cette thèse met à profit les performances offertes par le développement des solveurs FFT massivement parallèles pour améliorer la modélisation de ce phénomène crucial. Nous avons mis au point des méthodes de traitement permettant l'analyse systématique de la nature des bandes de localisation, ainsi que leur caractérisation quantitative, à partir des champs issus de la simulation haute résolution de cellules polycristallines. Elles ont permis de mettre en évidence les limites fondamentales de la plasticité cristalline classique, fondement des modèles de métaux irradiés actuels, quant à la prédiction des modes de localisation intra granulaire du glissement plastique. Pour y remédier, nous avons étudié en détail les prévisions analytiques et numériques d'un modèle de plasticité à gradient, en étendant l'implémentation du solveur AMITEX_FFTP à la résolution de problèmes non locaux. Nous avons pu montrer qu'il constitue un cadre prometteur pour une modélisation physiquement fidèle des modes de localisation intra granulaires dans les polycristaux adoucissants, donc a fortiori pour les métaux irradiés. Par ailleurs, nous avons également abordé ce problème par la modélisation explicite des bandes de glissement. Nous avons amélioré ses performances grâce au développement de modèles de voxels composites génériques, et montré que cette approche constitue une alternative efficace pour simuler les conséquences de la localisation de la déformation, comme la modification de la distribution de contraintes aux joints de grains, ou l'augmentation de l'écrouissage cinématique.

MOTS CLÉS

Plasticité cristalline, Localisation, Effets d'irradiation, Comportement mécanique, Solveurs FFT

ABSTRACT

Irradiated polycrystals are known to exhibit an intense localization of plastic deformation at the grain scale, responsible for a severe loss of ductility and increased sensitivity to intergranular stress corrosion cracking. This thesis takes advantage of the performances offered by the recent progresses of highly parallel FFT-based solvers, to improve the modeling of this crucial phenomenon. We developed field processing methods to produce a systematic analysis of the nature and quantitative characterization of localization bands, from high resolution polycrystalline simulation results. They allowed to evidence a fundamental shortcoming of classical crystal plasticity, cornerstone of all irradiated metals models, in the prediction of intragranular localization modes. To overcome this issue, we extended the scope of our FFT solver, AMITEX_FFTP, to non-local mechanics. We used it to extensively study the analytical and numerical predictions of a strain gradient plasticity model, showing that it is a promising way to achieve an accurate modeling of plastic slip localization modes in softening polycrystals, and a fortiori for irradiated metals. Additionally, we explored the explicit modeling of slip bands with FFT-based solvers. We developed generic composite voxel models allowing to strongly reduce its computational cost. We show that this approach provides an efficient way to simulate the consequences of strain localization, such as the evolution of the grain boundary stress distribution or the increased kinematic hardening.

KEYWORDS

Crystal plasticity, Localization, Irradiation effects, Mechanical Behavior, FFT based solvers